

Universiteit
Leiden
The Netherlands

Shedding light on anti-estrogen resistance and antigen presentation through biophysical techniques

Zwart, W.T.

Citation

Zwart, W. T. (2009, May 26). *Shedding light on anti-estrogen resistance and antigen presentation through biophysical techniques*. Retrieved from https://hdl.handle.net/1887/13809

Version:	Corrected Publisher's Version
License:	Licence agreement concerning inclusion of doctoral thesis in the Institutional Repository of the University of Leiden
Downloaded from:	https://hdl.handle.net/1887/13809

Note: To cite this publication please use the final published version (if applicable).

Shedding light on anti-estrogen resistance and antigen presentation through biophysical techniques

Wilbert Zwart

Cover: Cellen die fluorescent gekoppeld oestrogen receptor (voorkant) of MHC klasse II (achterkant) tot expressie brengen zijn gevisualiseerd met een confocal microscoop. Bij het optreden van Fluorescence Resonance Energy Transfer (FRET) kan de energie van het blauwe fluorofoor (achterkant) overgedragen worden naar het gele fluorofoor (voorkant). Cel fotografie is beschikbaar gesteld door mekentosj.com

Shedding light on anti-estrogen resistance and antigen presentation through biophysical techniques

Proefschrift

ter verkrijging van
de graad van Doctor aan de Universiteit Leiden,
op gezag van de Rector Magnificus prof.mr. P.F. van der Heijden,
volgens besluit van het College voor Promoties
te verdedigen op dinsdag 26 mei 2009
klokke 13.45 uur

door

Willem Teunis Zwart

geboren te Putten
in 1980

promotiecommissie

Promotor:	Prof. Dr. J.J. Neefjes
Copromotor:	Dr. R.J.A.M. Michalides *Het Nederlands Kanker Instituut*
Overige leden:	Prof. Dr. B. van de Water
	Prof. Dr. F. Koning
	Prof. Dr. J. Borst *Universiteit van Amsterdam*
	Prof. Dr. P. ten Dijke
	Prof. Dr. Ir. L. Brunsveld *Technische Universiteit van Eindhoven*
	Prof. Dr. J. Trapman *Erasmus MC*

© 2009 W.T. Zwart

Drukkerij: Wöhrmann Print Service

The work described in this thesis was performed at the Division of Tumor Biology of the Netherlands Cancer Institute (NKI-AVL), Amsterdam, The Netherlands. This work was supported by grants from The Dutch Cancer Society (KWF) and Top Institute Pharma (TI Pharma).
Financial support for the publication of this thesis was provided by: The Netherlands Cancer Institue (NKI-AVL), The Dutch Cancer Society (KWF) and 'de Stichting tot Bevordering van de Electronenmicroscopie in Nederland' (SEN).

Nothing great was ever achieved without enthusiasm.
Ralph Waldo Emerson (1803 - 1882)

aan mijn ouders,
die me de betekenis van
doorzetten hebben geleerd

Table of Contents

-Prologue 9

Part one: Shedding light on anti-estrogen resistance through biophysical techniques

	Introduction	
-Chapter 1.	Nuclear receptor dynamics and activity: fluorescence microscopy versus biochemistry	15
	Review	
-Chapter 2.	Visualizing the action of steroid hormone receptors in living cells. *Nucl Recept Signal. 2007 Mar 9;5:e003*	29
	Article	
-Chapter 3.	PKA-induced resistance to tamoxifen is associated with an altered orientation of ERα towards co-activator SRC-1. *EMBO J. 2007 Aug 8;26(15):3534-44.*	41
	Article	
-Chapter 4.	The AF-1 and hinge region of the human Estrogen Receptor cooperate in the quantitative response to estradiol and tamoxifen.	63
	Article	
-Chapter 5.	Classification of anti-estrogens according to intramolecular FRET effects on phospho-mutants of ERα. *Mol Cancer Ther. 2007 May;6(5):1526-33*	79
	Article	
-Chapter 6.	Resistance to anti-estrogen arzoxifene is mediated by overexpression of Cyclin D1. *Manuscript submitted*	93
	Article	
-Chapter 7.	Predictive algorithm for tamoxifen resistance in breast cancer patients based on PKA-induced phosphorylation of ERα at serine 305 and PAK1. *Manuscript submitted*	111
	Summary	
-Chapter 8.	Summary and discussion: anti-estrogen resistance	129

Continued on next page

Table of Contents

Continued from previous page

Part two: Shedding light on antigen presentation through biophysical techniques

	Review	
-Chapter 9.	Presenting antigen presentation in living cells using biophysical techniques. *Curr Opin Microbiol. 2005 Jun;8(3):338-43*	137
	Article	
-Chapter 10.	Spatial separation of HLA-DM/HLA-DR interactions within MIIC and phagosome-induced immune escape. *Immunity. 2005 Feb;22(2):221-33*	147
	Article	
-Chapter 11.	Activation of endosomal dynein motors by stepwise assembly of Rab7-RILP-p150^{Glued}, ORP1L, and the receptor betalll spectrin. *J Cell Biol. 2007 Feb 12;176(4):459-71*	173
	Article	
-Chapter 12.	Cholesterol sensor ORP1L organizes late endosomal contacts with the ER protein VAP that controls Rab7-RILP-p150^{Glued} and late endosomal positioning. *Manuscript submitted*	195
	Article	
-Chapter 13.	Invariant chain controls CD70 transport in dendritic cells and thereby regulates CD8+ T cell priming *Manuscript submitted*	231
	Summary	
-Chapter 14.	Summary and discussion: antigen presentation	249
	Nederlandse samenvatting	255
	Curriculum Vitae	261
	List of Publications	263

Prologue

In cell biology, a large spectrum of technical approaches are available to study the functional behaviour of proteins. However, extrapolating the acquired data towards the physiological context of a living cell can be cumbersome. Although biochemistry can provide insights in binding capacities of the involved molecules, it does not provide information about the dynamic behaviour of these proteins in intact cells. The confined localization of a protein to a specific cellular compartment can highly alter its functional behavior. Also the involvement of possible interaction-stabilizing proteins and chaperones may be lost when studying protein-protein interactions out of the physiological context.
These disadvantages are unknown when imaging living cells using fluorescence microscopy. However, conventional fluorescence microscopy only provides information of localizations at a maximum resolution of 250 nm. At this resolution, colocalization does not imply interaction but only a reasonably close proximity of the two proteins to each other. Although high resolutions in intact cells can be achieved using electron microscopy, the dynamics of interaction are lost and fixation of the cells might also lead to artifacts.
Biophysical microscopic techniques, such as FRET (Fluorescent Resonance Energy Transfer) allow high-resolution analysis of protein-protein interactions and protein conformation status in living cells and in real time.

In the following two research lines, techniques making use of this biophysical phenomenon are applied.

Part one

Shedding light on anti-estrogen resistance through biophysical techniques



Nuclear Receptor dynamics and activity: Fluorescence Microscopy versus Biochemistry

introduction

1

Nuclear receptor dynamics and activity: fluorescence microscopy versus biochemistry

Abstract
Nuclear receptors are key transcriptional regulators. The subfamily of steroid hormone receptors responds to hormones, small molecular ligands, which diffuse into the target cell from the blood stream. As a response to nuclear receptor activation, a specific set of responsive genes is transcribed that are involved in development, cell differentiation and organ physiology. Steroid hormone receptor functions have been the focus of intensive studies since their discovery in the 1960s, which produced detailed insights into the functioning of these key transcriptional regulators. This was achieved by applying a broad range of biochemical techniques. The emergence of genetically encoded fluorochromes from the beginning of the 1990s, like GFP, yielded a new set of tools to study the behavior of steroid hormone receptors in a living cell in time and space. Although biochemical and imaging based techniques differ profoundly and possess their own intrinsic strengths and weaknesses, integration of these techniques allows further and more detailed understanding of the hormone dependent transcription regulation of many genes. Here, we describe the benefits and possible pitfalls of both approaches when studying steroid hormone receptor activity and behavior. How the various techniques are applied for the different steps in receptor activation will be systematically and critically reviewed.

Introduction

The Nuclear Receptor super family contains many members. To date, 48 human nuclear receptors have been identified, which are involved in development, cell differentiation and organ physiology [1]. Steroid hormone receptors (SHRs) are a subgroup which can bind and respond to lipophilic hormones that have the capacity to diffuse to the target cell and permeate over the target cell membrane. This subgroup includes Estrogen Receptors (ER), Androgen Receptors (AR), progesterone Receptors (PR), Mineralocorticoid Receptors (MR) and Glucocorticoid Receptors (GR). SHRs share a conserved architecture and are composed of 4 core domains: The variable N-terminal (A/B) domain which contains the ligand independent AF-1 transactivation region, the DNA-binding domain (C) and the hinge region (D), a small flexible stretch connecting the DNA binding domain to the ligand/ hormone binding domain (E) (Figure 1).

The pathway of SHR activation can classically be divided in different steps (Figure 2):

1. Ligand binding, inducing a conformational change of the receptor.
2. Migration of the receptor from the cytosol into the nucleus.
3. Dimerization of the receptor with itself or with other transcription factors.
4. The binding of the receptor to coregulators.
5. The binding of the receptor the DNA on designated responsive sites.
6. The recruitment of the transcription complex, inducing chromatin remodeling and transcription.
7. Downstream protein production.

Each of these steps has been intensively studied using a series of techniques.

In this review, we will go through each individual step of SHR activation and describe which approach provides what kind of information and ultimately try to combine these. Due to the large group of nuclear receptors and the great availability of literature, this review focuses predominantly on estrogen receptor (ER), androgen receptor (AR) and glucocorticoid receptor (GR) functions. These receptors have been most extensively studied and we believe that many concepts found for these receptors will also apply to other SHRs.

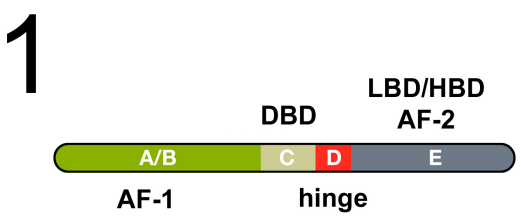


Figure 1. Domain structure of steroid hormone receptors. Indicated are:
- the N terminal (A/B) domain, containing the ligand independent AF-1 transactivation region
- the DNA binding domain (C)
- the flexible hinge region (D)
- the Ligand of Hormone Binding Domain (LBD/HBD), containing the ligand dependent AF-2 transactivation region

2

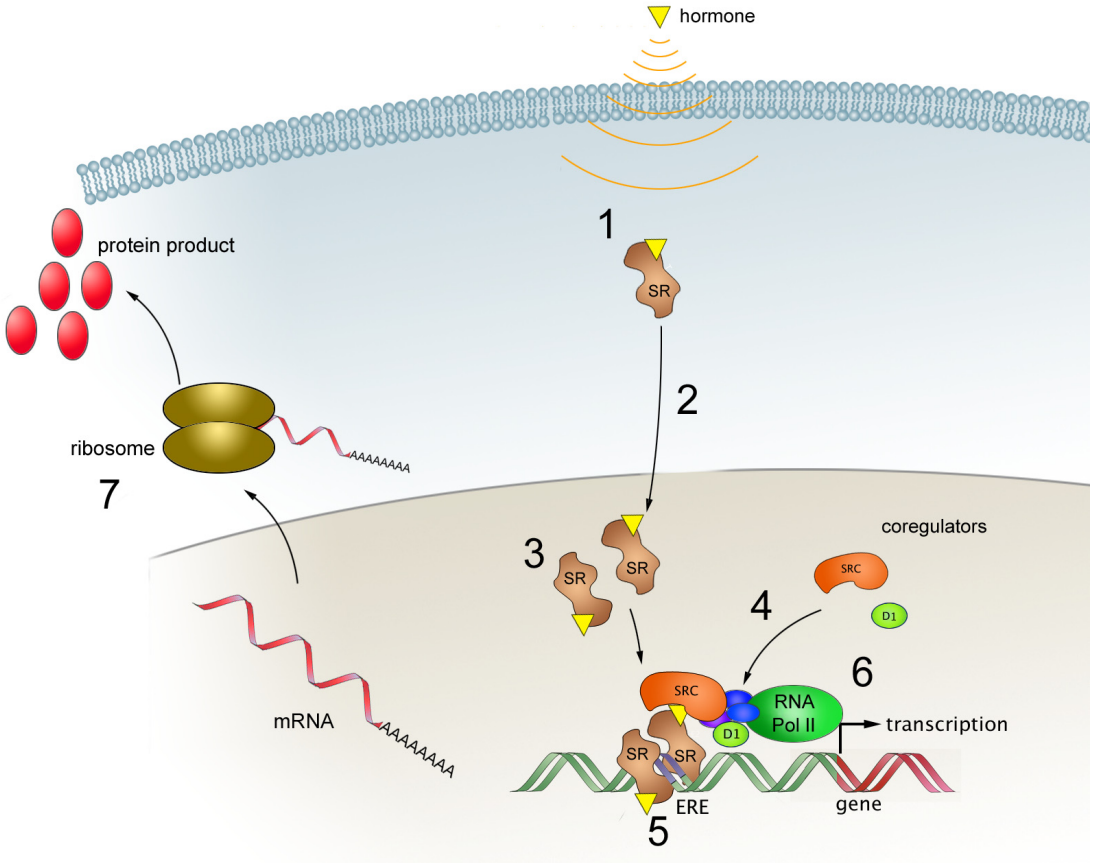


Figure 2. The pathway of steroid hormone receptor activation. After diffusion of the ligand into the target cell, it binds the receptor, which induces a conformational change (1). Subsequently, the receptor migrates into the nucleus (2) and dimerizes (3). Then, the receptor can recruit coregulators, such as SRC-1 and Cyclin D1 (4) and bind to the DNA (5). On the DNA, the rest of the transcription complex is recruited, inducing chromatin remodeling and transcription (6), eventually leading to protein production (7).

Conformational change of the receptor after ligand binding (1)

For a SHR to be activated, it has to bind its specific ligand. Dihydroxytestosterone and estradiol are the main ligands for AR and ER, respectively. These hormones circulate in the bloodstream, bound mostly to sex hormone-binding globulin (SHBG) and to some degree bound to serum albumin. Cortisol and progesterone on the other hand are the primary ligands for GR and PR, respectively. These hormones are mainly associated to Cortisol Binding Globulin (CBG) in the blood stream. Only a small fraction of these hormones is unbound in the blood and thus biologically active and able to diffuse into the cell and activate its receptor.

SHRs can adopt distinct conformations upon ligand binding, as has been directly shown in crystal structures of ligand binding domain (LBD) truncation mutants. A number of nuclear receptor LBDs have been crystallized, including ER [2], AR [3] and GR [4]. The major conformational alteration within the receptors' ligand binding domain is the reorientation of the most

carboxy-terminal α helix (named helix 12 in ER and AR, helix 11 in GR). This most C-terminally located α helix forms, together with the nuclear receptor-specific subset of α helices in the LBD, a docking platform where coregulators can bind. These include the members of the p160 family (SRC-1, SRC-2 and SRC-3). When an antagonist is bound, this most C-terminal α helix is repositioned over the coregulator binding cavity, thereby preventing these protein to associate. This is, however, not the only conformational change within a SHRs after ligand addition. Trypsin cleavage studies (illustrated in Figure 3) have illustrated that helix 6 within GR is made accessible for digestion after ligand addition [5]. While this approach can detect conformational changes, it has an intrinsic 'low resolution' as it does not discriminate an agonist- from an antagonist-associated receptor [6]. What these data did indicate was that conformational changes take place within the receptor upon ligand binding and might very well surpass the exclusivity of an altered carboxy-terminal α helix orientation in the ligand binding domain [7].

(Phage display based) peptide-binding studies (Figure 3) have verified these indications [8]. Specific, conformation-dependent binding of peptides could be monitored, providing a receptor fingerprint in a specific conformation. Interestingly, peptides derived from this phage display library can be applied as antagonistic agents [9,10], only blocking the receptor when its conformation is permissive for peptide binding, thus making these antagonistic probes ligand specific. This feature is an extremely useful application, opening the possibility of directly designing novel activation-specific, antagonistic compounds using the peptide backbone as a model. A prove of principle was shown for ERα, where transactivation potential was inhibited by specific peptides (Carraz, Zwart *et al*., submitted). These peptides were identified *in vitro* [8] and could enter the cells after addition of a small poly-arginine tag [11]. Within the cells, these peptides could bind ERα and compete with endogenous co-activators only when the receptor was in an estradiol bound conformation.

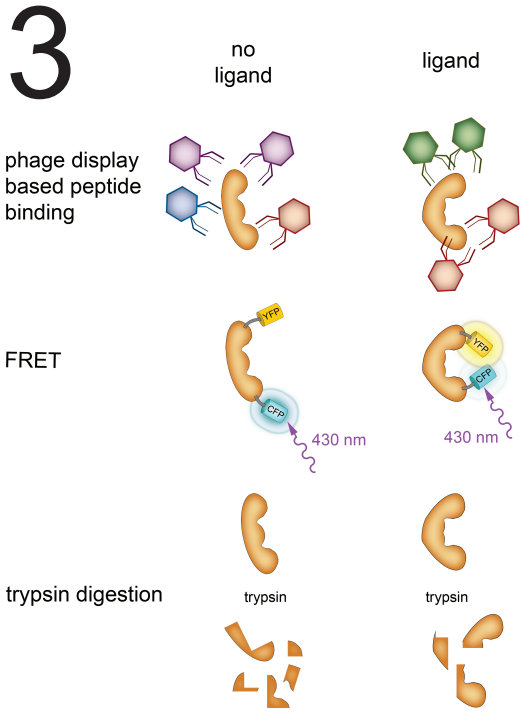


Figure 3. Methods to detect SHR conformational alterations.

Liganded SHRs can adopt distinct conformations from non-ligand bound receptors. These conformational alterations can be detected through differences in (phage display based) peptide binding (top panel), changes in FRET signal (middle panel) or specific trypsin digestion patterns (bottom panel).

Comparable data on conformational changes of ERα, ERβ and AR was provided by applying fluorescence resonance energy transfer (FRET) [12,13]. FRET is the radiationless transfer of energy from an excited donor fluorophore to a suitable acceptor fluorophore [14]. This process depends on spectral overlap and proper dipole alignment of the two fluorophores applied. The most commonly used genetically encoded FRET-pair is the combination of CFP (Cyan Fluorescent Protein) and YFP (Yellow Fluorescent Protein). The occurrence of FRET between CFP and YFP is characterized by an increase of YFP signal at the expense of CFP signal. Importantly, FRET is extremely sensitive to the distance between the fluorophores. For CFP and YFP, the characteristic half-maximum distance is 49–52 Å (Förster radius) with an upper limit of 80-100 Å [15]. In addition, FRET is also sensitive to the orientation between the two fluorophores. Thereby, FRET can be applied as a highly sensitive method to study conformational changes.

In the published cases, a YFP is cloned to the one terminus of the receptor and a CFP to the other. After a conformational change, the fluorophores may locate differentially in space thus affecting their orientations (Figure 3). This then results in a permissive orientation for FRET to occur, and YFP emission is increased at the expense of CFP signal. For ERα, a change in FRET was occurring only when the receptor adopted an inactive conformation upon antagonist binding [12,16]. In the case of resistance against an anti-estrogen, thus recongizing the inhibitor as an agonist instead of an antagonist, such a change in FRET was not observed (Chapters 5 and 6).

For AR, the increase in FRET upon ligand binding was found to be induced by agonist association rather than binding of antagonists [13]. For this receptor, the N- and C-termini directly interact after agonist binding, which results in a closer proximity between the CFP- and YFP fluorochromes and an increase in FRET. This agonist-induced N/C interaction was also illustrated in two-hybrid based assays [17]. In two-hybrid assays, protein-protein interactions are determined through the fusion of both proteins to truncations of a transcription factor, typically GAL4. The truncated fractions of GAL4 used in this setup are the DNA

binding domain and the transactivation domain of the protein. In the case of physical interaction of the fusion constructs, the modified GAL4 transcription factor is now functionally capable to induce transcription of a reporter gene or a selection marker (Chapter 3 and illustrated in Figure 4).

An increase in N/C interactions of AR was also correlated with nuclear import of this receptor. These N/C interactions are possibly involved in preventing unfavorable cofactor interactions when the receptor is imported into the nucleus [18], since this N/C interaction is lost when the AR is bound to the DNA and needs to associate with cofactors in order to induce transcription.

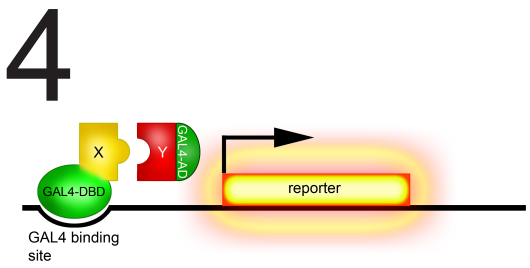


Figure 4. Principle of two-hybrid studies.

In two-hybrid assays, protein-protein interactions can be detected by fusing one interaction partner ('X') to the DNA binding domain of GAL4 (GAL4-DBD) and the other interaction partner ('Y') to the transactivating domain of GAL4 (GAL4-AD). When the two proteins interact, a functional GAL4 is formed and the reporter gene is transcribed.

While previously used techniques to study conformational changes where either completely *in vitro* based or had an *in vitro* component, these FRET-based assays allow for monitoring conformational changes in intact, living cells. This way, FRET data can provide temporal information on the SHR conformation status in the physiological context. A main drawback of FRET-technology is that it does not provide absolute information about the conformation of a molecule, but is also influenced by other factors. These include next to distance and orientation between the fluorophores also temperature and lipid environment (Dr. Kees Jalink, personal communication). These variables prevent translating FRET signals into exact molecular events. In the case of ER and AR, it does however provide qualitative information about the activation status of the receptor [12,13,16]. The structural implications of changes in FRET remain, however, illusive until a crystal structure of the full length receptor becomes available, ideally generated under comparable conditions as applied in the FRET experiments. Using these kinds of approaches, anti-hormones can be tested for sensitivity of the receptor to resistance-inducing conditions, such as phosphorylation of the receptor (Chapter 5) and coactivator overexpression (Chapter 6). In addition, the extent of FRET changes is highly reproducible thus facilitating high throughput screening for inhibitory compounds [19].

Recently, the first crystal structure of a full length nuclear receptor PPAR/RXR complex has been described, albeit without electron density of the N-termini of both proteins [20]. This study holds the promise that other full length nuclear receptors may be crystallized, providing high resolution information beyond the ligand binding domain. If such a complex could be crystallized with different ligands, FRET effects may finally be resolved and understood at the atomic level.

Intramolecular FRET can be monitored both *in vivo* and *in vitro*. Interestingly, changes in FRET for ERα after ligand addition cannot be detected *in vitro* (WZ, unpublished observations), indicating that a conformational change is not solely governed by the nuclear receptor but that additional factors may be required. The involvement of other factors is also suggested from the observation that, while a conformational change of ERα in response to ligand showed a small delay in time [12], the dissociation of a SRC-1/LBD binding peptide from the ER was initiated within seconds after anti-estrogen addition [21]. This difference in time may be ascribed to dissociation of interacting coregulators, which apparently precedes and might well be essential for the capacity of the receptor to change its complete conformation.

In summary, while conventional trypsin digestion studies cannot discriminate between agonist- and antagonist-bound SHRs, both FRET and (phage display-based) peptide binding studies can. Although the latter two techniques do provide essential information about receptor activation and conformation, the link between these two processes can only be fully understood when full length nuclear receptor crystal structures become available. In studying nuclear receptor conformational changes, both phage display-studies and FRET are very well capable in discriminating distinct conformations. Selecting technology depends on whether the focus is on sequential treatment and time resolution (FRET) or on directly generating ligand-specific inhibitory molecules (peptide-binding studies).

Nuclear presence and ligand-induced translocation (2)

SHRs are thought to reside in the cytosol of responding cells and translocate to the nucleus upon stimulation [22,23]. The factors responsible for this cytosolic confinement are hsp90 and hsp70 [24]. These heat shock proteins bind the nuclear receptor in the cytosol and ligand-binding leads to their dissociation. This dissociation allows the nuclear localization signals of the receptor to induce transport into the nucleus which enables the receptor to bind the DNA [25]. The presence or absence of receptors in the nucleus can be biochemically defined by separating the cytosolic from the nuclear fraction before receptor detection. Whether non-liganded receptors reside in the cytosol

of intact cells, as determined by biochemical analysis, was challenged for certain SHRs such as ER and PR [26,27]. Immuno-staining of intact cells shows, in contrast to the biochemical model, both the ER and PR already present in the nucleus in the absence of hormone and not exclusively localized in the cytosol. Staining intact cells for AR and GR did produce data in line with the biochemical ligand-induced translocation model, and translocation from the cytosol to the nucleus was observed after ligand addition for both receptors [28-30].

The discrepancy between biochemistry and visualizing the distribution of ER and PR by microscopy could be explained by a relatively low affinity of both receptors to DNA. The presence of ER and PR in the cytosolic fraction could be the result of nuclear extraction by the applied detergent and salt conditions. After agonist stimulation, ER and PR showed a higher binding-affinity to the DNA [17], resulting in a more nuclear restricted distribution, even after detergent treatment and nucleus/cytosol separation. In other words, the biochemical method used may result in apparent differences in nuclear/cytosol distribution but may in fact measure chromatin interactions. For AR and GR, the control of nuclear import forms a sophisticated way of regulating the receptor, introducing a spatial separation between the transcription factor and target genes. Inhibition of the receptor might already be achieved by nuclear exclusion. ER on the other hand is already present in the nucleus prior to ligand binding, and possibly requires more complex ways to inhibit transcriptional activation. The need for additional regulation of ER as compared to AR and GR is further illlustrated by the finding that non-liganded ER already associates to responsive elements in the DNA [31,32]. Here, the role of corepressors for inhibiting a DNA-associated but inactive ER seems to be indispensable. The pre-existing presence at a promoter could be an example of a rapidly responding 'loaded gun' model, in which ER and PR can efficiently respond to activating stimuli, a feature which is supported by the pre-existing interaction capacity with some coacitvators such as the members of the p160 family [31,33,34].

When studying translocation of SHRs from cytosolic to nuclear compartments, it is clear that the conventional biochemical approaches can introduce artifacts for some receptors (ER and PR), while this is less obvious for others (GR and AR). Cell fixation and analysis/quantification by microscopy is a perhaps an easier and more quantitative assay for the genuine effects of ligands on cellular distribution.

Hetero and homo-dimerization of SHRs (3)

After ligand binding and possible nuclear import of the liganded receptor, the next step in SHR activation is interaction with other factors. SHRs can homodimerize, heterodimerize with other nuclear receptors or associate with other transcription factors, such as SP-1, AP-1 or NFκB. The interaction partner determines which transcription complex is formed, eventually defining which hormonal-responsive element will be activated. The factors, which define the interaction partner and thereby eventually the biological output, are largely unknown. These factors might very well be influenced by tissue or cell-type specific expression patterns, which is shown for ERα and ERβ. The expression of ERα and ERβ is different in various tissues, ranging from exclusive expression of ERβ in colon and brain to variations in the ratios of ERα and ERβ expression in other tissues, including breast.

ERα and ERβ are highly homologous proteins that bind similar hormones and can homodimerize as well as hetrodimerize [35]. As a homodimer, ERβ has a significantly lower transactivation potential than ERα [36], which can be ascribed to specific characteristics of the AF-1 transactivation region (Chapter 4). In contrast to ERα, the AF-1 of ERβ lacks the capacity to interact with SRC-1. This feature of ERβ appears to be causal for the lower transcriptional response to stimuli. As a heterodimer, lack of SRC-1 binding capacity may influence the transcriptional response of the entire complex, since FCCS studies have illustrated that two estrogen receptors share one SRC-1 molecule [37]. This could imply that the characteristics of the ERβ-AF-1 are causal for the inhibitory behavior of ERβ in the ERα/ERβ hetero-dimer complex in transcription assays[35] and growth of T47D cells [38] .

Studies on ER dimerization have been performed with various techniques, including two-hybrid studies [39] and FRET [13,40,41]. When FRET was applied, ERα was CFP or YFP tagged, and dimerization could be monitored by an increase in FRET signal. Note that some GFP variants may homodimerize [42], which could induce artificial dimerization of the tagged proteins, in this case ER. This was directly tested using GFP variants manipulated to exclude dimerization [43]. The effect on ER-dimer FRET was measured with 'wildtype' CFP and YFP variants which were compared to monomeric CFP/YFP mutants. The kinetics of ERα/ERα dimer formation was not different between the 'wildtype' CFP/YFP FRET combination versus the monomeric mutant ones. Interestingly, the variation in FRET efficiency between different cells was lower in the case ER was tagged to CFP/YFP variants that were capable of dimerizing as compared to the non-dimerizing mutants. This indicates that the 'stickyness' of fluorochromes does not directly alter the protein-protein interaction. However, when the complex is formed, the dimerizing CFP/YFP variants are attracting each other, which might be responsible for the higher consistency between the measurements. Next to dimer formation, also interdomain conformations within the dimer could be studied through FRET, illustrating that ligand induced conformational alterations are C-terminally confined [41], providing significantly more information then just association dynamics.

Yeast two-hybrid based approaches have initially been used to monitor nuclear receptor

dimerization [44]. A major advantage of this technology is its high sensitivity; even low affinity interactions can be determined by yeast two-hybrid. The relatively long time before reading out the effects does not allow the determination of 'on' and 'off' rates. In addition, the role of modifications more specific to mammalian cells rather than yeast cells can not be determined.

When studying nuclear receptor dimerization, FRET based approaches have the benefit over two-hybrid and pull down studies that it allows for real-time visualization of complex formation, while the latter two approaches are end-point measurements. All three methods discussed here require overexpression, the necessity of which could be a pitfall.

Coregulator recruitment (4)

SHRs contain two transactivation regions; the AF-1 and AF-2. While the AF-1 is typically hormone independent, the AF-2 can be activated by ligand binding. Both AF regions are capable to directly interact with coactivators, an initial and essential step in the formation of an active transcription complex.
This interaction with coactivators is of special clinical interest, since expression levels of several coactivators, including cyclin D1 and SRC-1, can play a causal role in anti-hormone resistance [9] (Chapter 6). Among the first coactivators recruited by a hormone-bound ER is one of the three members of the p160 family; SRC-1, SRC-2 and SRC-3 [45]. It was initially thought that nuclear receptors only interact with p160 coregulators after stimulation with an agonist. This notion was strengthened by the crystal structure data, which suggested only liganded nuclear receptors form a coactivator binding pocket in its ligand binding domain. Next to the crystallized LBD, both ER and AR also possess the capacity to interact with p160 cofactors with its ligand-independent AF-1 region, implying that ligand independent cofactor recruitment can be achieved by both receptors. This appeared not to be the case for AR. Its AF-1 is shielded in the absence of ligands but becomes exposed upon agonist binding. Agonist binding is however not sufficient; An additional requirement for an exposed AF-1 of AR is the association with the DNA. In a non-DNA associated complex, the activated AR is still in a closed conformation, which is achieved by an interaction between its N and C termini [18].

An N/C interaction has also been described for ERα although this still allowed coactivator binding by ERα [33]. Since p160 coactivators are also recruited to the AF-1 of ERα when the receptor is devoid of hormone, binding studies such as co-immunoprecipitation, GST-pull down and CHIP to visualize cofactor-hormone receptor binding can not be interpreted as genuine ligand-induced transcription complex formation. When ERα is activated, SRC-1 can interact with both AF-1 and AF-2 regions on ERα, stabilizing the pre-existing ERα/SRC-1 interaction. The relevance of interactions through the AF-1 and AF-2 is illustrated in cases of anti-estrogen resistance. For the initiation of tamoxifen resistance, the most applied anti-estrogen, the interaction of ERα/AF-1 with SRC-1 is a prerequisite, enabling a reorientation between ERα/AF-2 and SRC-1 which permits activation of the complex under tamoxifen conditions (Chapter 3).
Interestingly, the ERβ/AF-1 does not bind SRC-1 and only a functional AF-2 remains accessible for cofactor interactions (Chapter 4). This feature appears to be dependent on promoter composition, since SRC-1 is reported to be specifically recruited to the AF-1 of ERβ on the TGFbeta-inducible early gene-1 (TIEG) [34]. Such promoter specific activities have also been reported for GR and are a consequence of variations in the nucleotides surrounding the nuclear receptor consensus sequence [46].

Direct interaction studies between ER and coactivators have been performed by GST pull down and co-immunoprecipitation studies. These studies can be hampered by SHR solubility since the presence of the receptor in the soluble fraction is greatly influenced by the ligand applied [47]. E2 treatment, for example, greatly enhances binding of the ERα to the DNA while ICI 182,780 (a full anti-estrogen) completely immobilizes the ER [48], followed by the receptors degradation. Such cell biological differences may also translate into biochemical differences when affecting solubility of the receptor in lysate fractions, available for immunoprecipitation.

A potential problem in both GST pull down and co-immunoprecipitation assays is the loss of physiological context, which is relevant since some interactions can be influenced by DNA binding, chromatin binding and promoter context. Therefore, lysate-based studies may suffer from dilution of relevant information, since the composition of the complex may be different for promoter- and non-promoter-bound populations. Interactions between ERα and SRC-1, for example, appear to be pre-existing, independent of DNA binding [31,32,41]. Other factors of the transcription complex are recruited dependent on DNA context, such as RNA Polymerase II. These differences make extrapolation of results obtained from lysis-based interaction studies cumbersome and should thereby be handled with caution. One approach which does not suffer from these problems, is Chromatin Immuno Precipitation (ChIP). Given that the complex is fixed and crosslinked on the promoter and subsequently lysed and detected, the complex is isolated in its native DNA-associated form and dilution of information specific for the DNA-bound complex is minimized [32,49].

DNA binding (5), transcription complex formation and transcription (6)

Interestingly, due to the limited number of nuclear receptor binding sites in the genome of eukaryotic cells [32,50], interaction studies in an overexpression setup represent the behavior of the

majority of proteins, that will as a consequence be non-promoter bound. Thereby, these studies suggest that (a proportion of) ERα and p160 coregulators in cells interact irrespective of DNA binding. This would imply that overexpression-based pull down studies [51], two-hybrid studies [31,33], CO-IPs [52] and FRET based assays [21,53] mainly visualize interactions of the non-DNA bound fraction of proteins. Although FRET has the advantage of temporal resolution which is a valuable feature when compared to the other methods, overexpression artifacts using this technique can be significant. The most obvious drawback in fluorescence-based studies is that overexpression is essential to visualize the fluorescently-tagged protein.

An additional drawback of fluorescence-based studies is that a light microscopy-based assay does not allow visualization of nuclear receptors exclusively on their responsive elements. Colocalization studies of ERα with RNA Polymerase II have been performed [54], showing hardly any overlap of the two signals. Interestingly, almost every defined ERα region did have an adjacent RNA Polymerase II positive structure, indicating that a functional connection between these two complexes may still exist. Comparable data were also found for AR [18], where DNA binding mutants lack the capacity to localize to defined foci. Although it is tempting to envision this lack of overlap as an intrinsic spacing between distant promoters and the start of association of RNA Polymerase II, or a RNA Polymerase II complex already being in the process of transcribing the gene, ChIP analysis has shown a functional interaction of ERα with RNA Polymerase II on responsive elements [55]. Since the size of DNA fragments amplified in these CHIP analyses is small [49], typically between 100 and 2000bp, such a fragment may fall below the resolution limit of light microscopy due to the condense chromatin structure. Thereby, the results obtained with both techniques can not be compared.

The identification of a DNA-associated nuclear receptor was greatly facilitated by the generation of cell lines possessing a tandem repeat of defined nuclear receptor binding regions, enabling live cell studies on the initial steps of transcription complex formation. At such a tandem repeat array structure, the nuclear receptor and associated cofactors could be visualized in real time. These nuclear receptor binding structures were either composed of a natural poly-repeat of a MMTV gene including promoter [56], or of an artificial poly-repeat of a Prolactin promoter/enhancer region with only one responsive mRFP-tagged reporter gene [57]. The array of nuclear receptor binding sites enables the association of enough fluorescently tagged receptor to the DNA to be visualized by light microscopy. This way, promoter-associated receptor can be distinguished from non promoter-bound receptor in intact cells. Both array structures provided great insights in nuclear receptor-DNA association in time and the recruitment of co-activators. Although ER is capable of interacting with its coregulator SRC-1 in the absence of DNA-binding, the nature of interaction might still be different between DNA- and non DNA-associated complexes. Measuring FRET efficiency between ER-CFP and SRC-1-YFP resulted in comparable FRET values between the defined DNA-bound ER and the receptor present in the rest of the nucleoplasm, indicating that the nature of the ER/SRC-1 complex bound to the DNA is comparable to that of the non-DNA-bound complex [31] (Chapter 3). Interestingly, the size of the array structure is tightly correlated with transcriptional activity, providing the opportunity to monitor profound DNA remodeling events in real time in living cells [57,58]. These data could be verified in an *in vitro* reconstituted system [59,60], where the recruitment of the SWI/SNF complex and subsequent chromatin remodeling could be visualized.

Although these array containing cell lines are very informative models that provide deep insights into ER and GR functioning in living cells, they are not devoid of potential pitfalls. It is tempting to generalize these data for ER/GR functioning. However, these data only provide formation for the activity of the analyzed promoter region. Promoter sequence, composition and location within the genome (which may have particular chromatin structures or modified histones) all affect the activity of the responsive gene [32,61,62]. These factors may differ in the array structure. In addition, the promoter sequence and its composition are fixed in this setup.

These limitations of array-containing cell lines may differ from ChIP approaches, that can yield dynamic and temporal insights in the recruitment of the transcriptional machinery to specified endogenous target genes [49]. This elegant study by Metivier and coworkers describes a cyclic turnover of the transcriptional machinery on the promoter. The authors showed that the sequential recruitment of (although already known) ERα cofactors to the promoter occurs in a highly sophisticated and ordered way. For the next transcriptional round to occur, the acting ERα has to be degraded first. A potential pitfall of these kinds of ChIP analyses is the necessity for synchronization of the cell population using DNA stripping agents. Comparable data were however obtained for the GR in an *in vitro* reconstituted system. In this system, the cycling of GR on the promoter of a MMTV reporter gene was visualized through the use of UV crosslinking techniques [63].

Still, the number of transcription cycles and factors determining this amount remain elusive and could easily represent another level of regulation. Acquiring information on the transcriptional output is commonly performed by Q-PCR, determining the total mRNA quantity of the gene of interest, or more general on whole-genome microarray analysis. The latter has the clear advantage that it does not suffer from a bias originating from focus. Still, since these assays are endpoint measurements, distinction between the factors which influence mRNA levels (i.e. transcriptional cycles, mRNA stability) can not be made by using these techniques.

In conclusion, although cell lines possessing

a tandem repeat of SHR responsive elements furthered our knowledge in the temporal regulation of nuclear receptor-DNA binding and transcription complex formation, they suffer from a bias of focus and their artificial nature. Thereby, any conclusions drawn from such cell lines should be verified on endogenous promoter sequences using alternative methods, such as ChIP or Q-PCR, in order to generalize such statements.

Protein production measured by vectors versus endogenous reporters (7)

Since the eventual outcome of nuclear receptor activation is the production of downstream proteins, many assays have been developed to study this event. Classical beta-galactosidase and luciferase reporter constructs, where a consensus NR responsive element is used as a promoter sequence for the reporter, have been applied for many years. Recently, GFP or its variants have been introduced as an alternative readout. Time resolution in protein production can be introduced by applying non-stable variants of these proteins [64]. These non-stable GFP variants give the advantage of measuring differences in reporter signal after inhibition or activation in real-time. The main drawback of these reporters is, however, that the classical promoter consensus sequence used within such a reporter only represents the vast minority of consensus variations present in the genome, greatly oversimplifying the system. Since the position of genes within the genome and distant regulation by promoter and enhancer sequences greatly affects their activities, exogenous vector-based reporters should be treated with caution.

Moreover, factors like RNA stability and translational efficiency, both defined by the untranslated regions in the mRNA, are lost in such a reporter gene setup. Endogenous reporters for nuclear receptor activity and factors influencing this activity are thereby the most reliable means of read-out, provided that specific anti-bodies are available and detection is not hampered by fixation. Detecting such reporters or proteins that affect nuclear receptor activity by conventional antibody staining on tumor tissue microarrays (Chapter 7) will most likely prove to be the most reliable read-out in a high-throughput fashion [65].

Concluding remarks

When studying nuclear receptor functioning and activity, many different techniques are applicable, which enable the study of the entire cascade of receptor activation, from ligand binding to eventual protein production (illustrated in Table 1). Although the choice of technology is often based on personal preference and expertise, one has to realize that every technique has its own limitations and intrinsic flaws. The most profound dangers may lie in the loss of physiological context and the risk of over interpretation of data. Both *in vitro* steps and overexpression in intact cells introduce non-physiological conditions, in which protein interactions, conformations, localizations and activities may differ from the non-manipulated situation. As such, many conclusions can only be drawn after verification of the results by alternative technical means, especially since the potential pitfalls of the techniques applied are not always fully understood nor predictable and may differ per protein studied.

When using exogenous reporter systems to study nuclear receptor activity in intact cells, one should realize that the reporter system contains a consensus sequence, which often illustrates activity of the vast minority of possible variations present in the genome. In addition, such a reporter provides information out of the correct chromatin and promoter context, greatly oversimplifying a complex and sophisticated system as the eukaryotic cell.

Table 1: Comparision of a subset of technical approaches applied to study nuclear receptor activity and dynamics

Step of nuclear receptor activation	Methodology		Comments	
	Biochemistry	Fluorescent microscopy	Advantage	Disadvantage
1. Ligand binding of the receptor, inducing a conformational change.	trypsin digestion			cannot discriminate between activated or inhibited receptor
	peptide-binding studies		can discriminate between activated or inhibited receptor/ enables generation of inhibitory small molecules	
		FRET	can discriminate between activated or inhibited receptor/ temporal resolution	receptor needs to be tagged and overexpressed
2. Migration of the receptor from the cytosol into the nucleus.	nucleus-cytosol separation			may measure chromatin interactions in stead of nuclear confinement
		in situ staining		need for specific antibodies or overexpression
3. Dimerization of the receptor with itself or with other transcription factors.	GST-pull down/ Yeast two hybrid		very sensitive	end-point measurement/ lack of mammalian-specific modifications/ receptor needs to be tagged and overexpressed
		FRET	temporal resolution	receptor needs to be tagged and overexpressed
4. The binding of the receptor to coregulators.	GST-pull down/ Co-IP			Ligand influences solubility of the receptor
		FRET	temporal resolution	receptor needs to be tagged and overexpressed
5/6A. The binding of the receptor the DNA on designated responsive sites. The recruitment of the transcription complex and the induction of chromatin remodeling	ChIP		endogenous proteins	need for specific antibodies/ need to synchronize cells for temporal resolution
	In vitro reconstitution		highly controlled	artificial
		colocalization on tandem repeat of responsive elements	temporal resolution	receptor needs to be tagged and overexpressed/ artificial system
6B. transcription induction.	Q-PCR		quantitative/ endogenous product	focus on 1 gene/ end-point measurement
	microarray		genome-wide	end-point measurement
7. The induction of protein production.	luciferase reporter constructs		sensitive	one consensus thus oversimplifying
		GFP reporter constructs	temporal resolution	one consensus thus oversimplifying
		tissue stainings/IHC	strictly endogenous/ within the tissue context	need for specific antibodies

References

1. Zhang, Z. *et al*. Genomic analysis of the nuclear receptor family: new insights into structure, regulation, and evolution from the rat genome. Genome Res 14, 580-590 (2004).

2. Shiau, A. K. *et al*. The structural basis of estrogen receptor coactivator recognition and the antagonism of this interaction by tamoxifen. Cell 95, 927-937 (1998).

3. He, B. *et al*. Structural basis for androgen receptor interdomain and coactivator interactions suggests a transition in nuclear receptor activation function dominance. Mol Cell 16, 425-438 (2004).

4. Bledsoe, R. K. *et al*. Crystal structure of the glucocorticoid receptor ligand binding domain reveals a novel mode of receptor dimerization and coactivator recognition. Cell 110, 93-105 (2002).

5. Xu, M., Modarress, K. J., Meeker, J. E. & Simons, S. S., Jr. Steroid-induced conformational changes of rat glucocorticoid receptor cause altered trypsin cleavage of the putative helix 6 in the ligand binding domain. Mol Cell Endocrinol. 155, 85-100 (1999).

6. Modarress, K. J., Opoku, J., Xu, M., Sarlis, N. J. & Simons, S. S., Jr. Steroid-induced conformational changes at ends of the hormone-binding domain in the rat glucocorticoid receptor are independent of agonist versus antagonist activity. J Biol Chem 272, 23986-23994 (1997).

7. Kraichely, D. M., Sun, J., Katzenellenbogen, J. A. & Katzenellenbogen, B. S. Conformational changes and coactivator recruitment by novel ligands for estrogen receptor-alpha and estrogen receptor-beta: correlations with biological character and distinct differences among SRC coactivator family members. Endocrinology 141, 3534-3545 (2000).

8. Paige, L. A. *et al*. Estrogen receptor (ER) modulators each induce distinct conformational changes in ER alpha and ER beta. Proc. Natl Acad. Sci. U. S. A 96, 3999-4004 (1999).

9. Norris, J. D. *et al*. Peptide antagonists of the human estrogen receptor. Science 285, 744-746 (1999).

10. Chang, C. *et al*. Dissection of the LXXLL nuclear receptor-coactivator interaction motif using combinatorial peptide libraries: discovery of peptide antagonists of estrogen receptors alpha and beta. Mol Cell Biol 19, 8226-8239 (1999).

11. Futaki, S. *et al*. Arginine-rich peptides. An abundant source of membrane-permeable peptides having potential as carriers for intracellular protein delivery. J Biol Chem 276, 5836-5840 (2001).

12. Michalides, R. *et al*. Tamoxifen resistance by a conformational arrest of the estrogen receptor alpha after PKA activation in breast cancer. Cancer Cell 5, 597-605 (2004).

13. Schaufele, F. *et al*. The structural basis of androgen receptor activation: intramolecular and intermolecular amino-carboxy interactions. Proc. Natl Acad. Sci. U. S. A 102, 9802-9807 (2005).

14. Förster T Zwischemolekulare energiewanderung und fluoreszenz. Ann Physik 2, 55-67 (1948).

15. Tsien, R. Y. The green fluorescent protein. Annu Rev Biochem 67, 509-544 (1998).

16. Zwart, W. *et al*. Classification of anti-estrogens according to intramolecular FRET effects on phospho-mutants of estrogen receptor alpha. Mol Cancer Ther. 6, 1526-1533 (2007).

17. Kemppainen, J. A. *et al*. Distinguishing androgen receptor agonists and antagonists: distinct mechanisms of activation by medroxyprogesterone acetate and dihydrotestosterone. Mol Endocrinol 13, 440-454 (1999).

18. van Royen, M. E. *et al*. Compartmentalization of androgen receptor protein-protein interactions in living cells. J Cell Biol 177, 63-72 (2007).

19. Jones, J. O. & Diamond, M. I. A cellular conformation-based screen for androgen receptor inhibitors. ACS Chem Biol 3, 412-418 (2008).

20. Chandra, V. *et al*. Structure of the intact PPAR-gamma-RXR-alpha nuclear receptor complex on DNA. Nature 350-356 (2008).

21. Llopis, J. *et al*. Ligand-dependent interactions of coactivators steroid receptor coactivator-1 and peroxisome proliferator-activated receptor binding protein with nuclear hormone receptors can be imaged in live cells and are required for transcription. Proc. Natl Acad. Sci. U. S. A 97, 4363-4368 (2000).

22. Renoir, J. M., Radanyi, C., Faber, L. E. & Baulieu, E. E. The non-DNA-binding heterooligomeric form of mammalian steroid hormone receptors contains a hsp90-bound 59-kilodalton protein. J Biol Chem 265, 10740-10745 (1990).

23. Press, M. F., Xu, S. H., Wang, J. D. & Greene, G. L. Subcellular distribution of estrogen receptor and progesterone receptor with and without specific ligand. Am J Pathol. 135, 857-864 (1989).

24. Sanchez, E. R., Faber, L. E., Henzel, W. J. & Pratt, W. B. The 56-59-kilodalton protein identified in untransformed steroid receptor complexes is a unique protein that exists in cytosol in a complex with both the 70- and 90-kilodalton heat shock proteins. Biochemistry 29, 5145-5152 (1990).

25. Denis, M., Poellinger, L., Wikstom, A. C. & Gustafsson, J. A. Requirement of hormone for thermal conversion of the glucocorticoid receptor to a DNA-binding state. Nature 333, 686-688 (1988).

26. King, W. J. & Greene, G. L. Monoclonal antibodies localize oestrogen receptor in the nuclei of target cells. Nature 307, 745-747 (1984).

27. Renoir, J. M., Radanyi, C., Jung-Testas, I., Faber, L. E. & Baulieu, E. E. The nonactivated progesterone receptor is a nuclear heterooligomer. J Biol Chem 265, 14402-14406 (1990).

28. Jenster, G., Trapman, J. & Brinkmann, A. O. Nuclear import of the human androgen receptor. Biochem J 293 (Pt 3), 761-768 (1993).

29. Madan, A. P. & DeFranco, D. B. Bidirectional transport of glucocorticoid receptors across the nuclear envelope. Proc Natl Acad Sci U S A 90, 3588-3592 (1993).

30. Kakar, M., Kanwal, C., Davis, J. R., Li, H. & Lim, C. S. Geldanamycin, an inhibitor of Hsp90, blocks cytoplasmic retention of progesterone receptors and glucocorticoid receptors via their respective ligand binding domains. AAPS J 8, E718-E728 (2006).

31. Zwart, W. *et al*. PKA-induced resistance to tamoxifen is associated with an altered orientation of ERalpha towards co-activator SRC-1. EMBO J 26, 3534-3544 (2007).

32. Carroll, J. S. *et al*. Genome-wide analysis of estrogen receptor binding sites. Nat. Genet. 38, 1289-1297 (2006).

33. Metivier, R., Penot, G., Flouriot, G. & Pakdel, F. Synergism between ERalpha transactivation function 1 (AF-1) and AF-2 mediated by steroid receptor coactivator protein-1: requirement for the AF-1 alpha-helical core and for a direct interaction between the N- and C-terminal domains. Mol Endocrinol. 15, 1953-1970 (2001).

34. Hawse, J. R. *et al*. Estrogen Receptor {beta} Isoform-Specific Induction of Transforming Growth Factor {beta}-Inducible Early Gene-1 in Human Osteoblast Cells: An Essential Role for the Activation Function 1 Domain. Mol Endocrinol. 22, 1579-1595 (2008).

35. Li, X. *et al*. Single-chain estrogen receptors (ERs) reveal that the ERalpha/beta heterodimer emulates functions of the ERalpha dimer in genomic estrogen signaling pathways. Mol Cell Biol 24, 7681-7694 (2004).

36. Yi, P., Bhagat, S., Hilf, R., Bambara, R. A. & Muyan, M. Differences in the abilities of estrogen receptors to integrate activation functions are critical for subtype-specific transcriptional responses. Mol Endocrinol. 16, 1810-1827 (2002).

37. Margeat, E. *et al*. The human estrogen receptor alpha dimer binds a single SRC-1 coactivator molecule with an affinity dictated by agonist structure. J Mol Biol 306, 433-442 (2001).

38. Sotoca, A. M. *et al*. Influence of cellular ERalpha/ERbeta ratio on the ERalpha-agonist induced proliferation of human T47D breast cancer cells. Toxicol Sci 105, 303-311 (2008).

39. Wang, H. *et al*. Yeast two-hybrid system demonstrates that estrogen receptor dimerization is ligand-dependent *in vivo*. J Biol Chem 270, 23322-23329 (1995).

40. Tamrazi, A., Carlson, K. E., Daniels, J. R., Hurth, K. M. & Katzenellenbogen, J. A. Estrogen receptor dimerization: ligand binding regulates dimer affinity and dimer dissociation rate. Mol Endocrinol 16, 2706-2719 (2002).

41. Padron, A., Li, L., Kofoed, E. M. & Schaufele, F. Ligand-selective interdomain conformations of estrogen receptor-alpha. Mol Endocrinol. 21, 49-61 (2007).

42. Gautier, I. *et al*. Homo-FRET microscopy in living cells to measure monomer-dimer transition of GFP-tagged proteins. Biophys J 80, 3000-3008 (2001).

43. Kofoed, E. M., Guerbadot, M. & Schaufele, F. Dimerization between aequorea fluorescent proteins does not affect interaction between tagged estrogen receptors in living cells. J Biomed Opt. 13, 031207 (2008).

44. Peters, G. A. & Khan, S. A. Estrogen receptor domains E and F: role in dimerization and interaction with coactivator RIP-140. Mol Endocrinol. 13, 286-296 (1999).

45. Xu, J. & Li, Q. Review of the *in vivo* functions of the p160 steroid receptor coactivator family. Mol Endocrinol. 17, 1681-1692 (2003).

46. So, A. Y., Chaivorapol, C., Bolton, E. C., Li, H. & Yamamoto, K. R. Determinants of cell- and gene-specific transcriptional regulation by the glucocorticoid receptor. PLoS Genet. 3, e94 (2007).

47. Damdimopoulos, A. E., Spyrou, G. & Gustafsson, J. A. Ligands differentially modify the nuclear mobility of estrogen receptors alpha and beta. Endocrinology 149, 339-345 (2008).

48. Long, X. & Nephew, K. P. Fulvestrant (ICI 182,780)-dependent interacting proteins mediate immobilization and degradation of estrogen receptor-alpha. J Biol Chem 281, 9607-9615 (2006).

49. Metivier, R. *et al*. Estrogen receptor-alpha directs ordered, cyclical, and combinatorial recruitment of cofactors on a natural target promoter. Cell 115, 751-763 (2003).

50. Lin, C. Y. *et al*. Whole-genome cartography of estrogen receptor alpha binding sites. PLoS Genet 3, e87 (2007).

51. Tremblay, A., Tremblay, G. B., Labrie, F. & Giguere, V. Ligand-independent recruitment of SRC-1 to estrogen receptor beta through phosphorylation of activation function AF-1. Mol Cell 3, 513-519 (1999).

52. Wu, R. C. *et al*. Selective phosphorylations of the SRC-3/AIB1 coactivator integrate genomic reponses to multiple cellular signaling pathways. Mol Cell 15, 937-949 (2004).

53. Weatherman, R. V. *et al*. Ligand-selective interactions of ER detected in living cells by fluorescence resonance energy transfer. Mol Endocrinol. 16, 487-496 (2002).

54. Stenoien, D. L. *et al*. Subnuclear trafficking of estrogen receptor-alpha and steroid receptor coactivator-1. Mol Endocrinol 14, 518-534 (2000).

55. Sun, J., Nawaz, Z. & Slingerland, J. M. Long-range activation of GREB1 by estrogen receptor via three distal consensus estrogen-responsive elements in breast cancer cells. Mol Endocrinol 21, 2651-2662 (2007).

56. McNally, J. G., Muller, W. G., Walker, D., Wolford, R. & Hager, G. L. The glucocorticoid receptor: rapid exchange with regulatory sites in living cells. Science 287, 1262-1265 (2000).

57. Sharp, Z. D. *et al*. Estrogen-receptor-alpha exchange and chromatin dynamics are ligand- and domain-dependent. J Cell Sci. 119, 4101-4116 (2006).

58. Muller, W. G., Walker, D., Hager, G. L. & McNally, J. G. Large-scale chromatin decondensation and recondensation regulated by transcription from a natural promoter. J Cell Biol 154, 33-48 (2001).

59. Nagaich, A. K., Walker, D. A., Wolford, R. & Hager, G. L. Rapid periodic binding and displacement of the glucocorticoid receptor during chromatin remodeling. Mol Cell 14, 163-174 (2004).

60. Fletcher, T. M. *et al*. ATP-dependent mobilization of the glucocorticoid receptor during chromatin remodeling. Mol Cell Biol 22, 3255-3263 (2002).

61. So, A. Y., Chaivorapol, C., Bolton, E. C., Li, H. & Yamamoto, K. R. Determinants of cell- and gene-specific transcriptional regulation by the glucocorticoid receptor. PLoS Genet. 3, e94 (2007).

62. Pickersgill, H. *et al*. Characterization of the Drosophila melanogaster genome at the nuclear lamina. Nat Genet 38, 1005-1014 (2006).

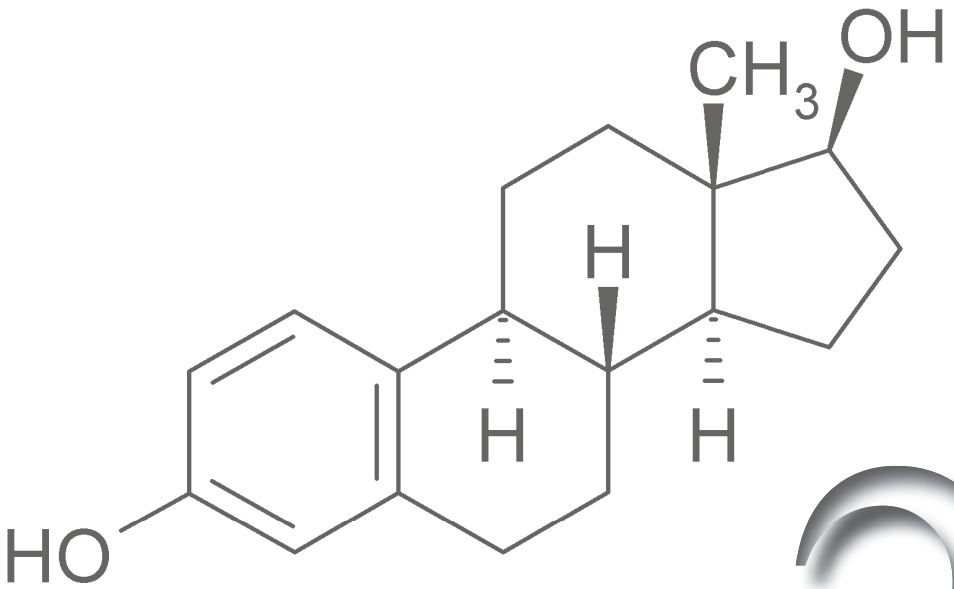
63. Fletcher, T. M. *et al*. ATP-dependent mobilization of the glucocorticoid receptor during chromatin remodeling. Mol Cell Biol 22, 3255-3263 (2002).

64. Andersen, J. B. *et al*. New unstable variants of green fluorescent protein for studies of transient gene expression in bacteria. Appl Environ Microbiol 64, 2240-2246 (1998).

65. Ponten, F., Jirstrom, K. & Uhlen, M. The Human Protein Atlas--a tool for pathology. J Pathol 216, 387-393 (2008).

Visualizing the action of steroid hormone receptors in living cells

Nuclear Receptor Signaling 2007, vol. 5: e003



2

Visualizing the action of steroid hormone receptors in living cells

Alexander Griekspoor, Wilbert Zwart, Jacques Neefjes and Rob Michalides[#].

Abstract
Transcription controlled by Steroid Hormone Receptors (SHRs) plays a key role in many important physiological processes like organ development, metabolite homeostasis, and response to external stimuli. Evidently, the members of this family have drawn a lot of attention from the scientific community since their discovery, four decades ago. Still, after many years of research we are only beginning to unravel the complex nature of these receptors. The pace at which we do has improved significantly in recent years with the discovery of genetically encoded fluorescent probes, and the accompanying revival of biophysical approaches that allow more detailed study of SHRs. Here, we will look into the different aspects of SHR signalling, and discuss how biophysical techniques have contributed to visualize their functioning in their native context, the living cell.

Steroid hormone receptors

Already in 1896 Thomas Beatson described that removal of the ovaries in advanced breast cancer patients often resulted in remarkable improvement [1]. With that he had revealed the stimulating effect of the female ovarian hormone estrogen on breast cancer, even before the hormone itself was discovered. His work provided a foundation for the modern use of hormone therapy in treatment and prevention of breast cancer. Only much later the cellular counterpart that mediated the described effects was revealed, the estrogen receptor (ER) [2,3].

As it turned out, this receptor plays a key role in the development and maintenance of the sexual reproductive tissues, and therefore, as Beatson had discovered, in breast cancer as well. We now know that the estrogen receptor is part of the nuclear receptor superfamily, and comes in two forms, ERα [NR3A1] and ERβ [NR3A2]. More specifically, both receptors are members of the subgroup of Steroid Hormone Receptors (SHRs), to which also the cortisol binding glucocorticoid receptor (GR) [NR3C1], the aldosterone binding mineralocorticoid receptor (MR) [NR3C2], the progesterone receptor (PR) [NR3C3], and the dihydrotestosterone (DHT) binding androgen receptor (AR) [NR3C4] belong (Figure 1A).

In addition, the SHR subgroup contains three orphan receptors closely related to ER: the estrogen related receptors α (ERRα) [NR3B1], β (ERRβ) [NR3B2], and γ (ERRγ) [NR3B3], for which a natural ligand remains to be identified. All SHRs function as nuclear transcription factors whose activity is regulated by small lipidsoluble ligands, and each member plays an important role in key physiological processes like reproduction, glucose metabolism, salt balance, and stress response.

Division of Tumor Biology,
The Netherlands Cancer Institute,
Plesmanlaan 121,
1066 CX Amsterdam,
The Netherlands
[#]Corresponding author
Email: r.michalides@nki.nl

Keywords:
Steroid Hormone Receptor / nuclear receptors / estrogen receptor / androgen receptor / glucocorticoid receptor / mineralocorticoid receptor / progesterone receptor / microscopy / FRAP / FRET / FCS / fluorescence / GFP

Structural overview

The members of the Steroid Hormone Receptor family share a similar, modular architecture, consisting of a number of independent functional domains (Figure 1B). Most conserved is the centrally located DNA binding domain (DBD) containing the characteristic zinc-finger motifs. The DBD is followed by a flexible hinge region and a moderately conserved Ligand Binding Domain (LBD), located at the carboxy-terminal end of the receptor. The estrogen receptor α is unique in that it contains an additional F domain of which the exact function is unclear. The LBD is composed of twelve α-helices (H1-H12) that together fold into a canonical α -helical sandwich. Besides its ligand binding capability, the LBD also plays an important role in nuclear translocation, chaperone binding, receptor dimerization, and coregulator recruitment through its potent ligand-dependent transactivation domain, referred to as AF-2. A second, ligand independent, transactivation domain is located in the more variable N-terminal part of the receptor, designated as AF-1. To date, no crystal structure of a full-length SHR exists, though structures of the DBD and LBD regions of most SHRs are available. These have helped significantly in understanding the molecular aspects of DNA and ligand binding, but have to some extent also led to biased attention to these parts of the receptor only. For example, many co-regulator interaction studies are still performed with the LBD only, while numerous

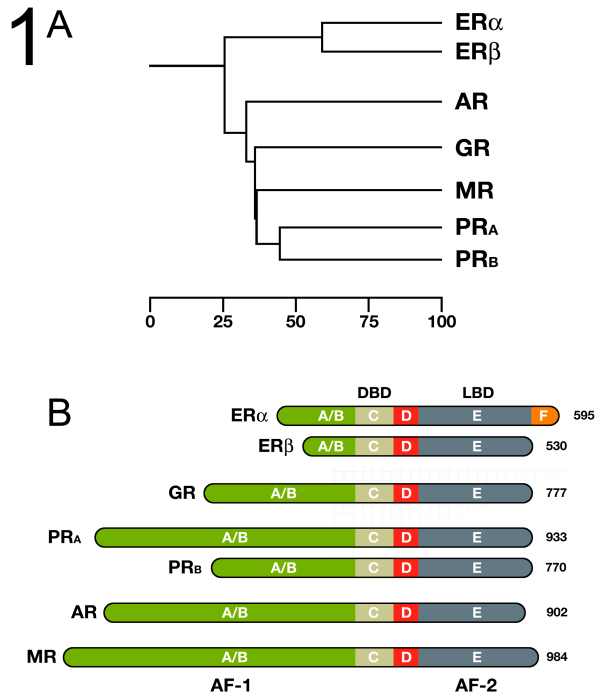


Figure 1 - Overview of the Steroid Hormone Receptor family

A. Phylogenetic tree of the Steroid Hormone Receptor (SHR) family showing the evolutionary interrelationships and distance between the various receptors. Based on alignments available at The NucleaRDB [56].
B. All steroid receptors are composed of a variable N-terminal domain (A/B) containing the AF-1 transactivation region, a highly conserved DNA Binding Domain (DBD), a flexible hinge region (D), and a C-terminal Ligand Binding Domain (LBD, E) containing the AF-2 transactivation region. The estrogen receptor α is unique in that it contains an additional C-terminal F domain. Numbers represent the length of the receptor in aminoacids. Abbreviations: ER - estrogen receptor, GR – glucocorticoid receptor, PR - progesterone receptor, AR - androgen receptor, MR - mineralocorticoid receptor.

studies have demonstrated that the AF-2 domain often tells only part of the story. With the help of biophysical techniques it is however feasible to study the full-length receptor in its native environment (Figure 2).

Ligand binding

Steroid Hormones (SHs) reach their target cells via the blood, where they are bound to carrier proteins. Because of their lipophilic nature it is thought that they pass the cell membrane by simple diffusion, although some evidence exist that they can also be actively taken up by endocytosis of carrier protein bound hormones [4]. For a long time it has been assumed that binding of the ligand resulted in a simple on/off switch of the receptor (Figure 2, step 1). While this is likely the case for typical agonists like estrogen and progesterone, this is not always correct for receptor antagonists. These antagonists come in two kinds, so-called partial antagonists (for the estrogen receptor known as SERMs for Selective Estrogen Receptor Modulators) and full antagonists. The partial antagonist can, depending on cell type, act as SHR agonist or antagonist. In contrast, full antagonists (for ER known as SERDs for Selective Estrogen Receptor Downregulators) always inhibit the receptor, independent of cell type, in part by targeting the receptor for degradation. Binding of either type of antagonist results in major conformational changes within the LBD and in release from heat shock proteins that thus far had protected the unliganded receptor from unfolding and aggregation (Figure 2, step 2). This process was nicely visualized for the estrogen receptor by Devin-Leclerc *et al*. who showed using fluorescence microscopy that the nuclear ER-HSP90 complex dissociates after addition of either agonist or antagonist, followed by rapid relocation of the heat shock protein to the cytoplasm [5].

Nuclear translocation

The constitutive nuclear localisation of ER is a unique feature of this SHR only. Although family members, SHRs are located differently in cells. The subcellular localisation of SHRs in living cells has been extensively studied using fusion constructs of green fluorescent protein (GFP). This showed that SHRs can be divided in three groups based on their unliganded distribution: ERα and ERβ are found predominantly in the nucleus [6], GR and AR are found primarily in the cytoplasm [7,8], while MR and PR have a mixed distribution over both cytoplasm and nucleus [9,10]. The progesterone receptor is of particular interest as it exists in two forms with different ratios of nuclear versus cytoplasmic localization of the unliganded receptor. In most cell contexts, the PRA isoform is a repressor of the shorter PRB isoform, and without hormone induc-

tion it is mostly located in the nucleus, whereas PRB distributes both in the nucleus and in the cytoplasm. PRB accumulates in the nucleus after progesterone binding, a process that directly correlates with PR mediated transcription [10,11].

Rapid and almost complete nuclear translocation following ligand addition is a common behavior observed for almost all SHRs (Figure 2, step 3). This translocation coincides with a striking alteration in receptor distribution within the nucleus, most apparent in case of the already nuclear ER. Htun *et al*. observed that GFP-ER's uniform distribution changes into a punctuated pattern upon the addition of either agonistic or antagonistic ligands [6]. A few years earlier the same group had already made similar observations for GFP-GR [8]. Other groups confirmed similar behavior for the other SHRs, some directly by tagging two receptors with different variants of GFP and following both at the same time [12]. Fejes-Toth and colleagues demonstrated that hormone-activated MRs accumulated in dynamic discrete clusters in the cell nucleus, a phenomenon that only concurred with agonistic mineralocorticoids and not with full antagonists [9]. Further work on MR and AR showed that the accumulation of these receptors in about 250-400 foci requires both the DBD and LBD regions, and is possibly influenced by AF-1 function [13-17]. The exact nature of these foci is still unclear and multiple roles have been proposed, in-

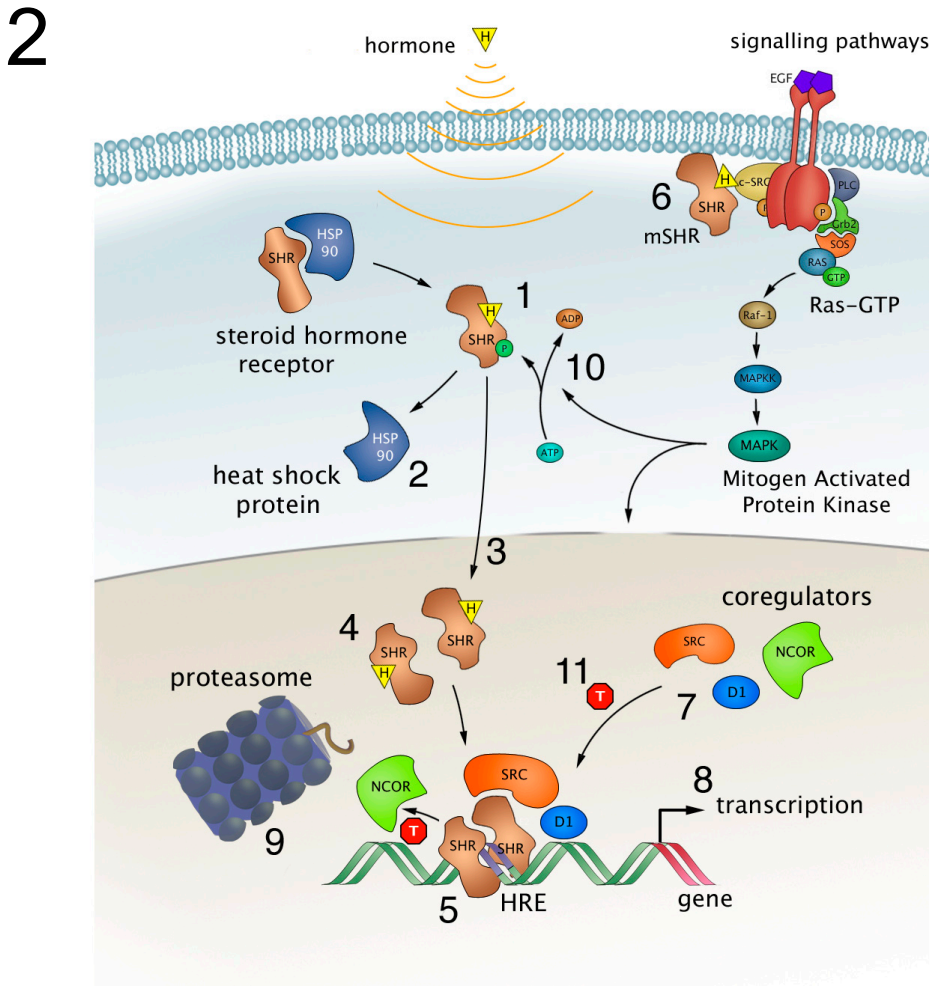


Figure 2 - Steroid Hormone Receptor signalling

Steroid Hormone Receptors (SHR) act as a hormone dependent nuclear transcription factor. Upon entering the cell by passive diffusion, the hormone (H) binds the receptor, which is subsequently released from heat shock proteins, and translocates to the nucleus. There, the receptor dimerizes, binds specific sequences in the DNA, called Hormone Responsive Elements or HREs, and recruits a number of coregulators that facilitate gene transcription. This latter step can be modulated by receptor antagonists like tamoxifen (T), and cellular signalling pathways. Examples of processes studied using biophysical techniques and discussed in this review include: hormone binding (1), chaperone interaction (2), nuclear translocation (3), receptor dimerization (4), DNA binding (5), putative membranebound receptors (6), coregulator recruitment (7), transcription (8), proteasomal degradation (9), modulation by cellular signalling pathways (10), and antagonist resistance (11).

cluding storage depots and sites of transcription, splicing, aggregation or degradation. What is clear however is that nuclear and subnuclear translocation of SHRs is ligand and concentration dependent. Martinez *et al*. recently made use of this finding to devise a molecular screen for ER ligands based on a fluorescent GR-ER chimera [18]. Instead of a constitutive nuclear localization, this chimeric receptor adapted the cytoplasmic localization of unliganded GR, and translocates to the nucleus upon ER ligand addition. Interestingly, the GR-ER chimera retained the (anti-) estrogen binding properties, and could thus be used to screen for new ER ligands.

Dimerization

Nuclear receptors that bind steroid hormones typically form homodimers (Figure 2, step 4). Dimer formation is facilitated mainly through interactions between the LBDs of both receptors, and is essential for their function, as mutations in the dimerization domain typically render the receptor inactive. ER has been reported to exist as a dimer even in the absence of ligand, although it is important to note that these studies have again been performed with the LBD domain only [19]. Biophysical *in vitro* studies, again with the LBD only, have confirmed these data and show slow dissociation of unliganded dimers, which is further retarded by ligand binding [20]. Recent *in vivo* studies suggested that this might not hold for full-length receptors though, at least not for AR. Schaufele *et al*. used Fluorescence Resonance Energy Transfer (FRET) to study AR dimer formation [21]. FRET is the radiationless transfer of energy from an excited donor fluorophore to a suitable acceptor fluorophore [22]. Importantly, FRET is extremely sensitive to the distance between the fluorophores fluorophores (its efficiency decays with the distance to the sixth power), and will therefore only occur when two proteins are on average no more than one molecule in distance apart, but usually they interact directly (Figure 3A). Schaufele and colleagues measured FRET between CFP and YFP labeled AR receptors, and their results suggest that dimerization only takes place after ligand binding, and predominantly in the nucleus. It should be noted that absence of FRET does not imply absence of protein-protein interaction since the relative orientation of two fluorophores is also critical for FRET to occur [22]. Further study is required to confirm these findings and

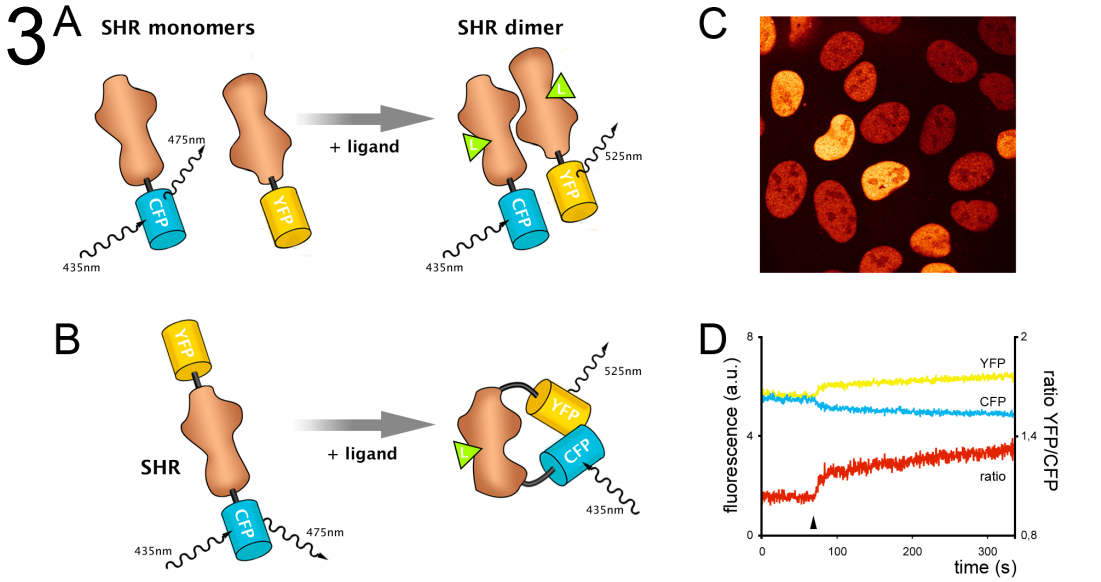


Figure 3 - Fluorescence resonance energy transfer (FRET).

A. Principle of FRET to measure intermolecular interaction. Exciting the blue variant of GFP (CFP) linked to one Steroid Hormone Receptor (SHR) monomer at 435nm results in emission at 475nm, unless energy is transferred to a SHR monomer coupled to the yellow variant of GFP (YFP). This phenomenon only occurs when both monomers physically interact as a dimer, and results in increased YFP emission at 525nm at the cost of CFP emission at 475nm. **B**. A similar protocol is followed to measure intramolecular FRET. A single SHR monomer is tagged with two variants of GFP. Ligand binding induces conformational changes within the receptor and alters the relative orientation and distance between the two fluorophores, leading to changes in FRET efficiency. **C**. A confocal microscopy image showing U2OS cells expressing nuclear YFP-ER-CFP to monitor conformational changes through intramolecular FRET. Fluorescence is depicted in false colors. **D**. An example FRET trace, measuring intramolecular FRET between CFP and YFP within a single nucleus of a YFP-ER-CFP expressing cell as shown in 3C. The fluorescent signal of YFP (yellow) and CFP (cyan) is arbitrarily set to the same level such that the ratio (red) is 1, and followed in time. After 80 seconds, tamoxifen is added to the cells (arrowhead) and a conformational change is observed in the form of a change in FRET; the YFP signal increases at the cost of CFP fluorescence.

to determine whether this behavior is unique for AR or also applies to other SHRs.

Dimers of SHRs are only efficiently formed between closely related receptors. In this light the previously mentioned two isoforms of the progesterone receptor and the two estrogen receptors are of particular interest. In both cases one of the two seems to exhibit a repressive function on the other. ERβ efficiently dimerizes with ERα and mixed dimers show identical subnuclear distribution as homodimers [23]. However, binding of ERβ suppresses ERα mediated gene transcription, accordingly the mouse knockouts of either receptor show completely opposing phenotypes [24].

DNA binding

Upon binding of ligand and translocation to the nucleus, SHRs bind to specific regions in the DNA called Hormone Responsive Elements (HREs) through zincfinger motifs present in the DBD (Figure 2, step 5). The exact mode of binding has been characterised in detail with help of available crystal structures and extensive biophysical *in vitro* measurements. Consensus nucleotide binding sequences have been determined for all SHRs, but these show a significant amount of ambiguity, making it hard to pinpoint true target HREs in the genome. A HRE is made up of two so-called half-sites that each binds one monomer of the SHR dimer. Interestingly, also single half-sites have been found in genes that clearly respond to hormone, hinting at a possible role for receptors in their monomeric configuration.

Immobilization of SHRs on DNA and other nuclear structures has been studied with photobleaching techniques like Fluorescence Recovery After Photobleaching (FRAP). By bleaching fluorescent molecules in a region of interest in a living cell and measuring recurrence of fluorescence levels in the bleached area, the mobility of the tagged molecules can be determined (Figure 4). Using this technique several groups could demonstrate a clear correlation between receptor immobilization in the nucleus and the appearance of the typical punctuated receptor distribution, which was most convincingly demonstrated by Schaaf and colleagues who compared 13 GR ligands [25]. FRAP measurements show that fluorescently tagged SHRs such as ER, GR, and AR are highly mobile and dynamic in the unliganded state, whereas ligand-bound forms are less mobile [26-28]. Stenoien *et al*. further showed that in the case of ERα, FRAP could discriminate between ligands with potential agonistic properties and full antagonists on the basis of receptor immobilization in the nucleus [28]. The nature of the substrate on which the receptor immobilizes remains uncertain, but almost certainly includes DNA. Carefully controlled FRAP measurements from Sprague *et al*. show that in free form GR is bound to a single type of substrate, most probably DNA, with each molecule binding on average 65 sites per second [27]. This rapid sampling of GR is likely to be important in finding a specific HRE. Upon ligand binding, the residence time on DNA is significantly increased. According to Farla *et al*. on average one out of five ARs is immobilized in the presence of ligand, each individual AR being immobile for 1-2 min. This immobilization is depended

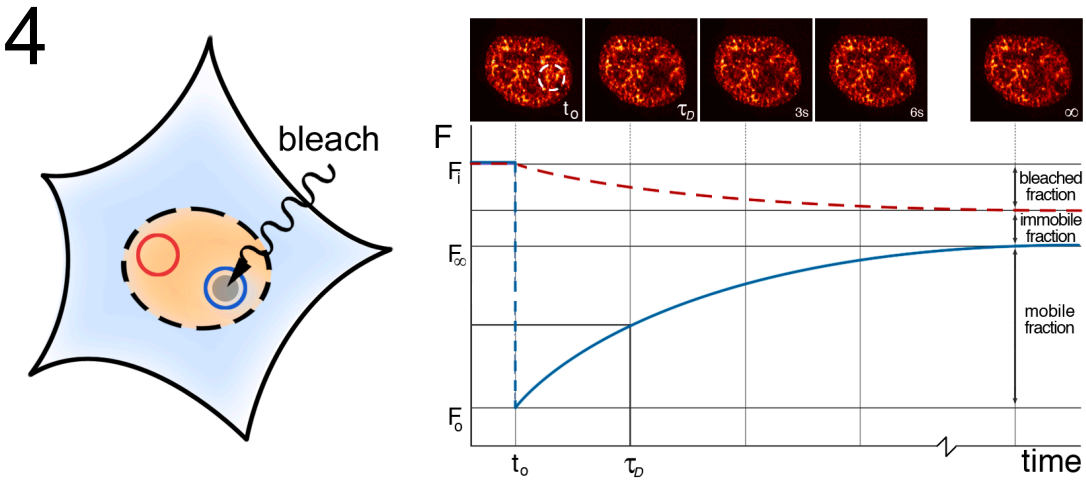


Figure 4 - Fluorescence Recovery After Photobleaching (FRAP)

By bleaching the indicated (blue) region in the fluorescent area (here the nucleus of a cell expressing ERα fused to GFP) is bleached at time t0, Fluorescence decreases from the initial fluorescence Fi to F0. The fluorescence recovers over time by diffusion. The characteristic diffusion time τD indicates the time at which half of the fluorescence has recovered. The mobile fraction can be calculated by comparing the fluorescence in the bleached region after full recovery (F∞) with the fluorescence in a distant region in the nucleus (red, dashed line).

on DNA binding since GFP-ARs mutated in the DNA-binding domain were not immobilized [26]. Likewise, FRAP analysis by Kino *et al*. on several GR mutant receptors showed a significantly increased nuclear motility and decreased chromatin retention, which correlated with impaired transcriptional activity [29].

DNA binding and transcription has been visualized directly by using cells that have stably integrated a tandem array of HREs. Pioneering work in this area has been performed by the Hager lab, which used this approach to study the interaction of GR with a natural promoter [30]. The promoter array allows significant amounts of GFPGR to accumulate for direct detection under the microscope. The recruitment of GFPGR leads to gross alterations in chromatin structure of the array that correlate with gene transcription [31]. Interestingly, FRAP analysis on the array again shows a rapid exchange of receptors between chromatin and the nucleoplasmic compartment. Further analysis demonstrated that following binding of GR to the promoter, the receptor is actively displaced from the template during a chromatin remodeling reaction facilitated by the hSWI/SNF complex [32]. Further evidence comes from work on PR by the same group, which showed that the exchange of PR-GFP on the array was slowed down (but still in the order of seconds) upon agonist addition, and even further slowed down after addition of a partial antagonist [33]. Strikingly, addition of a full-antagonist showed the opposite effect, with ongoing exchange at a rate faster than for an agonist bound receptor. In contrast to an agonist or partial antagonist bound receptor, addition of a full-antagonist does not lead to recruitment of the SWI/SNF chromatin remodeling complex, which may partly explain the above results. Together, these findings have led to the so-called hit-and-run model. In contrast to static binding of the receptor to a HRE and the subsequent build up of the transcription complex, this model suggests a receptor to continuously probe the DNA for potential binding sites. Transcriptional activation reflects the probability that all components required for activation will meet at a certain chromatin site.

Besides binding to Hormone Responsive Elements, SHRs can also exert their effects by binding directly to other transcription factors. For example, ERα is able to bind to fos/jun, and thus regulate AP-1 mediated transcription of genes like cyclin D1. Similarly, ERα can bind Sp1 proteins and regulate transcription of genes that contain an Sp1/ER binding site. Interestingly, antagonists often have agonistic effects in this setting, which may be important when it comes to resistance to antagonistic compounds. This is illustrated by work from Kim *et al*. who used FRET to visualize the interaction between ERα and Sp1 [34]. Addition of the full anti-estrogen ICI 182,780 inhibits normal ERα mediated transcription, yet like agonist estradiol induced a FRET signal between ERα and Sp1 that correlated with Sp1 mediated transcription of a reporter construct.

Recently a number of groups have claimed a role for SHRs in non-genomic, extranuclear signalling events (Figure 2, step 6). Targeting ERα artificially to the plasma membrane has marked influence on ERK1/2 signalling, which was not affected by full anti-estrogens [35]. Similar effects on the Mitogen Activated Protein Kinase (MAPK) and Protein Kinase A (PKA) pathways have also been attributed to the wild-type receptor [36,37]. However, most studies are based on biochemical approaches where post-lysis artefacts are hard to exclude. Moreover, convincing microscopic pictures of SHR membrane localization are still lacking. Nevertheless, accumulating evidence seems to point to possible functions for SHRs other than mediated by DNA binding.

Co-regulator recruitment

The classical mode of action of SHRs involves ligand and DNA binding. For transcription to occur the subsequent recruitment of co-regulator proteins is absolutely required (Figure 2, step 7). These regulatory proteins come in two types, co-activators and co-repressors that respectively enhance or diminish transactivation activity through various enzymatic activities, including acetylating, deactylating, methylating, ubiquitinating, and kinase activity. Ligand dependent recruitment of coregulators occurs through a hydrophobic cleft formed by helices 3, 4 and 12 in the AF-2 domain of the receptor [38]. In free receptors this pocket is shielded by a short amphipathic α- helix (H12) located at the carboxy-terminal end of the receptor that prevents AF-2 mediated coregulator binding in the absence of ligand. Upon hormone binding, this helix is repositioned, which opens a functional interface for coregulator recruitment through conserved LXXLL motifs in the co-factor. Antagonists exert their function by inducing a different conformational change of H12 that blocks or modulates the recruitment of these essential coregulators. However, not all coregulator binding occurs through the AF-2 region. Also other conformational changes within the receptor and events like dimerization are likely to be involved in coregulator recruitment. Moreover, the AF-1 region of SHRs plays an important role in ligand independent binding of coregulators. The exact coregulator requirements for transcription are dependent on cell type, and probably also on ligand and promoter context. This explains why partial antagonists can have antagonistic properties in one tissue, while exhibiting agonistic properties in another.

The most well studied coactivators are of

the Steroid Receptor Coactivator (SRC) family, which includes SRC-1 (or NcoA-1), SRC-2 (also known as TIF-2 or GRIP1, NcoA-2) and SRC-3 (also known as RAC3, ACTR, AIB1, P/CIP and TRAM). Llopis *et al.* were the first to directly visualize the interaction between SRC- 1 and a SHR in living cells using FRET [39]. They showed that the ERα LBD exhibited some basal interaction with coactivators in unstimulated cells that was increased upon agonist addition and abolished by receptor antagonists. A large number of publications have since confirmed these findings, also with full-length ER constructs. Interestingly, these studies clearly show that the receptor adopts a slightly different conformation for various ligands, and this conformation significantly influences the binding of specific coregulatory proteins [40-42]. Likewise, the small structural differences between the LBD of ERα and ERβ can result in profound differences in SRC-1 recruitment with the same ligand [43]. We have visualized these conformational changes by fusing full-length ERα with YFP to its N- and CFP to its C-terminus [44]. This allowed us to monitor conformational alterations of the receptor after ligand binding in the form of a change in FRET between CFP and YFP (Figure 3B). Indeed, subtle FRET differences between the various anti-estrogens tested were observed, showing that the receptor had adopted ligand specific conformations.

The stoichiometry of interaction between ERα and SRC-1 was studied using fluorescence correlation spectroscopy (FCS). By measuring the fluorescence signal from a very small excitation volume only, this technique allows precise determination of the diffusion coefficient of fluorescently labeled proteins, which is in part dependent on protein complex formation (Figure 5). In this way Margeat *et al.* could show that the ERα dimer binds a single SRC-1 coactivator molecule [45].

One caveat of the above experiments is the use of only the AF-2 binding part of SRC-1. This may give false impressions when conclusions are extrapolated to the full-length receptor. Work from others and unpublished data from our lab have demonstrated that full-length SRC-1 binds the receptor through its AF-1 domain in a ligand independent manner [46] (Zwart *et al*, manuscript in preparation). AF-2 binding still functions as a switch to invoke full transactivation activity, but in contrast to what the above studies suggest, SRC-1 is already bound to unliganded receptors. This was also demonstrated by Stenoien *et al.*, who used a fusion construct of CFP-ERα with a lac repressor domain to artificially target the receptor to an integrated lac operator array [47]. Even in the absence of ligand, significant levels of SRC-1 were already present on the array, which further increased upon addition of agonist, and decreased after addition of antagonist. Further work by this group suggested that agonist binding predominantly stabilized SRC-1 binding, which translated in identical mobility of both proteins [28]. Similar results were reported for other SHRs like GR and AR, and for other coregulators including CREB binding protein (CBP), glucocorticoid receptor (GR) interacting protein 1 (GRIP-1), and RIP140 [48-50]. Interestingly, in all cases dynamic DNA binding of SHRs was observed even in the presence of agonist and coregulators.

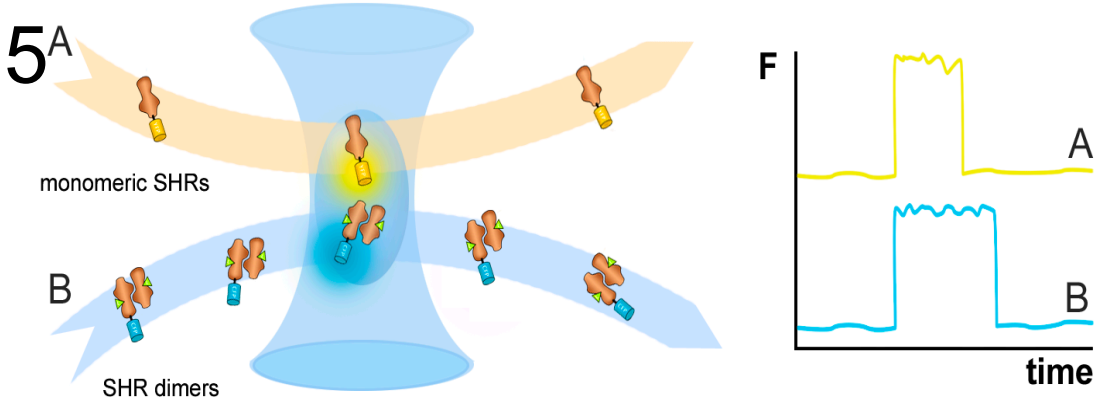


Figure 5 - Fluorescence Correlation Spectroscopy (FCS)

By using the microscope objective lens to focus the laser beam, a diffraction limited excitation volume is created. The emitted fluorescence signal (F) from this observation volume fluctuates as labeled molecules diffuse in and out, and the duration of the fluctuations are related to the average time individual models reside within the volume. One such an event is depicted in the graph. The residence time can be used to determine the diffusion coefficient for the fluorescent molecules, which is dependent on their size and interaction with other proteins. For example, it can be used to discriminate monomeric Steroid Hormone Receptors (SHRs, **A**) from dimeric complexes (**B**).

Transcription

Our view on SHR mediated transcription has more and more shifted from one in which a static holoenzyme of transcription factors is steadily build up after initial binding of the receptor to a response element, into a highly dynamic picture where different factors rapidly move in and out to perform temporary and local functions (Figure 2, step 8). In this so-called hit-and-run model, transcription only takes place when all factors coincidentally meet at the same time at the same location. Factors like DNA binding on specific HREs, and ligand dependent co-regulator recruitment simply increase the odds that a successful transcriptional unit is formed and a gene is transcribed. FRAP analysis shows that indeed the majority of nuclear proteins is highly mobile [51], except for Polymerase II, which once recruited has a residence time on the DNA in the order of minutes.

Whichever model is closer to reality, it is clear that transcription is a complex process, requiring dozens of proteins. Large-scale Chromatin IP assays have shown the recruitment of at least 46 factors to an empty promoter before continued transcription can take place [52]. Interestingly, these experiments revealed a striking ATP-dependent periodicity in the recruitment of these factors, which was confirmed using FRAP analysis [52,53]. The observed cycling time was in the order of 1h, much slower than the rapid exchange of SHRs on the template described earlier. Receptor degradation by the proteasome plays an important role in this process, as a block of proteasomal function halts the cycle after one round of transcription (Figure 2, step 9). This corresponds to previous observations that GR and ERα completely immobilize in the nucleus upon proteasome inhibition [28,54]. However, since proteasome inhibition rapidly de-ubiquitinates histones, these effects may also be indirect, and the result of chromatin alterations [55]. An important role to maintain proper cycling has also been suggested for heat shock proteins like HSP-90 [54]. The exact role of this cyclic recruitment of transcription factors to the promoter is still unclear. It is also difficult to interpret how this slower cycle relates to the rapid exchange of SHRs that forms the basis of the hit-and-run model. Interestingly, the cyclic pattern of transcription factor presence on the promoter does suggest that some form of order in the build up of a functional transcriptional unit must exist, resulting in a so-called transcription factory. This may very well represent the summation of all rapid exchange events over a longer period of time, which suggests that both models may not necessarily be mutually exclusive, and might act in subsequent steps of transcription initiation.

Note

The literature on steroid hormone receptors is extensive and only selected studies were cited in this review due to space limitation. We sincerely apologize to all investigators whose work was not mentioned.

References

[1] Beatson, G. W. Lancet 1896, 2, 104-107.

[2] Green, S.; Walter, P.; Kumar, V.; Krust, A.; Borert, J. M.; Argos, P.; Chambon, P. Nature 1986, 320, 134-139.

[3] Jensen, E. V. Perspect Biol Med 1962, 6, 47-59.

[4] Hammes, A.; Andreassen, T. K.; Spoelgen, R.; Raila, J.; Hubner, N.; Schulz, H.; Metzger, J.; Schweigert, F. J.; Luppa, P. B.; Nykjaer, A.; Willnow, T. E. Cell 2005, 122, 751-762.

[5] Devin-Leclerc, J.; Meng, X.; Delahaye, F.; Leclerc, P.; Baulieu, E. E.; Catelli, M. G. Mol Endocrinol 1998, 12, 842-854.

[6] Htun, H.; Holth, L. T.; Walker, D.; Davie, J. R.; Hager, G. L. Mol Biol Cell 1999, 10, 471-486.

[7] Georget, V.; Lobaccaro, J. M.; Terouanne, B.; Mangeat, P.; Nicolas, J. C.; Sultan, C. Mol Cell Endocrinol 1997, 129, 17-26.

[8] Htun, H.; Barsony, J.; Renyi, I.; Gould, D. L.; Hager, G. L. Proc Natl Acad Sci U S A 1996, 93, 4845-4850.

[9] Fejes-Toth, G.; Pearce, D.; Naray-Fejes-Toth, A. Proc Natl Acad Sci U S A 1998, 95, 2973-2978.

[10] Lim, C. S.; Baumann, C. T.; Htun, H.; Xian, W.; Irie, M.; Smith, C. L.; Hager, G. L. Mol Endocrinol 1999, 13, 366-375.

[11] Li, H.; Fidler, M. L.; Lim, C. S. Mol Pharm 2005, 2, 509-518.

[12] Nishi, M.; Ogawa, H.; Ito, T.; Matsuda, K. I.; Kawata, M. Mol Endocrinol 2001, 15, 1077-1092.

[13] Farla, P.; Hersmus, R.; Trapman, J.; Houtsmuller, A. B. J Cell Sci 2005, 118, 4187-4198.

[14] Goto, K.; Zhao, Y.; Saito, M.; Tomura, A.; Morinaga, H.; Nomura, M.; Okabe, T.; Yanase, T.; Takayanagi, R.; Nawata, H. J Steroid Biochem Mol Biol 2003,85, 201-208.

[15] Pearce, D.; Naray-Fejes-Toth, A.; Fejes-Toth, G. J Biol Chem 2002, 277, 1451-1456.

[16] Tomura, A.; Goto, K.; Morinaga, H.; Nomura, M.; Okabe, T.; Yanase, T.; Takayanagi, R.; Nawata, H. J Biol Chem 2001, 276, 28395-28401.

[17] Tyagi, R. K.; Lavrovsky, Y.; Ahn, S. C.; Song, C. S.; Chatterjee, B.; Roy, A. K. Mol Endocrinol 2000, 14, 1162-1174.

[18] Martinez, E. D.; Rayasam, G. V.; Dull, A. B.; Walker, D. A.; Hager, G. L. J Steroid Biochem Mol Biol 2005, 97, 307-321.

[19] Salomonsson, M.; Haggblad, J.; O'Malley, B. W.; Sitbon, G. M. J Steroid Biochem Mol Biol 1994, 48, 447-452.

[20] Tamrazi, A.; Carlson, K. E.; Daniels, J. R.; Hurth, K. M.; Katzenellenbogen, J. A. Mol Endocrinol 2002, 16, 2706-2719.

[21] Schaufele, F.; Carbonell, X.; Guerbadot, M.; Borngraeber, S.; Chapman, M. S.; Ma, A. A.; Miner, J. N.; Diamond, M. I. Proc Natl Acad Sci U S A 2005, 102, 9802-9807.

[22] Förster, T. Annalen Physik 1948, 6, 55-75.

[23] Matsuda, K.; Ochiai, I.; Nishi, M.; Kawata, M. Mol Endocrinol 2002, 16, 2215-2230.

[24] Couse, J. F.; Korach, K. S. Endocr Rev 1999, 20, 358-417.

[25] Schaaf, M. J.; Lewis-Tuffin, L. J.; Cidlowski, J. A. Mol Endocrinol 2005, 19, 1501-1515.

[26] Farla, P.; Hersmus, R.; Geverts, B.; Mari, P. O.; Nigg, A. L.; Dubbink, H. J.; Trapman, J.; Houtsmuller, A. B. J Struct Biol 2004, 147, 50-61.

[27] Sprague, B. L.; Pego, R. L.; Stavreva, D. A.; McNally, J. G. Biophys J 2004, 86, 3473-3495.

[28] Stenoien, D. L.; Patel, K.; Mancini, M. G.; Dutertre, M.; Smith, C. L.; O'Malley, B. W.; Mancini, M. A. Nat Cell Biol 2001, 3, 15-23.

[29] Kino, T.; Liou, S. H.; Charmandari, E.; Chrousos, G. P. Mol Med 2004, 10, 80-88.

[30] McNally, J. G.; Muller, W. G.; Walker, D.; Wolford, R.; Hager, G. L. Science 2000, 287, 1262-1265.

[31] Muller, W. G.; Walker, D.; Hager, G. L.; McNally, J. G. J Cell Biol 2001, 154, 33-48.

[32] Nagaich, A. K.; Walker, D. A.; Wolford, R.; Hager, G. L. Mol Cell 2004, 14, 163-174.

[33] Rayasam, G. V.; Elbi, C.; Walker, D. A.; Wolford, R.; Fletcher, T. M.; Edwards, D. P.; Hager, G. L. Mol Cell Biol 2005, 25, 2406-2418.

[34] Kim, K.; Barhoumi, R.; Burghardt, R.; Safe, S. Mol Endocrinol 2005, 19, 843-854.

[35] Rai, D.; Frolova, A.; Frasor, J.; Carpenter, A. E.; Katzenellenbogen, B. S. Mol Endocrinol 2005, 19, 1606-1617.

[36] Levin, E. R. Mol Endocrinol 2005, 19, 1951-1959.

[37] Razandi, M.; Pedram, A.; Merchenthaler, I.; Greene, G. L.; Levin, E. R. Mol Endocrinol 2004, 18, 2854-2865.

[38] Gronemeyer, H.; Gustafsson, J. A.; Laudet, V. Nat Rev Drug Discov 2004, 3, 950-964.

[39] Llopis, J.; Westin, S.; Ricote, M.; Wang, Z.; Cho, C. Y.; Kurokawa, R.; Mullen, T. M.; Rose, D. W.; Rosenfeld, M. G.; Tsien, R. Y.; Glass, C. K. Proc Natl Acad Sci U S A 2000, 97, 4363-4368.

[40] Schaufele, F.; Chang, C. Y.; Liu, W.; Baxter, J. D.; Nordeen, S. K.; Wan, Y.; Day, R. N.; McDonnell, D. P. Mol Endocrinol 2000, 14, 2024-2039.

[41] Tamrazi, A.; Carlson, K. E.; Rodriguez, A. L.; Katzenellenbogen, J. A. Mol Endocrinol 2005, 19, 1516-1528.

[42] Weatherman, R. V.; Chang, C. Y.; Clegg, N. J.; Carroll, D. C.; Day, R. N.; Baxter, J. D.; McDonnell, D. P.; Scanlan, T. S.; Schaufele, F. Mol Endocrinol 2002, 16, 487-496.

[43] Margeat, E.; Bourdoncle, A.; Margueron, R.; Poujol, N.; Cavailles, V.; Royer, C. J Mol Biol 2003, 326, 77-92.

[44] Michalides, R.; Griekspoor, A.; Balkenende, A.; Verwoerd, D.; Janssen, L.; Jalink, K.; Floore, A.; Velds, A.; van't Veer, L.; Neefjes, J. Cancer Cell 2004, 5, 597-605.

[45] Margeat, E.; Poujol, N.; Boulahtouf, A.; Chen, Y.; Muller, J. D.; Gratton, E.; Cavailles, V.; Royer, C. A. J Mol Biol 2001, 306, 433-442.

[46] Dutertre, M.; Smith, C. L. Mol Endocrinol 2003, 17, 1296-1314.

[47] Stenoien, D. L.; Nye, A. C.; Mancini, M. G.; Patel, K.; Dutertre, M.; O'Malley, B. W.; Smith, C. L.; Belmont, A. S.; Mancini, M. A. Mol Cell Biol 2001, 21, 4404-4412.

[48] Becker, M.; Baumann, C.; John, S.; Walker, D. A.; Vigneron, M.; McNally, J. G.; Hager, G. L. EMBO Rep 2002, 3, 1188-1194.

[49] Carascossa, S.; Gobinet, J.; Georget, V.; Lucas, A.; Badia, E.; Castet, A.; White, R.; Nicolas, J. C.; Cavailles, V.; Jalaguier, S. Mol Endocrinol 2006.

[50] Marcelli, M.; Stenoien, D. L.; Szafran, A. T.; Simeoni, S.; Agoulnik, I. U.; Weigel, N. L.; Moran, T.; Mikic, I.; Price, J. H.; Mancini, M. A. J Cell Biochem 2006.

[51] Phair, R. D.; Misteli, T. Nature 2000, 404, 604-609.

[52] Metivier, R.; Penot, G.; Hubner, M. R.; Reid, G.; Brand, H.; Kos, M.; Gannon, F. Cell 2003, 115, 751-763.

[53] Reid, G.; Hubner, M. R.; Metivier, R.; Brand, H.; Denger, S.; Manu, D.; Beaudouin, J.; Ellenberg, J.; Gannon, F. Mol Cell 2003, 11, 695-707.

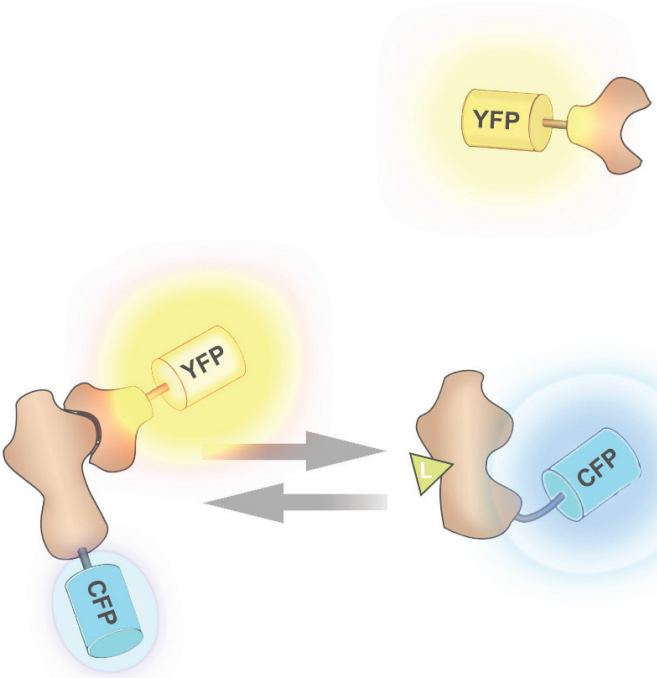
[54] Stavreva, D. A.; Muller, W. G.; Hager, G. L.; Smith, C. L.; McNally, J. G. Mol Cell Biol 2004, 24, 2682-2697.

[55] Dantuma, N. P.; Groothuis, T. A.; Salomons, F. A.; Neefjes, J. J Cell Biol 2006, 173, 19-26.

[56] Horn, F.; Vriend, G.; Cohen, F. E. Nucleic Acids Res 2001, 29, 346-349.

PKA-induced resistance to tamoxifen is associated with an altered orientation of ERα towards co-activator SRC-1

The EMBO journal 2007, vol. 26: 3534-3544



3

PKA-induced resistance to tamoxifen is associated with an altered orientation of ERα towards co-activator SRC-1

Wilbert Zwart[1], Alexander Griekspoor[1], Valeria Berno[2], Kim Lakeman[1], Kees Jalink[3], Michael Mancini[2], Jacques Neefjes[1] and Rob Michalides[1,4]

Abstract
Resistance to tamoxifen is observed in half of the recurrences in breast cancer where the anti-estrogen tamoxifen acquires agonistic properties for transactivating ERα. In a previous study, we showed that Protein Kinase A-mediated phosphorylation of serine 305 of ERα results in resistance to tamoxifen. Now, we demonstrate that phosphorylation of serine 305 in ERα by Protein Kinase A leads to an altered orientation between ERα and its coactivator SRC-1, which renders the transcription complex active in the presence of tamoxifen. This altered orientation involves the C-termini of ERα and SRC-1, which required a prolonged AF-1 mediated interaction. This intermolecular reorientation as a result of PKA-mediated phosphorylation of ERα-serine 305 and tamoxifen binding provides a unique model for resistance to the anti-cancer drug tamoxifen.

Introduction

Tamoxifen is a highly effective anti-cancer drug in Estrogen Receptor alpha (ERα) positive breast cancer patients. In recurrent disease however, still half of the patients develop resistance where tamoxifen acquires agonistic properties for transactivation of ERα. Various mechanisms may account for insensitivity to tamoxifen, including activation of the Mitogen Activated Protein Kinase (MAPK), Protein Kinase A (PKA) and p21-activated kinase-1 (PAK-1) signaling pathways that show enhanced activity in tamoxifen-resistant breast tumors (Michalides *et al*., 2004;Gutierrez *et al*., 2005;Holm *et al*., 2006). These kinases may directly target ERα. However, the molecular details of how these events contribute to tamoxifen resistance remain elusive. Antagonists of ERα act by altering the orientation of the C-terminally located α-helix 12 of the Ligand Binding Domain (LBD) of ER (Brzozowski *et al*., 1997). In the agonist-bound state, cofactors bind to the pocket composed of helices 3, 4, 5 and 12 (Pike, 2006). Anti-estrogens induce a distortion in α-helix 12 covering this binding pocket, thereby preventing the association with the p160 family of coactivators (Shiau *et al*., 1998). These cofactors are essential to initiate transcription (Kamei *et al*., 1996) and include SRC-1 (or NcoA-1), SRC-2 (also known as TIF-2, GRIP1 or NcoA-2) and SRC-3 (also known as RAC3, ACTR, AIB1, P/CIP or TRAM) (Xu and Li, 2003). SRC-1 can interact with CREB-binding protein (CBP), as well as with both the N-terminal AF-1 and the C-terminal AF-2 domains of ERα (Metivier *et al*., 2001). The AF-1 and AF-2 domains cooperate in transactivation of ERα (Metivier *et al*., 2002; Dutertre and Smith, 2003). Activity of SRC-1 is modified by phosphorylation at multiple sites, two of which are attributed to MAPK activation (Rowan *et al*., 2000b). The SRCs can have different cellular properties: while SRC-1 and SRC-3 can be recruited to unliganded ERα, SRC-3 is more readily displaced from ERα in the presence of antagonists as compared to SRC-1 (Sharp *et al*, 2006). Overexpression of SRC-1 and SRC-3 is correlated with tamoxifen resistance in breast cancer patients (Osborne *et al*., 2003;Myers *et al*., 2004). Moreover, agonistic activity of tamoxifen is enhanced by overexpression of SRC-1 in normal uterus tissue (Shang and Brown, 2002).

Previously we reported that tamoxifen resistance mediated by Protein Kinase A (PKA) is caused by phosphorylation of serine 305 (S305) of ERα (Michalides *et al*., 2004). Recently, S305 of ERα was also reported to be the target of p21-activated kinase-1, PAK-1 (Wang *et al*., 2002), and its overexpression correlates with resistance to tamoxifen in breast cancer patients (Holm *et al*., 2006). These findings identify S305 as a crucial site in ERα that upon phosphorylation by either PKA or PAK-1 is responsible for resistance to tamoxifen. This phosphorylation switches tamoxifen from an antagonist to an agonist of ERα and affects conformational changes in ERα following binding to tamoxifen and other anti-estrogens (Michalides *et al*., 2004; Zwart *et al*., 2007). The mechanistic details of this process are, however, still unclear. Here, we report that PKA mediated phosphorylation of ERα

Department of Tumor Biology[1] and Cellular Biology[3], the Netherlands Cancer Institute, Plesmanlaan 121, 1066CX Amsterdam, the Netherlands
[2]Department of Molecular & Cellular Biology, Baylor College of Medicine, Houston, Texas, USA
[4]Correspondence: r.michalides@nki.nl

Keywords: Estrogen Receptor α/ SRC-1/ tamoxifen resistance/ Protein kinase A/ conformational control of transcription factors/FRET/ FLIM

Running title: Mechanism of PKA-induced resistance to tamoxifen

Categories: Molecular Biology of Disease; Signal transduction

alters the orientation between ERα and coactivator SRC-1, without affecting the overall binding between ERα and SRC-1 in tamoxifen-treated cells. We applied Fluorescent Resonance Energy Transfer (FRET) in living cells to visualize changes in orientation between ERα and SRC-1 following tamoxifen binding, which was dependent on phosphorylation of the PKA target S305 in ERα. This affected the recruitment of RNA polymerase II and led to estrogen receptor mediated transcription in cells treated with tamoxifen. In summary, tamoxifen resistance via PKA or PAK-1 occurs through phosphorylation of S305 in ERα, which alters its orientation towards coactivator SRC-1 and recruitment of RNA polymerase II, thereby stimulating estrogen receptor driven transcription by the anti-estrogen tamoxifen.

Results

PKA phosphorylates ERα-serine 305.

To follow the immediate interactions between ERα and its cofactor SRC-1 in cells transfected with tagged ERα and SRC-1 constructs, U2OS cells were used as a model cell line, since they are easily transfectable. However, the same results were also obtained in HeLa cells and in breast cancer cells T47D and MCF7 (Michalides *et al*., 2004; this study). To show that serine 305 is indeed phosphorylated by PKA, U2OS cells transfected with ERα were treated with 8-Br-cAMP to activate PKA. This resulted in a specific phosphorylation of ERα-serine 305, see Figure 1A. The mutant $ERα_{S305A}$, where the serine 305 was replaced with an alanine to prevent phosphorylation of that site by PKA, was not detected with the ERα-serine 305 specific antibody. The ERα-serine 305 phosphate specific antibody did not detect the putative phosphomimics of ERα-S305, ERαS305E or ERαS305D, where serine 305 was replaced with glutamate or aspartate, respectively. We therefor preferred wild-type ERα treated with PKA activators 8-Br-cAMP or forskolin, with $ERα_{S305A}$ as a control. The concentration of (anti)-estrogens used in the study were similar to those used in the previous study (Michalides *et al*., 2004), and were optimally effective for the levels of ERα expressed in the cells.

Phosphorylation of ERα-serine 305 by PKA does not influence overall binding to SRC-1.

Since ligand-induced activation of ERα is generally followed by binding to a coactivator, we hypothesized that insensitivity to tamoxifen by PKA-mediated phosphorylation of serine 305 (S305) would affect the binding between ERα and cofactor SRC-1. This was first investigated in a mammalian 2-hybrid (M2H) assay. To distinguish between the interaction of SRC-1 with AF-1 and/or AF-2 domains of ERα, the SRC-1 truncation mutant, aa 623-711 ($SRC\text{-}1_{623\text{-}711}$) was used that only binds to the ligand binding AF-2 domain of ERa, as described previously (Llopis *et al*., 2000), as well as the full length SRC-1 ($SRC\text{-}1_{FL}$), which interacts with both AF-1 and AF-2 domains of ERα (Metivier *et al*., 2001). Expression of the fusion proteins was confirmed by Western blotting (Supplementary Data, Figure S1). Chimeras of ERα and the transactivation domain of GAL4 (TA-ERα), as well as $SRC\text{-}1_{623\text{-}711}$ or $SRC\text{-}1_{FL}$ fused to the DNA binding domain of GAL4 (DBD-SRC-1) were co-transfected with a GAL4-responsive luciferase expression construct and Renilla luciferase construct as a transfection control (Figure 1B). In this assay luciferase activity is directly related to the binding between the two fusion proteins. $SRC\text{-}1_{623\text{-}711}$ interacted with ERα in the presence of E2 and this was only slightly increased by preincubation of the cells with PKA-activator 8-Br-cAMP (Figure 1B, left panel). No binding was observed under tamoxifen and ICI 182,780 conditions, also not in the presence of 8-Br-cAMP. The binding of full length SRC-1 was increased by E2 and, surprisingly, also by the partial antagonist tamoxifen (Figure 1B, right panel). Treatment with the full ERα-antagonist ICI 182,780 resulted in a loss in binding. ICI 182,780 not only inhibits ERα activity, but also induces degradation of ERα, and defined the inactive state of ERα in our measurements. The interaction between ERα and $SRC\text{-}1_{FL}$ was not influenced by 8-Br-cAMP under all tested conditions. These results indicated that PKA activation does not affect the overall binding between ERα and SRC-1. In addition, whereas binding of SRC-1 to the AF-2 domain of ERα is induced by E2 and was abrogated by tamoxifen (Llopis *et al*., 2000), the binding of SRC-1 to the AF-1 domain of ERα prevailed under hormone-depleted conditions and in the presence of tamoxifen, as was reported previously (Metivier *et al*., 2001).

In order to verify the M2H results in living cells and in a dynamic context, we visualized interactions between ERα and SRC-1 using Fluorescence Recovery After Photobleaching (FRAP) in U2OS cells. In FRAP, fluorophores in the region of interest are bleached using a high intensity laser beam and recurrence of fluorescence is followed in time, as described before (Stenoien *et al*., 2001) and illustrated in Supplemental data, Figure S2. The mobility of the fluorophore-tagged protein of interest, whether alone or in (transient) complex with interaction partners, can be monitored in this way. The statistics of the t1/2 recovery values are given in Figure 1C. $SRC\text{-}1_{623\text{-}711}$ interacts with the AF-2 domain of ERα . When expressing $SRC\text{-}1_{623\text{-}711}$ in the absence of ERα, the t1/2 value was

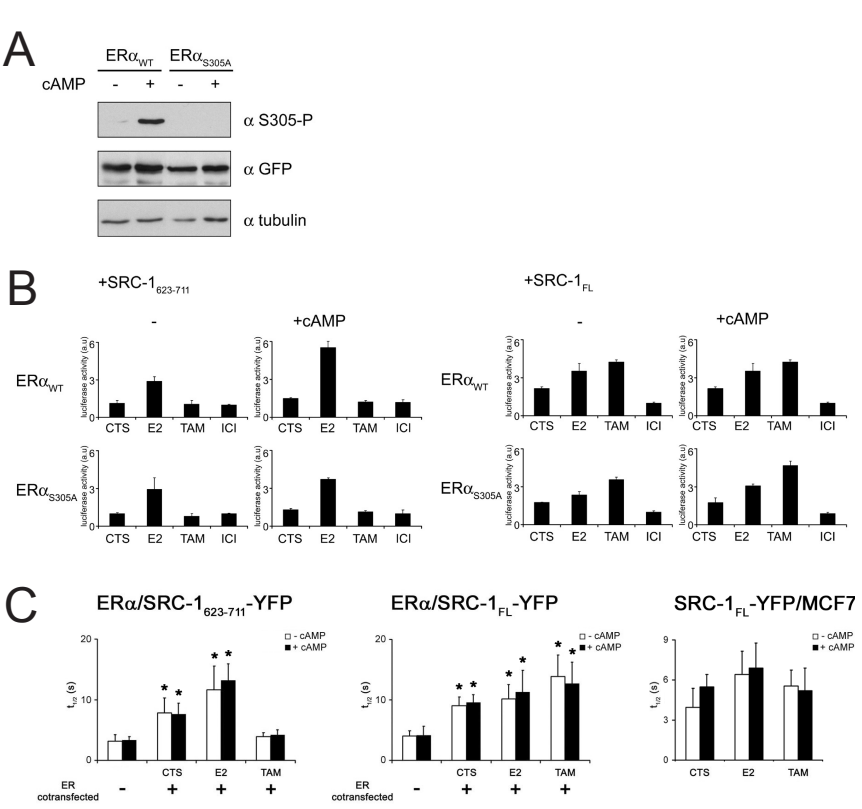


Figure 1: Binding between ERα and SRC-1 is not affected by PKA activation.

A. Characterization of S305-ERα as PKA target. U2OS cells were transfected with the wild-type YFP-ERα-CFP construct or the S305A mutant thereof, cultured in the presence or absence of 8-Br-cAMP and analyzed for S305 phosphorylation of wild-type ERα or the phospho-mutant of ERα. Anti-tubulin staining was used as a loading control, anti-GFP as an expression-control. Absence of the phosphorylated S305-ERα protein in the cells transfected with S305A, but its presence in the PKA treated cells transfected with wild-type indicates the inability to phosphorylate mutant ERα_{S305A} by PKA.

B. Mammalian 2 hybrid analysis of ERα/SRC-1 interactions. U2OS cells transfected with DBD-SRC-1 (623-711 or full length), TA-ERα (wt or S305A), GAL4-luciferase and Renilla luciferase were cultured in CTS containing medium only, or in the presence of 1 μM Estradiol (E2), 1 μM ICI 182,780 or 1 μM 4'OH-tamoxifen for 96 hours. 24 hours prior to analysis 100 μM 8-Br-cAMP was added where indicated. Luciferase activity was measured and related to ICI 182,780 values without cAMP for every transfectant and set to 1. Bars indicate standard deviations from 3 independent experiments.

C. FRAP analysis of ERα/SRC-1 interactions. U2OS cells were transfected with SRC-1$_{623-711}$-YFP (left panel) or SRC-1FL-YFP (middle panel) and ERα-CFP, MCF7 cells were transfected with SRC-1FL-YFP only (right panel). These were cultured in CTS containing medium and 1 μM Estradiol (E2) or 1 μM 4'OH-tamoxifen was added 15' prior to analysis were indicated. Cells were pretreated with 10 μM forskolin for 15 min where indicated. YFP was bleached and fluorescence intensities were followed in time in the bleach spot from which t1/2 (half-time to recovery) was calculated as described in Materials and Methods. Bars indicate standard deviations from >10 cells per condition. Student T-test was performed for each bar, compared to SRC-1$_{623-711}$-YFP or SRC-1FL-YFP expression alone. * = $p<0.05$

low (indicating rapid diffusion in the nuclear compartments) and was not changed after addition of E2 or tamoxifen (data not shown). When SRC-1$_{623-711}$ was coexpressed with ER, introduction of the hormone E2 decreased the mobility of SRC-1$_{623-711}$, suggesting interactions with ERα following binding to E2. The mobility of SRC-1$_{623-711}$ under conditions of CTS was slower than in the presence of tamoxifen, and was not affected by treatment with forskolin that activates PKA. The t1/2 recovery values for SRC-1$_{FL}$ indicated increased interactions between ERα and SRC-1$_{FL}$ under conditions of CTS, E2, and tamoxifen as well, since they were higher than the t1/2 recovery value of SRC-1$_{FL}$-YFP alone (Figure 1C, middle column). The latter was not affected by E2 or tamoxifen (data not shown). The mobility of SRC-1$_{FL}$-YFP in breast cancer MCF7 cells showed a similar pattern as was obtained in U2OS cells co-transfected with exogenous ERα (Figure 1C right column), indicating that the FRAP results are not cell type specific and are in U2OS cells with exogenous ERα comparable to the breast cancer MCF7 cells with an endogenous ERα only.

The combined results of the M2H and FRAP experiments indicated that SRC-1$_{FL}$ can interact with ERα in hormone depleted (CTS), as well as in E2 and tamoxifen-treated cells. They strongly suggested that the AF-1 domain of ERα is involved in binding under all three conditions, whereas the AF-2 domain is participating in binding only in the presence of E2. Importantly, PKA activation, which is known to induce tamoxifen resistance, did not influence the interaction between SRC-1 and ERα.

Phosphorylation of S305 by PKA alters the orientation between ERα and SRC-1 under tamoxifen conditions.

If binding is not affected by PKA-mediated phosphorylation of Erα-S305, does this phosphorylation have an effect on the mode of interaction between ERα and SRC-1? We investigated this by FRET (Fluorescence Resonance Energy Transfer) technology using confocal imaging in HeLa cells. FRET is the radiationless energy transfer from one fluorophore to the next and occurs when two dipole moments of overlapping fluorophores couple within a distance of ~80Å. Intermolecular FRET provides thereby a most direct method to study interactions between two pro-

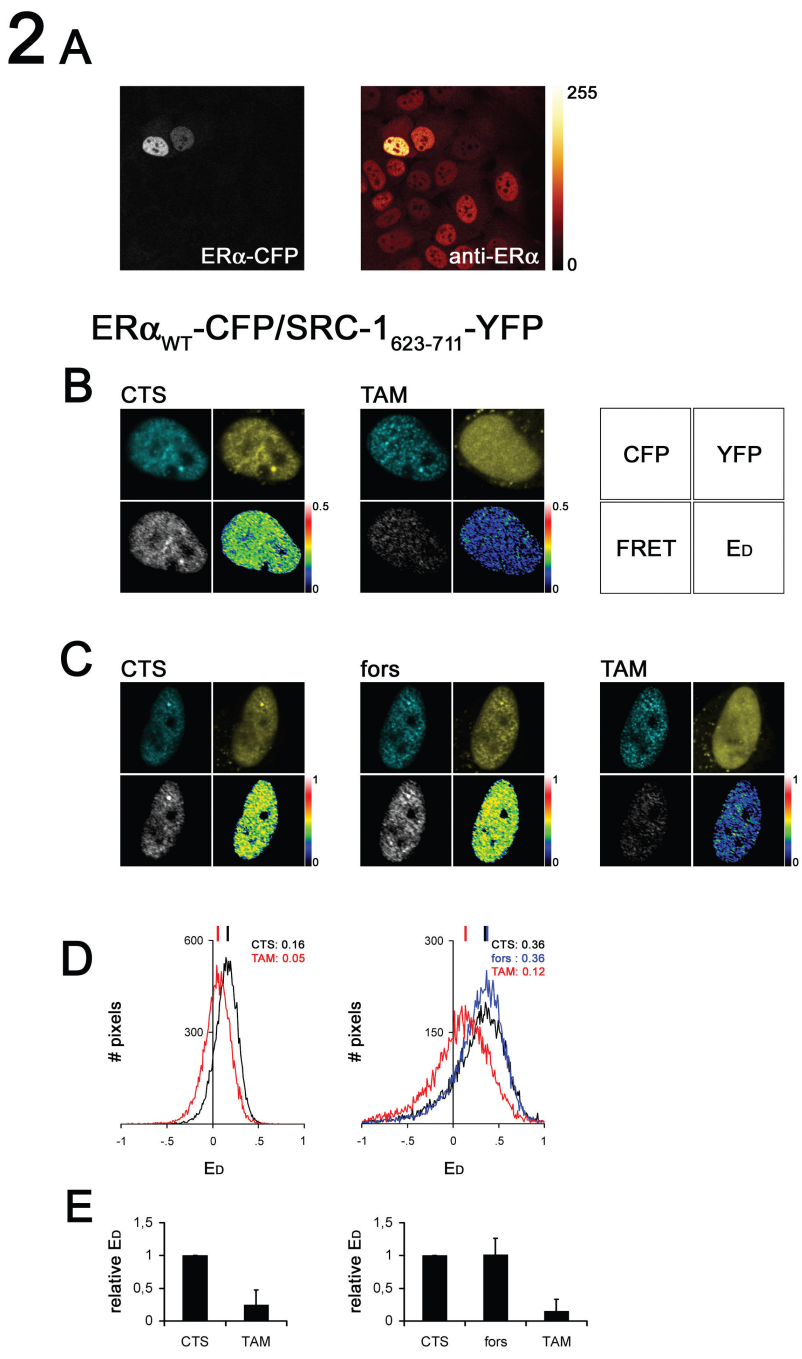


Figure 2: Orientation between ERα and SRC-1$_{623-711}$ is altered in the presence of tamoxifen and is independent of phophorylation of serine 305 of ERα by PKA.

A. Expression levels of ERα-CFP related to endogenous expression. MCF7 cells were transfected in ERα-CFP, fixed and stained for ERα. Cells with CFP-positive nuclei were compared to exclusively endogenous ER expressing cells. FRET measurements were performed on PRL array containing HeLa cells, transfected with ERα$_{wt}$-CFP and SRC-1$_{623-711}$-YFP (**B, C**). FRET images were generated from cells cultured in hormone-depleted (CTS) medium only (B and C, left panels) or after treatment with 10 µM forskolin prior to FRET measurements (C, middle panel). Subsequently, 1 µM 4'OH-tamoxifen (TAM) was added and after 15 min cells were imaged (B and C, right panels). FRET and donor FRET efficiency (E_D) were calculated as described in Materials and Methods. For each condition described in B and C, the raw E_D values from the whole nucleus were related to the total amount of pixels (**D**). Mean E_D is indicated and quantifications (**E**) are done on >10 independent measurements, where the E_D under CTS conditions is set to 1 for each experiment (relative E_D). Bars indicate standard deviations.

teins, and is strictly dependent on distance between the fluorophores as well as their relative orientations, allowing visualization of conformational changes within protein-protein complexes. In these experiments and in the FRAP experiments described above, we used cells with a 2-3 fold expression of exogenous ERα-CFP as compared to endogenous ERα expression in MCF-7 cells (see Figure 2A). FRET was detected between ERα-CFP and SRC-$1_{623\text{-}711}$-YFP (Figure 2B); here, excitation of CFP at 430nm yielded emission of YFP that, after correction of leak-through, only could have arisen from FRET (lower left panel). The observed FRET signal was normalized for the amount of CFP emission as is described in Materials and Methods, yielding the corrected donor FRET efficiency (E_D) that is presented in the lower right panel. E_D represents the FRET per donor-acceptor fluorophore pair and is independent of donor fluorescence. Under hormone-depleted conditions a high FRET donor efficiency was observed for ERα-CFP and SRC-$1_{623\text{-}711}$-YFP, which was strongly reduced by tamoxifen (Figure 2B), indicating that the interaction in CTS between ERα and SRC-$1_{623\text{-}711}$ was altered by tamoxifen. When FRET efficiency was quantified by determining the E_D per pixel as described in Materials and Methods, we observed that the average efficiency of 16% FRET between ERα-CFP and SRC-$1_{623\text{-}711}$-YFP under hormone depleted conditions was reduced to an average of 5% after addition of tamoxifen to this particular cell (Figures 2D) and others (Figure 2E). Note that the spread in pixel E_D values is due to contribution of noise. PKA activation by forskolin under conditions of CTS did not significantly influence FRET efficiency between ERα and SRC-$1_{623\text{-}711}$ (Figure 2C and quantified in Figure 2E). Subsequent treatment with tamoxifen still led to a substantial reduction in FRET efficiency. This indicated that PKA activation did not influence the binding between the AF-2 domain of ERα and SRC-$1_{623\text{-}711}$-YFP, which agrees with the results obtained by FRAP and M2H (Figure 1).

We next investigated whether PKA treatment had any effect on the orientation between full length SRC-1 and ERα using FRET (Figure 3). FRET between ERα and SRC-1_{FL} was less efficient as with SRC-$1_{623\text{-}711}$, which may be attributed to the much larger protein size of the full length SRC-1 and hence the larger distance between the fluorophores at the ends of the tagged proteins, but may also be the result of different orientation of the fluorophores. FRET between ERα-CFP and SRC-1_{FL}-YFP was detected in hormone-deprived cells and was reduced by tamoxifen (Figure 3A), supporting the FRAP experiments where these proteins could be found to interact under hormone-deprived conditions. The mean FRET efficiency of 9% in CTS was reduced to 3% when tamoxifen was added (Figure 3C). This is remarkable, since the M2H and FRAP experiments demonstrated that the interaction between ERα and SRC-1_{FL} was not affected by tamoxifen (Figure 1). This suggested that a loss of FRET under conditions of tamoxifen indicated an altered orientation between ERα and SRC-1, where the C-termini of ERα and SRC-1_{FL} that carry the fluorophores position differently in tamoxifen treated cells as under CTS conditions. We next investigated whether activation of PKA influenced this reorientation upon tamoxifen binding. PKA activation through forskolin had no effect on FRET efficiency under hormone-deprived conditions (Figure 3B). However, subsequent treatment with tamoxifen did not show alterations in FRET efficiency analogous to cells not pretreated with forskolin, indicating that the orientation between ERα and SRC-1_{FL} is stabilized by activation of PKA. The $ER\alpha_{S305A}$ mutant behaved similar as wild-type ERα under non-PKA stimulated conditions: forskolin treatment followed by tamoxifen still resulted in a loss of FRET (Figure 3D and Supplemental data S3). This indicates that phosphorylation of wild-type ERα-S305 by PKA affects the orientation between ERα and full length SRC-1 (quantified in Figures 3D and 3E). These data were verified in U2OS (not shown) and MCF7 cells (Supplemental data, Figure S4D, E and F), indicating that the results of these FRET experiments were cell type independent. These results were further confirmed by fluorescence lifetime imaging microscopy (FLIM), which is an alternative FRET approach (Zwart *et al*., 2005) (Supplemental data S4A, B and C). Taken together, these data showed that the orientation between ERα-CFP and SRC-1_{FL}-YFP is altered by tamoxifen, unless PKA phosphorylates S305 in ERα.

ERα interacts in the nucleus with SRC-1 irrespective of DNA promoter content.

Given the limits of resolution of the light microscope and the relatively low number of specific estrogen response elements (ERE) in the genome (Carroll *et al*., 2006), it is not possible to directly relate high FRET efficiency between ERα and SRC-1 to ERE-binding (Figures 3 and 4). Since the transcription function of ERα can be mediated by direct interaction with EREs at the promoters of target genes, we determined FRET signals in HeLa cells that contain a multicopy prolactin promoter/enhancer (PRL) DNA array containing natural ER binding sites. Transcription from this visible locus is regulated by ligand-bound ER, and ERα and recruited cofactors can be readily identified (Sharp *et al*., 2006). This permitted a clear distinction between defined ERE-associated ERα and SRC-1 events on the PRL array and in the remainder of the nucleus, as shown in Figures 3A and B (indicated by arrowheads). Here, we compared the FRET efficiency

on the PRL array with that throughout the remainder of the nucleus (Figure 3E). The levels of ERα-CFP, SRC-1-YFP proteins and FRET events were significantly higher on the PRL array than outside, as shown in Figures 3A and B. However, when FRET from these cells was related to the emission of the donor (E_D) to render the readout fluorophore concentration independent, similar E_D values were obtained on the array as compared to levels outside the array in the nucleus. Also, the effects on E_D of tamoxifen alone or in combination with forskolin on the PRL array were comparable with those detected outside the array (Figure 3E). These

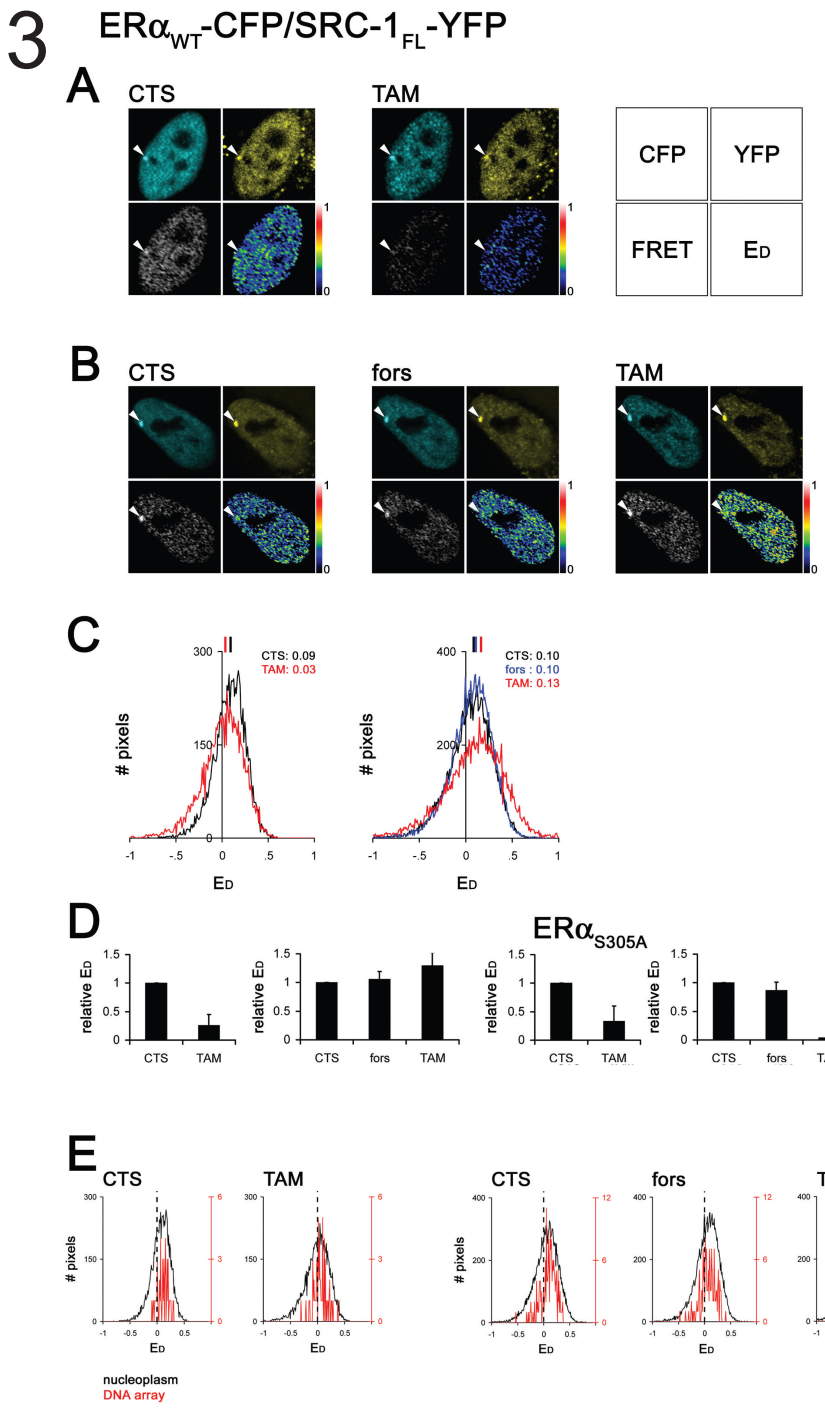


Figure 3: Orientation between ER and SRC-1FL¬ is altered by tamoxifen alone, but is stabilized by activation of PKA.

FRET experiments were performed analogous as described at Figure 2, now using SRC-1FL¬-YFP and wild-type ERα (**A-D**) or ERα$_{S305A}$ (D, right panel). Arrows indicate the PRL array (A, B), for which the raw E_D values (including noise) were related to the total amount of pixels and presented for both the PRL array (in red) and entire nucleus (in black) for the cells shown in Figures A and B (**E**).

results indicated that the interaction detected between ERα and SRC-1_{FL} on a genuine ER binding domain, the PRL array, reflects the interaction at other sites in the nucleus.

Phosphorylation of serine-305 of ERα by PKA enables recruitment of RNA polymerase II to the PRL transcription locus, enhancing transcription under tamoxifen conditions.

Genuine tamoxifen resistance would imply that the effect of PKA-induced phosphorylation of ERα-S305 on the positioning of SRC-1 and ERα following exposure to tamoxifen would lead to tamoxifen-mediated transactivation of ERα with recruitment of RNA polymerase II to the ERα/SRC-1 complex as a hallmark. Therefore, we investigated the RNA polymerase II recruitment in the PRL array containing cells that were transfected with ERα-CFP and SRC-1_{FL}-YFP and examined co-localization of ERα and SRC-1 with RNA polymerase II on the PRL array. Approximately half of the cells expressing both $ERα_{wt}$-CFP and SRC-1_{FL}-YFP showed co-localization with RNA-polymerase II on the PRL array under conditions of CTS and E2 (Figure 4A and quantified in 4B). The PRL array did show a more 'open', decondensed structure due to Estradiol (E2) when compared to hormone-depleted

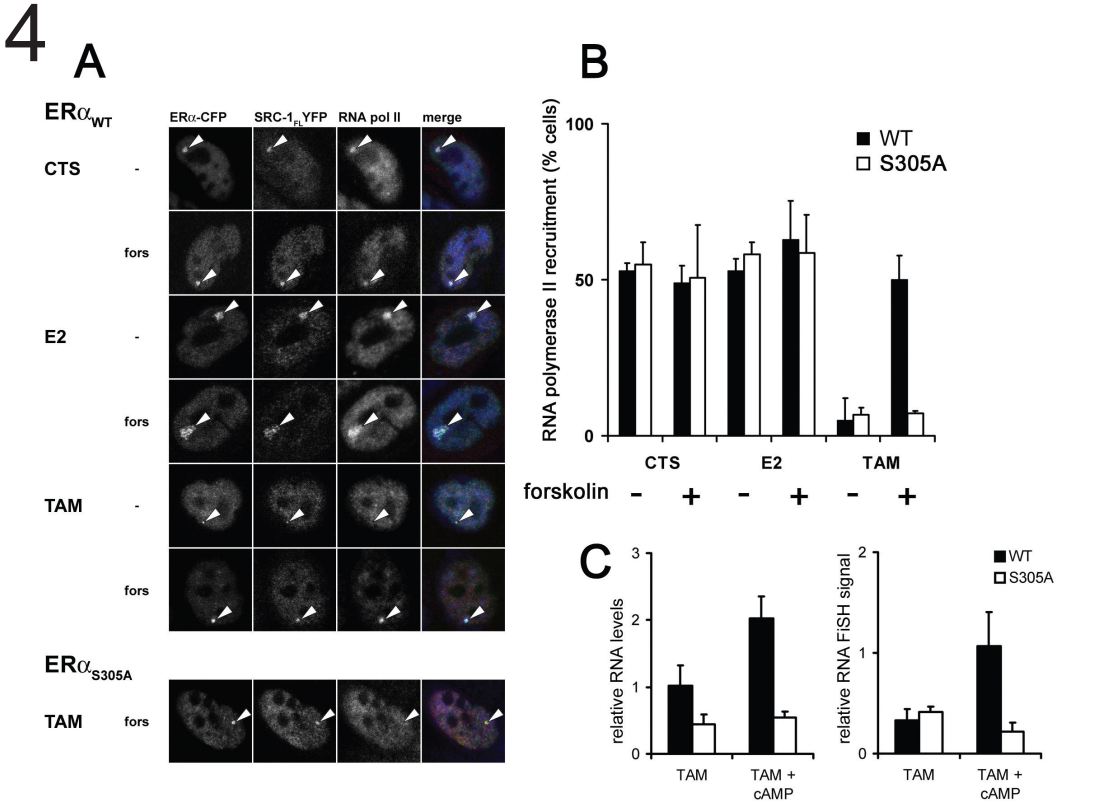


Figure 4: PKA-mediated phosphorylation of S305 of ERα is responsible for RNA polymerase II recruitment on the PRL array and for enhanced transcription of a hormone-responsive reporter gene under conditions of tamoxifen.

A. Staining for RNA polymerase II was performed on PRL array containing HeLa cells that were transfected with $ERα_{wt}$ or $ERα_{S305A}$-CFP and SRC1FL-YFP and cultured in hormone depleted (CTS) medium. Where indicated, they were pretreated with 10 μM forskolin. Subsequently cells were treated with 1 μM Estradiol (E2) or 1 μM 4'OH-tamoxifen for 2 hours and then fixed and stained for RNA Polymerase II. Arrowheads indicate the PRL array that was analyzed for RNA polymerase II staining.

B. Quantification of the RNA polymerase II signals on the PRL array under conditions as described in Figures 6A. Quantifications are from 3 independent experiments, n>40 cells each. Bars indicate standard deviations.

C. PKA-mediated phosphorylation of S305 on ERa enhances transcription of the PRL array under conditions of tamoxifen.

QPCR was performed on PRL array containing HeLa cells, transfected with $ERα_{wt}$-CFP or $ERα_{S305A}$-CFP, which were treated with 1 μM tamoxifen or left untreated (CTS). 16 hours prior to analysis 100 μM 8-Br-cAMP was added where indicated. mRNA levels were measured as described in Experimental Procedures, and related to CTS values which was set to 1. Bars indicate standard deviation from 2 independent experiments.

RNA FISH of the hormone responsive DsRed2 reporter gene behind the PRL-based promoter in PRL-Hela transfected with $ERα_{wt}$-CFP or $ERα_{S305A}$-CFP. 2 hours prior to analysis cells were treated with forskolin where indicated and subsequently with 1 μM 4'OH-tamoxifen. Signal intensity of the FISH DsRed2, as visualized by Alexa-546 is given. Bars indicate standard deviation from 2 independent experiments.

conditions (CTS). This open chromatin structure was previously reported to be tightly linked with increased transcriptional activity (Sharp *et al*., 2006). In our experiments, activation of PKA by forskolin did not affect co-localization of the three proteins (ERα, SRC-1 and RNA polymerase II) under conditions of CTS and E2. As reported previously (Sharp *et al*., 2006), tamoxifen-treated cells showed a more condensed PRL array, on which both ERα and SRC-1, but no RNA-polymerase II was recruited (Figure 4A). Strikingly, activation of PKA under tamoxifen conditions now resulted in recruitment of RNA polymerase II to the array, indicating that PKA activation influenced the orientation between ERα and SRC-1 such that RNA polymerase II recruitment to the PRL array is facilitated under tamoxifen conditions. The S305A mutant of ERα did not result in RNA polymerase II recruitment under identical conditions (Figure 4A and Supplementary Data S5). This indicates that RNA polymerase II recruitment to the ERα complex in tamoxifen-treated cells requires phosphorylation of ERα-S305 by PKA.
To directly investigate whether these events resulted in enhanced transcription, we measured transcription of the integrated DsRed2 reporter gene that is under control of the ER responsive elements on the PRL array (Sharp *et al*., 2006) by Quantitative RT-PCR and RNA FISH as described in Experimental Procedures (see Figure 4C). PKA activation led in tamoxifen-treated cells transfected with $ERα_{wt}$ to a two-fold increase in transcription of the DsRed2 gene as compared to tamoxifen alone, whereas no such effect was observed in cells transfected with $ERα_{S305A}$. Tamoxifen exposure resulted in a similar PKA induced increase in DsRed2 transcripts, which was specifically associated with the PRL array as shown by RNA FISH in cells transfected with wild-type ERα, but not in $ERα_{S305A}$ transfected cells.

Our results indicated that tamoxifen resistance is due to a change in the orientation between ERα and SRC-1, which was dependent on PKA-mediated phosphorylation of ERα-S305. This reorientation between the C-termini of ERα and $SRC\text{-}1_{FL}$ induced RNA polymerase II recruitment, resulting in enhanced transcription.

Interaction between ERα and AF-1 binding domain of SRC-1 is maintained under tamoxifen conditions.

Which domain outside the AF-2 binding domain on SRC-1 is responsible for the sustained interaction between ERα and the full length SRC-1 following tamoxifen exposure, as was observed in the FRET experiments? To study this, we determined co-localization of ERα-CFP, RNA Polymerase II and an AF-1 binding domain of SRC-1 (Onate *et al*.,1998; Metivier

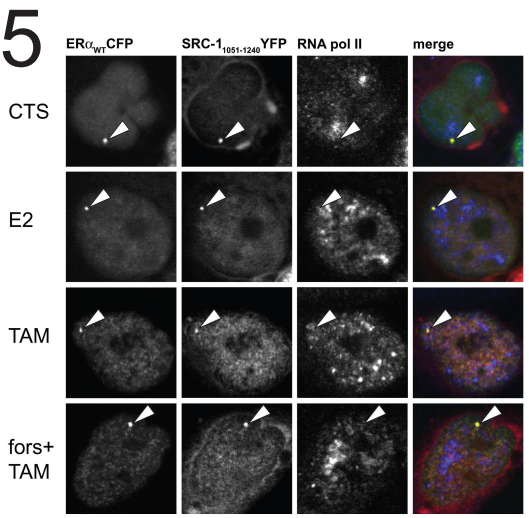


Figure 5: $SRC\text{-}1_{1051\text{-}1240}$-YFP recruitment to the PRL DNA array in the presence of tamoxifen.

Staining of RNA polymerase II was performed on PRL array containing HeLa cells, transfected with $ERα_{wt}$-CFP and $SRC1_{1051\text{-}1240}$-YFP and cultured in medium containing only CTS. Subsequently cells were treated with 1 μM E2 or 1 μM 4'OH-tamoxifen for 2 hours and then fixed and stained for RNA Polymerase II. Arrowheads indicate the PRL DNA array that was analyzed for RNA polymerase II staining.

et al., 2001; Webb *et al*., 1998; Glass *et al*., 2000). We reduced the SRC-1 fragment, which was previously reported to interact with the AF-1 of ERα by others (Metivier *et al*., 2001) to a $SRC\text{-}1_{1051\text{-}1240}$ fragment still showing interaction with the AF-1 of ERα (data not shown). We observed co-localization of ERα-CFP and $SRC\text{-}1_{1051\text{-}1240}$-YFP on the PRL array under conditions of CTS, E2 and tamoxifen, and also under tamoxifen conditions after PKA activation (Figure 5). No RNA Polymerase II was recruited under these conditions, which is explained by a dominant-negative function of the $SRC\text{-}1_{1051\text{-}1240}$ mutant. This may also be indicated by the condensed shape of the PRL-array in cells, also in the presence of E2, which is representative for the lack of transcriptional activity (Sharp *et al*., 2006).

The condensed shape of the PRL array in the presence of E2 when ERα was co-expressed with the dominant negative $SRC\text{-}1_{1051\text{-}1240}$ mutant also indicated that other endogenous SRCs do not compensate or otherwise influence our measurements. The combined results indicated that PKA mediated phosphorylation of ERα-S305 in the presence of tamoxifen resulted in a reorientation between the carboxy-termini of ERα and SRC-1, whereas the binding is sustained via an interaction between ERα and the AF-1 binding domain of SRC-1 in $SRC\text{-}1_{1051\text{-}1240}$. This altered orientation between the C-termini of ERα and SRC-1 resulted in RNA Polymerase II recruitment and transcriptional activity under tamoxifen conditions and explains how PKA activation can result in tamoxifen resistance.

Discussion

Regulated gene expression is achieved through the coordinated assembly of transcription factors, co-factors and the basal transcription machinery to transcription start sites, and demands a spatio-temporal coordination of interactions between these components. Traditional models of transcription tend to be static and depend on overall interactions measured by various kinds of binding assays, whereas the generation of transcription factor complexes requires a fine-tuned recruitment of components depending mainly on affinity of interfaces. The present study shows that the orientation of a tamoxifen-bound ERα transcription factor towards its coactivator SRC-1 is altered by PKA-mediated phosphorylation of S305 in the hinge region of ERα. This reorientation is responsible for RNA Polymerase II recruitment and ER dependent transcription in the presence of tamoxifen, as is illustrated in Figure 6. This reorientation was observed by a direct intermolecular FRET in living cells (Figures 2 and 3) that measures distance and/or orientation between the two fluorescently-tagged proteins. Other methods, such as M2H and FRAP (Figure 1) measure protein- protein interactions respectively interactions with more static complexes and stability of these complexes. These M2H and FRAP approaches did not show an effect of PKA on overall binding between ERα and SRC-1 under tamoxifen conditions. However, this PKA-mediated reorientation of ERα leads to recruitment of RNA polymerase II and to enhanced transcription from a hormone-responsive reporter gene (Figure 4). Our data indicate that the orientation of interfaces between ERα and SRC-1 in the transcription complex is crucial for efficacy of transcription and provides a molecular mechanism for tamoxifen resistance.

We found no differences in the FRET efficiency resulting from the interactions of ERα with SRC-1 on the PRL array as compared to FRET signals scattered in the nucleoplasm (Figure 3E). This indicates that ERα/SRC-1 interactions can be visualized throughout the nucleus, and that their relative orientations are unaltered by DNA binding. Possibly such complexes are not assembling at the transcription start sites but exist as preformed complexes in the nucleoplasm, as also suggested by others (Zheng *et al*., 2005). At present, it is technically impossible to determine if the nucleoplasmic hot spots are sites of active genes containing EREs, or non-promoter-associated EREs.

The PKA-mediated phosphorylation of S305 in the hinge region of ERα is responsible for a reorientation of the C-terminus of ERα under tamoxifen conditions, which we measured by FRET using C-terminally tagged ERα-CFP and SRC-1-YFP constructs (Figures 2 and 3). This reorientation alters the interaction between the C-termini of ERα and SRC-1 and depends on prolonged association via AF-1 of ERα (Figure 5). This was inferred from the absence of interactions between the AF-2 binding SRC-1 fragment and ERα under tamoxifen conditions. In addition, this AF-2/SRC-1 interaction was also not induced by PKA activation (Figures 1B, 1C and 2), whereas the AF-1 binding SRC-1 fragment did interact with ERα under tamoxifen conditions (Figure 5). Our results thus support previous findings that AF-1 binding is a prerequisite for resistance to tamoxifen (Glaros *et al*., 2006), whereas functional synergy between AF-1 and AF-2 enhances SRC-1 recruitment and subsequent transcription (Metivier *et al*., 2001). Since the PKA effect on orientation is visualized only in the presence of tamoxifen, and not under conditions of CTS, the AF-1 domain should be regarded as a ligand dependent (in this case tamoxifen-dependent) transactivation domain that requires PKA activation. The AF-2 binding fragment of the SRC-1 construct that we used in this study as an AF-2 probe, encompasses aa 623-711 and contains two LXXLL motives that interact with the cofactor binding pocket in the AF-2 of the ERα-LBD (Llopis *et al*., 2000). The results with this AF-2 probe in our M2H and FRAP experiments indicate that it binds to ERα under conditions of E2 and CTS, but not in the presence of tamoxifen. This binding was not influenced by activation of PKA. The full-length SRC-1_{FL}, however, binds to ERα under all three conditions when measured by M2H and FRAP, and was also observed on the PRL array in colocalization studies (Sharp *et al*., 2006) and FRET (Figure 3) as was also the case for the AF-1 binding SRC-$1_{1051-1240}$ fragment (Figure 5). This binding is also not affected by PKA activation. Since SRC-1_{FL} binds to both AF-1 and AF-2 domains of ERα (Metivier *et al*., 2001), and SRC-$_{623-711}$ only to the AF-2 domain, our results indicate that the AF-1 functional core in ERα, which is positioned at the start of the B-domain (aa 39-45 of ERα) (Metivier *et al*., 2001), is involved in the interaction between ERα and the aa 1051-1240 region of SRC-1 in tamoxifen-treated cells. Indeed, an SRC-1 mutant, previously described to bind the AF-1 region of ER (Metivier *et al*., 2001) was still capable interaction with ER on the PRL array in the presence of tamoxifen (Figure 5). Interaction between this AF-1 helical core and SRC-1 has been reported to be essential for ERα activity in the presence of tamoxifen (Glaros *et al*., 2006) and is most likely involved in the PKA-mediated reorientation between ERα and SRC-1 that we observed in our experiments under tamoxifen conditions. The outcome of our M2H and FRAP experiments, that measure interactions between ERα and SRC-1_{FL} molecules, was not influenced by tamoxifen. The outcome of the FRET experiments that measure distance and orientation between them, was however, affected by tamoxifen. From these results, we concluded that the orientation between the C-termini

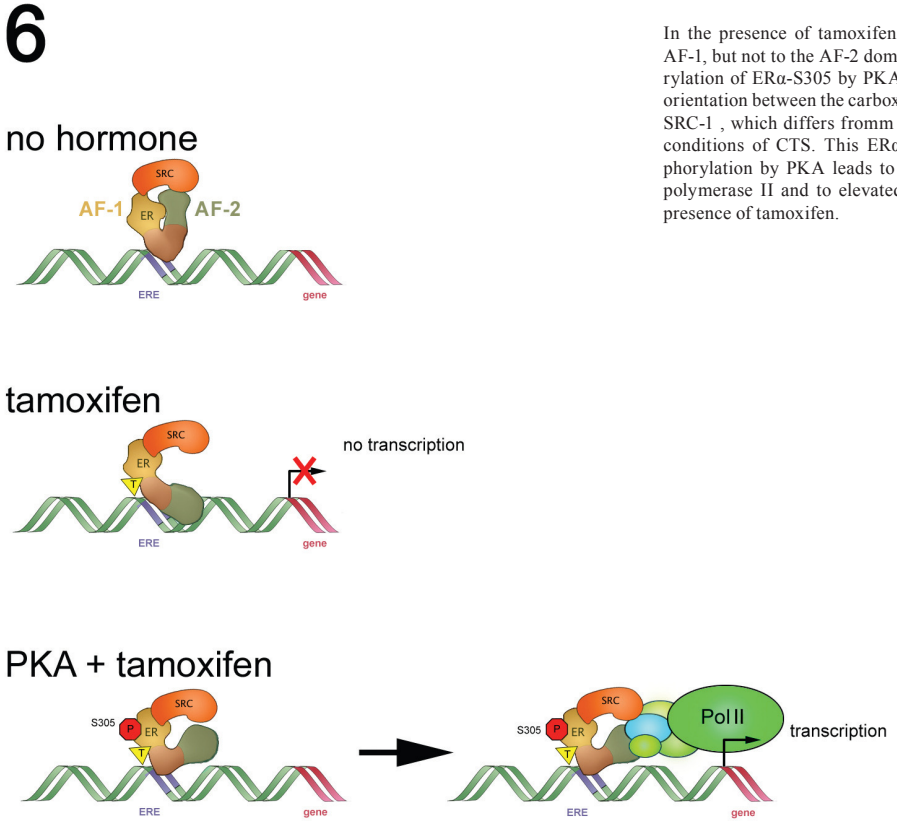


Figure 6: Model of the molecular mechanism of the PKA- or PAK1-induced tamoxifen resistance.

In the presence of tamoxifen, SRC-1 binds to the AF-1, but not to the AF-2 domain of ERα. Phosphorylation of ERα-S305 by PKA results in an altered orientation between the carboxy-termini of ERα and SRC-1 , which differs fromm the orientation under conditions of CTS. This ERα-S305-specific phosphorylation by PKA leads to recruitment of RNA polymerase II and to elevated transcription in the presence of tamoxifen.

of ERα and SRC-1_{FL}, rather than the interaction between the two proteins, was altered by tamoxifen. This tamoxifen-associated alteration is prevented by phosphorylation of S305 of ERα by PKA, which stabilizes in the presence of tamoxifen the orientation towards SRC-1 as it appears under CTS conditions (Figure 3 and Supplemental data S4). These findings led to a model where PKA-mediated phosphorylation of S305 results in a conformational state of ERα by which the orientation between ERα and SRC-1 facilitates recruitment of RNA polymerase II under conditions of tamoxifen. The effect of PKA on the conformation of ERα involves most likely the reorientation between the N- and C termini of ERα that we have observed by intramolecular FRET as has been reported before (Michalides *et al*., 2004). This intramolecular change was dependent on PKA-mediated phosphorylation of S305 and resulted in enhanced transactivation of ERα and tamoxifen dependent proliferation after PKA activation. In tamoxifen resistant ER positive patients, PKA activity was found increased, underlining the clinical relevance of these findings. The results of the present study strongly indicate that the change of ERα conformation upon PKA activation results in a permissive orientation between ERα and SRC-1 that facilitates transcription under tamoxifen conditions. Besides the phosphorylation of direct target sites in ERα, the phosphorylation of SRC-1 (Rowan *et al*., 2000a) and reduced association between ERα and transcriptional corepressors NCoR and SMRT (Wagner *et al*., 1998) may contribute to PKA-mediated resistance to antiestrogens. Since the PKA-induced reorientation, the RNA Polymerase II recruitment and enhanced transcription were not observed when the $ERα_{S305A}$ mutant was used (Figures 3D and supplemental Figure S3), we conclude that phosphorylation of S305 by PKA is the main target for PKA induced tamoxifen resistance that may still act in conjunction with phosphorylation of SRC-1 and NCoR/SMRT.

The reorientation of the C-terminus of tamoxifen-bound ERα towards SRC-1 that is induced by either PKA or PAK-1 mediated phosphorylation of S305 in the hinge region of ERα, provides a unique model for resistance to tamoxifen. It demonstrates that the effect of interacting agents can be nullified by activation of other signaling pathways, adding to the complexity of estrogen mediated transcriptional events and complicating interfering strategies. This

mechanism also provides a framework for selection and development of agents that are insensitive to these modifications on ERα and contributes to identification of conditions for tamoxifen resistance in breast cancer patients.

Materials and methods

Plasmids, cell culture and transfections

Human osteosarcoma U2OS, MCF7 and Hela cells were cultured in DMEM medium in the presence of 10% FCS and standard antibiotics. Cells containing ERα were cultured in phenol red-free DMEM medium containing 5% charcoal treated serum (CTS, Hyclone) 48 hours prior to analysis.
For characterization of the ERα-S305 phosphorylation of ERα by PKA, U2OS cells were transfected with the YFP-ERα-CFP construct or the S305A variant thereof (Michalides *et al*, 2004), treated with 100 μM 8-Br-cAMP (Sigma) and analyzed by Western blotting using antibodies against GFP (van Ham *et al*., 1997), against tubulin (Sigma) or against phospho-S305-ERα (Upstate, USA). Cloning strategies are described in the Supplemental data section.

Mammalian 2-hybrid assay

U2OS cells were cultured in 12 well plates 96 hours prior to analysis. 24 hours later cells were transfected using PEI (Polyethylenimine, MW 25kDa (Polysciences Inc.)) (Boussif *et al*., 1995) with TA-ERα_{wt} or TA-ERα_{S305A} (0.5μg), DBD-SRC-1-YFP (full length or aa 623-711) (0.5μg), GAL4 responsive Luciferase reporter construct (0.5μg) and ER-insensitive Renilla luciferase construct (1ng) as control for transfection efficiency (Michalides *et al*., 2004). Four hours after transfection, medium was replaced with Dulbecco's medium without phenol red, supplemented with 5% Charcoal Treated Serum (CTS, Hyclone) and cultured in the absence or presence of E2, ICI 182,780 (Tocris) or 4'OH-tamoxifen (Sigma) at a final concentration of 1 μM. 24 hours prior to analysis, medium with (anti-) estrogens was replaced and 8-Br-cAMP (Sigma) was added where indicated at a final concentration of 100 μM. Luciferase activity was determined as described previously (Bindels *et al*., 2002).

Fluorescence recovery after Photobleaching (FRAP) is described in the Supplemental data section.

FRET imaging by sensitized emission

HeLa cells were cultured on coverslips for 48 hours before imaging. 24 hours prior to imaging cells were transfected with the constructs indicated and medium was replaced with Dulbecco's medium without phenol red, supplemented with CTS. Mel JuSo cells, stably transfected with pcDNA3 constructs containing only CFP or YFP were included to the culture for leak-through corrections and internal controls. Coverslips were placed in 2 ml bicarbonate/Hepes-buffered saline and analyzed in a heated tissue culture chamber at 37°C under 5% CO2. Where indicated forskolin was added at a final concentration of 10 μM for 15'. FRET between CFP and YFP molecules was determined by calculating the sensitized emission (the YFP emission upon CFP excitation) using separately acquired donor and acceptor images as described previously (Zwart *et al*., 2005). In short, images were acquired on a TCS-SP2 confocal microscope (Leica). Three images were collected: CFP (excited at 430nm and detected between 470 and 490nm); indirect YFP (excited at 430nm and detected between 528 and 603nm) and direct YFP (excited at 514nm and detected between 528 and 603nm). Because of considerable overlap of CFP and YFP spectra, YFP emission was corrected for leak-through of CFP emission, and for direct excitation of YFP during CFP excitation. FRET was calculated using correction factors obtained from cells expressing either CFP or YFP alone, which were included for every image, as described before (van Rheenen *et al*., 2004). Then the apparent donor FRET efficiency (E_D) was calculated by relating the FRET to the total emission of the donor cell, after which the E_D picture was overlaid with a false color look up table. Using these methods, differences in FRET efficiency can be measured with an accuracy of 0.5% (Zwart *et al*., 2005). For graphic representation, the E_D was calculated for each pixel from the raw data files of the represented cell, and was exported to Microsoft Excel. Here, the amount of pixels was related to the corresponding E_D, and plotted in a histogram (Zwart *et al*., 2005).

RNA Polymerase II recruitment assay

For CLSM analysis prolactin promoter/enhancer (PRL) array containing HeLa cells (Sharp *et al*., 2006) were cultured in Dulbecco's medium containing CTS and were transfected with ERα_{wt}-CFP or ERα_{S305A}-CFP and SRC-1_{FL}-YFP or the aa 1051-1240 truncation mutant thereof, using PEI. After 4 hours the medium was replaced with Dulbecco's medium without phenol red supplemented with 5% CTS. Cells were cultured in CTS only or supplemented with 10 μM forskolin for 15 min. Subsequently, cells were treated for 2 hours with 1

μM Estradiol, 1 μM 4'OH-tamoxifen or left untreated, thereafter fixed with 3.7% formaldehyde in PBS and subsequently stained with anti-RNA polymerase II antibody 8WG16 (Covanche Research Products, Inc.) and secondary antibodies conjugated to Alexa 633 (Molecular Probes, Leiden, The Netherlands). Images were taken with a Leica TCS SP2 System equipped with a 63 x oil emersion objective. CFP was excited at 458 nm, and emission measured at 460-500 nm. YFP was excited at 514 nm, emission measured at 528-600 nm. Alexa 633 was excited at 633 nm, emission measured at 645-720 nm.

Quantitative RT-PCR and RNA FISH

Prolactin promoter/enhancer (PRL-) array containing HeLa cells (Sharp *et al*., 2006) were transfected with $ER\alpha_{wt}$-CFP or $ER\alpha_{S305A}$-CFP using electroporation, and subsequently cultured in Dulbecco's medium containing CTS. Immediately after seeding the cells, 1 μM 4'OH-tamoxifen was added or the cells were left untreated. After 6 hours, 8-Br-cAMP was added where indicated at a final concentration of 100 μM. After 16 hours, cells were lysed and RNA was extracted using Trizol (Invitrogen) according to the manufacturers protocol. RNA was reverse transcribed using SuperScript(tm) III Reverse Transcriptase (Invitrogen), on which QPCR was performed using CYBR Green (Applied Biosystems), according to the manufacturers protocols. The DsRed2 cDNA was amplified with forward primer 5' CCAGTTCCAGTACGGCTCCA and reverse primer 5' GCCGTCCTCGAAGTTCATCA. As a control, the observed DsRed2 signal was related to beta actin RNA levels, using a forward primer 5' CCTGGCACCCAGCACAAT and reverse primer 5' GGGCCGGACTCGTCATACT.
RNA FISH was performed as described previously (Sharp *et al*., 2006). PRL array containing HeLa cells were transfected with either CFP-$ER\alpha_{wt}$ or CFP-$ER\alpha_{S305A}$ and treated 2 hours before analysis with 10 μM forskolin for 15 minutes, followed by 1 μM 4'OH-tamoxifen or treated with 4'OH-tamoxifen only. The cells were stained with an antibody against ERα (Clone 60C, Upstate) and RNA FISH for DsRed2 transcripts was performed as described previously (Sharp *et al*., 2006). Informative arrays were analyzed for the Alexa-546 signal intensity of DsRed2 transcripts.

Acknowledgements

We thank Lennert Janssen for assistance in generating the chimeric mutants of ERα and SRC-1, dr. Rene Bernards (NKI) for the kind supply of plasmids pPC86, pPC97 and pCMV-SRC-1, Anja Duursma for help with the Q-RT-PCR, dr. Jacco van Rheenen for advice on the FRET procedures, Coenraad Kuijl for help with FRAP analysis and dr. Mariska Rondaij for critically reading of this manuscript and Mrs Maureen G. Mancini for technical advice on the PRL-HeLa cells. This study was supported by grant NKI 2005-3388 of the Dutch Cancer Society.

References

Bindels EM, Lallemand F, Balkenende A, Verwoerd D, and Michalides R (2002) Involvement of G1/S cyclins in estrogen-independent proliferation of estrogen receptor-positive breast cancer cells. Oncogene 21: 8158-8165.

Boussif O, Lezoualc'h F, Zanta MA, Mergny MD, Scherman D, Demeneix B, and Behr JP (1995) A versatile vector for gene and oligonucleotide transfer into cells in culture and *in vivo*: polyethylenimine. Proc Natl Acad Sci U S A 92: 7297-7301.

Brzozowski AM, Pike AC, Dauter Z, Hubbard RE, Bonn T, Engstrom O, Ohman L, Greene GL, Gustafsson JA, and Carlquist M (1997) Molecular basis of agonism and antagonism in the oestrogen receptor. Nature 389: 753-758.

Carroll JS, Meyer CA, Song J, Li W, Geistlinger TR, Eeckhoute J, Brodsky AS, Keeton EK, Fertuck KC, Hall GF, Wang Q, Bekiranov S, Sementchenko V, Fox EA, Silver PA, Gingeras TR, Liu XS, and Brown M (2006) Genome-wide analysis of estrogen receptor binding sites. Nat Genet 38:1289-1297.

Dutertre M and Smith CL (2003) Ligand-independent interactions of p160/steroid receptor coactivators and CREB-binding protein (CBP) with estrogen receptor-alpha: regulation by phosphorylation sites in the A/B region depends on other receptor domains. Mol Endocrinol 17: 1296-1314.

Glaros S, Atanaskova N, Zhao C, Skafar DF, and Reddy KB (2006) Activation function-1 domain of estrogen receptor regulates the agonistic and antagonistic actions of tamoxifen. Mol Endocrinol 20: 996-1008.
Glass CK and Rosenfeld MG (2000) The coregulator exchange in transcriptional functions of nuclear receptors. Genes Dev 14: 121-141.

Gutierrez MC, Detre S, Johnston S, Mohsin SK, Shou J, Allred DC, Schiff R, Osborne CK, and Dowsett M (2005) Molecular changes in tamoxifen-resistant breast cancer: relationship between estrogen receptor, HER-2, and p38 mitogen-activated protein kinase. J Clin Oncol 23: 2469-2476.

Holm C, Rayala S, Jirstrom K, Stal O, Kumar R, and Landberg G (2006) Association between Pak1 expression and subcellular localization and tamoxifen resistance in breast cancer patients. J Natl Cancer Inst 98: 671-680.

Kamei Y, Xu L, Heinzel T, Torchia J, Kurokawa R, Gloss B, Lin SC, Heyman RA, Rose DW, Glass CK, and Rosenfeld MG (1996) A CBP integrator complex mediates transcriptional activation and AP-1 inhibition by nuclear receptors. Cell 85: 403-414.

Llopis J, Westin S, Ricote M, Wang Z, Cho CY, Kurokawa R, Mullen TM, Rose DW, Rosenfeld MG, Tsien RY, and Glass CK (2000) Ligand-dependent interactions of coactivators steroid receptor coactivator-1 and peroxisome proliferator-activated receptor binding protein with nuclear hormone receptors can be imaged in live cells and are required for transcription. Proc Natl Acad Sci U S A 97: 4363-4368.

Metivier R, Penot G, Flouriot G, and Pakdel F (2001) Synergism between ERalpha transactivation function 1 (AF-1) and AF-2 mediated by steroid receptor coactivator protein-1: requirement for the AF-1 alpha-helical core and for a direct interaction between the N- and C-terminal domains. Mol Endocrinol 15: 1953-1970.

Metivier R, Stark A, Flouriot G, Hubner MR, Brand H, Penot G, Manu D, Denger S, Reid G, Kos M, Russell RB, Kah O, Pakdel F, and Gannon F (2002) A dynamic structural model for estrogen receptor-alpha activation by ligands, emphasizing the role of interactions between distant A and E domains. Mol Cell 10: 1019-1032.

Michalides R, Griekspoor A, Balkenende A, Verwoerd D, Janssen L, Jalink K, Floore A, Velds A, van't Veer L, and Neefjes J (2004) Tamoxifen resistance by a conformational arrest of the estrogen receptor alpha after PKA activation in breast cancer. Cancer Cell 5: 597-605.

Myers E, Fleming FJ, Crotty TB, Kelly G, McDermott EW, O'higgins NJ, Hill AD, and Young LS (2004) Inverse relationship between ER-beta and SRC-1 predicts outcome in endocrine-resistant breast cancer. Br J Cancer 91: 1687-1693.

Onate SA, Boonyaratanakornkit V, Spencer TE, Tsai SY, Tsai MJ, Edwards DP, and O'Malley BW (1998) The Steroid Receptor Coactivator-1 Contains Multiple Receptor Interacting and Activation Domains That Cooperatively Enhance the Activation Function 1 (AF1) and AF2 Domains of Steroid Receptors. J Biol Chem 273: 12101-12108.

Osborne CK, Bardou V, Hopp TA, Chamness GC, Hilsenbeck SG, Fuqua SA, Wong J, Allred DC, Clark GM, and Schiff R (2003) Role of the estrogen receptor coactivator AIB1 (SRC-3) and HER-2/neu in tamoxifen resistance in breast cancer. J Natl Cancer Inst 95: 353-361.

Pike AC (2006) Lessons learnt from structural studies of the oestrogen receptor. Best Pract Res Clin Endocrinol Metab 20: 1-14.

Rowan BG, Garrison N, Weigel NL, and O'Malley BW (2000a) 8-Bromo-cyclic AMP induces phosphorylation of two sites in SRC-1 that facilitate ligand-independent activation of the chicken progesterone receptor and are critical for functional cooperation between SRC-1 and CREB binding protein. Mol Cell Biol 20: 8720-8730.

Rowan BG, Weigel NL, and O'Malley BW (2000b) Phosphorylation of steroid receptor coactivator-1. Identification of the phosphorylation sites and phosphorylation through the mitogen-activated protein kinase pathway. J Biol Chem 275: 4475-4483.

Shang Y and Brown M (2002) Molecular determinants for the tissue specificity of SERMs. Science 295: 2465-2468.

Sharp ZD, Mancini MG, Hinojos CA, Dai F, Berno V, Szafran AT, Smith KP, Lele TT, Ingber DE, and Mancini MA (2006) Estrogen-receptor-{alpha} exchange and chromatin dynamics are ligand- and domain-dependent. J Cell Sci 119: 4101-4116.

Shiau AK, Barstad D, Loria PM, Cheng L, Kushner PJ, Agard DA, and Greene GL (1998) The structural basis of estrogen receptor/coactivator recognition and the antagonism of this interaction by tamoxifen. Cell 95: 927-937.

Stenoien DL, Patel K, Mancini MG, Dutertre M, Smith CL, O'Malley BW, and Mancini MA (2001) FRAP reveals that mobility of oestrogen receptor a is ligand- and proteasome-dependent. Nat Cell Biol 3, 15 - 23.

van Ham SM, Tjin EP, Lillemeier BF, Gruneberg U, van Meijgaarden KE, Pastoors L, Verwoerd D, Tulp A, Canas B, Rahman D, Ottenhoff TH, Pappin DJ, Trowsdale J, and Neefjes J (1997) HLA-DO is a negative modulator of HLA-DM-mediated MHC class II peptide loading. Curr Biol 7: 950-957.

van Rheenen J, Langeslag M, and Jalink K (2004) Correcting confocal acquisition to optimize imaging of fluorescence resonance energy transfer by sensitized emission. Biophys J 86: 2517-2529.

Wagner BL, Norris JD, Knotts TA, Weigel NL, and McDonnell DP (1998) The nuclear corepressors NCoR and SMRT are key regulators of both ligand- and 8-bromo-cyclic AMP-dependent transcriptional activity of the human progesterone receptor. Mol Cell Biol 18: 1369-1378.

Wang RA, Mazumdar A, Vadlamudi RK, and Kumar R (2002) P21-activated kinase-1 phosphorylates and transactivates estrogen receptor-alpha and promotes hyperplasia in mammary epithelium. EMBO J 21: 5437-5447.

Webb P, Nguyen P, Shinsako P, Anderson C, Feng W, Nguyen MP, Chen D, Huang S, Subramanian S, McKinerney E, Katzenellenbogen BS, Stallcup MR, and Kushner PJ (1998) Estrogen Receptor Activation Function 1 Works by Binding p160 Coactivator Proteins. Mol Endocrinol 12: 1605-1618.

Xu J and Li Q (2003) Review of the *in vivo* functions of the p160 steroid receptor coactivator family. Mol Endocrinol 17: 1681-1692.

Zheng FF, Wu RC, Smith CL, and O'Malley BW (2005) Rapid estrogen-induced phosphorylation of the SRC-3 coactivator occurs in an extranuclear complex containing estrogen receptor. Mol Cell Biol 25: 8273-8284.

Zwart W, Griekspoor A, Kuijl C, Marsman M, van Rheenen J, Janssen H, Calafat J, van Ham M, Janssen L, van Lith M, Jalink K, and Neefjes J (2005) Spatial separation of HLA-DM/HLA-DR interactions within MIIC and phagosome-induced immune escape. Immunity 22: 221-233.

Zwart W, Griekspoor A, Rondaij M, Verwoerd D, Neefjes J, and Michalides R (2007) Classification of anti-estrogens according to intramolecular FRET effects on phospho-mutants of estrogen receptor a. Mol Cancer Ther 6:1526-1533.

Supplemental Data

Supplementary materials and methods

Fluorescent constructs

For the construction of SRC-$1_{623-711}$-YFP fragment of SRC-1 was amplified by PCR from pCMV-SRC-1 (Zwijsen *et al*., 1997) (kind gift from dr. Rene Bernards) using forward primer 5' GGAATTCACCACCATGCCCAAGAAGAAGAGAAAGGTGGACAGTAAATACTCTCAA and reverse primer 5' CCCAGCGGCCGCTTATCAGGCTCGACAGACAA, introducing restriction sites for EcoRI and NotI. This fragment was subsequently inserted in a pcDNA3-YFP vector. For construct SRC-1_{FL}-YFP, full-length SRC-1 was amplified from pCMV-SRC-1 by PCR with forward primer 5' CCCAAGATCTACCACCATGAGTGGCCTTGGGGACAGTT and reverse primer 5' CCCAGCGGCCGCATCAGTAGC GCTGACGGAGG, introducing restriction sites for BglII and NotI and removing the stop codon. This fragment was subsequently inserted in a pcDNA3-YFP vector at these sites.
For the construction of SRC-$1_{1051-1240}$-YFP fragment of SRC-1 was amplified by PCR from pCMV-SRC-1 using forward primer 5' AATTGGATCCGCCACCATGCCTAACCAGCTTCGAC and reverse primer 5' AATTGAATTCTTGGGGAACCATTCCTGC, introducing restriction sites for EcoRI and BamHI. This fragment was subsequently inserted in a pcDNA3-YFP vector. $ER\alpha_{wt}$-CFP and $ER\alpha_{S305A}$-CFP were constructed as described previously (Michalides *et al*., 2004).

Mammalian 2-Hybrid constructs

For the Gal4 transactivating and DNA binding domain (TA and DBD, respectively), the TA and DBD containing yeast 2-hybrid vectors pPC86 and pPC97 (Invitrogen) were digested with HindIII and EcoRI, and were both inserted in a pcDNA3 vector. For the construct DBDSRC-$1_{623-711}$-YFP, SRC-$1_{623-711}$-YFP was isolated by PCR from pCMV-SRC-1 (Zwijsen *et al*., 1997) with forward primer 5' GGAATTCACCACCATGCCCAAGAAGAAGAGAAAGGTGGACAGTAAATACTCTCAA and reverse primer 5' CCCAGAATTCTCACTTGTACAGCTCGTCCATG, introducing restriction sites for EcoRI and XbaI, and was subsequently inserted in the DBD containing pcDNA3 vector. For the construct DBD-SRC-1_{FL}, SRC-1_{FL}-YFP was amplified by PCR from pCMVSRC-1 with forward primer 5' CCCACCCGGGATGAGTGGCCTTGGGGACA and reverse primer 5' CCCATCTAGATTATTCAGTCAGTAGCTGCTGACGGA, producing restriction sites for SmaI and XbaI. This fragment was subsequently inserted in the XbaI and EcoRI sites of pcDNA3 vector, where the EcoRI site was filled up. For the TA-$ER\alpha_{wt}$ and TA-$ER\alpha_{S305A}$ constructs, fragments were generated from $ER\alpha_{wt}$-CFP or $ER\alpha_{S305A}$-CFP by PCR with forward primer 5' CGGAATTCAAATGACCCTCCACACCAAAGCATCT and reverse primer 5' CCCAACTAGTTCAGACTGTGGCAGGGAAACCCT, introducing restriction sites for EcoRI and SpeI and inserted into the corresponding restriction sites of TA-containing pcDNA3 vector.

Fluorescence Recovery After Photobleaching (FRAP)
U2OS or MCF7 cells were cultured on coverslips for 48 h before treatment in CTS containing medium. 24 hours prior to imaging, cells were transfected with $ER\alpha_{wt}$-CFP, SRC-1_{FL}-YFP or SRC-$1_{623-711}$-YFP, as indicated. After transfection medium was replaced with Dulbecco's medium without phenol red, supplemented with CTS. Prior to analysis, coverslips were placed in 2 ml bicarbonate/Hepes-buffered saline (140 mM NaCl, 5mM KCl2, 2mM MgCl2, 1mM CaCl2, 23 mM NaHCO3, 10 mM D-Glucose, 10 mM Hepes pH 7.3) and analyzed in a heated tissue culture chamber at 37°C under 5% CO2. Where indicated cells were pretreated with 10 M forskolin for 15 min, and subsequently treated with E2, 4'OHtamoxifen or left untreated. Images were acquired on a TCS-SP2 confocal microscope (Leica), using a 63x oil immersion objective. Fluorescence intensities were measured at the bleach spot (FRAP), where t1/2 recovery time was the time at which the recovering signal reached (fluorescence∞-fluoresenceBLEACH)/2, where ∞ is the asymptotic value of the corresponding curve, as described before (Reits and Neefjes, 2001). Only cells expressing low ERα-CFP levels, but in excess related to SRC-1-YFP expression, were imaged. Zoom factor was set at 4x for all experiments.

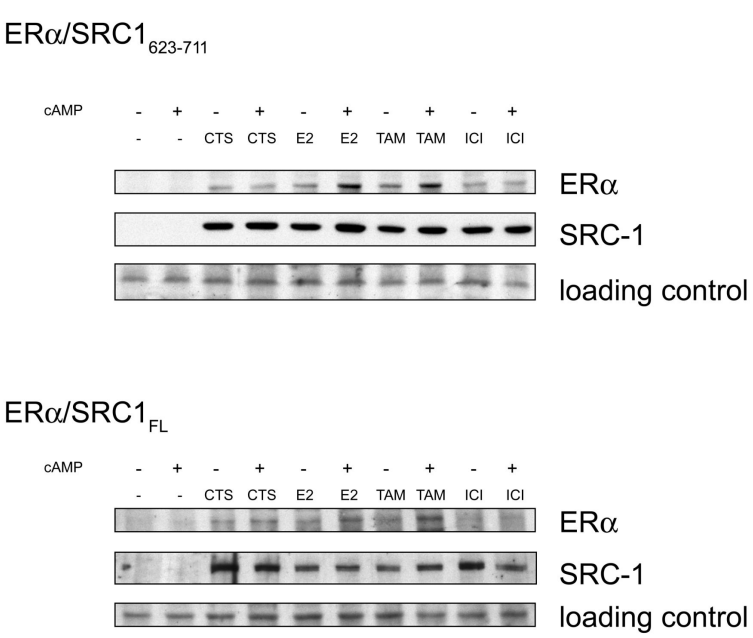
References

Michalides R, Griekspoor A, Balkenende A, Verwoerd D, Janssen L, Jalink K, Floore A, Velds A, van't Veer L, and Neefjes J (2004) Tamoxifen resistance by a conformational arrest of the estrogen receptor alpha after PKA activation in breast cancer. Cancer Cell 5: 597-605.

Reits EA and Neefjes JJ (2001) From fixed to FRAP: measuring protein mobility and activity in living cells. Nat Cell Biol 3: E145-E147.

Zwijsen R, Wientjens E, Klompmaker R, van der Sman J, Bernards R, and Michalides R (1997) CDK-Independent Activation of Estrogen Receptor by Cyclin D1. Cell 88: 405-415.

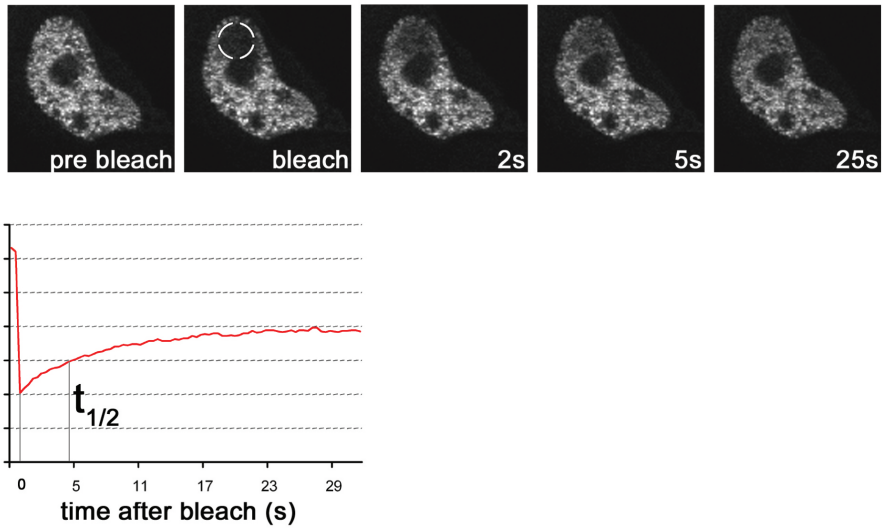
S1



Supplemental Figure S1: Expression verification of ERα and SRC-1 constructs in mammalian 2 hybrid analysis.

U2OS cells transfected with DBD-SRC-1 (623-711 or full length), TA-ERα (wt or S305A), GAL4-luciferase and Renilla luciferase were cultured in CTS containing medium only, or in the presence of 1 µM Estradiol (E2), 1 µM ICI 182,780 or 1 µM 4'OH-Tamoxifen for 96 hours. 24 hours prior to analysis 100 µM 8-Br-cAMP was added where indicated. Lysates were analyzed by Western blotting using antibodies against the transactivating domain of Gal4 (768, Santa Cruz) fused to ERα or against the DNA binding domain of Gal4 (N-19, Santa Cruz) fused to SRC-1. Aspecific background band is used as loading control. From 3 independent experiments, a representative blot is shown.

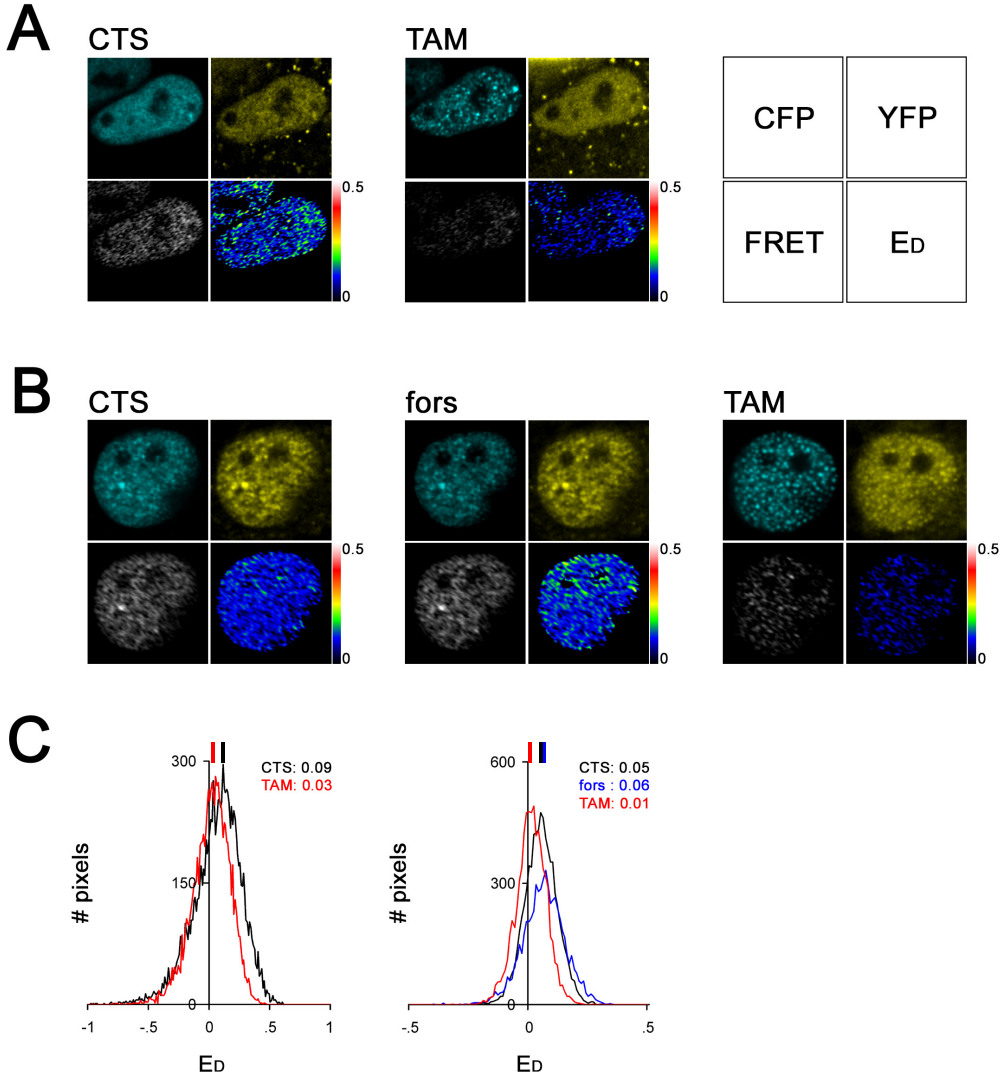
S2



Supplemental Figure S2: Example of FRAP measurements.

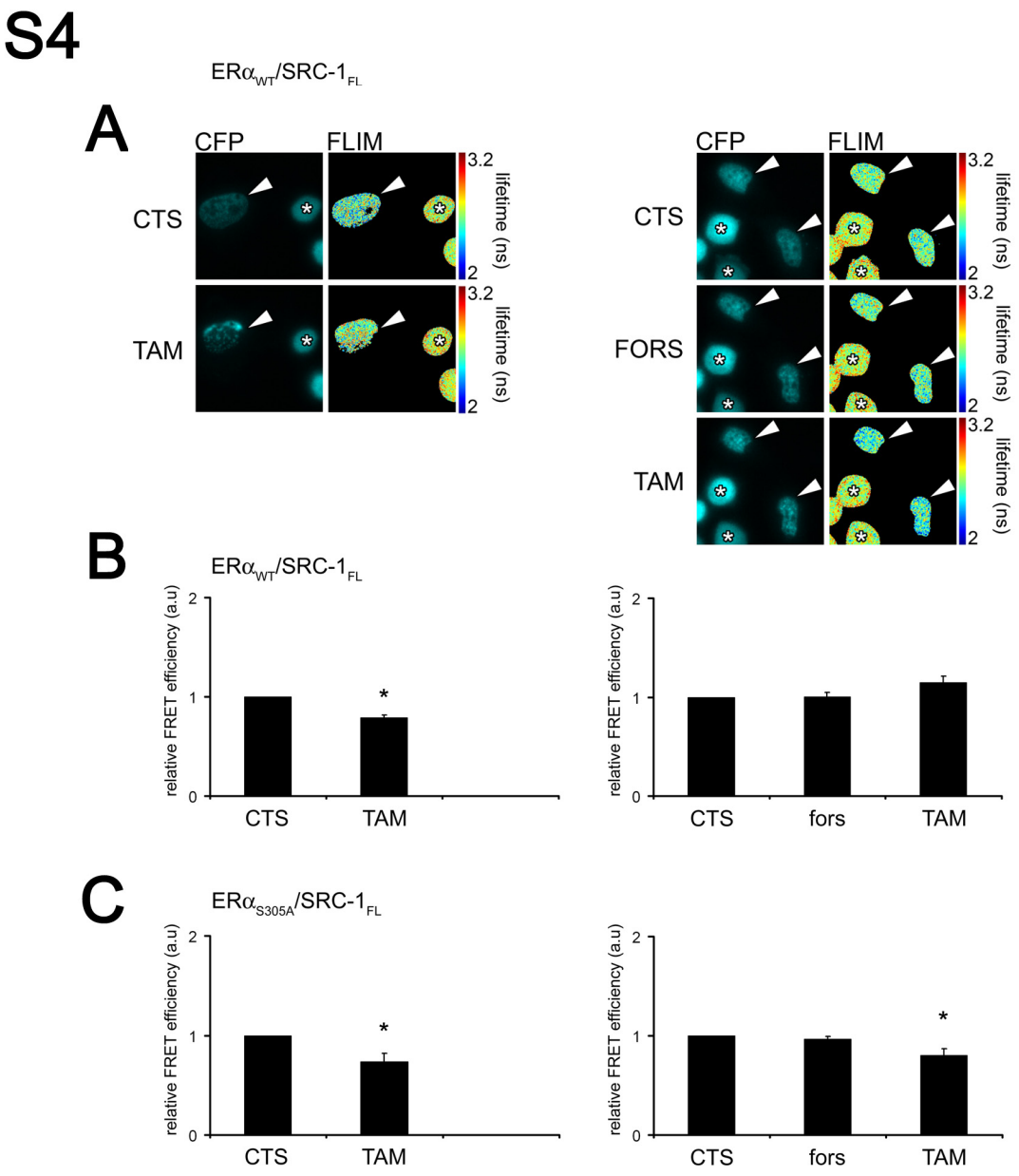
U2OS cells transfected with SRC-$1_{623-711}$-YFP and ERα-CFP were cultured in CTS containing medium, and treated with 1µM Estradiol (E2) 15 minutes prior to analysis. YFP was bleached and fluorescence intensities were followed in time in the bleach spot (crosshair), from which t1/2 (half-time to recovery) was calculated as described in Materials and Methods.

S3 ERα$_{305A}$-CFP/SRC-1$_{FL}$-YFP



Supplemental Figure S3: Orientation between ERα$_{S305A}$ and SRC-1$_{FL}$ is altered in the presence of tamoxifen and is not influenced by PKA.

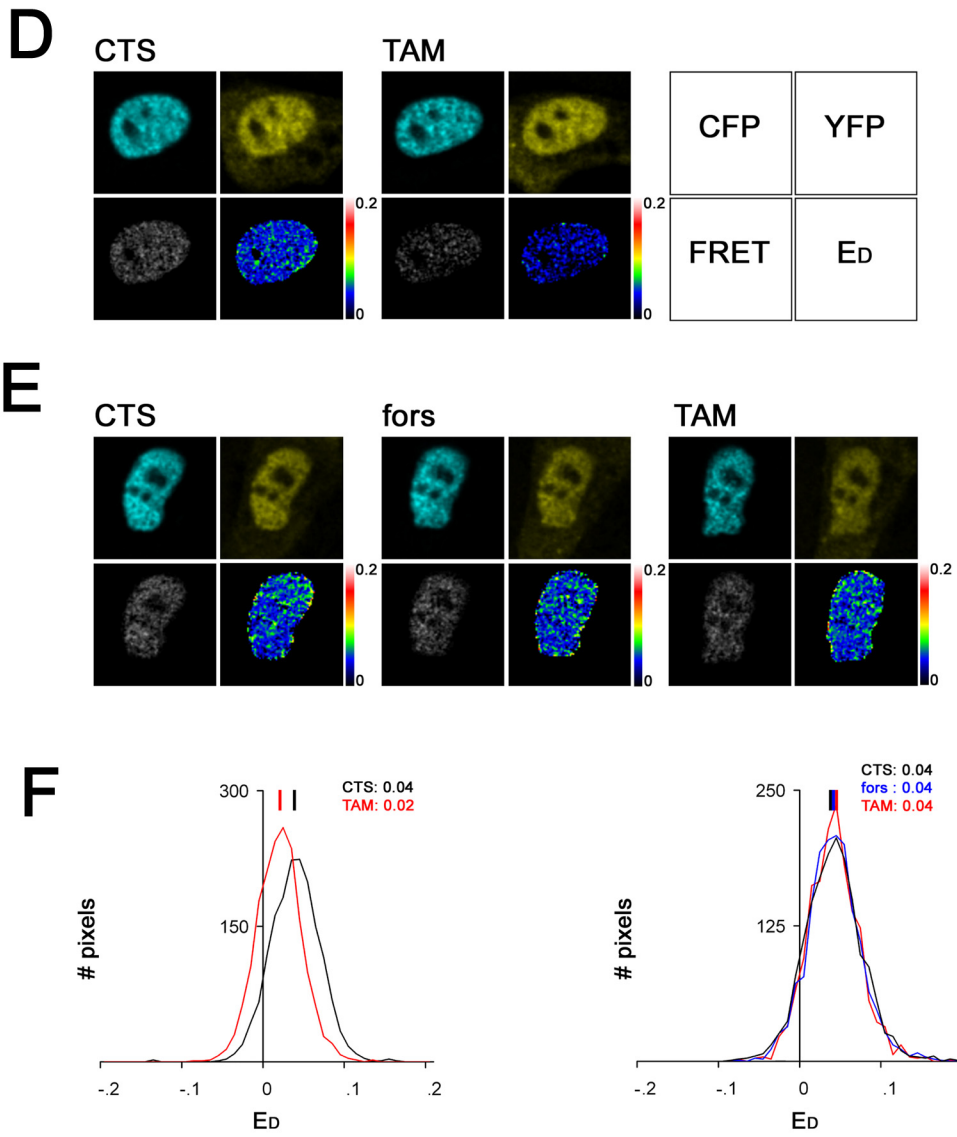
FRET measurements were performed on PRL array containing HeLa cells, transfected with ERα$_{S305A}$-CFP and SRC-1 FL-YFP (**A, B**). FRET images were generated from cells cultured in hormone-free (CTS) medium only (A and B, left panels) or after treatment with 10 µM forskolin prior to FRET measurements (B, middle panel). Subsequently, 1 µM 4'OH-tamoxifen (TAM) was added and after 15 minutes cells were imaged (A and B, right panels). FRET and donor FRET efficiency (E_D) were calculated as described in the experimental procedures section. For each condition described in A and B, the raw E_D values from the whole nucleus were related to the total amount of pixels (**C**).



Supplemental Figure S4: ERα-CFP/ SRC-1-YFP FRET analysis by FLIM and in MCF7 cells.

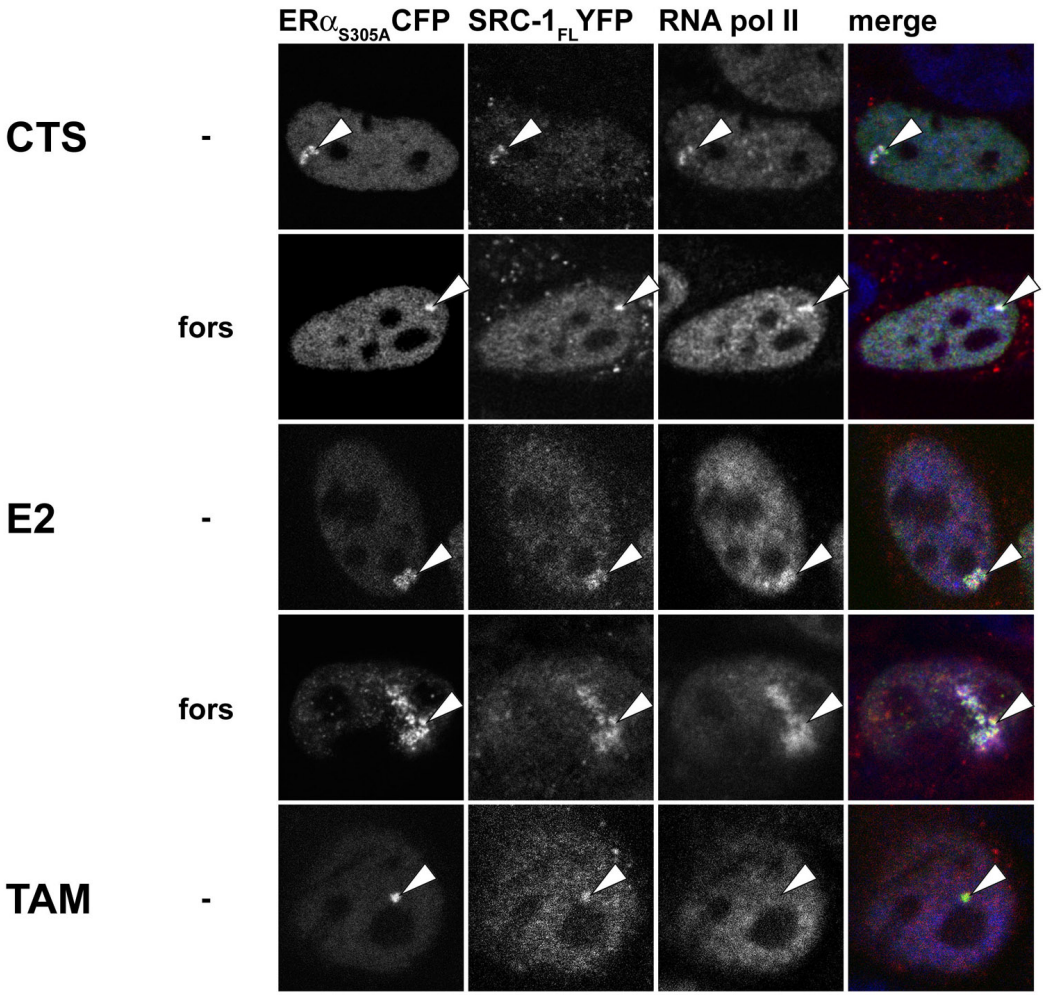
In FLIM, the lifetime of the CFP fluorophore determined (2.7 ns), which decreases in the case of FRET, thus if the energy of the CFP is transferred to the YFP. FLIM measurements were performed in U2OS cells, transfected with ERα$_{wt}$-CFP and SRC-1$_{FL}$-YFP (**A**, arrowhead). As an internal reference, these cells were cocultured in MelJuSo cells only expressing CFP (**A**, asterisk). FLIM images were generated from cells cultured in hormone-depleted (CTS) medium only (**A**) or after treatment with 10 µM forskolin prior to FRET measurements (A, right panel). Subsequently, 1 µM 4'OH-tamoxifen (TAM) was added and after 15 min cells were imaged. Donor FRET efficiency (E_D) was calculated as E_D=1- (lifetime cell of interest/ lifetime reference cell), where pair wise analysis was performed for ERα$_{wt}$-CFP (**B**) and ERα$_{S305A}$-CFP (**C**) under the conditions indicated above, where the E_D under CTS conditions is set to 1 for each experiment (relative E_D), bars indicate SEM from n>20 cells/condition. Student T-test was performed, *= $p < 0.05$.

S4



Supplemental Figure S4 C-E: FRET measurements were performed on MCF7 cells under conditions described in Supplemental Figure S3, now transfected with $ER\alpha_{wt}$-CFP and $SRC\text{-}1_{FL}$-YFP (**D, E**). For each condition described in D and E, the raw E_D values from the whole nucleus were related to the total amount of pixels (**F**).

S5



Supplemental Figure S5: RNA polymerase II recruitment on the PRL array is lost in $ER\alpha_{S305A}$ and $SRC1_{FL}$ expressing cells under conditions of tamoxifen.

Staining for RNA polymerase II was performed on PRL array containing HeLa cells that were transfected with $ER\alpha_{S305A}$-CFP and $SRC1_{FL}$-YFP and cultured in hormone-free (CTS) medium. Where indicated, they were pretreated with 10 µM forskolin. Subsequently cells were treated with 1 µM Estradiol (E2) or 1µM 4'OH-tamoxifen for 2 hours and then fixed and stained for RNA Polymerase II. Arrowheads indicate the PRL array that was analyzed for RNA polymerase II staining.

The AF-1 and hinge region of the human Estrogen Receptor cooperate in the quantitative response to estradiol and tamoxifen

In preparation for resubmission



4

The AF-1 and hinge region of the human Estrogen Receptor cooperate in the quantitative response to estradiol and tamoxifen.

Wilbert Zwart[1], Renée de Leeuw[1], Mariska Rondaij, Jacques Neefjes, Michael A Mancini[2] and Rob Michalides[3].

Abstract

Human Estrogen Receptor α and β greatly differ in their target genes, transcriptional potency, cofactor binding capacity and are differentially expressed in various tissues. In a classical ERE- mediated transactivation, ERβ has a markedly reduced activation potential as compared to ERα, for which the underlying mechanism is unclear. Here, we report that the binding between SRC-1 and the AF-1 domain of ERα is essential but not sufficient to facilitate AF-1/AF-2 synergy, which is required for an optimal agonistic response to E2 and tamoxifen. Complete synergy is achieved by the combined action of the AF-1 and AF-2 modulated by the distinct hinge domain of ERα. The AF-1 of ERβ lacks the capacity to interact with SRC-1, which explains the reduced E2-mediated transactivation by ERβ. The enhanced transactivation by ERα is due to the genuine interaction between AF-1 and AF-2, which depends on the distinct hinge region of ERα, whereas transactivation by ERβ solely depends on its AF-2 domain.

Introduction

Estrogen Receptors (ERα and ERβ) are homologous members of the nuclear receptor superfamily and are encoded by two different genes. They control critical processes in physiology and are prognostic markers in breast cancer, their expression determines whether or not endocrine treatment is to be given as an adjuvant therapy (1). On binding of agonistic ligands, the DNA-bound receptor recruits cofactors which permit the receptor to transmit its regulatory information to the cellular transcription complex (transactivation). ERα and ERβ mediate distinct profiles of gene expression (2;3), which is due to a combination of differential ligand response (4-7), distinct interaction with coactivators (8) and binding to specific, estrogen response elements (EREs) (9). Consequently, ERα and ERβ exert different effects on organization, growth and differentiation of various tissues, including colon, uterus, bone, brain and mammary gland (10-14). Moreover, transactivation by ER can occur in two different ways. One is by classical ER transactivation where two dimerized ER molecules bind to a palindromic ERE sequence (15). The other way is by non-classical transactivation where ER is tethered to other transcription factors, including the fos-jun complex, NFκB and Sp1, to render transcription of their genes responsive to ER activity (16;17). ERα and ERβ differ in the classical and non-classical transactivation by ER (4;18). These differences between ERα and ERβ are to be reduced to differences in the amino-acid sequence and/or a different interaction between the various domains of ER. ERα is composed of 595 amino acids, whereas ERβ is 530 amino acids long. The amino-terminal A/B domain contains a ligand-independent transactivation function (AF-1) and shows 17% amino-acid homology between the ERs. The highly conserved central C-region, with 96% homology, encompasses the DNA-binding domain. The flexible hinge or D region contains nuclear localization signal information and links the C-domain to the multifunctional carboxyl-terminal E/F domain. The E/F domains of the ERs share 53% amino-acid homology and contain the ligand binding domain and the ligand-dependent transactivation domain (AF-2 domain), including the cofactor-binding groove to which cofactors are recruited when ER becomes activated. For ERα it has been shown that the interaction between domains is essential for an effective transactivation (19;20).

Despite similar *in vitro* ERE binding capacities and comparable IC50 values for E2 (21;22), human ERβ has a substantially lower transactivation capacity than ERα in an E2-driven, ERE dependenttransactivation (21). This difference between ERα and ERβ is not found in the mouse

Department of Tumor Biology, The Netherlands Cancer Institute, Amsterdam, The Netherlands

[1]equal contribution
[2]Department of Molecular & Cellular Biology, Baylor College of Medicine, Houston, Tx, USA

[3]Correspondence: dr. R. Michalides

Department of Tumor Biology, The Netherlands Cancer Institute, Plesmanlaan 121, 1066CX Amsterdam, the Netherlands, phone +31205122022, fax +31205122029, Email:r.michalides@nki.nl

Running Title: Hinge and AF-1 mediate synergy in ERα.

Keywords: estrogen receptor alpha / estrogen receptor beta / Activation domain 1 / hinge region/ SRC-1/ transcriptional capacity/ tamoxifen agonism

This study was supported by Grant NKI 2005-3388 of the Dutch Cancer Society and was in part performed within the framework of Top Institute Pharma project: number T3-107.

isoforms (23). Also in the non-classical pathways, differences between human ERα and ERβ have been reported (24), where the underlying mechanisms for differences in transcription efficacies of ER subtypes are still unclear.

The precise transactivation process of genes by ER is still unresolved. ER can dimerize and bind to its cofactors even when the ER is not bound to DNA and this occurs also in the absence of ligands (25-27). For a proper recruitment of RNA polymerase II however, the ER needs to be bound to an ERE (25;27;28). Effective transactivation by ERα requires an interaction between the N-terminal and C-terminal regions of ERα (20;29), which is accomplished by the binding of ERα to cofactors (20). The anti-estrogen tamoxifen inhibits ERα-mediated transactivation by arresting the conformation of ERα as such that the SRC-cofactor interaction groove remains covered by the twelfth α-helix of the LBD (30). However, tamoxifen has also a weak agonistic activity. This mild agonistic behavior can be enhanced by phosphorylation of serine 305 in the hinge region of ERα by Protein Kinase A (31).

Here, we investigated the differences between human ERα and ERβ in E2-driven transactivation and the agonistic effect of tamoxifen. We show that the AF-1 region of ERα that specifically interacts with SRC-1 is in combination with the distinct hinge region of ERα responsible for hormone-independent transactivation and for an efficient transcription after estradiol stimulation. This AF-1 specific feature is absent in human ERβ. Although the AF-2 region of ERα is crucial for the agonistic behavior of tamoxifen, the extent of transactivation is dependent on the AF-1 domain under these conditions.

Results

Classical transactivation by ER is dependent on the AF-1 domain.

ERα and ERβ differ mostly in their N-terminal AF-1 regions, which share 17% sequence homology and differ 41 amino acids in size. We therefore examined the contribution of the AF-1 domains to maximal E2-driven transactivation and generated swap mutants, where the AF-1 of ERα (aa 1-185) was replaced by that of ERβ (aa 1-144) and vice versa, resulting in $ERα^{AF-1β}$ and $ERβ^{AF-1α}$ mutants, Figure 1A. All four of the ER variants were analyzed for the extent of E2-induced transcription using an ERE-luciferase reporter construct and various concentrations of ligand, Figure 1B. Maximal transactivation for ERα was considerably higher than that for ERβ, 60 versus 6 fold induction, respectively. Exchanging the AF-1 region of ERβ for that of ERα in $ERβ^{AF-1α}$ greatly affected this response, and increased the maximal transactivation from 6 to 16 fold. Exchanging the AF-1 of ERα for that of ERβ in $ERα^{AF-1β}$, however, reduced the transactivation from 60 to 6 fold, a level also reached by ERβ wild-type. The ERβ AF-1 domain therefore reduces the E2-induced transactivation, whereas the AF-1 domain of ERα is responsible for its enhancement. The EC50 values for E2 of ERα and ERβ differed slightly ($7.5*10^{-12}$ M and $2.5*10^{-11}$ M, respectively), which is to be ascribed to the AF-1 domain, since these values were exchanged in the AF-1 swap mutants. Although the exchange of the AF-1 of ERβ for that of ERα in $ERβ^{AF-1α}$ increased maximal transactivation approximately 3 fold in comparison to wild-type ERβ, the extent of transactivation still did not reach the level of ERα. This indicates that additional features are involved in maximal E2-driven transactivation.

We next examined whether also the ligand-independent and tamoxifen-associated transactivation are linked to the AF-1 of ERα. The AF-1 of ERα appeared responsible for the minor ligand-independent transactivation of ERα, since exchange of the AF-1 region between both ERs completely switched this ligand-independent transactivation, Figure 1D. These results indicate that the AF-1 domain of ERα mediates ligand-independent transactivation, whereas no such activity is observed for the AF-1 domain of ERβ.

Transactivation by tamoxifen resulted in a 3.5 fold enhancement over hormone depleted conditions for wild-type ERα, whereas ERβ did not respond to tamoxifen, Figure 1C. Interestingly, whereas transactivation by $ERα^{AF-1β}$, in which the AF-1 of ERα had been replaced with that of ERβ, was decreased compared to ERα, some dose-dependent response to tamoxifen still occurred. The transactivation response of $ERβ^{AF-1α}$ however, was similar to that of wild-type ERβ, showing no transcriptional activity under the tamoxifen conditions tested. These results indicate that the AF-1 domain of ERα is affecting the extent of tamoxifen-associated transactivation. Whether this tamoxifen-driven transactivation occurs or not, depends on the AF-2 domain of ERα

The AF-1 domain of ERα, but not of ERβ, binds to SRC-1.

Since the AF-1 of ERα appeared to be responsible for efficient transactivation of ERα in a ligand-dependent and –independent manner, unlike the AF-1 of ERβ that lacks this activity, we investigated the binding of these domains to the p160 coregulator SRC-1. SRC-1 binds to both the AF-1 and AF-2 domains of ERα; an interaction which generates a functional synergy between the two transactivation domains (20;32). Whereas the Q-rich region of SRC-1

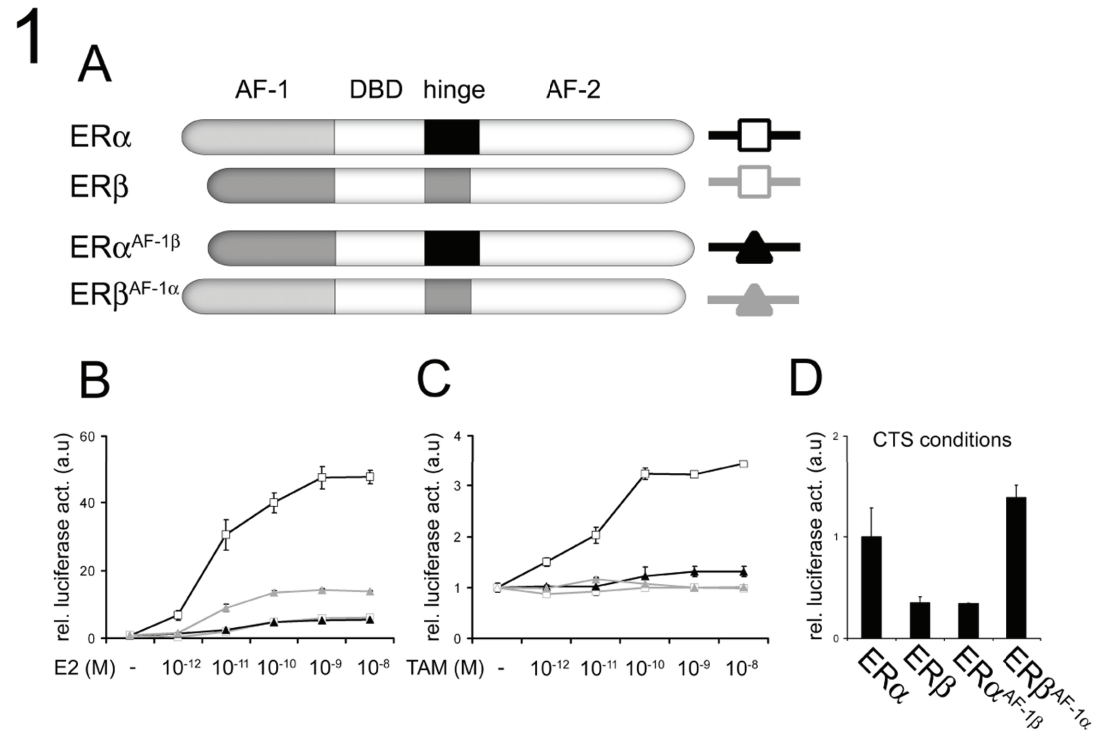


Figure 1. Extent of classical and ligand-independent transactivation by ER is dependent on the AF-1 domain of ERα

A. Structural overview of ERα, ERβ and AF-1 swap mutants.
B. E2 concentration-dependent transcription of an ERE-luciferase reporter. U2OS cells were transfected with ERα, ERβ, ERα$^{AF-1β}$ or ERβ$^{AF-1α}$, cotransfected with ERE-luciferase reporter gene and Renilla luciferase as control. Cells were treated with 10^{-12}, 10^{-11}, 10^{-10}, 10^{-9}, 10^{-8} M E2 for 36 hours or left untreated and luciferase activity was measured. A representative experiment out of 3 independent experiments is shown. Error bars indicate standard deviation from duplicate samples.
C. Same conditions as in 1B are applied, but now with 10^{-12}, 10^{-11}, 10^{-10}, 10^{-9}, 10^{-8} M 4-OH-tamoxifen.
D. Luciferase signal for the tested ER variants under hormone depleted conditions. Signal for ERα is set on 1. A representative experiment out of 2 independent experiments is shown. Error bars indicate standard deviation from duplicate samples.

can bind the AF-1 in ERα, the consensus LxxLL-containing middle region of SRC-1 binds to the ligand-dependent AF-2 domain of ERα (29).

We visualized these interactions in intact cells on a genuine ERE promoter sequence, the prolactin promoter/enhancer (PRL) region, in Hela cells. These cells contain a DNA array, consisting of ~200 copies of stably transfected modified PRL (28). The PRL array allowed visualization of a defined, ERE containing DNA structure in the nucleus, to which ERα and cofactors can be recruited. In addition, the size of this structure provides information on the transcriptional activity of the complex bound to this region (25;28), since widening of the DNA array structure has been reported to be associated with increased transcriptional activity (25;28;33). In our experiments, ERα, ERβ and both AF-1 swap mutants could recruit RNA Polymerase II to the array structure under E2 conditions, Figure 2. Under these conditions, the array structures were enlarged, which is associated with transcriptional activity. However, whereas ERα was already capable of recruiting RNA Polymerase II to the array under hormone-depleted conditions, ERβ failed to do so. This functional behavior was associated with the AF-1 domain of ERα, since swapping this region was sufficient to exchange the ability to recruit RNA polymerase II under hormone-deprived conditions. These results indicate that the AF-1 domain of ERα contains a ligand-independent transactivation activity, which is absent in ERβ, supporting the results of the transactivation studies presented in Figure 1. We confirmed these interactions using truncation mutants of SRC-1 that only bind AF-1 or AF-2. These truncation mutants of SRC-1 act as dominant-negative mutants over the endogenous coactivators (25). We used a truncation mutant of SRC-1 (aa 1051-1240), which was reported to bind to the AF-1 domain of ERα in a yeast two-hybrid assay (29), and tested this mutant under E2 conditions. When this SRC-1 mutant was cotransfected with ERα, RNA polymerase II was no longer recruited to the now condensed array structure, indicative of an inactive promoter region, Figure 3A. The SRC-$1_{1051-1240}$ mutant

2

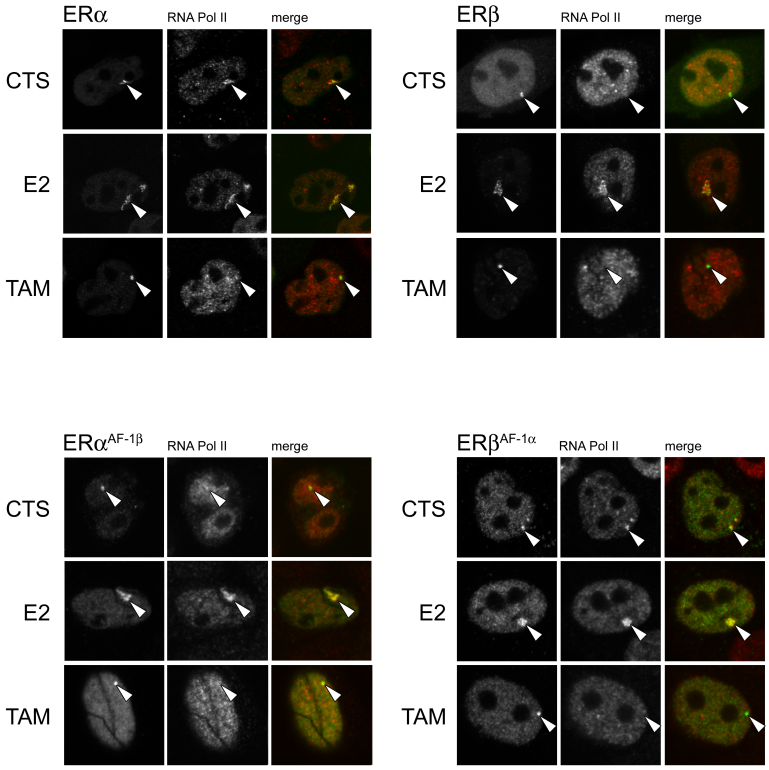


Figure 2. RNA Polymerase II recruitment by ERα, ERβ or AF-1 swap mutants.

PRL array containing HeLa cells were transfected with one of the different ER constructs and treated with 10^{-6} M E2, tamoxifen or left untreated. Cells were fixed and stained with antibodies recognizing ERα or ERβ and RNA Polymerase II. Arrowheads indicate array structure.

was not recruited to the array by ERβ and therefore could not prevent RNA Polymerase II accumulation on the array structure. Swapping the AF-1 domains of ERα and ERβ resulted in an exchange of the effect of the SRC-1 truncation mutant to interfere with accumulation of RNA polymerase II. The results of these inhibition studies indicated that the AF-1 domain of ERα is capable of binding to the Q-rich region of SRC-1, unlike the AF-1 domain of ERβ. These data were verified in a co-immunoprecipitation experiment, supplemental Figure S1.

In order to inhibit binding to the AF-2 domain we used a second SRC-1 truncation mutant (aa 623-711), which specifically binds to the AF-2 region of ER (34), figure 3B. All of the tested ER constructs were capable of recruiting the AF-2 binding SRC-1 mutant resulting in co-localization with the ER on the array structure. This prevented binding of RNA Polymerase II to the array structure and led to a condensed array.

The results of these binding studies indicate that the AF-2 domains of both ERα and ERβ directly interact with SRC-1, whereas only the AF-1 of ERα is capable of interacting with the AF-1 binding domain of SRC-1.

Maximal transactivation by synergism between the AF-1 and AF-2 domains of ERα is absent in ERβ.

We next investigated the functional consequences of the differences in SRC-1 binding between the AF-1 domains of ERα and ERβ. We therefore performed an ERE luciferase reporter assay, in which the function of AF-1, AF-2 or both, for each of the estrogen receptor constructs was inhibited using the different SRC-1 truncation mutants, Figure 4. 10nM E2 was added for all conditions, which resulted in a maximal transactivation for each construct, Figure 1B. The extent of transactivation by ERα was much higher than by ERβ. This response could be significantly reduced by cotransfection of either AF-1 or AF-2 inhibiting SRC-1 truncation mutants. Importantly, the simultaneous inhibition of both AF-1 and AF-2 domains reduced E2-associated transactivation even further, indicating that these two transactivation domains functionally cooperate in ERα, as has been demonstrated before (20). This appeared not to be the case for ERβ, where only AF-2, but not AF-1, inhibition blocked transactivation. Exchanging the AF-1 of ERβ for that of ERα in ERβ$^{AF\text{-}1\alpha}$, rendered this construct now sensitive to AF-1 inhibition and permitted a further inhibition with AF-2-binding SRC1 fragment.

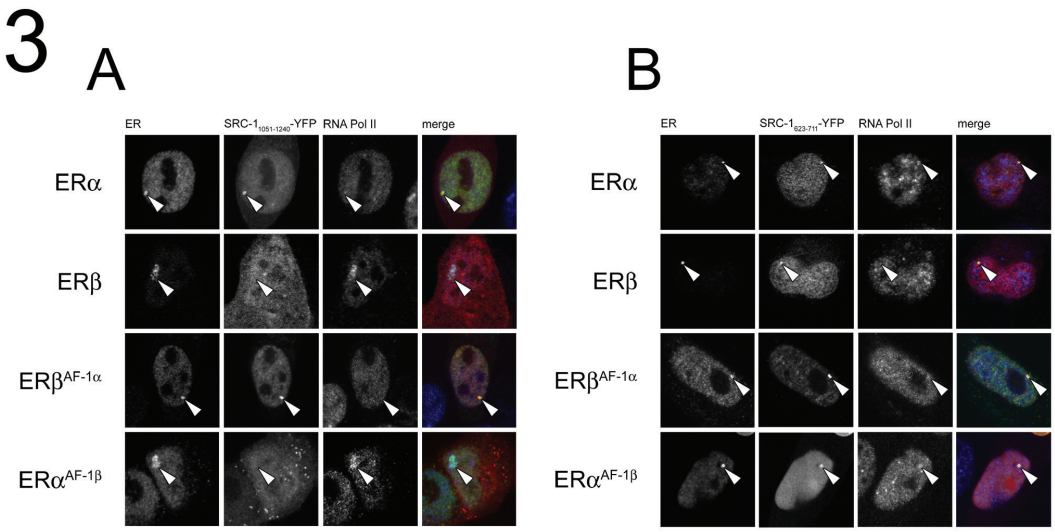


Figure 3. AF-1- and AF-2-dependent SRC-1 recruitment to the PRL array structures

PRL array containing HeLa cells were transfected with one of the different ER constructs and treated with 10^{-6} M E2, tamoxifen or left untreated. Cells were cotransfected with SRC-1 truncation mutants; **A**. SRC-1$_{1051-1240}$-YFP (AF-1 inhibiting) or **B**. SRC-1$_{623-711}$-YFP (AF-2 inhibiting). Arrowheads indicate array structure, analyzed for presence of the fragments of SRC-1-YFP and RNA Polymerase II.

These results indicate that the extent of transactivation by E2 is in ERα largely determined by the interaction between its AF-1 and AF-2 domains. Since the AF-1 domain of ERβ lacks the ability to bind to SRC-1, this synergism is absent in ERβ. The E2-mediated transactivation by ERβ, which is minor in comparison to that of ERα, is solely due to the transactivation capacity of its AF-2 domain. Replacement of the AF-1 of ERβ by the AF-1 domain of ERα in ERβ$^{AF-1α}$ restored the synergism between the domains, which did affect the extent of transactivation by E2 but not to the levels observed with ERα.

Effect of the hinge region on E2-driven transactivation by ER.

The difference in the extent of transactivation by E2 between wildtype ERα and ERβ$^{AF-1α}$ might be due to the hinge region, a non-conserved domain between the DNA binding and the AF-2 domain. Thereby, we exchanged the hinge region of ERα for that of ERβ and vice versa, Figure 5A, and tested these constructs in an ERE-dependent luciferase reporter assay using various concentrations of E2, Figure 5B. Two different hinge swaps were made for each ER subtype; a small swap where aa 294-309 in ERα were replaced for the corresponding aa 253-262 in ERβ and a larger swap where aa 256-332 in ERα were replaced for the corresponding aa 225-283 in ERβ. The small hinge swap in ERα, ERα^{Shingeβ}, showed a similar response to E2 as wildtype ERα. The large hinge swap, ERα^{Lhingeβ}, however, resulted in a decreased transactivation, which overlapped with that of ERβ$^{AF-1α}$, Figure 5B. These data suggest that the lack of a full response in this ERβ$^{AF-1α}$ mutant is due to the composition and/or total length of the hinge region. No effect on maximal transactivation by the hinge swap mutants of ERβ was observed; both mutants behaved similar as wild-type ERβ or ERα$^{AF-1β}$, which is likely due to the absence of AF-1 activity in ERβ.

Synergy between AF-1 and AF-2 is essential for agonistic behavior of tamoxifen (25). The role of the hinge region in this synergy was studied in the ERα hinge swap mutants. The tamoxifen response on the large hinge swap mutant was impaired, whereas that of the small hinge swap mutant overlapped with ERα, Figure 5C. Tamoxifen did not increase the response to any of the ERβ hinge swap mutants. Interestingly, exchanging the hinge region in ERα for that of ERβ, resulted in a 10 fold shift in EC50 values in the response curves for E2 (Figure 5B) as well as for tamoxifen (Figure 5C), indicating that the ligand efficacy is influenced by the hinge region. The EC50 of the ERβ hinge mutants was also affected, suggesting that EC50 is ER subtype specific, Figure 5C. This does not involve an AF-1/AF-2 functional synergy, but is determined by the hinge region alone.

Taken together, these results indicate that in ERα the maximal E2-driven transactivation is due to synergy between the AF-1 and AF-2 domains that

4

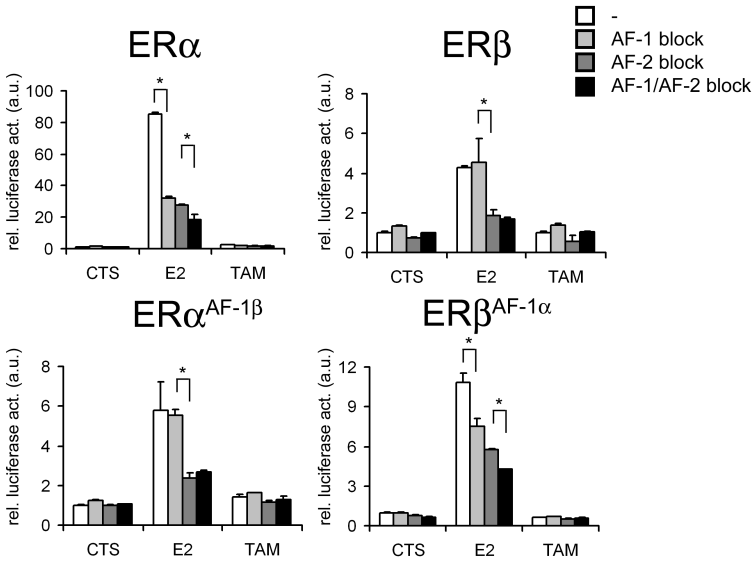


Figure 4. Functional synergy between AF-1 and AF-2 is ERα/AF-1 specific.

ERE-luciferase reporter assay was performed in U2OS cells transfected with ER variants, ERE-luciferase reporter construct and Renilla luciferase. Where indicated, cells were cotransfected with SRC-$1_{1051-1240}$ or SRC-$1_{623-711}$, inhibiting AF-1 or AF-2 respectively. Cells were treated with 10nM E2 or 100 nM tamoxifen or left untreated for 36 hours after which cells were lysed and luciferase activity was determined. Representative data from 2 independent experiments is shown; error bars indicate standard deviation from duplicate samples. * indicates a statistically significant reduction of luciferase signal, $p < 0.05$

is dependent on the length and/or composition of the hinge region. In ERβ, the E2-mediated transactivation is solely associated with its AF-2 domain.

Role of AF-1 in non-classical trans-activation by ER.

The AF-1 of ERα determines the transactivation capacity of ERα under E2 conditions in a classical ERE-mediated transactivation induction. In order to investigate the role of AF-1 in a non-classical transactivation reaction, we tested ERα, ERβ, and the AF-1 swap mutants in an AP-1 driven luciferase assay, Figure 6A. For ERα, AP-1-mediated transcription was inhibited by E2, and was not affected by tamoxifen, whereas no ERβ response was observed. The response on this AP-1 dependent reporter was exchanged by the AF-1 swap mutants, indicating that the effect of the ERα/AF-1 is not restricted to the classical ERE-mediated transcription, but also applies to non-ERE-mediated transactivation. This AF-1 effect was also evident from measuring progesterone receptor mRNA levels by Q-PCR in MCF-7 breast cancer cells. The promoter of the progesterone receptor gene contains AP-1, Sp-1 and imperfect ERE sites (35-38). In order to measure transactivation by the ER variants, MCF-7 cells were transfected with ERα, ERβ or the AF-1 swap mutants, and either or not treated with E2 or tamoxifen, Figure 6B. Whereas PR mRNA levels were elevated by E2 in ERα transfected cells, this was less in the presence of ERβ, Figure 6B. This ER-subtype specific effect on expression of PR mRNA was exchanged in the AF-1 swap mutants. These results indicate that the AF-1 of ERα plays a major role in the non-classical ER-mediated transactivation and determines expression level of PR mRNA in MCF-7 cells.

Discussion

ERβ arose from ERα by a duplication event to different chromosomes approximately 450 million years ago (39). The homology between them is largely maintained at the DNA binding domains (96%) and ligand binding domains (53%), which indicates a functional selection pressure for both domains. In the present study, we showed that the AF-1 domain of ERα binds to SRC-1, and that this binding, in combination with the hinge region of ERα, is responsible for the extent of transactivation by estradiol and for the ligand-independent transactivation. Both of these functions are lost in ERβ, which coincides with the largely deviating sequence of the AF-1 and the hinge region of ERβ compared to ERα. This evolutionary loss of the AF-1 domain of ERβ to interact with SRC-1 has also functional consequences, since ERβ poorly responds to E2. The expression of ERα and ERβ is different in various human tissues, ranging from exclusive expression of ERβ in colon and brain to variations in the ratios of ERα and ERβ expression in other tissues. This variation influences the extent of response to E2. Indeed, ERβ has been reported to interfere with E2-driven proliferation of breast cancer cells (40), either or not as heterodimers of ERα and ERβ (41). This deviation is relevant for the development of selective drugs that aim to maintain the E2-response in particular tissues, such as the colon and the brain, but to disrupt that response in target tissues in the case of breast cancer.

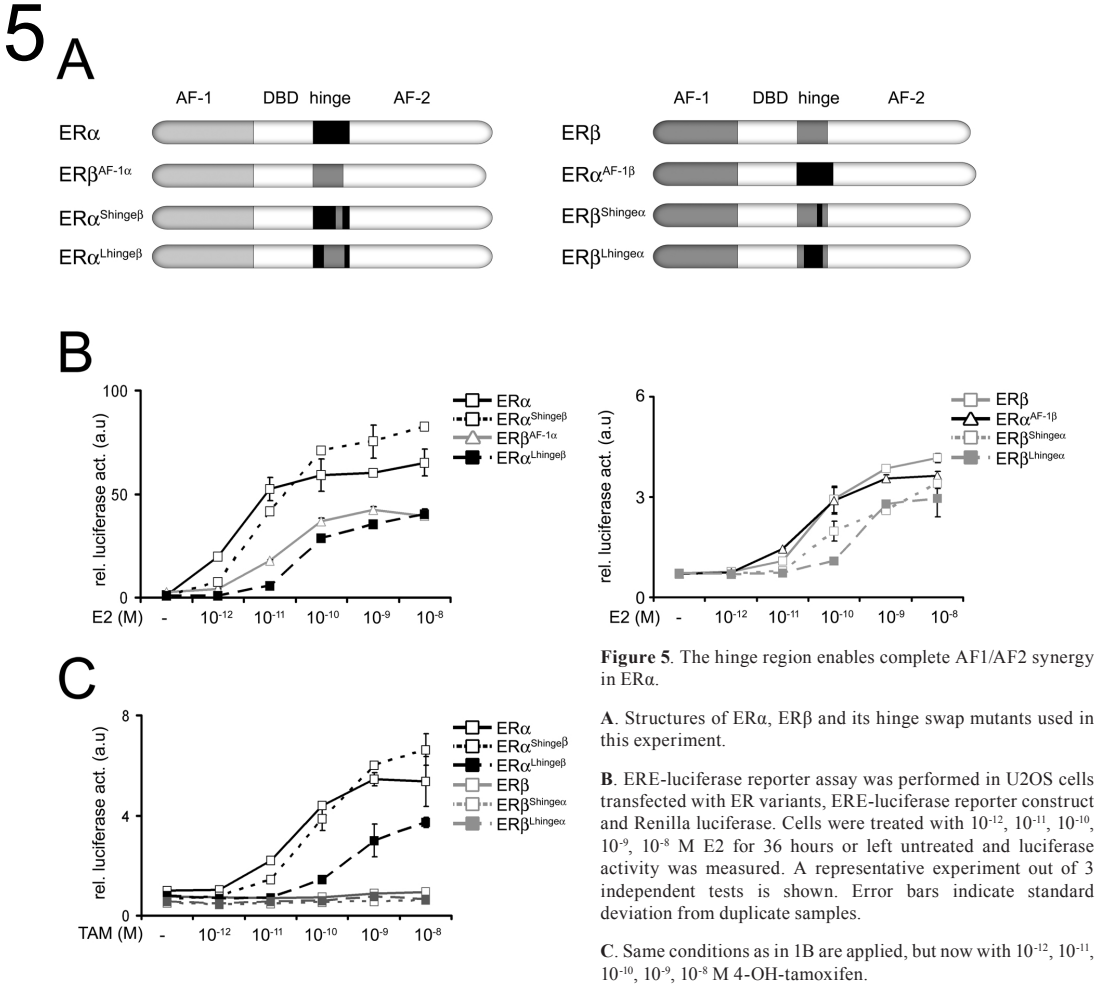


Figure 5. The hinge region enables complete AF1/AF2 synergy in ERα.

A. Structures of ERα, ERβ and its hinge swap mutants used in this experiment.

B. ERE-luciferase reporter assay was performed in U2OS cells transfected with ER variants, ERE-luciferase reporter construct and Renilla luciferase. Cells were treated with 10^{-12}, 10^{-11}, 10^{-10}, 10^{-9}, 10^{-8} M E2 for 36 hours or left untreated and luciferase activity was measured. A representative experiment out of 3 independent tests is shown. Error bars indicate standard deviation from duplicate samples.

C. Same conditions as in 1B are applied, but now with 10^{-12}, 10^{-11}, 10^{-10}, 10^{-9}, 10^{-8} M 4-OH-tamoxifen.

Our study emphasizes that the interaction between the AF-1 domain of ERα and the Q-rich region of SRC-1 is crucial for the enhanced transactivation by E2, and show that the orientation between the AF-1 and AF-2 domains, being determined by the composition and/or length of the hinge region, affects the final extent of E2-driven transactivation. Since this AF-1 function is lacking in human ERβ, the minor transactivation by E2 in ERβ is solely due to its AF-2 activity.

The results of the luciferase reporter studies (Figure 4) confirmed the co-immunoprecipitation experiments (Supplemental Figure S1) and in situ localization studies (Figure 3).These results showed that non-liganded ERα binds to SRC-1 via its AF-1 domain, which is sufficient for recruitment of RNA polymerase II. Recruitment of RNA Polymerase II by ERβ, however, was dependent on E2, and occurred via its AF-2 domain. Not only the composition of the AF-1 domain is crucial for binding to SRC-1, but also the spacing and/or orientation between the AF-1 and AF-2 domains is essential for transactivation of ERα. When the large hinge region of ERα was replaced for that of ERβ, the resulting ERα^{Lhingeβ} mutant was equally effective as the ERβ^{AF-1A} mutant (Figure 5). This suggests that the combination of AF-1/AF-2 interaction together with the hinge region, determines the vast E2-driven transactivation of ERα. This spatial positioning of the AF domains may also be relevant for resistance to particular antagonists, since phosphorylation of Serine 305 of ERα within the hinge region by Protein Kinase A or PAK-1 (31;42) results in resistance to tamoxifen. The mechanism for this is a repositioning of the AF-2 domain of ERα towards cofactor SRC-1 when Serine 305 of ERα was phosphorylated by PKA and ERα was bound to tamoxifen (25). This repositioning of ERα towards SRC-1 is in its turn the result of an internal reorientation of the AF-1 and AF-2 domains of ERα under these conditions (31). This reorientation permits recruitment of RNA polymerase II and thereby

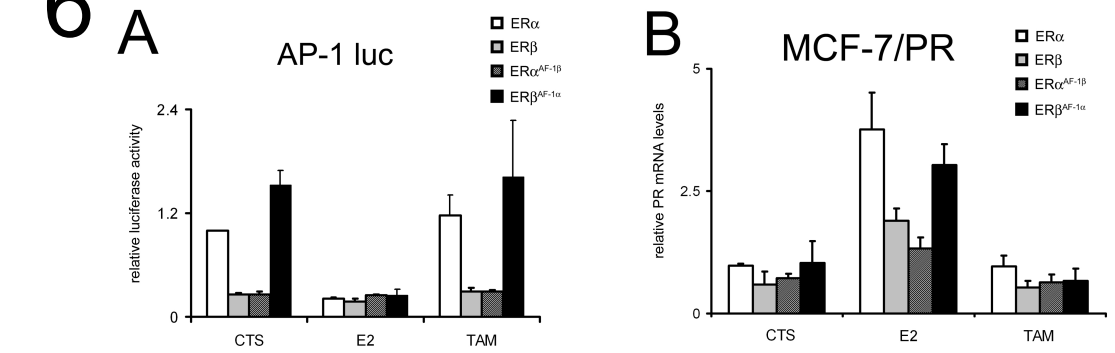


Figure 6. Non-classical transactivation by ER is influenced by AF-1 of ERα.

A. AP-1-luciferase reporter assay was performed in U2OS cells, transfected with ER variants, AP-1 luciferase reporter construct and Renilla luciferase. Cells were treated with 10^{-8} M E2, tamoxifen, or left untreated for 36 hours and luciferase activity was measured. A representative experiment out of 3 independent tests is shown. Error bars indicate standard deviation from triplicate samples.

B. MCF-7 cells were transfected with ER variants, and treated with E2, tamoxifen or left untreated. Five hours thereafter, RNA was isolated and mRNA levels of PR were determined by quantitative RT-PCR. mRNA levels were related to hormone deprived conditions of ERα, which was set at one. Data are from 2 independent experiments, both performed in duplicate. Error bars show standard deviations.

transcription of genes by ERα and proliferation of ER-dependent breast tumor cells in the presence of tamoxifen.

Not only the length, but also the composition of the hinge region may affect the capacity of transactivation, since the hinge region of ERα is a target of extensive posttranslational modifications which affect stability and or activity of the receptor. In particular, the residues in the hinge between K299 and S305 are target for acetylation, ubiquitylation, methylation and phosphorylation. These modifications may interfere with one another and affect final activation of ERα (31;43-46). These sequences and corresponding opportunities for modification and modulation of the receptor are unknown in the hinge region of ERβ.

The tissue-selective antagonist tamoxifen, which is widely applied in the treatment of ER-positive breast cancer, has also weak agonistic activity. This is due to a combined AF-1 and AF-2 activity on the proper ER background. The AF-1 domain of ERα largely enhanced this tamoxifen-mediated transactivation, but only on an ERα background (Figure 1C). This background involves the proper hinge region, which facilitates the interaction between the AF-1 and AF-2 and thereby the extent of transactivation for ERα, but not for ERβ (Figure 6C). The lack of any agonistic action of tamoxifen on ERβ can therefore be ascribed to the lack of interaction between AF-1 and AF-2 in combination with its hinge region.

We have performed these studies in U2OS osteosarcoma cells, a highly suitable cell line for testing the direct effects of transactivation of ERα and ERβ (31;47), that are themselves devoid of expression of endogenous ER. We have focused in this study on the interaction between ER and SRC-1 as a most relevant cofactor of ER. There are 3 different SRC cofactors, which all belong to the p160 cofactor family (48). They interact with the AF-2 domain of ERα and ERβ via their LxxLL motives (49). However, when we inhibited the interaction between AF-1 of ERα and SRC-1 with an AF-1 inhibiting fragment of SRC-1 (Figure 3), we did not observe any recruitment of RNA polymerase II under E2 conditions, excluding any residual interaction between ERα/AF-1 and SRC-2 or -3 that would have resulted in recruitment of RNA polymerase II.

Recently, it has been reported that the AF-1 of ERβ does bind to SRC-1 when the complex was bound to the SP-1 directed promoter of the TIEG gene in osteoblast cells and mediated its E2 mediated expression (50). Their study and our results indicate that the effects of ERα and ERβ are dependent on the promoter region to which they (in)directly bind, as has also been concluded by others (9). The results of our study emphasize that on the "classical", palindromic ERE containing promoters, the E2- and ligand-independent transactivation are determined by the binding of AF-1 of ERα and SRC-1, which is absent in ERβ. AF-1 of human ERβ does not bind to SRC-1, whereas this is the case for mouse ERβ (51). This corresponds with a difference in transactivation by E2 between human ERα and ERβ, whereas there is no such a difference between mouse ERα and ERβ (23). In the mouse, specific phosphorylation sites in the AF-1 domain of mouse ERβ can alter the activity of ERβ (51) and its stability (23).

This difference between human ERα and ERβ also stresses the importance of domain orientations in ERα. The orientation between the AF-1 and AF-2 domains in ERα is affected by selective anti-estrogens and can be subtly modified by the structure of these anti-estrogens. Moreover, the orientation between AF-1 and AF-2 is modulated by phospho-modifications of the receptor and/or overexpression of cofactors. How the various domains of ERα and co-factors collaborate in breast tumor growth and the responses to anti-estrogens is gradually becoming apparent.

Experimental Procedures

Cell culture, constructs and antibodies

Human osteosarcoma U2OS, MCF-7 and HeLa PRL array cells (28) were cultured in Dulbecco's Modified Eagle Medium in the presence of 10% FCS and standard antibiotics. Cells containing estrogen receptor constructs were cultured in phenol red-free DMEM medium containing 5% charcoal-treated serum (CTS; Hyclone).
The cloning prodecures for $ERα^{AF\text{-}1β}$, $ERβ^{AF\text{-}1α}$, $ERα^{Shingeβ}$, $ERα^{Lhingeβ}$, $ERβ^{Shingeα}$ and $ERβ^{Lhingeα}$ swap construct are described in the supplemental data section.
ERα, ERβ, SRC-1(aa623-711)-YFP and SRC-1(aa1051-1240)-YFP constructs were generated as described previously (25;31). Antibodies used were raised against ERα (Novocastra/ Cell Signaling), tubulin (Sigma), ERβ (Santacruz), RNA polymerase II (8WG16; Covance, Inc.) and GFP (52).

ERE and AP-1 dependent luciferase assay

Luciferase assays were performed as described previously (53), transfecting 2 ng of ER and 0.2 μg ERE-tk-Firefly luciferase or 0.2 μg of ER and 0.2 μg AP-1-tk-Firefly luciferase using PEI (Polyethylenimine, Mw 25kDa, Polysciences) (54) and 2 ng SV40 Renilla luciferase as a control. For specific inhibition of AF-1 or AF-2 activity of ERα, the SRC-1 truncation mutants of aa 1051-1240-YFP or aa 623-711-YFP (25) were cotransfected at 0.5 and 0.2 μg per well, respectively and supplemented with pcDNA 3 empty vector to equalize the total amount of DNA per well.

RNA Polymerase II recruitment assay

RNA Polemerase II recruitment was assayed as described before (25). Where indicated, cells were cotransfected with YFP-tagged SRC-1 fragments of aa 623-711 or aa 1051-1240. 2 hours before fixation, cells were treated with 1μM estradiol, tamoxifen or left untreated. Thereafter, cells were fixed with 3.7% formaldehyde in PBS and subsequently stained with antibodies detecting ERα, ERβ and RNA polymerase II, and secondary antibodies conjugated to Alexa 405 and Alexa 647 (Molecular Probes, Leiden, The Netherlands).

Quantitative RT-PCR

MCF-7 cells were cultured for 72 hours on CTS containing phenol red-free DMEM after which they were transfected with ERα, ERβ, $ERα^{AF\text{-}1β}$ or $ERβ^{AF\text{-}1α}$ using electroporation. 24 hours after seeding, the cells were treated with 10^{-8} M E2, 10^{-7} M tamoxifen or left untreated for 5 hours, and QPCR was performed using standard protocols. cDNA was amplified using oligo's described in the supplemental data section.

Acknowledgements

We thank Lennert Janssen and Cristiane Bentin-Toaldo for generating the chimeric mutants of ERα and SRC-1.

References

1. Speirs V, Carder PJ, Lane S, Dodwell D, Lansdown MR, Hanby AM 2004 Oestrogen receptor beta: what it means for patients with breast cancer. Lancet Oncol 5:174-181

2. Chang EC, Charn TH, Park SH, Helferich WG, Komm B, Katzenellenbogen JA, Katzenellenbogen BS 2008 Estrogen Receptors alpha and beta as determinants of gene expression: influence of ligand, dose, and chromatin binding. Mol Endocrinol 22:1032-1043

3. Williams C, Edvardsson K, Lewandowski SA, Strom A, Gustafsson JA 2008 A genome-wide study of the repressive effects of estrogen receptor beta on estrogen receptor alpha signaling in breast cancer cells. Oncogene 27:1019-1032

4. Paech K, Webb P, Kuiper GG, Nilsson S, Gustafsson J, Kushner PJ, Scanlan TS 1997 Differential ligand activation of estrogen receptors ERalpha and ERbeta at AP1 sites. Science 277:1508-1510

5. Paige LA, Christensen DJ, Gron H, Norris JD, Gottlin EB, Padilla KM, Chang CY, Ballas LM, Hamilton PT, McDonnell DP, Fowlkes DM 1999 Estrogen receptor (ER) modulators each induce distinct conformational changes in ER alpha and ER beta. Proc Natl Acad Sci U S A 96:3999-

6. Barkhem T, Carlsson B, Nilsson Y, Enmark E, Gustafsson J, Nilsson S 1998 Differential response of estrogen receptor alpha and estrogen receptor beta to partial estrogen agonists/antagonists. Mol Pharmacol 54:105-112

7. Van Den Bemd GJ, Kuiper GG, Pols HA, Van Leeuwen JP 1999 Distinct effects on the conformation of estrogen receptor alpha and beta by both the antiestrogens ICI 164,384 and ICI 182,780 leading to opposite effects on receptor stability. Biochem Biophys Res Commun 261:1-5

8. Kraichely DM, Sun J, Katzenellenbogen JA, Katzenellenbogen BS 2000 Conformational changes and coactivator recruitment by novel ligands for estrogen receptor-alpha and estrogen receptor-beta: correlations with biological character and distinct differences among SRC coactivator family members. Endocrinology 141:3534-3545

9. Klinge CM, Jernigan SC, Mattingly KA, Risinger KE, Zhang J 2004 Estrogen response element-dependent regulation of transcriptional activation of estrogen receptors alpha and beta by coactivators and corepressors. J Mol Endocrinol 33:387-410

10. Wada-Hiraike O, Hiraike H, Okinaga H, Imamov O, Barros RP, Morani A, Omoto Y, Warner M, Gustafsson JA 2006 Role of estrogen receptor beta in uterine stroma and epithelium: Insights from estrogen receptor beta-/- mice. Proc Natl Acad Sci U S A 103:18350-18355

11. Wada-Hiraike O, Imamov O, Hiraike H, Hultenby K, Schwend T, Omoto Y, Warner M, Gustafsson JA 2006 Role of estrogen receptor beta in colonic epithelium. Proc Natl Acad Sci U S A 103:2959-2964

12. Helguero LA, Faulds MH, Gustafsson JA, Haldosen LA 2005 Estrogen receptors alfa (ERalpha) and beta (ERbeta) differentially regulate proliferation and apoptosis of the normal murine mammary epithelial cell line HC11. Oncogene 24:6605-6616

13. Forster C, Kietz S, Hultenby K, Warner M, Gustafsson JA 2004 Characterization of the ERbeta-/-mouse heart. Proc Natl Acad Sci U S A 101:14234-14239

14. Kudwa AE, Bodo C, Gustafsson JA, Rissman EF 2005 A previously uncharacterized role for estrogen receptor beta: defeminization of male brain and behavior. Proc Natl Acad Sci U S A 102:4608-4612

15. Klein-Hitpass L, Tsai SY, Greene GL, Clark JH, Tsai MJ, O'Malley BW 1989 Specific binding of estrogen receptor to the estrogen response element. Mol Cell Biol 9:43-49

16. Sabbah M, Courilleau D, Mester J, Redeuilh G 1999 Estrogen induction of the cyclin D1 promoter: involvement of a cAMP response-like element. Proc Natl Acad Sci U S A 96:11217-11222

17. Pearce ST, Jordan VC 2004 The biological role of estrogen receptors alpha and beta in cancer. Crit Rev Oncol Hematol 50:3-22

18. Weatherman RV, Clegg NJ, Scanlan TS 2001 Differential SERM activation of the estrogen receptors (ERalpha and ERbeta) at AP-1 sites. Chem Biol 8:427-436

19. Yi P, Bhagat S, Hilf R, Bambara RA, Muyan M 2002 Differences in the abilities of estrogen receptors to integrate activation functions are critical for subtype-specific transcriptional responses. Mol Endocrinol 16:1810-1827

20. Metivier R, Penot G, Flouriot G, Pakdel F 2001 Synergism between ERalpha transactivation function 1 (AF-1) and AF-2 mediated by steroid receptor coactivator protein-1: requirement for the AF-1 alpha-helical core and for a direct interaction between the N- and C-terminal domains. Mol Endocrinol 15:1953-1970

21. Yi P, Driscoll MD, Huang J, Bhagat S, Hilf R, Bambara RA, Muyan M 2002 The effects of estrogen-responsive element- and ligand-induced structural changes on the recruitment of cofactors and transcriptional responses by ER alpha and ER beta. Mol Endocrinol 16:674-693

22. Bowers JL, Tyulmenkov VV, Jernigan SC, Klinge CM 2000 Resveratrol acts as a mixed agonist/antagonist for estrogen receptors alpha and beta. Endocrinology 141:3657-3667

23. Picard N, Charbonneau C, Sanchez M, Licznar A, Busson M, Lazennec G, Tremblay A 2008 Phosphorylation of activation function-1 regulates proteasome-dependent nuclear mobility and E6-associated protein ubiquitin ligase recruitment to the estrogen receptor beta. Mol Endocrinol 22:317-330

24. Gustafsson JA 2000 An update on estrogen receptors. Semin Perinatol 24:66-69

25. Zwart W, Griekspoor A, Berno V, Lakeman K, Jalink K, Mancini M, Neefjes J, Michalides R 2007 PKA-induced resistance to tamoxifen is associated with an altered orientation of ERalpha towards co-activator SRC-1. EMBO J 26:3534-3544

26. Padron A, Li L, Kofoed EM, Schaufele F 2007 Ligand-selective interdomain conformations of estrogen receptor-alpha. Mol Endocrinol 21:49-61

27. Carroll JS, Meyer CA, Song J, Li W, Geistlinger TR, Eeckhoute J, Brodsky AS, Keeton EK, Fertuck KC, Hall GF, Wang Q, Bekiranov S, Sementchenko V, Fox EA, Silver PA, Gingeras TR, Liu XS, Brown M 2006 Genome-wide analysis of estrogen receptor binding sites. Nat Genet 38:1289-1297

28. Sharp ZD, Mancini MG, Hinojos CA, Dai F, Berno V, Szafran AT, Smith KP, Lele TP, Ingber DE, Mancini MA 2006 Estrogen-receptor-alpha exchange and chromatin dynamics are ligand- and domain-dependent. J Cell Sci 119:4101-4116

29. Merot Y, Metivier R, Penot G, Manu D, Saligaut C, Gannon F, Pakdel F, Kah O, Flouriot G 2004 The relative contribution exerted by AF-1 and AF-2 transactivation functions in estrogen receptor alpha transcriptional activity depends upon the differentiation stage of the cell. J Biol Chem 279:26184-26191

30. Shiau AK, Barstad D, Loria PM, Cheng L, Kushner PJ, Agard DA, Greene GL 1998 The structural basis of estrogen receptor/coactivator recognition and the antagonism of this

interaction by tamoxifen. Cell 95:927-937

31. Michalides R, Griekspoor A, Balkenende A, Verwoerd D, Janssen L, Jalink K, Floore A, Velds A, van't Veer L, Neefjes J 2004 Tamoxifen resistance by a conformational arrest of the estrogen receptor alpha after PKA activation in breast cancer. Cancer Cell 5:597-605

32. Webb P, Nguyen P, Shinsako J, Anderson C, Feng W, Nguyen MP, Chen D, Huang SM, Subramanian S, McKinerney E, Katzenellenbogen BS, Stallcup MR, Kushner PJ 1998 Estrogen receptor activation function 1 works by binding p160 coactivator proteins. Mol Endocrinol 12:1605-1618

33. Hatzis P, Talianidis I 2002 Dynamics of enhancer-promoter communication during differentiation-induced gene activation. Mol Cell 10:1467-1477

34. Llopis J, Westin S, Ricote M, Wang Z, Cho CY, Kurokawa R, Mullen TM, Rose DW, Rosenfeld MG, Tsien RY, Glass CK 2000 Ligand-dependent interactions of coactivators steroid receptor coactivator-1 and peroxisome proliferator-activated receptor binding protein with nuclear hormone receptors can be imaged in live cells and are required for transcription. Proc Natl Acad Sci U S A 97:4363-4368

35. Petz LN, Ziegler YS, Schultz JR, Kim H, Kemper JK, Nardulli AM 2004 Differential regulation of the human progesterone receptor gene through an estrogen response element half site and Sp1 sites. J Steroid Biochem Mol Biol 88:113-122

36. Petz LN, Ziegler YS, Schultz JR, Nardulli AM 2004 Fos and Jun inhibit estrogen-induced transcription of the human progesterone receptor gene through an activator protein-1 site. Mol Endocrinol 18:521-532

37. Petz LN, Ziegler YS, Loven MA, Nardulli AM 2002 Estrogen receptor alpha and activating protein-1 mediate estrogen responsiveness of the progesterone receptor gene in MCF-7 breast cancer cells. Endocrinology 143:4583-4591

38. Schultz JR, Petz LN, Nardulli AM 2003 Estrogen receptor alpha and Sp1 regulate progesterone receptor gene expression. Mol Cell Endocrinol 201:165-175

39. Kelley ST, Thackray VG 1999 Phylogenetic analyses reveal ancient duplication of estrogen receptor isoforms. J Mol Evol 49:609-614

40. Strom A, Hartman J, Foster JS, Kietz S, Wimalasena J, Gustafsson JA 2004 Estrogen receptor beta inhibits 17beta-estradiol-stimulated proliferation of the breast cancer cell line T47D. Proc Natl Acad Sci U S A 101:1566-1571

41. Li X, Huang J, Yi P, Bambara RA, Hilf R, Muyan M 2004 Single-chain estrogen receptors (ERs) reveal that the ERalpha/beta heterodimer emulates functions of the ERalpha dimer in genomic estrogen signaling pathways. Mol Cell Biol 24:7681-7694

42. Rayala SK, Talukder AH, Balasenthil S, Tharakan R, Barnes CJ, Wang RA, Aldaz M, Khan S, Kumar R 2006 P21-activated kinase 1 regulation of estrogen receptor-alpha activation involves serine 305 activation linked with serine 118 phosphorylation. Cancer Res 66:1694-1701

43. Eakin CM, Maccoss MJ, Finney GL, Klevit RE 2007 Estrogen receptor alpha is a putative substrate for the BRCA1 ubiquitin ligase. Proc Natl Acad Sci U S A 104:5794-5799

44. Subramanian K, Jia D, Kapoor-Vazirani P, Powell DR, Collins RE, Sharma D, Peng J, Cheng X, Vertino PM 2008 Regulation of estrogen receptor alpha by the SET7 lysine methyltransferase. Mol Cell 30:336-347

45. Wang C, Fu M, Angeletti RH, Siconolfi-Baez L, Reutens AT, Albanese C, Lisanti MP, Katzenellenbogen BS, Kato S, Hopp T, Fuqua SA, Lopez GN, Kushner PJ, Pestell RG 2001 Direct acetylation of the estrogen receptor alpha hinge region by p300 regulates transactivation and hormone sensitivity. J Biol Chem 276:18375-18383

46. Kim MY, Woo EM, Chong YT, Homenko DR, Kraus WL 2006 Acetylation of estrogen receptor alpha by p300 at lysines 266 and 268 enhances the deoxyribonucleic acid binding and transactivation activities of the receptor. Mol Endocrinol 20:1479-1493

47. Stossi F, Barnett DH, Frasor J, Komm B, Lyttle CR, Katzenellenbogen BS 2004 Transcriptional profiling of estrogen-regulated gene expression via estrogen receptor (ER) alpha or ERbeta in human osteosarcoma cells: distinct and common target genes for these receptors. Endocrinology 145:3473-3486

48. Xu J, Li Q 2003 Review of the *in vivo* functions of the p160 steroid receptor coactivator family. Mol Endocrinol 17:1681-1692

49. Heery DM, Kalkhoven E, Hoare S, Parker MG 1997 A signature motif in transcriptional co-activators mediates binding to nuclear receptors. Nature 387:733-736

50. Hawse JR, Subramaniam M, Monroe DG, Hemmingsen AH, Ingle JN, Khosla S, Oursler MJ, Spelsberg TC 2008 Estrogen Receptor {beta} Isoform-Specific Induction of Transforming Growth Factor {beta}-Inducible Early Gene-1 in Human Osteoblast Cells: An Essential Role for the Activation Function 1 Domain. Mol Endocrinol 22:1579-1595

51. Tremblay A, Tremblay GB, Labrie F, Giguere V 1999 Ligand-independent recruitment of SRC-1 to estrogen receptor beta through phosphorylation of activation function AF-1. Mol Cell 3:513-519

52. van Ham SM, Tjin EP, Lillemeier BF, Gruneberg U, van Meijgaarden KE, Pastoors L, Verwoerd D, Tulp A, Canas B, Rahman D, Ottenhoff TH, Pappin DJ, Trowsdale J, Neefjes J 1997 HLA-DO is a negative modulator of HLA-DM-mediated MHC class II peptide loading. Curr Biol 7:950-957

53. Bindels EM, Lallemand F, Balkenende A, Verwoerd D, Michalides R 2002 Involvement of G1/S cyclins in estrogen-independent proliferation of estrogen receptor-positive breast cancer cells. Oncogene 21:8158-8165

54. Boussif O, Lezoualc'h F, Zanta MA, Mergny MD, Scherman D, Demeneix B, Behr JP 1995 A versatile vector for gene and oligonucleotide transfer into cells in culture and *in vivo*: polyethylenimine. Proc Natl Acad Sci U S A 92:7297-7301

Supplemental Data

materials and methods

cloning procedures and oligo's

The $ER\alpha^{AF\text{-}1\beta}$ and $ER\beta^{AF\text{-}1\alpha}$ swap constructs were made by pair wise ligation of four separate PCR fragments in a second PCR reaction. The AF-1α (aa 1-180) and AF-1β (aa 1-144) fragments were made using forward primer (A) 5'AATTGGATCCACCACCATGGCATAC CCATACGACGTCCCAGACTACGCTATGACCATG ACCCTCCACACC and reverse primer (B) 5'GCGCA GAAGTGAGCATCCTTGGCAGATTCCATAGCC or forward primer (C) 5'AATTGGATCCACCACCATG GCATACCCATACGACGTCCCAGACTACGCTATG-GATATAAAAAACTCACC and reverse primer (D) 5'GCACAGTAGCGAGTCTCCCTCTTTGAACCTG GACC respectively, introducing a BamHI restriction site and a HA-tag at the 5'-ends and a ERβ- or ERα-overhang at the 3'-ends of the fragments. The $ER\alpha^{\Delta AF\text{-}1}$ and $ER\beta^{\Delta AF\text{-}1}$ fragments lacking the AF-1 regions were made using forward primer (E) 5'GGTCCAGGTTC AAAGAGGGAGACTCGCTACTGTGC and reverse primer (F) 5'TGGGGGATCCTTATCAGACTGTGG CAGGGAAACC or forward primer (G) 5'GGCTATG GAATCTGCCAAGGATGCTCACTTCTGCGC and reverse primer (H) 5'AATTGGATCCTCACTGAGAC TGTGGGTTCTGG respectively, introducing a ERβ- or ERα-overhang at the 5'-ends and a stopcodon and BamHI restriction site at the 3'-ends of the fragments. The AF-1α and $ER\beta^{\Delta AF\text{-}1}$ and AF-1β and $ER\alpha^{\Delta AF\text{-}1}$ fragments were then ligated to each other in a second PCR reaction using forward primer (A) and reverse primer (H) or forward primer (C) and reverse primer (F). These swap constructs were cloned in the dephosphorylated BamHI site of the pcDNA3 vector.

$ER\alpha^{Shinge\beta}$, $ER\alpha^{Lhinge\beta}$, $ER\beta^{Shinge\alpha}$ and $ER\beta^{Lhinge\alpha}$ constructs were made by sequential PCR reactions, ligating ten separate smaller PCR fragments into four different, larger fragments containing the chimeric hinge regions.

The two PCR fragments used for the construction of $ER\alpha^{Shinge\beta}$ (aa 253-262) were made using forward primer (1) 5'AATTCCGCGGCCGCCGCCAACGCGCAGG and reverse primer (2) 5'GGCGTCCAGCAGCAGCT CCCGCACTCGGGGTGGCCAAAGGTTGGC and forward primer (3) 5'CCCCGAGTGCGGGAGCTGCT GCTGGACGCCCTGACGGCCGACCAG and reverse primer (4) 5'TGGTCTAGAAGGTGGACCTGATCAT GGAG, which were then ligated in a second PCR reaction using forward primer (1) and reverse primer (4) introducing a SacII restriction site at the 5'-end and a XbaI site at the 3'-end. This was then inserted into the corresponding restriction sites in a pcDNA3-ERα vector.

The two PCR fragments used for the construction of $ER^{\beta Shinge\alpha}$ (aa 294-309) were made using forward primer (5) 5'CCAGATATCACTATGGAGTCTGGTC GTGTG and reverse primer (6) 5'GGACAAGGCCA GGCTGTTCTTCTTAGAGCGTTTGATCATGAGCG-GGCTCGCGTGGCCGCCACTTCTCTTGGCC and forward primer (7) 5'AGCCCGCTCATGATCAAAC GCTCTAAGAAGAACAGCCTGGCCTTGTCCCTG AGCCCCGAGCAGCTAGTGCTCACC and reverse primer (8) 5'TGGGAATTCCTTCTACGCATTTCCC CTCATCC, which were then ligated in a second PCR reaction using forward primer (5) and reverse primer (8) introducing an EcoRV restriction site at the 5'-end and an EcoRI site at the 3'-end. This was then inserted into the corresponding restriction sites in a pcDNA3-ERβ vector.

The three PCR fragments used for the construction of $ER\alpha^{Lhinge\beta}$ (aa 220-283) were made using forward primer (1) and reverse primer (9) 5'CACATCTCTCTCTCCGT ATCCCACCTTTCATCATTCCC, forward primer (10) 5'CGGAGAGAGAGATGTGGGTACC and reverse primer (11) 5'GCGGCTGATCAGCACATGGGGC and forward primer (12) 5'TGTGCTGATCAGCCGC CCTACCAGACCCTTCAGTGAAGCTTCG and reverse primer (4), which were then sequentially ligated in a second and third PCR reaction using forward primer (1) and reverse primer (11) and forward primer (1) and reverse primer (4) respectively, introducing a SacII restriction site at the 5'-end and a XbaI site at the 3'-end. This was then inserted into the corresponding restriction sites in a pcDNA3-ERα vector.

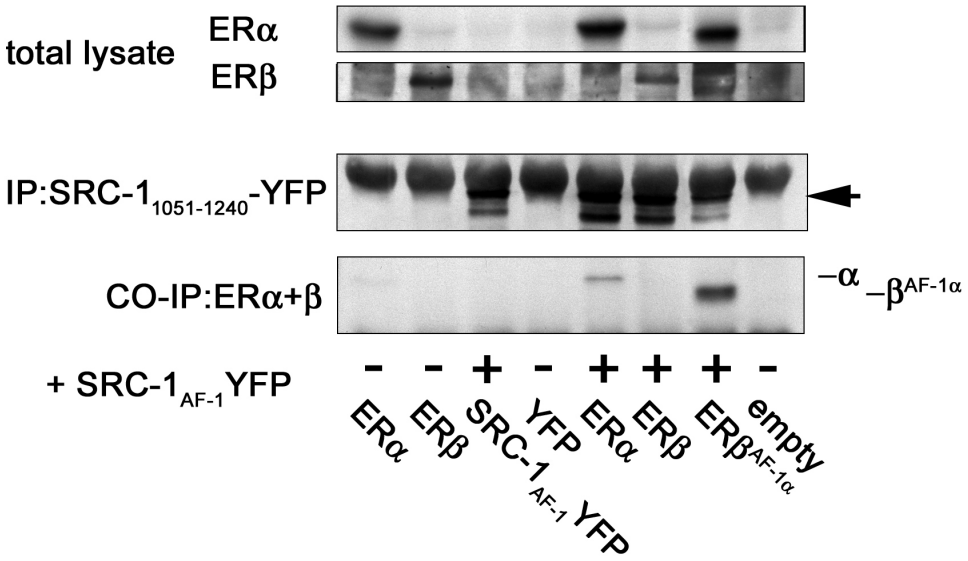
The three PCR fragments used for the construction of $ER\beta^{Lhinge\alpha}$ (aa 256-332) were made using forward primer (5) and reverse primer (13) 5 'CTCCTCTTCGGTCTTTTCGGGAGCCAC ACTTCACCATTCCC, forward primer (14) 5'CGAAAAGACCGAAGAGGAGGGAG and reverse primer (15) 5'ATCATACTCGGAATAGAGTATGGG and forward primer (16) 5'CTCTATTCCGAGTATG ATCCCAGTGCGCCCTTCACCGAGG and reverse primer (8), which were then ligated in a sequential second and third PCR reaction using forward primer (5) and reverse primer (15) and forward primer (5) and reverse primer (8) respectively, introducing an EcoRV restriction site at the 5'-end and an EcoRI site at the 3'-end. This was then inserted into the corresponding restriction sites in a pcDNA3-ERβ vector.

For QPCR analysis, primers were used for PR with the forward primer 5' CGCGCTACCCTGCACTC and the reverse primer 5' TGAATCCGGCCTCAGGTAGTT. As a control for equal loading, the observed PR signal was related to β-actin RNA levels, using a forward primer 5' CCTGGCACCCAGCACAAT and reverse primer 5' GGGCCGGACTCGTCATACT.

Immunoprecipitation

U2OS cells were transfected with ERα, ERβ or ERβ$^{AF-1α}$ either or not in the presence of SRC-$1_{1051-1240}$-YFP using PEI. 24 hours after transfections, cells were lysed in 125mM NaCl, 50mM HEPES (pH 7.5), 0,1% Nonidet P-40, 10mM MgCl2 and protease inhibitor cocktail (Roche) on ice, sonificated and debris was removed by centrifugation. The supernatant was used in immunoprecipitation using anti-GFP antibody immobilized on protein A Sepharose beads (Invitrogen) during incubation overnight. Samples were taken from the supernatant for analysis of the total lysate. Beads were extensively washed, boiled and samples were analyzed by Western blotting. For detection, antibodies identifying ERα, ERβ and GFP were used, and the signal was detected using an ECL detection kit (Amersham).

S1

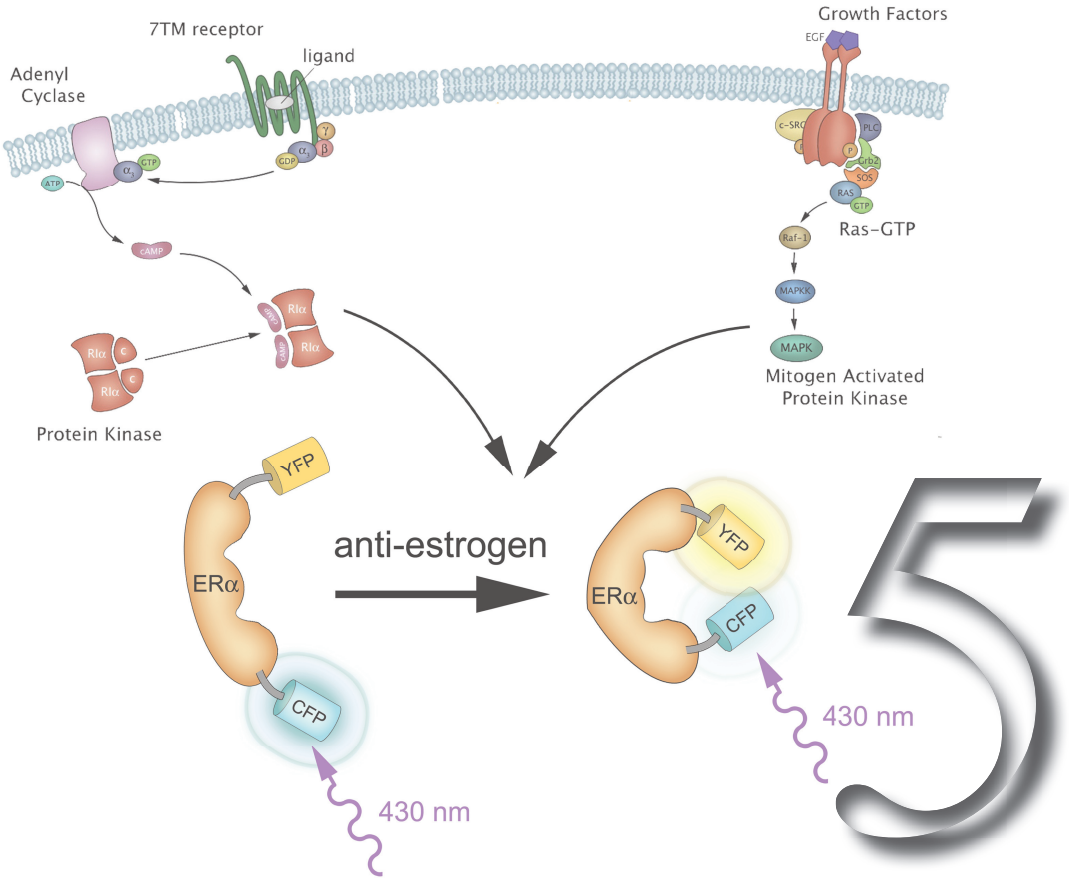


Supplemental Figure S1. The AF-1 domain of ERα but not of ERβ binds to SRC-1

U2OS cells were transfected with ERα, ERβ or one of the AF-1 swap mutants, and cotransfected with SRC-$1_{1051-1240}$-YFP where indicated. SCR-$1_{1051-1240}$ was immunoprecipitated after which the co-immunoprecipitated ER was identified using antibodies against ERα and ERβ. Arrow indicates SRC-$1_{1051-1240}$-YFP signal, detected below the IgG background band.

Classification of anti-estrogens according to intramolecular FRET effects on phospho-mutants of ERα

Molecular Cancer Therapeutics 2007, vol. 6: 1526-1633



Classification of anti-estrogens according to intramolecular FRET effects on phospho-mutants of ERα

Wilbert Zwart, Alexander Griekspoor, Mariska Rondaij, Desiree Verwoerd, Jacques Neefjes and Rob Michalides[1]

Abstract
Anti-estrogen resistance is a major clinical problem in the treatment of breast cancer. In this study, Fluorescence Resonance Energy Transfer (FRET) analysis, a rapid and direct way to monitor conformational changes of ERα upon anti-estrogen binding, was used to characterize resistance to anti-estrogens. Nine different anti-estrogens all induced a rapid FRET response within minutes after the compounds have liganded to ERα in live cells, corresponding to an inactive conformation of the ERα. Phosphorylation of serine 305 and/or serine 236 of ERα by protein Kinase A and of serine 118 by MAP kinase influenced the FRET response differently for the various anti-estrogens. PKA and MAPK are both associated with resistance to anti-estrogens in breast cancer patients, Their respective actions can result in seven different combinations of phospho-modifications in ERα where the FRET effects of (a) particular anti-estrogens(s) are nullified. The FRET response provided information on the activity of ERα under the various anti-estrogen conditions as measured in a traditional reporter assay. Tamoxifen and EM-652 were the most sensitive to kinase activities, whereas ICI-182,780 (Fulvestrant) and ICI-164,384 were the most stringent. The different responses of anti-estrogens to the various combinations of phospho-modifications in ERα elucidate why certain anti-estrogens are more prone than others to develop resistance. These data provide new insights into the mechanism of action of anti-hormones and are critical for selection of the correct individual patient-based endocrine therapy in breast cancer.

Introduction

Three quarter of breast cancer patients have Estrogen Receptor (ER) positive disease and are commonly treated with anti-estrogen tamoxifen. Despite a successful drug, almost 50% reduction in recurrence during 10 years of follow-up of ER-positive patients, and a reduction in mortality by a third, still a substantial proportion of BC patients who are treated with tamoxifen develop a relapse and are to be treated with different anti-estrogens and/or aromatase inhibitors (1-3). Early diagnosis of anti-estrogen resistance could therefore lead to a proper patient selection for adequate therapy.

A lead to early diagnosis of resistance to anti-estrogens is provided by the molecular mechanism of resistance to anti-estrogens. Anti-estrogens that bind the receptor inhibit its activity by modulating transactivation capacities of either the N-terminally located AF-1 and/or AF-2 at the C-terminus of ERα (4). The most carboxyl-terminal α-helix (H12) of the ER-LBD (Ligand Binding Domain) acts as a molecular switch for transactivation to occur. Its orientation determines the transcriptional read-out of the receptor. Binding of the different anti-estrogens to the LBD reorients H12 and conceals the coactivator-binding groove that consists of a pocket formed by α-helices 3, 4, 5 and 12 (5;6). This distortion of H12 is not fixed, but occurs to various extents, depending on the side chain and polarity of the anti-estrogen applied (7). The conformational state of ERα can be measured using biophysical methods such as fluorescence resonance energy transfer (FRET) (8). Using FRET, we have demonstrated that anti-estrogens induce a conformational change that is overridden by phosphorylation of particular target sites on ERα, resulting in resistance to that anti-estrogen (9). For instance, resistance to tamoxifen is caused by phosphorylation of serine-305 of ERα by Protein Kinase A (PKA). Tamoxifen binds but then fails to induce the inactive conformation, invoking ERα-dependent transactivation instead. PKA activity thus induces a switch from antagonistic to agonistic effects of tamoxifen on ERα. In a retrospective clinical study, we confirmed that an elevated PKA level is associated with tamoxifen resistance in ER positive breast cancer (9). Serine-305 is also the target of p21-activated kinase, PAK-1 (10), and overexpression of PAK-1 is in a similar way associated with resistance to tamoxifen (11). In addition, resistance to anti-estrogens is also associated with modification of ERα by MAPK (12-14) and by the expression levels and/or phosphorylation status of cofactors such as SRC-1 (15)

Department of Tumor Biology,
the Netherlands Cancer Institute, Plesmanlaan 121, 1066CX Amsterdam, the Netherlands
Running title: Anti-estrogen resistance and ERα phosphorylation
Keywords: estrogen receptor / resistance / anti-estrogens / FRET/ Tamoxifen/ Protein Kinase A / PKA / MAP kinase / MAPK
Abbreviations: CFP, cyano fluorescent protein; CTS, charcoal treated serum; ER, estrogen receptor; FRET, fluorescence resonance energy transfer; LBD, ligand binding domain; PAK-1, p21 activated kinase-1; PKA, protein kinase A; SERM, selective estrogen receptor modulator; SERD, selective estrogen receptor downregulator; SRC, steroid receptor co-activator, YFP, yellow fluorescent protein.
[1]Correspondence: r.michalides@nki.nl
phone : + 31 20 5122022

and SRC-3 (14;16). Aberrant activation of other signaling pathways in ER-positive breast cancer cells will result in post-translational modification(s) on the estrogen receptor that affect resistance to anti-estrogens. In this way, and of clinical relevance, resistance to two different anti-estrogens used in the clinic, tamoxifen and ICI-182,780 (Fulvestrant), was distinguishable: resistance to tamoxifen was due to PKA-mediated phosphorylation of serine-305, whereas resistance to ICI-182,780 (Fulvestrant) required additional overexpression of cofactors cyclin D1 and SRC-1. Anti-estrogen characteristic requirements for resistance are also foreseen by a different binding profile of randomly generated peptides to ERα in the presence of various anti-estrogens (17-19). Moreover, the 3D structures of the ligand binding domain of ERα bound to different anti-estrogens indicate anti-estrogen specific distortions of ERα (20).

In the present study we investigated the requirements for resistance to nine different anti-estrogens using a FRET approach, and related these to consecutive ER transactivation events. This led to seven different combinations of phospho-modifications in ERα, each of which is associated with a FRET-related resistance to (a) particular anti-estrogen(s). This anti-estrogen specific profile reveals a mechanism for anti-estrogen resistance and provides a molecular explanation for the outcome of anti-estrogen therapy.

Results

Characterization of the phospho-variants of ERα

In this study we used phospho-mutants of ERαthat were characterized by Western blotting using phospho-ERα-specific antibodies (Figure 1B). U2OS cells containing either wild-type ERα, a S118E mutant that mimics phosphorylation by MAPK at that site or a S305A mutant that cannot be phosphorylated by PKA at that site, all showed equal levels of ERα, which was detected with an antibody recognizing the GFP tags at both sides of the protein. These ERα-GFP bands were also visible with an antibody detecting ERα (data not shown). The S118E-ERα containing cells showed expression of this protein using an antiserum that specifically detects phosphorylated S118-ERα, whereas treatment with PKA activator 8-Br-cAMP and the use of an antiserum that detects phospho-S305-ERα revealed phospho-S305-ERα in the cells transfected with wild-type and S118E-ERα, but not in cells transfected with S305A-ERα.

Characteristics of anti-estrogens and FRET

Anti-estrogens can be distinguished in selective estrogen receptor modulators (SERMs), such as tamoxifen, and full anti-estrogens or selective estrogen receptor downregulators (SERDs), such as ICI compounds 182,780 (Fulvestrant) and 164,384 (21), whereas anti-estrogen GW5638 has mixed SERM/SERD properties (22). The compounds used in this study, and their structure are described in Figure 1A. They differ widely in biological effects *in vitro* and *in vivo* (23;24).

Anti-estrogens can form hydrogen bonds with the amino acid residues in ERα. Agonist estradiol binds to glu 353, arg 394 and his 524, whereas the anti-estrogens bind to additional amino acid residues, which together with the respective nature of the side chain of the anti-estrogens, results in different distortions of the LBD of ERα (7). We measured such distortions by FRET, where we applied the various anti-estrogens to ER-negative U2OS cells, now transfected with a recombinant ERα with Yellow Fluorescent Protein (YFP) at the N- and Cyan Fluorescent protein (CFP) at the C-terminus. Application of anti-estrogens to these cells resulted in an altered position/orientation that induced a change in energy transfer between the two fluorophores. Using this approach, we are able to measure intramolecular changes of ERα as a consequence of exposure to anti-estrogens, which occurred within 15 minutes after administration of the anti-estrogens. The recombinant YFP-ERα-CFP construct retained the properties of wild-type ERα, and an optimal amount of YFP-ERα-CFP for FRET detection (0.5 μg per 10^5 cells) in combination with an excess of anti-estrogens (10^{-6} M) was used in our FRET experiments (9). The principle of FRET and a representative experiment where FRET is detected in the form of the ratio between YFP and CFP following tamoxifen addition at 400 seconds, are presented in Figure 2.

Characterization of PKA-mediated resistance to anti-estrogens by FRET

The FRET changes induced by the various anti-estrogens in wt YFP-ERα-CFP containing U2OS cells are presented in box plots in Figure 3A, with the median value indicated. The box plots present data of at least three independent measurements. When the FRET changes showed variation, we included at least 10 additional measurement points. The data in Figure 3A demonstrated that anti-estrogens tamoxifen, EM-652, lasofoxifene, raloxifene, toremifene and GW5638 all showed a change in FRET (i.e. induced a conformational change in ERα) that was abolished by pretreatment of the cells with an immediate PKA activator

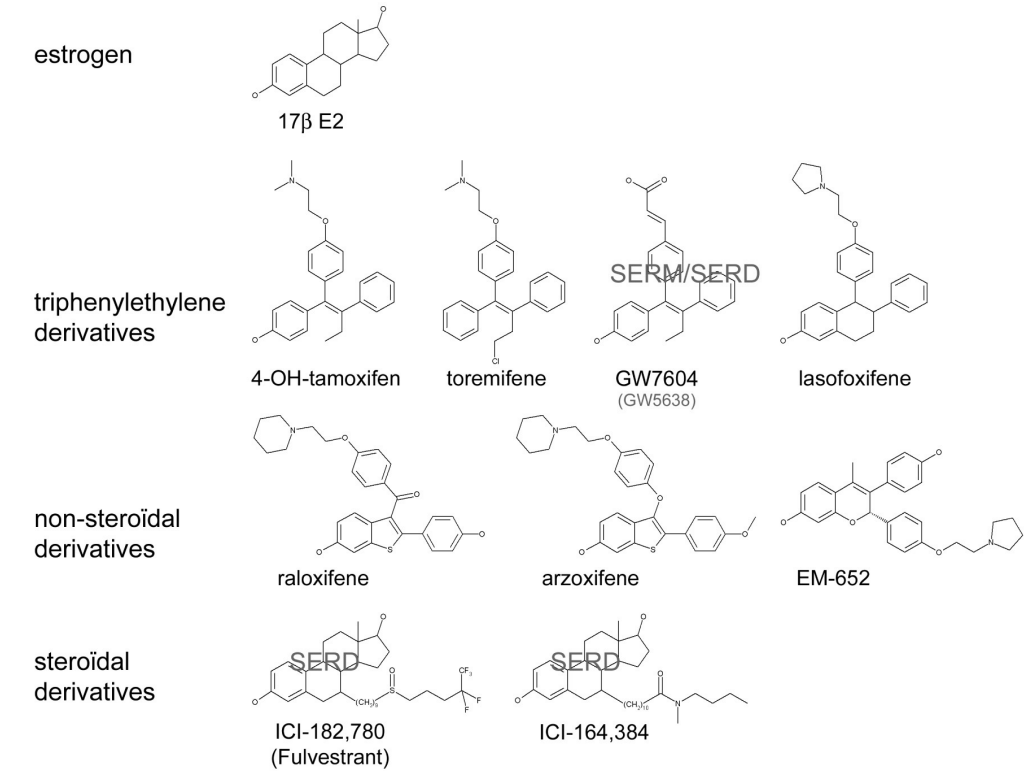


Figure 1

A. Structure of estrogen-like and anti-estrogen-like SERMs and SERDs used in this study.
B. Characterization of the phospho-ERα variants. U2OS cells were transfected with the wild-type YFP-ERα-CFP construct or S118E or S305A mutants thereof, cultured in the presence or absence of 8-Br-cAMP and analyzed for the expression of wild-type ERα or the phospho-mutants of ERα. Anti-tubulin staining was used as a loading control. Absence of the phosphorylated S305-ERα protein in the cells transfected with S305A, but its presence in the PKA treated cells transfected with wild-type or S118E- ERα indicates the inability to phosphorylate mutant S305A-ERα by PKA.

forskolin (25), as we had previously demonstrated for tamoxifen (9). The differences between the control and forskolin treated cells using these anti-estrogens were statistically significant ($p<0.05$). SERDs ICI-182,780 and ICI-164,384 showed a FRET change that was not affected by forskolin, whereas that of arzoxifene was reduced, but did not reach statistical significance.

Does PKA activation affect FRET changes for the sensitive anti-estrogens by phosphorylation of S305 of ERα, as we have demonstrated to be the case for tamoxifen (9)? To study this, we repeated the experiments using an YFP-ERα-S305A-CFP mutant, where serine-305 is replaced with alanine to prevent phosphorylation at this site, Figure 3B. Now PKA did not affect tamoxifen- and EM-652-induced FRET, indicating that PKA-associated resistance to these two anti-estrogens is dependent on PKA-mediated phosphorylation of S305. In case of the other SERMs, lasofoxifene, raloxifene, toremifene and GW5638, the FRET change was still abolished upon pretreatment with forskolin, suggesting that additional PKA driven events were responsible for FRET-predicted resistance to these anti-estrogens. The two other SERDs, ICI-182,780 (Fulvestrant) and ICI-164,384, were again insensitive to pretreatment with forskolin. Arzoxifene now showed a significant, but no absolute loss of FRET

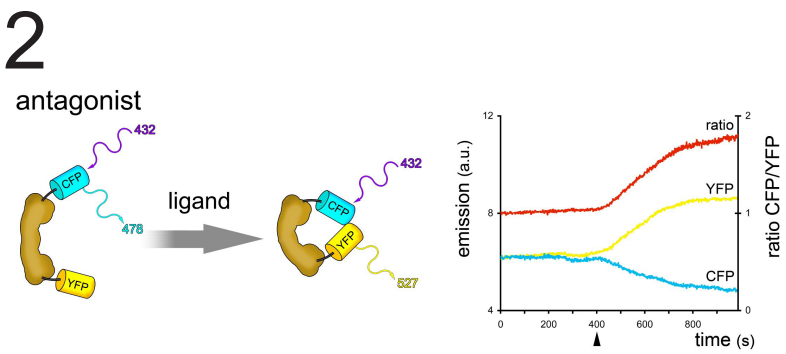


Figure 2. Inactivation of ERα by anti-estrogens measured by FRET.

A. Principle of FRET. Exciting CFP at 432nm results in emission at 478nm unless energy is transferred to YFP. Energy transfer depends on the orientation and distance between the two fluorophores and is highly sensitive to conformational changes. An increased YFP (at 527nm) at the expense of CFP emission can occur as the result of a conformational change of ERα.
B. FRET change induced by tamoxifen. Time course of emission of YFP and CFP and corresponding ratio of YFP/CFP emission of one YFP-wtERα-CFP containing U2OS cell after addition of 10^{-6} M 4'-OH-tamoxifen (TAM).

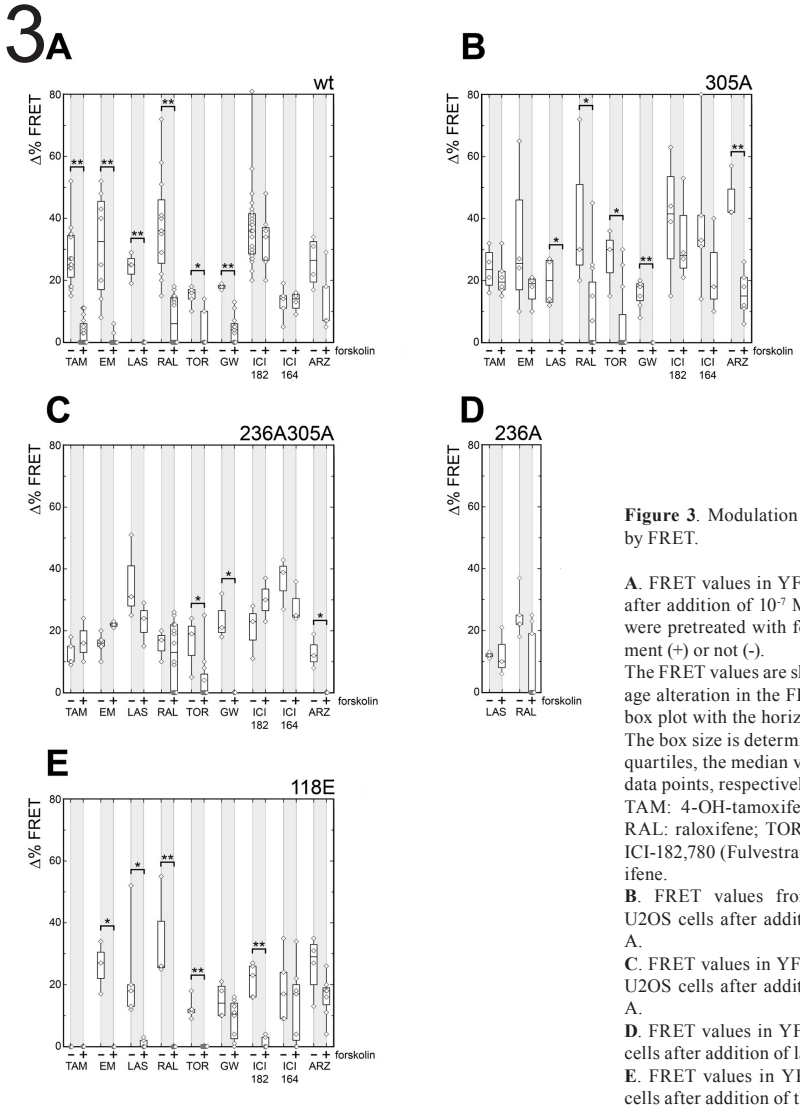


Figure 3. Modulation of anti-estrogen-induced inactivation by FRET.

A. FRET values in YFP-wtERα-CFP expressing U2OS cells after addition of 10^{-7} M of the indicated anti-estrogen. Cells were pretreated with forskolin 15 minutes prior to measurement (+) or not (-).
The FRET values are shown as separate values of the percentage alteration in the FRET ratio. The data are presented in a box plot with the horizontal bar indicating the median value. The box size is determined by the upper and lower quartiles, the median value of the upper and lower half of the data points, respectively.
TAM: 4-OH-tamoxifen; EM: EM-652; LAS: lasofoxifene; RAL: raloxifene; TOR: toremifene; GW: GW5638; ICI 182: ICI-182,780 (Fulvestrant); ICI 164: ICI-164,384; ARZ: arzoxifene.
B. FRET values from YFP-ERα-S305A-CFP expressing U2OS cells after addition of the anti-estrogens indicated in A.
C. FRET values in YFP-ERα-S236A:S305A-CFP expressing U2OS cells after addition of the anti-estrogens indicated in A.
D. FRET values in YFP-ERα-S236A-CFP expressing U2OS cells after addition of lasofoxifene or raloxifene.
E. FRET values in YFP-ERα-S118E-CFP expressing U2OS cells after addition of the anti-estrogens indicated in A.
* indicates a statistically significant FRET reduction between forskolin treated and untreated samples, $P < 0.05$
** indicates a statistically significant FRET reduction between forskolin treated and untreated samples, $P < 0.01$

change upon forskolin pretreatment, suggesting that the effect of this compound was influenced by PKA-modifications of ERα at other sites than S305. In order to investigate the participation of other PKA target sites in ERα (26), we performed the FRET experiments with the YFP-ERα-S236A:S305A-CFP double mutant construct, where both PKA targets in ERα, serine 236 and 305, were replaced with alanine (Figure 3C). PKA pretreatment did not influence the conformational changes of YFP-ERα-S236A:S305A-CFP in response to tamoxifen and EM-652, as to be expected. Importantly, no FRET change was observed for lasofoxifene and raloxifene when pretreated with forskolin, whereas they were recorded with the single S305A mutant. This indicated that resistance to lasofoxifene and raloxifene was due to PKA-mediated phosphorylation of either S236 alone or to a combination of serine sites at positions 236 and 305. Using this double mutant, the reduction in FRET change for toremifene, GW5638 and arzoxifene upon 8-Br-cAMP treatment was still observed, indicating that PKA-mediated resistance of wild-type ERα to these anti-estrogens required other PKA-associated events outside ERα. In order to determine whether resistance to lasofoxifene and raloxifene required PKA-associated phosphorylation of S236 alone or of a combination of S236 and S305, we investigated YFP-ERα-S236A-CFP transfected U2OS cells (Figure 3D). The FRET change induced by lasofoxifene was completely abrogated upon pretreatment with forskolin, whereas FRET change induced by raloxifene was only partially affected. This indicated that FRET-predicted resistance to lasofoxifene required PKA-mediated phosphorylation of S236, whereas resistance to raloxifene was generated by PKA-mediated phosphorylation of either S236 or S305, or of a combination of both sites.

With respect to PKA-mediated resistance, five groups of anti-estrogens can be distinguished:
A. Tamoxifen and EM-652, where resistance is associated with PKA-mediated phosphorylation of ERα at S305.
B. Lasofoxifene, where resistance is associated with PKA-mediated phosphorylation at S236 of ERα.
C. Raloxifene, where resistance is associated with PKA-mediated phosphorylation of ERα at either S236 or S305, or a combination of both.
D. Toremifene, GW5638 and arzoxifene, where resistance is associated with additional PKA-mediated events outside ERα.
E. SERDs ICI-182,780 (Fulvestrant) and ICI-164,384 that are PKA-insensitive with respect to resistance.

Characterization of MAPK/PKA associated resistance to anti-estrogens by FRET

In addition to the PKA pathway, activation of the MAPK pathway also influences activation of ERα (12) and may well be related to anti-estrogen resistance. We investigated this using an YFP-ERα-S118E-CFP construct in our FRET experiments, where serine-118 was replaced by glutamate, mimicking phosphorylation at that site by the activation of the MAPK pathway. A combination of this mutant with PKA activation by forskolin reflected the synergy between MAPK and PKA pathways in resistance to anti-estrogens. The ERα-S118E mutant did not show any conformational changes upon tamoxifen addition in the absence of PKA activation nor after forskolin pretreatment (Figure 3E), which supports previous reports that MAPK-mediated phosphorylation of S118 suffices to induce tamoxifen resistance of ERα (13). In contrast, the S118A mutant that cannot be phosphorylated by MAPK at this site behaved as wt ERα (data not shown). The other anti-estrogens still induced a conformational change of the ERα-S118E mutant, which was prevented by forskolin treatment for EM-652, lasofoxifene, raloxifene and toremifene, but not SERM/SERD GW5638 and SERD ICI-164,384. Importantly, PKA activation in cells expressing the ERα-S118E mutant did prevent a conformational change in response to SERD ICI-182,780 (Fulvestrant), suggesting that

4

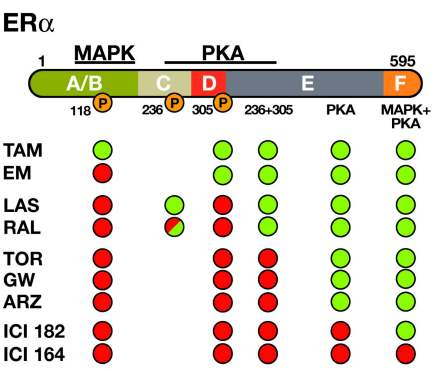


Figure 4. Summary of modifications in ERα that are associated with FRET-predicted resistance to anti-estrogens.

The modification sites in ERα by MAPK (S118) and PKA (S236 and S305) are indicated. When no conformational change in wild-type ERα occurs in response to the various anti-estrogens, this is marked in white, indicating that ERα is insensitive towards the anti-estrogen (thus transcriptionally active) for a given modification status. For instance, PKA-mediated phosphorylation of YFP-wt-ERα-CFP showed no conformational change upon addition of tamoxifen and is therefore indicated in white. A conformational change in ERα in response to the various anti-estrogens is marked in grey, indicating that ERα is sensitive towards the anti-estrogen (thus transcriptionally inactive) for a given modification status. A-F represent the various ER domains.

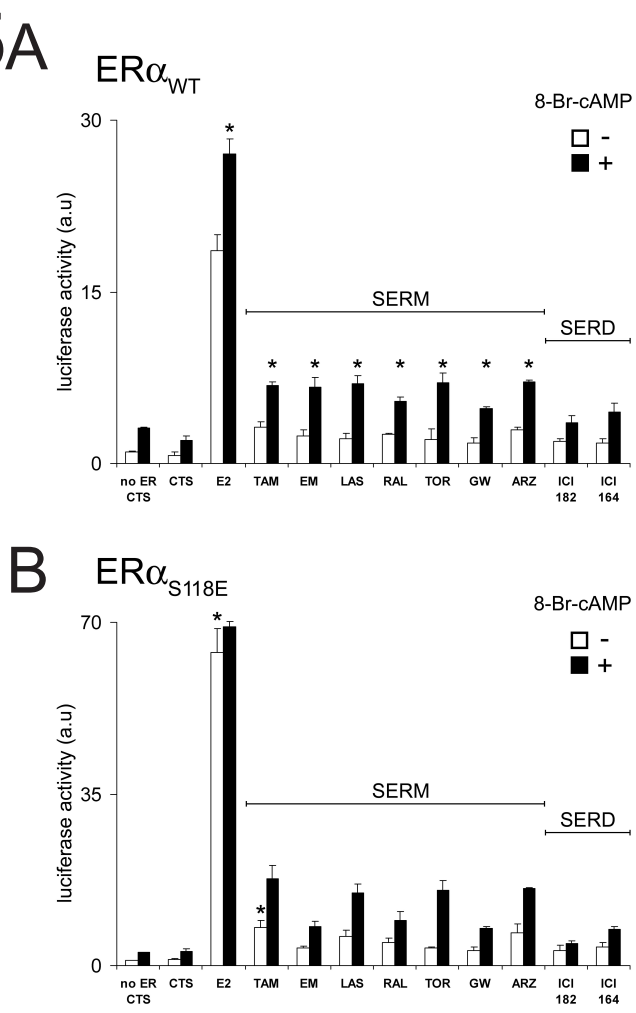


Figure 5. ER transcriptional activity measured by ERE-dependent luciferase assay.

U2OS cells were transfected and cultured for two days in the presence of either CTS medium, 10^{-8} M Estradiol (E2) or 10^{-7} M of the indicated anti-estrogens, and subsequently assayed by an ERE-luciferase assay. Bars indicate standard error in triplicate experiments. For abbreviations of the anti-estrogens, see legend Figure 3.

A. ER dependent transcriptional activity in YFP-wt-ERα-CFP transfected U2OS cells. The luciferase activity under conditions of CTS in the absence of ERα was set on 1.

* indicates a statistically significant ER dependent reporter read-out between forskolin treated and untreated samples, $P< 0.05$

B. ER dependent transcriptional activity in YFP-ERα-S118E-CFP transfected U2OS cells. The luciferase activity under conditions of CTS in the absence of ERα was set on 1.

* indicates a statistically significant ER dependent reporter read-out between the S118E mutant and wild type ERα values, $P< 0.05$

combined PKA and MAPK activity resulted in resistance to this compound on the basis of FRET measurements.

The results from the FRET experiments are summarized in Figure 4 and provide a profile of modifications in ERα where the combination of effects of PKA and MAPK on resistance to anti-estrogens can be divided in seven categories:

A. MAPK-mediated phosphorylation of S118 that is associated with resistance to tamoxifen

B. PKA-mediated phosphorylation of S305 that is associated with resistance to tamoxifen and EM-652

C. PKA-mediated phosphorylation of S236 that is associated with resistance to lasofoxifene

D. PKA-mediated phosphorylation of either S236 or S305, or a combination of both that is associated with resistance to raloxifene

E. PKA effects outside ERα that affect resistance to toremifene, GW5638 and arzoxifene

F. A combined effect of MAPK and PKA on ERα that is associated with resistance to ICI-182,780 (Fulvestrant)

G. Insensitivity to MAPK and PKA of ICI-164,384

Stimulation of anti-estrogen mediated transcriptional activation of ERα by PKA and MAPK

The compound-induced conformational changes of ERα indicated that phosphorylation of ERα by PKA and/or MAPK affected conformation of ERα and might turn an antagonist into an agonist, as it did for tamoxifen. We therefore investigated the ability of wt and mutant ERα to activate an ERE-containing reporter gene in the presence of these anti-estrogens

with or without PKA activator 8-Br-cAMP in U2OS cells. These U2OS cells, devoid of endogenous ER expression, were transfected with constructs of ERα (variant), an ER-responsive luciferase reporter and an ER-insensitive Renilla luciferase as control for transfection efficiency (Figure 5). The expression level of ERα in these transiently transfected U2OS cells was similar to endogenous expression of ERα in T47D breast cancer cells as detected by Western blotting (data not shown). The results are related to CTS, which was set at 1. Without expression of ER, there was only a slight variation in the background read-out of the ERE-reporter assay irrespective of the various anti-estrogens, which was elevated approximately three fold by PKA (data not shown). In the presence of ERα, treatment with 8-Br-cAMP enhanced the read-out of E2 (Figure 5A), as has been reported before (26). 8-Br-cAMP also enhanced transcriptional activity of ERα in the presence of SERMs tamoxifen, EM-652, lasofoxifene, raloxifene, toremifene, GW5638 and arzoxifene significantly as compared with the respective SERMs under CTS conditions, but this was not significant for the SERDs ICI-182,780 and ICI-164,384 (Figure 5A and Supplementary Data). This effect of PKA on transcriptional activation of ERα in the presence of anti-estrogens corresponded to the effect of PKA in the FRET experiments (Figure 3), indicating that an immediate measurement of the conformational change of ERα upon interaction with anti-estrogens provided information on the transactivation of ER that we measured 48 hours after addition of the anti-estrogens. Using the YFP-ERα-S118E CFP mutant, which mimics phosphorylation by MAPK at this site, we observed that the transcriptional activity of ERα-S118E in the presence of tamoxifen, but not for the other tested anti-estrogens, was significantly higher then for wt ERα (Figure 5B and Supplementary Data), corresponding to the FRET results. The transcriptional read-out for the S118E mutant in the presence of PKA stimulator 8-Br-cAMP differed significantly from control wild-type values for all tested anti-estrogens, including the two SERDs (Figure 5B and Supplementary data). This was in line with the absence of a conformational change in ERα of the S118E mutant in response to PKA activation in the presence of ICI-182,780, indicating an activated ERα (Figure 3E), but is in contrast to the conformational change observed under these conditions with ICI-164,384. The latter may well be due to differences in secondary effects between the two SERDs, which takes place after the first interaction (that we measured by FRET), but before the transactivation that we measured in the ERE-luc assay (27;28).

Discussion

In endocrine treatment of breast cancer, early diagnosis of sensitivity for anti-estrogens will contribute to proper selection of adequate anti-estrogens for individual patients. This is especially relevant since patients benefit from consecutive treatment with different types of anti-estrogens (29;30), which thus far is taking place on empirical basis. A profile of the modifications in ERα that are associated to resistance to anti-estrogens as presented here in Figure 4 may well contribute to rational matching of patients and compounds. This profile of ERα modifications is based on the immediate interaction between ERα and anti-estrogenic compounds, which takes place within 15 minutes after administration and is measured by FRET. Phosphorylation of direct target sites in ERα by PKA leads to resistance predicted by FRET for the anti-estrogens tamoxifen, EM-652, raloxifene and lasofoxifene (Figure 4), whereas indirect effects were measured for anti-estrogens GW5638, toremifene and arzoxifene. The PKA-associated targets outside ERα may well include SRCs, and the effect of PKA-mediated phosphorylation of these cofactors in other cell types might well differ from that in U2OS cells used for FRET experiments, due to different levels of SRCs (15;31).

Phosphorylation of ERα by PKA and/or MAPK is able to modulate the response to anti-estrogens, but does so differently for the various anti-estrogens, as is depicted in Figure 4. This can be explained by an anti-estrogen specific reorientation of the LBD of ERα, which is counteracted by a specific set of PKA and/or MAPK associated phosphorylations in ERα, thereby converting the action of the antagonist into that of an agonist. The PKA- and MAPK-mediated modifications that are associated with FRET-predicted resistance result in a ranking of anti-estrogens that largely agrees with the transcriptional activation of ERα, in particular for the SERMs tested in this study, and with previous biological findings (24) and structural differences between comparable compounds (Figure 1A and Figure 4). For the anti-estrogens in the triphenylethylene group (Figure 1A), the polarity of the side chain (COOH in GW5638 versus –N-C2H6 in tamoxifen) correlated with the effect in FRET analysis: resistance to anti-estrogen GW5638 required more stringent conditions than resistance to tamoxifen (Figure 4). The same applies to arzoxifene and raloxifene, and for ICI-164,384 in comparison with ICI-182,780 (Fulvestrant), where the former steroidal compound contains a more extended side chain and additional conditions appear to be required for resistance to these anti-estrogens.

The additional PKA-mediated events outside the ERα that are associated with resistance to toremifene, GW5638 and arzoxifene (Figure 4) may well

involve phosphorylation of cofactors for which it has been demonstrated that the expression levels and/or phosphorylation status affect the extent of E2-mediated transactivation of ERα and its sensitivity to tamoxifen (16). Our results do, however, show that PKA- and MAPK-mediated phosphorylation of particular sites of ERα, possibly in synergy with phosphorylation of SRCs, acts to confer resistance to anti-estrogens.

Although the results from our FRET and transactivation experiments do agree in general, loss of a change in FRET in the presence of anti-estrogens due to PKA activity does not lead to a full transactivation of ERα, as is observed in the presence of E2. Also proliferation under those conditions is only a fraction of that under E2 conditions (9). This suggests that, although the inactive state of ERα is abrogated by PKA pretreatment, the transcriptional active state of the ERα differs between activation by E2 and activation by PKA in the presence of anti-estrogens (W.Zwart *et al*., in preparation). As for the reporter assay, these differences could be explained by a different promoter preference between ERα activated by E2 versus ERα activated by PKA in the presence of anti-estrogens (32). This difference in target preference is also obvious from different RNA expression profiles of breast cancer cells (33), and more relevant to the present study, also of U2OS cells transfected with ERα (34), when E2 conditions are compared with conditions of different anti-estrogens.

Not only does the profile of modifications required for resistance provide a means for ranking anti-estrogens, it also suggests conditions in specimens of breast cancer patients where resistance to a particular anti-estrogen can be anticipated. We (9) and others (11;35) have demonstrated that elevated PKA and PAK-1 levels, as well as activation of PKA and PAK-1 in primary breast cancer is associated with resistance to tamoxifen. Resistance to tamoxifen treatment due to activation of the MAPK pathway has also been demonstrated before (36). The FRET profile based on ERα-modifications involved in resistance to tamoxifen, as presented in this study, may explain this form of anti-estrogen resistance, as well as a rationale for the selection of patients for adequate treatment with other anti-estrogens. When translated to the clinic the profile may predict the regimen of successive endocrine treatment modalities of breast cancer on the basis of modifications in ERα rather than by empirics.

Experimental procedures

Cell culture, and transfection

Human osteosarcoma U2OS cells were cultured in DMEM medium in the presence of 10% FCS and standard antibiotics. U2OS cells containing ERα constructs were cultured in phenol red-free DMEM medium containing 5% charcoal treated serum (CTS, Hyclone) 48 hours prior to analysis. For the FRET experiments, cells were cultured overnight on 2 cm round glass coverslips. 24 hours prior to analysis, cells were transfected with pcDNA3-YFP-ERα-CFP or mutants using PEI (Polyethylenimine, Mw 25kDa, Polysciences) (37). Estradiol (Sigma), 4-OH-tamoxifen (Sigma), raloxifene (Sigma), EM-652 (kindly provided by dr. C. Labrie, University of Quebec, Canada), toremifene (Schering), arzoxifene, lasofoxifene, ICI-164,384 (the last three kindly provided by Organon), GW7604, the active form of GW5638 (38) (kindly provided by GlaxoSmithKline), or ICI-182,780 (Tocris) were added at the concentrations indicated. Forskolin (Sigma) was added 15 min prior to measurements at a final concentration of 10−5 M.

YFP-ERα-CFP constructs

YFP-ER-CFP constructs were generated as described previously (9). Site-directed mutagenesis of serine-118, 236 and 305 to alanine or glutamate was performed with the YFP-ERα-CFP construct as a template using the appropriate modified oligonucleotides. All constructs were verified by sequence analysis. Protein expression was verified by Western blotting using antibodies against ERα (Stressgen Biotechnologies Corp) and GFP (39) and detected using an ECL detection kit (Amersham). The pcDNA3-YFP-ERα-CFP construct was transfected in U2OS cells that were inspected by confocal microscopy for YFP emission at 500–565 nm after 48 hours.

For characterization of the phospho-variants of ERα, U2OS cells were transfected with the YFP-ERα-CFP construct or S118E or S305A variants thereof, treated with 8-Br-cAMP and analyzed by Western blotting using antibodies against GFP (39) or against phospho-S118-ERα(#2515, Cell Signaling, USA) or against phospho-S305-ERα (Upstate, USA).

Fluorescence Resonance Energy Transfer (FRET)

Prior to FRET experiments, cells on coverslips were mounted in bicarbonate-buffered saline (containing: 140 mM NaCl, 5 mM KCl, 1 mM MgCl2, 1 mM CaCl2, 23 mM NaHCO3, 10 mM glucose and 10 mM HEPES at pH 7.2) in a heated tissue culture chamber at 37°C under 5% CO2. Cells were analyzed on an inverted Zeiss Axiovert 135 microscope equipped with a dry Achroplan 63× objective. FRET equipment was as described previously (40). CFP was excited at 432 ± 5 nm and emission of YFP was detected at 527 nm and CFP at 478 nm. FRET was expressed as the ratio of YFP to CFP signals. The ratio was arbitrarily set as 1.0 at the onset of the experiment. Changes are expressed as percent deviation from this initial value of 1.0. For data acquisition, Felix software (PTI Inc.) was used. Data were plotted using proFit (QuantumSoft).

ERE-luciferase reporter assays

Luciferase assays were performed as described previously (41). In short, 8x104 U2OS cells were plated in a 24-well plate culture dish and cultured overnight in CTS, after which cells were transfected with 10 ng of pcDNA3-YFP-ER-CFP or mutants, 0.2 µg ERE-tk-Firefly luciferase (Bindels *et al*., 2002) and 1 ng of SV40 Renilla luciferase construct using PEI. Directly after tranfection, 10−8 M estrogen or 10−7 M anti-estrogen was added to the cells that were cultured for 48 hr before harvesting. Membrane-permeable 8-Br-cAMP (Hordijk *et al*., 1994) was present during the last 16 hours at a final concentration of 0.1 mM.

Acknowledgements

We thank Lennert Janssen for assistance in generating the phospho-mutants of ERα, and dr. K. Jalink for initial help with the FRET equipment. We thank Dr. F. Dijcks and Dr. G. Veeneman (Organon, Oss, the Netherlands) for the kind supply of ICI-164,384, lasofoxifene and arzoxifene, Dr. C. Labrie (University of Quebec, Canada) for the kind supply of EM-652, and Mrs. L. Bray (GlaxoSmithKline, Herthfordshire, UK) for kindly providing us with GW7604. This study was supported by a grant of the Dutch Cancer Organization, KWF 2005-3388.

References

1. Dellapasqua S, Castiglione-Gertsch M. The choice of systemic adjuvant therapy in receptor-positive early breast cancer. Eur J Cancer 2005;41:357-64.

2. Polychemotherapy for early breast cancer: an overview of the randomised trials. Early Breast Cancer Trialists' Collaborative Group. Lancet 1998;352:930-42.

3. Endocrine responsiveness and tailoring adjuvant therapy for postmenopausal lymph node-negative breast cancer: a randomized trial. J Natl Cancer Inst 2002;94:1054-65.

4. Gronemeyer H, Gustafsson JA, Laudet V. Principles for modulation of the nuclear receptor superfamily. Nat Rev Drug Discov 2004;3:950-64.

5. Brzozowski AM, Pike AC, Dauter Z, *et al*. Molecular basis of agonism and antagonism in the oestrogen receptor. Nature 1997;389:753-8.

6. Shiau AK, Barstad D, Loria PM, *et al*. The structural basis of estrogen receptor/coactivator recognition and the antagonism of this interaction by tamoxifen. Cell 1998;95:927-37.

7. Nettles KW, Sun J, Radek JT, *et al*. Allosteric control of ligand selectivity between estrogen receptors alpha and beta: implications for other nuclear receptors. Mol Cell 2004;13:317-27.

8. Giepmans BN, Adams SR, Ellisman MH, Tsien RY. The fluorescent toolbox for assessing protein location and function. Science 2006;312:217-24.

9. Michalides R, Griekspoor A, Balkenende A, *et al*. Tamoxifen resistance by a conformational arrest of the estrogen receptor alpha after PKA activation in breast cancer. Cancer Cell 2004;5:597-605.

10. Rayala SK, Talukder AH, Balasenthil S, *et al*. P21-activated kinase 1 regulation of estrogen receptor-alpha activation involves serine 305 activation linked with serine 118 phosphorylation. Cancer Res 2006;66:1694-701.

11. Holm C, Rayala S, Jirstrom K, Stal O, Kumar R, Landberg G. Association between Pak1 expression and subcellular localization and tamoxifen resistance in breast cancer patients. J Natl Cancer Inst 2006;98:671-80.

12. Kato S, Endoh H, Masuhiro Y, *et al*. Activation of the estrogen receptor through phosphorylation by mitogen-activated protein kinase. Science 1995;270:1491-4.

13. Bunone G, Briand PA, Miksicek RJ, Picard D. Activation of the unliganded estrogen receptor by EGF involves the MAP kinase pathway and direct phosphorylation. EMBO J 1996;15:2174-83.

14. Osborne CK, Bardou V, Hopp TA, *et al*. Role of the estrogen receptor coactivator AIB1 (SRC-3) and HER-2/neu in tamoxifen resistance in breast cancer. J Natl Cancer Inst 2003;95:353-61.

15. Shang Y, Brown M. Molecular determinants for the tissue specificity of SERMs. Science 2002;295:2465-8

16. Lonard DM, Tsai SY, O'Malley BW. Selective estrogen receptor modulators 4-hydroxytamoxifen and raloxifene impact the stability and function of SRC-1 and SRC-3 coactivator proteins. Mol Cell Biol 2004;24:14-24.

17. Paige LA, Christensen DJ, Gron H, *et al*. Estrogen receptor (ER) modulators each induce distinct conformational changes in ER alpha and ER beta. Proc Natl Acad Sci USA 1999;96:3999-4004.

18. Norris JD, Paige LA, Christensen DJ, *et al*. Peptide antagonists of the human estrogen receptor. Science 1999;285:744-6.

19. Iannone MA, Simmons CA, Kadwell SH, *et al*. Correlation between *in vitro* peptide binding profiles and cellular activities for estrogen receptor-modulating compounds. Mol Endocrinol 2004;18:1064-81.

20. Pike AC. Lessons learnt from structural studies of the oestrogen receptor. Best Pract Res Clin Endocrinol Metab 2006;20:1-14.

21. McDonnell DP. The molecular pharmacology of estrogen receptor modulators: implications for the treatment of breast cancer. Clin Cancer Res 2005;11:871s-7s.

22. Wu YL, Yang X, Ren Z, *et al*. Structural basis for an unexpected mode of SERM-mediated ER antagonism. Mol Cell 2005;18:413-24.

23. Osborne CK, Zhao H, Fuqua SA. Selective estrogen receptor modulators: structure, function, and clinical use. J Clin Oncol 2000;18:3172-86.

24. Robertson JF. Selective oestrogen receptor modulators/new antioestrogens: a clinical perspective. Cancer Treat Rev 2004;30:695-706.

25. Hordijk PL, Verlaan I, Jalink K, van Corven EJ, Moolenaar WH. cAMP abrogates the p21ras-mitogen-activated protein kinase pathway in fibroblasts. J Biol Chem 1994;269:3534-8.

26. Chen D, Pace PE, Coombes RC, Ali S. Phosphorylation of human estrogen receptor alpha by protein kinase A regulates dimerization. Mol Cell Biol 1999;19:1002-15.

27. Van Den Bemd GJ, Kuiper GG, Pols HA, Van Leeuwen JP. Distinct effects on the conformation of estrogen receptor alpha and beta by both the antiestrogens ICI 164,384 and ICI 182,780 leading to opposite effects on receptor stability. Biochem Biophys Res Commun 1999;261:1-5.

28. Osborne CK, Wakeling A, Nicholson RI. Fulvestrant: an oestrogen receptor antagonist with a novel mechanism of action. Br J Cancer 2004;90:S2-S6.

29. Howell A, DeFriend D, Robertson J, Blamey R, Walton P. Response to a specific antioestrogen (ICI 182780) in tamoxifen-resistant breast cancer. Lancet 1995;345:29-30.

30. Osborne CK, Pippen J, Jones SE, *et al*. Double-blind, randomized trial comparing the efficacy and tolerability of fulvestrant versus anastrozole in postmenopausal women with advanced breast cancer progressing on prior endocrine therapy: results of a North American trial. J Clin Oncol 2002;20:3386-95.

31. Zheng FF, Wu RC, Smith CL, O'Malley BW. Rapid estrogen-induced phosphorylation of the SRC-3 coactivator occurs in an extranuclear complex containing estrogen receptor. Mol Cell Biol 2005;25:8273-84.

32. Levenson AS, Kliakhandler IL, Svoboda KM, *et al*. Molecular classification of selective oestrogen receptor modulators on the basis of gene expression profiles of breast cancer cells expressing oestrogen receptor alpha. Br J Cancer 2002;87:449-56.

33. Levenson AS, Svoboda KM, Pease KM, *et al*. Gene expression profiles with activation of the estrogen receptor alpha-selective estrogen receptor modulator complex in breast cancer cells expressing wild-type estrogen receptor. Cancer Res 2002;62:4419-26.

34. Monroe DG, Secreto FJ, Subramaniam M, Getz BJ, Khosla S, Spelsberg TC. Estrogen receptor alpha and beta heterodimers exert unique effects on estrogen- and tamoxifen-dependent gene expression in human U2OS osteosarcoma cells. Mol Endocrinol 2005;19:1555-68.

35. Miller WR. Regulatory subunits of PKA and breast cancer. Ann N Y Acad Sci 2002;968:37-48.

36. Schiff R, Massarweh SA, Shou J, Bharwani L, Mohsin SK, Osborne CK. Cross-talk between estrogen receptor and growth factor pathways as a molecular target for overcoming endocrine resistance. Clin Cancer Res 2004;10:331S-6S.

37. Boussif O, Lezoualc'h F, Zanta MA, *et al*. A versatile vector for gene and oligonucleotide transfer into cells in culture and *in vivo*: polyethylenimine. Proc Natl Acad Sci USA 1995;92:7297-301.

38. Dardes RC, O'Regan RM, Gajdos C, *et al*. Effects of a new clinically relevant antiestrogen (GW5638) related to tamoxifen on breast and endometrial cancer growth *in vivo*. Clin Cancer Res 2002;8:1995-2001.

39. van Ham SM, Tjin EP, Lillemeier BF, *et al*. HLA-DO is a negative modulator of HLA-DM-mediated MHC class II peptide loading. Curr Biol 1997;7:950-7.

40. van der Wal J, Habets R, Varnai P, Balla T, Jalink K. Monitoring agonist-induced phospholipase C activation in live cells by fluorescence resonance energy transfer. J Biol Chem 2001;276:15337-44.

41. Bindels EM, Lallemand F, Balkenende A, Verwoerd D, Michalides R. Involvement of G1/S cyclins in estrogen-independent proliferation of estrogen receptor-positive breast cancer cells. Oncogene 2002;21:8158-65.

Supplemental data

S1

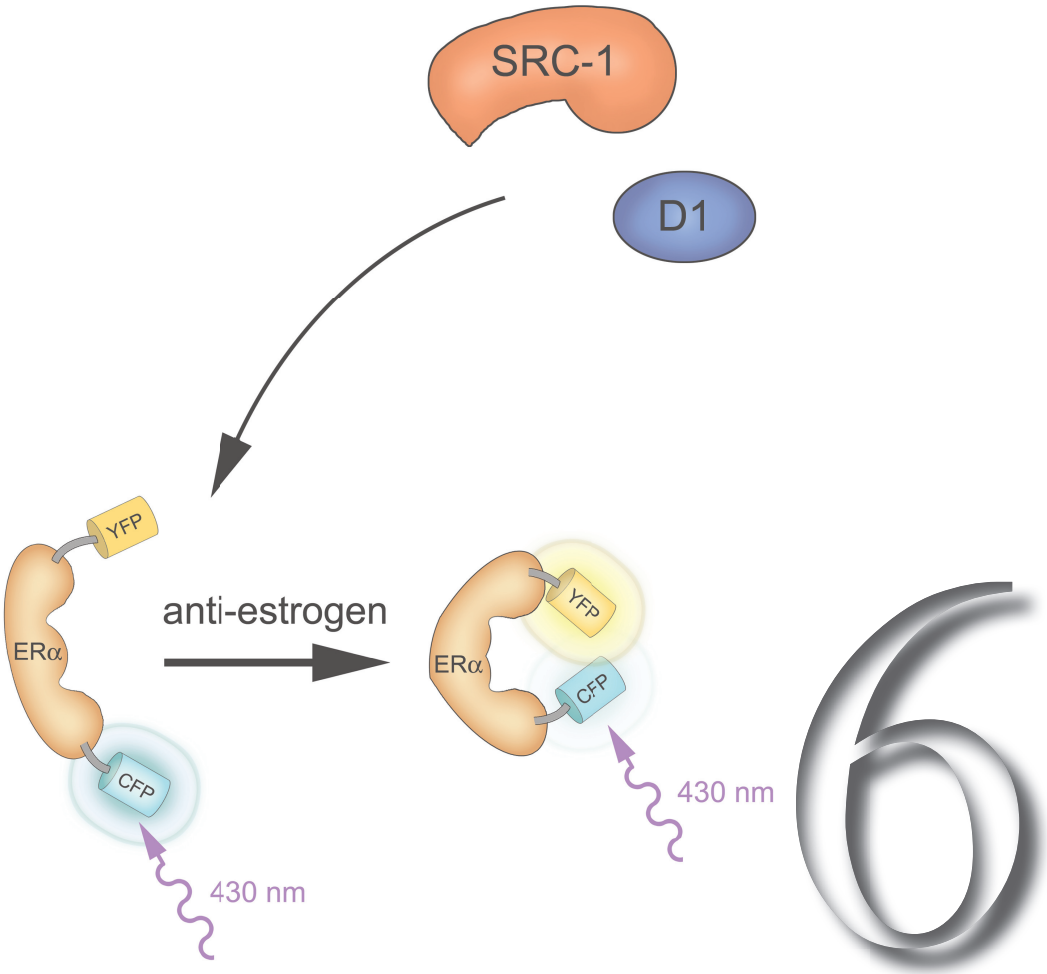
	1	2	3
CTS	0.01	0.51	0.05
E2	0.01	0.00	0.00
TAM	0.01	0.02	0.01
EM	0.02	0.34	0.02
LAS	0.01	0.06	0.01
RAL	0.01	0.08	0.03
TOR	0.04	0.34	0.01
GW	0.01	0.34	0.01
ARZ	0.00	0.12	0.00
ICI 182	0.08	0.31	0.02
ICI 164	0.05	0.12	0.00

1: $ER\alpha_{WT}$ -cAMP / $ER\alpha_{WT}$+cAMP
2: $ER\alpha_{WT}$ / $ER\alpha_{S118E}$
3: $ER\alpha_{WT}$ -cAMP/ $ER\alpha_{S118E}$+cAMP

Table S1. *Statistical analysis of ERα luciferase activity.* Student's t-test analysis of the ERE-luciferase reporter data for YFP-wt-ERα-CFP and YFP-ERα-S118E-CFP, with or without 8-Br-cAMP, as depicted in Figure 5. P values are presented, for $P<0.05$ in black, $P\geq0.05$ in grey.

Resistance to anti-estrogen arzoxifene is mediated by overexpression of Cyclin D1

Submitted



Resistance to anti-estrogen arzoxifene is mediated by overexpression of Cyclin D1

Wilbert Zwart[1], Mariska Rondaij[1], Kees Jalink[2], Z. Dave Sharp[3], Michael A. Mancini[4], Jacques Neefjes[1], and Rob Michalides[1,5].

Abstract
Resistance to tamoxifen treatment occurs in approximately 50% of the ERα positive breast cancer patients. Resistant patients would benefit from treatment with other available anti-estrogens. In this study, we show that overexpression of a regular component of the ERα transcription factor complex, cyclin D1, which occurs in approximately 40% of breast cancer patients, renders cells resistant to a new promising anti-estrogen arzoxifene. Arzoxifene is an effective growth inhibitor of ERα positive breast cancer cells, including tamoxifen resistant tumors. Overexpression of cyclin D1 alters the conformation of ERα in the presence of arzoxifene. In this altered conformation, ERα still recruits RNA polymerase II to an ERE-containing promoter, inducing transcription of an ERα-dependent reporter gene and of endogenous pS2, and promoting arzoxifene-stimulated growth of MCF-7 cells. By this, arzoxifene is converted from an ERα-antagonist into an agonist. This is explained by a stabilization of the ERα/SRC-1 complex in the presence of arzoxifene, only when cyclin D1 is overexpressed. These results indicate that subtle changes in the conformation of ERα upon binding to anti-estrogen are at the basis of resistance to anti-estrogens.

Introduction

Estrogen receptor alpha (ERα) positive breast cancer patients are commonly treated with either aromatase inhibitors or anti-estrogens. The clinically most frequently applied anti-estrogen, tamoxifen, leads in an adjuvant setting to an approximately 50% reduction in recurrence during 10 years of follow-up of ER-positive patients, and to a decrease in mortality by a third. Tamoxifen resistance is, however, still a major clinical problem in the treatment of breast cancer. Various mechanisms may account for insensitivity to tamoxifen, including activation of the mitogen-activated protein kinase (MAPK), protein kinase A (PKA) and p21-activated kinase-1 (PAK1) signaling pathways that show enhanced activity in tamoxifen-resistant breast tumors (1-3). All of these kinase activities directly phosphorylate ERα, resulting in anti-estrogen resistance. In the case of PKA- and MAPK-mediated resistance, tamoxifen binds but then fails to induce the inactive conformation of ERα (1;4). For PKA, we found that its activity alters the orientation between ERα and steroid receptor coactivator-1 (SRC-1) in the presence of tamoxifen, which ultimately leads to RNA Polymerase II recruitment and subsequently, to ERα-dependent transactivation instead (5).

Next to phosphorylation events on the ERα, expression levels and/or phosphorylation of cofactors such as SRC-1 (6) and SRC-3 (7;8) are reported to be associated with anti-estrogen resistance or tamoxifen non-responsiveness. Moreover, amplification of 11q13, a gene-rich region on Chromosome 11, that is found in approximately 15% of the primary human breast cancers (9-11), is associated with tamoxifen resistance. Among the genes present in this region are PAK1 and cyclin D1. PAK1 overexpression is correlated with tamoxifen resistance in patients, whereas cyclin D1 overexpression by itself fails to do so (3;12), nor did it enhance cell growth is tissue culture experiments under tamoxifen conditions (13). Cyclin D1 enhances ligand-independent activation of ERα activity (14;15). The cyclin D1 protein is overexpressed in approximately 40% of human breast cancers, yet it does not indicate a poor prognosis in ERα-positive cases (16;17).

New anti-estrogens are continuously generated and tested for clinical application. These anti-estrogens can be subdivided in Selective Estrogen Receptor Modulators (SERMs), such as tamoxifen, and Selective Estrogen Receptor Downregulators (SERDs), such as ICI-182,780 (Fulvestrant), whereas anti-estrogen GW5638 has mixed SERM/SERD properties (18). New compounds may then fall in one of these classes. Outcome to treatment and resistance to anti-estrogens

Departments of Tumor Biology[1] and Cellular Biology[2], The Netherlands Cancer Institute, Amsterdam, The Netherlands,

[3]The University of Texas Institute for Biotechnology, San Antonio, TX, USA
[4]Department of Molecular & Cellular Biology, Baylor College of Medicine, Houston, TX, USA

[5]Correspondence and reprint requests:
dr. R. Michalides
Department of Tumor Biology, The Netherlands Cancer Institute, Plesmanlaan 121, 1066CX Amsterdam, the Netherlands, phone + 31 20 5122022, fax + 31 20 5122029, Email: r.michalides@nki.nl

Keywords: Estrogen Receptor α/ Cyclin D1/ anti-estrogen resistance/ arzoxifene/ conformational control of transcription factors
Running Title: Anti-estrogen resistance through cyclin D1

This study was supported by Grant NKI 2005-3388 of the Dutch Cancer Society and was in part performed within the framework of Top Institute Pharma project: number T3-107.

are unpredictable parameters. Many factors may affect clinical response to new anti-estrogens, including overexpression of cyclin D1 and/or SRC-1 in possible conjunction with activation of PKA and or MAPK.

In the present study, we found that SRC-1 overexpression did not influence efficacy of anti-estrogens to inhibit ERα. Overexpression of cyclin D1, however, resulted in a conformational arrest of ERα, which indicated an activated ERα, but now in the presence of GW5638 and arzoxifene, two novel anti-estrogens that are at present in phase III clinical testing. In this conformation, the ERα was capable of recruiting RNA Polymerase II and inducing chromatin remodeling required for initiation of transcription. Whereas these events eventually enhanced ERα driven transcription and tumor cell growth by arzoxifene, the breakdown of ERα by GW5638 prevented these long-term effects. Arzoxifene resistance resulted from stabilization of the cyclin D1:ERα/SRC-1 complex. Cyclin D1 overexpression did not affect the capacity of the other anti-estrogens tested to inhibit ERα. Other modifications of ERα were required for induction of resistance by these anti-estrogens. These findings illustrate that estrogen receptor degradation is a dominant factor over a resistance-associated conformation. Moreover, they define the frequently overexpressed cofactor cyclin D1 as a causal factor in resistance to particular anti-estrogens, and show that subtle changes in the conformation of ERα are at the basis of resistance to anti-estrogens.

Results

Overexpression of cyclin D1/ SRC-1 induces resistance to anti-estrogens as measured by FRET

We determined the effect of overexpression of cyclin D1 and/or SRC-1 on the ability of a subset of anti-estrogens to inhibit transactivation of ERα. The anti-estrogens used in this study and their structure are depicted in Figure 1. They differ widely in biological effects *in vitro* and *in vivo* (19;20). These compounds were tested in U2OS osteosarcoma cells, a highly suitable cell line for testing activation status of ERα and ERβ (1;21), that are themselves devoid of expression of endogenous ER and did not show apparent overexpression of any of the p160 coactivators when related to other cell lines (22-25). As a first indication for the capacity of the tested anti-estrogens to inactivate ERα, we applied a Fluorescence Resonance Energy Transfer (FRET) assay. FRET is the energy transfer from a donor fluorophore to a suitable acceptor. When the two fluorophores come in close enough proximity, typically less than 80 Å, energy can be transferred from the CFP to the YFP fluorophore. This depends on the orientation and distance between the two fluorophores and intramolecular FRET is thus highly sensitive to conformational changes. In our setup, an YFP fluorophore was fused to the N-terminus and a CFP to the C-terminus of ERα, as illustrated in Figure 2A, left

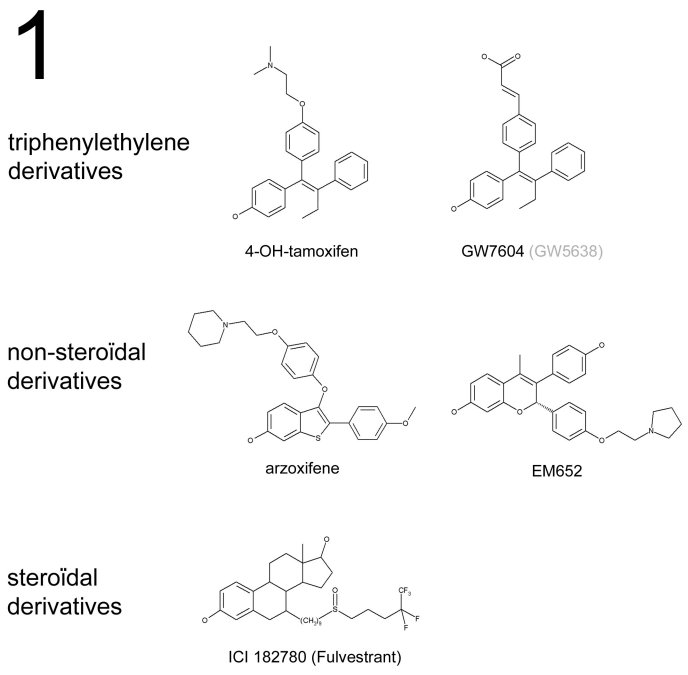


Figure 1. Structure of anti-estrogens used in this study.

panel. An inactive conformation of ERα is typically associated with an increase in FRET between the CFP and YFP fluorophores, as we reported previously (1;4). This enabled us to monitor the capacity of anti-estrogens to inactivate ERα and their sensitivity to overexpression of cyclin D1 and SRC-1.

To perform these experiments in a semi-high throughput manner, we applied Fluorescence Lifetime Imaging Microscopy (FLIM), a highly quantitative method for measuring FRET. In FLIM, the lifetime of the donor fluorophore emission is measured which is for the donor CFP typically 2.7 ns (26). This lifetime is reduced when the energy of the donor is transferred to the acceptor fluorophore in the case of FRET (27). In our assays, cells expressing YFP-ERα-CFP were cocultured with cells only expressing CFP, in order to provide an internal control for the FLIM measurements, Figure 2A, right panel. After addition of anti-estrogen ICI-182,780, the lifetime of CFP in the YFP-ERα-CFP expressing cells was reduced from 2.5 ns to 2.1 ns after treatment, indicating a donor FRET efficiency of 7% prior to treatment and 22% after treatment with ICI-182,780. The same cell was monitored before and after treatment with the ligand, where the FRET efficiency after treatment was related to the efficiency before, which was set at one. The final relative donor FRET efficiency was depicted in Figure 2B. The FRET efficiency prior to treatment was unaltered by co-expression of cyclin D1 or SRC-1 (data not shown). A significant increase in relative FRET efficiency was found for all anti-estrogens tested, Figure 2B. However, when SRC-1 and cyclin D1 were cotransfected, the relative FRET efficiency after EM-652, arzoxifene and GW5638 addition was significantly reduced. These data were verified using an alternative ratio-based FRET-approach (Supplemental Figure S1), where synergy between cyclin D1/SRC-1 overexpression and PKA activity could be observed, which had also been illustrated previously (1). When FRET was measured in cells overexpressing SRC-1 alone, no ef-

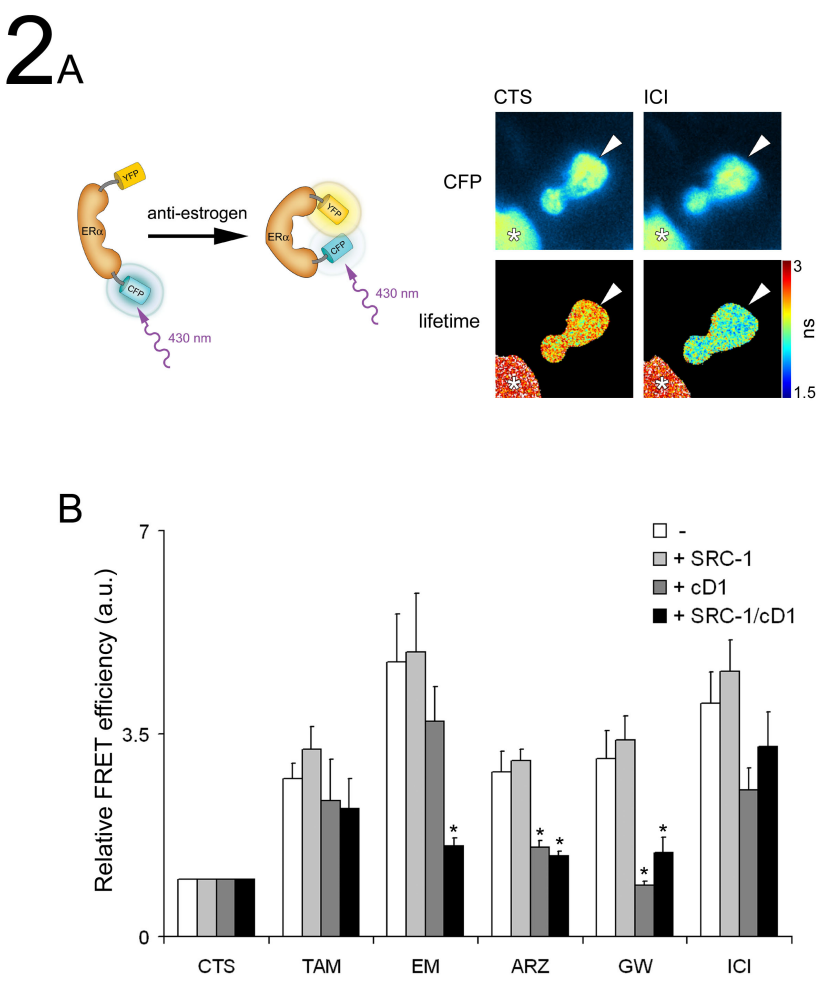


Figure 2. Inactivation of ERα by anti-estrogens measured by FRET.

A. left panel: Principle of FRET. Exciting CFP at 430 nm results in an emission from CFP unless energy is transferred to YFP, resulting in yellow light. An increased YFP emission at the expense of CFP emission can occur as the result of a conformational change of ERα affecting the orientation of the two fluorophores. Right panel: A representative image from a FLIM measurement before and after ICI-182,780 addition. FLIM measurements were performed in U2OS cells, transfected with YFP-ERα-CFP (arrowhead). As an internal reference, these cells were cocultured with MelJuSo cells only expressing CFP (asterisk). FLIM images were generated from cells cultured in hormone-depleted (CTS) medium only, or after treatment with 1 μM ICI-182,780 (ICI) prior to data acquisition and visualized with a lookup table with the corresponding lifetimes indicated in the bar.

B. FRET values as determined by FLIM in YFP-ERα-CFP expressing U2OS cells after addition of 1 μM of the indicated anti-estrogen. Donor FRET efficiency (E_D) was calculated as ED=1- (lifetime cell of interest/ lifetime reference cell). Pair-wise analysis was performed, where the ED under CTS conditions is set to 1 for each experiment (relative ED), bars indicate mean and standard error of the mean from n>20 cells/ condition. Student T-test was performed, * indicates a statistically significant relative ED reduction as compared with the control value, $p < 0.05$.

fect of SRC-1 overexpression was found on the relative FRET efficiency for any of the tested anti-estrogens. Cyclin D1 overexpression, however, did result in reduced FRET efficiency for arzoxifene and GW5638, indicating that an elevated cyclin D1 level is sufficient to induce resistance against these two compounds as determined by this biophysical approach.

Overexpression of cyclin D1 enhances recruitment of RNA Polymerase II to the ERα promoter in the presence of anti-estrogens.

Our FRET and FLIM results suggested that resistance to anti-estrogens GW5638 and arzoxifene may be due to overexpression of cyclin D1. To determine whether this altered conformation of ERα by cyclin D1 also induces transcription in the presence of these anti-estrogens, we assayed their effects on RNA Polymerase II binding to an artificial prolactin promoter/ enhancer (PRL) array in HeLa cells. These cells contain a DNA array, consisting of a ~200 copies of stably transfected modified PRL (28). The PRL array allowed visualization of a defined DNA structure in the nucleus where ERα and cofactors are recruited to regulate reporter gene mRNA synthesis. Resistance to particular anti-estrogens by overexpression of cyclin D1 may result in anti-estrogen mediated transactivation of ERα and consequently, to recruitment of RNA polymerase II to the PRL array. In order to ensure cyclin D1 co-expression in ERα expressing cells, five times more cyclin D1 expression vector was transfected than of ERα. This was verified in a separate staining experiment (see supplemental Figure S2), where overexpressed cyclin D1 was recruited to the PRL array structure, colocalizing with ERα. Cells expressing ERα-CFP showed co-localization with RNA-polymerase II at the DNA array when treated

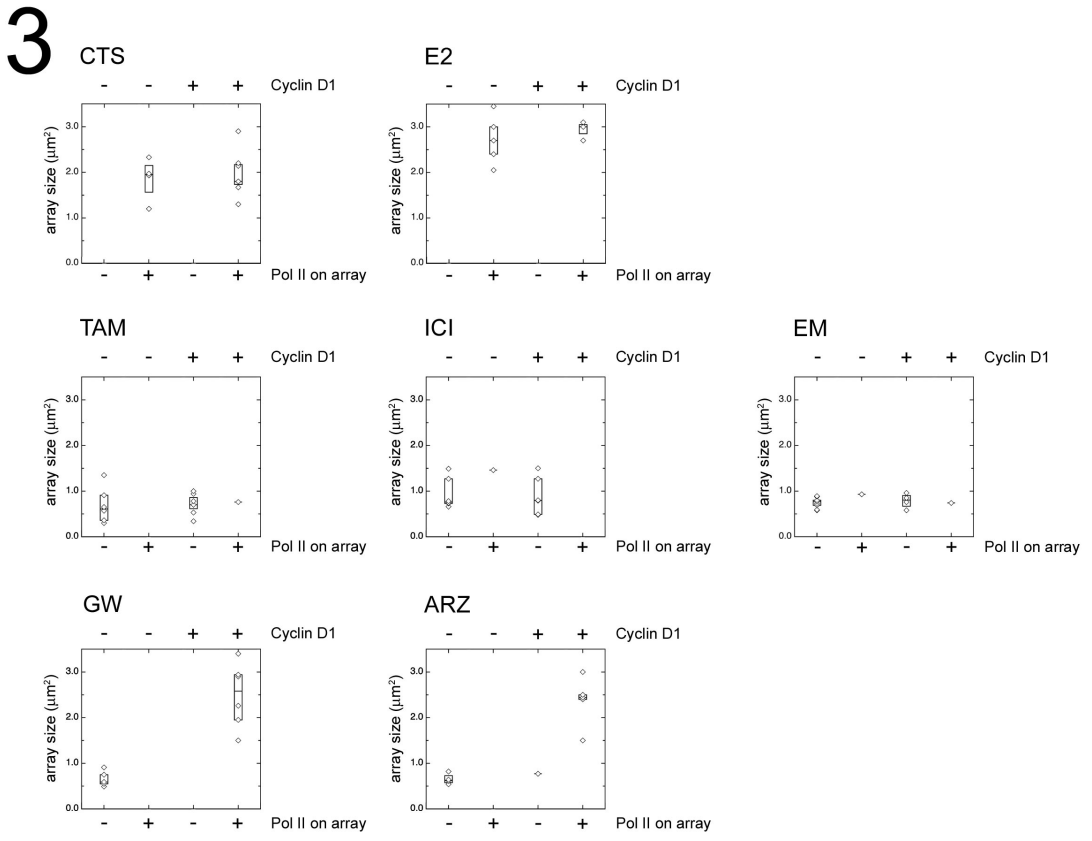


Figure 3. Cyclin D1 overexpression induces RNA polymerase II recruitment on the PRL array and increases array size in the presence of GW5638 and arzoxifene.

Staining for RNA polymerase II signals on the PRL array. PRL array containing HeLa cells were transfected with ERα-CFP alone or cotransfected with cyclin D1. Cells were cultured in hormone depleted (CTS) medium and treated with 1 µM estradiol (E2) or with 1 µM of the indicated anti-estrogen for 2 hours and then fixed and stained for RNA Polymerase II. The data are subdivided in the presence or absence of RNA Polymerase II on the array, and presented in a box plot with the horizontal bar indicating the median array size in µm2. The box size is determined by the upper and lower quartiles, the median value of the upper and lower half of the data points (for each experiment n > 10), respectively. Microscopic images of the cells are shown in supplemental Figure S3.

for 2 hours under conditions of charcoal treated serum (CTS; deprived of hormone) and estradiol (E2), as quantified in Figure 3 and shown in supplemental Figure S3. The average DNA array size was 1.9 μm2 under CTS conditions, which increased to 2.8 μm2 when E2 was added to the cells. This widening of the DNA array structure was previously reported to be associated with increased transcriptional activity (28;29). Overexpression of cyclin D1 did not significantly alter the array size or RNA Polymerase II recruitment under CTS conditions.

Addition of any of the tested anti-estrogens resulted in a loss of RNA Polymerase II from the PRL array structure, and in a marked condensation of the array size (Figure 3 and Figure S3), which is indicative of an inactive ERα (28). Cyclin D1 overexpression did not affect RNA Polymerase II recruitment for cells treated with tamoxifen, ICI-182,780 and EM-652 and the PRL array appeared condensed. However, when cyclin D1 was co-expressed, RNA Polymerase II recruitment was restored for cells treated with GW5638 and arzoxifene. In addition, the array size for both GW5638 and arzoxifene was increased from 0.7 to 2.4 μm2 in the presence of exogenous cyclin D1. Our findings demonstrated that cyclin D1 overexpression prevented an increase in the FRET signal for arzoxifene and GW5638 and resulted in a recruitment of RNA Polymerase II and in a subsequent widening of the array structure. All of these features indicate that resistance to GW5638 and arzoxifene can be induced by overexpression of cyclin D1.

Overexpression of cyclin D1 enhances ERα mediated transcription and subsequent growth of MCF-7 cells in the presence of arzoxifene.

To study the direct consequences of GW5638 and arzoxifene-driven, ERα-mediated RNA polymerase II recruitment under conditions of cyclin D1 overexpression as a means of drug resistance, we measured transcription of an integrated DsRed2 reporter gene that is under control of the ER-responsive elements on the PRL array (28) by quantitative RT–PCR (Figure 4B). These cells were transfected with ERα-CFP and treated overnight with the ligand, after which RNA was isolated for RT-PCR analysis, as described in the materials and methods section. Only cells treated with estradiol showed an increase in DsRed2 mRNA levels of 2.7 fold, this in contrast to any of the anti-estrogens tested. DsRed2 mRNA levels increased under hormone deprived conditions 1.8 fold over control CTS values when cyclin D1 was overexpressed, which is consistent with the hormone-independent activation of ERα in cyclin D1 overexpressing cells (15). When cyclin D1 was overexpressed, only cells treated with arzoxifene showed increased DsRed2 mRNA levels (from 0.7 to 1.7 times over control, respectively). No enhanced transcription was observed in GW5638 treated cells, for reasons described below. Not only activation of an exogenous reporter gene, but also transcription of an ERE-dependent endogenous gene was tested, namely pS2 in MCF-7 breast cancer cells. pS2 mRNA levels were enhanced by arzoxifene when cyclin D1 was overexpressed, whereas none of the other anti-estrogens tested did so (Figure 4C). The RT-PCR data for the levels of endogenous pS2 mRNA in MCF-7 cells showed similar results as was observed the for DsRed2 mRNA reporter signals in HeLa cells (Figure 4B). These data indicated that overexpression of cyclin D1 induced resistance to arzoxifene by enhancing expression of endogenous and of exogenously transfected, ER-dependent genes. Since transfection efficiency of cyclin D1 mutants was approximately 40-50 % in MCF7 and Hela cells (data not shown), the results obtained in Figure 4, represented underestimates of the effects of these mutants. Although overexpression of cyclin D1 also showed resistance to GW5638 as indicated by FRET and RNA Polymerase II recruitment analysis, this did not result in elevated transcription of ER-dependent genes in the presence of GW5638. GW5638 is, however, known to possess SERD capacities, which will lead to degradation of ERα. The discrepancy between the (short term) FRET and RNA Polymerase II recruitment assays which indicated resistance, and the (long term) absence of DsRed2 and pS2 mRNA induction could be explained by GW5638-associated degradation of ERα that will then prevent specific transcription on the long term. Western blot analysis on ERα–transfected PRL-HeLa cells and MCF-7 cells expressing only endogenous ERα which were treated with the different anti-estrogens with or without additional cyclin D1 overexpression, confirmed the SERD nature of GW5638, Figure 4A. The ERα protein levels in both ERα-transfected HeLa and MCF-7 cells corresponded in a comparable way to the treatment with (anti-)estrogens, where E2 lowered and tamoxifen stabilized the protein level of ERα, as compared with untreated cells. The ERα protein levels for cells treated with GW5638 or ICI-182,780, a widely accepted SERD, were similar and showed that treatment with these compounds leads to degradation of ERα. Treatment with arzoxifene and EM-562 however, stabilized the protein level of ERα similar as for tamoxifen. Cyclin D1 overexpression had no effect on the protein level of ERα in the cells treated with the various anti-estrogens.

In order to show a biological effect of cyclin D1 overexpression on resistance to arzoxifene, we performed a cell growth assay using the MCF-7 breast tumor cell line (Figure 4D), of which the proliferation is dependent on an activated ERα. The MCF-7 cells were

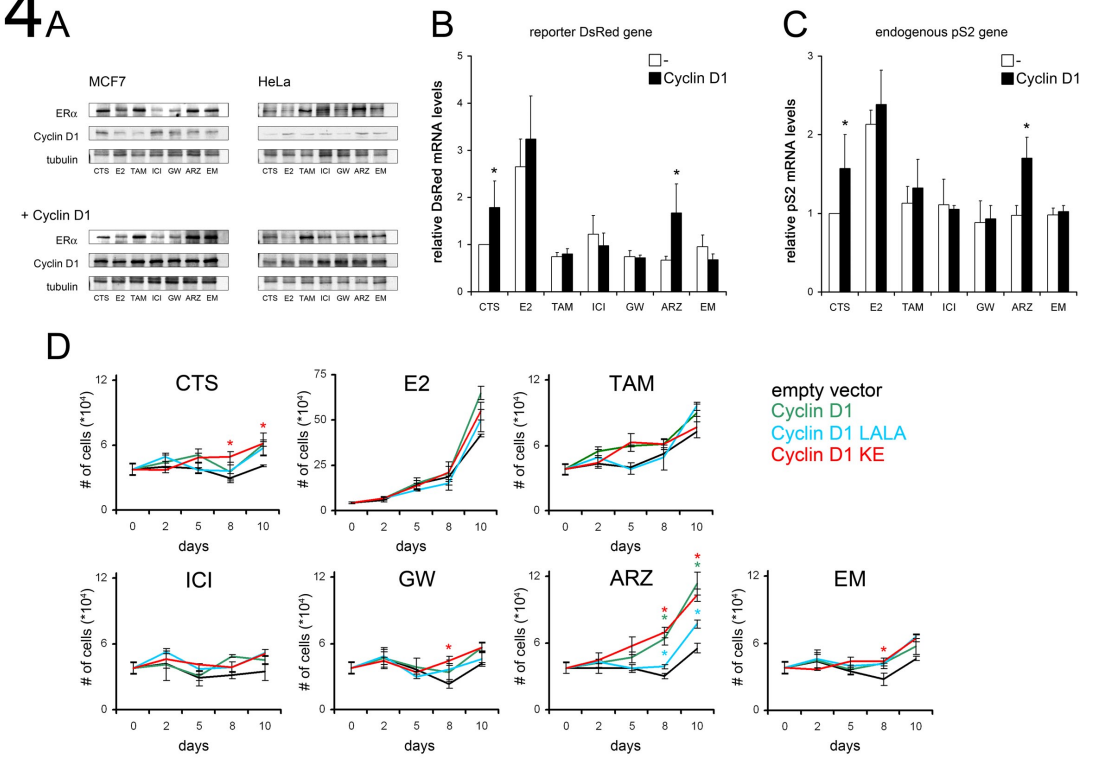


Figure 4. Cyclin D1 overexpression enhances ERα mediated transcription on an ERE-reporter and cell growth of MCF-7 cells in the presence arzoxifene.

A. ERα protein stability in MCF-7 and Hela cells, with expression of either endogenous ERα or exogenous ERα-CFP respectively. Where indicated, cells were cotransfected with cyclin D1. Cells were treated overnight with the indicated anti-estrogens, analyzed by Western blot, and stained for ERα and cyclin D1, using tubulin as a loading control.

B. QPCR was performed on Hela PRL array cells, which were transfected with ERα and cyclin D1 or empty vector as a control and treated overnight with estradiol, anti-estrogen or left untreated. mRNA levels were measured as described in the materials and methods section, and related to CTS values which were set to 1. Bars indicate standard deviation from 3 independent experiments. * indicates a statistically significant differences in DsRed mRNA levels for the cyclin D1 transfected cells compared to empty vector transfected cells treated with the same anti-estrogen; $p < 0.05$.

C. QPCR was performed on MCF-7 cells, transfected with cyclin D1 or empty vector as a control. Cells were treated with estradiol, anti-estrogen for 5 hours or left untreated. mRNA levels were measured as described in the materials and methods section, and related to CTS values which were set to 1. Bars indicate standard deviation from 2 independent experiments in duplicate. * indicates a statistically significant differences in pS2 mRNA levels for the cyclin D1 transfected cells compared to empty vector transfected cells treated with the same anti-estrogen; $p < 0.05$.

D. Cell growth of MCF-7 cells transfected with Cyclin D1, Cyclin D1 LALA, Cyclin D1 KE or empty vector. Cells were seeded in 24 well plates and cultured in the presence of the indicated anti-estrogens for 10 days, where samples were taken directly after seeding and after 2, 5, 8 and 10 days of ligand exposure. Shown are mean and standard deviation from triplicate samples. * indicates a statistically significant differences in cell growth for the cyclin D1 transfected cells compared to empty vector transfected cells (black lines) treated with the same anti-estrogen, within the same timepoint; $p < 0.05$ (green * for cyclin D1 wild type, blue * for cyclin D1 LALA and red * for cyclin D1 KE).

therefore, transfected with various mutants of cyclin D1 or with an empty pcDNA3-YFP vector as a negative control. In comparison to wild type cyclin D1, a cyclin D1 LALA mutant that fails to stabilize ERα/SRC-1 interaction, and a cyclin D1 KE mutant that prevents its binding to cdk (cyclin dependent kinase) (30) were used. The cyclin D1 KE mutant stimulates ERα/SRC-1 dependent cell growth, wheras the cyclin D1 LALA mutant might enhance proliferation, independent of ERα activity (29). Transfection efficiency in these experiments was approximately 50% (data not shown). Therefore, any effect of the cyclin D1 overexpression is an underestimate. The cells were cultured for 10 days in the presence of the anti-estrogens and samples were taken every few days for cell counting. For each ligand, except for arzoxifene, minor effects were observed on the cell growth when cyclin D1 variants were expressed. Cells treated with arzoxifene, however, significantly increased in number when cyclin D1 wild type was transfected. The cells transfected with the cyclin D1 KE mutant, stimulating ERα/SRC-1 dependent proliferation, showed a comparable growth

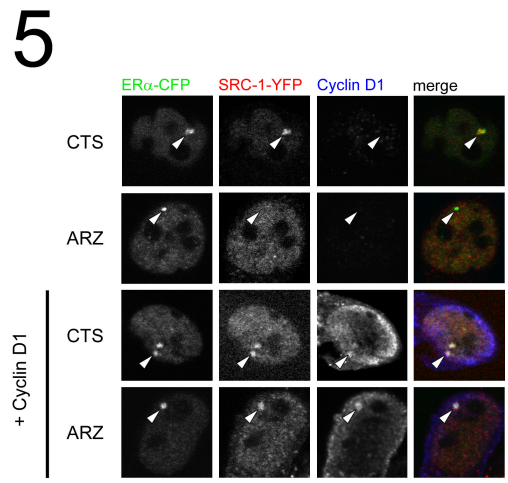


Figure 5. Cyclin D1 stabilizes ERα/SRC-1 complex under arzoxifene conditions.

Cyclin D1 overexpression stabilizes SRC-1 recruitment by ERα on the PRL. PRL array containing HeLa cells, transfected with ERα-CFP and SRC-1-YFP, were either cotransfected with cyclin D1 or with empty vector. Cells were cultured in hormone depleted (CTS) medium and treated with 1 μM arzoxifene for 2 hours or left untreated and then fixed and stained for cyclin D1. Arrowheads indicate the PRL array. For each condition, n > 15. No endogenous level of cyclin D1 could be detected with the antibody applied.

response. This in contrast to the cells, transfected with cyclin D1 LALA, where the cell growth was increased, but not to the extent of the cyclin D1 variants that are capable to stabilize ERα/SRC-1 interactions. These data showed that the cyclin D1 dependent cell growth of MCF-7 cells was stimulated in the presence of arzoxifene, indicating genuine anti-estrogen resistance to this compound by overexpression of cyclin D1.

Cyclin D1 stabilizes ERα/SRC-1 interactions in the presence of arzoxifene.

Overexpression of cyclin D1 apparently facilitates transcription and cell growth in the presence of arzoxifene, but the molecular mechanism for this effect is unclear. To investigate the mechanism of the arzoxifene-specific transcription under conditions of cyclin D1 overexpression, we investigated ERα/SRC-1 complex formation in the PRL array containing HeLa cells, with or without cyclin D1 overexpression, Figure 5. In nontreated cells, colocalization between ERα and SRC-1 occurred in the absence and presence of exogenous cyclin D1. In cells treated with arzoxifene, however, SRC-1 recruitment to the array was lost. But when cyclin D1 was cotransfected, both SRC-1 and cyclin D1 were recruited to the ERα-containing array structure. These data imply that, whereas arzoxifene induced dissociation of the ER/SRC-1 complex, this interaction was rescued by cyclin D1 overexpression. These results were verified by using a fluorescence recovery after photobleaching (FRAP) approach, presented in Figure S5. These results indicated that overexpression of cyclin D1 mediated resistance to arzoxifene by stabilizing the ERα/SRC-1 complex.

Discussion

Ligands of ERα induce specific conformations of the receptor, with alterations beyond the ligand binding domain of ERα. These altered conformations include distinctive orientations of the receptor's carboxyl-terminal transactivation helix (31), and are recognized by particular peptides which bind to distinct ERα-ligand conformations (32). A glimpse of these different conformations is revealed in X-ray crystallography studies of ERα-ligand interactions which are restricted to the AF-2 moiety of the receptor (33). We have demonstrated that these distinct ERα-ligand conformations have far reaching consequences, since they influence resistance to a particular anti-estrogen (1;4). Each anti-estrogen can be characterized by a specific set of phosphorylation sites in ERα that, when being phosphorylated by PKA and/or MAPK, are responsible for resistance to that particular anti-estrogen. These phosphorylations are responsible for an altered conformation of ERα that is measured by intramolecular FRET. In the present study, we showed that overexpression of cyclin D1, here a specific cofactor of ERα, renders ERα resistant to new 3rd generation anti-estrogens, arzoxifene and GW5638. Arzoxifene is an effective growth inhibitor of ERα positive human breast cancer cells, including tamoxifen resistant cells (34;35), and would be an alternative SERM in the clinic next to the broadly applied tamoxifen. We demonstrated that overexpression of cyclin D1, however, alters the conformation of ERα in the presence of arzoxifene (by FRET and FLIM), and showed that ERα in this altered conformation still forms a complex with SRC-1 and recruits RNA polymerase II to an ERE-containing promoter (Figures 2,3 and 5). This then promotes transcription of either endogenous or exogenously transfected, ER-dependent genes and stimulates growth of MCF-7 cells in an arzoxifene dependent manner (Figure 4). Overexpression of cyclin D1 thus converts arzoxifene from an antagonist into an agonist. This feature, among others, may have been causally involved in a significantly shorter progression-free survival and time to treatment failure of arzoxifene-treated patients as compared to tamoxifen in the treatment of locally advanced and metastatic breast cancer (36). However, no material of the breast tumors of these patients was available to study this. In previous studies, we have

demonstrated that FRET results in MCF7 cells are similar to those performed in U2OS cells, excluding any cell line specific FRET effect (1).

Overexpression of cyclin D1 is also responsible for the two short term markers of anti-estrogen resistance (a conformational change of the receptor and a recruitment of RNA Polymerase II) when the SERM/SERD compound GW5638 was used, but failed to stimulate GW5638-mediated gene expression and growth of MCF-7 cells. The SERD nature of the mixed antagonist GW5638 induced degradation of ERα, even in the presence of overexpressed cyclin D1, and prevented the late features of anti-estrogen resistance to occur (Figures 4A-D). This is comparable to the resistance found for Fulvestrant, ICI-182,780, where ERα becomes resistant to Fulvestrant when it is phosphorylated by both PKA at Serine 305 and by MAPK at Serine 118 (4), or by phosphorylation of Serine 305 by PKA in conjunction with overexpression of cyclin D1 and SRC-1 (1). This resistance is manifested by an altered ERα conformation, but is not sustained in enhanced Fulvestrant-dependent reporter read-out or proliferation. The two short term features of anti-estrogen resistance (conformational alteration and recruitment of co-factors and RNA polymerase II) are immediate effects upon the ERα-SERD binding, whereas the two long term features (transcription and cell growth) take place during, or after a SERD-mediated degradation of ERα. Apparently, degradation of ERα is not prevented by the modifications that render ERα resistant to SERMs.

Cyclin D1 forms a specific complex with the estrogen receptor that facilitates ligand-independent recruitment of co-activators to the receptor complex (15;37). It is noteworthy that cyclin D1 overexpression does not lead to resistance to tamoxifen under experimental conditions (13), and does not predict response to tamoxifen treatment in breast cancer patients (12;38). Our results confirmed these findings by the absence of a FRET change (Figure 2), RNA polymerase II recruitment (Figure 3), nor responsive gene activation and cell growth (Figure 4) under tamoxifen conditions when cyclin D1 is overexpressed.

Each anti-estrogen apparently binds to ERα in a distinct manner and induces a characteristic inhibitory conformation that is released by compound-specific modifications of the estrogen receptor. For arzoxifene and GW5638, we found in this study that overexpression of cyclin D1 renders ERα resistant to these compounds. Cyclin D1 protein binds to the 338-379 aa region of ERα (39), just adjacent to the hinge region, in which Serine 305, when phosphorylated by PKA, determines resistance to tamoxifen.

Our findings of anti-estrogen specific modifications of ERα that are responsible for resistance to particular anti-estrogens may be of clinical relevance, since they indicate resistance to a particular anti-estrogen in the treatment of breast cancer (40) and could provide guidelines for the development of new anti-estrogens. Both of these may aid in eventually developing personalized endocrine treatment in breast cancer, where different anti-estrogens are subsequently applied in a rationalized manner, instead of in an empirical order as is now common practice (41).

Materials and Methods

Cell culture, transfection, constructs and antibodies

Human osteosarcoma U2OS, MCF-7 and HeLa cells were cultured in DMEM medium in the presence of 10% FCS and standard antibiotics. Cells containing ERα were cultured in phenol red-free DMEM medium containing 5% charcoal-treated serum (CTS; Hyclone). For the FRET and FLIM experiments, cells were cultured overnight on 2 cm round glass coverslips. 24 hours prior to analysis, cells were transfected with pcDNA3-YFP-ERα-CFP or cotransfected with cyclin D1 and/or SRC-1, where indicated, using PEI (Polyethylenimine, Mw 25kDa, Polysciences) (42). 4-OH-tamoxifen (Sigma), EM-652 (kindly provided by dr. C. Labrie, University of Quebec, Canada), arzoxifene, GW7604, the active form of GW5638 (43) (kindly provided by GlaxoSmithKline), or ICI-182,780 (Tocris) were added at a final concentration of 1 μM, to ensure saturating ligand concentrations for overexpressed ERα. Forskolin (Sigma) was added 15 min prior to measurements at a final concentration of 10 μM. YFP-ERα-CFP, ERα-CFP, SRC-1, SRC-1(aa623-711)-YFP, SRC-1(aa1051-1240)-YFP and cyclin D1 constructs were generated as described previously (1;5;30). All used constructs and point mutants were sequence verified. Antibodies applied in this study were raised against ERα (Novocastra), tubulin (Sigma), cyclin D1 (Santa Cruz), RNA polymerase II (8WG16; Covance, Inc.) and GFP (44).

Fluorescence Lifetime Imaging Microscopy (FLIM)

Prior to FLIM experiments, cells on coverslips were mounted in bicarbonate-buffered saline in a heated tissue culture chamber at 37°C under 5% CO2. FLIM experiments were performed on a Leica inverted DM-IRE2 microscope equipped with a Lambert Instruments frequency domain lifetime attachment (Leutingewolde, The Netherlands), controlled by the vendors LI FLIM software. CFP was excited at 430nm with ~4mW power using a LED modulated at 40MHz. Emission was collected at 450-490nm using an intensified CCD camera. FLIM measurements were performed in

U2OS cells, transfected with YFP-ERα-CFP only or cotransfected with cyclin D1 and/or SRC-1 constructs. Calculated CFP lifetimes were referenced to a 1 μM solution of Rhodamine-G6 in medium that was set at 4.11ns lifetime, and internally calibrated using co-cultured CFP containing MelJuSo reference cells for which the lifetime was set to 2.7ns (26). Donor FRET efficiency (E_D) was calculated as E_D=1- (lifetime cell of interest/ lifetime reference cell). Pair wise analysis was performed for each cell prior and after addition of anti-estrogen, where the E_D under CTS conditions is set to 1 for each experiment (relative E_D).

CLSM analysis

For CLSM analysis, prolactin promoter/enhancer (PRL-) array containing HeLa cells (28) were cultured in Dulbecco's medium containing CTS and were transfected where indicated with ERα-CFP, SRC-1-YFP and/or cyclin D1 by electroporation and subsequently seeded in Dulbecco's medium without phenol red supplemented with 5% CTS. Cells were treated for 2 hours with 1 μM estradiol, 1 μM of the indicated anti-estrogen or left untreated, to ensure saturating ligand concentrations for overexpressed ERα. Thereafter, cells were fixed with 3.7% formaldehyde in PBS and subsequently stained with antibodies detecting RNA polymerase II (8WG16; Covance, Inc.) or anti-Cyclin D1 (Santa Cruz) and secondary antibodies conjugated to Alexa 647 (Molecular Probes, Leiden, The Netherlands). Images were taken with a Leica TCS SP2 System equipped with a 63 x oil emersion objective. CFP was excited at 458 nm, and emission measured at 460-500 nm. Alexa 647 was excited at 633 nm, emission measured at 645-720 nm. Array size quantification was performed using Leica software, and plotted using proFit (QuantumSoft).

Quantitative RT-PCR

Prolactin promoter/enhancer (PRL-) array containing HeLa cells (28) were transfected with ERα-CFP only or cotransfected with cyclin D1 by electroporation and subsequently cultured in phenol-red free Dulbecco's medium containing CTS. Immediately after seeding, the cells were treated with 10 nM estradiol or 100 nM anti-estrogen for 16 hours or the cells were left untreated. For quantitative RT-PCR in MCF-7 cells, cells were cultured in phenol red-free DMEM medium containing 5% charcoal-treated serum for 72 hours prior to transfection. Subsequently, cells were transfected with cyclin D1 or pcDNA3 empty vector and cultured overnight, after which cells were treated with 10 nM estradiol or 100 nM anti-estrogen for 5 hours or the cells were left untreated. After exposure to hormones, cells were lysed and RNA was extracted using Trizol (Invitrogen), according to the manufacturer's protocol. RNA was reverse transcribed using SuperScript(tm) III Reverse Transcriptase (Invitrogen), on which QPCR was performed using CYBR Green (Applied Biosystems), according to the manufacturer's protocols. The DsRed2 cDNA was amplified with the forward primer 5' CCAGTTCCAGTACGGCTCCA and the reverse primer 5' GCCGTCCTCGA AGTTCATCA. pS2 cDNA was amplified with the forward primer 5' CATCGA CGTCCCTCCAGAAGA and the reverse primer 5' CTCTGGGACTAATCACCG TGCT. As a control for equal loading, the observed signals were related to β-actin RNA levels, using a forward primer 5' CCTGGCACCCAGCACAAT and reverse primer 5' GGGCCGGACTCGTCA TACT.

Cell growth assay

MCF-7 cells, grown on 5% CTS serum containing phenol-red free Dulbecco's medium for 7 days, were electroporated with cyclin D1 wild type, cyclin D1-L244A/L245A (LALA), cyclin D1-K112E (KE) or pcDNA3-YFP empty vector as control. Immediately after electroporation, 40.000 cells were seeded in per well (24 well plate). Cells were treated with 10 nM E2, 100 nM anti-estrogen or left untreated and ligand-supplemented medium was replaced every 2 days. At 10 hours after seeding, cells were detached from the plate using trypsin and fixed in 3,7 % formaldehyde in PBS in triplicate. Similar samples were taken at 2, 5, 8 and 10 days after transfection. Total number of cells obtained from each well was determined using a Casy model TT cell counter (Schärfe-System GmbH, Germany).

Acknowledgements

We thank Lennert Janssen and Cristiane Bentin-Toaldo for assistance in generating the chimeric mutants of ER and SRC-1 and Coenraad Kuijl for help with FRAP analysis.

References

1. Michalides R, Griekspoor A, Balkenende A, Verwoerd D, Janssen L, Jalink K, Floore A, Velds A, van't Veer L, Neefjes J 2004 Tamoxifen resistance by a conformational arrest of the estrogen receptor alpha after PKA activation in breast cancer. Cancer Cell 5:597-605

2. Gutierrez MC, Detre S, Johnston S, Mohsin SK, Shou J, Allred DC, Schiff R, Osborne CK, Dowsett M 2005 Molecular changes in tamoxifen-resistant breast cancer: relationship between estrogen receptor, HER-2, and p38 mitogen-activated protein kinase. J Clin Oncol 23:2469-2476

3. Holm C, Rayala S, Jirstrom K, Stal O, Kumar R, Landberg G 2006 Association between Pak1 expression and subcellular localization and tamoxifen resistance in breast cancer patients. J Natl Cancer Inst 98:671-680

4. Zwart W, Griekspoor A, Rondaij M, Verwoerd D, Neefjes J, Michalides R 2007 Classification of anti-estrogens according to intramolecular FRET effects on phospho-mutants of estrogen receptor alpha. Mol Cancer Ther 6:1526-1533

5. Zwart W, Griekspoor A, Berno V, Lakeman K, Jalink K, Mancini M, Neefjes J, Michalides R 2007 PKA-induced resistance to tamoxifen is associated with an altered orientation of ERalpha towards co-activator SRC-1. EMBO J 26:3534-3544

6. Shang Y, Brown M 2002 Molecular determinants for the tissue specificity of SERMs. Science 295:2465-2468

7. Lonard DM, Tsai SY, O'Malley BW 2004 Selective estrogen receptor modulators 4-hydroxytamoxifen and raloxifene impact the stability and function of SRC-1 and SRC-3 coactivator proteins. Mol Cell Biol 24:14-24

8. Osborne CK, Bardou V, Hopp TA, Chamness GC, Hilsenbeck SG, Fuqua SA, Wong J, Allred DC, Clark GM, Schiff R 2003 Role of the estrogen receptor coactivator AIB1 (SRC-3) and HER-2/neu in tamoxifen resistance in breast cancer. J Natl Cancer Inst 95:353-361

9. Karlseder J, Zeillinger R, Schneeberger C, Czerwenka K, Speiser P, Kubista E, Birnbaum D, Gaudray P, Theillet C 1994 Patterns of DNA amplification at band q13 of chromosome 11 in human breast cancer. Genes Chromosomes Cancer 9:42-48

10. Ormandy CJ, Musgrove EA, Hui R, Daly RJ, Sutherland RL 2003 Cyclin D1, EMS1 and 11q13 amplification in breast cancer. Breast Cancer Res Treat 78:323-335

11. Schuuring E, Verhoeven E, Mooi WJ, Michalides RJ 1992 Identification and cloning of two overexpressed genes, U21B31/PRAD1 and EMS1, within the amplified chromosome 11q13 region in human carcinomas. Oncogene 7:355-361

12. Bostner J, Ahnstrom Waltersson M, Fornander T, Skoog L, Nordenskjold B, Stal O 2007 Amplification of CCND1 and PAK1 as predictors of recurrence and tamoxifen resistance in postmenopausal breast cancer. Oncogene 26:6997-7005

13. Pacilio C, Germano D, Addeo R, Altucci L, Petrizzi VB, Cancemi M, Cicatiello L, Salzano S, Lallemand F, Michalides RJ, Bresciani F, Weisz A 1998 Constitutive overexpression of cyclin D1 does not prevent inhibition of hormone-responsive human breast cancer cell growth by antiestrogens. Cancer Res 58:871-876

14. Zwijsen RM, Wientjens E, Klompmaker R, van der Sman J, Bernards R, Michalides RJ 1997 CDK-independent activation of estrogen receptor by cyclin D1. Cell 88:405-415

15. Zwijsen RM, Buckle RS, Hijmans EM, Loomans CJ, Bernards R 1998 Ligand-independent recruitment of steroid receptor coactivators to estrogen receptor by cyclin D1. Genes Dev 12:3488-3498

16. Michalides R, Hageman P, van Tinteren H, Houben L, Wientjens E, Klompmaker R, Peterse J 1996 A clinicopathological study on overexpression of cyclin D1 and of p53 in a series of 248 patients with operable breast cancer. Br J Cancer 73:728-734

17. van Diest PJ, Michalides RJ, Jannink L, van der Valk P, Peterse HL, de Jong JS, Meijer CJ, Baak JP 1997 Cyclin D1 expression in invasive breast cancer. Correlations and prognostic value. Am J Pathol 150:705-711

18. Wu YL, Yang X, Ren Z, McDonnell DP, Norris JD, Willson TM, Greene GL 2005 Structural basis for an unexpected mode of SERM-mediated ER antagonism. Mol Cell 18:413-424

19. Osborne CK, Zhao H, Fuqua SA 2000 Selective estrogen receptor modulators: structure, function, and clinical use. J Clin Oncol 18:3172-3186

20. Robertson JF 2004 Selective oestrogen receptor modulators/new antioestrogens: a clinical perspective. Cancer Treat Rev 30:695-706

21. Stossi F, Barnett DH, Frasor J, Komm B, Lyttle CR, Katzenellenbogen BS 2004 Transcriptional profiling of estrogen-regulated gene expression via estrogen receptor (ER) alpha or ERbeta in human osteosarcoma cells: distinct and common target genes for these receptors. Endocrinology 145:3473-3486

22. Levy N, Zhao X, Tang H, Jaffe RB, Speed TP, Leitman DC 2007 Multiple transcription factor elements collaborate with estrogen receptor alpha to activate an inducible estrogen response element in the NKG2E gene. Endocrinology 148:3449-3458

23. Monroe DG, Johnsen SA, Subramaniam M, Getz BJ, Khosla S, Riggs BL, Spelsberg TC 2003 Mutual antagonism of estrogen receptors alpha and beta and their preferred interactions with steroid receptor coactivators in human osteoblastic cell lines. J Endocrinol 176:349-357

24. Rogatsky I, Zarember KA, Yamamoto KR 2001 Factor recruitment and TIF2/GRIP1 corepressor activity at a collagenase-3 response element that mediates regulation by phorbol esters and hormones. EMBO J 20:6071-6083

25. Ball LJ, Levy N, Zhao X, Griffin C, Tagliaferri M, Cohen I, Ricke WA, Speed TP, Firestone GL, Leitman DC 2009 Cell type- and estrogen receptor-subtype specific regulation of selective estrogen receptor modulator regulatory elements. Mol Cell Endocrinol 299:204-211

26. Vermeer JE, Van Munster EB, Vischer NO, Gadella TW, Jr. 2004 Probing plasma membrane microdomains in cowpea protoplasts using lipidated GFP-fusion proteins and multimode FRET microscopy. J Microsc 214:190-200

27. Bastiaens PI, Squire A 1999 Fluorescence lifetime imaging microscopy: spatial resolution of biochemical processes in the cell. Trends Cell Biol 9:48-52

28. Sharp ZD, Mancini MG, Hinojos CA, Dai F, Berno V, Szafran AT, Smith KP, Lele TP, Ingber DE, Mancini MA 2006 Estrogen-receptor-alpha exchange and chromatin dynamics are ligand- and domain-dependent. J Cell Sci 119:4101-4116

29. Hatzis P, Talianidis I 2002 Dynamics of enhancer-promoter communication during differentiation-induced gene activation. Mol Cell 10:1467-1477

30. Bindels EM, Lallemand F, Balkenende A, Verwoerd D, Michalides R 2002 Involvement of G1/S cyclins in estrogen-independent proliferation of estrogen receptor-positive breast cancer cells. Oncogene 21:8158-8165

31. Brzozowski AM, Pike AC, Dauter Z, Hubbard RE, Bonn T, Engstrom O, Ohman L, Greene GL, Gustafsson JA, Carlquist M 1997 Molecular basis of agonism and antagonism in the oestrogen receptor. Nature 389:753-758

32. Wijayaratne AL, Nagel SC, Paige LA, Christensen DJ, Norris JD, Fowlkes DM, McDonnell DP 1999 Comparative analyses of mechanistic differences among antiestrogens. Endocrinology 140:5828-5840

33. Pike AC 2006 Lessons learnt from structural studies of the oestrogen receptor. Best Pract Res Clin Endocrinol Metab 20:1-14

34. Buzdar A, O'Shaughnessy JA, Booser DJ, Pippen JE, Jr., Jones SE, Munster PN, Peterson P, Melemed AS, Winer E, Hudis C 2003 Phase II, randomized, double-blind study of two dose levels of arzoxifene in patients with locally advanced or metastatic breast cancer. J Clin Oncol 21:1007-1014

35. Freddie CT, Larsen SS, Bartholomaeussen M, Lykkesfeldt AE 2004 The effect of the new SERM arzoxifene on growth and gene expression in MCF-7 breast cancer cells. Mol Cell Endocrinol 219:27-36

36. Deshmane V, Krishnamurthy S, Melemed AS, Peterson P, Buzdar AU 2007 Phase III double-blind trial of arzoxifene compared with tamoxifen for locally advanced or metastatic breast cancer. J Clin Oncol 25:4967-4973

37. Neuman E, Ladha MH, Lin N, Upton TM, Miller SJ, DiRenzo J, Pestell RG, Hinds PW, Dowdy SF, Brown M, Ewen ME 1997 Cyclin D1 stimulation of estrogen receptor transcriptional activity independent of cdk4. Mol Cell Biol 17:5338-5347

38. Michalides R, van Tinteren H, Balkenende A, Vermorken JB, Benraadt J, Huldij J, van Diest P 2002 Cyclin A is a prognostic indicator in early stage breast cancer with and without tamoxifen treatment. Br J Cancer 86:402-408

39. Wang C, Fan S, Li Z, Fu M, Rao M, Ma Y, Lisanti MP, Albanese C, Katzenellenbogen BS, Kushner PJ, Weber B, Rosen EM, Pestell RG 2005 Cyclin D1 antagonizes BRCA1 repression of estrogen receptor alpha activity. Cancer Res 65:6557-6567

40. Holm C, Kok M, Michalides R, Fles R, Koornstra RH, Wesseling J, Hauptmann M, Neefjes J, Peterse JL, Stal O, Landberg G, Linn SC 2009 Phosphorylation of the oestrogen receptor alpha at serine 305 and prediction of tamoxifen resistance in breast cancer. J Pathol 217:372-379

41. Jordan VC, O'Malley BW 2007 Selective estrogen-receptor modulators and antihormanal resistance in breast cancer. J Clin Oncol 25:5815-5824

42. Boussif O, Lezoualc'h F, Zanta MA, Mergny MD, Scherman D, Demeneix B, Behr JP 1995 A versatile vector for gene and oligonucleotide transfer into cells in culture and *in vivo*: polyethylenimine. Proc Natl Acad Sci U S A 92:7297-7301

43. Dardes RC, O'Regan RM, Gajdos C, Robinson SP, Bentrem D, Los Reyes A, Jordan VC 2002 Effects of a new clinically relevant antiestrogen (GW5638) related to tamoxifen on breast and endometrial cancer growth *in vivo*. Clin Cancer Res 8:1995-2001

44. van Ham SM, Tjin EP, Lillemeier BF, Gruneberg U, van Meijgaarden KE, Pastoors L, Verwoerd D, Tulp A, Canas B, Rahman D, Ottenhoff TH, Pappin DJ, Trowsdale J, Neefjes J 1997 HLA-DO is a negative modulator of HLA-DM-mediated MHC class II peptide loading. Curr Biol 7:950-957

Supplemental Data

Supplemental Materials and Methods

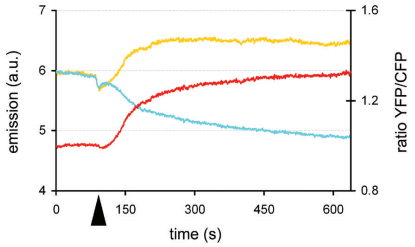
Ratio-Fluorescence Resonance Energy Transfer (FRET)

Prior to FRET experiments, cells on coverslips were mounted in bicarbonate-buffered saline (140 mM NaCl, 5 mM KCl, 1 mM MgCl2, 1 mM CaCl2, 23 mM NaHCO3, 10 mM glucose and 10 mM HEPES at pH 7.3) in a heated tissue culture chamber at 37°C under 5% CO2. Cells were analyzed on an inverted Zeiss Axiovert 135 microscope equipped with a dry Achroplan 63× objective. FRET equipment was as described previously (44). CFP was excited at 432 ± 5 nm and emission of YFP was detected with a 527 nm longpass filter and CFP using a 478-527 nm bandpass filter. FRET was expressed as the ratio of YFP to CFP signals. The ratio was arbitrarily set as 1.0 at the onset of the experiment. Changes are expressed as percent deviation from this initial value of 1.0. For data acquisition, Felix software (PTI Inc.) was used. Data were plotted using proFit (QuantumSoft).

Fluorescence Recovery After Photobleaching (FRAP) and Fluorecence Loss in Photobleaching (FLIP)

U2OS cells were cultured on coverslips in CTS containing medium. 24 hours prior to imaging, cells were transfected with ERα-CFP and/ or SRC-1 using PEI. Where indicated, cells were additionally cotransfected with exogenous cyclin D1. Prior to analysis, coverslips were placed in 2 ml bicarbonate-buffered saline and analyzed in a heated tissue culture chamber at 37°C under 5% CO2. Cells were treated with 100 nM arzoxifene or left untreated. Images were acquired on a TCS-SP2 confocal microscope (Leica, Mannheim, Germany), using a 63x oil immersion objective. Fluorescence intensities were measured at the bleach spot (FRAP) and at the far end of the nucleus (FLIP). Zoom factor was set at 4x for all experiments. t1/2 recovery value was calculated by t1/2 = FFRAP∞- FBLEACH /2, where ∞ is the asymptotic plateau value of the corresponding curve. Immobile fraction (IF) was calculated as IF = ((FFLIP∞- FBLEACH)- (FFRAP∞- FBLEACH))/ (FFLIP∞- FBLEACH) * 100%, where FFLIP∞ and FFRAP∞ are the fluorescence plateau levels of the corresponding curves and FBLEACH the fluorescence level immediately after bleach.

S1A



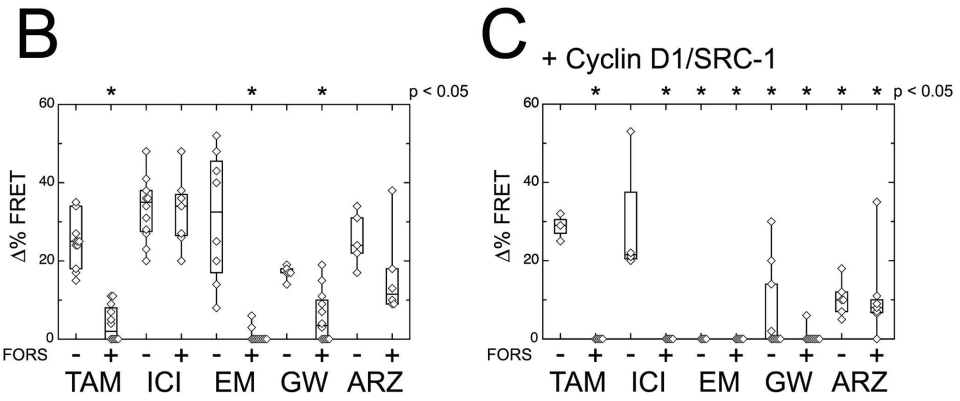


Figure S1. Inactivation of ERα by anti-estrogens measured by ratio-FRET.

A. Time course of emission of YFP (yellow line) and CFP (blue line) and corresponding ratio of YFP/CFP emission (red line) of one YFP-ERα-CFP containing U2OS cell after addition of 1 μM ICI-182,780, indicated by arrowhead. No effect of the ethanol solvent could be detected.
B. FRET values in YFP-ERα-CFP expressing U2OS cells after addition of 1 μM of the indicated anti-estrogens. Cells were either (+) or not (-) pretreated with forskolin 15 minutes prior to FRET measurements.
The FRET values are shown as separate values of the percentage alteration in the FRET ratio, where each square shows one experiment (n > 5 for each condition). The data are presented in a box plot with the horizontal bar indicating the median value. The box size is determined by the upper and lower quartiles, the median value of the upper and lower half of the data points, respectively.
C. FRET values in U2OS cells expressing YFP-ERα-CFP, SRC-1 and cyclin D1 after addition of 10^{-6} M of the indicated anti-estrogen. The FRET values are presented as under B.
TAM: 4-OH-tamoxifen; ICI: ICI-182,780 (Fulvestrant); EM: EM-652; GW: GW5638; ARZ: arzoxifene.
* indicates a statistically significant FRET reduction for conditions in both B and C, compared to the non-forskolin treated samples in B, $p < 0.05$

S2

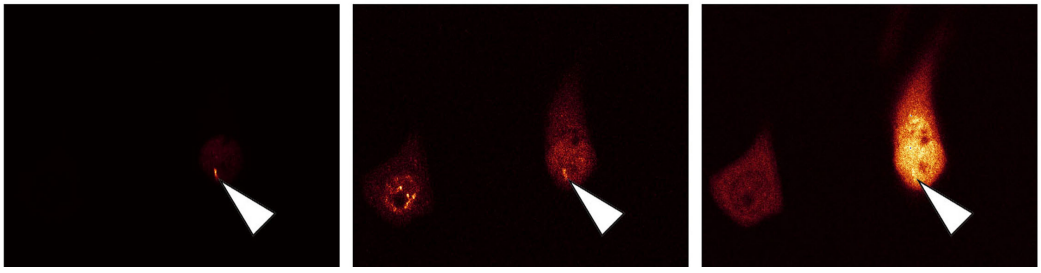


Figure S2. Cyclin D1 overexpression verified in PRL array containing HeLa cells.

Staining for cyclin D1 and RNA Polymerase II was performed on PRL array containing HeLa cells
that were cotransfected with ERα and excess cyclin D1. Cells expressing ERα overexpressed cyclin D1. ERα, cyclin D1 and RNA Polymerase II were all recruited to the array structure, indicated by arrowhead.

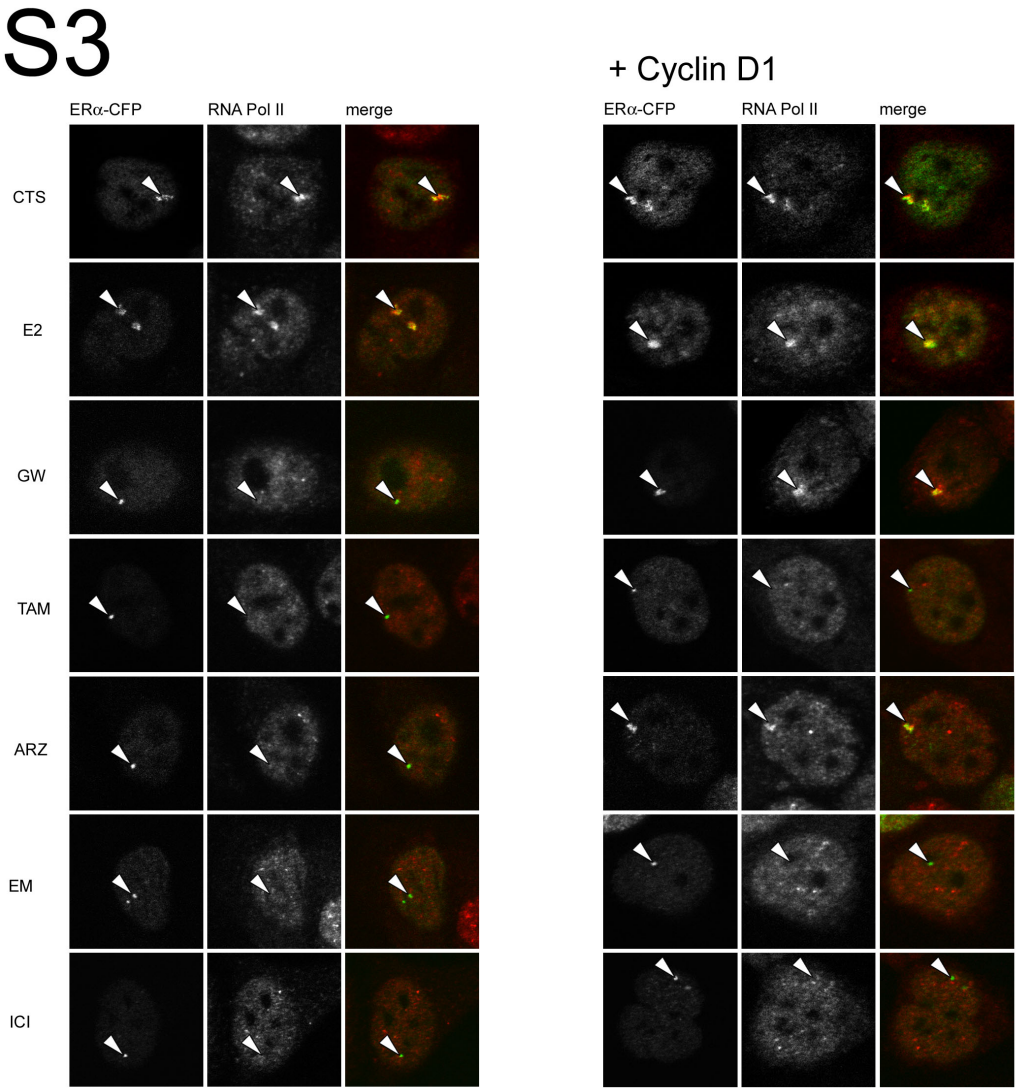


Figure S3. Cyclin D1 overexpression induces RNA polymerase II recruitment on the PRL array and increases array size in the presence of GW5638 and arzoxifene.

PRL array containing HeLa cells were transfected with ERα-CFP alone or cotransfected with cyclin D1 and stained for RNA polymerase II. Cells were cultured in hormone depleted (CTS) medium and treated with 1 μM estradiol (E2) or with 1 μM of the indicated anti-estrogen for 2 hours and then fixed and stained for RNA Polymerase II. Arrowheads indicate the PRL array that was analyzed for RNA polymerase II staining. Quantifications are shown in Figure 3.

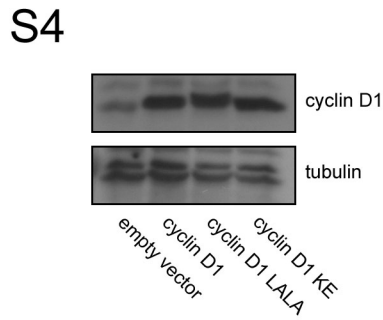


Figure S4. Overexpression of cyclin D1 wild type and mutants in MCF-7 cells.

Western blot analysis of MCF-7 cells, transfected by electroporation with an empty vector, cyclin D1 wild type, cyclin D1 LALA or cyclin D1 KE. Blots were stained with antibodies detecting cyclin D1 and tubulin, verifying equal overexpression of the applied cyclin D1 variants.

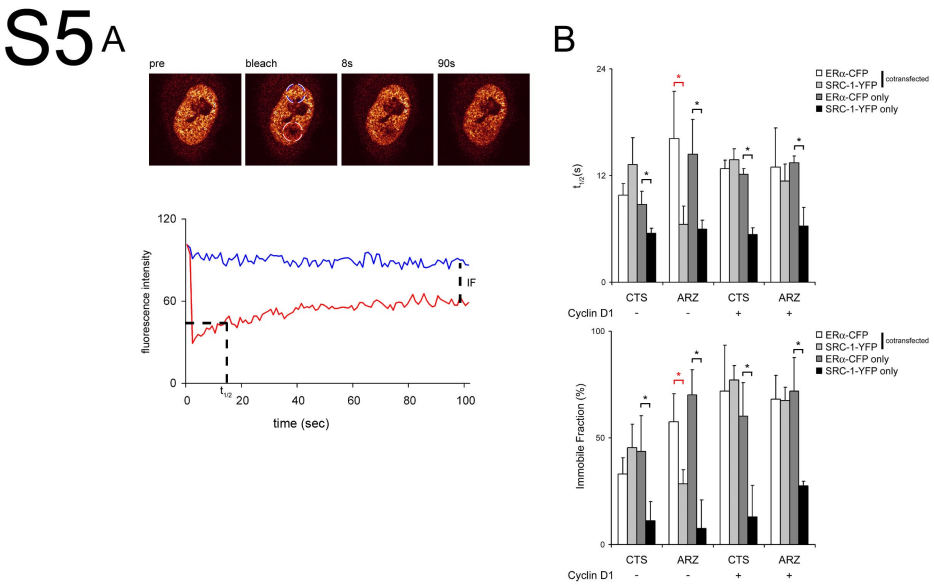
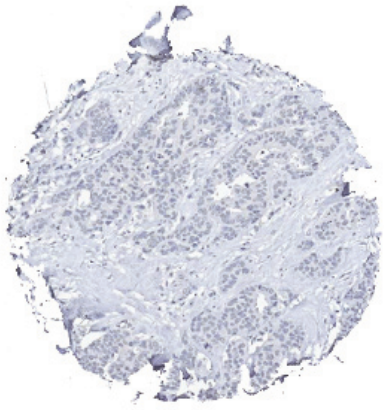


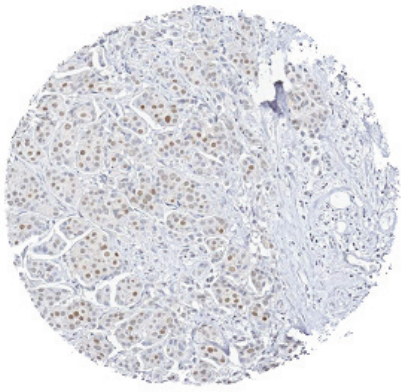
Figure S5. Cyclin D1 stabilizes ERα/SRC-1 complex under arzoxifene conditions

A. An example of FRAP analysis where the determination of T1/2 and Immobile fraction (IF) is illustrated. Underlying calculations are described in the supplemental materials and methods section.
B. FRAP analysis of U2OS cells expressing ERα-CFP and/or SRC-1-YFP, with or without cyclin D1 co-expression. Both t1/2 (top panel) and immobile fraction (bottom panel) are given. Mean and standard deviation for tested conditions is given. t1/2 and immobile fraction of SRC-1-YFP was altered by co-expression of ERα-CFP, suggesting an interaction. Arzoxifene treatment induced a deviation between ERα-CFP and SRC-1-YFP dynamics, thus interaction is lost. When cyclin D1 was overexpressed, SRC-1-YFP t1/2 and immobile fraction were again comparable to those of ERα-CFP under arzoxifene conditions, implying a stabilization of the complex. * indicates a statistically significant differences in between ERα-CFP and SRC-1-YFP (black for controls, red for cotransfected ERα-CFP and SRC-1-YFP) within the same treatment; $p < 0.05$.

Predictive algorithm for tamoxifen resistance in breast cancer patients based on PKA-induced phosphorylation of ERα at serine 305 and PAK1

Submitted





7

Predictive algorithm for tamoxifen resistance in breast cancer patients based on PKA-induced phosphorylation of ERα at serine 305 and PAK1

Marleen Kok[1] MD, Wilbert Zwart[2] MSc, Caroline Holm[3,4] MSc, Renske Fles[1] BSc, Michael Hauptmann[5] PhD, Laura J. Van 't Veer[6] PhD, Lodewyk F.A. Wessels[5] PhD, Prof Jacques Neefjes[2] PhD, Prof Olle Stål[7] MD, Sabine C. Linn[5,8] MD, Prof Göran Landberg[3,4] MD and Rob Michalides[2] PhD

Summary

Background

p21-activated kinase (PAK1) and protein kinase A (PKA) may induce phosphorylation of oestrogen receptor α at serine 305 (ERαS305-P). ERαS305-P leads to tamoxifen resistance *in vitro*. We aimed to develop a clinical test incorporating ERαS305-P, PAK1 and, PKA to predict tamoxifen resistance in breast cancer patients.

Methods

Phosphorylation of ERαS305 was studied in MCF7 cells. Pathways were analysed in 58 tumours using gene expression microarrays. Immunohistochemistry of PAK1, phosphorylated PKA (pPKA) and, ERαS305-P was evaluated in 132 patients (trainingset) who received tamoxifen for metastatic disease (endpoint: time to tumour-progression, TTP). Patients (n=231) who had been randomised between adjuvant tamoxifen and no treatment (endpoint: recurrence-free survival, RFS) were used for validation.

Findings

In the trainingset, PAK1 (HR=1.64, 95% CI 1.05-2.58) predicted TTP. In addition, tumours with both pPKA and ERαS305-P (pPKA/ERαS305-P) showed a shorter TTP (HR 1.94, 95% CI 1.14-3.63). In MCF7 cells, PKA induced ERαS305-P, while PAK1 did not. ERαS305-P was associated with PKA-pathways (p=0.019) and not with PAK1-pathways.

Subsequently, an algorithm was developed that combined PAK1 and pPKA/ERαS305-P immunohistochemistry. In the validation, patients with no PAK1 and no pPKA/ERαS305-P benefitted from tamoxifen (HR=0.54, 95% CI 0.34-0.87), while patients with either PAK1 or pPKA/ERαS305-P expression had no significant benefit (HR 0.88, 95% CI 0.42-1.82). Effects of tamoxifen on RFS in subgroups defined by the algorithm were different (interaction, p=0.037).

Interpretation

PAK1 and pPKA/ ERαS305-P identify tumours with poor outcome after tamoxifen. An algorithm including PAK1 and pPKA/ER305-P identifies one-third of ERα-positive breast cancer patients as unlikely to benefit from tamoxifen.

Introduction

Resistance to anti-oestrogens is one of the major challenges in breast cancer treatment. For more than 25 years, the gold standard for endocrine treatment of breast cancer has been tamoxifen. However, approximately half of the patients with oestrogen receptor alpha (ERα)-positive tumours do not respond to tamoxifen [1]. More recently, novel classes of endocrine agents have been introduced, including aromatase inhibitors and fulvestrant [2]. These drugs have a different mechanism of action compared to tamoxifen [3,4], and consequently, clinical trials in metastatic breast indicate a non-cross-resistance between tamoxifen and the more recently developed endocrine agents [5-7]. To select an optimal adjuvant treatment [8], additional biomarkers are necessary to identify patients who have no benefit from tamoxifen and should be treated according to alternative anti-oestrogen strategies.

Various mechanisms can contribute to tamoxifen resistance [9]. For example, kinases can modify ERα via phosphorylation [10]. Phosphorylation of ERα at serine 305 (ERαS305-P) leads to activation of ERα and transcription of ERα-responsive genes in response to tamoxifen exposure [11,12], thus inducing resistance. Functional studies showed that tamoxifen resistance mediated by protein kinase A (PKA) is caused by ERαS305-P [11,12]. In addition, ERαS305-P has been associated with p21-activated kinase (PAK1)[13-15], and nuclear expression and amplification of PAK1 correlates with tamoxifen resistance as well [16,17].

Recently, we have presented the first clinical

Departments of Experimental Therapy[1], Cell Biology[2], Molecular Biology[5], Pathology[6] and Medical Oncology[8], Netherlands Cancer Institute, Amsterdam, the Netherlands
Center for Molecular Pathology[3], Lund University, Malmö University Hospital, Malmö, Sweden
Breakthrough Breast Cancer Research Unit[4], Paterson Institute for Cancer Research, Manchester, UK
Division of Oncology[7], Department of Clinical and Experimental Medicine, Linköping University, Linköping, Sweden

Corresponding author
Dr. Rob Michalides, Division of Cell Biology
Netherlands Cancer Institute
Plesmanlaan 121, 1066 CX Amsterdam, The Netherlands
Phone 0031 20 5122022
Fax 0031 20 5122029
Email r.michalides@nki.nl

data suggesting that ERαS305-P may be a biomarker that, as suggested by the experimental studies, can identify patients unlikely to respond to tamoxifen [18]. So far, translational studies have only provided indirect evidence that PKA and PAK1 are linked to ERαS305-P in breast cancer patients [11,17]. In order to gain insight into the association between both PKA as well as PAK1 with ERαS305-P and to determine their clinical relevance, we studied the three putative markers in a clinical setting (n=363). We developed and validated an algorithm containing PKA, PAK1 and, ERαS305-P that identified a substantial fraction of patients who fail to respond to tamoxifen.

Methods

NKI-AVL, Lund and Linköping Universities ethical boards approved the studies. The data are presented according to the REMARK recommendations [19].

Patients training series

As previously described ([18] and partly in [20]), a consecutive series of breast cancer patients who had been treated at the NKI-AVL were selected according to the following criteria: 1) invasive ERα-positive breast carcinoma, 2) no adjuvant systemic treatment, 3) development of relapse before 2002, for which first-line tamoxifen mono-therapy had been given. Tamoxifen was administered according to national guidelines of that time. Ten patients were excluded due to insufficient tumour material. Analyses presented here are based on 132 patients.

Patients validation series

As described before, 564 premenopausal patients were randomised to either 2 years of tamoxifen (n=276) or no systemic treatment (control) (n=288) [17,18,21,22]. Here, we analyse ERα-positive tumours of 231 patients for whom PAK1, PKA and, ERαS305-P immunohistochemistry was available.

Clinical endpoints

In the training series, time to tumour progression (TTP) was considered primary endpoint measured from start tamoxifen until treatment was ended because of progression. In the validation series, recurrence-free survival (RFS) was primary endpoint measured from surgery to either local, regional, or distant recurrences or breast cancer specific death.

Immunohistochemistry (IHC)

Tissue microarrays (TMAs) were constructed using formalin-fixed paraffin-embedded (FFPE) tumour blocks [23].

Details regarding IHC are presented in Table S1. ERα was considered positive when > 10% of invasive cells showed nuclear reactivity [22]. IHC and scoring with the monoclonal ERαS305-P antibody (Millipore # 124-9-4) has been described previously [18]. PAK1 staining was performed and scored as described before and nuclear expression was assessed [17]. For antigen retrieval of phosphorylated PKA-catalytic subunit (threonine 197) (pPKA) (Cell Signaling, #4781), citrate buffer (10 mM, pH 6.0) was pre-heated; slides were added for 15 minutes (microwave 300W), incubated overnight with the antibody (dilution 1:40) and detected by diaminobenzidine. pPKA cytoplasmatic intensity was evaluated. As this is the first report describing this antibody for IHC, we used a simple cut-off comparing no pPKA with any pPKA expression. Scoring of the TMAs was performed without any information on disease outcome of the patients. To control phospho-specificity, a sample expressing pPKA was dephosphorylated with 1000 U lambda phosphatase (2 hours, 37° C)(Millipore). TMA images are available (http://telepathology.nki.nl login: ER305PAK1PKA, password:tamoxifen).

Cell culture, transfection, western blotting

MCF-7 cells were cultured in DMEM supplemented with 10% fetal calf serum and standard antibiotics. Two days before transfection, cells were kept in phenolred-free DMEM containing 5% charcoal-treated serum (Hyclone). 3 x 10^6 cells were transfected [12], with expression constructs encoding PAK1 K423E [24], and/or a catalytic PKA subunit [25] and after two days prepared for western blotting [18]. Forskolin (Sigma) was added 15 min prior to lysis at a concentration of 10^{-5} M. Antibodies against ERα (Stressgen Biotechnologies Corp), ERαS305P (Millipore), PAK1 (Cell Signaling, #2602), PKA C-α (Cell Signaling, #4782), and, β-tubulin (Sigma) were used at the recommended concentrations.

Gene expression analysis

The gene expression dataset has been described previously and are part of the training series described in this paper [20]. Agilent 44K expression data are available at http://research.agendia.com. Analyses were performed using BRB Array Tools (version 3.6). First, using the gene set expression comparison tool, 302 pathways as defined by Biocarta were analysed.

Fisher's Least Square (LS) statistic (10,000 permutations) was used to test which pathways were differentially expressed in ERαS305-P-positive tumours. Second, we related the pathways to either PKA or PAK1 using the Cancer Genome Anatomy Project (http://cgap.nci.nih.gov/Genes/GeneFinder) and 27 and 12 pathways were found to be related to PKA and PAK1, respectively. Next, we tested whether the list of significant pathways as defined by the LS statistic ($p<0.05$) was enriched for PKA-related pathways using Fisher's Exact test.

Statistics

Level of agreement between observers for pPKA staining was expressed by means of kappa. Clinicopathological characteristics according to pPKA were compared using Fisher's exact or Mann-Whitney U tests. Hazard ratios (HRs) were calculated using Cox regression analysis. Variables were entered into the multivariate model in one single step and to allow comparison with previous studies the same clinicopathological variables were added [17,18]. Analyses were performed using SPSS (version 15.0.1).

Table 1. Patient characteristics training series (tamoxifen for metastatic disease, NKI, n=132)

Variable	Category	Number	%
Year of diagnosis	Range	1977-1997	
Time to tumour progression*	Median in months (range)	15 (1-169)	
Disease-free interval**	Median in years (range)	5.1 (0.6-16.6)	
Age at surgery	Median in years (range)	59 (36-83)	
Grade***	I/II III	98 34	74% 26%
Lymph Node Status (2 unknown)	Negative Positive	86 44	66% 34%
WHO subtype (4 unknown or other subtype)	Invasive Ductal Carcinoma Invasive Lobular Carcinoma	111 17	87% 13%
Size (1 unknown)	≤ 20 mm >20 mm	77 54	59% 41%
Progesterone Receptor (IHC) (1 unknown)	≤ 10 % >10 %	48 83	37% 63%
HER2 (IHC)	0,1,2 3	118 14	89% 11%
ERαS305-P (IHC) (3 unknown)	Negative Positive	107 22	83% 17%
pPKA (IHC)	Negative Positive	37 95	28% 72%
PAK1 (IHC) (25 unknown)	Negative Positive	78 29	73% 27%

* Measured from start tamoxifen until stop tamoxifen treatment. ** Measured from date primary surgery till recurrence of disease.
*** According Nottingham Grading system (Elston et al. Histopathology 1993).

Role of funding source

The study was supported by the Dutch Cancer Society, TI Pharma, A Sister's Hope, Swedish Cancer Society, Malmö University Hospital Research and Cancer Funds and Astra Zeneca. Funding sources had no role in the study.

1

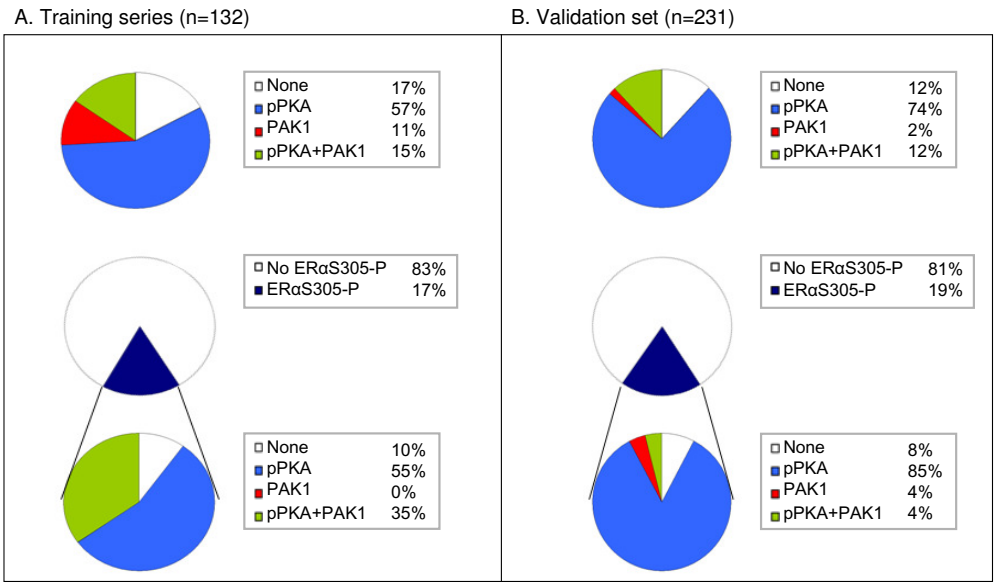


Figure 1. Expression on PAK1, pPKA and ERαS305-P in human breast tumours

Proportion of tumours that express nuclear PAK1, pPKA and/or ERαS305-P. In addition, the co-expression of PAK1 and pPKA with ERαS305-P is depicted. A) Training series consisting of patients treated with tamoxifen for metastatic disease, B) Validation series consisting of premenopausal patients who have participated in a randomised controlled trial that evaluated adjuvant tamoxifen versus no adjuvant systemic treatment.

Results

In order to determine the clinical relevance of both PAK1, PKA and phosphorylation of the PKA target, ERα at serine 305, we evaluated the expression of the three markers in a series of breast cancer patients (n=132) who had received tamoxifen for metastatic disease (training series, clinical characteristics in Table 1). Tests for PAK1 and ERαS305-P have been described before [17,18]. Active PKA was determined using an antibody detecting PKA phosphorylated at threonine 197 of the catalytic subunit (pPKA) [26]. To ensure that the antibody detects the phosphorylated form of PKA in FFPE tissues, sections were dephosphorylated prior to IHC. After treatment with lambda-phosphatase, no pPKA was detected (Figure S1). Scoring of the intensity of pPKA staining by two observers resulted in a kappa of 0.84 (p<0.0001). Clinico-pathological parameters according to pPKA are shown in Table S2. Figure 1A shows the proportion of tumours that express PAK1, pPKA or both. In addition, the co-expression of PAK1 and pPKA with ERαS305-P is summarised.

Previously we had shown that ERαS305-P status may predict tamoxifen response in the adjuvant setting [18]. The predictive value was less pronounced for outcome after tamoxifen in the metastatic disease setting (Figure 2A) [18]. pPKA was not associated with TTP after tamoxifen treatment (Figure 2B). However, patients with a tumour that co-expressed pPKA and ERαS305-P had a significantly worse outcome after tamoxifen (Figure 2C, univariate HR=1.94, p=0.014). In addition, PAK1 was related to short TTP after tamox-

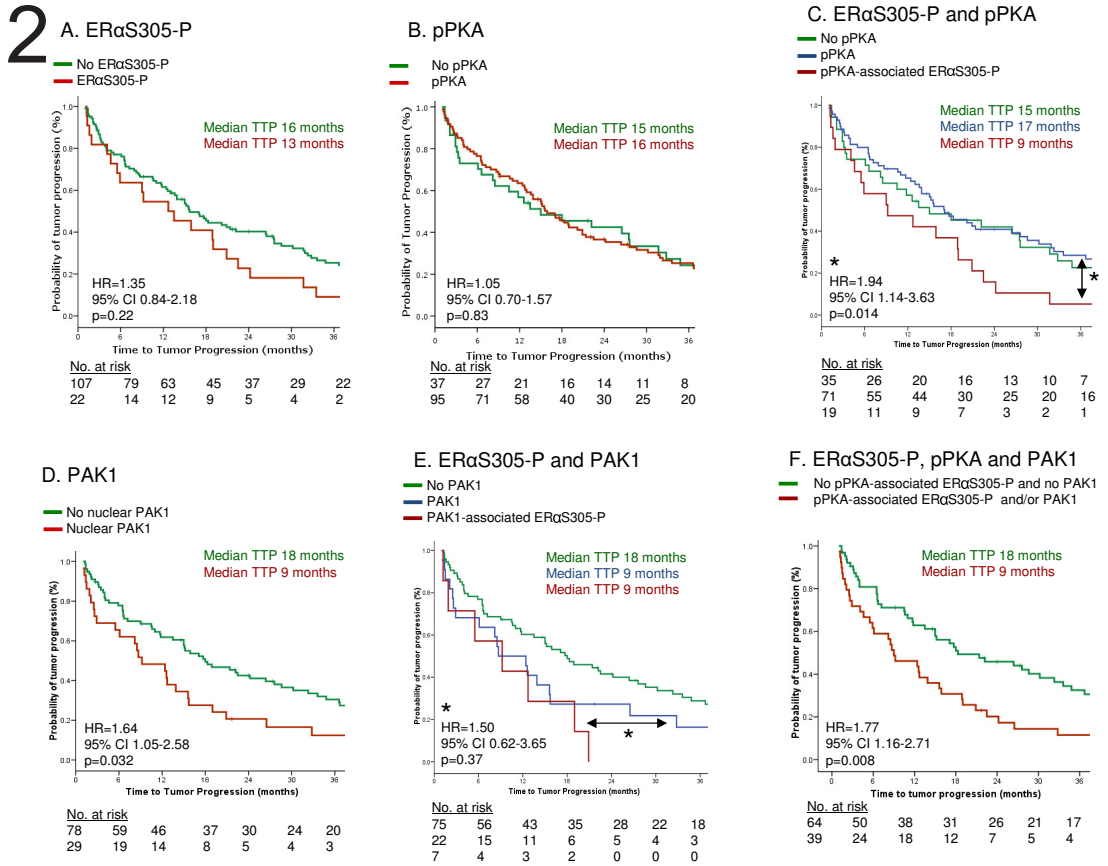


Figure 2. Relation of ERαS305-P, pPKA and PAK1 with outcome after tamoxifen treatment for metastatic disease (training series)

Kaplan-Meier analysis according to ERαS305-P, pPKA and nuclear PAK1 expression in 132 patients. HR and p-values are based on univariate Cox regression analysis. A) Time to tumour progression (TTP) according to ERαS305-P, B) TTP according to pPKA, C) TTP according to ERαS305-P and pPKA. Red line represents patients with a tumour co-expressing ERαS305-P and pPKA. Blue line represents patients with a tumour expressing pPKA but no ERαS305-P. HR and p-value is based on univariate Cox regression analysis and estimates the difference between the groups depicted in blue and red, D) TTP according to nuclear PAK1, E) TTP according to ERαS305-P and nuclear PAK1. Red line represents patients with a tumour co-expressing ERαS305-P and PAK1. Blue line represents patients with a tumour expressing PAK1 but no ERαS305-P. HR and p-value is based on univariate Cox regression analysis and estimates the difference between the groups depicted in blue and red. F) TTP according to the ERαS305-P/pPKA and PAK1. Red line represents patients with a tumour expressing pPKA-associated ERαS305-P, and/or nuclear PAK1. Green line represents patients with a tumour that is neither expressing nuclear PAK1 nor expressing pPKA-associated ERαS305-P.

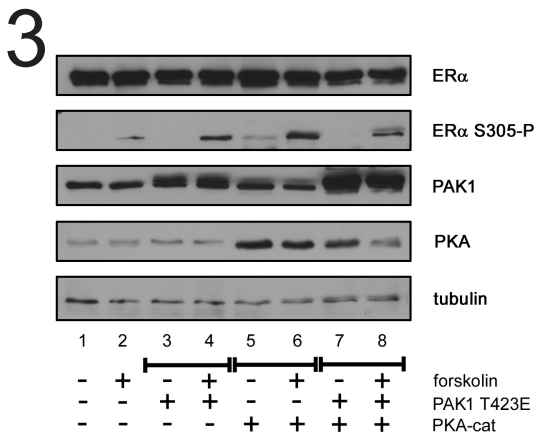


Figure 3. PAK1 does not directly phosphorylate ERαS305 in MCF-7 cells

Western blot analysis of MCF-7 breast cancer cells expressing kinase-active PAK1 T423E (lanes 3,4,7,8) either or not in combination with the catalytic subunit of PKA, PKA-cat, (lanes 5-8). In the even lanes, cells were treated for 30 minutes prior to lysis with 10μM forskolin for PKA activation, whereas cells were untreated in uneven lanes. Protein was analysed for expression of ERα, ERαS305-P, PAK1, PKA and α-tubulin (loading control). While both PKA activation and PKA-cat overexpression induced phosphorylation of ERαS305-P, this did not occur when overexpressing PAK1.

ifen (Figure 2D, univariate HR 1.64, p=0.032), which is in line with our previous results [17]. Although PAK1 has been linked to ERαS305-P *in vitro* [13], the tumours that co-expressed PAK1 and ERαS305-P did not show a shorter TTP compared to tumours that expressed PAK1 alone (Figure 2E).

These data suggest that PKA is linked to ERαS305-P since tumours expressing both pPKA and ERαS305-P have a poor outcome after tamoxifen, while activation of PAK1 seems to be related to tamoxifen resistance independent of ERαS305-P. To verify the connection between pPKA and ERαS305-P in a direct manner, we activated PKA in the mammary tumour cell line MCF7 by forskolin (activator of PKA via cAMP induction) treatment. Upon PKA activation the levels of ERαS305-P were increased (Figure 3, lane 2). To confirm this observation we activated PKA via over-expression of its catalytic subunit and this induced ERαS305-P (Figure 3, lane 5). Next, we over-expressed PAK1 (kinase-active construct), which did not affect ERαS305-P levels in MCF7 cells (Figure 3, lane 3).

To test whether ERαS305-P is indeed associated with PKA in human breast tumours, we evaluated gene expression of 11 tumours known to have a phosphorylated ERα at serine 305 and 47 ERαS305-P-negative tumours. These 58 tumours were selected because for these we had both IHC and gene expression data available. The ERαS305-P-positive tumours were not significantly different from the rest of the trainingset presented above with respect to the proportion of PAK1 and pPKA expression. Of the 302 pathways tested [19], were differentially expressed in ERαS305-P-positive tumours (permutated p<0.05, Table S3). The enrichment for pathways (5/19=26%) that include one or more PKA subunits was significant (p=0.019), while none of the 12 PAK1-related pathways were present in the list.

The *in vitro* experiments, the gene expression analysis as well as the clinical data in the training series, indicated that ERαS305-P is associated with pPKA but not with PAK1, suggesting that PAK1 induces tamoxifen resistance via a mechanism indepen-

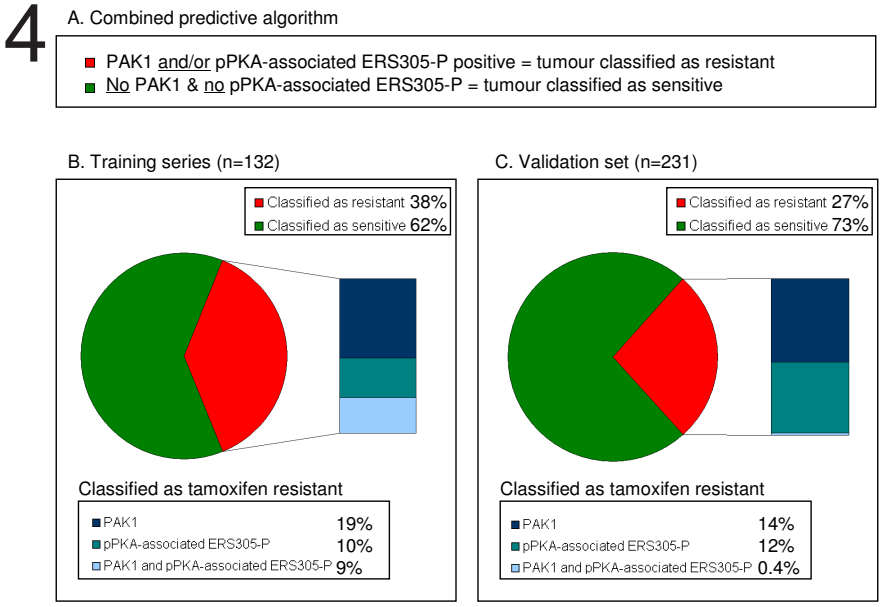


Figure 4. Illustration of the predictive algorithm

A) Categories defined by the algorithm including PAK1, pPKA and ERαS305-P.
B) and **C)** Illustration of the predictive algorithm and the proportion of patients that is classified as resistant.

Table 2. Multivariate Cox regression analysis of the risk of progression after tamoxifen according to ERαS305-P, pPKA and PAK1

A. Trainingset, NKI, tamoxifen for metastatic disease

Variable	Category	HR	95% CI	P-value
Grade*	I/II III	1 1.38	1.09-1.76	0.008
Lymph node status	Negative Positive	1 1.30	0.83-2.05	0.26
Age	Continuous (per year)	1.00	0.98-1.02	0.68
Algorithm	No pPKA-associated ERαS305-P and no PAK1 pPKA-associated ERαS305-P and/or PAK1	1 1.91	1.23-2.95	0.004

Due to missing values in the factors used for adjustment, the analysis was based on 101 cases with 89 events. Variables included as previously described for this series (16,17). Including variables that performed significant in this trainingset in univariate analyses (progesterone receptor, HER2 and disease-free interval) did not signifcantly change the HR for the Algorithm.
Ki67 was not available for this series. * Nottingham grading system

B. Validationset, Lund, adjuvant tamoxifen versus no systemic treatment in randomized trial

Variable	Category		HR	95% CI	P-value
Grade*	I/II III		1 1.74	1.07-2.84	0.026
Lymph node status	Negative Positive		1 0.94	0.58-1.55	0.82
Age	Continuous (per year)		0.95	0.91-1.00	0.052
Ki67	≤25 % > 25%		1 1.22	0.70-2.13	0.47
Algorithm	No pPKA-associated ERαS305-P and no PAK1 pPKA-associated ERαS305-P and/or PAK1		1 0.71	0.37-1.35	0.29
Tamoxifen**	No pPKA-associated ERαS305-P and no PAK1	-Control	1		
		-Tamoxifen	0.44	0.26-0.74	0.002
	pPKA-associated ERαS305-P and/or PAK1	-Control	1		
		-Tamoxifen	1.22	0.55-2.74	0.62

Due to missing values in the factors used for adjustment, the analysis was based on 201 cases with 88 events. Variables included as previously described for this series (16,17)
* Nottingham grading system
** Test of homogeneity of tamoxifen treatment effects by the Algorithm: p = 0.037 (based on interaction term).

Table 3. Patient characteristics validation series (randomized controlled trial, Lund, n=231)

Variable	Category	Number	%
Year of diagnosis	Range	1986-1991	
Follow-Up	Median in years (range)	12 (0-17)	
Age at surgery	Median in years (range)	45 (26-57)	
Grade* (3 unknown)	I/II III	151 77	66% 34%
Lymph Node Status	Negative Positive	55 176	24% 76%
WHO subtype (12 unknown or other subtype)	Invasive Ductal Carcinoma Invasive Lobular Carcinoma	196 23	89% 11%
Size (1 unknown)	≤ 20 mm >20 mm	97 134	42% 58%
Progesterone Receptor (IHC) (13 unknown)	≤ 10 % >10 %	22 196	10% 90%
Ki67 (IHC) (28 unknown)	≤25% > 25%	165 38	81% 19%
ERαS305-P (IHC) (18 unknown)	Negative Positive	178 35	84% 16%
pPKA (IHC) (41 unknown)	Negative Positive	25 165	13% 87%
PAK1 (IHC) (6 unknown)	Negative Positive	191 34	85% 15%

* According Nottingham Grading system (Elston et al. Histopathology 1993).

5

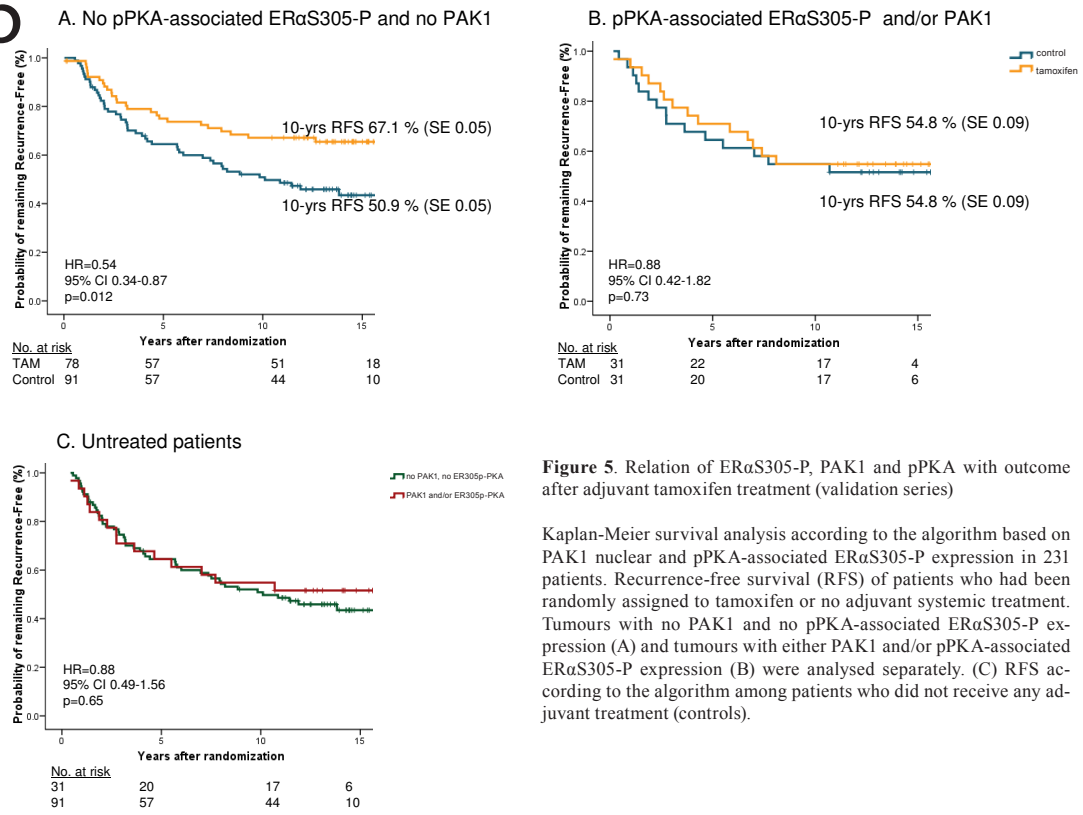


Figure 5. Relation of ERαS305-P, PAK1 and pPKA with outcome after adjuvant tamoxifen treatment (validation series)

Kaplan-Meier survival analysis according to the algorithm based on PAK1 nuclear and pPKA-associated ERαS305-P expression in 231 patients. Recurrence-free survival (RFS) of patients who had been randomly assigned to tamoxifen or no adjuvant systemic treatment. Tumours with no PAK1 and no pPKA-associated ERαS305-P expression (A) and tumours with either PAK1 and/or pPKA-associated ERαS305-P expression (B) were analysed separately. (C) RFS according to the algorithm among patients who did not receive any adjuvant treatment (controls).

dent of ERαS305-P. In order to capture both resistance mechanisms in a putative diagnostic test, we developed an IHC-based algorithm including PAK1 as well as pPKA-associated ERαS305-P (Figure 4A and 4B), which classified 38% (39/103) of the patients as resistant in the training series. Those had a significantly higher risk for progression after tamoxifen (HR=1.77, p=0.008)(Figure 2F). Multivariate Cox regression analysis revealed that the algorithm can identify a group of breast cancer patients who have a poor outcome after tamoxifen independent of traditional factors (Table 2A, multivariate HR=1.91, p=0.004).

Next, we validated the algorithm in an independent series (n=231), which was a subgroup of patients from a trial for whom sufficient material was available in order to assess the markers. They were not significantly different from the remaining group of patients with ERα-positive tumours who were included in the trial but for whom we couldn't analyse the algorithm (Figure S2, Table S4). The proportions of tumours expressing ERαS305-P, pPKA or PAK1 were similar as in the training series (Figure 1B, Table 3). 27% of the tumours had either PAK1 expression and/or pPKA-associated ERαS305-P (Figure 4C). Patients with either PAK1 expression and/or pPKA-associated ERαS305-P had no significant benefit from adjuvant tamoxifen (Figure 5B, HR=0.88, p=0.73), whereas patients with neither PAK1 nor pPKA-associated ERαS305-P benefitted from tamoxifen (Figure 5A, HR=0.54, p=0.012). In multivariate analysis, the effect of tamoxifen on RFS was statistically significantly different between subgroups defined by the algorithm (interaction, p=0.037, Table 2B). Notably, the algorithm was not significantly associated with RFS in patients not treated with tamoxifen (Figure 5C, HR=0.88, p=0.65), indicating that the algorithm is a marker for treatment outcome rather than prognosis.

Discussion

Here, we present a comprehensive algorithm, using IHC of two independent datasets. This algorithm identifies breast cancer patients who will become resistant to tamoxifen and who should be offered alternative treatment options. Besides assessment of the modification of the drug target (ERα), the algorithm incorporated information on kinase activities potentially modified the drug target. The algorithm has several advantages over the use of a single marker: Firstly, a combination of markers may capture several resistance mechanisms, which is relevant for a heterogeneous disease such as breast cancer. Secondly, involvement of a particular signalling pathway is more reliably assessed

by multiple measurements within that pathway, in particular in archived material using semi-quantitative assays. Our data validate this concept.

Although tamoxifen has reduced breast cancer mortality by 30%, one third of the patients still develop a relapse despite adjuvant tamoxifen treatment [27]. It has been cumbersome to identify the endocrine agent most effective for an individual patient at high risk for recurrent disease. At present, the only validated predictive biomarker for tamoxifen response used in the clinic ERα expression, but this test has suboptimal positive predictive value. Data on the predictive value of PR are conflicting [22,28,29].

We confirmed findings of Holm *et al*. that PAK1 is correlated with tamoxifen resistance [17]. Holm *et al*. assumed that PAK1 identified ERαS305-P positive breast tumours, based on indirect evidence from *in vitro* studies [13,14]. Our study indicated no direct link between PAK1 and ERαS305-P. Outcome of the PAK-positive group was not significantly affected by adding ERαS305-P to the identification of tumours with poor outcome (see Figure 2E). In addition, our expression analysis showed no clear link between ERαS305P and PAK1-related pathways. Finally, *in vitro* PAK1 overexpression did not induce ERαS305P. This is the first report assessing the interaction between PAK1 and ERαS305P in patients using a novel monoclonal antibody against ERαS305-P. Our data suggest that PAK1 is not directly involved in phosphorylation of ERαS305 but PAK1 is still an important additional marker in the identification of tamoxifen non -responders.

Our gene expression analysis revealed that pathways including PKA activity are overrepresented in tumours with a phosphorylated ERα at serine 305. This mechanism of PKA activation was first described by Miller *et al*., who showed a correlation between tamoxifen response and mRNA downregulation of a negative regulator of PKA (PKA-RIα) [30]. This supported our previous work in which we correlated mRNA levels of PKA-RIα to outcome after adjuvant tamoxifen treatment and, more importantly, showed that PKA activity induced a modification of ERα which in turn caused tamoxifen resistance [11]. Although phosphorylation of ERαS305 by PKA is clearly associated with tamoxifen resistance, pPKA expression alone appeared not to be sufficient to predict tamoxifen response (Figure 2B). The majority of breast tumours expressed pPKA, while approximately 20% of the tumours showed ERαS305-P. This suggests that additional factors like phosphatases may play additional roles in causing detectable ERαS305-P. The weak association between the markers may also be due to the application of antibodies detecting phospho-proteins in archived samples, which may, in some cases, be complicated by fixation procedures potentially affecting the stability of phospho-proteins. However, the algorithm was validated in an independent dataset from another hospital with stainings performed in a different laboratory. Even though the designs and patient selections were different in the training and validation series, the performance of the algorithm was significant in both locations. Further research is needed to determine the diagnostic accuracy of the algorithm, e.g. sensitivity, specificity etc. Since patients in the validation series received only two years of tamoxifen, further validation of the algorithm has to be done for the currently prescribed five years of adjuvant endocrine treatment.

How should our predictive algorithm be implemented in clinical practice for selecting correct endocrine treatment (marker-based strategy, calculations provided in Figure S3)? If the observed effect is representative for a general breast cancer population and using empirical rates from our validation set, tailoring adjuvant tamoxifen treatment to the 73% of the patients classified by the algorithm as tamoxifen sensitive and not treating the remaining 27% would result in an estimated 10-year RFS similar to the 10-year RFS if all patients are treated with adjuvant tamoxifen irrespective of the predictive algorithm. Therefore, treatment guided by the algorithm may save unnecessary treatment for approximately one third of the ER-positive breast cancer patients, while approximately maintaining a similar 10-year RFS. If such patients receive correct anti-estrogens or aromatase inhibitors that would still inhibit the activities of ERαS305P [11,12], their clinical prospects should be improved over the current situation. The best alternative treatment for the patients predicted as resistant by the algorithm needs further study but will most likely result in a better 10-year RFS compared to the untreated situation.

In this study, we confirmed the correlation between PAK1 and tamoxifen resistance and provide evidence for cooperation between pPKA and ERαS305-P that is relevant for tamoxifen response in patients. The proportion of tumours that have both PAK1 as well as pPKA-associated ERαS305-P is limited (9% in training, 0.4% in validation, Figure 1B and 1D) suggesting that the three markers reflect two different mechanisms. Previously we had shown that the effects of tamoxifen on RFS in subgroups defined by PAK1 alone are different [17]. This study provides evidence that pPKA/ERαS305-P is a marker for tamoxifen resistance not related to PAK1. Using both markers resulted in the identification of an increased proportion of patients (27% based on the algorithm versus 15% based on PAK1 alone) who have a high chance to be resistant to tamoxifen (Figure S3).

Only few candidate biomarkers predicting drug response progress from laboratory to the clinic. Patient stratification into responders and non-responders on the basis of one single biomarker will be rare. The strength of the predictive algorithm presented here

is not only that it contains three markers and consequently captures PKA/PAK1-pathway activities at different levels in the signalling cascade, but that the implication of all three markers in tamoxifen resistance is supported by extensive functional experiments [11-15,17].

This algorithm will provide an important step towards personalised anti-estrogen therapy as tamoxifen-resistant patients have alternative treatment options such as fulvestrant or aromatase inhibitors and thus may improve the outcome of breast cancer.

Acknowledgements

The authors would like to thank Renate de Groot for the construction of the tissue microarrays, Desiree Verwoerd for technical assistance in the western blots, Agendia BV. for performing the microarray experiments and Marieke Vollebergh, Stella Mook, Els Berns and Stefan Sleijfer for critical reading of the manuscript. We are indebted to Donne Majoor and Jacinta Aantjes for their help and advice regarding the immunohistochemistry and Guus Hart for statistical advice. We thank dr Jonathan Chernoff for the PAK1 expression constructs, and dr M Zaccolo for the generous gift of the PKA expression constructs. The authors would like to commemorate Hans Peterse, an excellent surgical pathologist and a highly esteemed colleague, who passed away unexpectedly during the course of this project. The anti ERαS305-P monoclonal antibody (Millipore #124-9-4) has been developed in close collaboration with Upstate USA Inc, presently part of Chemicon Int, Millipore.

Contributors

MK, WZ, CH, MH, LJvtV, LFAW, JN, OS, SCL, GL and RM designed the study and interpretated the data. MK, WZ, CH and RF performed the experiments. GL evaluated the pathology and immunohistochemistry. MK, CH, LFAW, MH performed or supervised the statistical and bioinformatical analyses. MK, WZ, MH, LFAW, JN, SCL and RM wrote the paper. All authors read, revised and approved the paper. MK and RM had full access to all data in the study and RM had final responsibility for the decision to submit for publication.

Conflicts of interest

LJ Van ‘t Veer is an employee of, and holds shares in, Agendia BV. All other authors declared no conflict of interest.

References

1. Pritchard KI. Endocrine therapy of advanced disease: analysis and implications of the existing data. Clin Cancer Res 2003; 9: 460S-7S.

2. O’Regan RM, Jordan VC. The evolution of tamoxifen therapy in breast cancer: selective oestrogen-receptor modulators and down-regulators. Lancet Oncol 2002; 3: 207-14.

3. Johnston SR, Dowsett M. Aromatase inhibitors for breast cancer: lessons from the laboratory. Nat Rev Cancer 2003; 3: 821-31.

4. Wakeling AE, Dukes M, Bowler J. A potent specific pure antiestrogen with clinical potential. Cancer Res 1991; 51: 3867-73.

5. Osborne CK, Pippen J, Jones SE, Parker LM, Ellis M, Come S, *et al*. Double-blind, randomized trial comparing the efficacy and tolerability of fulvestrant versus anastrozole in postmenopausal women with advanced breast cancer progressing on prior endocrine therapy: results of a North American trial. J Clin Oncol 2002; 20: 3386-95.

6. Howell A, Robertson JF, Quaresma Albano J, Aschermannova A, Mauriac L, Kleeberg UR, *et al*. Fulvestrant, formerly ICI 182,780, is as effective as anastrozole in postmenopausal women with advanced breast cancer progressing after prior endocrine treatment. J Clin Oncol 2002; 20: 3396-403.

7. Miller WR, Bartlett JM, Canney P, Verrill M. Hormonal therapy for postmenopausal breast cancer: the science of sequencing. Breast Cancer Res Treat 2007; 103: 149-60.

8. Rabaglio M, Aebi S, Castiglione-Gertsch M. Controversies of adjuvant endocrine treatment for breast cancer and recommendations of the 2007 St Gallen conference. Lancet Oncol 2007; 8: 940-9.

9. Jordan VC, O’Malley BW. Selective estrogen-receptor modulators and antihormonal resistance in breast cancer. J Clin Oncol 2007; 25: 5815-24.

10. Ali S, Coombes RC. Endocrine-responsive breast cancer and strategies for combating resistance. Nat Rev Cancer 2002; 2:101-12.

11. Michalides R, Griekspoor A, Balkenende A, Verwoerd D, Janssen L, Jalink K, *et al*. Tamoxifen resistance by a conformational arrest of the estrogen receptor alpha after PKA activation in breast cancer. Cancer Cell 2004; 5: 597-605.

12. Zwart W, Griekspoor A, Berno V, Lakeman K, Jalink K, Mancini M, *et al*. PKA-induced resistance to tamoxifen is associated with an altered orientation of ERalpha towards co-activator SRC-1. EMBO J 2007; 26: 3534-44.

13. Wang RA, Mazumdar A, Vadlamudi RK, Kumar R. P21-activated kinase-1 phosphorylates and transactivates estrogen receptor-alpha and promotes hyperplasia in mammary epithelium. EMBO J 2002; 21: 5437-47.

14. Rayala SK, Talukder AH, Balasenthil S, Tharakan R, Barnes CJ, Wang RA, *et al*. P21-activated kinase 1 regulation of estrogen receptor-alpha activation involves serine 305 activation linked with serine 118 phosphorylation. Cancer Res 2006; 66: 1694-701.

15. Balasenthil S, Barnes CJ, Rayala SK, Kumar R. Estrogen receptor activation at serine 305 is sufficient to upregulate cyclin D1 in breast cancer cells. FEBS Lett 2004; 567: 243-7.

16. Bostner J, Ahnstrom Waltersson M, Fornander T, Skoog L, Nordenskjold B, Stal O. Amplification of CCND1 and PAK1 as predictors of recurrence and tamoxifen resistance in postmenopausal breast cancer. Oncogene 2007; 26: 6997-7005.

17. Holm C, Rayala S, Jirstrom K, Stal O, Kumar R, Landberg G.

Association between Pak1 expression and subcellular localization and tamoxifen resistance in breast cancer patients. J Natl Cancer Inst 2006; 98: 671-80.

18. Holm C, Kok M, Michalides R, Fles R, Koornstra R, Wesseling J, *et al*. Phosphorylation of the oestrogen receptor alpha at serine 305 and prediction of tamoxifen resistance in breast cancer. J Pathol 2009; 217; 372-9.

19. McShane LM, Altman DG, Sauerbrei W, Taube SE, Gion M, Clark GM. Reporting recommendations for tumor marker prognostic studies (REMARK). J Natl Cancer Inst 2005; 97: 1180-4.

20. Kok M, Linn SC, Van Laar RK, Jansen MP, van den Berg TM, Delahaye LJ, *et al*. Comparison of gene expression profiles predicting progression in breast cancer patients treated with tamoxifen. Breast Cancer Res Treat 2009; 113: 275-283.

21. Ryden L, Jirstrom K, Bendahl PO, Ferno M, Nordenskjold B, Stal O, *et al*. Tumor-specific expression of vascular endothelial growth factor receptor 2 but not vascular endothelial growth factor or human epidermal growth factor receptor 2 is associated with impaired response to adjuvant tamoxifen in premenopausal breast cancer. J Clin Oncol 2005; 23: 4695-704.

22. Ryden L, Jonsson PE, Chebil G, Dufmats M, Ferno M, Jirstrom K, *et al*. Two years of adjuvant tamoxifen in premenopausal patients with breast cancer: a randomised, controlled trial with long-term follow-up. Eur J Cancer 2005; 41: 256-64.

23 Liu CL, Montgomery KD, Natkunam Y, West RB, Nielsen TO, Cheang MC, *et al*. TMA-Combiner, a simple software tool to permit analysis of replicate cores on tissue microarrays. Mod Pathol 2005; 18: 1641-8.

24. Beeser A, Jaffer ZM, Hofmann C, Chernoff J. Role of group A p21-activated kinases in activation of extracellular-regulated kinase by growth factors. J Biol Chem 2005; 280: 36609-15.

25. Zaccolo M, De Giorgi F, Cho CY, Feng L, Knapp T, Negulescu PA, *et al*. A genetically encoded, fluorescent indicator for cyclic AMP in living cells. Nat Cell Biol 2000; 2: 25-9.

26. Moore MJ, Kanter JR, Jones KC, Taylor SS. Phosphorylation of the catalytic subunit of protein kinase A. Autophosphorylation versus phosphorylation by phosphoinositide-dependent kinase-1. J Biol Chem 2002; 277: 47878-84.

27. Early Breast Cancer Trialists' Collaborative Group. Effects of chemotherapy and hormonal therapy for early breast cancer on recurrence and 15-year survival: an overview of the randomised trials. Lancet 2005; 365: 1687-717.

28. Bezwoda WR, Esser JD, Dansey R, Kessel I, Lange M. The value of estrogen and progesterone receptor determinations in advanced breast cancer. Estrogen receptor level but not progesterone receptor level correlates with response to tamoxifen. Cancer 1991; 68: 867-72.

29. Viale G, Regan MM, Maiorano E, Mastropasqua MG, Dell'Orto P, Rasmussen BB, *et al*. Prognostic and predictive value of centrally reviewed expression of estrogen and progesterone receptors in a randomized trial comparing letrozole and tamoxifen adjuvant therapy for postmenopausal early breast cancer: BIG 1-98. J Clin Oncol 2007; 25: 3846-52.

30. Miller WR, Hulme MJ, Bartlett JM, MacCallum J, Dixon JM. Changes in messenger RNA expression of protein kinase A regulatory subunit ialpha in breast cancer patients treated with tamoxifen. Clin Cancer Res 1997; 3: 2399-404.

Supplemental data

Figure 1. Staining for the catalytic subunit of PKA phosphorylated at threonine 197.

A) Representative example of positive pPKA staining**. B**) Absence of pPKA expression after dephosphorylation via incubation with lambda phosphatase on the tumour slide prior to immunohistochemistry.

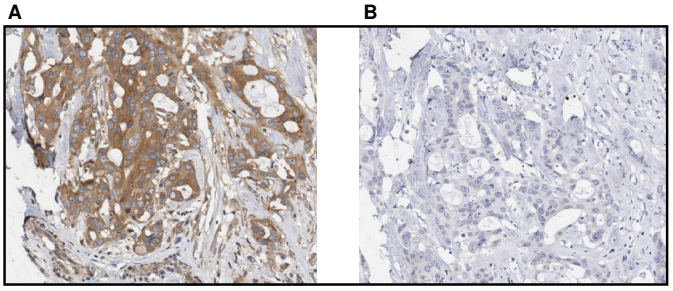


Figure 2. Flow diagram of patients

Flow of patients through the study including number of patients in each stage. Reasons for dropout and number of events (recurrence) in each subgroup are listed.

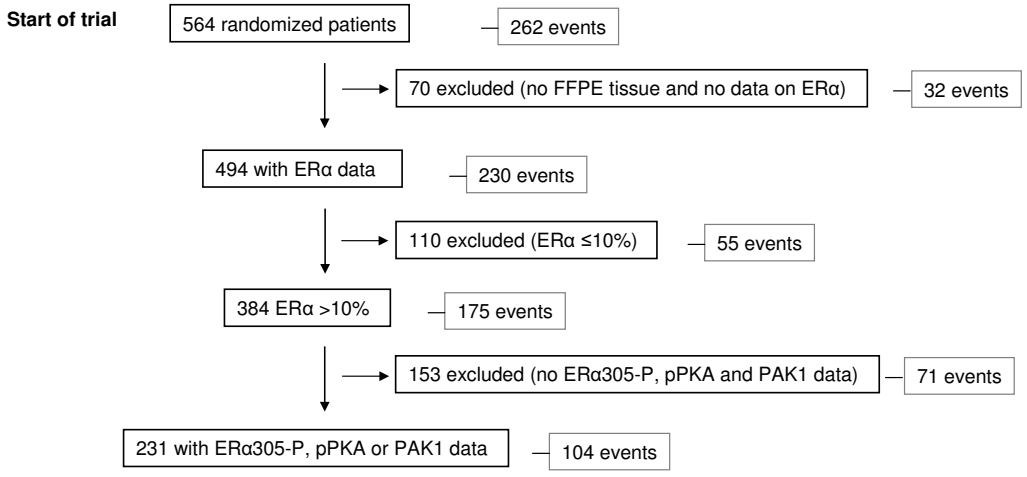


Figure 3. Potential clinical implication of application of predictive algorithm

Proportions of patients and 10-years Recurrence-Free Survival (RFS) rates are derived from Figure 5 as shown in the manuscript.

A. No marker used: all patients receive tamoxifen

- All patients receive tamoxifen.
- 67.1% is 10-yrs RFS in subgroup with no PAK1 and no PKA-associated ERα305-P that receive tamoxifen
- 54.8% is 10-yrs RFS in subgroup with PAK1 or PKA-associated ERα305-P that receive tamoxifen

10-yrs RFS = (((78+91)*67.1%)+ ((31+31)*54.8*))/231)=64%

B. Predictive algorithm used: 73% of patients will receive tamoxifen

- Only patients with no PAK1 and no PKA-associated ERα305-P receive tamoxifen
- 67.1% is 10-yrs RFS in subgroup with no PAK1 and no PKA-associated ERα305-P that receive tamoxifen
- 54.8% is 10-yrs RFS in subgroup with PAK1 or PKA-associated ERα305-P will not receive tamoxifen

10-yrs RFS = (((78+91)*67.1%)+ ((31+31)*54.8*))/231)=64%

C. PAK1 used: 85% of patients will receive tamoxifen (calculations based on data presented in ref. 16)

- Only patients with no PAK1 (85%) receive tamoxifen
- 69% is 10-yrs RFS in subgroup with no PAK1 that receive tamoxifen
- 44% is 10-yrs RFS in subgroup with PAK1 that will not receive tamoxifen

10-yrs RFS = (0.85*0.69 + 0.15*0.44)=65%

Table 1. Details immunohistochemistry

NKI-AVL (training series)

Protein	Supplier	Catalogusnr	Dilution	Pretreatment	Scoring	Reference
ERα	Labvision/Neomarkers	MS-750-S	50x	citrate	nuclear, percentage of cells	Hannemann et al.
PR	Immunologic	ACD 14	400x	citrate	nuclear, percentage of cells	Kok et al.
HER2	Thermo Scientific	RM-9103-S	25x	citrate	membranous, 0/1/2/3	Van de Vijver et al.
PAK1	Cell Signaling	2602.00	25x	citrate	intensity 0-5, nuclear 0/1	Holm et al.
Phospho-ERα-S305	Millipore	x	20x	citrate	nuclear, percentage of cells	Holm et al.
Phospho-PKA	Cell Signaling	4781	40x	citrate	intensity 0-5, nuclear 0/1	x

Lund (validation series)

Protein	Supplier	Catalogusnr	Dilution	Pretreatment	Scoring	Reference
ERα	Ventana Medical Systems	clone 6F11	prediluted	citrate	nuclear, percentage of cells	Ryden et al.
Ki-67	Dako	M7240	200x	citrate	nuclear, percentage of cells	Jirstrom et al.
PAK1	Cell Signaling	2602.00	25x	citrate	intensity 0-5, nuclear 0/1	Holm et al.
Phospho-ERα-S305	Millipore	x	20x	citrate	nuclear, percentage of cells	Holm et al.
Phospho-PKA	Cell Signaling	4781	40x	citrate	intensity 0-5, nuclear 0/1	x

Table 2. Distribution of pPKA according to clinicopathological parameters (training series NKI)

		pPKA-negative		pPKA-positive		p
		n	(%)	n	(%)	
Total		37	(28)	95	(72)	
Median age at surgery		58		59		0.52 *
Grade	I/II	27	(73)	71	(75)	0.83
	III	10	(27)	24	(25)	
LN status	0	30	(81)	56	(60)	0.025
(2 unknown)	>0	7	(19)	37	(40)	
WHO subtype	IDC	28	(80)	83	(89)	0.24
(4 unknown or other subtype)	ILC	7	(20)	10	(11)	
Size	<=20 mm	20	(54)	57	(61)	0.56
(1 unknown)	> 20 mm	17	(46)	37	(39)	
ERα (IHC)	11-79%	14	(38)	23	(24)	0.13
	>= 80%	23	(62)	72	(76)	
PR (IHC)	<= 10%	18	(49)	30	(32)	0.110
(1 unknown)	> 10%	19	(51)	64	(68)	
HER2 (IHC)	0,1,2	33	(89)	85	(90)	1.00
	3	4	(11)	10	(11)	

PKA scoring is based on expression in the cytoplasm

Percentages might not add up to 100% because of rounding

P-value are based on Fisher's Exact tests (* Mann-Whitney U test)

Abbreviations:

pPKA= phosphorylation of protein kinase A at threonine 197

Grade= histological grading based on Nottingham Grading system

LN= lymph node

IDC= invasive ductal carcinoma

ILC= invasive lobular carcinoma

ERα= oestrogen receptor α

PR=progesterone receptor

HER2= human epidermal growth factor 2

IHC= immunohistochemistry

Table 3. Pathways which have genes differentially expressed in ERαS305-P positive tumours

Rank	Biocarta pathway	PKA subunit in pathway	LS permuted p-value *
1	Rho-selective guanine exchange factor AKAP13 mediates stress fiber formation	PRKAR2A, PRKAR2B, PRKACA	0.006
2	AKAP95 role in mitosis and chromosome dynamics	PRKAR2A, PRKAR2B, PRKACA	0.007
3	Transcription regulation by methyltransferase of CARM1	PRKAR1B	0.008
4	Inhibition of Matrix Metalloproteinases		0.012
5	Y branching of actin filaments		0.012
6	Role of MAL in Rho-mediated activation of SRF		0.014
7	IFN alpha signaling pathway		0.022
8	mCalpain and friends in Cell motility	PRKAR1B	0.023
9	BCR signaling pathway		0.023
10	Steps in the glycosylation of mammalian N-linked oligosaccarides		0.025
11	Actions of Nitric Oxide in the Heart	PRKAR1B	0.031
12	EGF signaling		0.035
13	Generation of amyloid b-peptide by PS1		0.036
14	HIV Induced T cell apoptosis		0.038
15	Hypoxia and p53 in the cardiovascular system		0.042
16	Phosphorylation of MEK1 by cdk5/p35 downregulates the MAP kinase pathway		0.042
17	CDK regulation of DNA replication		0.044
18	Nuclear receptors coordinate the activities of chromatin remodeling complexes and coactivators to facilitate initiation of transcription in carcinoma cells		0.046
19	Bone remodelling		0.046

ERαS305-P positive tumours (n=11) were compared with ERαS305-P negative tumours (n=47) using gene expression profiling.
42,034 genes were used for the analysis. 302 pathways as defined by Biocarta were tested using the Gene Set Comparison Tool in BRB array tools. The pathways that had a permuted p-value <0.05 are included in the table. In the 302 pathways tested, 27 are known to be related to PKA (Cancer Genome Anatomy Project). The expression of 5 out of the 27 pathways turned out to be significantly associated with ERαS305-P status.
Enrichment, within the significant pathways, for PKA-related pathways was tested using Fisher's Exact test: odds ratio= 4.24, p=0.019

* Based on 100,000 permutations. The Fishers's LS (least squares) summary statistic uses the average log P values for the genes in that class.

Table 4 . Randomized controlled trial (Lund) used as validation series. Distribution of clinico-pathological parameters in the excluded cases (ERα>10%, no data to generate algorithm, n=153) vs included patients in the validation series (n=231).

		Insufficient data for Algorithm		Data for Algorithm available		
Variable	Category	n	%	n	%	P-value
Total		153		231		
Age at surgery	Median in years (range)	45	(27-57)	45	(26-57)	0.25¶
Grade*	I/II III Unknown	101 39 13	72% 28%	151 77 3	66% 34%	0.25
Lymph node status	Negative Positive	39 114	25% 75%	55 176	24% 76%	0.72
WHO subtype	Invasive Ductal Carcinoma Invasive Lobular Carcinoma Unknown or other type	104 14 35	88% 12%	196 23 12	89% 11%	0.72
Size	≤ 20 mm > 20 mm Unknown	64 88 1	42% 58%	97 134	42% 58%	1.00
Progesterone receptor (IHC)	≤ 10% > 10% Unknown	11 94 48	10% 90%	22 196 13	10% 90%	1.00
Ki67 (IHC)	≤ 25% > 25% Unknown	86 14 53	86% 14%	165 38 28	81% 19%	0.34

* According Nottingham Grading system (Elston et al.).

Summary and Discussion anti-estrogen resistance

summary



Summary and discussion: anti-estrogen resistance

Breast cancer is the most frequently occurring cancer in women, with over a million of newly diagnosed cases worldwide each year. 70% of all breast tumors are positive for estrogen receptor alpha (ERα) signal and presumably grow dependent on the activity of this hormonal receptor. The ERα was thereby recongized is a potential drug target and most therapeutic strategies are currently focused on inhibiting the activity of this transcription factor. In 1966, tamoxifen was developed and eventually found its way to the clinic. Tamoxifen can compete with estradiol, the natural ligand of the estrogen receptor, and thus inhibits the function of the receptor. This drug proved to be a highly successful one, saving the lives millions of breast cancer patients worldwide by reducing the recurrence rate by 50%. However, in the patients who did develop a recurrence despite tamoxifen treatment, resistance to this drug occurs by mechanisms largely unknown. One mechanism of tamoxifen resistance turned out to be induced by activation for Protein Kinase A (PKA). PKA can phosphorylate the estrogen receptor at serine 305, a residue close to the small flexible hinge region in ERα. This phosphorylation is causal for the receptor to recognize the inhibitor tamoxifen as an activator of transcription (reviewed in Chapters 1 and 2).

Physicians determine their prescriptions of anti-estrogenic compounds, such as tamoxifen, on the basis of an empirical order and not dependent on individual tumor characteristics. Determining classification criteria, by which the effectiveness of anti-estrogenic compounds can be predicted, may result in tailoring endocrine therapy for each patient, enabling selection of the most optimal first line treatment. Thereby, we set forth in defining the criteria a cell has to meet in order to become resistant to compounds which would otherwise inhibit estrogen receptor function.

As a first study dicussed in this thesis, we describe the molecular mechanism by which phosphorylation of ERα on serine 305 induces resistance to tamoxifen (Chapter 3). In the transcription complex, estrogen receptor interacts with p160 family members including steroid receptor coactivator 1 (SRC-1). ERα can interact with SRC-1 through its two transactivation regions, AF-1 and AF-2. This interaction of ERα with SRC-1 is an initial and essential step in the formation of an active transcription complex. While the AF-1 function of ERα is ligand independent, the AF-2 activity is induced by agonist binding. We fused ERα to a CFP and SRC-1 to an YFP, and monitored Fluorescence Resonance Energy Transfer (FRET) between these two tagged molecules. FRET is the radiationless energy transfer from a donor fluorophore to a suitable acceptor fluorophore, and is highly dependent on the distance between the fluorophores applied. This way, conformational changes within the ERα/SRC-1 complex could be monitored. Interestingly, after tamoxifen treatment, SRC-1 was still capable to interact with ERα through its AF-1 region, while the AF-2 interaction was lost. When serine 305 is phosphorylated in a tamoxifen-bound ERα, the AF-2 region of ERα alters its orientation towards SRC-1. In this altered orientation, RNA polymerase II is recruited and transcription is activated thus leading to tamoxifen resistance. The results from this study indicated the importance of using full length proteins when studying nuclear receptor functions. While most research on nuclear receptors is performed using truncation mutants only empassing the AF-2, the explanation for tamoxifen-resistance as described here shows that a role of the AF-1 may not be ignored. As illustrated, a functional AF-1 is a prerequisite for the altered orientation of AF-2 towards SRC-1 under resistant conditions. One additional message of this chapter is that protein-protein binding is not always informative for a biological readout. Both in the absence and presence of tamoxifen, also under tamoxifen resistant conditions, no influence was observed on ERα/SRC-1 physical interactions. Information on the inhibition of the receptor or concerning the induction of resistance could only be meassured by determining conformational changes between these two proteins.

In 1996, a second estrogen receptor was discovered, named estrogen receptor beta (ERβ). The expression of ERα and ERβ is different in various human tissues, ranging from exclusive expression of ERβ in colon and brain to variations in the ratios of ERα and ERβ expression in other tissues, including breast. In breast cancer, the exact role of ERβ is still under discussion, but high expression levels are correlated with good prognosis, thought to function by inhibiting ERα in a hetero-dimeric complex. While ERα can interact with its ligand independent AF-1 transactivation region with SRC-1, ERβ fails to do so (Chapter 4). This incapacity to interact with SRC-1 in a ligand independent manner appeared to be causal for the lower transactivation capacity of ERβ when compared to ERα. Also the agonistic response to tamoxifen, an essential step in tamoxifen resistance, did not occur in ERβ, which

could be ascribed to specific capacities of its AF-2. In addition, the AF-1 cooperates with the specific hinge in ERα to facilitate a maximal AF-2 activity. An obvious question that arose from this research is why a functional AF-1 is already sufficient to enhance the transcriptional response to agonist. One possibility, is that this preformed ERα/SRC-1 complex rules out the factor of stochastics. While ERα is already bound to part of the transcription complex in the absence of hormone, all components still have to be recruited after hormone binding in the case of ERβ. This delay in the formation of the transcription complex may render the agonistic response significantly less profound. This may also be the molecular basis for the inhibitory effect of ERβ in an ERα/ERβ hetero-dimer complex.

New anti-estrogens are constantly developed and find their way into the clinic, each with compound-specific behavior and characteristics. After we determined the mechanism of tamoxifen resistance induced by PKA, the question of what alternative anti-estrogenic compounds could be applied arose. Seven anti-estrogens were tested, all currently in phase III clinical trials or recently introduced into the clinic (Chapter 5). We tested the effects of PKA and MAP kinase activation on anti-estrogen function. Both kinases are reported to influence tamoxifen action. While PKA activation leads to phosphorylation of ERα on serine residues 236 and 305, MAP kinase activation leads to phosphorylation of ERα on serine residue 118. The sensitivity of these seven anti-estrogens for kinase activation was tested by a FRET assay, where an YFP was tagged to the ERα N terminus and a CFP to the C terminus. By tagging the same ERα molecule with these two fluorochromes, a change in ER-conformation could be measured by differences in FRET signal. A change in FRET was indicative for an inactivated ERα, allowing us to monitor the effect of kinase activity on anti-estrogen functioning in living cells. This way, a profile was constructed, defining for each anti-estrogen the specific phospho-modifications leading to resistance of the receptor.

Not only kinase action, but also expression levels of co-activators have been reported to be involved in resistance to anti-estrogenic compounds. To test the sensitivity of novel anti-estrogens for these variables, five anti-estrogens were selected, as representatives of the subgroups for MAPK and PKA sensitivity (Chapter 6). The coactivators we selected in this study were SRC-1 and cyclin D1. Previous reports have described a resistance to tamoxifen to be correlated with high SRC-1 expression levels. In addition, cyclin D1 is amplified in 15% of the breast tumors and overexpressed in 40%. These coactivators were separately tested as well as in combination with each other and in a possible synergy with PKA activity. Again, a FRET-based profile of combinations could be constructed for resistance to each anti-estrogen to occur. Notably, we found that for arzoxifene and GW-5638, both drugs currently in phase III clinical trials, resistance is induced by cyclin D1 overexpression. While this did result in reporter gene activation and growth of the ERα-dependent MCF-7 breast cancer cell line when treated with arzoxifene, this did not occur after GW-5638 treatment. The latter compound proved to induce estrogen receptor degradation, even in a resistant conformation, illustrating that estrogen receptor degradation is a dominant factor over initial resistance. A comparative study by others between tamoxifen and arzoxifene action in breast cancer patients illustrated that tamoxifen-treated patients had a better prognosis then those treated with arzoxifene. However, since 40% of the breast cancer patients do overexpress cyclin D1, this could be a causal factor in the non-favorable response to arzoxifene.

Other studies have reported a correlation between PAK-1 expression levels and tamoxifen resistance in patients. In addition, indirect data were acquired, indicating that PAK-1 phosphorylates ERα at serine 305, which would be a causal factor in this resistance. We tested this hypothesis, where PAK-1 expression levels were visualized in combination with PKA activity and ERα-S305 phosphorylation in patients (Chapter 7). Although PAK-1 levels did correlate with tamoxifen resistance, there was no correlation of PAK-1 intensity with ERα-S305 specific signal. pPKA positivity did however correlate with ER-S305 signals, implying a functional relationship between these two proteins. More importantly, the combination of these three antibodies, detecting tamoxifen resistance via two distinct pathways, enabled us to detect one third of all patients likely to fail to respond to tamoxifen treatment. If patient samples were to be stained with the combination of these antibodies prior to endocrine therapy, the patients who are positive for these markers may be selected in receiving an alternative endocrine treatment instead.

The results presented here clarify the molecular mechanism of PKA-induced tamoxifen resistance and define the functional differences between the two ER isoforms. Furthermore, profiles were generated for anti-estrogen resistance induced by ERα-phosphorylation and cofactor expression levels. Lastly, an algorithm was presented by which we can predict tamoxifen-resistance in one third of all breast cancer patients. Still, a number of questions remain open. Whether the resistance profiles we constructed for the tested anti-estrogens also holds true in the clinical setting still is an essential point needed to be addressed. Although the FRET profiles were verified in transactivation-assays and cell growth assays, tissue culture based experiments never encapsulate the complexity of the human body. In addition, metabolites of the applied anti-estrogen may have unpredictable ef-

fects on ER function and stability. Since it is hard to gain access to material from patients treated with these novel anti-estrogens and the follow-up of these patients is largely still incomplete, translation of our profiles directly into the clinic is still not applicable.

The induction of transcription by ERα, phosphorylated at serine 305 and bound to tamoxifen, may result in the activation of a specific gene subset, distinct from the estradiol or tamoxifen responsive genes. These genes could be not only the causal factors for the found cell proliferation and non-favorable prognosis, but could also serve as additional markers that may be applicable in the clinic. Therefore, defining these genes may aid in a further refinement of personalized breast cancer therapy next to the markers descibed here.

Next to SRC-1, also SRC-2 and SRC-3 expression levels may play a role in anti-estrogen resistance. For the beneficial response to tamoxifen, a negative correlation has already been discribed with SRC-3 levels. The underlying mechanism is reported to be mediated by a specific enhanced activity of the HER2/neu gene. But the effect of SRC-3 on other anti-estrogen functions and any effect of SRC-2 levels on anti-hormone efficacy are still unknown. These questions are still unresolved and the focus of current research, both in tissue culture and patient material.

Defining markers that can predict response for the remaining group of tamoxifen-resistant breast cancer patients, who can not be identified by the presented algorithm, will be the biggest challenge for the near future, of which the first steps are being made.

Part two

Shedding light on antigen presentation through biophysical techniques



Presenting antigen presentation in living cells using biophysical techniques

Current Opinion in Microbiology 2005, vol. 8: 338-343

introduction

9

Presenting antigen presentation in living cells using biophysical techniques

Wilbert Zwart*, Alexander Griekspoor* and Jacques Neefjes

Abstract
The combination of genetically encoded fluorescent probes and advanced microscopic techniques has dramatically propelled the understanding of cell biology. Highly complex reactions can now be studied in detail in a relatively cost-effective and easy manner and, perhaps most importantly, in the context of a single living cell. In the past decade, numerous reports have uncovered the localization of key molecules in virtually all cellular processes. However, there remains a need for more accurate determination of genuine protein–protein interactions and quantification of highly dynamic processes, which has resulted in the revival of several biophysical techniques. Recent applications of these techniques have deepened understanding of processes involved in antigen presentation to the immune system.

Introduction

Antigen presentation forms the basis on which the adaptive immune response is built. In humans, three different protein families facilitate the cell-surface presentation of antigens to cells of the immune system. Each family utilizes a separate antigen presentation pathway that contains distinct steps of antigen processing and loading. Whereas the CD1 molecule presents lipids of both endogenous and exogenous origin, the major histocompatibility complex (MHC) class I and MHC class II molecules present peptides. The MHC class II pathway is only operational in professional antigen presenting cells (APCs). In this pathway, endocytosed material forms the source of the antigens that are presented. By contrast, the MHC class I pathway is functional in all nucleated cells, and continuously samples the intracellular peptide pool derived from degraded old and incorrectly synthesized new proteins. In this review, we will follow both peptide presenting pathways in a stepwise manner, and will discuss how biophysical techniques have visualized their functioning in a highly relevant situation — the living cell.

The MHC class I pathway

By sampling protein breakdown products in the form of peptides, theMHCclass I pathway facilitates the display of a representation of the intracellular protein content to the immune system. This allows detection of changes to the intracellular protein repertoire, including malignant alterations and foreign intracellular content such as the presence of viral proteins.Byway of a complicated cascade of events, degradation products from, for example, viral proteins are intracellularly processed and are presented at the cell surface by so-called MHC class I molecules (for details see Figure 1). Viruses have developed many strategies to inhibit the MHC class I pathway, and hence to prevent their own presentation to the immune system. Ironically, as this pathway is active in almost all cells, some viruses have even evolved to exploit these molecules as co-receptors for cell entry [1].

Viral entry

To demonstrate that the interaction between a cell surface protein, glucose regulated protein 78 (GRP78), and MHC class I molecules is essential for coxsackievirus internalization, Triantafilou *et al*. [1] made use of a physical phenomenon known as fluorescence resonance energy transfer (FRET). FRET is the radiationless transfer of energy from an excited donor fluorophore to a suitable acceptor fluorophore — a physical process that depends on spectral overlap and proper dipole alignment of the two fluorophores. The occurrence of FRET is characterized by a decrease in donor emission and by simultaneously sensitized (increased) acceptor emission. Importantly, FRET is extremely sensitive to the distance between the fluorophores (its efficiency decays proportional to the sixth power of distance). Also, the characteristic half-maximum distance (Förster radius) is in the same order of size as most cellular proteins. FRET will therefore only occur when two proteins are, on average, no more than one molecule in distance apart, which usually mean that they interact directly (Figure 2). However, if they are present at very high concentrations,

Division of Tumor Biology, The Netherlands Cancer Institute, Plesmanlaan 121, 1066 CX Amsterdam, The Netherlands

Corresponding author: Neefjes, Jacques (j.neefjes@nki.nl)

* equal contribution

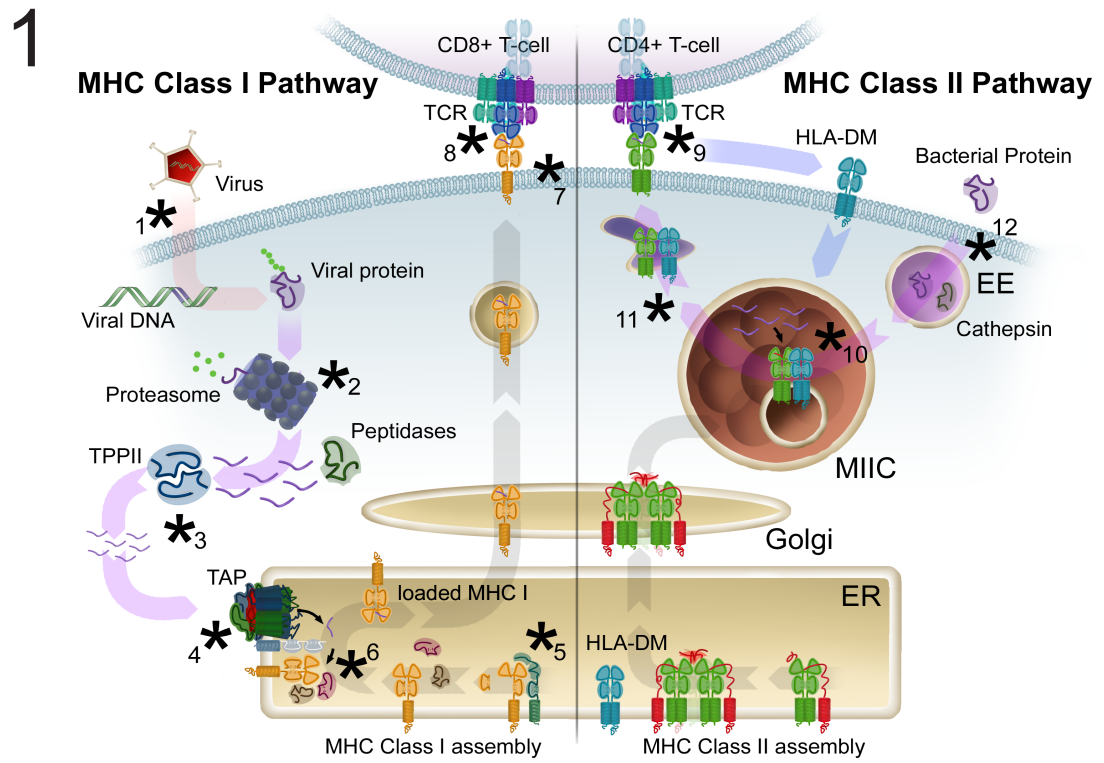


Figure 1. Schematic overview of the major histocompatibility complex (MHC) class I and II antigen presentation pathways.

MHC class I molecules are assembled in the endoplasmic reticulum (ER), with the help of the chaperones calnexin, calreticulin and ERp57, after which they dock onto the ER-resident peptide transporter associated with antigen processing (TAP). This docking is facilitated by the specialized chaperone tapasin. TAP pumps antigenic peptides into the ER lumen. These peptides are of cellular or viral origin, and are produced in the cytosol or in the nucleus by the proteasome, tripeptidyl peptidase II (TPPII), and other peptidases. Once in the ER, peptides can bind to MHC class I molecules, which are subsequently released from the TAP–tapasin loading complex. MHC class I–peptide complexes can then leave the ER for transport to the plasma membrane. Here they can be inspected by the T-cell receptor of CD8+ T cells. Examples of processes studied using biophysical techniques that are discussed in this review include: (1) viral entry, (2) proteasome compartmentalization, (3) TPPII and peptidase activity, (4) TAP activity, (5) MHC class I a sembly, (6) peptide loading, (7) plasma membrane behaviour and (8) interaction of the T-cell receptor with peptide-loaded MHC class I molecules. (b) MHC class II molecules are assembled as dimers in the ER. This assembly process is supported by the specialized chaperone invariant chain, which in addition occupies the peptide-binding groove. Three of these MHC class II–invariant chain complexes form a nonameric complex that is transported to the MHC class II containing compartment (MIIC). Here the invariant chain is degraded by cathepsins and other proteases until only the part that occupies the peptide-binding groove is left. This is called class II-associated invariant chain peptide (CLIP). In these compartments, MHC class II molecules also encounter antigenic peptide fragments derived from proteins that have been degraded in the endocytic route. CLIP is then exchanged for one of these fragments with help of the chaperone HLA-DM, and the peptide-loaded MHC class II molecules are transported to the plasma membrane for presentation of their cargo (peptides) to the immune system. Examples of processes studied using biophysical techniques that are discussed in this review include: (9) interaction of the T-cell receptor with peptide-loaded MHC class II molecules, (10) peptide loading, (11) cellular transport and (12) immune evasion.

FRET will occur by simple collision. FRET offers an important advantage over fluorescence colocalization studies that reveal whether two proteins are in close vicinity (>200 nm), but do not indicate if they really interact. To detect FRET, Triantafilou *et al.* [1] used a technique called acceptor photobleaching, in which bleaching of the acceptor molecules abrogates energy transfer from the donor molecules. This results in increased donor emission. After the Cy5-labeled GRP78 molecules were bleached, Triantafilou *et al.* detected an increase in fluorescence from the Cy3-labeled MHC class I molecules, which demonstrates a genuine interaction between these molecules. In a more recent study, Martin-Fernandez *et al.* [2] also used FRET techniques to characterize the entry and the disassembly of adenovirus particles in living cells.

Proteasomal degradation

Viral infection of cells is detected by the immune system as soon as the viral products contribute to the intracellular protein pool and subsequently join the household degradation pathway by way of the proteasome. This megadalton large proteolytic complex is present in both the cytosol and the nucleus. The

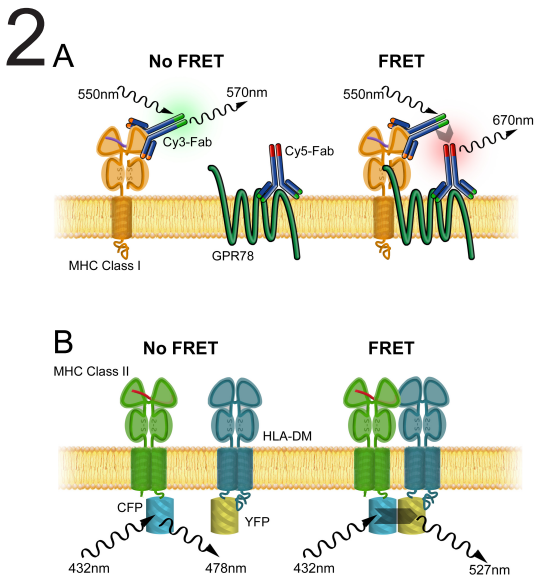


Figure 2. Fluorescence resonance energy transfer (FRET).

(**A**) A schematic that demonstrates the principle of FRET. Exciting Cy3 that is linked to a MHC class I bound Fab fragment (Cy3–Fab) at 550 nm results in emission at 570 nm, unless energy is transferred to a GRP78-bound Fab fragment that is labelled with Cy5 (Cy5–Fab). This phenomenon only occurs when MHC class I and GRP78 physically interact, and results in increased Cy5 emission (at 670 nm). (**B**) A similar protocol is followed for green fluorescent protein (GFP)-modified proteins. MHC class II molecules tagged with the blue variant of GFP (cyan fluorescent protein; CFP) can transfer energy to HLA-DM tagged with the yellow variant of GFP (yellow fluorescent protein; YFP), but only when they are within 5 nm distance (i.e. when MHC class II molecules and HLA-DM are directly interacting). As a result, the observed emission spectrum after excitation with light at 432 nm will shift from 478 nm (emission of CFP) to 527 nm (emission of YFP).

presence of proteasomes in the latter location is rather remarkable. Given the size of the complex, it is hard to imagine that it can be transported through nuclear pores. To test whether both compartments show exchange of particular proteins, two variants of a bleaching technique can be applied: fluorescence recovery after photobleaching (FRAP) and fluorescence loss in photobleaching (FLIP). By bleaching fluorescent molecules in a region of interest within a living cell and by measuring changes of fluorescence levels in the same (FRAP) or a distant (FLIP) area, one can determine the exchange rate between these two compartments (Figure 3). Reits *et al*. [3] used these techniques to demonstrate that the nucleus and cytoplasm harbor spatially separated pools of proteasomes that do not efficiently exchange.

Peptidases

The proteasome cleaves substrates into smaller peptides, which then become the targets of various cytosolic peptidases for further processing into single amino acids. A minor percentage of these peptides is rescued from degradation however, and sampled by the MHC class I pathway. To determine the average half-life of peptides *in vivo* and to calculate the fraction sampled by the MHC class I pathway, Reits *et al*. [4] microinjected chemically synthesized peptides that contain both a fluorescent group and a quencher moiety (so-called internally quenched peptides) into living cells. When intact, energy of the excited fluorophore is absorbed by the quencher group, analogous to the quenching of the donor observed in FRET, albeit without fluorescence emission by the acceptor molecule. Yet, cleavage by peptidases will spatially separate the quencher from the fluorophore, allowing fluorescence to be detected (Figure 4). Using this approach, the authors showed that the majority of peptides are lost for antigen presentation owing to the remarkable cellular capacity to recycle peptides back to single amino acids. 9-mer peptides have an *in vivo* halflife of around 5 s, with 1 amino acid removed every 1–2 s. More recently, the same approach was used to show that individual classes of peptidases exhibit subspecialization for defined lengths of substrates. Tripeptidyl peptidase II (TPPII), for example, cleaves proteasome substrates that are longer than 15 amino acids into peptides that are highly relevant for presentation by MHC class I molecules [5].

Transporter associated with antigen processing

Peptides sampled by the MHC class I pathway are captured by the transporter associated with antigen processing (TAP), a transmembrane ATP-binding cassettetransporter that pumps cytosolic peptides into the lumen of the endoplasmic reticulum (ER). The functioning of this transporter was elegantly studied using FRAP [6]. The Brownian motion of particles in solution was first described by Einstein [7], who indicated that diffusion was proportional to the inverse third of the mass (D M1/3). This was later modified for tran membrane proteins, in which diffusion is proportional to the viscosity of the lipid bi-layer and is related to the radius of the transmembrane segment (for details see [8]). When TAP transports a peptide, it probably changes the diameter of the transmembrane pore, which results in a reduced lateral mobility of the complex in the ER membrane. This can be measured using FRAP on green fluorescent protein (GFP)-tagged TAP. From their experiments, Reits *et al*. [8] were able to characterize TAP activity in living cells, which cor-

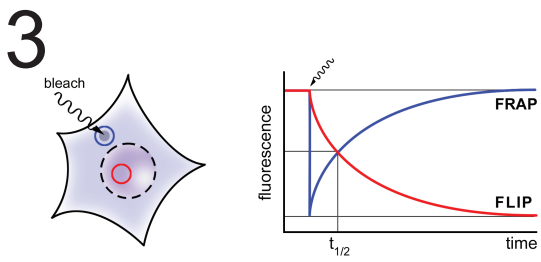


Figure 3. Fluorescence recovery after photobleaching (FRAP) and fluorescence loss in photobleaching (FLIP).

By bleaching fluorescent molecules in a region of interest in a living cell (marked by the arrow) and measuring changes of fluorescence levels in the same area (FRAP, blue circle) or in a distant area (FLIP, red circle), the exchange rate of fluorescent molecules between two compartments can be determined. (b) Shown is
a theoretical example of a FRAP (blue line) and FLIP (red line) experiment, in which the fluorescence is measured in the circles marked in (a). From these curves, the tl/2 (half-time of recovery) can be deduced — a measure of process dynamics. The timescale for FRAP and FLIP do not necessarily have to be the same, and are dependent on the experimental setup.

relates with the size of the intracellular peptide pool. They concluded that the major sources of peptides under steady state conditions are newly synthesized rather than old proteins.Thus, besides determination of proteincompartmentalization, FRAP is a valuable tool to study process dynamics and is used in this study as a biochemical tool to visualize enzyme activity in living cells.

Antigen loading

In addition to pumping peptides, TAP acts as a scaffold during antigen loading onto class I molecules, a process in which the ER chaperone tapasin also plays an essential role. Tapasin forms a bridge between TAP and newly synthesized MHC class I molecules that are waiting for peptides to dock. Again, using FRAP, Marguet *et al*. [9] showed that empty MHC class I molecules adapted the relatively slow lateral mobility of the TAP transporter, whereas binding of peptides resulted in release from this loading complex. This was measured as an increase in mobility. Both tapasin and unassembled MHC class I molecules are retained in the ER and are excluded from ER exit sites, yet each in a different manner. All tapasin molecules are located in dynamic clusters, whereas unassembled MHC class I molecules are excluded from clusters, as determined by FRET measurements [10,11]. Using FRET and polarized fluorescence measurements, the same group showed that peptide-loaded MHC class I molecules cluster at ER exit sites for transport through the Golgi to the plasma membrane [12,13].

Antigen presentation

Once the antigen-loaded MHC class I molecules arrive at the plasma membrane, they are accessible for inspection by CD8+ T cells. Using fluorescently tagged Fab fragments and FRET measurements, Catipovic *et al*. [14] demonstrated that peptide-loaded MHC class I molecules attached to the cell surface adopt a more compact structure than their empty counterparts. The interaction between MHC molecules and T-cell receptors, and the subsequent recruitment of co-receptors, has also been studied using FRET measurements. Lee and Kranz [15] visualized the recruitment of CD8 to the MHC class Ibound T-cell receptor, whereas Zal *et al*. [16] studied the interaction between the CD4 co-receptor and the MHC class II-bound T-cell receptor. Interestingly, this last step of antigen presentation is highly similar for both pathways, although the source of the presented antigen and its processing is completely different.

The MHC class II pathway

MHC class II molecules present antigens from extracellular origins that are degraded by way of the endocytic route on the surface of so-called professional APCs. Correct folding of these molecules in the ER requires the invariant chain, a dedicated chaperone that stabilizes the empty MHC class II molecules by occupying its peptide-binding groove (for details see Figure 1). In addition, the invariant chain targets the MHC class II complex to the MHC class II containing compartments (MIICs), which are late endosomal and/or lysosomal vesicles that have a multi-vesicular or multi-lamellar architecture. These vesicles form the environment in which MHC class II molecules meet

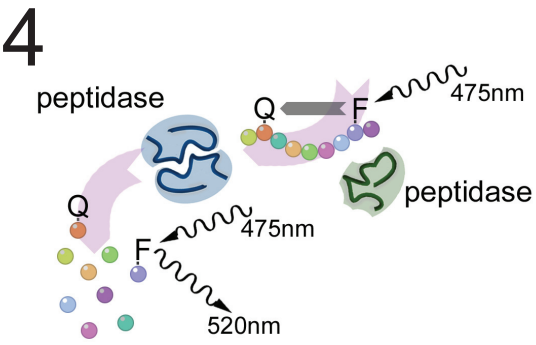


Figure 4. Internally quenched peptides. Peptidase activity can be measured in living cells using, so-called, internally quenched peptides. These chemically synthesized peptides contain both a fluorescent group (F) and a quencher moiety (Q), and do not emit fluorescence when excited with 475 nm light when the peptide is intact. Upon microinjection and cleavage by peptidases, the quencher will be spatially separated from fluorophore, and fluorescence-emitted light of 520 nm can be detected.

potential antigens, such as bacterial-derived peptides, and acquire fragments from them.

Antigen loading

When in the MIIC, the invariant chain is degraded by lysosomal proteases until only the part remains that occupies the peptide-binding groove of MHC class II molecules. This is known as the class II-associated invariant chain peptide (CLIP) fragment. The crucial exchange of this CLIP fragment for an antigenic peptide is facilitated by a second dedicated chaperone, human leukocyte antigen (HLA)-DM. As the size of the average MIIC compartment is smaller than the wavelength of visible light, conventional colocalization studies did not suffice to study the interaction between HLA-DM and MHC class II molecules. We therefore applied confocal laser scanning microscopy (CLSM) FRET measurements [17], which enabled us to visualize the interaction between MHC class II molecules and HLA-DM in the MIIC of living cells (Figure 2b; [18]). By reconstituting the MHC class II pathway with fluorescently tagged molecules, we were able to demonstrate that the interaction between HLA-DM andMHC class II molecules in native MIIC is pH independent, and that it only occurs on the internal structures, and not at the limiting membrane [18]. The internal membranes of the MIIC thus form a MHC class II loading microdomain in which the CLIP fragment is exchanged for an antigenic peptide.

Transport to the plasma membrane

After successful antigen loading, the MHC class II molecules traffic to the cell surface. The transport pathways involved in this have been quite thoroughly studied by use of a wide variety of techniques. Key regulators in this pathway are the small GTPases from the Rab family, most notably Rab5 and Rab7, which control the activity of microtubule-based motor proteins. These proteins are socalled molecular switches that cycle between an inactive cytosolic- and an active membrane-associated state. Their cycling has been successfully studied with FRAP, in which the membrane-bound fraction was bleached and recovery of fluorescence was quantified [19,20]. In addition, Galperin and Sorkin [21] used FRET measurements to visualize the interaction between the Rab5 protein and its effector (which only binds to the active form of the Rab protein).

Immune evasion

Intracellular bacteria, such as Mycobacterium tuberculosis and Salmonella, affect the endocytic pathway and multivesicular body formation. By doing this they form a phagosome that does not fuse with lysosomes [22]. By manipulation of the small GTPases Rab5 and Rab7, these bacteria manage to diverge from the normal endocytic pathway to create their own cellular compartment (the phagosome) in which they survive and replicate. Here, they are usually unrecognized by the immune system. Manipulation of the endocytic pathway starts immediately after bacteria have entered into cells by phagocytosis. This is a complex process that was elegantly studied using FRET by Hoppe and Swanson [23]. Importantly, the creation of a phagosome allows these bacteria to evade the immune system; for example, our FRET measurements show that HLA-DMandMHCclass II molecules do not interact on the membrane of the phagosome, thus preventing antigen loading [18]. These bacteria can locally evade the immune system by disruption of formation of the required internal MHC class II loading microdomains, a conclusion that could not have been drawn without the use of advanced biophysical techniques.

Conclusions

The two antigen presentation pathways discussed in this review are prime examples of multi-step and highly dynamic cellular processes. To unravel their details, sensitive microscopic measurements are required that have high temporal and spatial resolution in single living cells. In this review, we have discussed several techniques that satisfy these requirements, and recent advances in both microscopic techniques and fluorescent probes further extend the array of possibilities. For example, the discovery of photoactivatable fluorescent proteins [24,25] provides new ways in which to study cellular trafficking and compartmentalization. Likewise, many of the advanced microscopic techniques described in this review are becoming commercially available for use by cell biologists and microbiologists, rather than by biophysicists only. Taken together, this promises the onset of many more studies that apply biophysical techniques to gain further insight into antigen presentation as well as into many other processes, all in living cells.

Acknowledgements

We would like to thank Kees Jalink and Jacco van Rheenen for helpful discussions.

References

1. Triantafilou K, Fradelizi D, Wilson K, Triantafilou M: GRP78, a coreceptor for coxsackievirus A9, interacts with major histocompatibility complex class I molecules which mediate virus internalization. J Virol 2002, 76:633-643.

2.Martin-Fernandez M, Longshaw SV, Kirby I, Santis G, Tobin MJ, Clarke DT, Jones GR: Adenovirus type-5 entry and disassembly followed in living cells by FRET, fluorescence anisotropy, and FLIM. Biophys J 2004, 87:1316-1327.

3. Reits EA, Benham AM, Plougastel B, Neefjes J, Trowsdale J: Dynamics of proteasome distribution in living cells. EMBO J 1997, 16:6087-6094.

4. Reits E, Griekspoor A, Neijssen J, Groothuis T, Jalink K, van Veelen P, Janssen H, Calafat J, Drijfhout JW, Neefjes J: Peptide diffusion, protection, and degradation in nuclear and cytoplasmic compartments before antigen presentation by MHC class I. Immunity 2003, 18:97-108.

5. Reits E, Neijssen J, Herberts C, Benckhuijsen W, Janssen L, Drijfhout JW, Neefjes J: A major role for TPPII in trimming proteasomal degradation products for MHC class I antigen presentation. Immunity 2004, 20:495-506.

6. Reits EA, Vos JC, Gromme M, Neefjes J: The major substrates for TAP *in vivo* are derived from newly synthesized proteins. Nature 2000, 404:774-778.

7. Loudet JC, Hanusse P, Poulin P: Stokes drag on a sphere in a nematic liquid crystal. Science 2004, 306:1525.

8. Reits EA, Neefjes JJ: From fixed to FRAP: measuring protein mobility and activity in living cells. Nat Cell Biol 2001, 3:E145-E147.

9. Marguet D, Spiliotis ET, Pentcheva T, Lebowitz M, Schneck J, Edidin M: Lateral diffusion of GFP-tagged H2Ld molecules and of GFP-TAP1 reports on the assembly and retention of these molecules in the endoplasmic reticulum. Immunity 1999, 11:231-240.

10. Spiliotis ET, Pentcheva T, Edidin M: Probing for membrane domains in the endoplasmic reticulum: retention and degradation of unassembled MHC class I molecules. Mol Biol Cell 2002, 13:1566-1581.

11. Pentcheva T, Spiliotis ET, Edidin M: Cutting edge: tapasin is retained in the endoplasmic reticulum by dynamic clustering and exclusion from endoplasmic reticulum exit sites. J Immunol 2002, 168:1538-1541.

12. Pentcheva T, EdidinM: Clustering of peptide-loaded MHC class I molecules for endoplasmic reticulum export imaged by fluorescence resonance energy transfer. J Immunol 2001, 166:6625-6632.

13. Rocheleau JV, Edidin M, Piston DW: Intrasequence GFP in class I MHC molecules, a rigid probe for fluorescence anisotropy measurements of the membrane environment. Biophys J 2003, 84:4078-4086.

14. Catipovic B, Talluri G, Oh J, Wei T, Su XM, Johansen TE, Edidin M, Schneck JP: Analysis of the structure of empty and peptide-loaded major histocompatibility complex molecules at the cell surface. J Exp Med 1994, 180:1753-1761.

15. Lee PU, Kranz DM: Allogeneic and syngeneic class I MHC complexes drive the association of CD8 and TCR on 2C T cells. Mol Immunol 2003, 39:687-695.

16. Zal T, Zal MA, Gascoigne NR: Inhibition of T cell receptor–coreceptor interactions by antagonist ligands visualized by live FRET imaging of the T-hybridoma immunological synapse. Immunity 2002, 16:521-534.

17. van Rheenen J, Langeslag M, Jalink K: Correcting confocal acquisition to optimize imaging of fluorescence resonance energy transfer by sensitized emission. Biophys J 2004, 86:2517-2529.

18. Zwart W, Griekspoor A, Kuijl C, Marsman M, van Rheenen J, Janssen H, Calafat J, van Ham M, Janssen L, van Lith M *et al.*: Spatial separation of HLA-DM/HLA-DR interactions within MIIC, and phagosomal immune escape. Immunity 2005, 22:221-233.

19. Vieira OV, Bucci C, Harrison RE, Trimble WS, Lanzetti L, Gruenberg J, Schreiber AD, Stahl PD, Grinstein S: Modulation of Rab5 and Rab7 recruitment to phagosomes by phosphatidylinositol 3-kinase. Mol Cell Biol 2003, 23:2501-2514.

20. Jordens I, Fernandez-Borja M, Marsman M, Dusseljee S, Janssen L, Calafat J, Janssen H, Wubbolts R, Neefjes J: The Rab7 effector protein RILP controls lysosomal transport by inducing the recruitment of dynein-dynactin motors. Curr Biol 2001, 11:1680-1685.

21. Galperin E, Sorkin A: Visualization of Rab5 activity in living cells by FRET microscopy and influence of plasma-membrane-targeted Rab5 on clathrin-dependent endocytosis. J Cell Sci 2003, 116:4799-4810.

22. Harrison RE, Bucci C, Vieira OV, Schroer TA, Grinstein S: Phagosomes fuse with late endosomes and/or lysosomes by extension of membrane protrusions along microtubules: role of Rab7 and RILP. Mol Cell Biol 2003, 23:6494-6506.

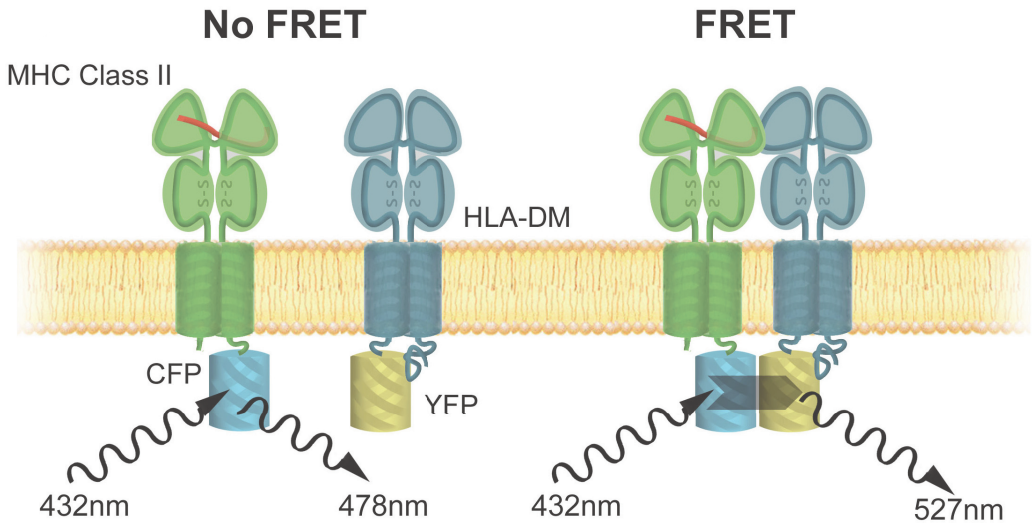
23. Hoppe AD, Swanson JA: Cdc42, Rac1, and Rac2 display distinct patterns of activation during phagocytosis. Mol Biol Cell 2004, 15:3509-3519.

24. Patterson GH, Lippincott-Schwartz J: A photoactivatable GFP for selective photolabeling of proteins and cells. Science 2002, 297:1873-1877.

25. Chudakov DM, Verkhusha VV, Staroverov DB, Souslova EA, Lukyanov S, Lukyanov KA: Photoswitchable cyan fluorescent protein for protein tracking. Nat Biotechnol 2004, 22:1435-1439.

Spacial Separation of HLA-DM/HLA-DR Interactions within MIIC and Phagosome-Induced Immune Escape

Immunity 2005, vol. 22:221-233



10

Spatial separation of HLA-DM/HLA-DR interactions within MIIC, and phagosome-induced immune escape.

Wilbert Zwart[+], Alexander Griekspoor[+], Coenraad Kuijl, Marije Marsman, Jacco van Rheenen[1], Hans Janssen[1], Jero Calafat[1], Marieke van Ham, Lennert Janssen, Marcel van Lith, Kees Jalink[1] and Jacques Neefjes[#].

Abstract
MHC class II molecules including HLA-DR present peptide fragments from proteins degraded in the endocytic pathway. HLA-DR is targeted to late endocytic structures named MIIC where it interacts with HLA-DM. This chaperone stabilizes HLA-DR during peptide exchange, and is critical for successful peptide loading. To follow this process in living cells, we have generated cells containing HLA-DR3/CFP, HLA-DM/YFP and invariant chain. HLA-DR/DM interactions were observed by FRET. These interactions were pH insensitive, yet occurred only in internal structures and not at the limiting membrane of MIIC. In a cellular model of infection, phagosomes formed a limiting membrane surrounding internalized Salmonella. HLA-DR and HLA-DM did not interact in Salmonella-induced vacuoles, and HLA-DR was not loaded with antigens. The absence of HLA-DR/DM interactions at the limiting membrane prevents local loading of MHC class II molecules in phagosomes. This may allow these bacteria to successfully evade the immune system.

Introduction

MHC class II molecules present peptide fragments of antigens degraded in the endocytic pathway to CD4+ T cells (Bryant *et al*., 2002). This is a prerequisite for efficient antibody responses and the establishment of an effective immunological memory. In order to contact antigens, MHC class II molecules like HLA-DR (DR) are chaperoned from the endoplasmic reticulum (ER) to late endocytic structures (called MHC class II containing compartments, or MIIC (Peters *et al*., 1991)) by the invariant chain. Here, the invariant chain is degraded, except for a small fragment called CLIP, which remains in the peptide-binding groove of DR (Cresswell, 1992). HLA-DM (DM), a second dedicated chaperone, is required to stabilize the 'empty' MHC class II molecules and supports the exchange of both CLIP and low affinity peptides for a peptide with high affinity (Denzin and Cresswell, 1995; Kropshofer *et al*., 1997; Sherman *et al*., 1995) that fills pocket 1 in the peptide binding groove (Chou and Sadegh-Nasseri, 2000). The direct interaction between DM and DR has been shown in *in vitro* reconstitution experiments and co-isolations. This interaction was pH sensitive and of low affinity (Sanderson *et al*., 1996; Vogt *et al*., 1999). DM interacts with a lateral site on DR via hydrophobic surfaces, but the exact factors that contribute to this process remain unclear (Doebele *et al*., 2000; Pashine *et al*., 2003; Ullrich *et al*., 1997). More recently, a non-polymorphic MHC class II homologue has been identified, called HLA-DO (DO). DO stably interacts with DM, reducing its chaperoning activity on DR in a pH-dependent manner (Denzin *et al*., 1997; Liljedahl *et al*., 1998; van Ham *et al*., 1997). Like the DR/DM complex, the DM/DO complex is targeted to the MIIC.

MIIC are characterized by a multilamellar and/or multivesicular structure. Multivesicular bodies (MVB) can be converted into multilamellar structures by changes in protein content (Calafat *et al*., 1994) and both type of structures most likely reflect different maturation states (Kleijmeer *et al*., 1997). The internal structures differ from the limiting membrane by both protein and lipid composition. Whereas DR and DM can be found in both domains, other late endocytic proteins like tetraspans, and lipids like cholesterol and lyso-bis-PA, are usually located at the internal structures (Gruenberg, 2003; Wubbolts *et al*., 2003). Although tetraspans like CD63 and CD82 interact with DM or DR (Escola *et al*., 1998; Hammond *et al*., 1998), the functional consequences are unclear. Still, internal structures differ in composition from the limiting membrane, and this may affect the interaction between DR and its chaperone DM, and ultimately antigen pre-

Divisions of Tumor Biology and 1Cell Biology,
The Netherlands Cancer Institute,
Plesmanlaan 121,
1066 CX Amsterdam,
The Netherlands

#Corresponding author
Email: J.NEEFJES@NKI.NL
+Equal contribution

Short title: HLA-DM/-DR interactions *in vivo*

Present address MvL: Department of Biological and Biomedical Sciences, University of Durham, Durham, U.K.
MvH: Sanquin Research at CLB, Amsterdam, The Netherlands

Keywords:
MHC class II / antigen presentation / HLA-DR / HLA-DM / HLA-DO / FRET / FLIM / MIIC / phagosome / microdomains / immune escape / MHC class II loading microdomain / Salmonella / SCV / VPS34 / M. tuberculosis

sentation (Kropshofer *et al*., 2002). The failure to visualize these interactions due to the limited resolution of light microscopy prevented any conclusion about spatial specialization within MIIC.

The formation of internal structures that characterize the morphology of a MVB is the result of a complicated series of events. It requires the activities of a PI 3-kinase hVPS34, ESCRT complexes, ubiquitination and acidification (Katzmann *et al*., 2002). Inhibition of hVPS34 or acidification results in expanded late endosomal structures without internal vesicles (Fernandez-Borja *et al*., 1999). Such treatments also affect the MIIC, and inhibit antigen presentation by MHC class II molecules (Morrison *et al*., 1986; Song *et al*., 1997). Pathogens like Salmonella typhimurium, Mycobacterium tuberculosis, and Mycobacterium leprae survive in phagosomes (Brumell and Grinstein, 2004; Russell, 2003), structures composed of only a limiting membrane surrounding the bacteria. These intracellular bacteria have been reported to reduce or even eliminate antigen presentation by MHC class II molecules (Harding *et al*., 2003; Ramachandra *et al*., 2001; Ullrich *et al*., 2000), but the underlying mechanism remains elusive.

Here, we studied the interaction between DM and DR3 in living cells by Fluorescence Resonance Energy Transfer (FRET). Applying CLSM-FRET microscopy allowed us to visualize these interactions at unprecedented resolution within MIIC of living cells. This interaction was not affected by neutralization of pH, and occurred exclusively in the internal structures of MIIC. No interaction was observed in MIIC devoid of internal structures after long-term chloroquine treatment or knockdown of hVPS34. Similarly, phagosomes in which many intracellular pathogens survive often lack internal membranes. This can occur when hVPS34 is inactivated (Vergne *et al*., 2003), or when a downstream product of hVPS34 (PI(3,5)P2) is hydrolyzed by the Salmonella secreted PIP2-phosphatase SopB (Hernandez *et al*., 2004). We show that at the limiting membrane of a Salmonella-induced phagosome (SCV) DM failed to interact with DR3, again using FRET. Consequently, DR3 was not loaded with antigens within the SCV while antigen loading within multivesicular MIIC continued in the infected cells. Local MHC class II-restricted immune escape of intracellular pathogens like Salmonella appears to be a consequence of subvesicular structural differences within the MIIC, where HLA-DM interacts with HLA-DR in MHC class II loading microdomains in the internal structures, but not at the limiting membrane.

Results

A system to monitor HLA-DR3 interaction with DM

To study the interaction between DR and DM, the molecules were tagged with two variants of the Green Fluorescent Protein, CFP attached to the cytoplasmic tail of DR3β and YFP linked to the cytoplasmic tail of DMα. GFP tagging of the DR3β chain has been successfully used before, without measurable effects on MHC class II behavior (Boes *et al*., 2002; Wubbolts *et al*., 1996). The DMβ chain contains the lysosomal targeting information (Marks *et al*., 1995), therefore the DMα chain was used for YFP tagging. To investigate whether the various modifications still allowed a productive interaction between DR3/CFP and DM/YFP, the DRα and DR3β/CFP chains were stably expressed into Human Embryo Kidney (HEK) 293 cells along with the DMα/YFP and DMβ chains. We generated three cell lines: HEK293 cells expressing only DR3/CFP, HEK293 cells expressing DR3/CFP and DM/YFP, and HEK293 cells expressing DR3/CFP, DM/YFP and the p30 form of the invariant chain (Ii). By introducing these chains in a non–immune cell line, DR3/CFP peptide loading could only be supported by YFP-tagged DM, since no endogenous DM was present. First, expression of the various subunits was confirmed by Western blotting (Fig 1A). Subsequent analysis of the stable cell lines by Confocal Laser Scanning Microscopy (CLSM) revealed that DM/YFP was efficiently targeted to endosomal structures, whereas DR3/CFP was mainly retained in the ER unless the invariant chain was co-expressed (suppl. Fig S1). In the presence of the invariant chain, DM/YFP and DR3/CFP were both efficiently transported to endosomal structures containing CD63 as a marker, and DR3/CFP arrived at the plasma membrane with similar efficiency as observed in cells endogenously expressing DR3 (Fig 1B and suppl. Fig S2). These endosomal compartments had the characteristic morphology of MIIC and were a mixture of multilamellar and multivesicular bodies, as shown by immuno-electron microscopy (EM) (Fig 1C). Note that DM/YFP and DR3/CFP were both distributed over the limiting membrane and the internal vesicles of the MIIC.

Peptide loading was assayed biochemically. DR3 with high affinity peptides will not dissociate in SDS-loading buffer when incubated at room temperature, resulting in slower migration of the so-called compact form by SDS-PAGE analysis (Germain and Hendrix, 1991; Neefjes and Ploegh, 1992). A substantial amount of compact DR3/CFP molecules was detected only when DM/YFP and the invariant chain were co-expressed (Fig 1D). This was confirmed by surface iodination and analysis of DR3/CFP for tem-

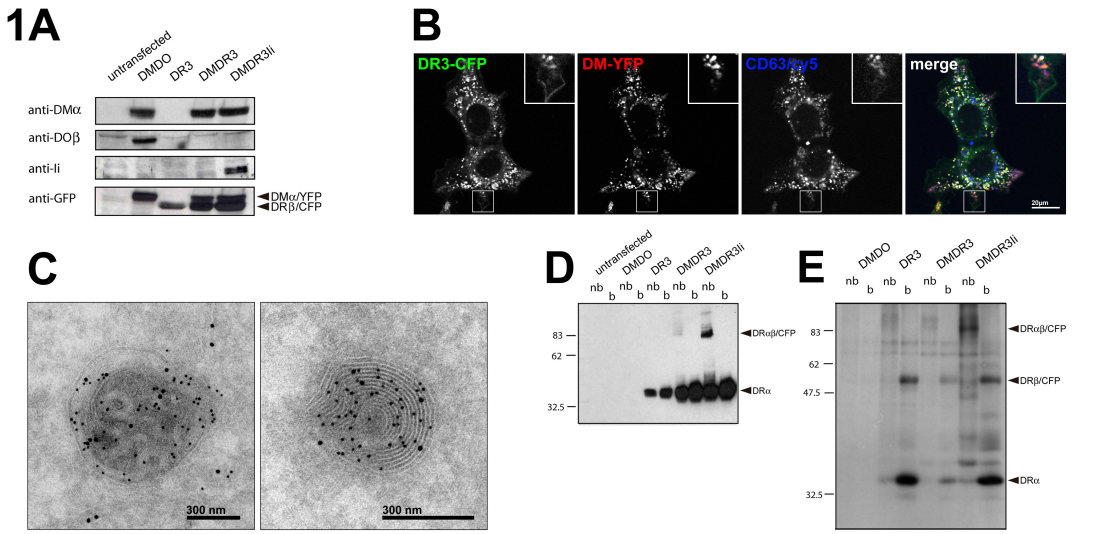


Figure 1. Characterization of the HEK293 Transfectants expressing HLA-DR3/CFP and HLA-DM/YFP

(**A**) HEK293 cells expressing DM/YFP, DO/CFP, DR3/CFP, and the invariant chain (Ii) were analyzed by SDS-PAGE and Western blotting with the antibodies indicated.
(**B**) Intracellular distribution of DR3/CFP and DM/YFP in Ii-expressing HEK293 cells. Cells were fixed and stained with anti-CD63 antibody, and the various fluorophores were analyzed as indicated. A strong colocalization between DR3, DM, and CD63 is observed. Inset shows the selective surface expression of DR3/CFP.
(**C**) DR3/CFP and DM/YFP localize to multivesicular and multilamellar structures. HEK293 cells expressing DR3/CFP, DM/YFP, and Ii were fixed and prepared for cryo-immuno-EM. DM (10 nm gold) and DR3 (15 nm gold) localize to both the internal structures and the limiting membrane of MIIC.
(**D**) Analysis of DR3/CFP peptide loading. Lysates of the different transfectants were incubated in SDS-loading buffer and split in two. One half was boiled at 100°C for 5 min (lanes "b" for boiled) and the other left at room temperature (lane "nb" for nonboiled) before separation by SDS-PAGE. Proteins were transferred to nitrocellulose and stained with antibody against DRα chain. Free DRα (35 kDa) and DRαβ/CFP complexes (83 kDa) are indicated. Compact, DR3/CFP-peptide complexes are only detected when cells coexpress DM/YFP and Ii.
(**E**) Analysis of cell surface-expressed MHC class II complexes. The various transfectants were cell surface iodinated and MHC class II complexes were immune precipitated. The immune isolates were either boiled in SDS loading buffer (lanes "b") or left at room temperature (lanes "nb") before separation by SDS-PAGE. The position of DRα, DR3β-CFP and the DR3αβ/CFP-peptide complex is indicated. Compact, DR3/CFP-peptide complexes are only detected at the plasma membrane when cells coexpress DM/YFP and Ii.

perature stability (Fig 1E). DM/YFP supported peptide loading of DR3/CFP, implying that the CFP/YFP-modifications did not prevent a successful interaction between the two partners. Since the expression, distribution, MHC class II loading with peptides, and transport to the plasma membrane mimicked the situation in antigen presenting cells, we continued our studies with the HEK293 cells stably transfected with DR3/CFP, DM/YFP and the invariant chain.

FRET analyses and the interaction of HLA-DM with HLA-DR3 or HLA-DO

FRET is the radiationless transfer of energy from an excited donor fluorophore to a suitable acceptor fluorophore, a physical process that depends on spectral overlap and proper dipole alignment of the two fluorophores. The occurrence of FRET between CFP and YFP is characterized by a decrease in CFP emission, and simultaneously sensitized (increased) YFP emission. Importantly, FRET is extremely sensitive to the distance between the fluorophores (its efficiency decays with the distance to the sixth power) (Förster, 1948). For CFP and YFP, the characteristic half-maximum distance is 49-52Å (Förster radius), with an upper limit of ~80Å (Tsien, 1998). Given the dimensions of GFP and its color variants (Ormo *et al*., 1996), DM (Mosyak *et al*., 1998) and DR3 (Ghosh *et al*., 1995), FRET between DR3/CFP and DM/YFP will only occur when both proteins are no more than one molecule in distance apart (Fig 2). Thus, if FRET is observed, DM almost certainly interacts with DR3. FRET was studied by calculating the sensitized emission from confocal CFP and YFP images, as described in depth (Van Rheenen *et al*., 2004). Leakthrough factors (due to spectral overlap of the fluorophores) were calculated from cells expressing histon 2B (H2B) coupled to CFP or YFP that were co-cultured with the cells under study (see Methods and supplementary material). No FRET signal of H2B-CFP and H2B-YFP should be observed in the final (fully corrected) sensi-

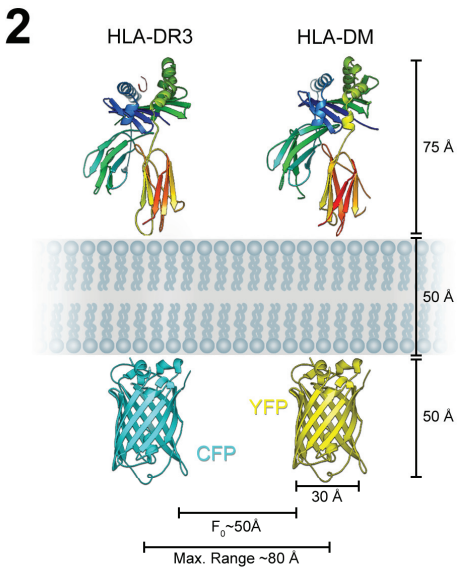


Figure 2. Dimensions of HLA-DR3/CFP, HLADM/YFP, and FRET

The structures of DR and DM are projected above a membrane of about 50 Å thick. The transmembrane regions of both molecules are undefined and not shown. CFP and YFP have a barrel shape of 30 × 50 Å with a fluorescent moiety inside. Shown are both the maximal distance (w80 Å) that can be detected by fluorescence resonance energy transfer (FRET), and the Förster radius (F0), the distance at which FRET between CFP and YFP is half maximal (50 Å).

tized emission pictures. Fig 3A shows a representative example of our experimental procedure using CLSM-FRET. The H2B-C/YFP expressing control cells could be easily recognized by their nuclear fluorescence. Sensitized emission (further referred to as 'FRET') between DM and DR3 was only detected in vesicles, as the algorithm used to correct for leakthrough terms effectively removed both the DR3 signal at the plasma membrane and the nuclear H2B-C/YFP fluorescence (Fig 3A, panel FRET).

The efficiency of DR3 interactions with DM was deduced from the donor FRET efficiency (E_D), the FRET signal relative to the amount of donor fluorescence, which is DR3/CFP. A donor FRET efficiency of ~5.3% was detected, far above the minimal efficiency detectable by this technique (see Methods). Little variation was observed between the various MIIC structures within one cell (Fig 3A, panel E_D), and in cells with different ratios of DR3/CFP versus DM/YFP, suggesting saturating amounts of DM/YFP for the catalysis of peptide loading of DR3/CFP in these vesicles (suppl. Fig S3). This was further visualized by plotting for each pixel the FRET efficiency versus the DR3/CFP and DM/YFP intensities (Fig 3E). No correlation was observed between FRET efficiency and the intensity of CFP and YFP, showing that this represented true interactions rather than accidental collision of both proteins.

GFP and its color variants can be sensitive to environment, for example to hydrophobicity and pH (Tsien, 1998). Since they are situated in acidic vesicles with many membranes, alterations in FRET could be the result of an altered environment in which the CFP/YFP molecules reside. As a control, we generated a stable HEK293 cell line expressing DM/YFP and DO/CFP. DO is homologous to DR (DOβ shares ~75% amino acid sequence identity with DR3β), but unlike DR interacts stably with DM. Consequently, if a change in FRET efficiency between DO and DM is observed, this could be the result of an altered environment of the fluorophores. DO is targeted mainly by DM to MIIC and is virtually absent from the plasma membrane. DO/CFP and DM/YFP localized to the same late endocytic, CD63-containing structures as DM/YFP and DR3/CFP, as shown by CLSM (Fig 3B) and immuno-EM with anti-GFP antibodies (Fig 3C). As observed before (van Lith *et al*., 2001), DM/YFP, DO/CFP was mainly located on the limiting membrane but also on internal structures of characteristic multivesicular/multilamellar MIIC. These DM/YFP, DO/CFP cells were used as controls in further experiments.

FRET was measured between DO and DM under conditions identical to those described for Fig 3A. Efficient FRET was detected between these molecules (Fig 3D). The FRET efficiency for the interaction between DO and DM was 23.2% (S.D. 3.5%) compared to 5.3% (S.D. 1.5%) observed for DR3 and DM (Fig 3F), and is obviously not affected by acceptor (YFP) concentrations (Fig 3E). This ratio in FRET efficiency was determined by both wide field (not shown) and CLSM-FRET, and confirmed by FLIM (Fluorescence Lifetime Imaging Microscopy) analysis, an alternative technique to monitor FRET (Bastiaens and Squire, 1999). The lifetime (the average duration of the excited state) for the donor CFP is typically 2.7ns (Vermeer *et al*., 2004), but is reduced when energy is transfered to YFP following the same rules for FRET as described earlier. FLIM offers the advantage that it reports FRET in a highly quantitative manner, but as implemented here, lacks confocal sectioning capacity. Also, it requires relatively long sampling times (~12s) to accurately determine the lifetime of the fluorophore (a problem for moving vesicles). Fig 3G shows wide-field FLIM measurements of the DM/YFP and DR3/CFP or DO/CFP cells, co-cultured with the H2B-CFP containing Mel JuSo cells in the presence of nocodazole to block vesicle transport. Arrows indicate examples of vesicles that were immobile during the measurement. The DR3/CFP lifetime was on average 2.49ns in the presence of DM/YFP, and 1.52ns in that of DO/CFP. These values correspond to a FRET efficiency ratio of 1:5.6 ((2.7 – 2.49) / (2.7 – 1.52)), similar as detected with CLSM-FRET.

The higher FRET efficiency between DM

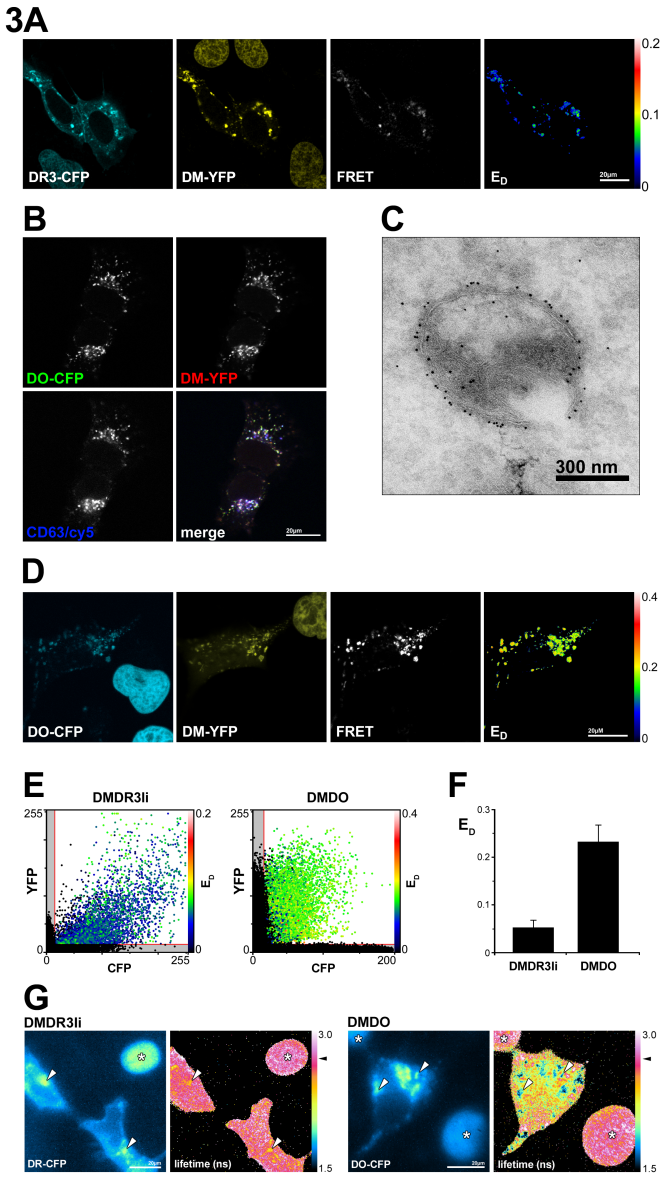


Figure 3. FRET Measurements

(**A**) FRET between DR3/CFP and DM/YFP with internal controls by CLSM. HEK293 cells with DR3/CFP, DM/YFP, and Ii were cocultured with Mel JuSo cells expressing H2B-CFP or H2B-YFP, and FRET was measured in living cells at 37°C. Nuclear fluorescence identifies control cells. After correction for fluorescent leakthrough (see Supplemental Experimental Procedures), FRET between DR3 and DM is observed as sensitized emission (panel "FRET"). The efficiency of interaction is shown in false colors by the donor FRET efficiency, the FRET signal related to the amount of donor fluorescence (panel "ED"). DR3/CFP is located in MIIC and at the plasma membrane, and DM/YFP only in MIIC. FRET between these complexes is solely observed in the endosomal structures. The relative FRET efficiency values corresponding to the respective colors are indicated.

(**B**) Intracellular distribution of DO/CFP andDM/YFP in HEK293 cells. The stable transfectants were methanol fixed, incubated with anti-CD63 antibodies labeled with Cy5, and analyzed by CLSM. DM/DO colocalizes with CD63 in endosomal structures.

(**C**) Distribution of DO/CFP and DM/YFP in MIIC. HEK293 cells transfected with the DO/CFP and DM/YFP were fixed, and sections were labeled with anti-GFP antibodies before analysis by immuno-EM. GFP labeling is observed at the limiting membrane and in internal structures.

(**D**) CLSM-FRET with internal controls of living HEK293 cells expressing DO/CFP and DM/YFP. The protocol is described under (A). High donor FRET efficiency (E_D) is observed between DO and DM in endosomal structures.

(**E**) Analysis of FRET efficiency images. From the images in (A) and (D), CFP, YFP, and FRET efficiency values were extracted for all pixels and plotted on the x and y axis, respectively, with corresponding FRET efficiencies (E_D) depicted in the false colors. The threshold set to exclude background fluorescence is indicated with a red line.

(**F**) Quantification of the donor FRET efficiency (E_D). E_D observed in endosomal structures between DR3/CFP and DM/YFP, and between DO/CFP and DM/YFP was determined in, respectively, 16 and 11 individual experiments made on various days. (G) FLIM measurements of the interactions between CFP/YFP-labeled DR3 and DM, or DO and DM in HEK293 cells, cocultured with H2B-CFP internal controls and treated withnocodazole to disrupt vesicle transport. Fluorophore excited state lifetime decreases upon FRET. Left panel shows wide field CFP fluorescence, right panel shows calculated lifetime (in ns) in false colors. The average lifetime of CFP in the absence of FRET (2.7 ns) is indicated with a black arrowhead. Only vesicles immobile during data sampling (w12 s) were considered, of which two examples are indicated in both images by white arrowheads. These vesicles had a shorter CFP lifetime than the H2B-CFP controls (indicated by asterisk).

and DO is not surprising since these molecules continuously interact, whereas DM will interact transiently with DR3 as long as the class II molecule contains CLIP or another non-stably binding peptide. Together, these data show that we have established a cell system to follow interactions between DR3 and its dedicated chaperone DM in MIIC of living cells by FRET.

HLA-DR3 interactions with HLA-DM are not pH dependent in vivo unless HLA-DO is present

The interaction between DM and DR3 is sensitive to pH, at least *in vitro*. DM mediated peptide exchange on DR is optimal at pH 4.5 and about 4 times less efficient at pH 7 (van Ham *et al*., 2000). Also, DM can only be co-isolated with DR at acidic pH (Sanderson *et al*., 1996). Furthermore, prolonged incubation with lysosomotropic agents like NH4Cl and chloroquine inhibits MHC class II antigen presentation

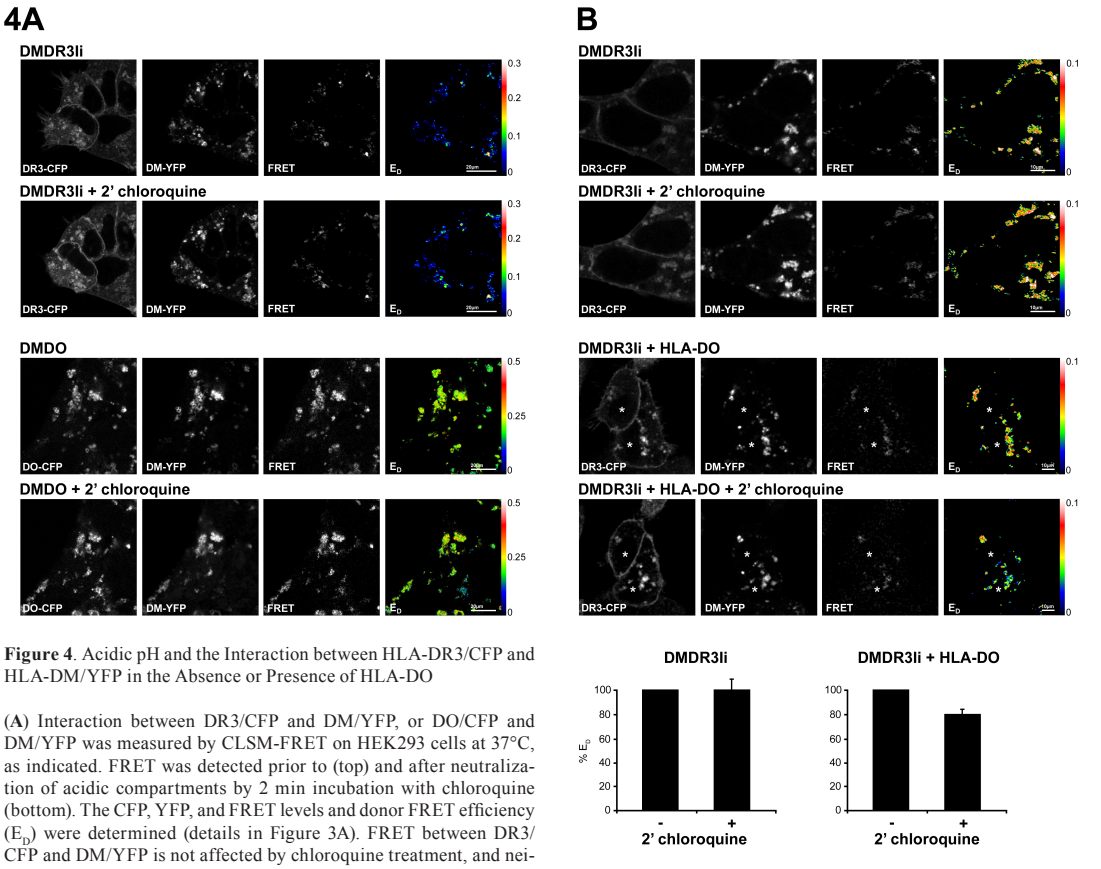


Figure 4. Acidic pH and the Interaction between HLA-DR3/CFP and HLA-DM/YFP in the Absence or Presence of HLA-DO

(**A**) Interaction between DR3/CFP and DM/YFP, or DO/CFP and DM/YFP was measured by CLSM-FRET on HEK293 cells at 37°C, as indicated. FRET was detected prior to (top) and after neutralization of acidic compartments by 2 min incubation with chloroquine (bottom). The CFP, YFP, and FRET levels and donor FRET efficiency (E_D) were determined (details in Figure 3A). FRET between DR3/CFP and DM/YFP is not affected by chloroquine treatment, and neither did neutralization affect DO and DM (n > 50 independent measurements).

(**B**) The interaction between DR3/CFP and DM/YFP becomes pH dependent upon DO expression. The same analysis as in (A) was performed on the DR3/CFP, DM/YFP and invariant chain-expressing HEK293 transfectants (upper panel), and the same cells overexpressing unlabeled DO with H2B-mRFP as a transfection marker (lower panel). The H2B-mRFP signal is not shown (see Figure S5). Interaction between DR3/CFP and DM/YFP is not affected by DO expression at normal acidic pH but is reduced upon neutralization with chloroquine. FRET efficie cies measured on the identical vesicles prior to and after neutralization are depicted in the bar diagrams with the SD indicated (n > 50 pairwise measurements).

(Morrison *et al*., 1986). We tested whether neutralization of MIIC by two minutes of chloroquine treatment (suppl. Fig S4), affected the interaction between DM and DR3 *in vivo* in intact MIIC, as could now be visualized by FRET. The DM/YFP, DO/CFP cells were taken to control for potential influences of pH changes on the fluorophores. Neutralization of acidic structures did not affect FRET efficiency between DM and DO but, surprisingly, neither between DR3 and DM (Fig 4A). Only when the pH sensor DO (van Ham *et al*., 2000) was overexpressed in the DR3/CFP, DM/YFP cells (suppl. Fig S5), a reduction in FRET efficiency between DR3 and DM was observed upon chloroquine treatment (Fig 4B). Overexpression of DO apparently does not change the relative orientation of DM to DR3, at least not at acidic pH, suggesting that DO does not act as a DR mimmick, but merely as a pH sensor for DM mediated peptide loading of DR (van Ham *et al*., 2000). Still, there is an apparent discrepancy between the *in vitro* experiments where DR and DM require acidic pH for activity, and the *in vivo* FRET data. Possibly, DR3 and DM localize in microdomains within the MIIC that stabilize their interaction, even under conditions of neutral pH.

Spatial differences within MIIC affect HLA-DR3 interactions with HLA-DM

It has been known for over 20 years that long-term treatment with chloroquine or NH4Cl induces swelling of lysosomes (Ohkuma and Poole, 1981). We demonstrate that the membranes needed for swelling are provided by internal vesicles that fuse back to the limiting membrane. This is concluded since 1. MIIC swelled after chloroquine treatment in our transfectants under conditions that vesicle transport was blocked (by destroying the microtubular network with nocoda-

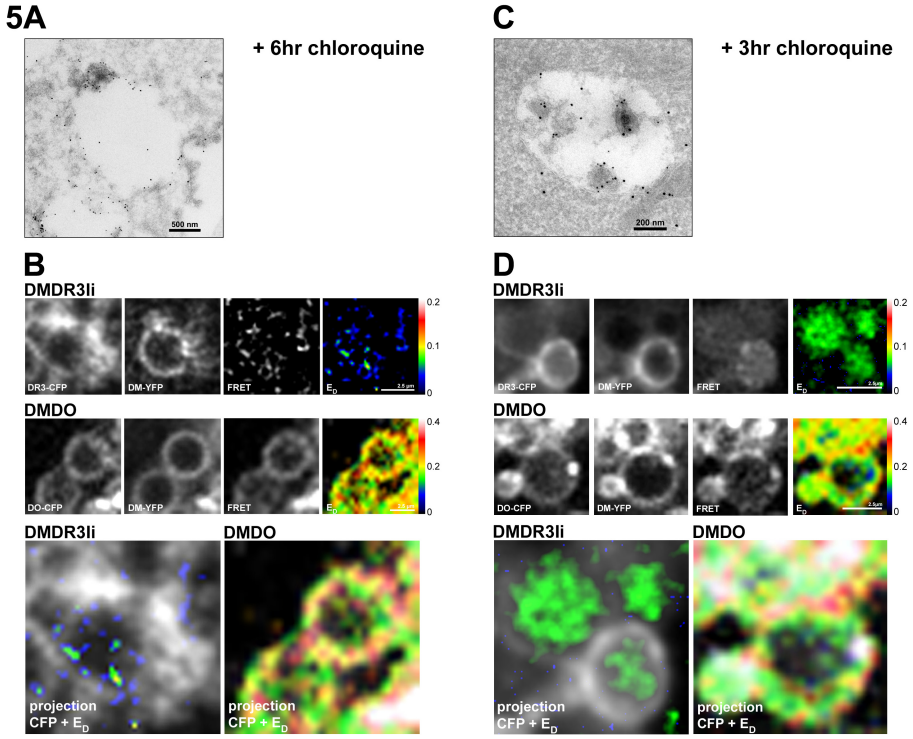


Figure 5. HLA-DR Interactions with HLA-DM on the Internal Structures of MIIC

(**A**) Six-hour chloroquine treatment relocalizes DR3/CFP and DM/YFP to the limiting membrane of empty expanded MIIC. HEK293 cells expressing DR3/CFP, DM/YFP, and Ii were processed for cryo immuno-EM after 6 hr incubation with chloroquine. DR3, 15 nm gold; DM, 10 nm gold. Both proteins localize to the limiting membrane in structures lacking internal vesicles.
(**B**) DR3/CFP does not interact with DM/YFP at the limiting membrane. HEK293 cells expressing DR3/CFP, DM/YFP, and Ii (upper panel) or DO/CFP and DM/YFP (middle panel) were analyzed by CLSM-FRET at 37°C after 6 hr of chloroquine treatment. The CFP, YFP, FRET levels, and donor FRET efficiency (E_D) were determined (details in Figure 3A). The lower panel shows the E_D in false colors projected on the CFP signal in white. Whereas DM and DO interact on the limiting membrane, no interaction is observed for DR3 and DM (n > 50 observations).
(**C**) The structure of partially swollen MIIC after 3 hr chloroquine treatment. HEK293 cells expressing DR3/CFP, DM/YFP and Ii were cultured for 3 hr in the presence of chloroquine before analysis by cryo immuno-EM. Swollen MIIC are observed still containing internal structures. DR (15 nm gold) and DM (10 nm gold) are located on both the internal vesicles and limiting membrane.
(**D**) DR3/CFP interacts with DM/YFP on the internal structures of MIIC. Living HEK293 cells transfected with DR3/CFP, DM/YFP, and Ii (upper panel) or DO/CFP, DM/YFP (middle panel) were analyzed by CLSM-FRET at 37°C after 3 hr of chloroquine treatment. Panels are organized identical as in (B). Whereas DM and DO interact on both the internal structures and the limiting membrane, DR3 and DM only interact on the internal structures (n > 100 observations).

zole), and consequently input of new membrane material prevented (suppl. Fig S6 inset). Membranes for the expanding limiting membrane can only be supplied by the internal structures under this condition. 2. Markers for internal vesicles like CD63 were found at the limiting membrane after long-term chloroquine treatment (data not shown). 3. EM showed that the swollen MIIC did not contain internal vesicles after 4-6h chloroquine treatment, as these had supplied the material for the expanding limiting membrane. Indeed, also DR3/CFP and DM/YFP were located at the limiting membrane by immuno-EM (Fig 5A) and CLSM (Fig 5B) in structures without internal vesicles. Thus, long-term chloroquine treatment, which is known to prevent MHC class II antigen presentation, appears to alter the architecture of an MIIC structure by backfusion of the internal vesicles with the limiting membrane.

We made use of this MIIC remodeling in subsequent experiments where the interaction between DM and DR3 (and between DM and DO as a control) was measured in cells treated for 6h with 200 μM chloroquine (Fig 5B). The interaction (as visualized by CLSM-FRET) between DM and DO was not affected on swollen late endosomal structures (middle panel), whereas DM and DR3 did not interact on the limiting membrane (the only membrane) of these structures (upper panel). The concentration of DR3/CFP and DM/YFP does not decrease when the expansion of MIIC is the result of backfusion of internal structures. This implies that the FRET observed in Fig 3A and Fig 4A was

not caused by coincidental collisions, but resulted from more stable interactions. This suggested that interactions between DR3 and DM in MIIC occur exclusively at the internal structures.

The size of MIIC (~500nm) is too small to distinguish between limiting and internal membranes by light microscopy. The swelling of MIIC by chloroquine occurs gradually. Therefore, we expected to obtain partially swollen structures with internal vesicles 2-3h after chloroquine addition, providing sufficient spatial resolution to distinguish internal and limiting membranes by CLSM-FRET. Immuno-EM 3h after chloroquine treatment showed swollen structures of around 1-2 µm with internal vesicles still containing DR3 and DM molecules (Fig 5C). These MIIC were sufficiently large to resolve internal and limiting membranes by CLSM, and FRET between DR3/CFP and DM/YFP in the partially swollen MIIC was measured (Fig 5D, upper panel). Although DM and DR3 are both present on the limiting and internal membranes, a substantial interaction was only observed in the internal structures and not at the limiting membrane. To exclude a decrease in DM and/or DR3 concentration due to the addition of membranes derived from fused vesicles, we repeated the experiment on nocodazole treated cells. This gave identical results (suppl. Fig S6). As a control, DM and DO showed FRET at both the limiting and internal membranes under identical conditions (Fig 5D, middle panel). These data indicate that MIIC are not homogeneous structures, but that they contain various subdomains that allow a productive interaction between DM and DR3 only on the internal structures but not the limiting membrane.

Inhibition of formation of internal structures prevents the interaction between HLA-DR3 and HLA-DM.

The PI 3-kinase VPS34 is required to initiate a cascade of events resulting in recruitment of ESCRT complexes, and ultimately formation of internal structures within multivesicular bodies (Katzmann *et al*., 2002). Inhibition of hVPS34, either genetically or with chemical inhibitors (Fernandez-Borja *et al*., 1999), results in swollen structures only containing a limiting membrane. Inhibition of hVPS34 would thus be an alternative to recruit DR3/CFP and DM/YFP to the limiting membrane. However, unlike the situation for chloroquine, the structures remain acidic (suppl. Fig S7). An RNAi construct targeting hVPS34 was co-transfected with mRFP in HEK293 cells expressing DR3/CFP, DM/YFP and the invariant chain, as well as in cells expressing DO/CFP, DM/YFP as a control. Only mRFP-positive cells were analyzed for swollen structures, and FRET and donor FRET efficiency were determined (Fig 6). Whereas DM/YFP

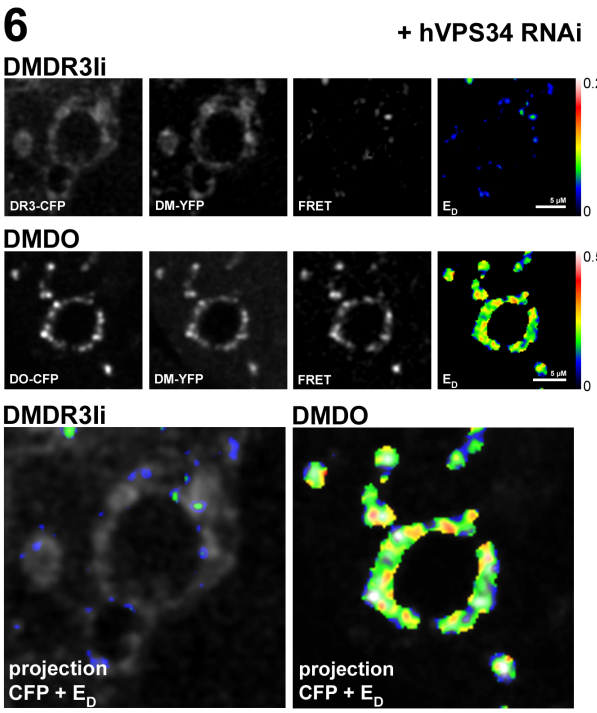


Figure 6. Inhibition of MVB Formation and the Interaction of HLA-DR3 with HLA-DM

HEK293 cells expressing DR3/CFP, DM/YFP and Ii, or DO/CFP and DM/YFP were transfected with two constructs encoding the RNAi for hVPS34 and soluble mRFP, respectively. After 72 hr, living cells expressing mRFP (not shown) with swollen MIIC were analyzed. A zoom-in of an expanded structure is shown. The CFP signal, YFP signal, FRET, and donorFRET efficiency (E_D) measurements are indicated (details in Figure 3A). The lower panel shows the E_D projected in false colors on the CFP signal in white. Whereas both DR3/CFP and DM/YFP are present at the limiting membrane of the expanded MIIC, they do not interact (n > 50 independent measurements).

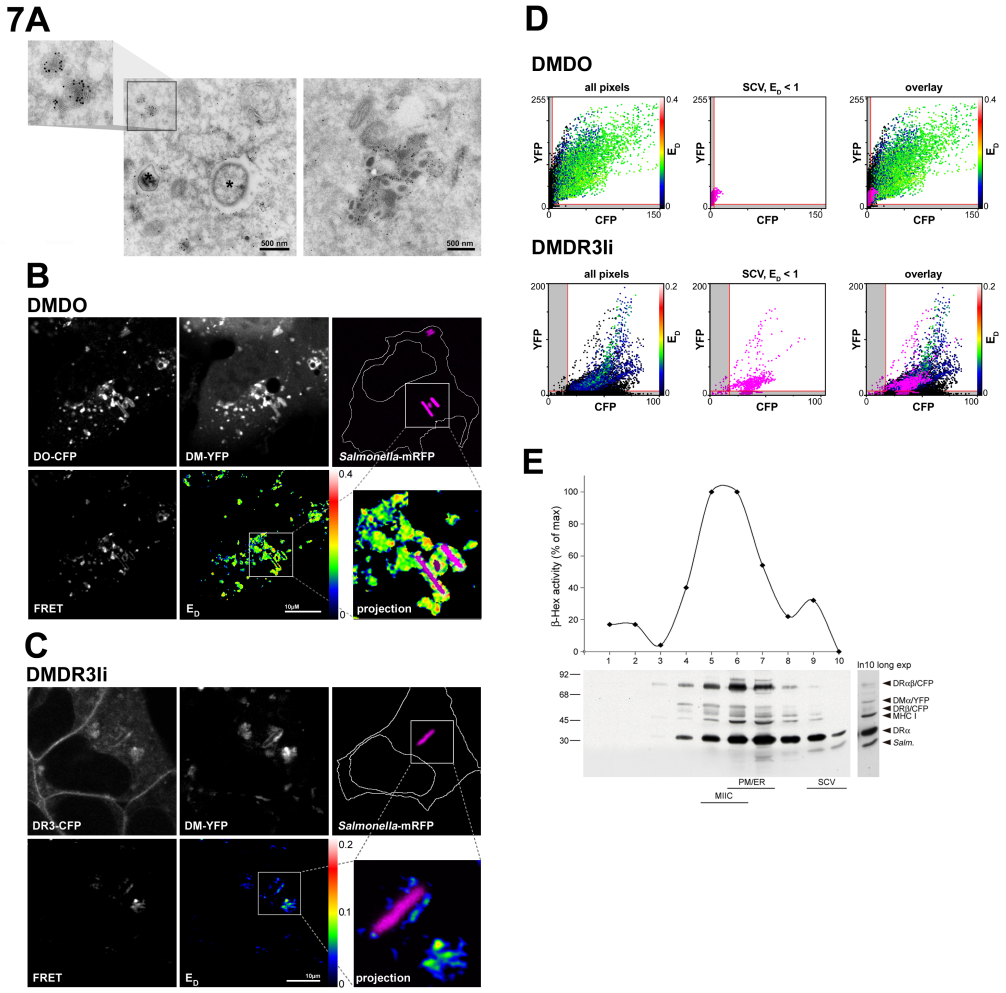


Figure 7. Interactions between HLA-DR3 and HLA-DM on Phagosomal Membranes

(**A**) Salmonella containing vacuoles (SCV), MIIC and internal vesicles. HEK293 cells expressing DR3/CFP, DM/YFP and Ii were infected with Salmonella for 4 hr prior to fixation and processing for immuno-EM. Left panel shows two SCV that have considerably expanded (asterices). The SCV label for DR (15 nm gold) and DM (10 nm gold) at the limiting membrane, and lack internal structures. Inset: higher magnification of MIIC labeling for DR and DM within the same section. Right panel: formation of internal structures upon Salmonella death. The typical dense structures represent remnants of Salmonella in a structure labeling for DR and DM. Note the appearance of internal structures.
(**B**) Interactions between DO/CFP and DM/YFP on SCV. HEK293 cells expressing DO/CFP and DM/YFP were infected by mRFP expressing Salmonella for 4 hr before imaging by CLSM-FRET at 37°C. DO/CFP, DM/YFP and mRFP-Salmonella can be simultaneously detected, as indicated. The cell boundary and the nucleus are drawn in the image showing the location of the bacterium. The expanded SCV are detectable in the CFP and YFP channels. Donor FRET efficiency (E_D) is shown in false colors with the corresponding values. The efficiency of interaction between DO and DM is not affected on the Salmonella-containing vacuoles. Inset: magnification of the SCV region depicted in the E_D picture with a projection of Salmonella in pink (n > 50 observations).
(**C**) DR3/CFP and DM/YFP fail to interact in mRFP-expressing Salmonella containing vacuoles. HEK293 cells expressing DR3/CFP, DM/YFP and Ii were infected with mRFP-Salmonella for 4 hr before analysis by CLSM-FRET at 37°C. The various fluorophores were detected as in B. mRFP-Salmonella containing phagosomes with DR3/CFP and DM/YFP did not show FRET in contrast to normal MIIC in the same cell. (n > 60 observations). Note that a number of these normal MIIC are located close to the SCV.
(**D**) Analysis of FRET efficiency images. The images in (B) and (C) were analyzed as described in Figure 3E. The gray region depicts the treshold settings in these experiments. The CFP and YFP intensities of the pixels corresponding to the limiting membrane of the SCV, where no FRET was detected, are indicated in purple in the DO/CFP, DM/YFP (top), and the DR3/CFP and DM/YFP (bottom) plots. The intensities of DR3/CFP and DM/YFP on the SCV are comparable to MIIC within the same cell where normal FRET is measured.
(**E**) Peptide loading of DR3/CFP in subcellular fractions. HEK293 cells expressing DR3/CFP, DM/YFP, and Ii were infected with Salmonella for 4 hr, followed by subcellular fractionation (fraction 1–10). After fractionation, the vesicles were pelleted, incubated in SDS-loading buffer, and analyzed by SDS-PAGE and Westernblotting with various antibodies (bottom panel). The position of the various proteins is indicated. Fraction 5–6 showed β-hexosaminidase activity (top panel), and corresponded to MIIC. Fraction 6,7, marked by MHC class I, contained the plasma membrane (PM/ER). The SCV ran at a high density and contained a 30 kDa protein (fraction 9,10). Right lane: longer exposure of fraction 10. The conditions used, separated unstable (DRα, 35 kDa) from compact DR3/CFP molecules (DRαβ-CFP, 85 kDa). Compact DR/CFP molecules were located in the MIIC and PM/ER fractions, but were virtually absent in the SCV fractions.

and DO/CFP showed FRET with normal efficiency, no FRET was detected between DR/CFP and DM/YFP at the limiting membrane of these swollen structures, analogous to the situation where MIIC was expanded by chloroquine (Fig 6). In conclusion, two treatments known to inhibit antigen presentation by MHC class II molecules (Allen and Unanue, 1984; Song *et al*., 1997), also induce localization of DR3 and DM to the limiting membrane of MIIC, where the interaction between these two proteins is prevented.

HLA-DR3 interactions with HLA-DM and peptide loading on phagosomal membranes.

If DR3 and DM fail to interact efficiently on limiting membranes, this may explain examples of immune escape observed under physiological conditions. In particular, bacterial pathogens like Mycobacterium tuberculosis and Salmonella typhimurium survive and propagate in acidified, self-induced phagosomes often unnoticed by the immune system (Ramachandra *et al*., 2001). Phagosomes contain a limiting membrane only, unless the pathogen is killed. Recently, it has been shown that Salmonella secretes the PIP2-phosphatase SopB into the cytoplasm of infected cells that hydrolyzes a downstream product of hVPS34 (PI(3,5)P2), thus inducing phagosome formation (Hernandez *et al*., 2004). Hence, is the interaction between DR3 and DM inhibited at the phagosomal membrane? We infected HEK293 cells expressing DR3/CFP, DM/YFP and invariant chain with Salmonella for 4h and processed the cells for immuno-EM (Fig 7A, left panel). Intracellular Salmonella was found in a typical phagosome (termed the Salmonella-containing vacuole or SCV), containing DR3 and DM at the limiting membrane. No internal vesicles were found, unless the bacterium was degraded (Fig 7A, right panel). Conventional, unaffected MIIC were also found in the same cell (Fig 7A, left panel insert). Next, we determined whether FRET between DR3/CFP and DM/YFP could be detected in SCV. As a control, we measured FRET between DM/YFP and DO/CFP on the same compartment. To allow simultaneous visualization of the intracellular bacteria, we generated mRFP-expressing Salmonellae. Fig 7B shows CLSM-FRET images of SCV and MIIC after 4h Salmonella infection in cells expressing DM and DO. The interaction between DO/CFP and DM/YFP was not affected on the phagosomal membrane. The interaction of DM and DR3 on SCV is shown in Fig 7C. To exclude the possibility that FRET between DR3/CFP and DM/YFP was not observed because their fluorescent intensities fell below the treshold set for background fluorescence, we analyzed the data in Fig 7B and 7C by the same 2D intensity plot approach used in Fig 3E. In addition, the CFP and YFP intensities of the pixels corresponding to the limiting membrane of the SCV where FRET was not detected are indicated in purple (Fig 7D). The limiting membrane of SCV contained hardly any pixels without FRET between DO/CFP and DM/YFP (resulting in only few purple dots in the middle panel). In contrast, pixels lacking FRET efficiency at the SCV membrane were abundantly found in the DR3/CFP, DM/YFP cells. The intensities of CFP and YFP in the majority of these SCV pixels corresponded to those found for MIIC in the same cell with positive FRET efficiencies. This analysis was repeated by considering the poisson distributed noise for the calculated E_D per pixel (suppl. Fig S8). Collectively, these data show an equally efficient interaction between DO and DM in MIIC and SCV, whereas the interaction between DR3 and DM was only observed in the MIIC and not the SCV membrane. Thus, within the same cell, two types of MHC class II containing compartments were found: MIIC, where DM and DR3 could engage in antigen loading, and SCV, where DM and DR3 were prevented from interacting. MIIC vesicles showed continuous kiss and run type of contacts with the SCV (data not shown), but no DM/DR3 interaction was observed on the limiting membrane in more than 60% of the SCV (41 negative, 25 positive SCVs, n=66). When Salmonella was intracellularly degraded, internal structures re-appeared (Fig 7A, right panel), probably leading to some SCVs with detectable FRET between DM and DR3. Thus, the interaction between DR3 and DM was obstructed in intact phagosomal structures, similar to the situation in swollen MIIC, apparently because the micro-environment of internal endosomal membranes is a prerequisite for this interaction.

Is the loading of MHC class II molecules in SCV affected, as would be predicted from the FRET data? HEK293 cells expressing DR3/CFP, DM/YFP and the invariant chain were infected with Salmonella for 4h before subcellular fractionation. 20% of each fraction was used to measure β-hexosaminidase activity to position the late endosomes and lysosomes (Fig 7E, upper panel). The rest was incubated in SDS-sample buffer at room temperature before separation by SDS-PAGE and Western blotting. This procedure should allow detection of compact type, SDS-stable, peptide-loaded DR3/CFP molecules (Germain and Hendrix, 1991). The nitrocellulose filter was probed sequentially with antibodies directed against the DRα chain and DR3αβ-peptide complex, against GFP, MHC class I molecules, and against a 30kD Salmonella protein. The position of the various proteins is given in the compilation (Fig 7E, lower panel). MHC class I marks the plasma membrane and ER (fraction 6,7), β-hexosaminidase and DMα-YFP the MIIC (fractions 5,6), and the Salmonella protein the SCV (fractions 9,10). SCV contained both DM/YFP and DR3/CFP, as

was also shown by CLSM and EM (Fig 7A-C). Still, whereas a large portion of DR3/CFP was in a compact state in the plasma membrane and MIIC-containing fractions, hardly any peptide-loaded DR3 molecules were observed in SCV (compare lanes 5 and 9 figure 7E). Peptide loading of DR3 in SCV was apparently very inefficient, corresponding with the poor interaction observed between DM and DR3 on the limiting membranes of SCV and MIIC.

Discussion

The MIIC was defined in 1991 as a late endosomal compartment with a multilamellar morphology containing MHC class II molecules (Peters *et al*., 1991). Since then, a number of factors have been defined, notably cathepsins (Honey and Rudensky, 2003) and DM (Denzin and Cresswell, 1995; Sherman *et al*., 1995), required for successful antigen loading of MHC class II molecules. The localization of DM to MIIC, defined it as the major site for antigen loading of MHC class II molecules (Sanderson *et al*., 1994). The interaction between DM and MHC class II molecules has been shown *in vitro* and by co-isolation (Doebele *et al*., 2000; Sanderson *et al*., 1996; Ullrich *et al*., 1997). Critical for this interaction is acidic pH, as expected for a late endosomal chaperone. How DM and DR interact in living cells has been unclear. For this reason, we generated cells expressing DR3 conjugated to CFP and YFP-labeled DM. DR3/CFP required the invariant chain for efficient release from the ER and transport to MIIC. The CFP/YFP modifications did not block peptide loading of DR3 since compact, SDS-stable, DR3/CFP molecules were formed with the support of DM/YFP. Next, we studied the interaction between DR3 and DM in living cells by FRET analysis. As a control, we used a cell line expressing DM/YFP and DO/CFP. DO is very similar to DR3, but stably interacts with DM. Because of their high similarity, DO may mimic DR for DM molecules. However, since overexpressed DO does not affect the FRET efficiency between DR3 and DM, this is unlikely. DO is apparently not a competitor for DR3 binding to DM but probably binds at another site thus affecting the (pH-dependent) chaperoning activity of DM.

The internal membranes of the MIIC have a different protein and lipid composition than the limiting membrane. DM and DR can be found in both endosomal subcompartments, albeit in variable amounts (Kleijmeer *et al*., 1997). We have investigated DR/DM interactions in the MIIC by FRET. Like their untagged counterparts, the DR3/CFP and DM/YFP molecules localized to both the internal structures and the limiting membrane, but FRET between these molecules was only seen on the internal structures. In order to optically separate internal and limiting membranes, the MIIC was swollen by chloroquine treatment. Chloroquine induces the fusion of internal structures with the limiting membrane, which subsequently expands at the cost of the internal structures. Long-term treatment with chloroquine completely depleted the internal structures and DR3 and DM resided at the limiting membrane where they failed to interact. Chloroquine treatment is a common way to inhibit (most) MHC class II responses. This could be the result of decreased antigen degradation by lysosomal proteases due to neutralization (although most cathepsins are active at neutral pH), less efficient support by DM (yet we show that the interaction with DR3 is not disturbed by neutralization), but may also be the result of repositioning DM and DR3 to the limiting membrane where they do not interact.

How is the interaction between DM and DR3 supported at the internal structures? Obvious candidates are the tetraspans CD63 and CD82, given their almost exclusive location in the internal structures and their interaction with MHC class II and DM (Escola *et al*., 1998; Hammond *et al*., 1998). It has been suggested that microdomain clusters of DR/DM and the tetraspans could have different peptide loading properties (Kropshofer *et al*., 2002). However, the tetraspans CD63 and CD82 are also relocated to the limiting membrane following chloroquine treatment (not shown) where DR3 and DM do not interact. Thus, the tetraspans CD63 and CD82 are not sufficient, if at all required, for stable DR3/DM interactions. Whether other proteins or lipids are involved in the formation of a putative 'MHC class II loading microdomain' inside the MIIC, is as yet unclear.

Phagosomes are endosomal structures where intracellular bacteria survive and even propagate. Morphologically, these structures resemble a swollen MIIC, and can be considered a limiting membrane around the bacterium. Various studies describe the effect of intracellular bacteria on antigen presentation. CD4+ T cells can be easily isolated after most bacterial infections, but it is unclear whether this is a response to a killed bacterium or a viable one. In vitro T cell assays yield mixed conclusions (Zur Lage *et al*., 2003). T cell responses against other antigens co-incubated with the bacterium are usually not affected, although some infections can reduce or inhibit antigen presentation by MHC class II (Flynn and Chan, 2003). Whereas various bacteria neutralize phagosomes, Salmonella allows acidification, which is even required for the secretion of effector proteins (Beuzon *et al*., 1999). Salmonella apparently forms phagosomes by secreting a PIP2-phosphatase, SopB, thus inactivating the hVPS34-ESCRT system of internal vesicle formation (Hernandez *et al*., 2004). Likewise, M. tuberculosis toxin directly inactivates hVPS34 (Vergne *et al*., 2003). Downregula-

tion of hVPS34 by RNAi induced expanded MIIC and prevented the interaction between DR3/CFP and DM/YFP on the limiting membrane. This also inhibits antigen presentation by MHC Class II (Song *et al*., 1997). In addition, the expression of DM/YFP and DR3/CFP at the SCV was lower. Whether this is the consequence of the altered interactions is unclear.

Still, the effect on DM/DR interactions is local. In the same cells, 'normal' MIIC were found where DM and DR3 associated both in biochemical and FRET assays. Fractionation studies indicated that MHC class II loading occurs in MIIC structures, but poorly in SCV. This suggests that intracellularly growing bacteria prevent local MHC class II presentation by preventing the formation of the typical architecture found in MIIC. At present, it is unclear whether this is just the result of their physical size or a situation actively maintained by the bacterium. In approximately 35% of the cases, we detected FRET between DM and DR3 in Salmonella containing phagosomes, which could be the result of death and disintegration of the bacterium; conditions where internal DM and DR3 containing structures reappear in the SCV. However, surviving and viable intracellular pathogens will remain undetected by CD4+ T cells as long as they prevent leakage of antigens into conventional MIIC. This local immune evasion may explain why other antigen presenting molecules have been developed, the CD1 family, to present antigens in a manner independent of DM (Vincent *et al*., 2003).

We have visualized the interaction of DM and DR3 in living cells by FRET and have defined an MHC class II loading microdomain. DR3 interacted with its chaperone DM only on the internal membranes within an MIIC. Consequently, structures containing only a limiting membrane will not support efficient interactions between these two molecules, a situation observed in phagosomes. By preventing the formation of the conventional architecture of MIIC, Salmonella excludes the creation of 'MHC class II loading microdomains', resulting in ineffective antigen presentation by MHC class II molecules.

Methods are described in the Supplementary section.

Acknowledgements

We thank Eric Reits, Tom Groothuis, Joost Neijssen, and Ingrid Jordens for discussions, Lauran Oomen for help with CLSM images, Nico Ong for photography, and Adam Benham and Nicole van der Wel for reading the manuscript. This work was supported by grants from the Dutch Cancer Society KWF and the Netherlands Scientific Organization N.W.O.

References

Allen, P. M., and Unanue, E. R. (1984). Antigen processing and presentation by macrophages. Am J Anat 170, 483-490.

Bastiaens, P. I., and Squire, A. (1999). Fluorescence lifetime imaging microscopy: spatial resolution of biochemical processes in the cell. Trends Cell Biol 9, 48-52.

Beuzon, C. R., Banks, G., Deiwick, J., Hensel, M., and Holden, D. W. (1999). pH-dependent secretion of SseB, a product of the SPI-2 type III secretion system of Salmonella typhimurium. Mol Microbiol 33, 806-816.

Boes, M., Cerny, J., Massol, R., Op den Brouw, M., Kirchhausen, T., Chen, J., and Ploegh, H. L. (2002). T-cell engagement of dendritic cells rapidly rearranges MHC class II transport. Nature 418, 983-988.

Brumell, J. H., and Grinstein, S. (2004). Salmonella redirects phagosomal maturation. Curr Opin Microbiol 7, 78-84.

Bryant, P. W., Lennon-Dumenil, A. M., Fiebiger, E., Lagaudriere-Gesbert, C., and Ploegh, H. L. (2002). Proteolysis and antigen presentation by MHC class II molecules. Adv Immunol 80, 71-114.

Calafat, J., Nijenhuis, M., Janssen, H., Tulp, A., Dusseljee, S., Wubbolts, R., and Neefjes, J. (1994). Major histocompatibility complex class II molecules induce the formation of endocytic MIIC-like structures. J Cell Biol 126, 967-977.

Chou, C. L., and Sadegh-Nasseri, S. (2000). HLA-DM recognizes the flexible conformation of major histocompatibility complex class II. J Exp Med 192, 1697-1706.

Cresswell, P. (1992). Chemistry and functional role of the invariant chain. Curr Opin Immunol 4, 87-92.

Denzin, L. K., and Cresswell, P. (1995). HLA-DM induces CLIP dissociation from MHC class II alpha beta dimers and facilitates peptide loading. Cell 82, 155-165.

Denzin, L. K., Sant'Angelo, D. B., Hammond, C., Surman, M. J., and Cresswell, P. (1997). Negative regulation by HLA-DO of MHC class II-restricted antigen processing. Science 278, 106-109.

Doebele, R. C., Busch, R., Scott, H. M., Pashine, A., and Mellins, E. D. (2000). Determination of the HLA-DM interaction site on HLA-DR molecules. Immunity 13, 517-527.

Escola, J. M., Kleijmeer, M. J., Stoorvogel, W., Griffith, J. M., Yoshie, O., and Geuze, H. J. (1998). Selective enrichment of tetraspan proteins on the internal vesicles of multivesicular endosomes and on exosomes secreted by human B-lymphocytes. J Biol Chem 273, 20121-20127.

Fernandez-Borja, M., Wubbolts, R., Calafat, J., Janssen, H., Divecha, N., Dusseljee, S., and Neefjes, J. (1999). Multivesicular body morphogenesis requires phosphatidyl-inositol 3-kinase activity. Curr Biol 9, 55-58.

Flynn, J. L., and Chan, J. (2003). Immune evasion by Mycobacterium tuberculosis: living with the enemy. Curr Opin Immunol 15, 450-455.

Förster, T. (1948). Zwischenmolekulare energiewandering und fluoreszenz. Annalen Physik 6, 55-75.

Germain, R. N., and Hendrix, L. R. (1991). MHC class II structure, occupancy and surface expression determined by post-endoplasmic reticulum antigen binding. Nature 353, 134-139.

Ghosh, P., Amaya, M., Mellins, E., and Wiley, D. C. (1995). The

structure of an intermediate in class II MHC maturation: CLIP bound to HLA-DR3. Nature 378, 457-462.

Gruenberg, J. (2003). Lipids in endocytic membrane transport and sorting. Curr Opin Cell Biol 15, 382-388.

Hammond, C., Denzin, L. K., Pan, M., Griffith, J. M., Geuze, H. J., and Cresswell, P. (1998). The tetraspan protein CD82 is a resident of MHC class II compartments where it associates with HLA-DR, -DM, and -DO molecules. J Immunol 161, 3282-3291.

Harding, C. V., Ramachandra, L., and Wick, M. J. (2003). Interaction of bacteria with antigen presenting cells: influences on antigen presentation and antibacterial immunity. Curr Opin Immunol 15, 112-119.

Hernandez, L. D., Hueffer, K., Wenk, M. R., and Galan, J. E. (2004). Salmonella modulates vesicular traffic by altering phosphoinositide metabolism. Science 304, 1805-1807.

Honey, K., and Rudensky, A. Y. (2003). Lysosomal cysteine proteases regulate antigen presentation. Nat Rev Immunol 3, 472-482.
Katzmann, D. J., Odorizzi, G., and Emr, S. D. (2002). Receptor down-regulation and multivesicular-body sorting. Nat Rev Mol Cell Biol 3, 893-905.

Kleijmeer, M. J., Morkowski, S., Griffith, J. M., Rudensky, A. Y., and Geuze, H. J. (1997). Major histocompatibility complex class II compartments in human and mouse B lymphoblasts represent conventional endocytic compartments. J Cell Biol 139, 639-649.

Kropshofer, H., Arndt, S. O., Moldenhauer, G., Hammerling, G. J., and Vogt, A. B. (1997). HLA-DM acts as a molecular chaperone and rescues empty HLA-DR molecules at lysosomal pH. Immunity 6, 293-302.

Kropshofer, H., Spindeldreher, S., Rohn, T. A., Platania, N., Grygar, C., Daniel, N., Wolpl, A., Langen, H., Horejsi, V., and Vogt, A. B. (2002). Tetraspan microdomains distinct from lipid rafts enrich select peptide-MHC class II complexes. Nat Immunol 3, 61-68.

Liljedahl, M., Winqvist, O., Surh, C. D., Wong, P., Ngo, K., Teyton, L., Peterson, P. A., Brunmark, A., Rudensky, A. Y., Fung-Leung, W. P., and Karlsson, L. (1998). Altered antigen presentation in mice lacking H2-O. Immunity 8, 233-243.

Marks, M. S., Roche, P. A., van Donselaar, E., Woodruff, L., Peters, P. J., and Bonifacino, J. S. (1995). A lysosomal targeting signal in the cytoplasmic tail of the beta chain directs HLA-DM to MHC class II compartments. J Cell Biol 131, 351-369.

Morrison, L. A., Lukacher, A. E., Braciale, V. L., Fan, D. P., and Braciale, T. J. (1986). Differences in antigen presentation to MHC class I-and class II-restricted influenza virus-specific cytolytic T lymphocyte clones. J Exp Med 163, 903-921.

Mosyak, L., Zaller, D. M., and Wiley, D. C. (1998). The structure of HLA-DM, the peptide exchange catalyst that loads antigen onto class II MHC molecules during antigen presentation. Immunity 9, 377-383.

Neefjes, J. J., and Ploegh, H. L. (1992). Inhibition of endosomal proteolytic activity by leupeptin blocks surface expression of MHC class II molecules and their conversion to SDS resistance alpha beta heterodimers in endosomes. Embo J 11, 411-416.

Ohkuma, S., and Poole, B. (1981). Cytoplasmic vacuolation of mouse peritoneal macrophages and the uptake into lysosomes of weakly basic substances. J Cell Biol 90, 656-664.

Ormo, M., Cubitt, A. B., Kallio, K., Gross, L. A., Tsien, R. Y., and Remington, S. J. (1996). Crystal structure of the Aequorea victoria green fluorescent protein. Science 273, 1392-1395.

Pashine, A., Busch, R., Belmares, M. P., Munning, J. N., Doebele, R. C., Buckingham, M., Nolan, G. P., and Mellins, E. D. (2003). Interaction of HLA-DR with an acidic face of HLA-DM disrupts sequence-dependent interactions with peptides. Immunity 19, 183-192.

Peters, P. J., Neefjes, J. J., Oorschot, V., Ploegh, H. L., and Geuze, H. J. (1991). Segregation of MHC class II molecules from MHC class I molecules in the Golgi complex for transport to lysosomal compartments. Nature 349, 669-676.

Ramachandra, L., Noss, E., Boom, W. H., and Harding, C. V. (2001). Processing of Mycobacterium tuberculosis antigen 85B involves intraphagosomal formation of peptide-major histocompatibility complex II complexes and is inhibited by live bacilli that decrease phagosome maturation. J Exp Med 194, 1421-1432.

Russell, D. G. (2003). Phagosomes, fatty acids and tuberculosis. Nat Cell Biol 5, 776-778.

Sanderson, F., Kleijmeer, M. J., Kelly, A., Verwoerd, D., Tulp, A., Neefjes, J. J., Geuze, H. J., and Trowsdale, J. (1994). Accumulation of HLA-DM, a regulator of antigen presentation, in MHC class II compartments. Science 266, 1566-1569.

Sanderson, F., Thomas, C., Neefjes, J., and Trowsdale, J. (1996). Association between HLA-DM and HLA-DR *in vivo*. Immunity 4, 87-96.

Sherman, M. A., Weber, D. A., and Jensen, P. E. (1995). DM enhances peptide binding to class II MHC by release of invariant chain-derived peptide. Immunity 3, 197-205.

Song, W., Wagle, N. M., Banh, T., Whiteford, C. C., Ulug, E., and Pierce, S. K. (1997). Wortmannin, a phosphatidylinositol 3-kinase inhibitor, blocks the assembly of peptide-MHC class II complexes. Int Immunol 9, 1709-1722.

Tsien, R. Y. (1998). The green fluorescent protein. Annu Rev Biochem 67, 509-544.

Ullrich, H. J., Beatty, W. L., and Russell, D. G. (2000). Interaction of Mycobacterium avium-containing phagosomes with the antigen presentation pathway. J Immunol 165, 6073-6080.

Ullrich, H. J., Doring, K., Gruneberg, U., Jahnig, F., Trowsdale, J., and van Ham, S. M. (1997). Interaction between HLA-DM and HLA-DR involves regions that undergo conformational changes at lysosomal pH. Proc Natl Acad Sci U S A 94, 13163-13168.

van Ham, M., van Lith, M., Lillemeier, B., Tjin, E., Gruneberg, U., Rahman, D., Pastoors, L., van Meijgaarden, K., Roucard, C., Trowsdale, J., *et al*. (2000). Modulation of the major histocompatibility complex class II-associated peptide repertoire by human histocompatibility leukocyte antigen (HLA)-DO. J Exp Med 191, 1127-1136.

van Ham, S. M., Tjin, E. P., Lillemeier, B. F., Gruneberg, U., van Meijgaarden, K. E., Pastoors, L., Verwoerd, D., Tulp, A., Canas, B., Rahman, D., *et al*. (1997). HLA-DO is a negative modulator of HLA-DM-mediated MHC class II peptide loading. Curr Biol 7, 950-957.

van Lith, M., van Ham, M., Griekspoor, A., Tjin, E., Verwoerd, D., Calafat, J., Janssen, H., Reits, E., Pastoors, L., and Neefjes, J. (2001). Regulation of MHC class II antigen presentation by sorting of recycling HLA-DM/DO and class II within the multivesicular body. In J Immunol, pp. 884-892.

Van Rheenen, J., Langeslag, M., and Jalink, K. (2004). Correcting confocal acquisition to optimize imaging of fluorescence resonance energy transfer by sensitized emission. Biophys J 86, 2517-2529.

Vergne, I., Chua, J., and Deretic, V. (2003). Tuberculosis toxin blocking phagosome maturation inhibits a novel Ca2+/calmodulin-PI3K hVPS34 cascade. J Exp Med 198, 653-659.

Vermeer, J. E., Van Munster, E. B., Vischer, N. O., and Gadella, T. W., Jr. (2004). Probing plasma membrane microdomains in cowpea protoplasts using lipidated GFP-fusion proteins and multimode FRET microscopy. J Microsc 214, 190-200.

Vincent, M. S., Gumperz, J. E., and Brenner, M. B. (2003). Understanding the function of CD1-restricted T cells. Nat Immunol 4, 517-523.

Vogt, A. B., Arndt, S. O., Hammerling, G. J., and Kropshofer, H. (1999). Quality control of MHC class II associated peptides by HLA-DM/H2-M. Semin Immunol 11, 391-403.

Wubbolts, R., Fernandez-Borja, M., Oomen, L., Verwoerd, D., Janssen, H., Calafat, J., Tulp, A., Dusseljee, S., and Neefjes, J. (1996). Direct vesicular transport of MHC class II molecules from lysosomal structures to the cell surface. J Cell Biol 135, 611-622.

Wubbolts, R., Leckie, R. S., Veenhuizen, P. T., Schwarzmann, G., Mobius, W., Hoernschemeyer, J., Slot, J. W., Geuze, H. J., and Stoorvogel, W. (2003). Proteomic and biochemical analyses of human B cell-derived exosomes. Potential implications for their function and multivesicular body formation. J Biol Chem 278, 10963-10972.

Zur Lage, S., Goethe, R., Darji, A., Valentin-Weigand, P., and Weiss, S. (2003). Activation of macrophages and interference with CD4+ T-cell stimulation by Mycobacterium avium subspecies paratuberculosis and Mycobacterium avium subspecies avium. Immunology 108, 62-69.

Supplemental Data

Supplemental Experimental Procedures

Antibodies and Fluorophores

The following antibodies were used. Mouse monoclonal antibodies HC-10 (class I Heavy Chain) (Stam *et al*.,1986); anti-CD63 (NKI-C3) (Vennegoor and Rumke, 1986); HLA-DR–specific mAbs 1B5 (Adams *et al*., 1983) and Tü36 (Shaw *et al*., 1985), and the HLA-DMα-specific mAb 5C1 (Sanderson *et al*., 1996). Rabbit polyclonal sera anti-DR (Neefjes *et al*., 1990), anti-GFP, anti-Salmonella (Salmonella 30 kDa) and rabbit anti-DOβ serum (van Ham *et al*., 1997), and the Ii-specific polyclonal serum ICN2 (Morton *et al*., 1995) have previously been described. The Cy5 and horseradish peroxidase–conjugated secondary antibodies were from Sigma-Aldrich co. (Steinheim, Germany). Fluorescent secondary antibodies were from Molecular Probes (Leiden, The Netherlands).

DNA Constructs and the Generation of Transfectants

Constructing pcDNA3.1 Zeo DMβ-IRES-DMα/YFP
A fusion construct between YFP and the C terminus of DMα was generated by PCR. pcDNA3.1 Zeo vector (Invitrogen) was digested with BamHI and EcoRI and ligated to an IRES sequence, digested with BamHI and EcoRI, forming IRES pcDNA3.1 Zeo. IRES pcDNA3.1 Zeo was subsequently digested with EcoRI and XhoI. The digest was ligated with DMα-YFP, digested with EcoRI and XhoI, forming pcDNA3.1 Zeo IRES DMαYFP. pcDNA3.1 Zeo-IRES-DMα/YFP was subsequently digested with NheI and NotI and ligated with DMβ (Copier *et al*., 1996), digested with NheI and NotI in presence of 0.5% BSA, forming pcDNA3.1 Zeo-DMβ-IRES-DMαYFP.

Constructing pCEP4Δ DOα−IRES-DOßCFP

Generation of a fusion construct between CFP and the C terminus of DOβ (Copier *et al*., 1996) was achieved via PCR. pCEP4Δ vector (van Ham *et al*., 2000) was digested with KpnI and HindIII. The digest was ligated with DOα (Marks *et al*., 1995), digested with KpnI and HindIII, forming pCEP4Δ DOα This construct was subsequently digested with EcoRV and NheI and ligated with IRES sequence, digested with EcoRV and NheI. Next, pCEP4Δ DOα-IRES was digested with NheI and XhoI and ligated with DOßCFP, digested with NheI and XhoI, forming pCEP4Δ DOα-IRES-DOßCFP. The same construct was generated without CFP attached to DOβ for use in HLA-DO overexpression experiments.

Constructing pcDNA3 DRα-IRES-DR3β/CFP

The fusion construct between CFP and the C terminus of DR3β was generated via PCR. pcDNA3 DOβ/GFP vector (van Ham *et al*., 1997) was digested with HindIII and BamHI and ligated with DR3β, digested with HindIII and BamHI, forming pcDNA3 DOα-GFP/DR3β. Subsequently, pcDNA3 DOα-GFP/DR3β was digested with BamHI and EcoRI and ligated with IRES, digested with EcoRV and NheI, forming pcDNA3 DRα-IRES. pcDNA3 DRα-IRES was subsequently digested with EcoRI and XhoI and ligated with DR3βCFP, digested with EcoRI and XhoI in Buffer H, forming pcDNA3 DRα-IRES-DR3β/CFP.

Constructing PSV51Ii, pcDNA3-H2B/CFP and -H2B/YFP

P30 invariant chain fragment was cut (EcoRI-BamHI) from Gem4sp6Ii vector and ligated blunt into the SmaI site of the PSV51L vector (gift from O.Bakke, Oslo). For selection, PSV51LIi was cotransfected with pcDNA3 ouabaine vector (Nijenhuis *et al*., 1994). GFP was swapped for CFP or YFP in H2B-GFP cloned in

pcDNA3 (Kanda *et al*., 1998) (by digestion with NotI and BamHI).

Constructing pSUPER- hVPS34

To generate the RNAi construct targeting the PIK3C3 gene (hVPS34), the RNAi vector pSUPER (Brummelkamp *et al*., 2002) was digested with BglII and HindIII and the annealed oligos containing the sequence AGTAGATTGGCTGGATAGA specific for hVPS34 were ligated into the vector.

Constructing mRFP-expressing Salmonella

Salmonella typhimurium strain SL1344 was transformed with a bacterial expression vector for mRFP (kind gift of R. Tsien). mRFP expressing bacteria were selected by fluorescence microscopy and further purified before use in tissue culture FRET experiments. All DNA manipulations were performed using standard procedures, and verified by sequencing.

Human Embryo Kidney (HEK) 293 cells were stably transfected with DOαIRESDOβ/CFP, DRα-IRESDR3β/CFP, DMβ-IRES-DMα/YFP, p30 invariant chain and/or pcDNA3 Ouabaine vector or left untransfected. These cells were grown on Dulbecco's modified Eagle's medium (DMEM) supplemented with 7.5% fetal calf serum (Gibco, Paisley, UK) in the presence or absence of 1000 µg/ml G418, 300µg/ml Hygromycin (Gibco, Paisley, UK), 500 µg/ml Zeocine (Invitrogen, Carlsbad, USA) and/or 2µM Ouabaine (Invitrogen, Carlsbad, USA), at 37°C in a humidified atmosphere containing 5% CO2. Stable expression of the CFP- and YFP-tagged proteins was ensured by regular selection of the CFP- and YFP-positive cells by FACS sorting. Stable transfectants of the melanoma cell line Mel JuSo (H2B-CFP, H2B-YFP) were grown in Iscove's medium with 7.5% FCS supplemented with 1000 µg/ml G418. For the HLA-DO competition experiments, 293 cells stably expressing HLA-DR3/CFP, HLA-DM/YFP and invariant chain were transiently transfected with DOαIRESDOβ and an empty vector mRFP vector (in 50:1 molar ratio) and analyzed 48 hr after transfection.

Biochemical and Western Blot Analyses

Cell surface protein labeling was performed by lactoperoxidase-catalyzed iodination with 1mCi Na125I on cells grown to subconfluency in a 75-cm2 tissue culture flask. Cells were washed four times with cold PBS, lysed in Tris-lysis buffer (pH 7.4) containing 0.5% NP-40 and 5mM MgCl2, and used for immunoprecipitations with antibody recognizing MHC ClassII αβ complexes (Tü36). Samples were analyzed by 10% SDS-PAGE. Total protein expression levels were analyzed by growing HEK293 cells, stably transfected with HLADR3/CFP, HLA-DM/YFP,-DR/CFP, HLA-DM/YFP,-DR/CFP and Ii, HLA-DM/YFP,-DO/CFP or left untransfected, to subconfluency in Ø 10cm dishes. Cells were washed four times with cold PBS, lysed in Tris lysis buffer (pH 7.4) containing 0.5% NP-40, 50mM Tris-HCl pH 7.4 and 5mM MgCl2. Lysates were split into two halves. One was incubated in SDS-sample buffer at 95°C for 5 min, the other left at room temperature. Samples were separated by 10% SDS-PAGE, transferred to nitrocellulose and immunolabeled with antibodies against GFP, HLA-DM, -DR, and -DO. To test for stability of the class II complex, boiled and unboiled samples were separated by 10% SDS-PAGE, transferred to nitrocellulose and incubated with antibody recognizing the DRα chain, both in the stable class II complex and as a free α chain (1B5). Equal amounts of protein were loaded.

CLSM and Immuno-Electronmicroscopy Analysis

For CLSM analysis, coverslips were coated with 5µg/ml fibronectin (Sigma-Aldrich co., Steinheim, Germany) in PBS for 1h at 37°C. Subsequently, HEK293 transfectants were seeded on the coated coverslips. These were fixed with methanol and stained with anti-CD63 antibodies NKI-C3, and secondary antibodies conjugated to Cy5. Images were taken with a Leica TCS SP2 System (Leica, Mannheim, Germany). HEK293 transfectants were fixed in a mixture of paraformaldehyde (4%) and glutaraldehyde (0.5%) prior to processing for immuno-electronmicroscopy. Cells were incubated with 200µM chloroquine for 3h or 6h before processing. For the Salmonella infection, Salmonella strain SL1344 was cultured o/n followed by renewed culture for 3h. For immuno-labeling, sections were incubated with purified mAb anti-human DMα (5C1), followed by incubations with rabbit anti-mouse IgG and 10nm protein A-conjugated colloidal gold. Subsequently, the sections were treated with 1% gluteraldehyde, followed by another incubation with rabbit anti-human class II serum and 15nm protein A-conjugated colloidal gold. After embedding in a mixture of methyl-cellulose and uranyl acetate, sections were analyzed with a Philips CM10 electron microscope (Eindhoven, the Netherlands).

Confocal FRET (CLSM-FRET) Imaging by Sensitized Emission

The HEK293 transfectants were grown on the coated coverslips for 72h before imaging. 24h prior to imaging, Mel JuSo cells, stably transfected with H2B-CFP or H2B-YFP were added to the culture. Prior to CLSM, culture medium was changed for 2ml CBS medium (140mM NaCl, 5mM KCl2, 2mM MgCl2, 1mM CaCl2, 23mM NaHCO3, 10mM D-Glucose, 10mM Hepes pH 7.3) under 5% CO2, and the coverslips were analyzed in a heated tissue culture chamber at 37°C. Where indicated, chloroquine was added at a final concentration of 200μM for 2.5-3h or 6h prior to analysis. In the short-term pH neutralization experiments, the same cell was analyzed prior to and directly after a 2′ chloroquine treatment. For the RNAi experiments, cells were transfected with the pSUPER construct targeting hVPS34 and an empty mRFP vector as a transfection marker in a 10:1 ratio. 72h after transfection, mRFP positive cells were analyzed. Fluorescence Resonance Energy Transfer between CFP and YFP molecules was studied by calculating the sensitized emission (the YFP emission upon CFP excitation) from separately acquired donor and acceptor images. Images were acquired on a DM-Ire2 inverted microscope fitted with TCS-SP2 scanhead (Leica, Mannheim, Germany). Three images were collected: CFP excited at 430nm and detected between 470 and 490 nm; indirect YFP: excited at 430nm and detected between 528 and 603nm; and direct YFP excited at 514nm, and detected between 528 and 603nm. When simultaneously mRFP-Salmonella was monitored, CFP emission was detected between 455 and 510nm for noise reduction, and YFP emission was detected between 525 and 550 nm to minimize leakage of mRFP signal into the YFP channel. mRFP was excited at 568nm, and detected between 582nm and 675nm. Remaining mRFP bleedthrough was eliminated by masking all pixels in the CFP, indirect YFP, and direct YFP images that corresponded to mRFP-positive pixels in the image taken of the mRFP-Salmonellae. Because of considerable overlap of CFP and YFP spectra, YFP emission was corrected for leakthrough of CFP emission and for direct excitation of YFP during CFP excitation. FRET was calculated from these data as described in detail (Van Rheenen *et al*., 2004). In brief, the images were shade-corrected and optionally smoothed. Sensitized emission (F_{Sen}) was calculated using correction factors obtained from cells expressing either CFP or YFP alone, which were updated for every image. Then the apparent FRET efficiency was calculated by relating the F_{Sen} to the total donor level (E_D). See supplementary information for more details. Given the microscope used, the fluorescence intensities measured, and the number of pixels analyzed, FRET efficiencies as low as ~0.5% can be measured reliably (K.J. unpublished observations). Resulting FRET efficiency images were analyzed by plotting the CFP and YFP intensities for all pixels in a 2D plot, with the corresponding FRET efficiency in false colors. Using MatLab7 software (The Mathworks, Natick, USA) a mask was generated to select all pixels above the threshold set for both the CFP and YFP intensities (to exclude background fluorescence). For each pixel the CFP, YFP and FRET efficiency values were extracted and plotted using pro Fit 6 software (Quansoft, Uetikon am See, Switzerland). In case of the Salmonella experiments, pixels representing the SCV were extracted that 1) were contained within a region of interest drawn around the bacterium, 2) had intensities of both CFP and YFP that were above the set treshold to exclude background fluorescence, and 3) had a FRET efficiency of 0. Also for these pixels, the CFP and YFP values were extracted and plotted. For the E_D histograms shown in Fig S8, all pixels of an MIIC and SCV with a donor or acceptor fluorescent intensity between 10 and 250 were considered. Donor FRET efficiencies of these pixels were binned in 30 categories from -0.75 to +0.75 and plotted in a histogram.

Fluorescence Lifetime-Imaging Microscopy

Fluorescence Lifetime-Imaging (FLIM) experiments were performed on a Leica inverted DM-IRE2 microscope equiped with a Lambert Instruments frequency domain lifetime attachment (Leutingewolde, The Netherlands), controlled by the vendors EZflim software. CFP was excited at 430nm with ~4mW power using a LED modulated at 40MHz. Emission was collected at 450-490nm using an intensified CCD camera. Calculated CFP lifetimes were referenced to a 1 μM solution of Rhodamine-G6 in medium that was set at 4.11ns lifetime, and calibrated using co-expressed H2B-CFP containing cells for which the lifetime was set to 2.7ns (Vermeer *et al*., 2004).

Subcellular Fractionation

HEK293 transfectants were infected with Salmonella for 4h. Cells were washed with PBS and scraped from the plate prior to dounching by an EMBL Cell Cracker. Debris was removed by a low spin centrifugation step and the post-nuclear supernatant was loaded on a 0.4-2.4M step-wise sucrose gradient (steps of 0.4M) in 10μM Tris-HCl pH8.0. This was centrifuged for 3h in a swing-out rotor (Beckman 40.1Ti) at 28.000 rpm. 0.5ml samples from the gradient were diluted 1:1 with PBS and 200μl was used in a standard β-hexosaminidase assay. The rest of the vesicles was pelleted by cen-

trifugation (15 min, 12.000g), and incubated in SDS-loading buffer for 5 min at room temperature prior to separation by 10% SDS-PAGE and Western blotting.

Information on FRET Calculations

For more details on FRET Calculations, see van Rheenen *et al*. (2004). FRET between CFP and YFP can be studied by calculating the sensitized emission (F_{Sen}), the acceptor emission upon donor excitation, from separately acquired CFP and YFP images. CFP and YFP have a spectral overlap. Therefore, the detected sensitized emission must be corrected for CFP leakthrough into the acceptor channel and direct excitation of YFP during CFP excitation to obtain the measured sensitized emission (M_{Sen}). Consequently, three images were acquired, MCFP; CFP excitation, and CFP detection, $M_{IndirectYFP}$; CFP excitation and YFP detection, $M_{DirectYFP}$; YFP excitation and YFP detection. From the M_{IndYFP} image, sensitized emission was calculated using the following equation:

$M_{Sen} = (M_{IndirectYFP} - \beta M_{CFP} - (\gamma-\alpha\beta)\ M_{DirectYFP}$ image)/ $(1-\beta\delta)$,

where α is the correction factor for YFP fluorescence excited and detected at CFP wavelength, β the leakthrough factor of fluorescence of CFP into YFP filters, δ the leakthrough factor of sensitized emission back onto the CFP filters, and γ the excitation efficiency of the YFP upon CFP excitation. These correction factors were obtained by co-culturing the cells of interest with cells expressing CFP and YFP only. α, γ, δ are obtained by imaging a cell containing only YFP and calculated as:

$\alpha = M_{CFP}/M_{DirectYFP}$
$\gamma = M_{IndirectYFP}/M_{DirectYFP}$
$\delta = M_{CFP}/M_{IndirectYFP}$
β is obtained by imaging a cell containing CFP only and calculated as:
$\beta = M_{IndirectYFP}/M_{CFP}$.

To obtain the efficiency of FRET, CFP fluorescence lost by FRET and measured in the MCFP channel (LostCFP) is related by the total CFP fluorescence measured in the MCFP channel (CFP fluorescence when FRET equals zero, $Total_{CFP}$) as:

$E_D = Lost_{Sen}/Total_{CFP}$,

where $Lost_{CFP}$ relates to the sensitized emission measured in the $M_{IndirectYFP}$ channel (M_{sen}) as:
$Lost_{CFP} = (Q_{CFP}/Q_{YFP})(C/(\beta D))M_{sen}$, and the total CFP fluorescence as:

$Total_{CFP} = (1+\zeta)M_{CFP} - (\zeta/\beta)M_{IndirectYFP} - (\alpha-\zeta((\gamma-\alpha\beta)/\beta))\ M_{DirectYFP}$,

where Q_{CFP} and QYFP are the quantum yield of respectively CFP and YFP, C is the fraction of CFP spectrum in the YFP channel, D the fraction of YFP spectrum in the YFP channel and ζ is a constant which can be derived from:

$\zeta = (\delta\beta - ((CQ_{CFP}/DQ_{YFP})/(1-\beta\delta)))$.

To reliably calculate sensitized emission, corrections should be performed on major sources of error and variability in confocal acquisition of M_{CFP}, $M_{IndirectYFP}$ and $M_{DirectYFP}$ images. Since different laser lines are used to excite CFP and YFP (430nm for MCFP and MIndirectYFP and 514 nm for MDirectYFP), chromatic aberrations within the objective and other optics, and small collimation differences in the laser beams result in an axial offset in the optical section of the acquired CFP and YFP images. To correct for this, M_{CFP} and $M_{IndirectYFP}$ images were acquired using 430nm excitation (optimal excitation for measuring FRET). Then, using the Z-galvanometer of the microscope stage, the preparation is refocused to minimize the axial offset where after the $M_{DirectYFP}$ image is acquired using 514nm excitation. After image acquisition, images were corrected for lateral image errors. The excitation intensity varies within an image (most apparent at the borders of an image), especially in confocal acquisition since the different excitation sources give different excitation intensity distributions. Because these excitation inhomogeneities are constant over time, they were corrected by normalizing the acquired images by reference images (e.g. images of CFP and YFP solutions). The excitation intensity not only varies laterally, but temporally as well, which makes the calculation of sensitized emission extremely difficult, since the correction factors α and γ will change in time. To correct for this, for every pair of images acquired, new control cells were imaged to reliably recalculate the correction factors. For exact details, see van Rheenen and coworkers (2004).
Of note: parts of these algorithms will be implemented in new software commercially available from Leica Microsystems AG.

Supplemental References

Adams, T.E., Bodmer, J.G., and Bodmer, W.F. (1983). Production and characterization of monoclonal antibodies recognizing the alpha-chain subunits of human ia alloantigens. Immunology 50, 613–624.

Brummelkamp, T.R., Bernards, R., and Agami, R. (2002). A system for stable expression of short interfering RNAs in mammalian cells. Science 296, 550–553.

Copier, J., Kleijmeer, M.J., Ponnambalam, S., Oorschot, V., Potter, P., Trowsdale, J., and Kelly, A. (1996). Targeting signal and subcellular compartments involved in the intracellular trafficking of HLA-DMB. J. Immunol. 157, 1017–1027.

Kanda, T., Sullivan, K.F., and Wahl, G.M. (1998). Histone-GFP fusion protein enables sensitive analysis of
chromosome dynamics in living mammalian cells. Curr. Biol. 8, 377–385.

Marks, M.S., Roche, P.A., van Donselaar, E., Woodruff, L., Peters, P.J., and Bonifacino, J.S. (1995). A lysosomal targeting signal in the cytoplasmic tail of the beta chain directs HLA-DM to MHC class II compartments. J. Cell Biol. 131, 351–369.

Morton, P.A., Zacheis, M.L., Giacoletto, K.S., Manning, J.A., and Schwartz, B.D. (1995). Delivery of nascent MHC class II-invariant chain complexes to lysosomal compartments and proteolysis of invariant chain by cysteine proteases precedes peptide binding in B-lymphoblastoid cells. J. Immunol. 154, 137–150.

Neefjes, J.J., Stollorz, V., Peters, P.J., Geuze, H.J., and Ploegh, H.L. (1990). The biosynthetic pathway of MHC class II but not class I molecules intersects the endocytic route. Cell 61, 171–183.

Nijenhuis, M., Calafat, J., Kuijpers, K.C., Janssen, H., de Haas, M., Nordeng, T.W., Bakke, O., and Neefjes, J.J. (1994). Targeting major histocompatibility complex class II molecules to the cell surface by invariant chain allows antigen presentation upon recycling. Eur. J. Immunol. 24, 873–883.

Sanderson, F., Thomas, C., Neefjes, J., and Trowsdale, J. (1996). Association between HLA-DM and HLA-DR *in vivo*. Immunity 4, 87–96.

Shaw, S., Ziegler, A., and DeMars, R. (1985). Specificity of monoclonal antibodies directed against human and murine class II histocompatibility antigens as analyzed by binding to HLA-deletion mutant cell lines. Hum. Immunol. 12, 191–211.

Stam, N.J., Spits, H., and Ploegh, H.L. (1986). Monoclonal antibodies raised against denatured HLA-B locus heavy chains permit biochemical characterization of certain HLA-C locus products. J. Immunol. 137, 2299–2306.

van Ham, M., van Lith, M., Lillemeier, B., Tjin, E., Gruneberg, U., Rahman, D., Pastoors, L., van Meijgaarden, K., Roucard, C., Trowsdale, J., *et al*. (2000). Modulation of the major histocompatibility complex class IIassociated peptide repertoire by human histocompatibility leukocyte antigen (HLA)-DO. J. Exp. Med. 191, 1127–1136.

van Ham, S.M., Tjin, E.P., Lillemeier, B.F., Gruneberg, U., van Meijgaarden, K.E., Pastoors, L., Verwoerd, D.,

Tulp, A., Canas, B., Rahman, D., *et al*. (1997). HLA-DO is a negative modulator of HLA-DM-mediated MHC class II peptide loading. Curr. Biol. 7, 950–957.

van Rheenen, J., Langeslag, M., and Jalink, K. (2004). Correcting confocal acquisition to optimize imaging of fluorescence resonance energy transfer by sensitized emission. Biophys. J. 86, 2517–2529.

Vennegoor, C., and Rumke, P. (1986). Circulating melanoma-associated antigen detected by monoclonal antibody NKI/C-3. Cancer Immunol. Immunother. 23, 93–100.

Vermeer, J.E., Van Munster, E.B., Vischer, N.O., and Gadella, T.W., Jr. (2004). Probing plasma membrane microdomains in cowpea protoplasts using lipidated GFP-fusion proteins and multimode FRET microscopy. J. Microsc. 214, 190–200.

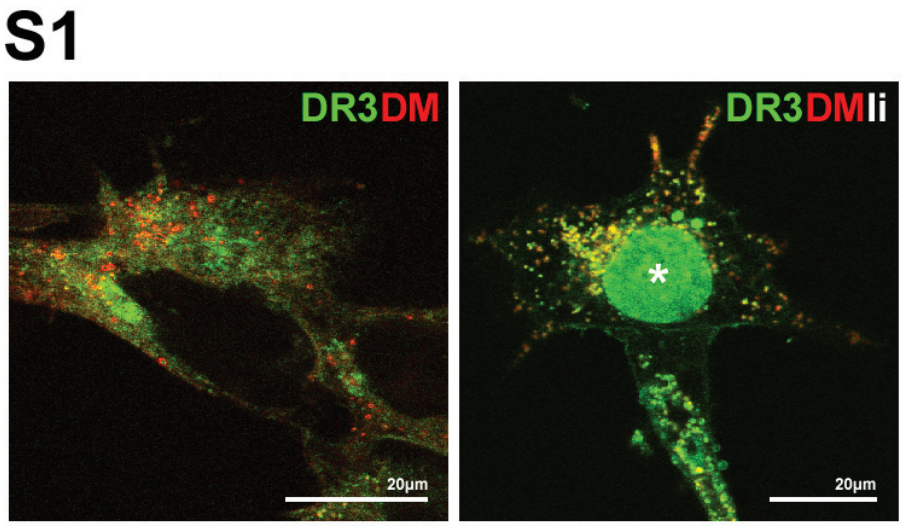


Figure S1. The Invariant Chain Ii Releases HLA-DR/CFP from the ER for Transport to HLA-DM Containing MIIC and the Plasma Membrane

HEK293 cells stably expressing DR3/CFP and DM/YFP (left panel) were microinjected with expression vectors for Ii and H2B-GFP (asterix). The position of DR3 (in green) and DM (in red) was subsequently monitored. In the absence of Ii, DR3/CFP is strongly expressed in the ER. Ii induces ER release and transport to DM containing vesicles and the plasma membrane.

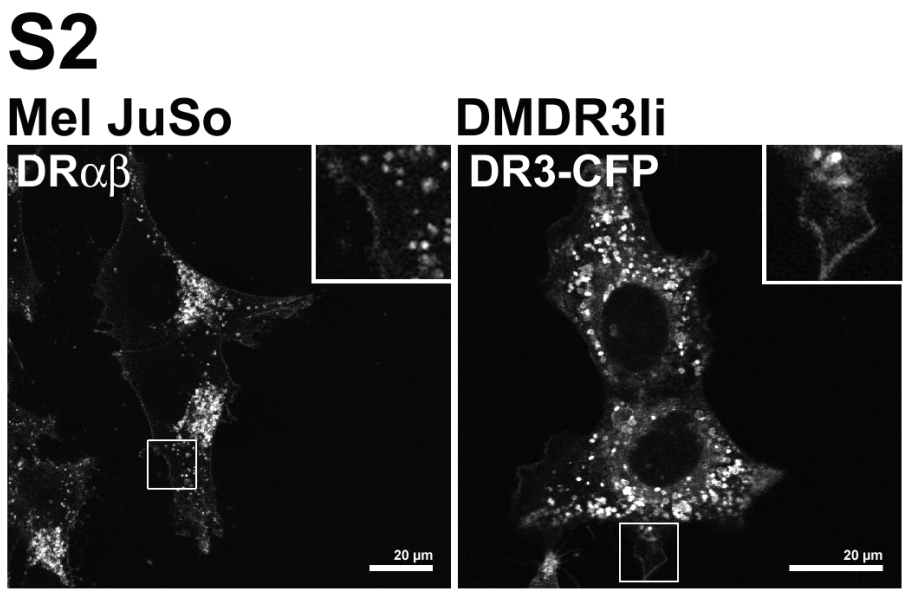


Figure S2. HLA-DR3/CFP Has a Similar Intracellular Distribution Compared to HLA-DR3 Expressed endogenously

Mel JuSo cells endogenously expressing DR were fixed with methanol and stained with anti-DRαβ antibody (left panel). Both intracellular distribution and cell surface expression of DR is comparable to that of DR3/CFP in the HEK293 transfectant also expressing DM/YFP and Ii (right panel). Inset shows a zoom-in of the surface expression.

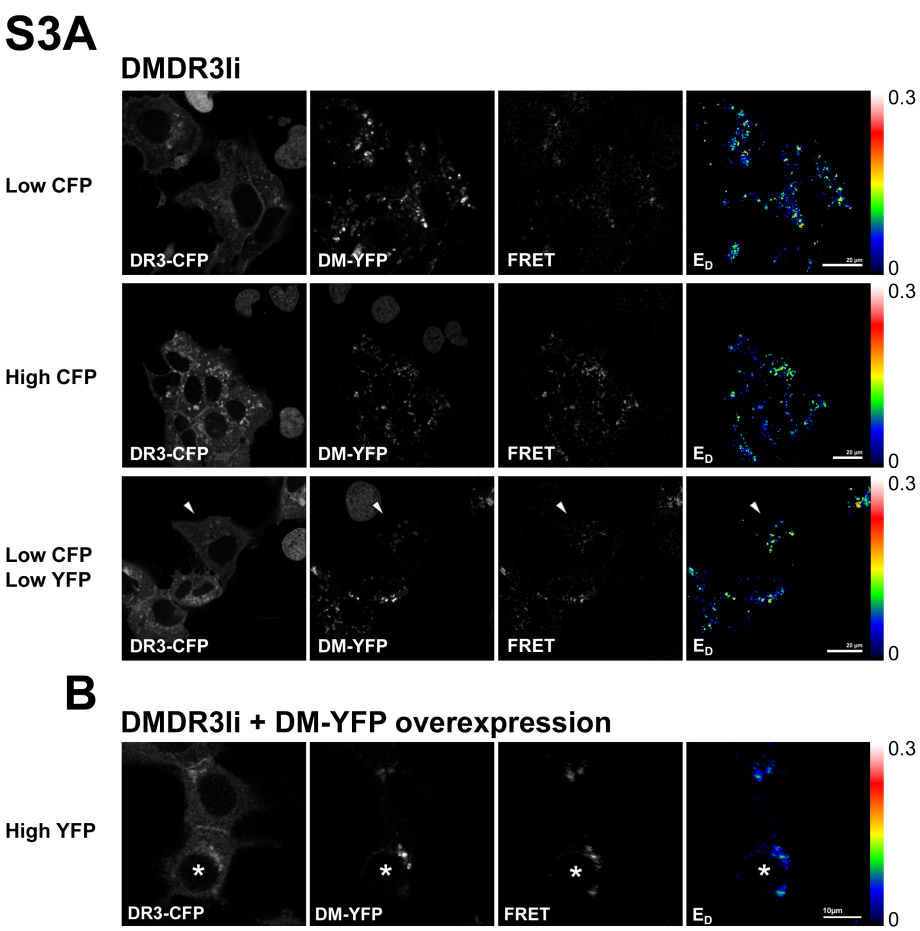


Figure S3. MIIC of HEK293 Cells Expressing Different Ratios of HLA-DR/CFP versus HLA-DM/YFP Show Similar Donor FRET Efficiencies

(**A**) The interaction between DR3/CFP and DM/YFP was measured by confocal-FRET on stable HEK293 transfectants at 37°C. Cells with different levels of DR/CFP were selected as indicated. The CFP signal, YFP signal, FRET and donor FRET efficiency (E_D) measurements are depicted (details in Figure 3A). FRET efficiency between DR3/CFP and DM/YFP is not affected by varying levels of donor DR3/CFP molecules, suggesting saturating amounts of DM/YFP in these vesicles.
(**B**) The interaction between DR3/CFP and DM/YFP was measured by confocal-FRET on stable HEK293 transfectants transiently overexpressing DM/YFP (marked with an asterix). The CFP signal, YFP signal, FRET and donor FRET efficiency (E_D) measurements are depicted. FRET efficiency between DR3/CFP and DM/YFP is not altered by the increasing levels of acceptor DM/YFP molecules.

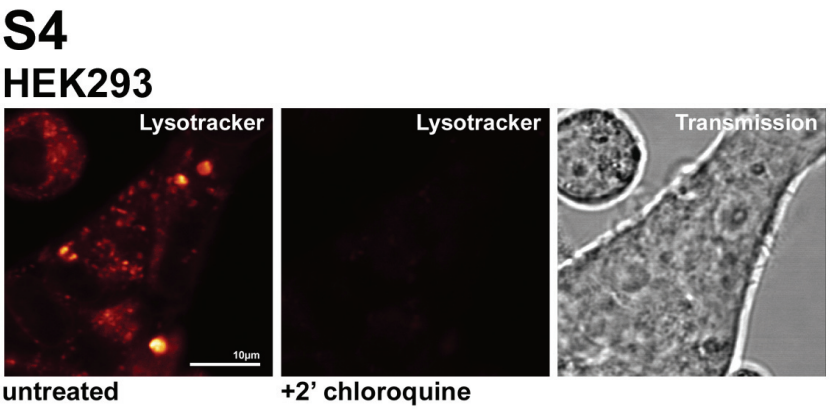


Figure S4. 2′ Chloroquine Treatment Suffices to Neutralize MIIC

Living HEK293 cells were incubated at 37°C with Lysotracker-Red to visualize acidic vesicles, including MIIC (Left panel). This fluorescence was lost within 2 min after addition of 100µM chloroquine (Middle panel). Right panel, transmission image of the assayed cell.

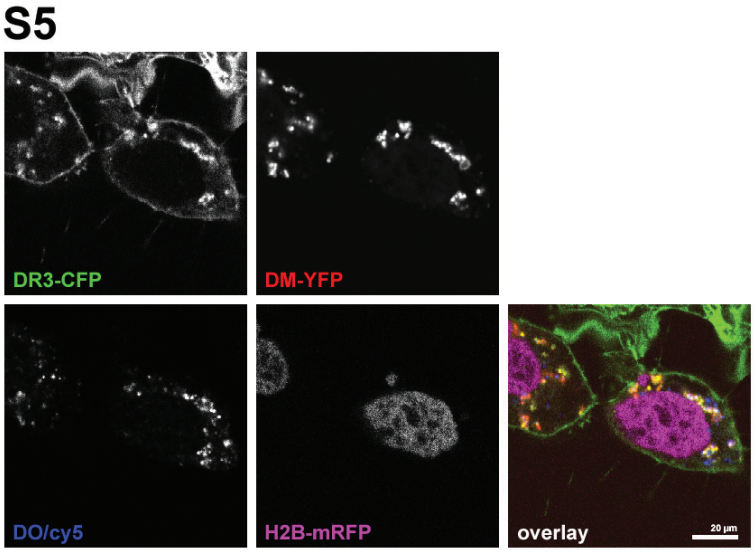


Figure S5. HLA-DO Overexpression in Fixed Cells

HEK293 cells stably expressing DR3/CFP and DM/YFP, and overexpressing unlabeled DO and H2B-mRFP as an transfection marker, were fixed with formaldehyde and stained with anti-DOβ antibody (van Ham *et al*., 2000). Cells expressing nuclear mRFP also contain DO, which colocalizes with DM/YFP and DR/CFP in perinuclear vesicles.

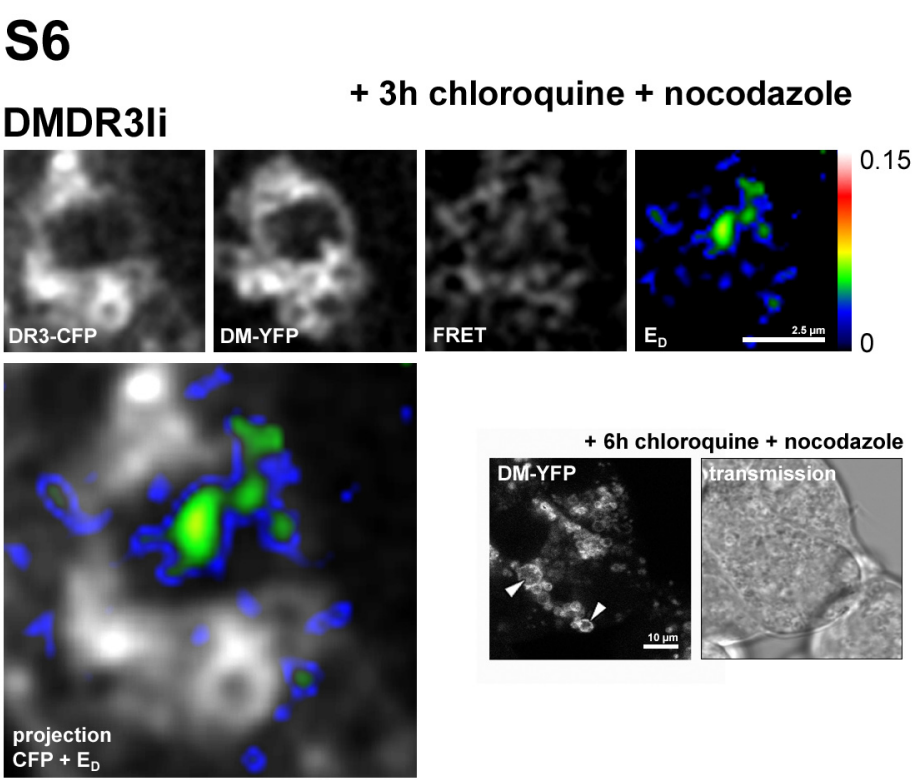


Figure S6. Vesicle Transport Is Not Required for Chloroquine-Induced Expansion of MIIC

HEK293 cells expressing DR/CFP, DM/YFP and Ii were treated with nocodazole to disrupt the microtubulular network, and block vesicular transport. Subsequently, the cells were cultured in the presence of 100µM chloroquine, and FRET was measured between DR3/CFP and DM/YFP on the expanded structures (shown is a zoom-in of the expanded structure). No efficient FRET was detected on the limiting membrane of the (expanded) MIIC. The subpanel shows the location of DM/YFP after 6 hr culture in the presence of chloroquine and nocodazole. MIIC completely expanded in the absence of microtubule-based vesicle transport, which suggests that the lipids required for the expanded limiting membrane almost exclusively derive from internal vesicles. Note that long-term treatment with nocodazole altered the morphology of the cells.

S7

DMDR3Ii

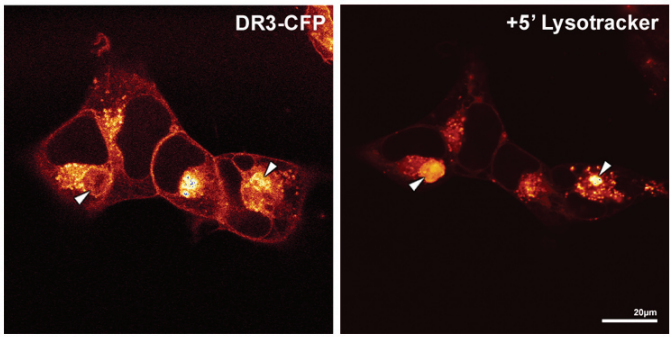


Figure S7. Swollen MIICs Induced by Knockdown of VPS34 Remain Acidic

HEK293 cells expressing DR/CFP, DM/YFP and Ii were transfected with an RNAi construct for hVPS34. Imaging 72 hr after transfection revealed swollen DR/CFP containing vesicles (indicated by arrows in left panel). These vesicles accumulated Lysotracker-Red (right panel), indicating that they were acidic.

S8

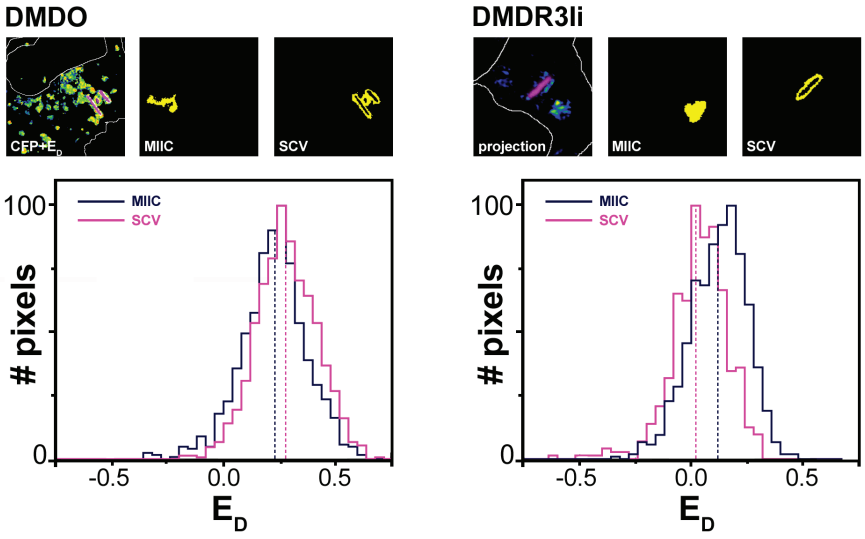
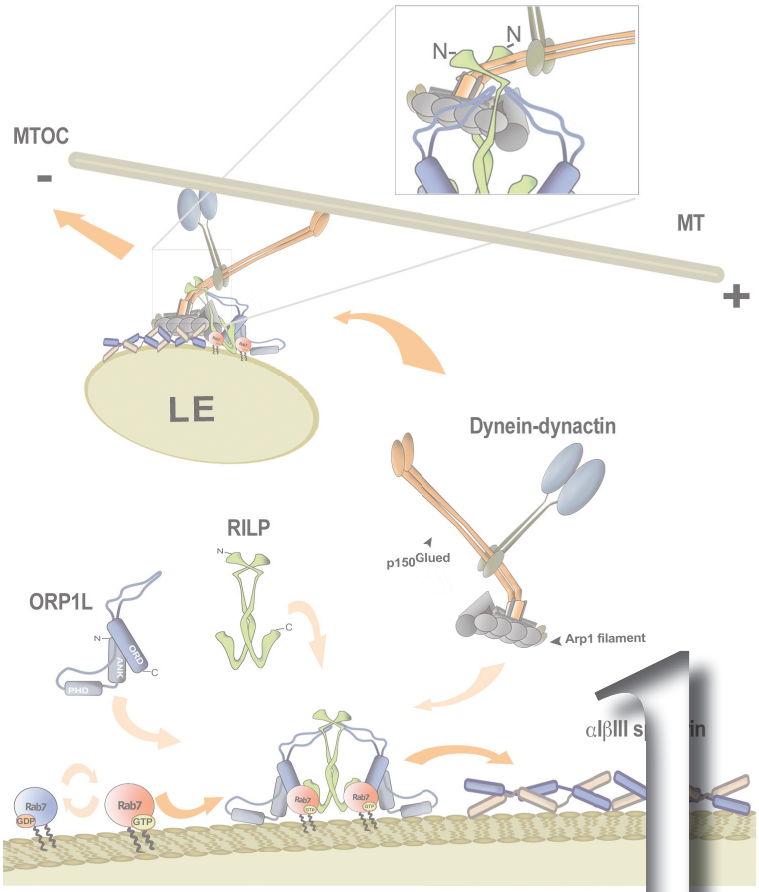


Figure S8. Donor FRET Efficiency Distribution of Pixels Representing SCV and MIIC

The data shown in Figure 7 were analyzed for donor FRET efficiency (E_D) distribution. MIIC or SCV pixels from the cells expressing DO/CFP, DM/YFP, or DR3/CFP, DM/YFP and Ii were extracted as shown in the top panel. The distribution of the donor FRET efficiencies of these selected pixels were plotted in a histogram (bottom panel). The average values are indicated by the dotted lines. Note the Poisson distribution of the E_D values, which is a consequence of noise in the measurements. Whereas E_D distribution for DO/CFP and DM/YFP is identical on both MIIC and SCV, a clear difference is observed for DR3/CFP and DM/YFP. No interaction between DR3 and DM is observed at the SCV.

Activation of endosomal dynein motors by stepwise assembly of Rab7-RILP-P150^{Glued}, ORP1L, and the receptor betaIII spectrin

The Journal of Cell Biology 2007, vol. 176: 459-471



11

The RILP-Rab7-ORP1L tripartite complex binds p150^{Glued} to recruit the dynein-dynactin motor to late endocytic structures

Marie Johansson[1#], Nuno Rocha[2#], Wilbert Zwart[2], Ingrid Jordens[2†], Lennert Janssen[2], Coenraad Kuijl[2], Vesa M. Olkkonen[1] and Jacques Neefjes[2*]

Abstract
The small GTPase Rab7 controls late endocytic transport by the minus end–directed motor protein complex dynein–dynactin, but how it does this is unclear. Rab7-interacting lysosomal protein (RILP) and oxysterol-binding protein–related protein 1L (ORP1L) are two effectors of Rab7. We show that GTP-bound Rab7 simultaneously binds RILP and ORP1L to form a RILP–Rab7–ORP1L complex. RILP interacts directly with the C-terminal 25-kD region of the dynactin projecting arm p150^{Glued}, which is required for dynein motor recruitment to late endocytic compartments (LEs). Still, p150^{Glued} recruitment by Rab7–RILP does not suffice to induce dynein-driven minus-end transport of LEs. ORP1L, as well as ßIII spectrin, which is the general receptor for dynactin on vesicles, are essential for dynein motor activity. Our results illustrate that the assembly of microtubule motors on endosomes involves a cascade of linked events. First, Rab7 recruits two effectors, RILP and ORP1L, to form a tripartite complex. Next, RILP directly binds to the p150^{Glued} dynactin subunit to recruit the dynein motor. Finally, the specific dynein motor receptor Rab7–RILP is transferred by ORP1L to ßIII spectrin. Dynein will initiate translocation of late endosomes to microtubule minus ends only after interacting with ßIII spectrin, which requires the activities of Rab7–RILP and ORP1L.

Introduction

The location and movement of intracellular vesiculotubular structures is controlled by microtubule-dependent kinesin and dynein motor proteins, as well as actin-dependent myosin motor proteins. Microtubule-based vesicle motility usually occurs in a bidirectional, stop-and-go manner because of the alternating activities of kinesin motors for plus-end movement and dynein motors for minus-end movement toward the microtubule organizing center (MTOC; Hirokawa, 1998; Wubbolts *et al*., 1999; Vale, 2003). How motor proteins are targeted to individual vesicles, how they dock on specific receptors, and how motor activity is controlled in a spatial and temporal manner are all processes that are poorly understood.

Cytoplasmic dynein is an 1.2-MD multisubunit protein complex, and it is the major motor for centripetal transport of membranous cargoes along microtubules (Schroer *et al*., 1989). Dynactin, which is also an 1.2-MD multisubunit complex, is a critical component of most, if not all, of the cytoplasmic dynein–driven activities. Dynactin participates in motor binding to microtubules (Waterman-Storer *et al*., 1995), increases motor processivity (King and Schroer, 2000; Culver-Hanlon *et al*., 2006), and acts as a multifunctional adaptor connecting cargo and dynein motor (Karki and Holzbaur, 1999; Schroer, 2004). At least 15 subunits of the dynein–dynactin motor are identified. The 1-MD dynein heavy chain dimer and the 300-kD p150^{Glued} dimer of the projecting arm of dynactin contact microtubules (Culver-Hanlon *et al*., 2006). p150^{Glued} is connected to the dynein heavy chain via the dynein intermediate chains (Waterman-Storer *et al*., 1995) and increases dynein motor processivity (King and Schroer, 2000; Culver-Hanlon *et al*., 2006). The actin-related protein 1 (Arp1) subunit forms a short filament at the base of dynactin and can bind membrane-associated ßIII spectrin, which probably acts as the membrane receptor for the dynein–dynactin motor complex (Holleran *et al*., 2001; Muresan *et al*., 2001). IßIII spectrin is located on the cytosolic side of late endocytic compartments (LEs), Golgi, and other subcellular compartments (De Matteis and Morrow, 2000), implying that compartment-selective dynein motor recruitment cannot be controlled by ßIII spectrin itself.

Small GTPases of the Rab family are present on specific subcellular compartments to regulate

[1]Department of Molecular Medicine, National Public Health Institute, Biomedicum, P.O.Box 104, FI-00251 Helsinki, Finland;

[2]Division of Tumor Biology, The Netherlands Cancer Institute, Plesmanlaan 121, 1066CX Amsterdam, The Netherlands; †Present address: Department of Biochemistry, Cellular Biology & Molecular Biology, Northwestern University, Evanston, USA

*Author for correspondence (e-mail: j.neefjes@nki.nl)

[#]The authors contributed equally to this work

Key words: dynactin, dynein, late endosome, lysosome, ORP1L, oxysterol binding protein, Rab7, RILP, p150^{Glued}

Running title: ORP1L–Rab7–RILP–P150^{Glued} complex and βIII spectrin

Abbreviations used in this paper: Arp, actin-related protein; FLIM, fluorescence lifetime imaging microscopy; FRET, fluorescence resonance energy transfer; LE, late endocytic compartment; MIIC, major histocompatibility complex class II–containing compartment; MBP, maltose-binding protein; mRFP, monomeric red fluorescent protein; MTOC, microtubule organizing center; ORD, oxysterolbinding protein–related domain; ORP, oxysterol-binding protein–related protein; RILP, Rab7-interacting lysosomal protein; shRNA, short hairpin RNA.

vesicle transport and fusion. They are ideal candidates for orchestrating the spatiotemporal regulation of motor-driven vesicle trafficking. Several Rab GTPases have been shown to interact directly or indirectly with motor proteins. These include members of the kinesin motor family (Rab4, Rab5, and Rab6), the dynein motor (Rab6 and Rab7), and the myosin motors (Rab8, Rab11, and Rab27a; Jordens *et al*., 2005). Rab6, which regulates Golgi transport, requires the effector bicaudal-D1 and -D2 (BicD1/2) to interact with the $p50^{dynamitin}$ subunit of dynactin (Hoogenraad *et al*., 2003; Matanis *et al*., 2002) or a third protein, egalitarian (Egl), which directly interacts with the dynein light chain in Drosophila melanogaster (Navarro *et al*., 2004). An activation state–dependent interaction of Rab6 with $p150^{Glued}$ has also been observed in a directed two-hybrid analysis (Short *et al*., 2002). We have studied another Rab protein, Rab7, which, through its effector Rab7-interacting lysosomal protein (RILP), recruits the dynein–dynactin motor to LEs, resulting in minus end–driven vesicular transport to the MTOC (Jordens *et al*., 2001). The Rab7–RILP–dynein motor cascade has been shown to act on many Rab7-containing compartments, including Salmonella-containing phagosomes (Harrison *et al*., 2004; Marsman *et al*., 2004), early melanosomes (Jordens *et al*., 2006), major histocompatibility complex class II–containing compartments (MIICs; Jordens *et al*., 2001), and cytolytic granules (Stinchcombe *et al*., 2006). The crystal structure of Rab7 in complex with a C-terminal domain of RILP revealed the details of this interaction. RILP forms a coiled-coil homodimer with two symmetric surfaces that bind two separate Rab7–GTP molecules to form a tetrameric complex (Wu *et al*., 2005), which has been confirmed in biochemical experiments (Colucci *et al*., 2005; Marsman *et al*., 2006). The recent finding that a member of the oxysterol-binding protein–related protein (ORP) family, ORP1L, also interacts with Rab7 and induces clustering of LEs (Johansson *et al*., 2005) complicated a simple interpretation of Rab7–RILP–controlled dynein motor recruitment. ORPs have been implicated in diverse aspects of cellular processes, including sterol and phospholipid metabolism, vesicle transport, and cell signaling (Lehto and Olkkonen, 2003). The mechanisms by which ORP proteins contribute to these processes have, however, remained largely unknown. We recently showed that ORP1L localizes to LEs and interacts via its ankyrin repeat region with the small GTPase Rab7 (Johansson *et al*., 2005). ORP1L was shown to stabilize the GTP-bound active form of Rab7 on LEs and to affect the subcellular distribution of these organelles, analogously, to RILP (Jordens *et al*., 2001). A third Rab7 effector, Rabring7 (Mizuno *et al*., 2003), clusters LEs, much like the other effectors, and induces lysosomal acidification, but dynein motor recruitment has not been shown. Surprisingly, no obvious sequence similarity is found between the three Rab7 effectors.

Apparently, multiple effectors interact with Rab7. They could be mutually exclusive, but they may also interact simultaneously with this Rab GTPase. How the Rab7 effector complexes recruit the dynein motor complex is also unclear. We have studied the interaction of RILP and ORP1L with the Rab7 GTPase, as well as their interactions with dynein–dynactin motor subunits. We show that Rab7 is part of a tripartite complex binding RILP and ORP1L simultaneously. RILP is essential for dynein motor recruitment through a direct interaction with the C-terminal portion of the $p150^{Glued}$ subunit of the dynein–dynactin motor. ORP1L recruits this complex to ßIII spectrin domains, which appears to be critical for dynein motor activation and minus-end transport of LEs. Rab7, thus, recruits two proteins with diverse functions in the control of dynein motor–driven transport: RILP for motor binding and ORP1L for transport to the membrane-associated late endocytic ßIII spectrin receptor for motor activation. The dynein–dynactin motor, thus, requires two receptors before actively transporting LEs to the microtubule minus end. Its projecting arm, $p150^{Glued}$, is recruited by RILP bound by active Rab7 in LE membranes. The other Rab7 effector, ORP1L, then transfers the Rab7–RILP–$p150^{Glued}$–dynein motor complex to ßIII spectrin interacting with the base of the dynactin complex Arp1. Only after completion of this "mass protein action" does the dynein motor transport LEs to the microtubule minus end.

Results

ORP1L and RILP colocalize on juxtanuclear late endocytic clusters as part of a physical complex

Both RILP and ORP1L have been reported to localize on LEs, and their overexpression induces juxtanuclear clustering of these compartments, suggesting involvement in microtubule-dependent LE motility (Jordens *et al*., 2001; Johansson *et al*., 2005). We studied the distribution of GFP-tagged RILP and Xpress-tagged ORP1L expressed in HeLa cells, and we visualized the proteins by confocal laser-scanning fluorescence microscopy. The proteins showed extensive colocalization on compact juxtanuclear organelle clusters (Fig. 2 A). We studied the contribution of their various domains to this phenotype (Fig. 1 A). The N-terminal portion of ORP1L, consisting of the ankyrin repeat region (ANK; aa 1–237; Fig. 2 A) or the ANK and the PH domain regions (ANK + PH; aa 1–408; not depicted), displayed colocalization with RILP similar

to that of full-length ORP1L (Fig. 2 A), demonstrating that the N-terminal Rab7-interacting ANK region of ORP1L suffices to specify this localization. We have previously shown that the ANK and ANK + PH domain regions of ORP1L induce clustering of LEs in the absence of ectopically expressed RILP (Johansson *et al*., 2003, 2005). We tested whether a truncated RILP that fails to recruit the dynein–dynactin motor, but still binds to the switch and interswitch regions of small GTPase Rab7 (N-RILP; Jordens *et al*., 2001; Wu *et al*., 2005), affects the LE-clustering phenotype induced by the ORP1L ANK domain (Fig. 2 A). Overexpression of N-RILP inhibited clustering by ANK, although the two proteins still colocalized on the scattered LEs.

To determine whether ORP1L and RILP might interact physically, HeLa cells were transected with Xpress-tagged RILP and subjected to immunoprecipitation with the Xpress mAb or irrelevant mouse IgG. Western blotting of the isolates with anti-ORP1L antibody revealed coprecipitation of endogenous ORP1L with Xpress-RILP (Fig. 2 B). To study the interaction in an endogenous setting, HeLa cell lysates were incubated with anti-RILP antibody or irrelevant rabbit IgG. Endogenous ORP1L was detected in the immunoprecipitates by Western blotting (Fig. 2 C), suggesting that ORP1L and RILP not only colocalize on LEs but are also part of a physical complex in cells.

ORP1L and RILP interactions with Rab7 in living cells

We then applied fluorescence resonance energy transfer (FRET) techniques to test whether a

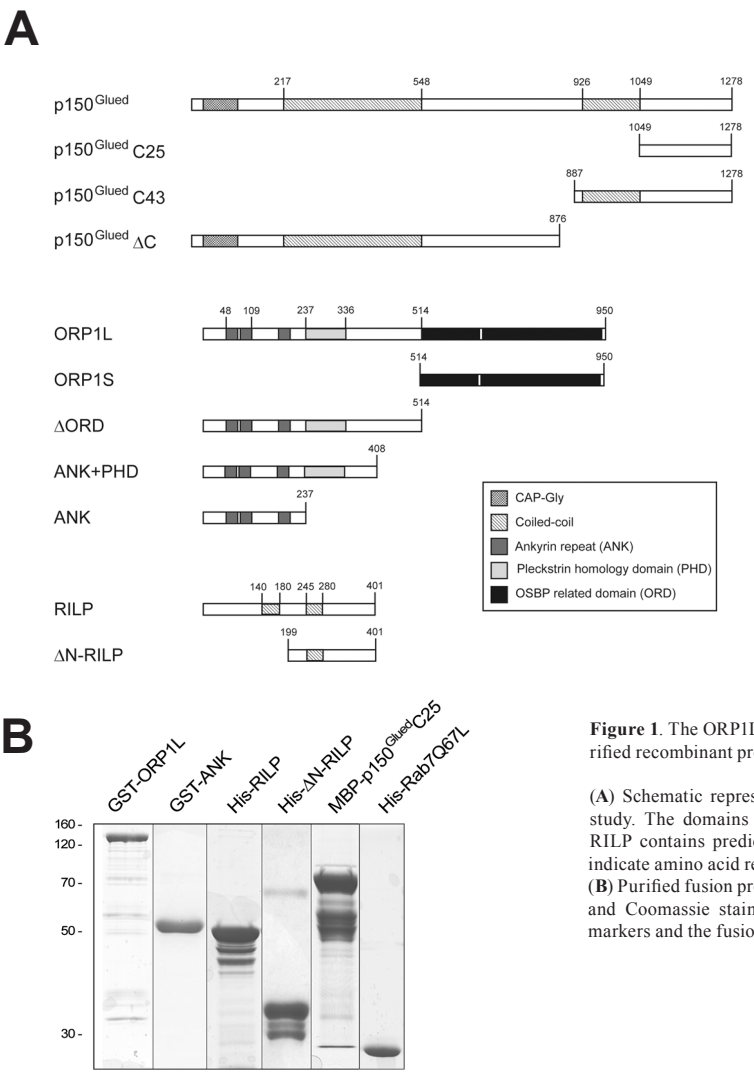


Figure 1. The ORP1L, RILP, and p150^{Glued} constructs and purified recombinant proteins.

(**A**) Schematic representation of the constructs used in this study. The domains in ORP1L and p150^{Glued} are indicated. RILP contains predicted coiled-coil regions only. Numbers indicate amino acid residue positions.
(**B**) Purified fusion proteins were resolved by 10% SDS-PAGE and Coomassie stained. Positions of the molecular weight markers and the fusion proteins are indicated.

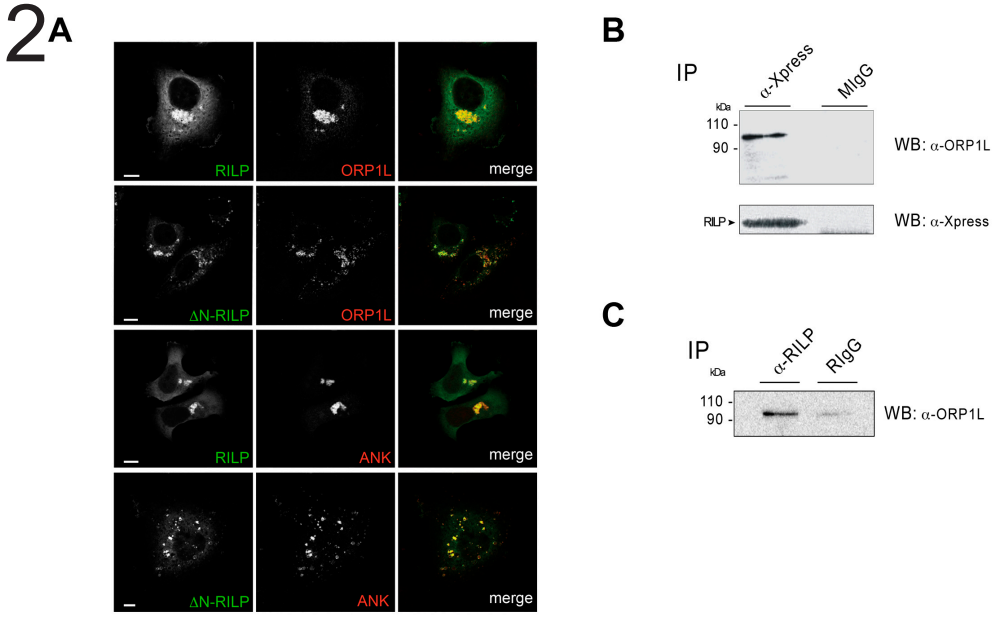


Figure 2. ORP1L and RILP colocalize and are part of a physical complex.

(**A**) ORP1L and RILP colocalize on juxtanuclear late endocytic clusters. HeLa cells were transfected with GFP–RILP or GFP–N-RILP, together with Xpress-tagged ORP1L or Xpress-tagged ORP1L–ANK domain (red), as indicated in the images. ANK and ORP1L colocalize with RILP or N-RILP (right, merge). Bars, 10 µm. (**B**) ORP1L co-isolates with expressed RILP. HeLa cells were transfected with Xpress-tagged RILP and immunoprecipitated with anti-Xpress antibody (-Xpress) or irrelevant mouse IgG (MIgG). The isolates were Western blotted with anti-ORP1L antibodies (WB: -ORP1L). (bottom) Corresponding lanes probed with anti-Xpress antibody (WB: -Xpress). (**C**) Coimmunoprecipitation of endogenous RILP and ORP1L. HeLa cell lysates were immunoprecipitated with rabbit anti-RILP serum (-RILP) or irrelevant rabbit IgG (RIgG). The isolates were Western blotted with anti-ORP1L antibodies (WB: -ORP1L).

RILP–Rab7–ORP1L interaction could be visualized in living cells using fluorescently labeled proteins. When two fluorophores are in close proximity (<8 nm) and the fluorophores show spectral overlap, FRET can occur (Förster, 1948). FRET can be detected by sensitized emission (when the acceptor emits light at the cost of donor fluorescence) or fluorescence lifetime imaging microscopy (FLIM). FLIM detects the time between photon absorbance by the donor fluorophore and its emission (in nanoseconds), which decreases when energy is transferred to acceptor fluorophores. FLIM, which, in principle, is more quantitative than sensitized emission for detecting FRET and FRET efficiencies (Wallrabe and Periasamy, 2005), was applied to study interactions between Rab7, RILP, and ORP1L in living HeLa cells.

HeLa cells transfected with GFP–RILP and monomeric red fluorescent protein (mRFP)–Rab7, GFP–ORP1L and mRFP–Rab7, or GFP–ORP1L and mRFP–RILP, were analyzed by FLIM, and the lifetime of the GFP fluorophore was measured. The cells were cocultured with Mel JuSo cells stably expressing histone 2B (H2B)–GFP, which were used as an internal null FRET control. Because RILP and Rab7 have been previously shown to interact (Cantalupo *et al*., 2001; Jordens *et al*., 2001) and cocrystallize (Wu *et al*., 2005), these proteins constituted a positive control for the experimental setup. When GFP–RILP and mRFP–Rab7 were coexpressed, discrete perinuclear clusters were formed. A substantial decrease in GFP fluorescence lifetime on the GFP–RILP–positive structures was observed in the presence of mRFP–Rab7. The measured lifetime was 2.29 ± 0.06 ns (Fig. 3 A), when the lifetime for H2B–GFP in control cells (indicated by an asterisk) was at 2.56 ± 0.03 ns (Bastiaens and Squire, 1999). The calculated donor FRET efficiency, or E_D (see Materials and methods), between GFP–RILP and mRFP–Rab7 was 11.2 ± 2.5% (Fig. 3 B), indicating efficient FRET and close spacing of RILP and Rab7 in living cells. Measuring FLIM between GFP–ORP1L and mRFP–Rab7 resulted in a comparable reduced lifetime of the GFP fluorophore, 2.23 ± 0.03 ns (Fig. 3 A), corresponding to an E_D of 12.5 ± 1.85% (Fig. 3 B).

To determine whether ORP1L and RILP are in close proximity not only to Rab7 but also to each other, FLIM was performed between GFP–ORP1L and mRFP–RILP. The decrease of fluorescence lifetime was somewhat less pronounced, but still significant (2.35 ± 0.04 ns; E_D = 7.0 ± 1.8%; Fig. 3, A and B). Similar results were obtained when measuring FRET by sensitized emission (unpublished data). These data suggest that ORP1L is part of the same complex as

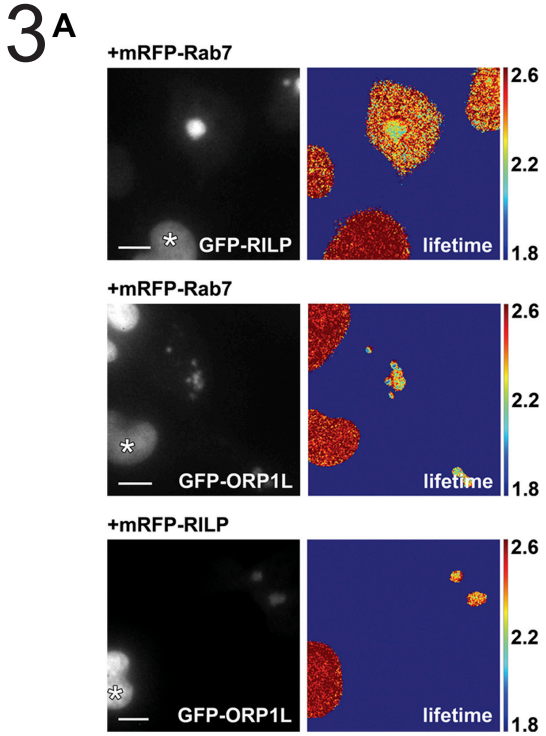


Figure 3. FRET between ORP1L, Rab7, and RILP.

(**A**) HeLa cells were transfected with GFP–RILP or GFP–ORP1L and cotransfected with mRFP–Rab7 or mRFP–RILP, as indicated. The transfected HeLa cells were cocultured with Mel JuSo cells stably expressing H2B–GFP (indicated by *) as an internal marker with a lifetime of 2.6 ns. (left) Wide-field image of the transfected and internal control cells. (right) FLIM image of the same cells, in which the fluorescence lifetime is depicted in false colors. The color scale with the respective lifetimes (in nanoseconds) is indicated. The fluorescence lifetime of GFP–RILP or GFP–ORP1L was determined on vesicles immobile during data acquisition (12 s). Bar, 10 µm. (**B**) The donor FRET efficiencies (E_D) between the GFP- and mRFP-tagged proteins were determined and plotted in the bar diagram. Mean ± the SD. n > 20.

RILP and Rab7. The absolute distances between the proteins cannot, however, be determined from these data because FRET efficiency is not only determined by the Förster distance (distance between the fluorescent groups) but also by the orientation factor and flexibility of the fluorophores (Förster, 1948).

The Rab7–RILP–ORP1L tripartite complex

Having established that ORP1L and RILP are part of a physical complex (Fig. 2, A and B), we set out to study the interaction between the two proteins by a series of pull-down experiments. Endogenous RILP was pulled down from HeLa cell lysate using purified, matrix-immobilized GST–ORP1L (Fig. 4 A). To study whether this interaction between ORP1L and RILP is direct, we used purified His_6-tagged RILP or the constitutively active GTP-loaded Rab7 mutant Q67L, which is produced in E. coli, to pull down purified GST–ORP1L. These experiments revealed that, although His_6–Rab7Q67L efficiently pulled down GST–ORP1L in accordance with our previous results (Johansson *et al*., 2005), no interaction was detected between His_6–RILP and GST–ORP1L (Fig. 4 B). Because both RILP and ORP1L bind to Rab7, we next tested, using purified proteins, whether Rab7 is able to bridge the two effectors and thereby form a tripartite complex. Because soluble full-length recombinant GST–ORP1L is produced in limiting amounts, GST–ANK, which suffices to bind Rab7 and can be efficiently produced, was used to perform the binding assay. GST fusion proteins of the Rab7-interacting ORP1L ANK fragment (GST–ANK) were incubated with His_6–RILP, GTP-loaded His_6–Rab7Q67L, or a mixture of both His_6-tagged proteins. As expected, GST–ANK pulled down His_6–Rab7Q67L, but not His_6–RILP. However, His_6–RILP was pulled down by GST–ANK when the incubation was performed in the presence of GTP-loaded His_6–Rab7Q67L (Fig. 4 C). This indicated that Rab7 is required to bridge RILP and ORP1L, and that the two effectors do not compete for the same binding site on Rab7.

To test whether ORP1L and RILP interacted cooperatively with Rab7, we immobilized GTP-loaded GST–Rab7 and pulled down *in vitro*–translated and radiolabeled ORP1L or RILP. This experiment was performed in the presence of a step gradient of increasing amounts of purified RILP, N-RILP, or ORP1L fusion proteins, respectively. GTP-loaded GST–Rab7 pulled down ^{35}S-labeled ORP1L to a significant extent in the absence of RILP, but further addition of His_6–RILP to the reaction mixture increased ORP1L binding to Rab7 in a dose-dependent manner. ^{35}S-labeled ORP1L binding to immobilized Rab7 increased up to approximately fourfold in the presence of His_6–RILP (Fig. 4, D [I] and E). Addition of His_6–RILP had no effect on the binding of ORP1L ANK (not depicted) or ANK +

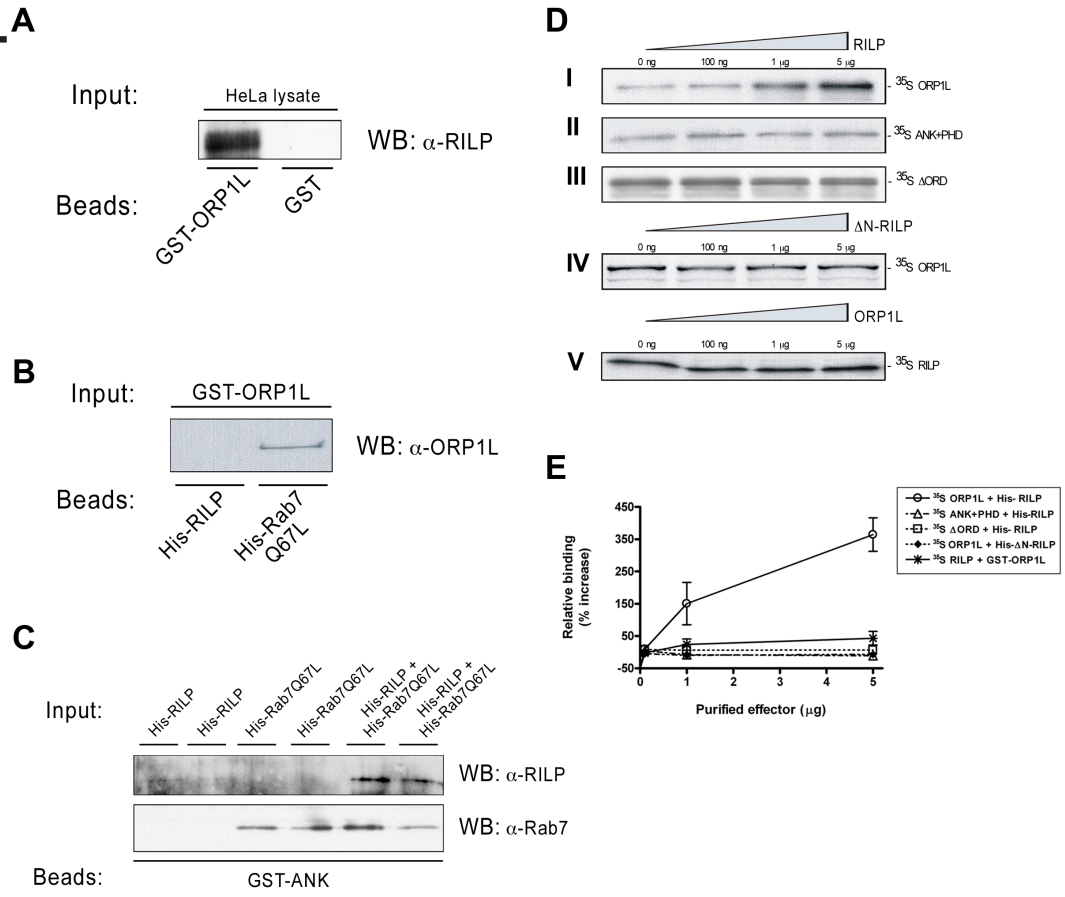


Figure 4. The ORP1L–Rab7–RILP heterotrimeric complex.

(**A**) Proteins were pulled down from HeLa cell lysates with GST–ORP1L or GST and Western blotted with anti-RILP antiserum (WB: -RILP). Pull-down assays were performed with purified proteins. (**B**) His_6–RILP or His_6–Rab7Q67L were immobilized on a matrix and used to pull down GST–ORP1L. Isolates were Western blotted with anti-ORP1L antibodies (WB: -ORP1L). (**C**) GST–ORP1L ANK fragment (GST–ANK) was immobilized and incubated with His_6–RILP, GTP-loaded His_6–Rab7Q67L, or a mixture containing both His_6–RILP and GTP-loaded His_6– Rab7Q67L. The material pulled down by the ANK fragment was Western blotted with antibodies against Rab7 or RILP (indicated on the right). Duplicate samples are shown for each condition. (**D**) RILP enhances ORP1L binding to Rab7. GST–Rab7 was immobilized on a matrix, loaded with GTP, and incubated with *in vitro*–translated ^{35}S-labeled ORP1L in the presence of increasing amounts of His_6–RILP. ^{35}S-labeled ORP1L protein pulled down by GST–Rab7 was visualized by SDS-PAGE and autoradiography (I). Similar pull-down experiments were performed with *in vitro*–translated ^{35}S-labeled ORP1L ANK + PHD (II) or ^{35}S-labeled ORP1L ORD fragments (III). Pull-down of full-length ^{35}S-labeled ORP1L by active GST–Rab7 in the presence of increasing amounts of His_6–N-RILP (indicated above the lanes) (IV). A reciprocal pull-down experiment in which *in vitro*–translated ^{35}S-labeled RILP was incubated with immobilized His_6–Rab7–GTP in the presence of increasing amounts of GST–ORP1L (indicated above the lanes; V). (**E**) Quantification of the radioactive bands in D by phosphorimaging. The plotted data shows the relative increase in binding of *in vitro*–translated proteins to immobilized Rab7–GTP in the presence of a step-gradient of effector proteins. Binding of ORP1L to Rab7 was enhanced up to fourfold in the presence of RILP. The plotted data represents the mean of three independent experiments ± the SD (error bars).

PHD fragments to Rab7–GTP (Fig. 4, D [II] and E). To further map the region of ORP1L involved in the observed stabilization, we extended the ANK + PHD domain to contain a region upstream of the oxysterol-binding protein–related domain (ORD) displaying a high probability of forming a coiled coil (ORD; Fig. 1 A; Lupas *et al*., 1991; Berger *et al*., 1995). Also this construct failed to produce the effect observed with full-length ORP1L (Fig. 4, D [III] and E), suggesting that the ORD of ORP1L is involved in the stabilization effect observed in the presence of His_6–RILP.

To determine if the N-terminal region of RILP, which is required for dynein–dynactin motor recruitment to LEs (Jordens *et al*., 2001), is necessary for facilitating the ORP1L–Rab7 interaction, the pull-down experiment with GTP-loaded Rab7 was repeated with *in vitro*–translated ^{35}S-labeled ORP1L in the presence of His_6–N-RILP. This truncated form of RILP failed to increase ORP1L binding to Rab7–GTP (Fig. 4, D [IV] and E), demonstrating that the same domain

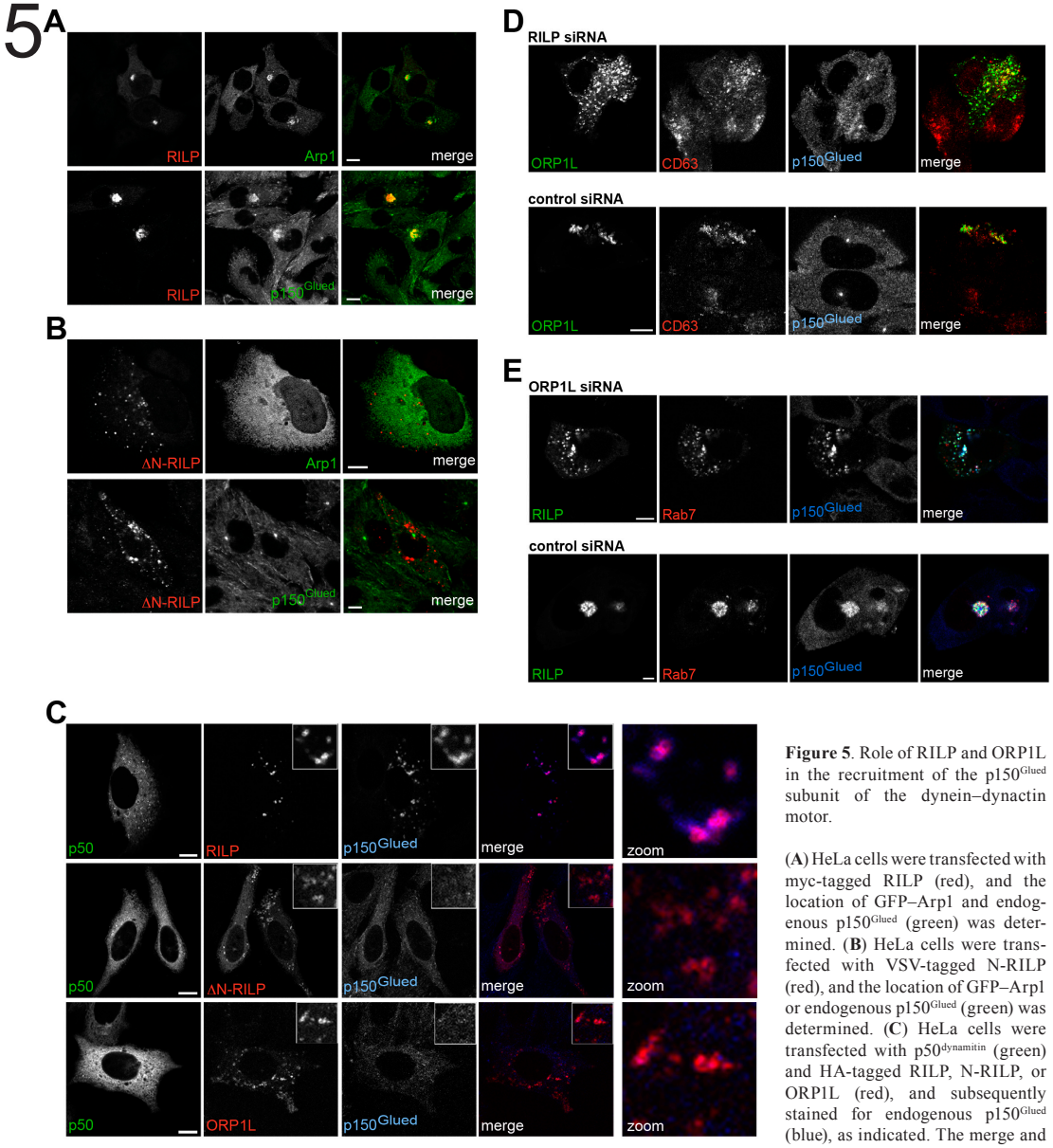


Figure 5. Role of RILP and ORP1L in the recruitment of the p150^{Glued} subunit of the dynein–dynactin motor.

(**A**) HeLa cells were transfected with myc-tagged RILP (red), and the location of GFP–Arp1 and endogenous p150^{Glued} (green) was determined. (**B**) HeLa cells were transfected with VSV-tagged N-RILP (red), and the location of GFP–Arp1 or endogenous p150^{Glued} (green) was determined. (**C**) HeLa cells were transfected with p50^{dynamitin} (green) and HA-tagged RILP, N-RILP, or ORP1L (red), and subsequently stained for endogenous p150^{Glued} (blue), as indicated. The merge and the magnified merge (zoom) images only show the stainings in the red and blue images. (D) HeLa cells were transfected with GFP–ORP1L (green) and RILP siRNA or scrambled siRNA, as indicated. At 72 h after transfection, cells were fixed and stained for endogenous CD63 (red) and p150^{Glued} (blue). The merge shows only the ORP1L and CD63 labeling. (E) HeLa cells were transfected with GFP–RILP (green), mRFP–Rab7 (red), and ORP1L siRNA or a scrambled siRNA, as indicated, and fixed at 48 h after transfection. Cells were stained for endogenous p150^{Glued} (blue). Bars, 10 μm.

of RILP essential in dynein–dynactin motor recruitment to LEs (Jordens *et al*., 2001) is also involved in the stabilization of the Rab7–ORP1L interaction.

To test if the observed cooperativity of ORP1L binding to Rab7 in the presence of RILP is reciprocal, we pulled down *in vitro*–translated ^{35}S-labeled RILP with immobilized His$_6$–Rab7–GTP, followed by incubation with increasing amounts of GST–ORP1L. RILP was observed to bind to immobilized Rab7, but the addition of GST–ORP1L had no effect on RILP binding (Fig. 4, D [V] and E). These experiments suggest that RILP might stabilize the Rab7–ORP1L interaction in a unidirectional manner, and again indicate that binding of the two effectors to Rab7 is not mutually exclusive.

RILP–Rab7 recruits p150^{Glued} to LEs, whereas ORP1L is required for actual minus-end transport

GTP-loaded Rab7 collects RILP and ORP1L into a complex, and then recruits the dynein–dynactin motor protein complex to LE membranes. The dynein–dynactin motor complex interacts via the Arp1 filament with the ß chain of membrane-associated IßIII spectrin (Holleran *et al*., 2001), which thereby acts as a membrane receptor for the motor. Fluorescence microscopy analyses performed in HeLa cells demonstrated that the dynein–dynactin motor subunits Arp1, p50^{dynamitin} (not depicted), and p150^{Glued} were selectively recruited to LEs by myc-tagged RILP (Fig. 5 A). N-RILP, in contrast, failed to recruit these dynein–dynactin motor subunits (Fig. 5 B).

To identify the dynein–dynactin motor subunit required for the RILP-mediated targeting to LEs, we tested whether ectopically expressed RILP or ORP1L could selectively stabilize particular dynein–dynactin motor subunits on LE membranes when the dynein–dynactin motor complex is dissociated. Overexpression of (GFP–)p50^{dynamitin} displaces the projecting arm of dynactin from the rest of the dynactin complex, leaving Arp1 membrane associated, whereas p150^{Glued} and other more distal dynein–dynactin motor subunits are dispersed in the cytosol (Echeverri *et al*., 1996; Burkhardt *et al*., 1997; Eckley *et al*., 1999). GFP–p50^{dynamitin} was overexpressed in HeLa cells in the absence or presence of HA-RILP or Xpress–ORP1L. Cells were fixed and stained for endogenous p150^{Glued} (Fig. 5 C). Expression of RILP alone, but not ORP1L (or ANK; unpublished data), sufficed to rescue p150^{Glued} localization on LEs when the dynein motor complex was dissociated by p50^{dynamitin} overexpression. It is noteworthy that the dynein–dynactin motor complex is no longer assembled into a functional motor when p50^{dynamitin} is overexpressed, resulting in scattered vesicles still containing RILP and p150^{Glued}. To further test the involvement of endogenous RILP or ORP1L in motor recruitment and minus end–directed transport, the proteins were down-regulated by specific siRNAs, and the localizations of RILP (ectopically expressed), ORP1L (ectopically expressed), late endocytic markers, and p150^{Glued} were determined (Fig. 5, D and E). Down-regulation of endogenous RILP or ORP1L induced scattering of LEs. p150^{Glued} was recruited to the scattered vesicles only when RILP was overexpressed (Fig. 5 E). Importantly, p150^{Glued} recruitment by RILP in the absence of ORP1L did not suffice to drive minus-end transport of LEs into a characteristic perinuclear cluster around the MTOC (Fig. 5 E). This suggests that RILP, but not ORP1L, interacts with the p150^{Glued} subunit of the dynein–dynactin motor complex. However, interactions of RILP or ORP1L with other stabilizing motor subunits, or the involvement of additional proteins linking p150^{Glued} and RILP, cannot be excluded by these experiments.

RILP interacts with the C-terminal domain of p150^{Glued}

To identify the potential interaction between RILP and p150^{Glued}, we first determined the p150^{Glued} region recruited by RILP. C, the GFP-tagged N-terminal 95-kD fragment of p150^{Glued} (aa 1–876) was coexpressed with mRFP–RILP (Fig. 6 A). Although decorating microtubules and the MTOC, this fragment failed to be recruited to the RILP cluster. This suggested that RILP interacts (directly or indirectly) with the C-terminal 55-kD portion of p150^{Glued}. The coiled coil–containing region in p150^{Glued} CC2 (aa 887–1,063) also failed to be recruited by RILP (not depicted), whereas GFP–p150^{Glued} C25 (aa 1,049–1,278), representing the most C-terminal 25-kD region after the coiled coil, was recruited to the mRFP–RILP cluster (Fig. 6 A). This construct did not colocalize with mRFP–N-RILP (Fig. 6 A), in agreement with the observation that this dominant-negative RILP variant inhibits p150^{Glued} recruitment to LEs (Fig. 5, B–D; Jordens *et al*., 2001). These data suggest that the N-terminal half of RILP interacts with the most C-terminal region of p150^{Glued} to recruit the dynein–dynactin motor complex to LEs. To test whether this p150^{Glued} fragment also inhibited minus-end transport by acting as a dominant-negative dynein motor fragment, analogously to overexpression of p50^{dynamitin} (Burkhardt *et al*., 1997), the GFP-tagged versions of both proteins were overexpressed in HeLa cells, and late endocytic structures were visualized by labeling with anti-CD63 antibodies (Fig. 6 B). Overexpression of the C-terminal fragment of p150^{Glued} induced a mild, but reproducible, scattering of LEs, whereas the effect of p50^{dynamitin} overexpression was considerably more pronounced. This suggests that overexpression of the (presumably) monomeric version of the p150^{Glued} C-terminal fragment competes weakly with the endogenous p150^{Glued} homodimer for binding to the RILP homodimer.

A direct interaction between RILP and the most C-terminal region of p150^{Glued} can only be studied using purified proteins. GST–Rab7, GST–ORP1L, maltose-binding protein (MBP)–p150^{Glued} C25, His_6–RILP, and His_6–N-RILP were expressed in E. coli and purified. GST–Rab7 was immobilized on beads and loaded with GTPS. To reconstitute the tripartite complex *in vitro*, the beads were subsequently loaded with His_6–RILP or His_6–N-RILP in the presence or absence of ORP1L. The beads were washed, and equal amounts of purified MBP–p150^{Glued} C25 were added to all reactions before another washing step. To determine specific binding, which is binding-dependent on the active

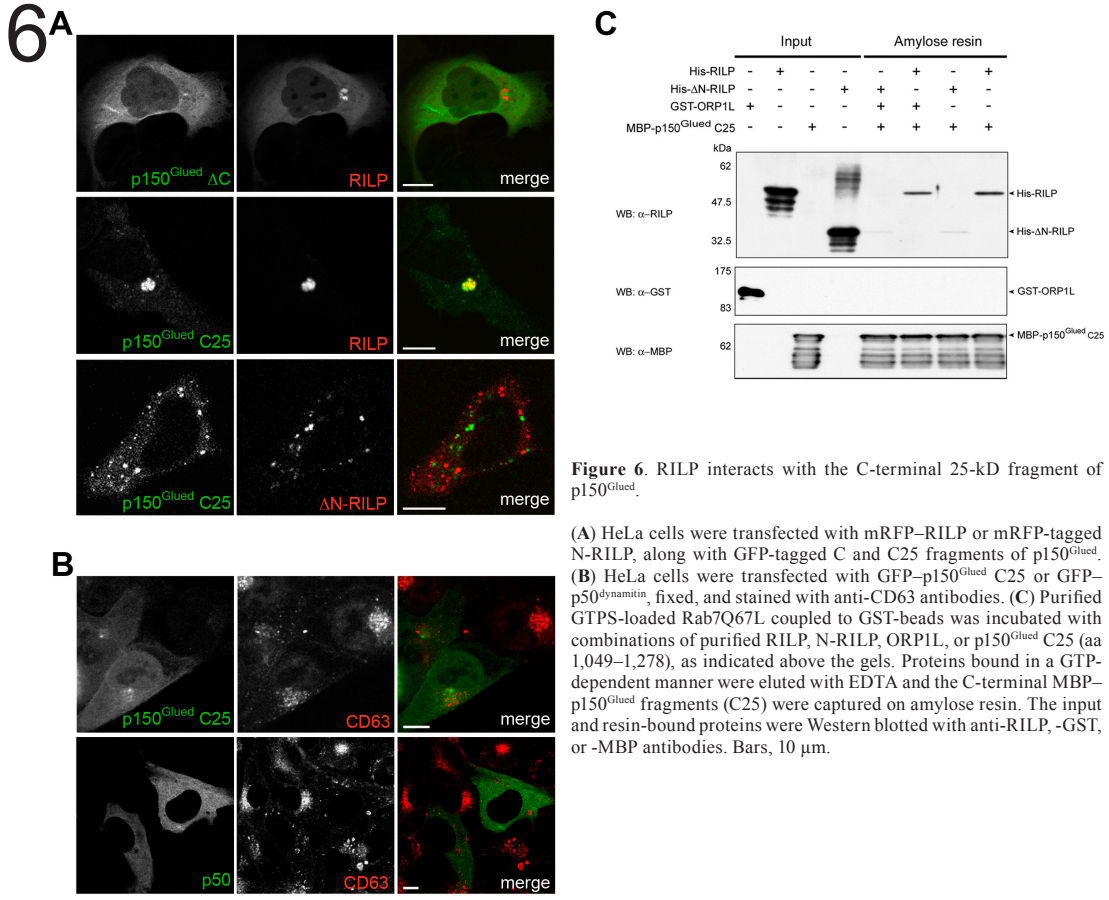


Figure 6. RILP interacts with the C-terminal 25-kD fragment of p150^{Glued}.

(**A**) HeLa cells were transfected with mRFP–RILP or mRFP-tagged N-RILP, along with GFP-tagged C and C25 fragments of p150^{Glued}. (**B**) HeLa cells were transfected with GFP–p150^{Glued} C25 or GFP–p50^{dynamitin}, fixed, and stained with anti-CD63 antibodies. (**C**) Purified GTPS-loaded Rab7Q67L coupled to GST-beads was incubated with combinations of purified RILP, N-RILP, ORP1L, or p150^{Glued} C25 (aa 1,049–1,278), as indicated above the gels. Proteins bound in a GTP-dependent manner were eluted with EDTA and the C-terminal MBP–p150^{Glued} fragments (C25) were captured on amylose resin. The input and resin-bound proteins were Western blotted with anti-RILP, -GST, or -MBP antibodies. Bars, 10 μm.

GTP-bound conformation of Rab7, GTPS was eluted by EDTA and replaced by excess GDP. The eluates were then incubated with amylose resin to capture the MBP–p150^{Glued} C25 fusions before extensive washing. The bound fractions were analyzed by SDS-PAGE and Western blotting (Fig. 6 C). Only RILP, but not N-RILP or ORP1L, was recovered from the amylose-bound MBP–p150^{Glued} C25 fractions, in line with the observations above. This interaction was also reproduced in the absence of immobilized Rab7, suggesting that the GTPase is not required for binding *in vitro* of p150^{Glued} to RILP (unpublished data). These results support a model in which the C-terminal domain of RILP interacts with active GTP-loaded Rab7 and the N-terminal domain of RILP (which is absent in N-RILP) interacts with the C-terminal 25-kD fragment of the dynein–dynactin motor subunit p150^{Glued}.

ORP1L recruits the Rab7–RILP–p150^{Glued} complex to the membrane-associated receptor ßIII spectrin

If the Rab7–RILP complex recruits the dynein motor through the p150^{Glued} stalk, it could act as a second dynein motor receptor in parallel with ßIII spectrin on the membrane of LEs. ßIII spectrin has an N-terminal actin-binding domain that interacts with the base of the dynein–dynactin motor Arp1 (Holleran *et al*., 2001) and is required for anchoring this motor to the membrane and for motor activity (Muresan *et al*., 2001). IßIII spectrin is likely to be the only spectrin family member present on LEs (Stankewich *et al*., 1998; De Matteis and Morrow, 2000). To test whether IßIII spectrin is located on LEs, and whether RILP or the dominant-negative form N-RILP affects spectrin localization, we introduced GFP-tagged RILP or N-RILP in Mel JuSo cells and stained these with antibodies for I or ßIII spectrin (Fig. 7 A). I and ßIII spectrin localized to various subcellular structures, including RILP- and N-RILP–containing vesicles. Although full-length RILP was required for p150^{Glued} recruitment, IßIII spectrin remained membrane associated, even when N-RILP was expressed. The membrane association of IßIII spectrin is, thus, independent of RILP, and probably occurs through association with various (unidentified) late endocytic transmembrane proteins and phospholipids (De Matteis and Morrow, 2000).

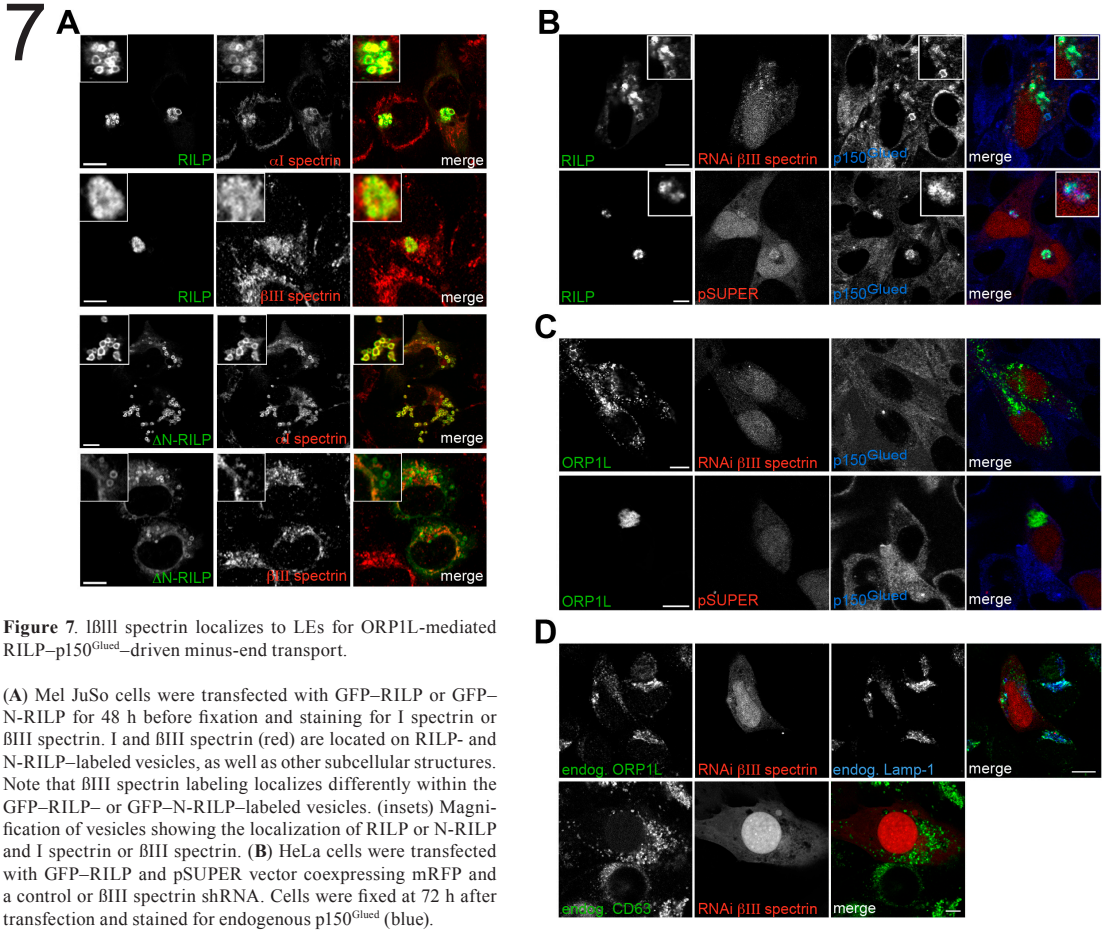


Figure 7. lßlll spectrin localizes to LEs for ORP1L-mediated RILP–p150^{Glued}–driven minus-end transport.

(**A**) Mel JuSo cells were transfected with GFP–RILP or GFP–N-RILP for 48 h before fixation and staining for I spectrin or ßIII spectrin. I and ßIII spectrin (red) are located on RILP- and N-RILP–labeled vesicles, as well as other subcellular structures. Note that ßIII spectrin labeling localizes differently within the GFP–RILP– or GFP–N-RILP–labeled vesicles. (insets) Magnification of vesicles showing the localization of RILP or N-RILP and I spectrin or ßIII spectrin. (**B**) HeLa cells were transfected with GFP–RILP and pSUPER vector coexpressing mRFP and a control or ßIII spectrin shRNA. Cells were fixed at 72 h after transfection and stained for endogenous p150^{Glued} (blue). (**C**) HeLa cells were transfected with GFP–ORP1L and pSUPER vector coexpressing mRFP and a control or ßIII spectrin shRNA. At 72 h after transfection, cells were fixed and stained for endogenous p150^{Glued} (blue). (**D**) Endogenous ORP1L and spectrin. HeLa cells were transfected with a ßIII spectrin shRNA pSUPER construct coexpressing mRFP. At 72 h after transfection, cells were fixed and stained for endogenous ORP1L (green) or endogenous CD63 (green) and the late endocytic marker Lamp-1 (blue). Bars, 10 µm.

If RILP and ßIII spectrin are receptors for the same motor protein, do they act in concert or independently? HeLa cells were transfected with GFP–RILP and a pSUPER construct that coexpresses mRFP and a control or ßIII spectrin short hairpin RNA (shRNA). The cells were fixed and stained for endogenous p150^{Glued}. Although (GFP–)RILP recruited p150^{Glued}, down-regulation of ßIII spectrin prevented transport of the RILP–p150^{Glued}–positive vesicles to the microtubule minus ends, which is similar to the situation observed after down-regulation of ORP1L (Fig. 7 B and Fig. 5 E). We subsequently tested whether the clustering of LEs imposed by ORP1L was also dependent on ßIII spectrin. HeLa cells were transfected with GFP–ORP1L– and pSUPER vector–coexpressing mRFP and control or ßIII spectrin shRNA. Cells were fixed and stained for p150^{Glued} (Fig. 7 C). GFP–ORP1L clustered vesicles without recruiting detectable p150^{Glued}, which is in accordance with the finding that RILP is responsible for recruiting p150^{Glued}. Silencing of ßIII spectrin expression resulted in scattering of ORP1L-positive vesicles, implying that minus-end transport of ORP1L and RILP-positive vesicles requires ßIII spectrin (Fig. 7, B and C). Unlike RILP, endogenous ORP1L was detectable with the available antibodies. We tested whether down-regulation of ßIII spectrin also induced scattering of organelles positive for endogenous ORP1L and other late endocytic markers. HeLa cells were transfected with the pSUPER vector coexpressing mRFP and a shRNA for ßIII spectrin before labeling (Fig. 7 D). Scattering of the ORP1L-, Lamp-1–, and CD63-positive LEs was only detected in the mRFP-expressing transfected cells. These results suggest that ßIII spectrin is required for minus-end transport of LEs labeled with endogenous or ectopically expressed ORP1L (Fig. 7, C and D). Notably, silencing of ßIII spectrin (Fig. 7 B), as well as ORP1L (Fig. 5 E), prevents LEs labeled with Rab7–RILP–p150^{Glued} complexes to be actively transported to the minus end of microtubules.

Discussion

Most intracellular organelles are transported along microtubules in a bidirectional manner, driven by at least two oppositely directed motor proteins. Late endosomes, like MIICs, move bidirectionally by the alternating activities of the dynein–dynactin motor (for minus-end transport) and the kinesin motor (for plus-end transport; Wubbolts *et al*., 1999). The function of motor proteins must be spatially and temporally coordinated to explain this complex pattern of organelle motility. We show how minus-end transport of LEs by the dynein–dynactin motor is regulated by the tripartite complex ORP1L–Rab7–RILP. We show that RILP directly interacts with the 25-kD C-terminal region of $p150^{Glued}$. This explains how activation of Rab7, via RILP, recruits the dynein–dynactin motor to LEs. However, we also show that this motor recruitment does not suffice for minus-end microtubular transport of LEs. ORP1L is presumably essential for translocation of Rab7–RILP–$p150^{Glued}$ to ßIII spectrin, which acts as the general dynein receptor on LEs and other organelles (De Matteis and Morrow, 2000). Only then does dynein motor–driven minus-end transport ensue. Rab7–RILP is the late endocytic–specific dynein motor receptor that cooperates with the general dynein receptor ßIII spectrin for active dynein motor activity on LEs. This $p150^{Glued}$–RILP–Rab7–ORP1L–ßIII spectrin cascade explains one critical step in the spatiotemporal control of late endocytic motility.

ßIII spectrin pairs with I spectrin and the IßIII spectrin heterodimer localizes to the cytosolic side of LEs, Golgi, and other organelles (Stankewich *et al*., 1998; De Matteis and Morrow, 2000). However, its presence does not suffice to recruit the dynein motor. Instead, activation of Rab7 specifies the target membrane for RILP- and ORP1L-mediated dynein–dynactin motor activities rather than the more ubiquitous spectrin receptor. Several Rab proteins have recently been found to control motor proteins either via a direct interaction or via effector proteins (Jordens *et al*., 2005). In all cases, it is unclear whether additional membrane motor receptors on specific compartments are also involved in RabGTPase-controlled, motor-driven transport.

We define a novel interaction where Rab7 recruits RILP to interact with the C terminus of $p150^{Glued}$. This may stabilize the projecting motor arm on the dynein–dynactin base comprised of Arp1, $p50^{dynamitin}$, and other subunits (Schroer, 2004). The C-terminal fragment of $p150^{Glued}$ also interacts with dynein intermediate chain and Arp1 (Kumar *et al*., 2001) in a manner that still leaves space for RILP interactions. That RILP interacts with a fragment near the dynein–dynactin motor base is not unexpected because the Rab7–RILP complex is membrane embedded and not likely to protrude far from the membrane. We have previously failed to detect this by cryoelectronmicroscopy (Jordens *et al*., 2001), probably because of the inefficiency of immunolabeling.

In this study, we have used a series of techniques to study the interaction between Rab7 and two of its effectors, RILP and ORP1L. The FRET results indicate that Rab7, RILP, and ORP1L are in close proximity in living cells, and our *in vitro* experiments indicate that RILP and ORP1L can bind simultaneously to the same active GTP-loaded Rab7 molecule. In fact, the binding of ORP1L to Rab7 is stabilized by RILP. The N-terminal ANK region of ORP1L specifies the Rab7 interaction (Johansson *et al*., 2005). We now show that the ANK region binds directly to active GTP-loaded Rab7, but additional determinants in the C-terminal half of ORP1L stabilize the RILP–Rab7–ORP1L tripartite complex. Because the crystal structure of the Rab7–RILP complex revealed that two GTP-loaded Rab7 molecules bind on opposite sides of a RILP homodimer (Wu *et al*., 2005), the RILP–Rab7–ORP1L complex is probably a heterotrimeric dimer with ORP1L positioned at the boundaries of the complex (Fig. 8).

How does the RILP–Rab7–ORP1L complex recruit the dynein motor to LEs? Rab7 associates with LEs after GTP binding and recruits the effectors RILP and/or ORP1L, thus forming a tripartite complex. In theory, both effectors could mediate the recruitment of the motor. When we overexpressed $p50^{dynamitin}$ to dissociate the dynein–dynactin motor complex such that the $p150^{Glued}$ subunit becomes solubilized, RILP, but not ORP1L, was able to recruit soluble $p150^{Glued}$ to LEs. $p150^{Glued}$ is in fact the most membrane-distal subunit that becomes detached from the Arp1 filament at the base of dynactin after $p50^{dynamitin}$ overexpression (Echeverri *et al*., 1996; Burkhardt *et al*., 1997; Ahmad *et al*., 1998; Eckley *et al*., 1999). Using $p150^{Glued}$ deletion constructs, we identified the RILP-interacting determinant as the most C-terminal 25-kD part of $p150^{Glued}$. In vitro reconstitution experiments confirmed that RILP, unlike N-RILP or ORP1L, directly interacts with this C-terminal region of $p150^{Glued}$. Thus, the C-terminal half of RILP interacts with GTP–Rab7 and the N-terminal half interacts with the C-terminus of $p150^{Glued}$, and probably with the C-terminus of ORP1L (Fig. 8). The N-terminal half of RILP could not be successfully produced in E. coli because of aggregation of the expressed protein and was not recruited to LEs. Thus, a direct interaction of this domain with $p150^{Glued}$ could not be tested. Because both RILP and $p150^{Glued}$ are homodimers, these two proteins may bind as dimer–dimer, but this has not been experimentally verified.

If the Rab7–RILP complex recruits the dynein–dynactin motor complex by directly interacting

8

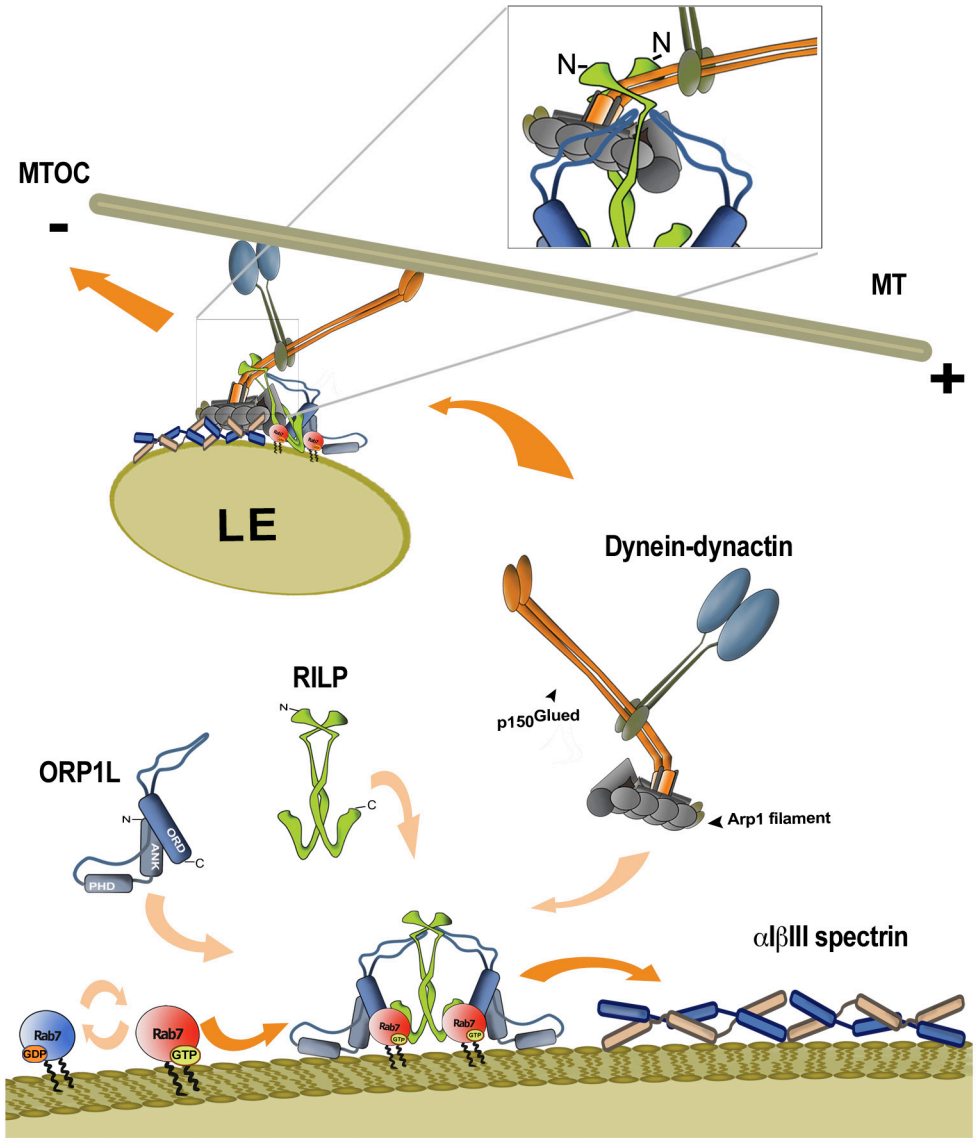


Figure 8. Model for function of ORP1L in the translocation of the Rab7–RILP–p150^{Glued}–dynein motor complex to ßIII spectrin for minus-end transport.

Active GTP-loaded Rab7 localizes to membranes of LEs and recruits the effectors RILP and ORP1L to form a dimer of a heterotrimeric complex. The C-terminal domain of RILP interacts with the switch and interswitch (RabSF1 and RabSF4) regions of Rab7, and the N-terminal half of RILP binds to the C-terminal domain of p150^{Glued} (shown in detail in the box). Subsequently, the 2.4-MD dynein–dynactin motor is recruited by the 0.35-MD ORP1L–Rab7–RILP complex on LEs. ORP1L is required to direct the entire complex to the 0.6-MD IßIII spectrin. The interaction is mediated by Arp1 binding to ßIII spectrin. IßIII spectrin localizes to several different compartments, but it is not sufficient on its own to recruit dynein motors. Microtubule-based, dynein motor–driven minus-end transport of LEs can only occur after the specific late endocytic dynein receptor Rab7–RILP has interacted with the general dynein membrane receptor ßIII spectrin, a process that is facilitated by ORP1L.

with p150^{Glued}, the function of ORP1L remains elusive. RILP mainly contains coiled-coil regions, whereas ORP1L is composed of multiple defined domains, including three ankyrin repeats, a PH domain, and an oxysterol-binding domain. Both ßIII spectrin and ORP1L contain a PH domain with similar specificity (Rameh *et al*., 1997; Johansson *et al*., 2005). It is possible that ORP1L is required for Rab7–RILP–dynein motor targeting to specific microdomains on LEs to deliver the dynein motor to its spectrin receptor. This is likely to be the 622-kD IßIII spectrin heterodimer (Stankewich *et al*., 1998; De Matteis and Morrow, 2000), which remains bound to late endosomes when RILP is inactivated (Fig. 7 A). The 272-kD ßIII spectrin protein contains two Arp1-binding sites (Holleran *et al*., 2001), repeat regions involved in several protein–protein interactions and a C-terminal PH domain (De Matteis and Morrow, 2000). Via its various molecular interactions, spectrin is strongly associated with multiple membrane compartments, including LEs. Using RNAi, we show that ßIII spectrin is critical for minus-end dynein-mediated transport of LEs. Surprisingly, inactivation of ORP1L or ßIII spectrin prevented minus-end dynein-mediated transport of LEs, even when Rab7–RILP recruited the p150^{Glued} subunit of dynactin onto the membranes of LEs. The similarity of phenotypes suggests that ORP1L and spectrin are functionally connected. ORP1L could interact directly with IßIII spectrin, perhaps via its ankyrin repeats. Because the PH domains of ORP1L and ßIII spectrin have overlapping specificities (Rameh *et al*., 1997; Johansson *et al*., 2005), ORP1L may also transfer the Rab7–RILP–p150^{Glued} complex to the correct microdomains for docking the dynein motor on ßIII spectrin. This transfer could be required for dynein motor activation by an unknown mechanism.

In addition, such microdomains may contain a GTPase-activating protein to inactivate GTP–Rab7 and dissociate the RILP–dynein motor complex from LEs. This may be essential because a kinesin and/or dynein motor should be cyclically recruited or activated to drive the bidirectional transport of LEs in a stop-and-go fashion (Wubbolts *et al*., 1999). How the kinesin motor is recruited and whether this requires dissociation of the Rab7–RILP–dynein motor complex is unclear. Kinesin II can associate with p150^{Glued} (Deacon *et al*., 2003; Gross, 2003), and the bidirectional movement may be driven by alternating activities of the kinesin and dynein motors on the ORP1L–Rab7–RILP-recruited–p150^{Glued} complex docked on ßIII spectrin, which acts as a receptor for both motor activities.

Based on the data presented here, we propose the following model for Rab7-controlled recruitment of the dynein motor complex to its receptor IßIII spectrin on LEs (Fig. 8). After GTP binding, Rab7 is recruited to late endocytic membranes. Active Rab7 binds two proteins with different functions. The RILP homodimer binds to the switch and interswitch regions of Rab7, arresting Rab7 in the active membrane-bound state (Jordens *et al*., 2001; Wu *et al*., 2005; Marsman *et al*., 2006). ORP1L binding to Rab7 is stabilized by RILP to form a 360-kD complex. Within this complex, the RILP dimer associates with the base of p150^{Glued} to facilitate the recruitment of the dynein–dynactin motor. ORP1L then targets the Rab7–RILP–dynein motor complex to the spectrin receptor on LEs. ORP1L and ßIII spectrin are both required for a functional dynein motor, suggesting that RILP-mediated recruitment of the dynein motor to LEs does not suffice for correct docking on the LE–dynein receptor ßIII spectrin. The dynein motor is apparently only activated with full cooperation of Rab7, RILP, and ORP1L. The complicated bidirectional motility of LEs is regulated by networks of macromolecular complexes controlled by the small GTPase Rab7.

Materials and Methods

cDNA constructs and vectors

ORP1L, RILP, N-RILP, and Rab7 cDNA constructs have been previously described (Fig. 1 A; Jordens *et al*., 2001; Johansson *et al*., 2003, 2005; Marsman *et al*., 2004). The mammalian expression vectors used were pcDNA4HisMax (Invitrogen), pcDNA3.1 (Invitrogen), and pEGFP-C (BD Biosciences). The mRFP–RILP and mRFP–Rab7 fusion constructs were generated by amplification of full-length mRFP by PCR (template plasmid provided by R.Y. Tsien, University of California, San Diego, La Jolla, CA) using forward primer 5'-CCCAGCTAGCACCACCATGGCCTCCTCCGAGGACGTCAT-3' and reverse primer 5'-GAAGATCTGGCGCCGGTGGAGTG-3'. The mRFP fragment was ligated into the NheI and BglII sites in vector pEGFP-C1, from which the GFP moiety had been removed. The GFP–Arp1 construct was a gift from C. Hoogenraad (Erasmus Medical Centre, Rotterdam, Netherlands). The C-terminal fragments of p150^{Glued} encoding aa 887–1,278 and 1,049–1,278 were generated by PCR and ligated into the EcoRI and BamHI sites of vector pEGFP-C2 (CLONTECH Laboratories, Inc.). For production of MBP–p150^{Glued} fusion proteins, the same fragments were cloned into the EcoRI and BamHI sites of vector pMAL-c2X (New England Biolabs). A pSUPER vector coexpressing mRFP (Bergink *et al*., 2006) was used to express short hairpins to downregulate human ßIII spectrin (the sequence targeted by the expressed RNAi is 5'-CGTGGCACGGCTCTGGGAC-3'). siRNA for human RILP was obtained from Dharmacon (ON-TARGETplus SMARTpool for ac-

cession no. NP_113618) and cotransfected with a vector expressing GFP–ORP1L (Johansson *et al*., 2005), using DharmaFECT 1 transfection reagent (Dharmacon). Human ORP1L siRNA oligos with sequence 5'-UrGrCrCrArGUrGrCrCrGrGrAUUrCUrGrATT -3' were obtained from Proligo and were cotransfected with a vector expressing GFP–RILP (Marsman *et al*., 2006) using Lipofectamine 2000 (Invitrogen).

For production of hexahistidine (His_6)-tagged proteins, full-length Rab7, or Rab7Q67L, cDNAs were subcloned into the BamHI and XhoI sites of pET-28a (Novagen). A cDNA fragment encoding full-length RILP was subcloned into the NcoI–HindIII sites of vector pETM-11 (a gift from G. Stier, European Molecular Biology Laboratory, Heidelberg, Germany) for production of His_6-tagged RILP. N-RILP was subcloned as a BglII fragment into a BamHI-digested vector pRSET-C (Invitrogen).

Vector pRP265, which is a derivative of pGEX-2T (GE Healthcare) with a modified multiple cloning site, was used to generate GST–Rab7 fusion protein. Full-length ORP1L, ORP1S, and ANK fragment inserts were subcloned into the BamHI site of vector pGEX-1T (GE Healthcare) for production of GST fusion proteins. Constructs are depicted in Fig. 1 A.

Antibodies

GST–ORP1 and GST–RILP fusion proteins were used for generation of rabbit polyclonal antibodies (Jordens *et al*., 2001; Johansson *et al*., 2003, 2005). The other antibodies used were chicken anti-Rab7 (a gift from A. Wandinger-Ness, University of New Mexico, Albuquerque, NM), rabbit anti-Rab7 (Santa Cruz Biotechnology, Inc.), rabbit anti–human I spectrin and rabbit anti–human ßIII spectrin (Santa Cruz Biotechnology, Inc.), mouse anti-Xpress (Invitrogen), mouse anti-myc (Santa Cruz Biotechnology, Inc.), mouse anti-$p150^{Glued}$ (BD Biosciences), HRP-conjugated monoclonal anti-MBP (New England Biolabs), and polyclonal goat anti-GST (GE Healthcare).

Protein purification

His_6-tagged RILP was produced in the E. coli strain Rosetta (DE3) pLysS (Novagen) in autoinduction high-density shaking cultures (Studier, 2005) at 24°C for 20 h. Cells were collected and resuspended in buffer A (25 mM Hepes, pH 7.5, 300 mM NaCl, Complete EDTA-free Protease Inhibitor Cocktail [Roche], 1 mM PMSF, 5 mM ß-mercaptoethanol, 10 mM imidazole, and 0.05% [vol/vol] Triton X-100), and then lysed by sonication on ice. The cleared lysate was incubated with preequilibrated Talon Co2+ resin (CLONTECH Laboratories, Inc.) for 1 h. The resin was packed into a column and washed with buffer A containing 20 mM imidazole, and His_6-RILP was eluted by a step-gradient of imidazole in buffer A. The eluted protein was concentrated in 25 mM Hepes, pH 7.5, 300 mM NaCl, and 10% (vol/vol) glycerol in 10-kD cut-off concentrators (Vivaspin-2; Sartorius).

GST–ORP1L was produced in a similar manner at an induction temperature of 30°C for 18 h. Cells were harvested and lysed in buffer B (25 mM Hepes, pH 8.0, 150 mM NaCl, 1 mM PMSF, Complete Protease Inhibitor Cocktail, 0.1% Triton X-100, and 1 mM DTT). The soluble fraction was combined with glutathione–Sepharose 4B beads (GE Healthcare) and washed extensively with buffer (25 mM Hepes, pH 7.6, and 100 mM NaCl), and the protein was eluted with 15 mM reduced glutathione. The protein was concentrated in 25 mM Hepes, pH 7.6, 150 mM NaCl, 15% (vol/vol) glycerol, and 1 mM DTT.

GST–ANK expression was induced in BL21(DE3) (Stratagene) with 1.0 mM IPTG for 4 h at 37°C. Cells were harvested, resuspended in PBS, and lysed by freeze–thaw cycles followed by sonication. The cleared lysate was incubated with glutathione–Sepharose 4B and washed with PBS, and the protein was eluted with 20 mM reduced glutathione in PBS.

His_6-tagged Rab7 and His_6-tagged Rab7Q67L were expressed in BL21(DE3) (Stratagene) by induction with 0.5 mM IPTG for 5 h at 30°C. After harvesting, the cells were resuspended in 25 mM Hepes, pH 8.0, 300 mM NaCl, 5 mM MgCl2, Complete EDTA-free Protease Inhibitor Cocktail, 1 mM PMSF, 5 mM ß-mercaptoethanol, and 10 mM imidazole, and lysed by sonication on ice. The clarified lysates were passed through a HiTrap Chelating HP column (GE Healthcare) charged with Co2+ and further purified using a HiTrap SP HP column (GE Healthcare) in 20 mM Mes, pH 6.0, 100 mM NaCl, 5 mM MgCl2, and 5 mM ß-mercaptoethanol.

E. coli BL21(DE3) cells harboring the GST–Rab7 construct were induced with 0.5 mM IPTG for 5 h at 30°C. Cells were harvested, resuspended in a buffer containing 50 mM Tris-HCl, pH 7.5, 200 mM NaCl, 1 mM PMSF, Complete EDTA-Free Protease Inhibitor Cocktail, 5 mM MgCl2, and 1 mM DTT, and lysed by sonication on ice. The cleared lysate was loaded on a preequilibrated GSTrap FF column (GE Healthcare) and washed extensively with the same buffer. GST–Rab7 was eluted with 50 mM Tris-HCl, pH 8.0, 100 mM NaCl, 5 mM MgCl2, 1 mM DTT, and 20 mM reduced glutathione.

The MBP–p150^{Glued} fusion proteins were expressed in E. coli strain Rosetta (DE3) pLysS (Novagen) and affinity purified using an amylose resin column (New England Biolabs) according to the manufacturer's instructions. All fusion proteins made were analyzed by SDS-PAGE and Coomassie staining; they are depicted in Fig. 1 B.

Immunoprecipitations

Transfected HeLa cells (2 x 106) were washed with ice-cold PBS and scraped into 400 µl of lysis buffer (20 mM Hepes, pH 7.6, 150 mM NaCl, 2 mM MgCl2, 10% glycerol, 0.5% Triton X-100, and 1 mM DTT) with Complete EDTA-free Protease Inhibitor Cocktail. Cells were kept on ice for 15 min and centrifuged for 15 min at 16,000 g at 4°C, and the supernatant was preadsorbed at 4°C for 30 min with 30 µl of protein G-Sepharose 4 Fast Flow (GE Healthcare). The recovered supernatant was incubated with Xpress or irrelevant control antibodies at 4°C overnight. The lysate–antibody mixture was incubated at 4°C with protein G-Sepharose for 4 h, followed by washing with lysis buffer. For immunoprecipitation of endogenous ORP1L from HeLa lysates, cells (107) were lysed and preadsorbed as described for supernatant. The recovered supernatant was incubated with RILP or irrelevant control antibodies at 4°C for 2 h. The lysate–antibody mixture was incubated at 4°C with protein G–Sepharose for 2 h, followed by washing with lysis buffer. The immunoprecipitates were analyzed by SDS-PAGE and Western blotting.

Pull-down of endogenous RILP

100 µg GST–ORP1L fusion protein and an approximately equimolar amount of 25 µg GST were coupled to 30 µl glutathione–Sepharose 4B beads in coupling buffer (PBS, 2 mM MgCl2, and 1 mM DTT) for 2 h at 4°C. Beads were washed with coupling buffer and equilibrated in lysis buffer (20 mM Hepes, pH 7.6, 150 mM NaCl, 2 mM MgCl2, 10% glycerol, 0.5% Triton X-100, and 1 mM DTT). HeLa cells were lysed as described in the immunoprecipitations section. After centrifugation of the lysates for 15 min at 16,000 g at 4°C, the supernatant was added to the beads and incubated for 2 h at 4°C. Beads were washed extensively with lysis buffer, and bound proteins were eluted with 20 mM glutathione. The eluted proteins were analyzed by SDS-PAGE and Western blotting.

Pull-down of *in vitro*–translated fragments

^{35}S-labeled full-length and truncated proteins were generated by *in vitro* transcription/translation using the TnT coupled reticulocyte system (Promega) according to the manufacturer's instructions. 50 µg wild-type GST–Rab7 fusion protein was coupled to 20 µl glutathione–Sepharose 4B beads in coupling buffer (PBS, 2 mM MgCl2, and 1 mM DTT) for 2 h at 4°C. Beads were washed with coupling buffer and equilibrated in 20 mM Hepes, pH 7.5, 100 mM KAc, 0.5 mM MgCl2, 1 mM DTT, 2 mM EDTA, and 10 mg/ml albumin. The beads were incubated with 10 µM GTP for 10 min at room temperature, after which MgCl2 was added to a final concentration of 10 mM and the incubation was continued for an additional 30 min. Purified His_6–RILP, His_6–N-RILP, or GST–ORP1L (0 ng, 100 ng, 1 µg, and 5 µg) and *in vitro*–translated proteins (22 µl) were added to the beads and incubated in a total volume of 0.5 ml for 2 h at 4°C. Beads were washed extensively with wash buffer (20 mM Hepes, pH 7.5, 100 mM KAc, 5 mM MgCl2, and 1 mM DTT), and proteins were eluted with 20 mM glutathione in wash buffer and resolved by SDS-polyacrylamide gels, which were exposed on x-ray film (Kodak) or analyzed by phosphor imaging (FLA-3000; Fujifilm).

Pull-down of purified ORP1L

50 µg His_6–RILP and 50 µg His_6–Rab7Q67L were coupled to 20 µl Talon Co2+ resin (CLONTECH Laboratories, Inc.) in coupling buffer (20 mM Hepes, pH 7.5, 150 mM NaCl, 2 mM MgCl2, 10% glycerol, and 5 mM ß-mercaptoethanol) for 1 h at 4°C. Beads were washed and equilibrated in coupling buffer with 10 mM imidazole. 2.3 µg purified GST–ORP1L or 5 µg plain GST was added to the beads and incubated for 2 h at 4°C. Beads were washed extensively with binding buffer (20 mM Hepes, pH 7.5, 150 mM NaCl, 2 mM MgCl2, 10% glycerol, 5 mM ß-mercaptoethanol, and 10 mM imidazole) and eluted with 750 mM imidazole in 20 mM Hepes, pH 7.5, 150 mM NaCl, 10% glycerol, and 5 mM ß-mercaptoethanol. Samples were analyzed by SDS-PAGE and Western blotting.

Pull-down of purified His_6–RILP

100 µg GST–ANK was coupled to glutathione–Sepharose 4B beads in PBS for 2 h at 4°C, after which the beads were washed and equilibrated in binding buffer (20 mM Hepes, pH 7.5, 150 mM NaCl, 2 mM MgCl2, 10% glycerol, 0.5% Triton X-100, and 1 mM DTT). 10 µg purified His_6–RILP and/or 20 µg His_6–Rab7Q67L were added to the beads and incubated for 4 h at 4°C.

Beads were washed with binding buffer and eluted with 20 mM glutathione (30 µl) in binding buffer. Samples were analyzed by SDS-PAGE and Western blotting.

p150^{Glued}-binding assay

30 µg GST–Rab7 was coupled to 15 µl glutathione–Sepharose 4B beads and preloaded with GTPS as described for the pull-down of *in vitro*–translated fragments. Beads were washed to remove unbound proteins, and recombinant purified His_6–RILP (3 µg), His_6–N-RILP (2 µg), or GST–ORP1L (8 µg) was added to the beads and incubated in a total volume of 0.4 ml for 2 h at 4°C. Beads were washed extensively with detergent/salt buffer (20 mM Hepes, pH 7.5, 300 mM NaCl, 1 mM DTT, 2 mM MgCl2, and 0.1% [vol/vol] Triton X-100), and 4 µg of either MBP–p150^{Glued} (aa 887–1,278) or MBP–p150^{Glued} (aa 1,049–1,278) was added to the beads. Proteins were incubated further in a total volume of 0.4 ml of detergent/salt buffer for 30 min at 22°C. Beads were washed and proteins bound to GTP–Rab7 were eluted by supplementing the 0.4 ml of detergent/salt reaction buffer with EDTA to a final concentration of 20 mM. To precipitate the MBP–p150^{Glued} C25 fusion (aa 1,049–1,278), the elution fractions were combined with 20 µl of amylose resin and incubated for 1 h at 4°C. The resin was washed extensively with detergent/salt buffer before analysis by SDS-PAGE and Western blotting.

Immunofluorescence microscopy

Transfected cells were fixed either with 4% formaldehyde in PBS for 30 min and permeabilized for 5 min with 0.05% Triton X-100 in PBS or with methanol (–20°C) for 5 min. Nonspecific binding of antibodies was blocked by 10% FBS/PBS for 30 min, after which cells were incubated with primary antibody in 5% FBS/PBS for 30 min at 37°C. Bound primary antibodies were visualized with Alexa Fluor secondary antibody conjugates (Invitrogen). Cells were mounted in Mowiol (Calbiochem) containing 50 mg/ml 1,4-diazocyclo-[2,2,2]octane (Sigma-Aldrich) or in Vectashield mounting medium (Vector Laboratories). The specimens were analyzed with confocal laser scanning microscopes (TCS SP1 or TCS SP2) equipped with HCX PL APO and HCX PL APO lbd.bl 40x/NA 1.32 objective lenses (all Leica). The acquisition software used was Leica LCS.

FLIM

FLIM experiments were performed at 37°C in a 5% CO2 culture hood on an inverted microscope (DM-IRE2; Leica) fitted with a TCS SP2 scanhead and HCX PL APO lbd.bl 40x/NA 1.32 objective lenses and equipped with Lambert Instruments frequency domain lifetime attachment, controlled by EZflim software (Lambert Instruments). Cells were cultured in Delta T dishes (Bioptechs) in CBS medium (140 mM NaCl, 5 mM KCl, 2 mM MgCl2, 1 mM CaCl2, 23 mM NaHCO3, 10 mM [D-]glucose, and 10 mM Hepes, pH 7.3, under 5% CO2 condition). GFP was excited with 4 mW of 488-nm light from a LED modulated at 40 MHz, and emission was collected at 490–550 nm using an intensified charge-coupled device camera (CoolSNAP HQ; Roper Scientific). To calculate the GFP lifetime, the intensities from 40 phase-shifted images (modulation depth 70%) were fitted with a sinus function, and lifetimes were derived from the phase shift between excitation and emission. For internal control, cells were cocultured with Mel JuSo cells expressing H2B–GFP only. Lifetimes were referenced to a 1-µM solution of rhodamine-G6 in saline that was set at a 4.11-ns lifetime. The donor FRET efficiency E_D was calculated as $E_D = 1 - (\text{measured lifetime/GFP lifetime in control cells})$ (Zwart *et al*., 2005).

Acknowledgements

We are grateful to Seija Puomilahti and Pirjo Ranta for skilled technical assistance. Angela Wandinger-Ness, Roger Y. Tsien, Casper Hoogenraad, and Gunther Stier are acknowledged for providing antibodies and cDNA constructs; Ira Mellman, Marije Marsman, and Peter Peters for support and critical reading of the manuscript; and Kees Jalink for help with FLIM.

Marie Johansson was supported by the Helsinki Graduate School of Biotechnology and Molecular Biology, a European Molecular Biology Organization short-term fellowship, The Finnish Cultural Foundation, and the Alfred Kordelin Foundation. Nuno Rocha was supported by a Portuguese Foundation for Science and Technology FCT/ FSE PhD scholarship within the Third Framework Program and a grant from the Dutch Cancer Society KWF. This study was further supported by the Academy of Finland (grants 206298 and 113010), the Sigrid Juselius Foundation, and the Finnish Foundation for Cardiovascular Research (to V.M. Olkkonen).

References

Ahmad, F.J., C.J. Echeverri, R.B. Vallee, and P.W. Baas. 1998. Cytoplasmic dynein and dynactin are required for the transport of microtubules into the axon. J Cell Biol. 140:391-401.

Bastiaens, P.I., and A. Squire. 1999. Fluorescence lifetime imaging microscopy: spatial resolution of biochemical processes in the cell. Trends Cell Biol. 9:48-52.

Berger, B., D.B. Wilson, E. Wolf, T. Tonchev, M. Milla, and P.S. Kim. 1995. Predicting coiled coils by use of pairwise residue correlations. Proc Natl Acad Sci U S A. 92:8259-63.

Burkhardt, J.K., C.J. Echeverri, T. Nilsson, and R.B. Vallee. 1997. Overexpression of the dynamitin (p50) subunit of the dynactin complex disrupts dynein-dependent maintenance of membrane organelle distribution. J Cell Biol. 139:469-84.

Cantalupo, G., P. Alifano, V. Roberti, C.B. Bruni, and C. Bucci. 2001. Rab-interacting lysosomal protein (RILP): the Rab7 effector required for transport to lysosomes. Embo J. 20:683-93.

Colucci, A.M., M.C. Campana, M. Bellopede, and C. Bucci. 2005. The Rab-interacting lysosomal protein, a Rab7 and Rab34 effector, is capable of self-interaction. Biochem Biophys Res Commun. 334:128-33.

Culver-Hanlon, T.L., S.A. Lex, A.D. Stephens, N.J. Quintyne, and S.J. King. 2006. A microtubulebinding
domain in dynactin increases dynein processivity by skating along microtubules. Nat Cell Biol. 8:264-70.

Deacon, S.W., A.S. Serpinskaya, P.S. Vaughan, M. Lopez Fanarraga, I. Vernos, K.T. Vaughan, and V.I. Gelfand. 2003. Dynactin is required for bidirectional organelle transport. J Cell Biol. 160:297-301.

Echard, A., F. Jollivet, O. Martinez, J.J. Lacapere, A. Rousselet, I. Janoueix-Lerosey, and B. Goud. 1998. Interaction of a Golgi-associated kinesin-like protein with Rab6. Science. 279:580-5.

Echeverri, C.J., B.M. Paschal, K.T. Vaughan, and R.B. Vallee. 1996. Molecular characterization of the 50-kD subunit of dynactin reveals function for the complex in chromosome alignment and spindle organization during mitosis. J Cell Biol. 132:617-33.

Eckley, D.M., S.R. Gill, K.A. Melkonian, J.B. Bingham, H.V. Goodson, J.E. Heuser, and T.A. Schroer. 1999. Analysis of dynactin subcomplexes reveals a novel actin-related protein associated with the arp1 minifilament pointed end. J Cell Biol. 147:307-20.

Förster, T. 1948. Zwischenmolekulare energiewandering und fluoreszenz. Annalen Physik. 6:55-75.

Gross, S.P. 2003. Dynactin: coordinating motors with opposite inclinations. Curr Biol. 13:R320-2.

Hammer, J.A., 3rd, and X.S. Wu. 2002. Rabs grab motors: defining the connections between Rab GTPases and motor proteins. Curr Opin Cell Biol. 14:69-75.

Harrison, R.E., J.H. Brumell, A. Khandani, C. Bucci, C.C. Scott, X. Jiang, B.B. Finlay, and S. Grinstein. 2004. Salmonella impairs RILP recruitment to Rab7 during maturation of invasion vacuoles. Mol Biol Cell. 15:3146-54.

Hirokawa, N. 1998. Kinesin and dynein superfamily proteins and the mechanism of organelle transport. Science. 279:519-26.

Hoepfner, S., F. Severin, A. Cabezas, B. Habermann, A. Runge, D. Gillooly, H. Stenmark, and M. Zerial. 2005. Modulation of receptor recycling and degradation by the endosomal kinesin KIF16B. Cell. 121:437-50.

Holleran, E.A., L.A. Ligon, M. Tokito, M.C. Stankewich, J.S. Morrow, and E.L. Holzbaur. 2001.
beta III spectrin binds to the Arp1 subunit of dynactin. J Biol Chem. 276:36598-605.

Hoogenraad, C.C., A. Akhmanova, S.A. Howell, B.R. Dortland, C.I. De Zeeuw, R. Willemsen, P. Visser, F. Grosveld, and N. Galjart. 2001. Mammalian Golgi-associated Bicaudal-D2 functions in the dynein-dynactin pathway by interacting with these complexes. Embo J. 20:4041-54.

Hoogenraad, C.C., P. Wulf, N. Schiefermeier, T. Stepanova, N. Galjart, J.V. Small, F. Grosveld, C.I. de Zeeuw, and A. Akhmanova. 2003. Bicaudal D induces selective dynein-mediated microtubule minus end-directed transport. Embo J. 22:6004-15.

Imamura, T., J. Huang, I. Usui, H. Satoh, J. Bever, and J.M. Olefsky. 2003. Insulin-induced GLUT4 translocation involves protein kinase C-lambda-mediated functional coupling between Rab4 and the motor protein kinesin. Mol Cell Biol. 23:4892-900.

Johansson, M., V. Bocher, M. Lehto, G. Chinetti, E. Kuismanen, C. Ehnholm, B. Staels, and V.M. Olkkonen. 2003. The two variants of oxysterol binding protein-related protein-1 display different tissue expression patterns, have different intracellular localization, and are functionally distinct. Mol Biol Cell. 14:903-15.

Johansson, M., M. Lehto, K. Tanhuanpaa, T.L. Cover, and V.M. Olkkonen. 2005. The oxysterolbinding
protein homologue ORP1L interacts with Rab7 and alters functional properties of late endocytic compartments. Mol Biol Cell. 16:5480-92.

Jordens, I., M. Fernandez-Borja, M. Marsman, S. Dusseljee, L. Janssen, J. Calafat, H. Janssen, R. Wubbolts, and J. Neefjes. 2001. The Rab7 effector protein RILP controls lysosomal transport by inducing the recruitment of dynein-dynactin motors. Curr Biol. 11:1680-5.

Jordens, I., M. Marsman, C. Kuijl, and J. Neefjes. 2005. Rab proteins, connecting transport and vesicle fusion. Traffic. 6:1070-7.

Jordens, I., W. Westbroek, M. Marsman, N. Rocha, M. Mommaas, M. Huizing, J. Lambert, J. Naeyaert, and J. Neefjes. 2006. Rab7 and Rab27a control two motor protein activities involved in melanosomal transport. Pigment Cell Res. In Press.

Karki, S., and E.L. Holzbaur. 1999. Cytoplasmic dynein and dynactin in cell division and intracellular transport. Curr Opin Cell Biol. 11:45-53.

King, S.J., and T.A. Schroer. 2000. Dynactin increases the processivity of the cytoplasmic dynein motor. Nat Cell Biol. 2:20-4.

Kumar, S., Y. Zhou, and M. Plamann. 2001. Dynactin-membrane interaction is regulated by the Cterminal
domains of p150(Glued). EMBO Rep. 2:939-44.

Lehto, M., and V.M. Olkkonen. 2003. The OSBP-related proteins: a novel protein family involved in vesicle transport, cellular lipid metabolism, and cell signalling. Biochim Biophys Acta. 1631:1-11.

Lupas, A., M. Van Dyke, and J. Stock. 1991. Predicting coiled coils from protein sequences. Science. 252:1162-4.

Marsman, M., I. Jordens, C. Kuijl, L. Janssen, and J. Neefjes. 2004. Dynein-mediated vesicle transport controls intracellular Salmonella replication. Mol Biol Cell. 15:2954-64.

Marsman, M., I. Jordens, N. Rocha, C. Kuijl, L. Janssen, and J. Neefjes. 2006. A splice variant of RILP induces lysosomal clustering independent of dynein recruitment. Biochem Biophys Res Commun. 344:747-56.

Matanis, T., A. Akhmanova, P. Wulf, E. Del Nery, T. Weide, T. Stepanova, N. Galjart, F. Grosveld, B. Goud, C.I. De Zeeuw, A. Barnekow, and C.C. Hoogenraad. 2002. Bicaudal-D regulates COPI-independent Golgi-ER transport by recruiting the dynein-dynactin motor complex. Nat Cell Biol. 4:986-92.

Mizuno, K., A. Kitamura, and T. Sasaki. 2003. Rabring7, a novel Rab7 target protein with a RING
finger motif. Mol Biol Cell. 14:3741-52.

Muresan, V., M.C. Stankewich, W. Steffen, J.S. Morrow, E.L. Holzbaur, and B.J. Schnapp. 2001. Dynactin-dependent, dynein-driven vesicle transport in the absence of membrane proteins: a role for spectrin and acidic phospholipids. Mol Cell. 7:173-83.

Navarro, C., H. Puthalakath, J.M. Adams, A. Strasser, and R. Lehmann. 2004. Egalitarian binds dynein light chain to establish oocyte polarity and maintain oocyte fate. Nat Cell Biol. 6:427-35.

Schroer, T.A. 2004. Dynactin. Annu Rev Cell Dev Biol. 20:759-79.

Schroer, T.A., E.R. Steuer, and M.P. Sheetz. 1989. Cytoplasmic dynein is a minus end-directed motor for membranous organelles. Cell. 56:937-46.

Short, B., C. Preisinger, J. Schaletzky, R. Kopajtich, and F.A. Barr. 2002. The Rab6 GTPase regulates recruitment of the dynactin complex to Golgi membranes. Curr Biol. 12:1792-5.

Studier, F.W. 2005. Protein production by auto-induction in high density shaking cultures. Protein Expr Purif. 41:207-34.

Vale, R.D. 2003. The molecular motor toolbox for intracellular transport. Cell. 112:467-80.

Wallrabe, H., and A. Periasamy. 2005. Imaging protein molecules using FRET and FLIM microscopy. Curr Opin Biotechnol. 16:19-27.

Waterman-Storer, C.M., S. Karki, and E.L. Holzbaur. 1995. The p150^{Glued} component of the dynactin complex binds to both microtubules and the actin-related protein centractin (Arp-1). Proc Natl Acad Sci U S A. 92:1634-8.

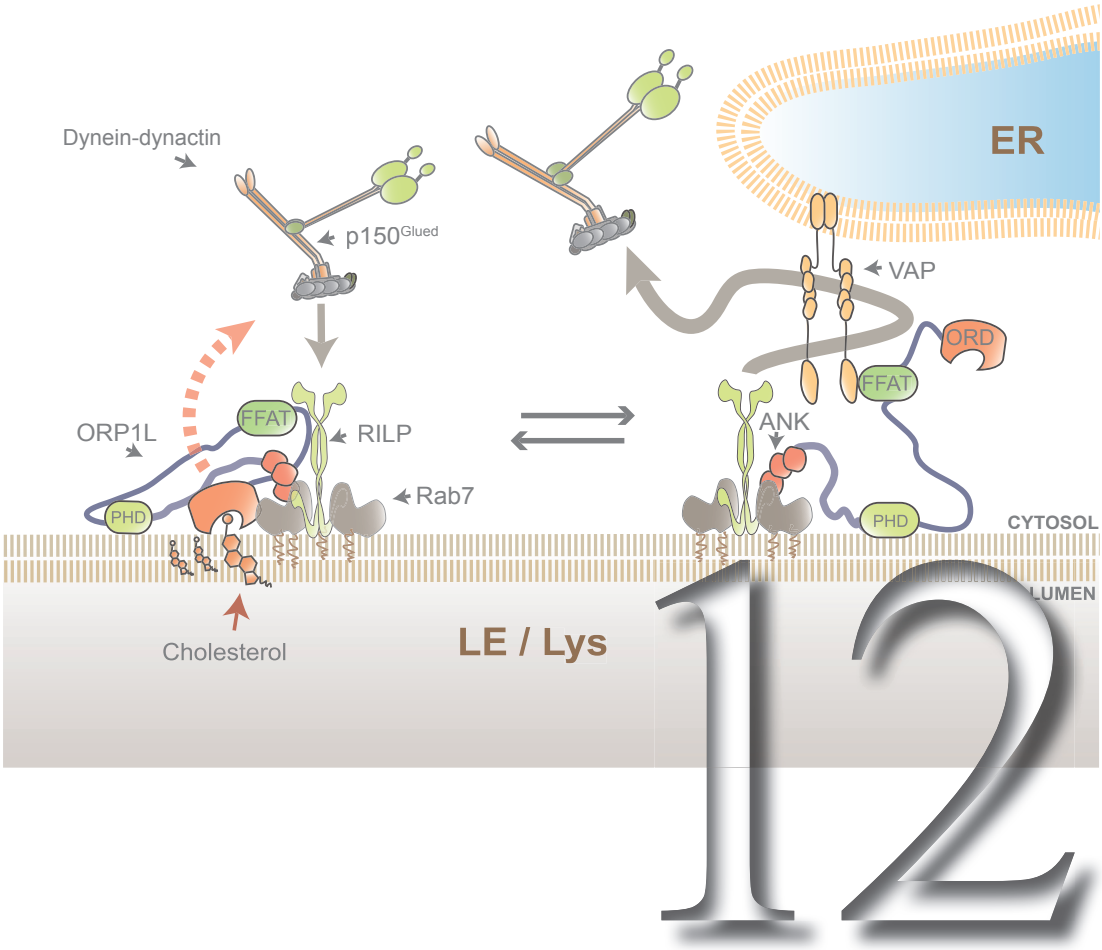
Wu, M., T. Wang, E. Loh, W. Hong, and H. Song. 2005. Structural basis for recruitment of RILP by small GTPase Rab7. Embo J. 24:1491-501.

Wubbolts, R., M. Fernandez-Borja, I. Jordens, E. Reits, S. Dusseljee, C. Echeverri, R.B. Vallee, and J. Neefjes. 1999. Opposing motor activities of dynein and kinesin determine retention and transport of MHC class II-containing compartments. J Cell Sci. 112 (Pt 6):785-95.

Zwart, W., A. Griekspoor, C. Kuijl, M. Marsman, J. van Rheenen, H. Janssen, J. Calafat, M. van Ham, L. Janssen, M. van Lith, K. Jalink, and J. Neefjes. 2005. Spatial separation of HLADM/HLA-DR interactions within MIIC and phagosome-induced immune escape. Immunity.22:221-33.

Cholesterol sensor ORP1L organizes late endosomal contacts with the ER protein VAP that controls Rab7-RILP-p150^{Glued} and late endosomal positioning

Submitted



Cholesterol sensor ORP1L organizes late endosomal contacts with the ER protein VAP that controls Rab7-RILP-p150^{Glued} and late endosomal positioning

Nuno Rocha, Coenraad Kuijl[+], Rik van der Kant[+], Lennert Janssen, Diane Houben, Hans Janssen, Wilbert Zwart[*] and Jacques Neefjes[*].

Abstract
Late endosomes and lysosomes have characteristic intracellular distributions determined by various motor proteins. The Rab7 effector RILP interacts with the oxysterol-binding protein ORP1L and is the receptor for the dynactin subunit p150^{Glued} and associated motor proteins on late endosomes. We show that cholesterol levels in late endosomes determine the conformational of ORP1L. Cholesterol in the cytosolic leaflet of late endosomes is sensed by ORP1L and cholesterol levels are lower in peripheral vesicles than in vesicles residing near the microtubule minus-end. Under low cholesterol conditions, ORP1L conformation induces formation of ER-late endosomal membrane contact sites (ER-LE-MCS). Here the ER protein VAP can interact *in trans* with the Rab7-RILP complex to remove p150^{Glued} and associated motors. As a result, late endosomes move to the microtubule plus-end. Under high cholesterol conditions, as in Niemann-Pick type C disease, this process is prevented resulting in accumulation of late endosomes at the microtubule minus-end due to dynein motor activity. These data explain how cholesterol through ORP1L controls late endosomal positioning in cells.

Introduction

Late endosomes, lysosomes and lysosome-related organelles (hereafter collectively called LE) have characteristic positions in cells through interactions with cytoskeletal elements usually through motor proteins. Whereas most LE locate near the nucleus at the minus-end of microtubules, more peripheral LE move along polarized microtubules in a bidirectional and stop-and-go fashion. This dynamic behaviour is dependent on the activities of microtubule-based motors of opposite polarities. The dynein-dynactin motor drives minus-end (inward-directed) transport and at least two kinesin motor proteins (KIF5 and KIF3) have been implicated in plus-end (outward-directed) transport of late endosomal compartments (Brown *et al*., 2005; Haimo and Rozdzial, 1989; Hollenbeck and Swanson, 1990; Vale *et al*., 1992; Wubbolts *et al*., 1999). The net balance between movements dictates the typical steady-state perinuclear positioning of late endosomal compartments close to the microtubule-organizing centre (MTOC) (Brown *et al*., 2005; Burkhardt *et al*., 1997; Harada *et al*., 1998; Santama *et al*., 1998; Wubbolts *et al*., 1999). In addition to dynein-dynactin and kinesin motors, other factors are involved in maintaining the typical distribution of LE including small GTPases and their effectors, kinases (Pelkmans *et al*., 2005), motor-associated factors like huntingtin (htt) (Colin *et al*., 2008) and cholesterol (Lebrand *et al*., 2002; Sugii *et al*., 2006).

Rab GTPases specify organelle identity (Pfeffer, 2001; Zerial and McBride, 2001) and control selective motor activity on defined compartments (Echard *et al*., 1998; Hoepfner *et al*., 2005; Jordens *et al*., 2001; Jordens *et al*., 2005). The small GTPase Rab7 associates with LE (Zerial and McBride, 2001) and supports dynein motor recruitment recruiting its effector RILP and then the p150^{Glued} subunit of the dynactin protein complex (Johansson *et al*., 2007; Jordens *et al*., 2001). p150^{Glued} can bind the Dynein Heavy Chain (DHC) through the Dynein Intermediate Chain (DIC) but also the oppositely-directed kinesin II (KIF3A) motor through the KAP3 adaptor (Brown *et al*., 2005; Deacon *et al*., 2003; Wubbolts *et al*., 1999). Kinesin I (KIF5) is also involved in plus-end transport of LE (Hollenbeck and Swanson, 1990; Nakata and Hirokawa, 1995) but interacts through different receptors. Therefore inactivation of p150^{Glued} binding to LE still results in net plus-end transport by the remaining kinesin I motor. Although Rab7 and RILP are sufficient for the recruitment of p150^{Glued}-associated motor protein complexes to LE, the actual translocation

Division of Cell Biology
The Netherlands Cancer Institute
Plesmanlaan 121
1066CX Amsterdam
The Netherlands

TEL 31-20-5122012
[*] Corresponding authors; email
J.NEEFJES@NKI.NL; W.ZWART@NKI.NL

[+] Equal contribution

Short title: Cholesterol, late endosomes and the ER.

Keywords: Rab7/ RILP/ ORP1L/ cholesterol/ dynein motor/ p150^{Glued}/ late endosomes/ lysosomes/ MIIC/ cytolytic granules/ U18666A/ LRO/ FLIM/ FRET/ Niemann-Pick/ Tangier/ Fabry/ NPC1/ ORD/ oxysterol-binding domain/ FFAT domain/ MHC class II molecules/ VAP-A/ VAP-B/ amyotrophic lateral sclerosis/ ER/ ER-late endosomal membrane contact sites/ ER-LE-MCS/ cross-presentation/ TAP

of LE towards the MTOC further requires βIII spectrin and the oxysterol-binding protein (OSBP)-related protein 1L (ORP1L) (Johansson *et al*., 2007) that contains a pleckstrin homology (PH) domain which binds phosphoinositides (Johansson *et al*., 2005), a protein-interacting FFAT (Two Phenylalanines (FF) in an Acidic Tract) motif (Loewen and Levine, 2005; Loewen *et al*., 2003) and a C-terminal OSBP-related domain (ORD) able to bind 25-hydroxycholesterol (Im *et al*., 2005; Suchanek *et al*., 2007). The ER protein OSBP is related to ORP1L and also contains a FFAT motif. This FFAT motif interacts with the vesicle-associated membrane protein (VAMP)-associated proteins (VAP)-A and VAP-B (Loewen and Levine, 2005). VAP-A and -B are homo- or heterodimeric integral ER proteins (Hamamoto *et al*., 2005; Nishimura *et al*., 1999) and participate in export of proteins and lipids from the ER (Wyles *et al*., 2002).

Ectopic expression of RILP redistributes LE, causing these to cluster tightly around the MTOC. In contrast, loss-of-function mutants of RILP cause centrifugal translocation of LE (Bucci *et al*., 2000; Jordens *et al*., 2001; Santama *et al*., 1998).

Cholesterol has also been implicated in the control of LE positioning. In the case of human Niemann-Pick type C disease, cholesterol-laden LE cluster around the MTOC (Mukherjee and Maxfield, 2004). This phenotype is shared with other lysosomal storage diseases like Tangier, Fabry and Gaucher (Maxfield and Tabas, 2005; Neufeld *et al*., 2004). Increasing endosomal cholesterol levels with the chemical compound U-18666A mimics this phenotype (Koh and Cheung, 2006; Roff *et al*., 1991; Sobo *et al*., 2007) and requires Rab7 and Rab9 GTPases as well as RabGDI for clustering (Chen *et al*., 2008; Lebrand *et al*., 2002; Narita *et al*., 2005). Conversely, cholesterol depletion results in LE translocation in the opposite direction, toward the plus-end of microtubules (Sugii *et al*., 2006). This suggests that motor protein activities controlling LE positioning are dependent on an interplay between Rab GTPases and cholesterol, but how is unclear.

We here show that cholesterol in LE is sensed by ORP1L which transmits this information to the Rab7-RILP-p150^{Glued} complex through the formation of ER-late endosome membrane contact sites (ER-LE-MCS). Here, ER protein VAP enters the Rab7-RILP complex to control p150^{Glued} binding and positioning of LE. The characteristic clustering of LE at the microtubule minus-end in Niemann-Pick type C and other lysosomal storage diseases is a result of this process.

Results

Chemical and genetic cholesterol manipulations in late endosomes and their positioning.

Cholesterol is an essential component of cellular membranes and contributes to a host of different processes. To visualize the effects of intracellular cholesterol levels on LE, MelJuSo cells were cultured under control, cholesterol-depleting or cholesterol-increasing conditions. Cholesterol depletion was achieved by culturing cells in lipid-free medium supplemented with a statin to prevent synthesis of endogenous cholesterol (Sugii *et al*., 2006). Cholesterol increase was achieved in two different ways. Firstly, cells were cultured in the presence of U-18666A, which increases cholesterol levels in LE (Kobayashi *et al*., 1999; Liscum and Faust, 1989). Alternatively, cholesterol was increased by transfecting MelJuso cells with small interfering RNA (siRNA) to silence NPC1 and mimic Niemann-Pick type C disease (Ikonen and Holtta-Vuori, 2004; Carstea *et al*., 1997).

To visualize the effect of these treatments, cells were fixed and stained with filipin (a cholesterol-binding fluorescent probe (Sobo *et al*., 2007; Sokol *et al*.,1988)) to detect cholesterol (Figures 1A, S1B) or stained for CD63 to label LE (Figure 1B,S1B). Images were made at identical microscope settings and show that these cholesterol-manipulating treatments decreased (Statin) or increased (U-18666A or siNPC1) intracellular cholesterol levels (Figure 1A,S1B). Cholesterol-depletion resulted in scattering of CD63-positive structures whereas the U-18666A compound and NPC1 silencing caused these structures to concentrate in the perinuclear region (Figures 1B, S1B; quantified in S1A).

Does cholesterol affect the bidirectional motility of LE? Therefore, these experiments were repeated where LysoTracker-RED-labelled MelJuSo cells were followed by time-lapse fluorescent microscopy when intracellular cholesterol levels were manipulated (movies M1-3 available online). A fraction of the LE in cells exposed to low or high cholesterol conditions still moved in a bidirectional and stop-and-go manner, as in control cells. Cholesterol determines net positioning but not the rapid bidirectional transport of LE.

To assess whether this re-positioning of LE near the MTOC under high cholesterol concentrations imposed by silencing NPC1 required the dynein-dynactin motor, dynactin's subunit p50^{dynamitin} was over-expressed to physically disrupt the motor complex (Burkhardt *et al*., 1997) in NPC1-silenced cells. p50^{dynamitin}-overexpression abrogated clustering of CD63-bearing structures in NPC1-silenced MelJuSo cells, suggesting that functional dynein-dynactin

complexes are involved in LE clustering in NPC1-deficient cells (Figure 1C).

ORP1L controls p150^{Glued} binding to Rab7-RILP and cholesterol-dependent LE positioning.

ORP1L binds to Rab7 via its N-terminal ankyrin repeats and is required for the regulation of late endosomal transport by the dynein motor (Johansson *et al*., 2005; Johansson *et al*., 2007). To resolve the ORP1L domains involved in the control of LE transport, a series of C-terminal truncations of ORP1L fused to mRFP (Shaner *et al*., 2004) (Figures 2A, S2A) were co-expressed with GFP-RILP in MelJuSo cells. The nature of the vesicles labelled by the mRFP-ORP1L constructs was determined by fixing the cells and immunostaining for different organelle markers. These vesicles were defined as CD63- and LAMP-1-containing LE (Figure S2B) labelling for Rab7 and for cholesterol as detected by filipin (Figure S2C). No co-labelling was detected with markers for ER, Golgi or early endosomes (Figure S2D).

To assess the effect of ORP1L and ORP1L mutants on LE positioning, cells were fixed and stained for the dynactin motor subunit p150^{Glued} and dynein intermediate chain (DIC). Co-expression of ORP1L and RILP resulted in recruitment of p150^{Glued} (Figure 2B) and DIC to LE (Figure 2C) and to LE clustering near the MTOC. Removal of the C-terminal ORD (ΔORD) prevented p150^{Glued} and DIC recruitment by RILP, resulting in relocation of RILP-containing compartments to the periphery of the cell (Figures 2B, 2C). OSBP/ORPs are involved in non-vesicular transport of sterols and their ORDs bind and possibly extract sterols from membranes (Ikonen, 2008). The ΔORD

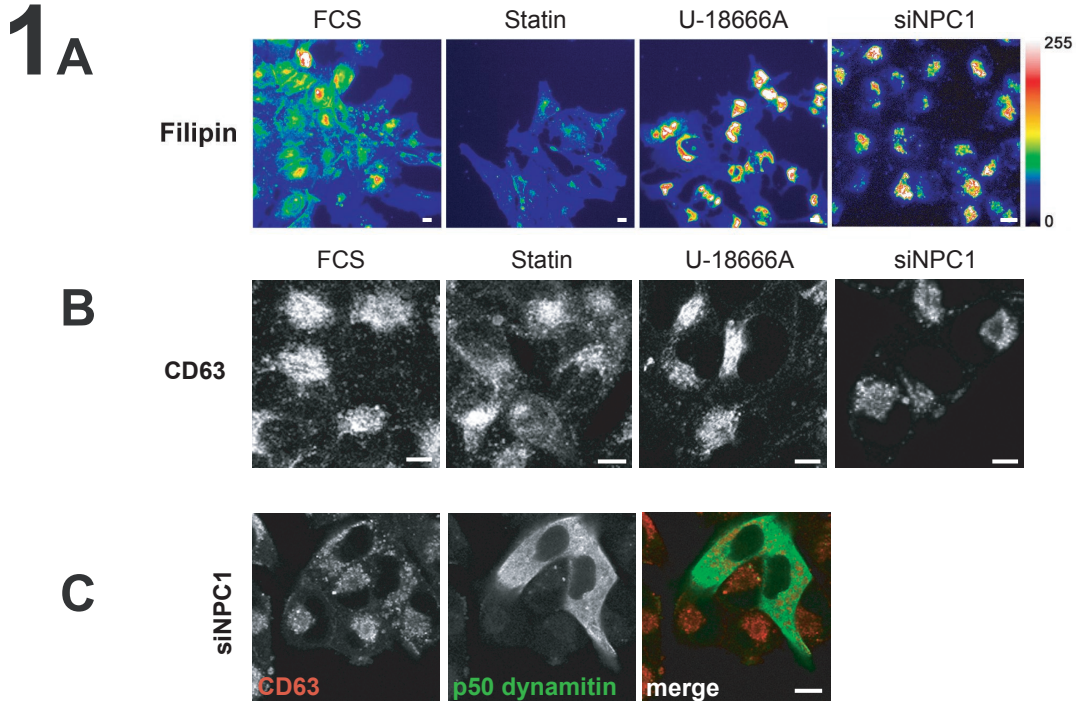
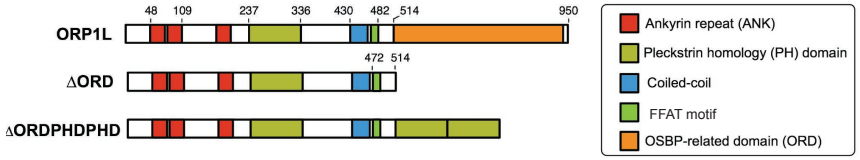
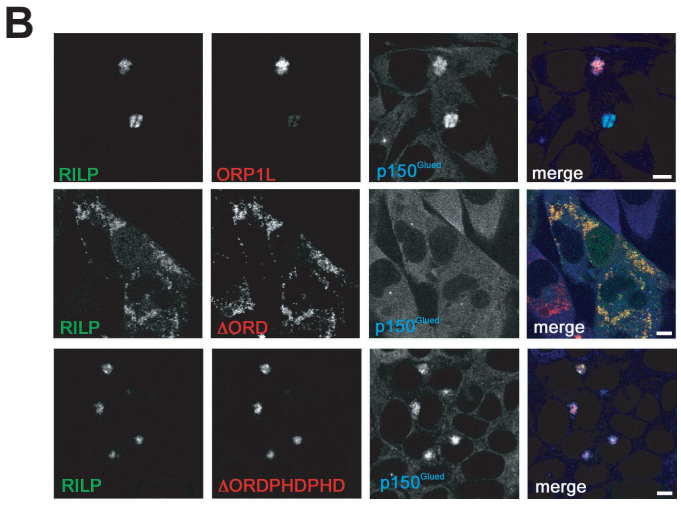


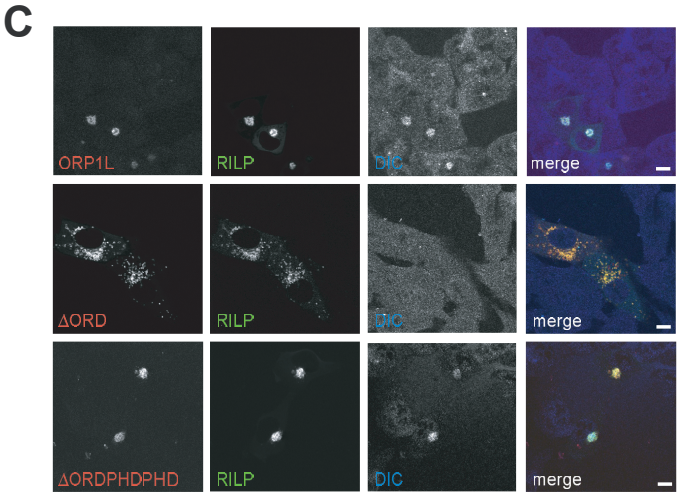
Figure 1. Chemical and genetic cholesterol manipulations and late endosomes.

(**A**) Modulation of intracellular cholesterol levels. MelJuSo cells were cultured in normal medium (FCS), cholesterol-depleted medium supplemented with Lovastatin (Statin) or in normal medium supplemented with U-18666A, as indicated. Cells were fixed and stained with filipin to detect cholesterol. Images were obtained using identical settings on the microscope. A colour LUT is applied to illustrate the differences in cholesterol. n>100 for each condition. Scale bars, 10μm.
(**B**) Effects of intracellular cholesterol manipulation on late endosomal positioning. MelJuSo cells were cultured under the three different cholesterol-manipulating conditions before fixation and analyzed by immunofluorescence microscopy with antibodies against the late endosomal marker CD63. n>100 (quantification see Figure S1A). Scale bars, 10 μm.
(**C**) Dynein motor and clustering of late endosomes in NPC1-silenced cells. MelJuSo cells were transfected with siRNA for NPC1 for 72 hrs and after 48 hrs transfected with an expression construct for p50^{dynamitin} to disrupt the dynein-dynactin motor. Cells were fixed and stained CD63 and p50^{dynamitin} to mark the cells overexpressing this inhibitory subunit of dynactin. n> 100. Scale bars, 10μm.

2A







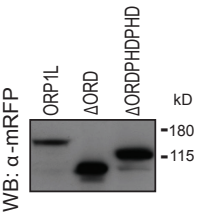


Figure 2. ORP1L controls recruitment of p150^{Glued} to the Rab7-RILP receptor.

(**A**) ORP1L domain structure and constructs. Five domains can be distinguished in ORP1L. A series of C-terminal truncation mutants were generated. Numbers indicate amino acid residue positions. All constructs were N-terminally tagged with mRFP. The ΔORDPHDPHD chimera had ORD exchanged for a tandem PH domain derived from ORP1L.
(**B**) Effect of ORP1L deletion or chimeric constructs on RILP-mediated p150^{Glued} recruitment. Left panel: MelJuSo cells were transfected with GFP-RILP and mRFP-ORP1L constructs. Cells were fixed and stained with anti-p150^{Glued} antibodies prior to CLSM. Pixel analyses of the images is shown in Figure S6. n>200 for each condition. Scale bars, 10μm. Right panel: MelJuSo cells were transfected with the indicated mRFP-ORP1L constructs and whole-cell lysates were analyzed by immunoblotting with anti-mRFP antibodies (WB: α-mRFP).The molecular weights are indicated.
(**C**) Effect of ORP1L constructs on RILP-recruitment of the p150^{Glued} associated Dyenin motor adaptor DIC. MelJuSo cells were transfected with GFP-RILP and mRFP-ORP1L constructs as indicated. Cells were fixed and stained with anti-DIC antibodies prior to CLSM. n>100 for each condition. Scale bars, 10μm.

mutant of ORP1L cannot bind sterols in the membrane, and may mimic a cholesterol-free conformation of ORP1L. To further test whether p150^{Glued} exclusion from Rab7-RILP requires ORD binding to membranes, another mutant was created where ORD was exchanged for two ORP1L PH domains in tandem (ΔORDPHDPHD). Tandem PH domains will increase the avidity of binding to phosphoinositides (Lemmon and Ferguson, 2000) and were used to mimic the ORD in a membrane-associated (cholesterol-interacting) state. The ΔORDPHDPHD chimera allowed p150^{Glued} and DIC recruitment by RILP, resulting in clustering of RILP-positive compartments at the minus-end of microtubules (Figures 2B, 2C). Silencing ORP1L with siRNA against ORD before ectopic expression of ΔORD or ΔORDPHDPHD showed no contribution of endogenous ORP1L on the phenotypes caused by the ORP1L mutants (data not shown). The re-positioning of LE by expression of the different ORP1L variants was confirmed in time-lapse experiments (Movies M4, M5; available online).

To test whether LE positioning controlled by cholesterol (Figure 1) is dependent on cholesterol sensing by ORP1L, MelJuSo cells were transfected with mRFP-ORP1L before manipulating cholesterol levels. Cholesterol reduction by statin and lipid-free medium resulted in scattering of mRFP-ORP1L-positive vesicles whereas U-18666A treatment resulted in LE positioning around the MTOC (Figures 3A, S3), as confirmed by quantification (Figure S1A). Removal of the cholesterol-binding domain ORD or its replacement by a tandem of PH domains rendered positioning of LE insensitive to cholesterol levels. ΔORD induced scattering of LE under all cholesterol-manipulated conditions whereas ΔORDPHDPHD always induced dense clustering (Figures 3B, S3A). We conclude that functional ORP1L is required for translating cholesterol content in LE into LE positioning.

Late endosomal cholesterol affects the conformation of ORP1L

To determine whether LE cholesterol content affects the conformation of ORP1L, an mRFP-ORP1L-GFP fusion protein was expressed to monitor intramolecular Fluorescence Resonance Energy Transfer (FRET). The radiation-less energy transfer from a donor fluorophore to a suitable acceptor (Förster, 1948) is highly dependent on distance and orientation between the two fluorophores (Calleja *et al.*, 2003;

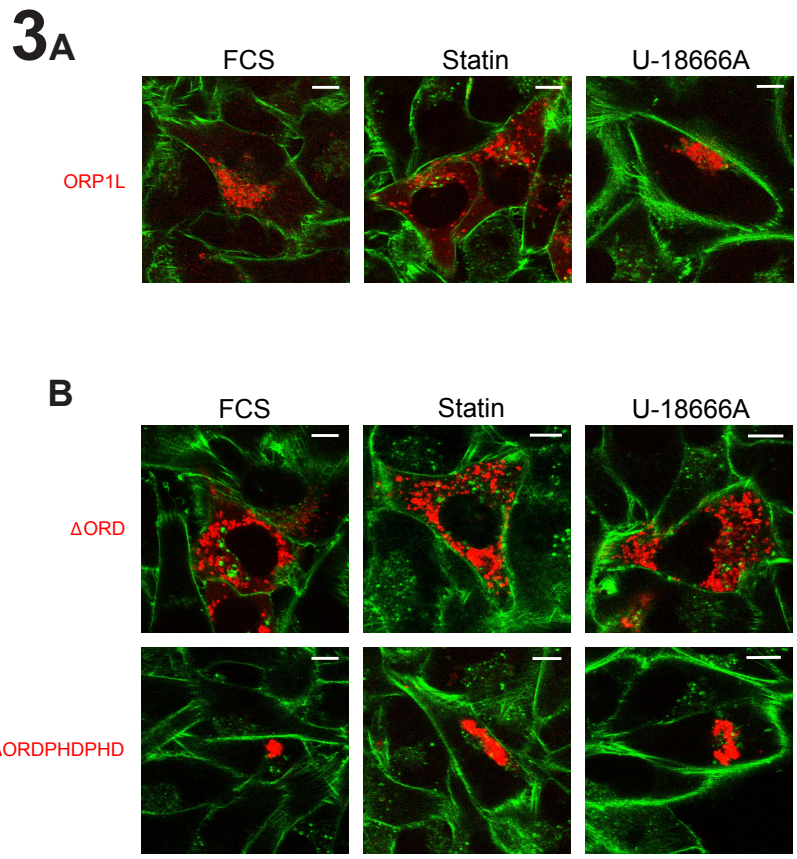


Figure 3. ORP1L controls cholesterol-dependent late endosomal positioning.

(**A**) Cholesterol-dependent ORP1L vesicle positioning. MelJuSo cells expressing mRFP-ORP1L were cultured under control conditions (FCS), conditions decreasing (Statin) or increasing (U-18666A) cholesterol. Subsequently, cells were fixed and actin stained with falloidin (green) to mark the cell boundaries before analyses by CLSM. n>100; scale bars, 10μm. (**B**) ORP1L is dominant in vesicle repositioning as the result of cholesterol manipulations. MelJuSo cells expressing mRFP-ΔORDPHDPHD or mRFP-ΔORD were treated and imaged as described in Figure 3A. n>100; scale bars, 10μm.

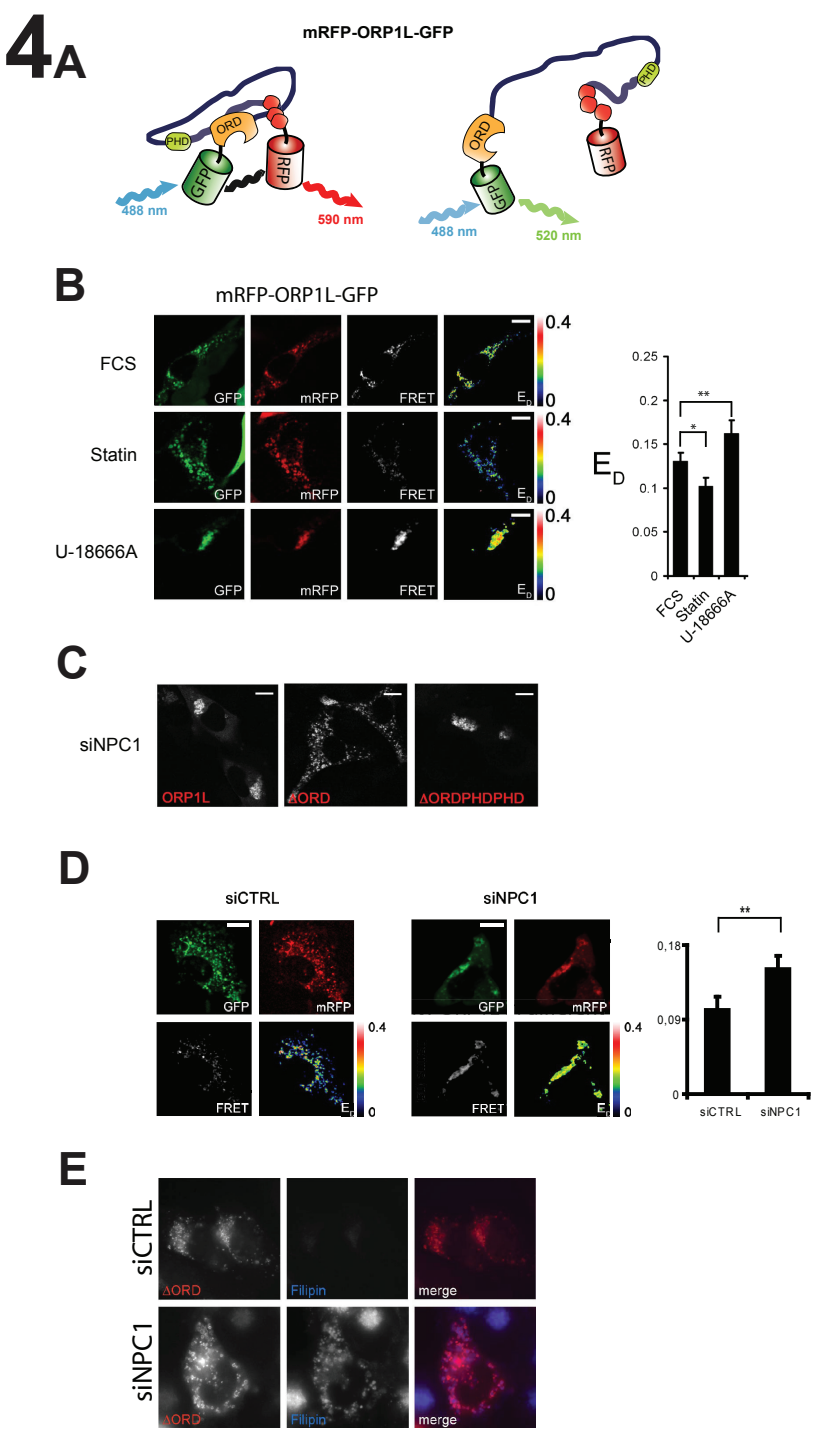


Figure 4. Late endosomal cholesterol alters the conformation of ORP1L

(**A**) Concept of intramolecular FRET for mRFP-ORP1L-GFP. GFP and mRFP are attached to the same molecule allowing fluorescence energy transfer (FRET) from donor GFP to acceptor mRFP. FRET depends on distance and orientation and thus visualizes conformational changes. FRET can be detected by sensitized emission where GFP is excited by 488 nm light and 582-675 nm light emission by mRFP (as the result of energy transfer from GFP) is detected.

(**B**) Cholesterol effects on ORP1L conformation detected by sensitized emission. MelJuSo cells expressing the intramolecular mRFP-ORP1L-GFP FRET probe were cultured under control (FCS), cholesterol-depleting (Statin) or -enhancing (U-18666A) conditions prior to imaging by CLSM for FRET determination. Panels show the GFP signal, the mRFP signal, calculated FRET and FRET related to donor fluorophore input: the donor FRET efficiency (E_D). The colour LUT visualizes the differences in the E_D panels. Scale bars, 10µm. Right panel: quantification of the donor FRET efficiency detected for mRFP-ORP1L-GFP under the different conditions of cholesterol manipulation. The mean and SD from 2 independent experiments (>10 cells analyzed for each condition) are shown (*p=0.05; **p=0.03).

(**C**) ORP1L controls late endosome positioning in NPC1-silenced cells. MelJuSo cells were transfected with mRFP-ORP1L, -ΔORD or -ΔORDPHDPHD and siRNA for NPC1. Cells were fixed and analyzed by CLSM. n>100; scale bars, 10µm.

(**D**) Sensitized emission and ORP1L conformation in NPC1-deficient cells. mRFP-ORP1L-GFP-expressing MelJuSo cells were transfected with control (siCTRL) or NPC1 (siNPC1) siRNAs before imaging by confocal FRET. Scale bars, 10 µm. Right panel: Donor FRET efficiencies determined in >10 control siRNA or NPC1 siRNA-transfected cells. Shown is the mean + SD (*p=5.1*10^{-6}).

(E) NPC1, cholesterol and late endosomal clustering. MelJuSo cells were transfected with control or NPC1 siRNA and subsequently mRFP-ΔORD. Subsequently, cells were fixed and stained for cholesterol with filipin. Pixel analyses in Figure S6. n>50 for each condition. Scale bars, 10 µm.

Förster, 1948) and thus reveals conformational changes within mRFP-ORP1L-GFP (Figure 4A).

FRET was determined by sensitized emission using CLSM. Here, GFP is excited with 488 nm light and the mRFP signal (after energy transfer from GFP) is determined. mRFP-ORP1L-GFP-expressing MelJuSo cells were co-cultured with MelJuSo cells expressing only GFP or mRFP for imaging at 37°C. These co-cultured cells serve as internal controls to calculate correction factors for bleed-through of GFP into the mRFP channel and for direct excitation of mRFP by the 488 nm laser (Zwart *et al*., 2005). FRET and donor FRET efficiency (E_D; i.e. FRET normalized to donor fluorophore input) were determined under the various conditions of cholesterol manipulation (Figure 4B). Cholesterol depletion decreased FRET efficiency E_D, whereas this was increased following late endosomal cholesterol accumulation (Figure 4B, right panels), implying that ORP1L changes conformation dependent on the cholesterol content of LE.

To exclude that the observed differences in E_D were due to clustering or aggregation of individual ORP1L molecules under the various conditions rather than conformational changes of each ORP1L molecule, the experiments were repeated with cells expressing both GFP-ORP1L and mRFP-ORP1L (Figure S4B). If changes in E_D were due to intermolecular, and not due to intramolecular FRET, E_D would also change in this situation. E_D values were not affected by cholesterol manipulation implying that the FRET differences in cholesterol-manipulated cells expressing mRFP-ORP1L-GFP results from conformational changes within mRFP-ORP1L-GFP rather than aggregation or clustering.

Two constructs, mRFP-ΔORD-GFP and mRFP-ΔORDPHDPHD-GFP, were used to test whether cholesterol-dependent conformational changes in ORP1L were mediated by the ORD. mRFP-ΔORD-GFP and mRFP-ΔORDPHDPHD should not respond to variations in cholesterol levels since they lack ORD, but may still respond to effects on the PH domain or other domains present in ORP1L. However, no effect of cholesterol manipulation on intramolecular donor FRET efficiency E_D was detected with these constructs, suggesting that cholesterol-induced conformational changes in mRFP-ORP1L-GFP were mediated by the cholesterol-sensing ORD (Figure S4A).

FRET efficiencies can also be calculated from differences in donor fluorophore lifetime, which is believed to be more quantitative than sensitized emission (Bastiaens and Squire, 1999). The FRET experiments discussed above were repeated where FRET was determined by fluorescence lifetime imaging microscopy (FLIM). The lifetime of GFP is typically 2.7 ns (Pepperkok *et al*., 1999), but decreases in the case of FRET, when energy is transferred to the acceptor fluorophore mRFP. mRFP-ORP1L-GFP-expressing cells were imaged along with GFP-only-expressing control cells to determine GFP lifetime under non-FRET conditions, and cholesterol levels were manipulated. Consistent with our observations using sensitized emission, FRET efficiency E_D decreased by cholesterol depletion and increased following enhanced cholesterol levels (Figure S4C). The various control conditions were also imaged by FLIM and showed no response to cholesterol manipulation, as also observed when FRET was measured by sensitized emission (Figures S4D and S4E).

These results demonstrate that the Rab7-RILP-interacting protein ORP1L senses cholesterol content in LE through the C-terminal ORD.

ORP1L, cholesterol and Niemann-Pick type C disease.

Silencing NPC1 increases cholesterol in LE and endosomal clustering. These intraluminal high levels of cholesterol could generate high levels of cholesterol in the cytosolic leaflet of LE after transfer over the limiting membrane by flip-flop and/or specific transporters. ORP1L senses cholesterol only in the cytosolic leaflet of the limiting membrane of LE before translating this into LE positioning. To test whether cholesterol sensing by ORP1L is required for LE clustering in Niemann-Pick type C disease, NPC1-silenced MelJuSo cells (Figure S1B) were transfected with different mRFP-ORP1L constructs before analysis by CLSM (Figure 4C). Whereas ORP1L and ΔORDPHDPHD induced clustering of LE, ΔORD induced scattering of LE even when NPC1 is silenced (Figure S4F). This suggests that functional ORP1L is required to translate increased cholesterol levels in NPC1-deficient cells into LE positioning.

To test whether NPC1-deficiency affects the cholesterol levels at the cytosolic leaflet of LE, intramolecular FRET of mRFP-ORP1L-GFP was measured by sensitized emission in cells transfected with control or NPC1 siRNAs (Figure 4D). The FRET efficiency E_D increased when NPC1 was silenced (Figure 4D). These results were confirmed in FLIM measurements (Figure S4G). The donor FRET efficiencies (E_D) for mRFP-ORP1L-GFP in NPC1-downregulated cells are similar to those observed with U-18666A treatment, which mimics NPC1 deficiency (Koh and Cheung, 2006; Sobo *et al*., 2007) (Figure 4B).

Cholesterol accumulation in LE of NPC1-silenced cells may be a cause or a consequence of the LE clustering observed in cells of Niemann-Pick type C patients (Kobayashi *et al*., 1999). To segregate cholesterol accumulation from LE clustering mRFP-

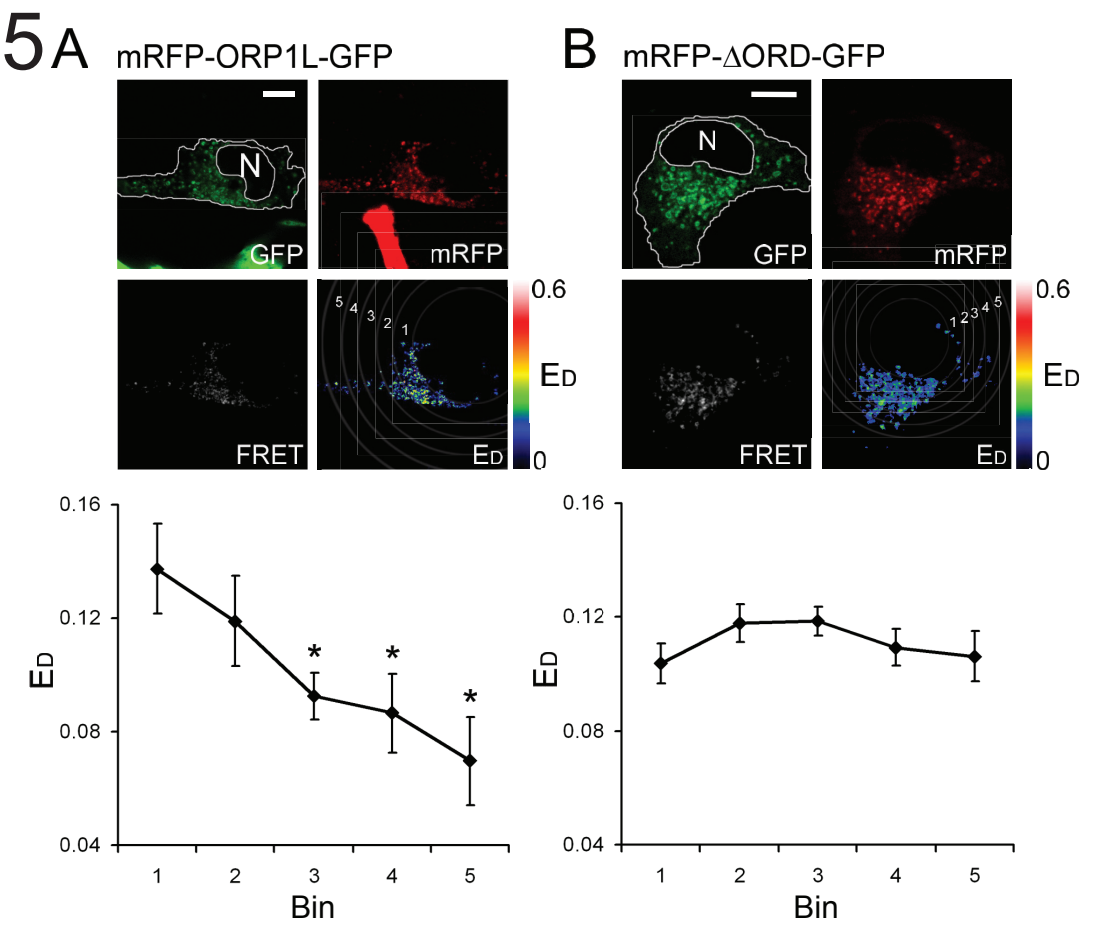


Figure 5. ORP1L conformation and late endosomal positioning.

Top: MelJuSo cells expressing mRFP-ORP1L-GFP (**A**) or mRFP-ΔORD-GFP (**B**) were imaged for FRET by CLSM. The GFP image, mRFP image, calculated FRET and donor FRET efficiency E_D images are indicated. E_D values are shown in false colours (LUT shows the corresponding values). The position of the nucleus (N) and cell boundaries are drawn in the GFP channel. The cytosol is divided by 5 concentric rings, as indicated in the E_D panel. Bar: 10µm.

Bottom: E_D values for the constructs were collected and binned for the different rings. Values are shown for the different rings under the corresponding images. Shown are mean +/- SEM of E_D values collected for more than 10 cells analyzed per construct. * indicates a statistically significant difference in E_D collected in bin 1 (the most internal ring) (respectively p= 0.024, 0.026 and 0.0063).

ΔORD was expressed in NPC1 silenced cells, since ΔORD induced scattering of LE (Figure 4C). Cells were fixed and stained for cholesterol with filipin (Figure 4E) and CD63 (Figure S4H). The CD63-positive LE structures scattered by ΔORD expression still accumulated cholesterol when NPC1 was silenced. This suggests that the characteristic clustering of LE near the MTOC, as typical in Niemann-Pick type C (and other lysosomal storage diseases), is a consequence of cholesterol accumulation as sensed by ORP1L (and is abrogated by ΔORD). ORP1L transmits this information to the Rab7-RILP-p150^{Glued}-dynein motor complex for microtubule minus-end-driven vesicle transport resulting in clustering of LE.

ORP1L conformation differs between peripheral and perinuclear LE.

If cholesterol levels in LE determine intracellular positioning of LE, these levels should be different between peripheral and perinuclear LE. ORP1L can sense cholesterol present in the cytosolic leaflet of LE only (the lumen of LE is not accessible to ORP1L). Cholesterol levels in the cytosolic leaflet can not be detected by any currently available probe other than by the mRFP-ORP1L-GFP sensor as used above (Figure 4). We re-analyzed the images of cells expressing the mRFP-ORP1L-GFP FRET probe (Figure 5A) and—as a control—the mRFP-ΔORD-GFP FRET probe (Figure 5B). The latter construct

lacks the ORD that senses cholesterol. Donor FRET efficiency E_D was determined in five regions spanning the nucleus and the cell surface, as indicated (Figure 5). The results were binned and quantified, shown in the graphs under the figures. E_D as determined with mRFP-ORP1L-GFP was higher on LE in the perinuclear region than in the cell periphery (Figure 5A). These differences were sensed by ORD since no differences in E_D were observed with the mRFP-ΔORD-GFP construct (Figure 5B). These data suggest that the positioning of LE within one cell correlates with different conformations of ORP1L as induced by different levels of cholesterol in the cytosolic leaflet of LE.

ORP1L dependent recruitment of VAP and removal of the p150^{Glued} dynactin subunit.

ORP1L allows RILP-induced clustering of LE whereas ΔORD re-locates such LE to the cell periphery. Somehow ΔORD excludes p150^{Glued} from RILP. Removal of an additional 20kDa region preceding the ORD restored RILP-induced clustering and p150^{Glued} binding to RILP (Figure S2A). This region contains a predicted coiled-coil region (aa 430-463) (Johansson *et al*., 2007) followed by a FFAT motif (aa 472-482; sequence SEDEFYDALSD) (Loewen *et al*., 2003) (Figure 2A) and should contain the information for removal of p150^{Glued} from RILP. To test whether the FFAT motif was involved in controlling p150^{Glued} binding to RILP, an inactivating point mutation (D478A) in the FFAT motif (Loewen *et al*., 2003) was introduced in mRFP-ΔORD. This mutant was co-expressed with GFP-RILP in cells before fixation and staining for p150^{Glued} (Figure 6A). Whereas ΔORD excludes RILP-mediated recruitment of p150^{Glued} (resulting in LE scattering), the ΔORDFFAT(D478A) FFAT motif point mutant rescued p150^{Glued} binding to RILP thus clustering LE around the MTOC.

The FFAT motif in the ER-located ORP1L homologue OSBP can interact with the type IV ER proteins VAP-A and VAP-B, which are involved in protein and lipid export from the ER (Loewen and Levine, 2005; Wyles *et al*., 2002). VAP is an integral ER protein and therefore not an obvious candidate for controlling p150^{Glued} release from Rab7-RILP on LE membranes. To test whether VAP is involved in this process, MelJuSo cells were transfected with mRFP-ΔORD and GFP-RILP, in combination with siRNA against VAP-A (Figure 6B, right panel). Subsequently, ΔORD-expressing cells transfected with control or VAP-A siRNA were fixed and stained for p150^{Glued} (Figure 6B).

As expected, ΔORD expression again removed p150^{Glued} from RILP in cells transfected with control siRNA resulting in LE positioning in the cell periphery. When VAP-A was silenced, ΔORD was no longer able to remove p150^{Glued} from RILP and the LE moved to the minus-end of microtubules to cluster around the MTOC. Identical results were obtained when VAP-B was silenced (data not shown). VAP-A and -B can form heterodimers (Hamamoto *et al*., 2005). Both proteins are probably required for stable expression since silencing one subunit affects expression of both VAP-A and –B (Figure 6B and data not shown).

To test whether VAP suffices to control p150^{Glued} binding to RILP, this interaction was reconstituted with purified proteins. We had already shown that the C-terminal domain of p150^{Glued} interacts with the Rab7-RILP complex (Johansson *et al*., 2007). To determine the effects of VAP-A on the Rab7-RILP-p150^{Glued} complex, the ORP1L-Rab7-RILP-p150^{Glued} complex was first assembled with purified proteins (Figure 6C). Therefore, His-tagged [GTP-loaded]-Rab7 was bound to metal affinity-beads before addition of RILP and ORP1L. The complex was completed by the C-terminal fragment of p150^{Glued}(C25) and non-bound proteins were removed in every step during the construction of the complex by washing. Subsequently, purified VAP-A was added to the complex followed by washing of the beads. The effect on the ORP1L-Rab7-RILP-p150^{Glued}(C25) complex was determined by Western blotting (Figure 6C). Soluble VAP-A removed the C25-fragment of p150^{Glued} from the pre-assembled Rab7-RILP-ORP1L complex.

To test whether VAP-A prevented binding of p150^{Glued} to the Rab7-RILP complex or whether VAP-A induced the release of p150^{Glued}, and to determine the role of ORP1L in this process, various purified Rab7-RILP complexes were assembled *in vitro* (Figure 6D). When VAP-A was included during the assembly of the complex, the p150^{Glued} C25 fragment could still enter the complex, whereas VAP-A was again able to remove the preassembled p150^{Glued} fragment (Figure 6D, lanes 1,2). VAP-A is probably removed by washing during the assembly of the Rab7-RILP complex, which explains why VAP-A did not affect C25 binding under these conditions. The presence or absence of ORP1L in the preassembled Rab7-RILP complex did not affect the ability of VAP-A to remove the C25 fragment of p150^{Glued} (Figure 6D, lanes 3,4). These data suggest that ORP1L is not directly involved in the VAP-A mediated removal of p150^{Glued} from the Rab7-RILP complex but probably recruits VAP into this complex in intact cells.

To test whether VAP-A directly interacts with the C25-fragment of p150^{Glued}, GST-VAP-A or GST (as a control) was bound to GST-beads and purified p150^{Glued} C25 fragment was added. VAP-A interacted with the C-terminal (C25) p150^{Glued} fragment (Figure 6E). This *in vitro* reconstitution experiment reveals

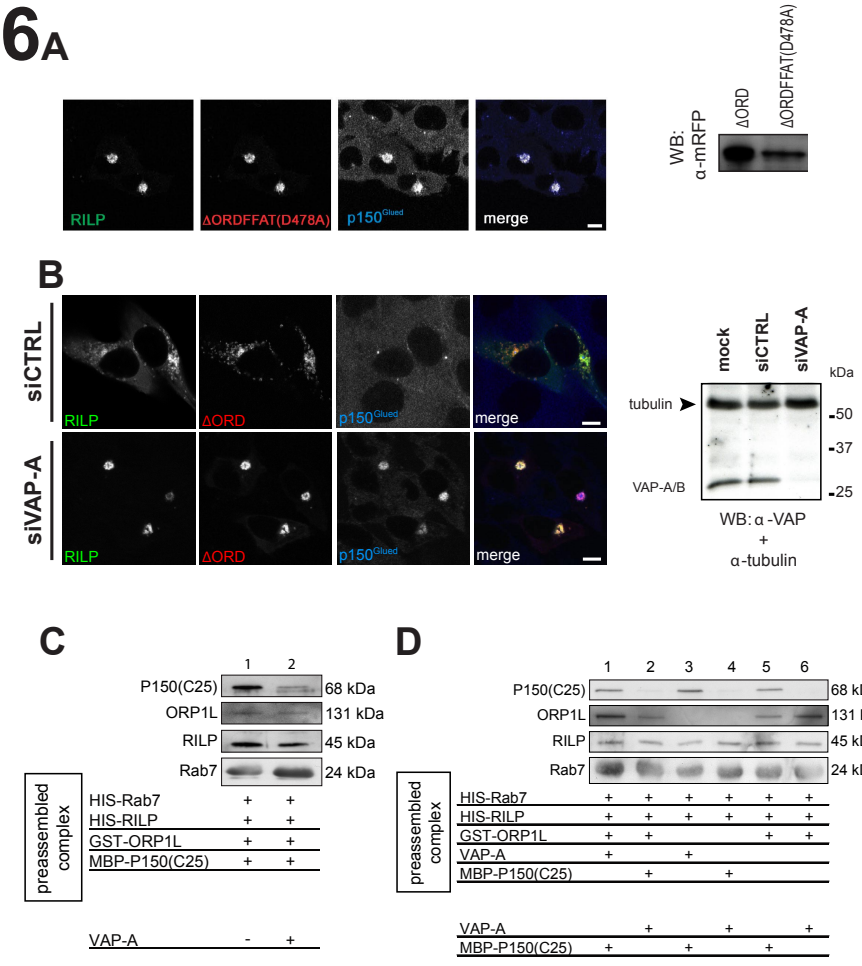


Figure 6. ORP1L requires VAP to remove p150^{Glued} from Rab7-RILP.

(**A**) Effect of the FFAT motif in ΔORD on RILP-mediated p150^{Glued} recruitment. Left panel: MelJuSo cells transfected with GFP-RILP and mRFP-ΔORD with the point mutation in its FFAT motif, ΔORDFFAT(D478A). Cells were fixed and stained with anti-p150^{Glued} antibodies before analyses by CLSM. n>200. Scale bar, 10μm. Right panel: MelJuSo cells were transfected with the indicated mRFP-ΔORD or mRFP-ΔORDFFAT(D478A) constructs and whole-cell lysates were subjected to immunoblot analysis using anti-mRFP antibodies (WB: α-mRFP).

(**B**) p150^{Glued} exclusion by ΔORD and VAP-A. VAP-A was silenced by siRNA in cells expressing GFP-RILP and mRFP-ΔORD. Left panel: cells were fixed and stained for p150^{Glued} before analyses by CLSM. Pixel analyses in Figure S6. n>100 for each condition. Scale bars, 10 μm. Right panel: Western blot analyses of cells transfected with transfection reagent only (mock), control (siCTRL) or VAP-A siRNA (siVAP-A) and probed for α-tubulin (as loading control) and an antibody recognizing both VAP-A and VAP-B.

(**C**) VAP-A removes p150^{Glued} from Rab7-RILP. GTP-locked His-Rab7(Q67L) was coupled to Talon-beads and loaded with GTP before purified RILP, ORP1L and the p150^{Glued}(C25) fragments were added in equimolar amounts to form a pre-assembled ORP1L-Rab7-RILP-p150^{Glued}(C25) complex. Subsequently, the complex was incubated in the presence or absence of purified VAP-A for 30 min at 20ºC. After washing, the proteins immobilized on the beads were analyzed by SDS-PAGE and Western blotting. The molecular weights are indicated.

(**D**).ORP1L requirements for p150^{Glued} removal by VAP-A. GTP-locked His-Rab7(Q67L) was coupled to Talon Co^{2+}-beads and loaded with GTP before any of the isolated proteins indicated was added in equimolar amounts to form a pre-assembled complex, as indicated. After washing, these complexes were exposed to isolated VAP-A or the p150^{Glued}(C25) fragment, as indicated, and the effects on the pre-formed complex assessed by SDS-PAGE and Western blot analyses with antibodies, as indicated. Molecular weights are indicated.

(**E**) VAP-A interacts with p150^{Glued}. GST or GST-VAP-A were coupled to GST beads before exposure to the p150^{Glued}(C25) fragment. After washing, the complexes were analyzed by SDS-PAGE and Western blotting. Molecular weights are indicated.

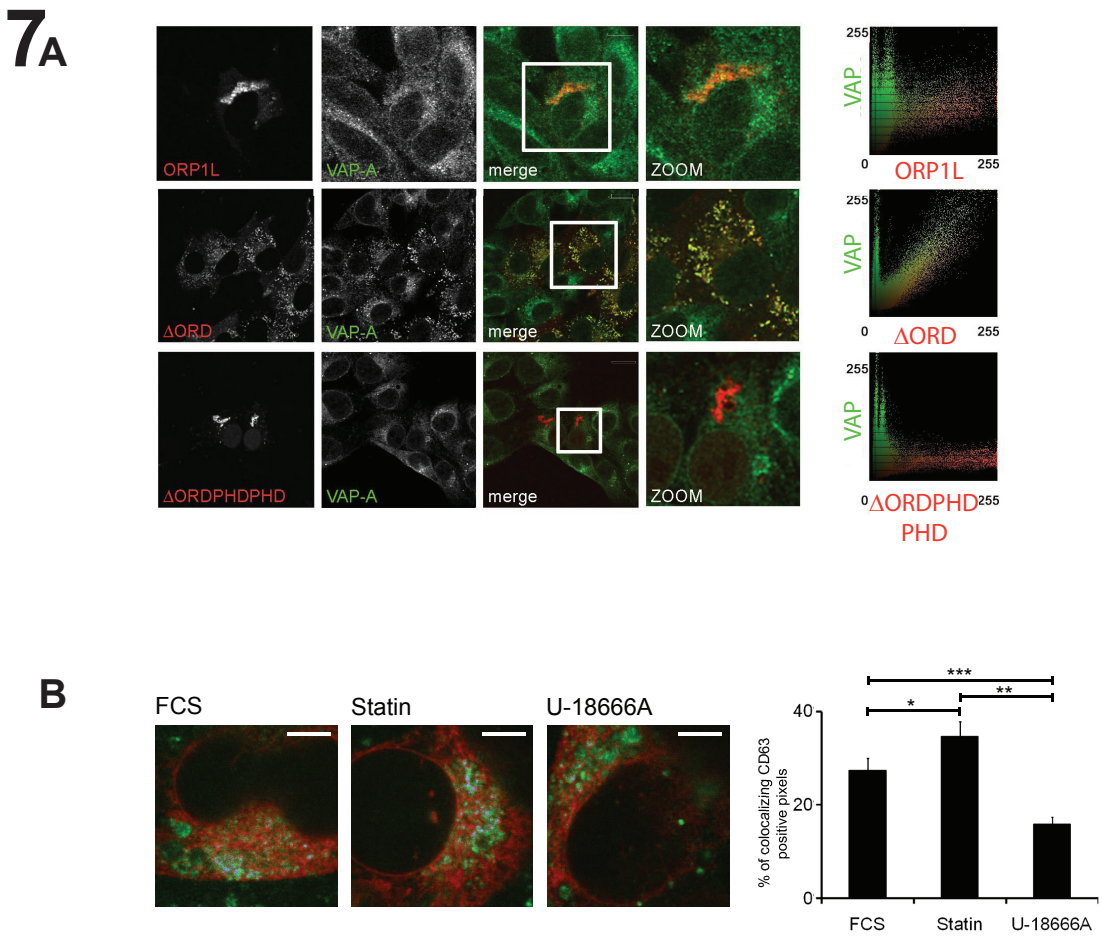


Figure 7. Cholesterol-dependent late endosomal membrane-contact-sites with the ER for *in trans* VAP interactions with the Rab7-RILP complex.

(**A**) ΔORD recruits endogenous VAP-A. MelJuSo cells expressing mRFP−ΔORD, -ORP1L or -ΔORDPHDPHD were fixed and stained for VAP-A, as indicated. Merge shows an overlay of the two channels and the box shows a zoom-in area. Pixel analyses of the zoom-in area for fluorescence distribution of the mRFP-ORP1L variants and VAP-A is shown in the last panel. n> 100; scale bars, 10 μm.
(**B**) MelJuso cells expressing TAP1-GFP (color-coded red) were exposed to different cholesterol manipulating conditions, as indicated. Cells were fixed and stained with antibodies for CD63 (color-coded green). Co-localization of both markers by pixel analyses was determined by computational analysis and visualized in blue; scalebar, 5 μm. Right panel: quantification of the co-localizing surface of CD63-positive structures is represented in the right panel. Shown are mean + SEM collected for more than 20 cells analyzed per condition. (*p=0.068; **p=1.55*10-6; ***p=0.0003).

a minimal unit of proteins controlling dynein motor binding to LE that includes Rab7, RILP, p150^{Glued} and the ER protein VAP.

ORP1L and VAP are involved in inducing ER-late endosome membrane contacts.

If the integral ER protein VAP controls motor binding to LE after recruitment by ORP1L, VAP should somehow contact these vesicles. To visualize how ORP1L controls the recruitment of the ER protein VAP to LE, MelJuSo cells were transfected with the various ORD variants of mRFP-ORP1L. Cells were fixed and stained for endogenous VAP (Figure 7A). Endogenous VAP accumulated on ΔORD- and to a lesser extent on ORP1L-containing vesicles but was excluded from vesicles labelled by ΔORDPHDPHD, indicating that VAP recruitment is dependent on the conformation of ORP1L, illustrated in the zoom-in and pixel analysis of Figure 7A. These results were confirmed in photo-activation experiments of MelJuSo cells expressing PA-GFP tagged VAP-A and mRFP-ORP1L variants (Figure S5A, Movies M6-8 available online). Accumulation of the ER protein VAP on LE by ΔORD expression also coincided with removal of p150^{Glued} from RILP (Figure S5B). We also tested whether the same results could be obtained by

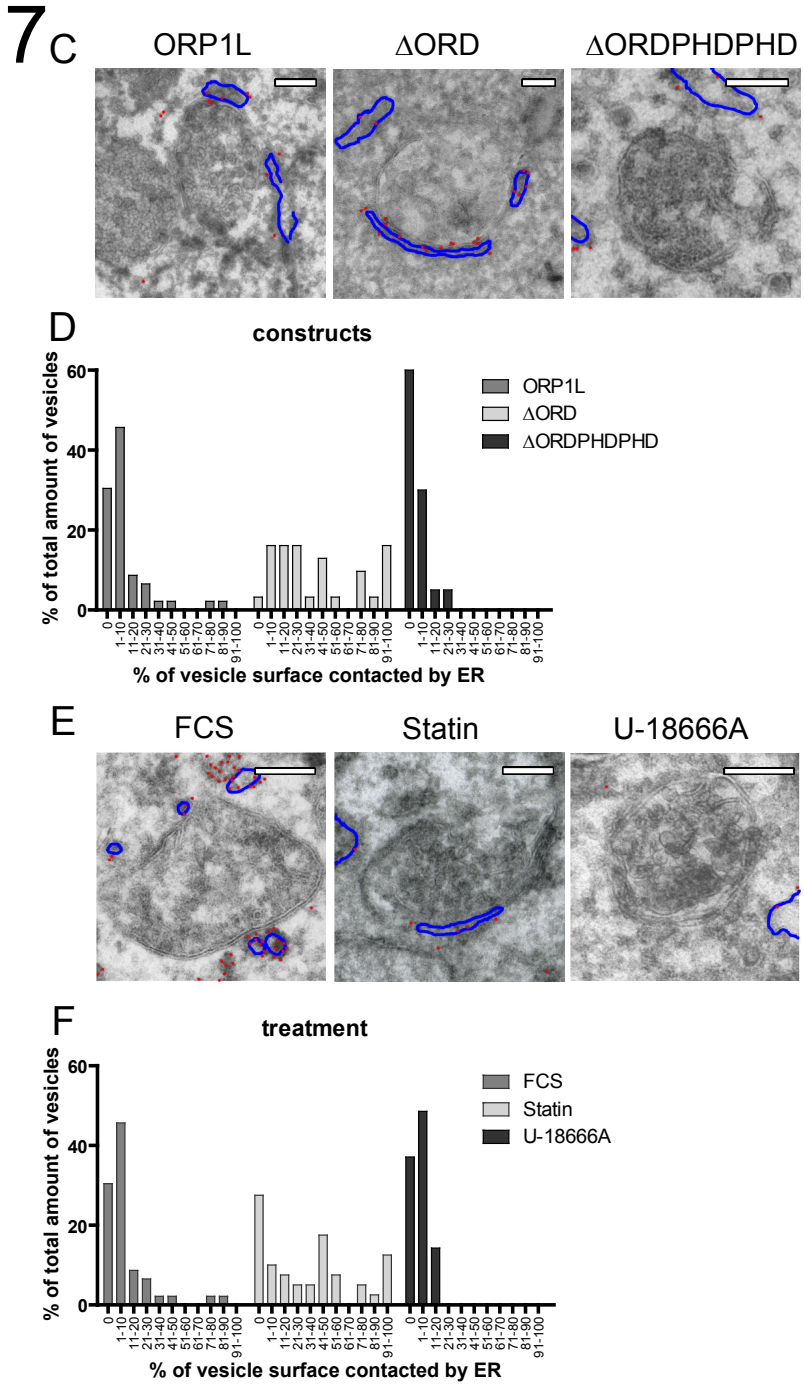


Figure 7 C-E.

(**C**) Electron micrographs of multivesicular bodies in MelJuSo cells expressing HA-VAP and different variants of GFP-ORP1L, as indicated. Cells were fixed and cryosections stained with anti-HA antibodies detected with 15 nm gold particles. The gold particles are highlighted by red dots and the ER membrane (containing HA-VAP) shown by blue lines. The original images are shown in Figure S7A. Scale bar, 200 nm.

(**D**) The percentage of multivesicular bodies contacting ER structures and the contact area between ER and late endosomal membranes were determined in MelJuSo cells expressing the ORP1L variants as shown in Figure 7C. More than 50 multivesicular bodies were considered per condition. The data on contact area were binned as indicated.

(**E**) Electron micrographs of multivesicular bodies in HA-VAP and GFP-ORP1L expressing MelJuSo cells exposed to different cholesterol manipulating conditions, as indicated. Cells were fixed and stained with anti-HA antibodies marked by 15 nm gold particles. The gold particles are highlighted by red dots and the ER membrane (containing HA-VAP) shown by blue lines. The original images are shown in Figure S7B. Bar; 200 nm.

(**F**) The percentage of multivesicular bodies contacting ER structures and the contact area between ER and LE membranes from MelJuSo cells expressing the ORP1L under various conditions of cholesterol manipulation (as shown in Figure 7E). More than 50 multivesicular bodies were considered per condition. The data on contact area were binned as indicated.

manipulation of cholesterol in MelJuSo cells were the ER was visualized by TAP1-GFP expression (Reits *et al*., 2000). Decreasing cholesterol levels sufficed to induce the arrival of ER markers on LE, as analyzed by CLSM and quantified by pixel analyses (Figure 7B).

To visualize the localization and interaction of VAP and ORP1L in more detail, we employed cryo-electron microscopy (EM). EM has a significantly higher spatial resolution than CLSM, which has a maximal resolution of ~240 nm. MelJuSo cells were transfected with GFP-ΔORD, -ORP1L or -ΔORDPHDPHD together with HA-tagged VAP-A. After expression of the ORP1L variants was observed (by GFP), cells were fixed, processed for cryo-immunoelectron microscopy

and stained with HA-antibodies to detect VAP-A (Figure 7C). The frequency of ER contacts with LE and the surface of the LE covered by ER structures was quantified (Figure 7D). Note that HA-VAP was never detected at LE membranes excluding fusion of LE and ER under these conditions. The ER, as labelled by HA-tagged VAP-A, had to be within 40 nm from the LE limiting membrane to be considered a contact. Most LE (>95%) interacted –often over large surface areas- with the ER when ΔORD was expressed. Both the number of ER-LE interactions and the surface covered by the ER decreased when ORP1L was expressed and contact sites were almost absent when the 'high-cholesterol conformation' of ORP1L (ΔORDPHDPHD) was expressed. This suggests that the cholesterol-dependent conformational state of ORP1L determines ER contact site formation with LE.

To directly test whether cholesterol levels indeed determine the formation of these contact sites, cells expressing GFP-ORP1L were cultured under control ('FCS'), cholesterol-increasing ('U-18666A') or –depleting ('Statin') conditions. Cells were fixed and sections stained for HA-tagged VAP-A (Figure 7E). Under control conditions some ER-LE interactions could be observed, usually over small late endosomal surfaces. Whereas cholesterol accumulation in LE (as the result of U-18666A) diminished these contacts, cholesterol depletion markedly induced formation of ER-LE contact sites (Figure 7F). These data suggest that the conformational state of ORP1L, as controlled by cholesterol levels, determines whether the ER will contact LE. This is required for the ER protein VAP to contact (and manipulate) the Rab7-RILP-p150^{Glued} complex on LE.

Discussion

Cholesterol is a hydrophobic molecule essential for fluidity and microdomain formation in biomembranes. Transfer of cholesterol over membranes requires transporters like ABCA1 and possibly NPC1 (Ikonen, 2008), but flip-flop of cholesterol over the limiting late endosomal membrane may be another possibility (Hamilton, 2003). If so, high concentrations of cholesterol in the LE lumen should be reflected by high concentrations of cholesterol in the cytosolic leaflet of LE.

The transfer of cholesterol to other organelles requires specific cholesterol-binding chaperones. A series of proteins with cholesterol-binding domains, like the StAR-related lipid transfer (StART) domain and ORD, have been identified in various compartments (Holthuis and Levine, 2005). Two such proteins, MLN64 and ORP1L, are located at LE membranes (Ikonen, 2008).

High cholesterol content in LE is typical for a series of lysosomal storage diseases with characteristic LE clustering at the minus-end of microtubules. It has been suggested that cholesterol influences LE transport in a process involving Rab GTPases (Holtta-Vuori *et al*., 2000; Lebrand *et al*., 2002). Minus-end transport of LE involves the dynein-dynactin motor complex and its receptor complex, Rab7-RILP-ORP1L. Since ORP1L binds both Rab7-RILP (Johansson *et al*., 2007) and cholesterol (Suchanek *et al*., 2007), we tested whether ORP1L could transfer information on LE cholesterol content to Rab7-RILP and then to p150^{Glued} associated motor proteins like the dynein motor. Using intramolecular FRET, we showed that the C-terminal ORD of ORP1L senses cholesterol in (the cytosolic leaflet of) LE resulting in a conformational change. ORD can be in a membrane-bound state (when cholesterol levels are high) or in a cytosolic, membrane-free orientation (when cholesterol levels are low). Overexpression of ORP1L or one of its mutants did not change cholesterol levels in LE (not shown), which suggests that ORP1L is merely a cholesterol sensor rather than actively contributing to extracting and redistributing cholesterol.

When ORD is in its cytosolic orientation or absent (as in the truncation mutant ΔORD), the FFAT motif of ORP1L prevents access of p150^{Glued} to Rab7-RILP. This does not occur when ORD is in the membrane-associated state (as in the chimera ΔORDPHDPHD). The FFAT motif in the ORP1L homologue OSBP interacts with VAPs in the ER (Loewen and Levine, 2005; Loewen *et al*., 2003) and modifies protein and lipid export from the ER (Wyles *et al*., 2002). Silencing of VAP restores p150^{Glued} binding to ΔORD-Rab7-RILP-containing vesicles, suggesting that VAP is directly involved in the removal of dynein-dynactin subunit p150^{Glued} from the Rab7-RILP complex. This was confirmed using isolated proteins where purified VAP-A removed p150^{Glued} from the RILP-Rab7-ORP1L complex (which also indicated that the minimal unit of proteins involved in this process had been identified).

The ER protein VAP would not be an obvious candidate for regulating LE positioning. Light microscopy suggested that VAP localized to LE when ΔORD was expressed (indicating ER-LE fusion) However, visualization of this process at a higher resolution by EM revealed that the ER (containing VAP) aligned to, rather than fused with LE creating LE-ER contact sites. The formation of these contact sites is dependent on the conformation of ORP1L. ΔORD or low cholesterol levels in the LE increased the number and area of contact sites, whereas ΔORDPHDPHD or high cholesterol decreased these interactions. ER-LE contact sites were proposed as sites where lipids like cholesterol could be transferred from LE to the

8

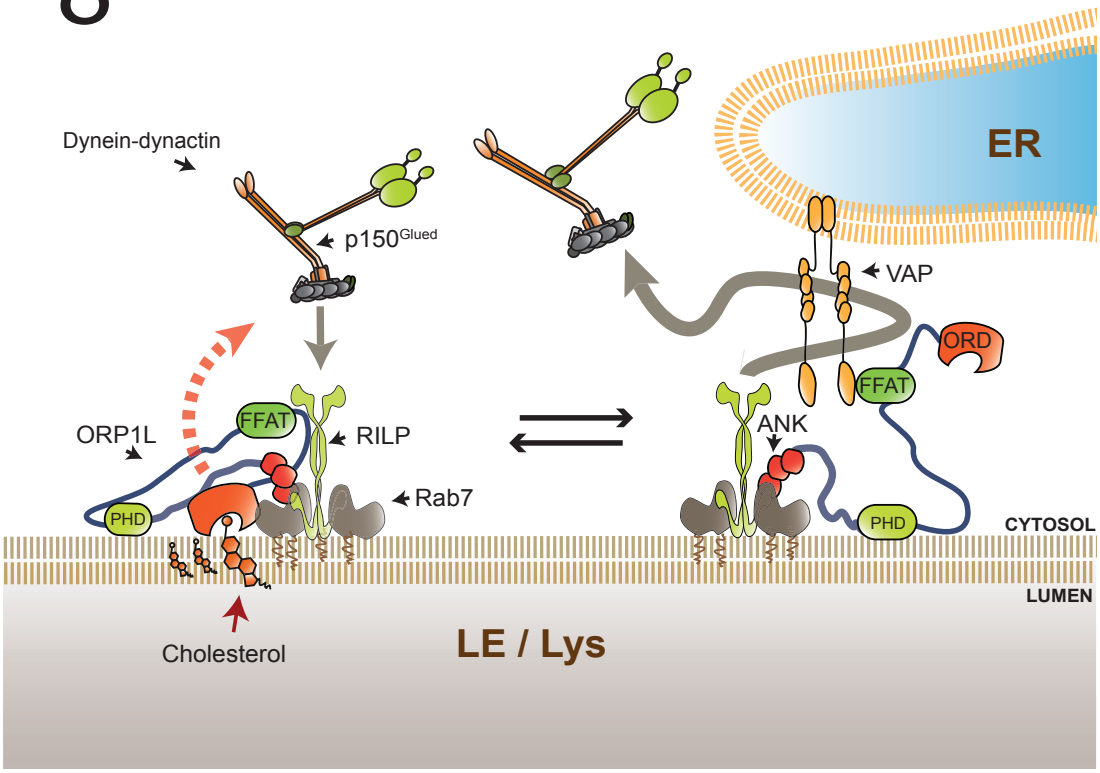


Figure 8. Model showing how the ER protein VAP controls late endosomal Rab7-RILP-p150^{Glued}-motor protein complexes and how this is controlled by cholesterol and sensor ORP1L.

Rab7 recruits the homodimeric effector protein RILP to late endosomes and lysosomes. The p150^{Glued} subunit of the dynein-dynactin motor directly interacts with RILP. ORP1L also binds to the Rab7-RILP complex. ORP1L has a C-terminal cholesterol-sensing domain ORD that exist in different conformational states, determined by late endosomal cholesterol At low cholesterol levels, ORD adopts a conformation where the preceding FFAT motif is exposed which can be detected by the ER protein VAP in ER-late endosomal membrane-contact-sites. VAP binds *in trans* to the Rab7-RILP-p150^{Glued} complex and removes p150^{Glued} thus preventing minus-end-directed transport. High cholesterol conditions initiate a different ORP1L conformation, preventing formation of ER-late endosomal membrane contact sites and VAP cannot interact with the Rab7-RILP-p150^{Glued} complex. Cholesterol levels in late endosomes thus determine the conformation of ORP1L and then VAP recruitment in ER-late endosome contact-sites. The ER protein VAP then controls the late endosomal motor protein receptor Rab7-RILP resulting in scattering of cholesterol-poor and clustering of cholesterol-laden late endosomes and lysosomes, as in Niemann-Pick type C disease.

ER (Underwood *et al*., 1998). The ER-LE contact sites are however predominantly observed under cholesterol depleted conditions, and to a lesser extent under control conditions. It is possible that they are transiently formed when ORP1L changes conformation to expose the FFAT domain, and released when ORP1L adopts the membrane associated 'cholesterol-high' state. Under low cholesterol conditions when the ER-LE membrane contact sites form, the ER protein VAP can interact *in trans* with the Rab7-RILP receptor on LE to release p150^{Glued}. This then results in microtubule plus-end transport and scattering of LE. Bleaching experiments suggest that GFP-VAP dynamically associates with ER-LE contact sites (not shown). Whether other proteins contribute to stabilizing interactions between these domains is unclear. When NPC1 is depleted or mutated, as in Niemann-Pick type C disease (Carstea *et al*., 1997), or when chemical drugs raise cholesterol levels of LE (Roff *et al*., 1991; Sobo *et al*., 2007), the ORD of ORP1L is membrane-associated preventing formation of ER-LE membrane contact sites. This allows enduring binding of p150^{Glued}-DIC-dynein motor complexes to Rab7-RILP and transport to the microtubule minus-end.

Why cholesterol is selected for determining late endosomal positioning is unclear. Cholesterol is present in the lumen as well as the cytosolic leaflet of LE allowing cytosolic exposure of intraluminal conditions. If cholesterol levels increase with maturation of LE, the resulting ORP1L controlled Rab7-RILP-p150^{Glued}-

DIC-dynein motor interactions would position the most matured compartments at the extreme minus-end of microtubules with 'shells' of less matured vesicles surrounding these at more plus-end locations. Newly arriving LE would then first encounter the 'youngest' LE automatically resulting in spatial maturation before encountering lysosomes. Cholesterol exposed at the LE cytosolic leaflet would thus control the positioning of these organelles. We have tested this by analyzing the conformation of the cholesterol sensor ORP1L by FRET on LE located in the perinuclear area versus the periphery. Donor FRET efficiency was lower in the cell periphery indicating a lower cholesterol concentration. This suggests that differences in LE cholesterol levels -as sensed by ORP1L- determine the intracellular location of LE.

We have visualized how the Rab7-RILP complex controls intracellular positioning of LE. This process is controlled by cholesterol levels sensed and translated by ORP1L to induce ER-LE contact sites via interaction with ER protein VAP. In these contact sites, VAP interacts *in trans* with the Rab7-RILP receptor, promoting dissociation of $p150^{Glued}$ and its associated motor proteins (Figure 8). This model explains why cholesterol depletion causes LE scattering and why high cholesterol levels induce LE clustering, as observed in Niemann-Pick type C disease. We reveal an unexpected contribution of ER proteins in the control of LE intracellular positioning by motor proteins in a process controlled by cholesterol.

Materials and methods

Reagents

Rab7, RILP, VAP-A, VAP-B, $p150^{Glued}$(C25) and ORP1L cDNA constructs have been described previously (Johansson *et al*., 2007; Jordens *et al*., 2001; Marsman *et al*., 2004; Wyles *et al*., 2002). Rabbit anti-GFP and rabbit anti-mRFP antibodies were generated using purified His-mRFP or His-GFP recombinant proteins as immunogens, respectively. Cross-reactivity was excluded by Western blot analyses with various mRFP- or GFP-labelled fusion proteins. Other antibodies used were rabbit polyclonal anti-NPC1 (Novus Biologicals, Inc.), rat monoclonal anti-tubulin antibody (Abcam plc), rabbit anti-human VAP antiserum (recognizing VAP-A and VAP-B; a kind gift of Dr. N. Ridgway; Dalhousie University, Canada), mouse anti-calnexin AF8 (David *et al*., 1993), mouse anti-LAMP1 (BD Transduction Laboratories), mouse anti-CD63 (Vennegoor *et al*., 1985), mouse monoclonal anti-EEA1 (Transduction Labs), rabbit anti-Rab7 and rabbit anti-HA epitope tag (Santa Cruz Biotechnology, Inc.), rabbit anti-human PDI (a kind gift of Dr. N. Bulleid (University of Manchester, UK), mouse monoclonal Golgi-97 (Molecular Probes), mouse monoclonal anti-HA epitope tag (12CA5) (Roche Applied Science), and mouse monoclonal anti-dynein intermediate chain (DIC) (BD Biosciences). Fluorescent secondary antibodies were from Molecular Probes.

Lovastatin (or Mevinolin) was purchased from Calbiochem (Darmstadt, Germany) and converted from its inactive prodrug form to its open acid form prior to use, by first dissolving the prodrug in ethanol and heating to 50°C for 2 hr in NaOH. Sodium-phosphate buffer was then added and this solution was heated to 40°C for 30 min. Finally, the pH was adjusted to 7.3 with concentrated HCl. Mevalonate was prepared by dissolving Mevalonolactone (Sigma-Aldrich, Schnelldorf, Germany) in a 0.05 M NaOH solution. The pH was adjusted to 7.0 with 0.1 M HCl.

U-18666A (Calbiochem) was dissolved in ethanol to a final concentration of 10 mg/ml.

The lipoprotein-deficient serum (LPDS) was prepared as described (Goldstein *et al*., 1983) and was a kind gift from Dr. M. Jauhiainen (National Public Health Institute, Helsinki, Finland).

cDNA constructs and vectors

Rab7, RILP, TAP1-GFP and ORP1L cDNA constructs have been described previously (Johansson *et al*., 2007; Jordens *et al*., 2001; Marsman *et al*., 2004; Reits *et al*., 2000). GST-VAP-A was a kind gift from Dr. M. Hardy and K. Ettayebi (Montana State University, USA) and HA-VAP-A and HA-VAP-B from Dr. C. Hoogenraad (Teuling *et al*., 2007). VAP-A was cut with BamHI-XhoI and cloned into both a pAGFP-C1 vector and a pYFP-C1 vector (in the BglII-Sal I site). GFP-ANKPHD and mRFP-ANKPHD were generated by subcloning the ANKPHD fragment from pCDNA4-ANKPHD (Johansson *et al*., 2007) into a pEGFP-C1 (BD Biosciences Clonetech, USA) or into a custom made pmRFP-C1 vector (Johansson *et al*., 2007), respectively, using the BamHI and XbaI sites.

ΔORD was generated by PCR using primers 5'-ACT CGGATCCATGAACACAGAAGCGGAGCAACA-3' and 5'-AAAGGATCCCTATCTGTGTTTTCTACT GCCCAAATGC-3' and inserted into the BamHI site of pcDNA4HisMax (Invitrogen) and the BglII site of pmRFP-C1 vectors (Johansson *et al*., 2007).

To generate mRFP-ΔORDPHDPHD, mRFP-ΔORD was digested with XbaI and EcoRI. The remainder of ΔORD was amplified by PCR using primers 5'-C TCAAAATGATTAAGGAGTGTGACATGGCTA -3' and 5'-CCGGAATTCCATTCTGTGTTTTCTA CTGCCCAAATGCTC-3'. The amplified fragment was inserted into the XbaI and EcoRI sites of the

previously digested mRFP- ΔORD vector. The first PH domain was generated by PCR using primers 5'-C CGGAATTCCGATATGAGGGCCCTCTCTGGAAG A-3' and 5'-CGGGGTACCGCTGTAAGCAGAATG TTCTTCTATTGC-3' and ligated into the EcoRI and KpnI sites. Subsequently, the second PH domain was also generated by PCR using primers 5'-CGGGGTA CCCGATATGAGGGCCCTCTCTGGAAGA-3' and 5'-CGGGATCCATTCTAGCTGTAAGCAGAATGT TCTTCTATTGC-3' and inserted using the KpnI and BamHI sites.

mRFP-ΔORDFFAT(D478A) was generated by PCR using mRFP-ΔORD as template and 5'-CCCAGAA TTCTATGCGGCGCTGTCAGATTCCGAGTC-3' and 5'-AAGCAAGTAAAACCTCTACAAATG-3' as primers, followed by swapping of the wild-type FFAT motif in mRFP-ΔORD for the mutated FFAT using the EcoRI and BamHI restriction sites.

The ORP1L-FRET construct (mRFP-ORP1L-GFP) was generated in two steps. First, mRFP-ORP1L was digested with NheI-SacI (internal site in ORP1L) which was subsequently cloned into pEGFP-N1 (Clontech) to obtain an N-terminal region of ORP1L which was N-terminally tagged to mRFP and C-terminally tagged to GFP. In the second step, the C-terminal part of ORP1L was produced by PCR with a forward primer 5'-GGAGTGTGACATGGCTAA-3' and a reverse primer 5'-CGGGATTCCATAAATGTCAGG CAAATTGAAG-3', mutating the ORP1L stop codon. The PCR product was digested using SacI and BamHI, and cloned into the intermediate construct described above.

To obtain mRFP-ΔORDPHDPHD-GFP, mRFP-ΔORDPHD was subcloned into pEGFP-N3 (Clontech) using the restriction sites NheI and KpnI in mRFP-ΔORDPHDPHD (described above). The second PH domain in the tandem was generated by PCR using primers 5'-CGGGGTACCCGATATGAGGGCCCT CTCTGGAAGA-3', and 5'-CGGGGTACCGCTGTA AGCAGAATGTTCTTCTATTGC-3' and cloned into the KpnI restriction site.

To obtain mRFP-ΔORD-GFP, mRFP-ΔORD was cloned into pEGFP-N2 (Clontech) using the restriction sites NheI and EcoRI in mRFP-ΔORDPHDPHD (described above).

For the generation of mRFP-ORP1L, ORP1L cDNA was cloned into mRFP-C1 using the BglII and BamHI restriction sites.

siRNAs for human NPC1 and ORP1L were obtained from Dharmacon (ON-TARGETplus SMARTpool for accession no. NM_000271 and NM-018030, respectively) and transfected using DharmaFECT 1 transfection reagent (Dharmacon).

All constructs were sequence verified. Expressed proteins had the expected molecular weight as confirmed by SDS-PAGE and Western blot analyses.

Cell culture and drug treatment

Monolayers of MelJuSo cells were maintained in Iscoves Modified Dulbecco's Medium (IMDM) medium (Gibco) supplemented with 8% FCS, in 5% CO_2 at 37°C.

For cholesterol-depleting conditions, MelJuSo cells were washed with PBS and then cultured in IMDM supplemented with 5% LPDS, 50 μM lovastatin to inhibit HMG-CoA reductase, and 230 μM mevalonate to supply essential non-sterol isoprenoids for cell growth and survival (Liscum *et al*., 1989; Sugii *et al*., 2006), for 4 hr before analyses. For cholesterol-enhancing conditions, cells were washed with PBS and cultured in IMDM supplemented with 8% FCS and 3 μg/ml of U18666A for 15 hr before analyses.

Microscopy

Transfected cells were fixed at 48 hr (DNA), 48 hr (RNAi) or 72 hr (RNAi and DNA) post-transfection with 4% formaldehyde in PBS for 30 min and permeabilized for 5 min with 0.05% Triton X-100 in PBS, at room temperature. Nonspecific binding of antibodies was blocked by 0.5% BSA/PBS for 40 min, after which cells were incubated with primary antibody in 0.5% BSA/PBS for 1 hr at room temperature. Bound primary antibodies were visualized with Alexa Fluor secondary antibody conjugates (Invitrogen). Cells were mounted in Vectashield mounting medium (Vector Laboratories, USA). The specimens were analyzed with confocal laser scanning microscopes (TCS-SP1, -SP2 or AOBS) equipped with HCX PL APO 63x/NA 1.32 and HCX PL APO lbd.bl 63×/NA 1.4 oil corrected objective lenses (all from Leica, Mannheim, Germany). The acquisition software used was Leica LCS.

Colocalization analysis for TAP-1 and CD63 was performed using Matlab, where images were stretched to 255 grey values and colocalization was performed on the pixels with intensities between100-255. The amount of colocalizing pixels was related to the total CD63 pixels for quantifications. The colocalizing pixels were projected on the CD63/TAP-1 overlay image for representation.

Photo-activation experiments were performed in MelJuSo cells transfected with photoactivatable GFP tagged to VAP-A, cotransfected with mRFP-tagged-ORP1L, -ORP1LΔORD or -ORP1LΔORDPDHPDH. Cells were mounted in phenolRed-free DMEM (Invitrogen), limiting autofluorescence of the medium. All measurements were performed on a on a Leica AOBS system equipped with a 37°C culture chamber and a 63x λ-blue-corrected PL APO 63x/NA 1.4 lens. Cells were imaged using a 488 nm and 561 nm laser, to visualize the activated PA-GFP and mRFP tagged

proteins, respectively. Point-activation with full power from the 405 nm laser was performed for 3 seconds at the nuclear region, where ER could be activated outside of the confocal plain. To prevent PA-GFP/VAP-A activation already present on late endosomal/lysosomal structures, a Z-stack was made before activation.

Fluorescence Lifetime Imaging Microscopy (FLIM)

FLIM experiments were performed with MelJuSo cells stably expressing mRFP-ORP1L-GFP cultured on Delta T dishes (Bioptechs). Prior to measurements, cells were mounted in bicarbonate-buffered saline medium (140 mM NaCl, 5 mM KCl, 2 mM $MgCl_2$, 1 mM $CaCl_2$, 23 mM $NaHCO_3$, 10 mM [D-]glucose, and 10 mM Hepes, pH 7.3) and analyzed at 37°C in a 5% CO_2 culture hood surrounding the objective stage of the microscope. Images were taken on a Leica inverted DM-IRE2 microscope with a HCX PL APO 63x/NA 1.35 glycerol corrected objective lens equipped with a Lambert Instruments (LI) frequency domain lifetime attachment (Leutingewolde, The Netherlands), controlled by the manufacturer's LI FLIM software. GFP was excited with ~4 mW of 488 nm light from a LED modulated at 40 MHz, and emission was collected at 490–550 nm using an intensified charge-coupled device camera (CoolSNAP HQ; Roper Scientific). To calculate the GFP lifetime, the intensities from 12 phase-shifted images (modulation depth ~70%) were fitted with a sinus function, and lifetimes were derived from the phase shift between excitation and emission. For internal controls, cells were co-cultured with MelJuSo cells expressing GFP only. Lifetimes were referenced to a 1 μM solution of rhodamine-G6 in saline that was set at a 4.11 ns lifetime. The donor FRET efficiency E_D was calculated as $E_D = 1 - (\text{measured lifetime/GFP lifetime in control cells})$ (Zwart *et al*., 2005).

Sensitized emission FRET by confocal microscopy

FRET between GFP and mRFP molecules was determined by calculating the sensitized emission (the mRFP emission following GFP excitation) from separately acquired donor and acceptor images (using a Leica AOBS system with 37°C culture device at 5% CO_2). Three images were collected: GFP excited at 488 nm and detected between 500 and 549 nm; indirect mRFP excited at 488 nm and detected between 581 and 675 nm and direct mRFP excited at 561 nm. Because of GFP-mRFP spectral overlap, indirect mRFP emission was corrected for bleed through of GFP in the 581-675 nm filter and for direct excitation of mRFP by 488 nm light. The correction factors were determined experimentally for each image by co-culturing the mRFP-ORP1L-GFP (or any of the ORP1L variants) expressing cells with cells expressing only GFP (to detect the bleed through in the mRFP channel) or mRFP (to detect direct excitation with 488 nm light). FRET and donor FRET efficiency E_D were calculated from these data as described in detail previously (van Rheenen *et al*., 2004; Zwart *et al*., 2005). For quantification of the intramolecular FRET gradient of mRFP-ORP1L-GFP and mRFP- ΔORD-GFP, E_D was measured in 5 equally sized concentric rings covering the area between the nucleus and the cell surface at the most distant point. The E_D in each circle was collected, binned and expressed per cell analyzed. The mean E_D and SEM of the different cells analyzed is calculated for the different rings.

Cryo-immunoelectron microscopy

Cells were fixed in a mixture of paraformaldehyde (4%) and glutaraldehyde (0.5%) prior to processing for immunoelectron microscopy. Cryosections were prepared and labeled with the various antibodies and secondary antibodies conjugated to protein A-colloidal gold. After embedding in a mixture of methyl-cellulose and uranyl acetate, sections were analyzed with a Philips CM10 electron microscope (Eindhoven, the Netherlands). The 40 nm spacing between ER and late endosomal membranes was derived from both digital and printed electron micrographs.

Filipin stainings

Filipin staining was performed on formaldehyde-fixed cells for 2 hr at room temperature with 0.05 mg/ml freshly dissolved Filipin (Sigma) in PBS supplemented with 0.5 % BSA, and imaged using a Zeiss AxioObserver Z1 microscope equipped with an Hamamatsu ORCA-ER CCD camera and a 63x / 1.25 Plan-Neofluar oil corrected objective lens. Filipin signal was recorded using a 390-415 nm BP excitation filter with a 450-470 nm BP emission filter. FITC signal was recorded with a 480-510 nm BP excitation filter with a 515-550 nm BP emission filter. mRFP signal was recorded with a 555-590 nm BP excitation filter with a 605- 655 nm BP emission filter (Zeiss). For data acquisition, the manufacturers' software was used.

Protein purification

His-Rab7, His-RILP, and GST-ORP1L were produced as previously described (Johansson *et al*., 2007). Cells were lysed in 0.5% Triton X-100, 20 mM Hepes (pH

7.5), 200 mM NaCl, 8 mM β-mercaptoethanol and Complete EDTA-free Protease Inhibitors Cocktail (Roche Diagnostics). The lysate was cleared by centrifugation and the supernatant was incubated with pre-equilibrated Talon Co^{2+} resin (Clontech Laboratories, Inc.) for 30 min. The resin was then washed extensively with 20 mM Hepes (pH7.5), 200 mM NaCl and 8 mM β-mercaptoethanol. Proteins were stored in 8.7% glycerol at -80°C until use in protein reconstitution experiments. GST-VAP-A construct in pGEX was a kind gift of Dr. N. Ridgway (Wyles *et al*., 2002). GST was removed by cleavage with thrombin by incubation at 30°C for 2 hr before inactivation and precipitation by 0.1mM PMSF. The GST moiety was removed using a glutathione-sepharose column and purity of GST-free VAP-A was confirmed by SDS-PAGE and Coomassie staining.

In vitro motor removal by and binding to VAP-A

The reconstitution assay was performed in a detergent/salt buffer (20 mM Hepes, pH 7.5, 200 mM NaCl, 4 mM β-mercaptoethanol, 5 mM $MgCl_2$, 0.05% [vol/vol] Triton X-100, and 50 µM GTP). 15 µg His-Rab7(Q67L) was coupled to 3 µl Talon Co^{2+} beads and preloaded with GTP. Beads were washed to remove unbound His-Rab7(Q67L) and recombinant purified proteins were added in equimolar concentrations. His-RILP (3 µg), GST-ORP1L (8.7 µg), VAP-A (2.2 µg) and MBP-$p150^{Glued}$(C25) (4.5 µg) were added to the beads as indicated and incubated in a total volume of 0.4 ml for 2 h at 4°C. Beads were washed extensively and MBP-$p150^{Glued}$(C25) (4.5 µg) or VAP-A (2.2 µg) was added to the beads as indicated. Proteins were subsequently incubated in a total volume of 0.4 ml of detergent/salt buffer for 30 min at 22°C. Beads were washed extensively and proteins bound to His-Rab7(Q67L) were analyzed by SDS-PAGE and Western blotting. Proteins were detected with the following antibodies: α-His (Amersham Biosciences), α-MBP (New England Biolabs), α-GST (kind gift of W. Moolenaar, NKI, Amsterdam). Direct binding of $p150^{Glued}$ to VAP-A was assayed as follows. 30 µg GST-VAP-A or 15 µg GST was coupled to 15 µl glutathione-Sepharose 4B beads. Beads were washed to remove unbound proteins, and MBP-$p150^{Glued}$(C25) (4.5 µg) was added to the beads in a total volume of 0.4 ml for 30 min at 22°C. Beads were washed extensively and proteins bound to the glutathione-Sepharose 4B beads were analyzed by SDS-PAGE and Western blotting.

Supplemental Material

This manuscript is accompanied by 18 Supplemental Figures and 8 Supplemental Movies (available online). Figure S1A shows quantification of LE distribution when cholesterol is manipulated or ORP1L mutants are expressed. Figure S1B shows controls for NPC1 silencing. Figure S2A shows the effects of further ORP1L mutants on LE and Figure S2B co-localization of the ORP1L mutants with the LE markers CD63 and lamp-1. Figure S3A shows co-localization of ORP1L mutants and CD63 under various conditions of cholesterol manipulation. Figure S4A and S4B shows control sensitized emission FRET images with various ORP1L mutants. Figure S4C-E shows FLIM images of mRFP-ORP1L-GFP and various control constructs under different cholesterol conditions. Figure S4F shows FLIM of mRFP-ORP1L-GFP in cells silenced for NPC1. Figures S4G-H shows the effect of NPC1 silencing on cholesterol accumulation in LE. Figure S5A shows snap-shots of photoactivation of PA-GFP tagged VAP-A in cells expressing mRFP labelled ORP1L mutants (corresponding to Movies M6-8). Figure S5B shows $p150^{Glued}$ distribution in cells expressing HA-VAP-A, GFP-RILP and different mRFP-OP1L variants. Figure S6 shows a pixel analyses of Figures 2B, 4E, 6B and S2. Figures S7A-B show the original electronmicrographs of Figures 7C and 7E.
Movies M1-3 show time-lapse experiments of MelJuSo cells LysoTrackerRED when cholesterol levels were manipulated. Movies M4 and M5 show time-lapse experiments of MelJuSo cells were expression of mRFP-ΔORD and mRFP-ΔORDPHDPHD is induced and distribution of LE is followed. Movies M6-8 show time-lapse experiments in MelJuSo cells expressing mRFP-ORP1L, mRFP-ΔORD and mRFP-ΔORDPHDPHD combined with photoactivation of PA-GFP tagged VAP-A.

Acknowledgements

K. Jalink for support with sensitized emission and FLIM measurements, P. Peters for support with electron microscopy and V. Olkkonen and M. Johansson for ORP1L reagents and constructs; N. Ridgway, M. Hardy, K. Ettayebi, and C. Hoogenraad for VAP-A and –B reagents. N. Ong for processing electron micrographs. We thank Helen Pickersgill, Rob Michalides and Victoria Menendez-Benito for critically reading the manuscript and Sabine Krom for helping with experiments. Nuno Rocha was supported by a Portuguese Foundation for Science and Technology FCT/ FSE PhD scholarship within the Third Framework Program. This work was supported by grants from the Dutch Cancer Society KWF and the Chemical Sciences Section of NWO (TOP grant).

References

Bastiaens, P.I., and A. Squire. 1999. Fluorescence lifetime imaging microscopy: spatial resolution of biochemical processes in the cell. Trends Cell Biol. 9:48-52.

Brown, C.L., K.C. Maier, T. Stauber, L.M. Ginkel, L. Wordeman, I. Vernos, and T.A. Schroer. 2005. Kinesin-2 is a motor for late endosomes and lysosomes. Traffic. 6:1114-24.

Bucci, C., P. Thomsen, P. Nicoziani, J. McCarthy, and B. van Deurs. 2000. Rab7: a key to lysosome biogenesis. Mol Biol Cell. 11:467-80.

Burkhardt, J.K., C.J. Echeverri, T. Nilsson, and R.B. Vallee. 1997. Overexpression of the dynamitin (p50) subunit of the dynactin complex disrupts dynein-dependent maintenance of membrane organelle distribution. J Cell Biol. 139:469-84.

Calleja, V., S.M. Ameer-Beg, B. Vojnovic, R. Woscholski, J. Downward, and B. Larijani. 2003. Monitoring conformational changes of proteins in cells by fluorescence lifetime imaging microscopy. Biochem J. 372:33-40.

Carstea, E.D., J.A. Morris, K.G. Coleman, S.K. Loftus, D. Zhang, C. Cummings, J. Gu, M.A. Rosenfeld, W.J. Pavan, D.B. Krizman, J. Nagle, M.H. Polymeropoulos, S.L. Sturley, Y.A. Ioannou, M.E. Higgins, M. Comly, A. Cooney, A. Brown, C.R. Kaneski, E.J. Blanchette-Mackie, N.K. Dwyer, E.B. Neufeld, T.Y. Chang, L. Liscum, J.F. Strauss, 3rd, K. Ohno, M. Zeigler, R. Carmi, J. Sokol, D. Markie, R.R. O'Neill, O.P. van Diggelen, M. Elleder, M.C. Patterson, R.O. Brady, M.T. Vanier, P.G. Pentchev, and D.A. Tagle. 1997. Niemann-Pick C1 disease gene: homology to mediators of cholesterol homeostasis. Science. 277:228-31.

Chen, H., J. Yang, P.S. Low, and J.X. Cheng. 2008. Cholesterol level regulates endosome motility via Rab proteins. Biophys J. 94:1508-20.

Colin, E., D. Zala, G. Liot, H. Rangone, M. Borrell-Pages, X.J. Li, F. Saudou, and S. Humbert. 2008. Huntingtin phosphorylation acts as a molecular switch for anterograde/retrograde transport in neurons. Embo J. 27:2124-34.

David, V., F. Hochstenbach, S. Rajagopalan, and M.B. Brenner. 1993. Interaction with newly synthesized and retained proteins in the endoplasmic reticulum suggests a chaperone function for human integral membrane protein IP90 (calnexin). J Biol Chem. 268:9585-92.

Deacon, S.W., A.S. Serpinskaya, P.S. Vaughan, M. Lopez Fanarraga, I. Vernos, K.T. Vaughan, and V.I. Gelfand. 2003. Dynactin is required for bidirectional organelle transport. J Cell Biol. 160:297-301.

Echard, A., F. Jollivet, O. Martinez, J.J. Lacapere, A. Rousselet, I. Janoueix-Lerosey, and B. Goud. 1998. Interaction of a Golgi-associated kinesin-like protein with Rab6. Science. 279:580-5.

Förster, T. 1948. Zwischenmolekulare energiewandering und fluoreszenz. . Annalen Physik. 6:55–75.

Goldstein, J.L., S.K. Basu, and M.S. Brown. 1983. Receptor-mediated endocytosis of low-density lipoprotein in cultured cells. Meth Enzymol. 98:241-60.

Gruenberg, J., and H. Stenmark. 2004. The biogenesis of multivesicular endosomes. Nat Rev Mol Cell Biol. 5:317-23.

Haimo, L.T., and M.M. Rozdzial. 1989. Lysed chromatophores: a model system for the study of bidirectional organelle transport. Methods Cell Biol. 31:3-24.

Hamamoto, I., Y. Nishimura, T. Okamoto, H. Aizaki, M. Liu, Y. Mori, T. Abe, T. Suzuki, M.M. Lai, T. Miyamura, K. Moriishi, and Y. Matsuura. 2005. Human VAP-B is involved in hepatitis C virus replication through interaction with NS5A and NS5B. J Virol. 79:13473-82.

Hamilton, J.A. 2003. Fast flip-flop of cholesterol and fatty acids in membranes: implications for membrane transport proteins. Curr Opin Lipidol. 14:263-71.

Harada, A., Y. Takei, Y. Kanai, Y. Tanaka, S. Nonaka, and N. Hirokawa. 1998. Golgi vesiculation and lysosome dispersion in cells lacking cytoplasmic dynein. J Cell Biol. 141:51-9.

Hoepfner, S., F. Severin, A. Cabezas, B. Habermann, A. Runge, D. Gillooly, H. Stenmark, and M. Zerial. 2005. Modulation of receptor recycling and degradation by the endosomal kinesin KIF16B. Cell. 121:437-50.

Hollenbeck, P.J., and J.A. Swanson. 1990. Radial extension of macrophage tubular lysosomes supported by kinesin. Nature. 346:864-6.

Holthuis, J.C., and T.P. Levine. 2005. Lipid traffic: floppy drives and a superhighway. Nat Rev Mol Cell Biol. 6:209-20.

Holtta-Vuori, M., J. Maatta, O. Ullrich, E. Kuismanen, and E. Ikonen. 2000. Mobilization of late-endosomal cholesterol is inhibited by Rab guanine nucleotide dissociation inhibitor. Curr Biol. 10:95-8.

Ikonen, E. 2008. Cellular cholesterol trafficking and compartmentalization. Nat Rev Mol Cell Biol. 9:125-38.

Im, Y.J., S. Raychaudhuri, W.A. Prinz, and J.H. Hurley. 2005. Structural mechanism for sterol sensing and transport by OSBP-related proteins. Nature. 437:154-8.

Johansson, M., M. Lehto, K. Tanhuanpää, T.L. Cover, and V.M. Olkkonen. 2005. The oxysterol-binding protein homologue ORP1L interacts with Rab7 and alters functional properties of late endocytic compartments. Mol Biol Cell. 16:5480-92.

Johansson, M., N. Rocha, W. Zwart, I. Jordens, L. Janssen, C. Kuijl, V.M. Olkkonen, and J. Neefjes. 2007. Activation of endosomal dynein motors by stepwise assembly of Rab7-RILP-p150^{Glued}, ORP1L, and the receptor betalll spectrin. J Cell Biol. 176:459-71.

Jordens, I., M. Fernandez-Borja, M. Marsman, S. Dusseljee, L. Janssen, J. Calafat, H. Janssen, R. Wubbolts, and J. Neefjes. 2001. The Rab7 effector protein RILP controls lysosomal transport by inducing the recruitment of dynein-dynactin motors. Curr Biol. 11:1680-5.

Jordens, I., M. Marsman, C. Kuijl, and J. Neefjes. 2005. Rab proteins, connecting transport and vesicle fusion. Traffic. 6:1070-7.

Kobayashi, T., M.H. Beuchat, M. Lindsay, S. Frias, R.D. Palmiter, H. Sakuraba, R.G. Parton, and J. Gruenberg. 1999. Late endosomal membranes rich in lysobisphosphatidic acid regulate cholesterol transport. Nat Cell Biol. 1:113-8.

Koh, C.H., and N.S. Cheung. 2006. Cellular mechanism of U18666A-mediated apoptosis in cultured murine cortical neurons: bridging Niemann-Pick disease type C and Alzheimer's disease. Cell Signal. 18:1844-53.

Lebrand, C., M. Corti, H. Goodson, P. Cosson, V. Cavalli, N. Mayran, J. Faure, and J. Gruenberg. 2002. Late endosome motility depends on lipids via the small GTPase Rab7. Embo J. 21:1289-300.

Lemmon, M.A., and K.M. Ferguson. 2000. Signal-dependent membrane targeting by pleckstrin homology (PH) domains. Biochem J. 350 Pt 1:1-18.

Liscum, L., R.M. Ruggiero, and J.R. Faust. 1989. The intracellular transport of low density lipoprotein-derived cholesterol is defective in Niemann-Pick type C fibroblasts. J Cell Biol. 108:1625-36.

Loewen, C.J., and T.P. Levine. 2005. A highly conserved binding site in vesicle-associated membrane protein-associated protein (VAP) for the FFAT motif of lipid-binding proteins. J Biol Chem. 280:14097-104.

Loewen, C.J., A. Roy, and T.P. Levine. 2003. A conserved ER targeting motif in three families of lipid binding proteins and in Opi1p binds VAP. Embo J. 22:2025-35.

Marsman, M., I. Jordens, C. Kuijl, L. Janssen, and J. Neefjes. 2004. Dynein-mediated vesicle transport controls intracellular Salmonella replication. Mol Biol Cell. 15:2954-64.

Maxfield, F.R., and I. Tabas. 2005. Role of cholesterol and lipid organization in disease. Nature. 438:612-21.

Mukherjee, S., and F.R. Maxfield. 2004. Lipid and cholesterol

trafficking in NPC. Biochim Biophys Acta. 1685:28-37.

Nakata, T., and N. Hirokawa. 1995. Point mutation of adenosine triphosphate-binding motif generated rigor kinesin that selectively blocks anterograde lysosome membrane transport. J Cell Biol. 131:1039-53.

Narita, K., A. Choudhury, K. Dobrenis, D.K. Sharma, E.L. Holicky, D.L. Marks, S.U. Walkley, and R.E. Pagano. 2005. Protein transduction of Rab9 in Niemann-Pick C cells reduces cholesterol storage. Faseb J. 19:1558-60.

Neufeld, E.B., J.A. Stonik, S.J. Demosky, Jr., C.L. Knapper, C.A. Combs, A. Cooney, M. Comly, N. Dwyer, J. Blanchette-Mackie, A.T. Remaley, S. Santamarina-Fojo, and H.B. Brewer, Jr. 2004. The ABCA1 transporter modulates late endocytic trafficking: insights from the correction of the genetic defect in Tangier disease. J Biol Chem. 279:15571-8.

Nishimura, Y., M. Hayashi, H. Inada, and T. Tanaka. 1999. Molecular cloning and characterization of mammalian homologues of vesicle-associated membrane protein-associated (VAMP-associated) proteins. Biochem Biophys Res Commun. 254:21-6.

Pelkmans, L., E. Fava, H. Grabner, M. Hannus, B. Habermann, E. Krausz, and M. Zerial. 2005. Genome-wide analysis of human kinases in clathrin- and caveolae/raft-mediated endocytosis. Nature. 436:78-86.

Pepperkok, R., A. Squire, S. Geley, and P.I. Bastiaens. 1999. Simultaneous detection of multiple green fluorescent proteins in live cells by fluorescence lifetime imaging microscopy. Curr Biol. 9:269-72.

Pfeffer, S.R. 2001. Rab GTPases: specifying and deciphering organelle identity and function. Trends Cell Biol. 11:487-91.

Reits, E.A., J.C. Vos, M. Gromme, and J. Neefjes. 2000. The major substrates for TAP *in vivo* are derived from newly synthesized proteins. Nature. 404:774-8.

Roff, C.F., E. Goldin, M.E. Comly, A. Cooney, A. Brown, M.T. Vanier, S.P. Miller, R.O. Brady, and P.G. Pentchev. 1991. Type C Niemann-Pick disease: use of hydrophobic amines to study defective cholesterol transport. Dev Neurosci. 13:315-9.

Santama, N., J. Krijnse-Locker, G. Griffiths, Y. Noda, N. Hirokawa, and C.G. Dotti. 1998. KIF2beta, a new kinesin superfamily protein in non-neuronal cells, is associated with lysosomes and may be implicated in their centrifugal translocation. Embo J. 17:5855-67.

Shaner, N.C., R.E. Campbell, P.A. Steinbach, B.N. Giepmans, A.E. Palmer, and R.Y. Tsien. 2004. Improved monomeric red, orange and yellow fluorescent proteins derived from Discosoma sp. red fluorescent protein. Nat Biotechnol. 22:1567-72.

Sobo, K., I. Le Blanc, P.P. Luyet, M. Fivaz, C. Ferguson, R.G. Parton, J. Gruenberg, and F.G. van der Goot. 2007. Late endosomal cholesterol accumulation leads to impaired intra-endosomal trafficking. PLoS ONE. 2:e851.

Suchanek, M., R. Hynynen, G. Wohlfahrt, M. Lehto, M. Johansson, H. Saarinen, A. Radzikowska, C. Thiele, and V.M. Olkkonen. 2007. The mammalian oxysterol-binding protein-related proteins (ORPs) bind 25-hydroxycholesterol in an evolutionarily conserved pocket. Biochem J. 405:473-80.

Sugii, S., S. Lin, N. Ohgami, M. Ohashi, C.C. Chang, and T.Y. Chang. 2006. Roles of endogenously synthesized sterols in the endocytic pathway. J Biol Chem. 281:23191-206.

Teuling, E., S. Ahmed, E. Haasdijk, J. Demmers, M.O. Steinmetz, A. Akhmanova, D. Jaarsma, and C.C. Hoogenraad. 2007. Motor neuron disease-associated mutant vesicle-associated membrane protein-associated protein (VAP) B recruits wild-type VAPs into endoplasmic reticulum-derived tubular aggregates. J Neurosci. 27:9801-15.

Underwood, K.W., N.L. Jacobs, A. Howley, and L. Liscum. 1998. Evidence for a cholesterol transport pathway from lysosomes to endoplasmic reticulum that is independent of the plasma membrane. J Biol Chem. 273:4266-74.

Vale, R.D., F. Malik, and D. Brown. 1992. Directional instability of microtubule transport in the presence of kinesin and dynein, two opposite polarity motor proteins. J Cell Biol. 119:1589-96.

van Rheenen, J., M. Langeslag, and K. Jalink. 2004. Correcting confocal acquisition to optimize imaging of fluorescence resonance energy transfer by sensitized emission. Biophys J. 86:2517-29.

Vennegoor, C., J. Calafat, P. Hageman, F. van Buitenen, H. Janssen, A. Kolk, and P. Rumke. 1985. Biochemical characterization and cellular localization of a formalin-resistant melanoma-associated antigen reacting with monoclonal antibody NKI/C-3. Int J Cancer. 35:287-95.

Wubbolts, R., M. Fernandez-Borja, I. Jordens, E. Reits, S. Dusseljee, C. Echeverri, R.B. Vallee, and J. Neefjes. 1999. Opposing motor activities of dynein and kinesin determine retention and transport of MHC class II-containing compartments. J Cell Sci. 112 (Pt 6):785-95.

Wyles, J.P., C.R. McMaster, and N.D. Ridgway. 2002. Vesicle-associated membrane protein-associated protein-A (VAP-A) interacts with the oxysterol-binding protein to modify export from the endoplasmic reticulum. J Biol Chem. 277:29908-18.

Zerial, M., and H. McBride. 2001. Rab proteins as membrane organizers. Nat Rev Mol Cell Biol. 2:107-17.

Zwart, W., A. Griekspoor, C. Kuijl, M. Marsman, J. van Rheenen, H. Janssen, J. Calafat, M. van Ham, L. Janssen, M. van Lith, K. Jalink, and J. Neefjes. 2005. Spatial separation of HLA-DM/HLA-DR interactions within MIIC and phagosome-induced immune escape. Immunity. 22:221-33.

Supplemental Data.

Figure S1. Cholesterol, NPC1, ORD domain and vesicle distribution.

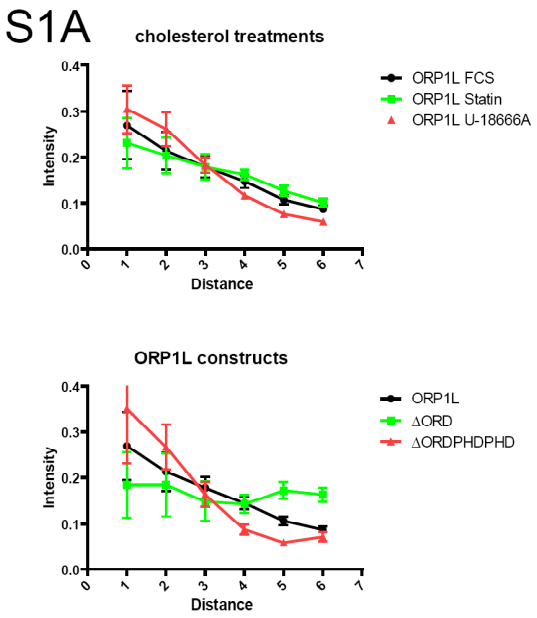


Figure S1A. Late endosomal distribution under expression of ORP1L and mutants or cellular cholesterol content modifications. Upper panel: Cells were transfected with ORP1L and treated with U-18666A to enhance cellular cholesterol content (red) or with statin and delipidated FCS to decrease cellular cholesterol content (green) or not treated (black). Endogenous CD63 was stained with anti CD63 (NKI-C3) the radial distribution of the fluorescence was measured in 6 bins with CellProfiler, where bin 1 start in the center of gravity of the CD63 stain and subsequent bins are progressively closer to the edge of the cell. Lower panel: Cells were transfected with ORP1L (black), ΔORD (green) and ΔORDPHDPHD (red). The distribution of the endogenous CD63 molecule was measured as described above. Vesicles cluster when the Cholesterol content of cells is increased or when ΔORDPHDPHD is expressed. Scattering is observed when cholesterol content of cells is decreased or when ΔORD is expressed. Shown are mean and SEM values of >20 cells per condition. The slopes of the curves were determined and the dependence of vesicle distribution (based on mean intensity per bin) on cholesterol content was tested (Jonckheere-Terpstra Test) from enhanced (U-18666A) to control (FCS) to decreased cholesterol (Statin) content (p=0.0002572). In case of the different ORP1L constructs (Figure 2) vesicle distribution was tested from ΔORDPHDPHD (high cholesterol mimic) to ORP1L to ΔORD (low cholesterol mimic) (p=5.122e-5).

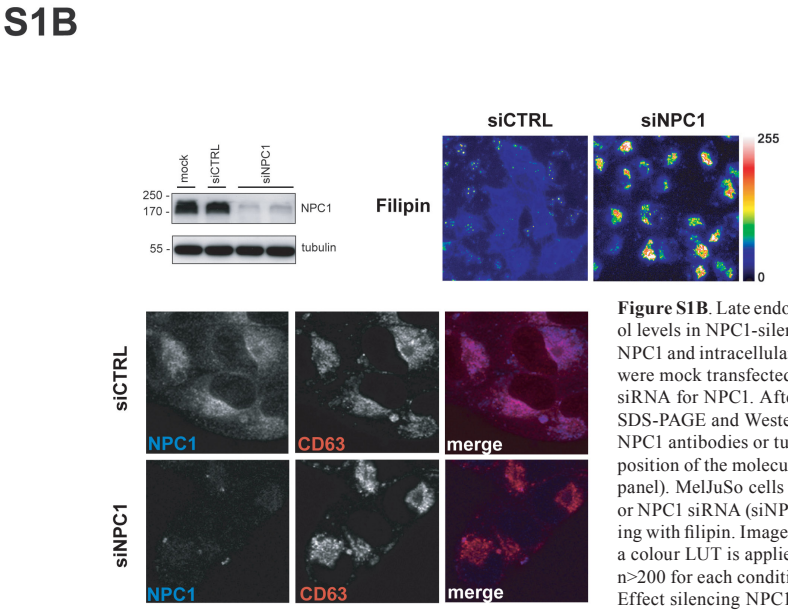


Figure S1B. Late endosomal vesicle distribution and cholesterol levels in NPC1-silenced cells. siRNA-mediated silencing of NPC1 and intracellular cholesterol. (Left panel). MelJuSo cells were mock transfected or transfected with a control siRNA or siRNA for NPC1. After 72 hrs, cell lysates were separated by SDS-PAGE and Western blotting and filters probed with anti-NPC1 antibodies or tubulin antibodies as loading control. The position of the molecular weight standards is indicated. (Right panel). MelJuSo cells were transfected with control (siCTRL) or NPC1 siRNA (siNPC1) for 72 hrs prior to fixation and staining with filipin. Images were made under identical settings and a colour LUT is applied to illustrate differences in intensities. n>200 for each condition. Scale bars, 10 µm.
Effect silencing NPC1 on late endosomal positioning. MelJuSo cells were transfected with control of NPC1 siRNA before fixations and staining for NPC1 and the late endosomal marker CD63, as indicated. n>100. Scale bars, 10 µm.

Figure S2. Co-localization studies of RILP and ORP1L variants with compartment markers and dynein motor subunits.

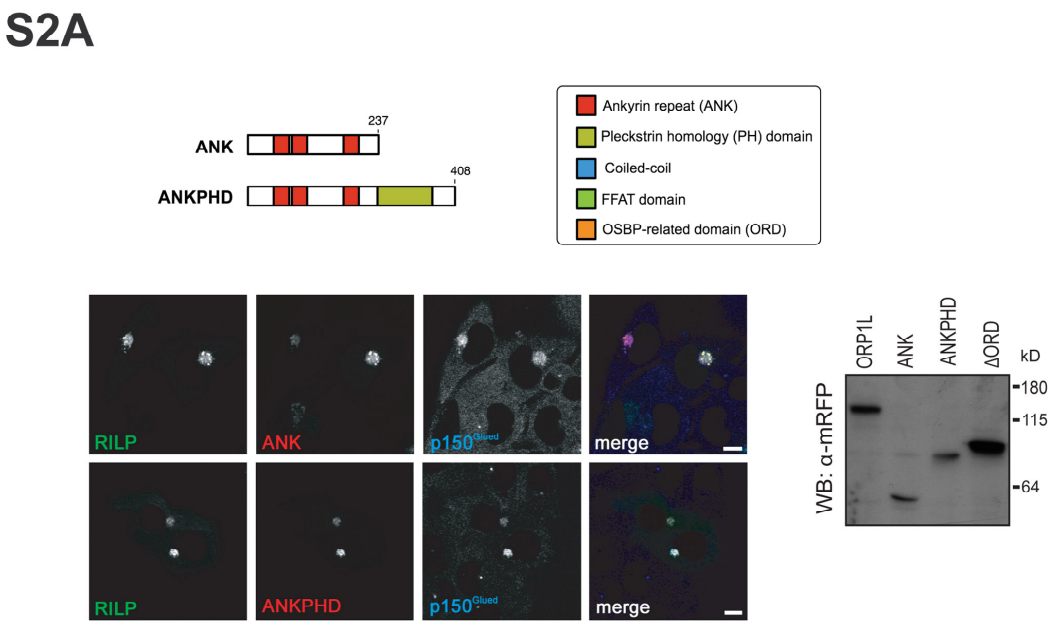


Figure S2A. ANK and ANKPHD enable recruitment of p150^{Glued} to the Rab7-RILP receptor.

Top panel: ANK and ANKPHD domain structure and constructs. Numbers indicate amino acid residue positions. Both constructs were N-terminally tagged with mRFP.
Bottom panels: Effect of ANK and ANKPHD chimeric constructs on RILP-mediated p150^{Glued} recruitment. Left panel: MelJuSo cells were transfected with GFP-RILP and mRFP-ORP1L constructs. Cells were fixed and stained with anti-p150^{Glued} antibodies prior to confocal microscopy, n>200 for each condition. Scale bars, 10 µm. Right panels: MelJuSo cells were transfected with the indicated mRFP-ORP1L, -ANK, -ANKPHD and -ΔORD constructs and whole-cell lysates were analyzed by SDS-PAGE and Western blotting with anti-mRFP antibodies (WB: α-mRFP). Position of the molecular weight standards is indicated.

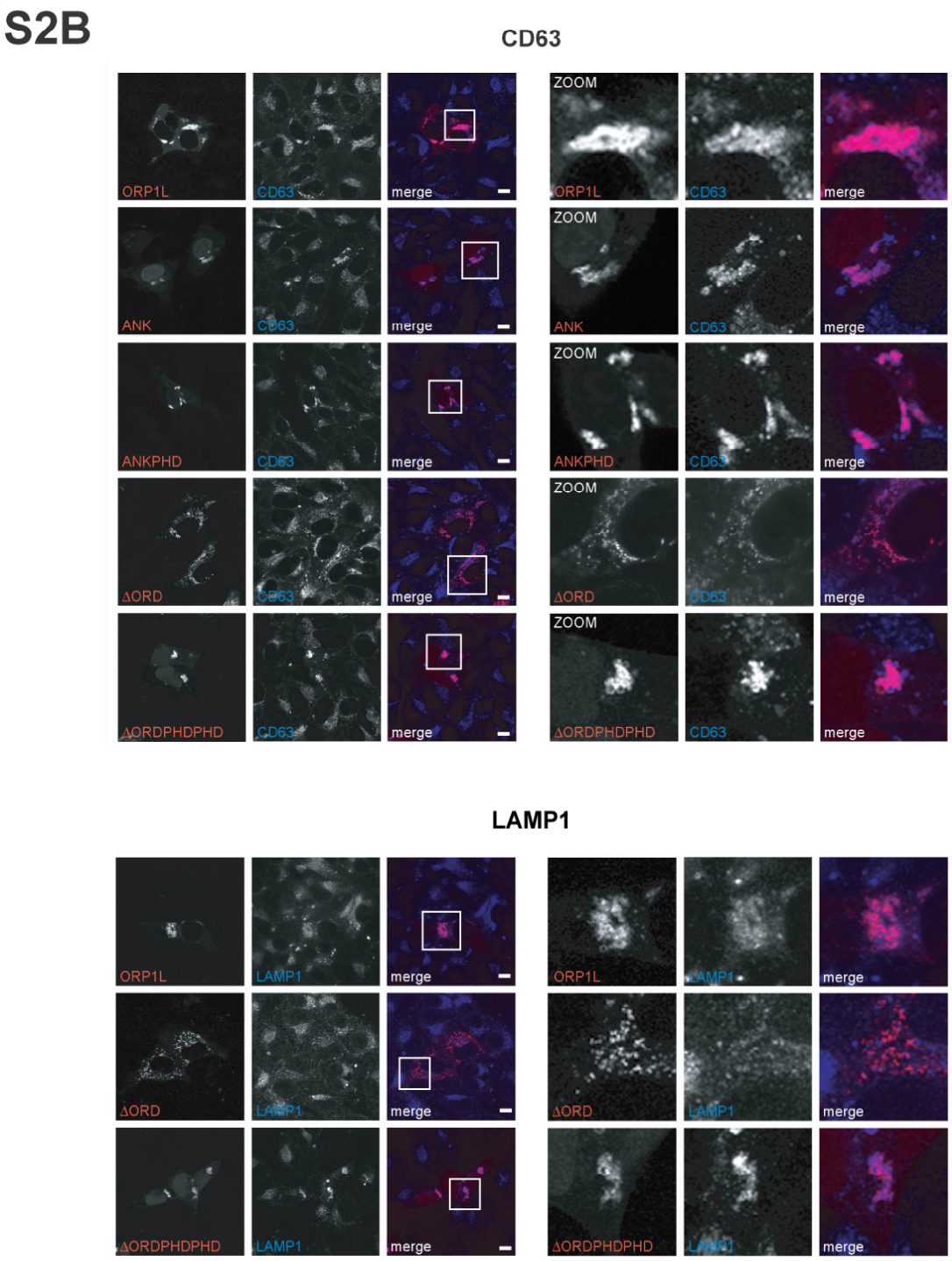


Figure S2B. ORP1L and variants label CD63 and LAMP1 positive late endosomes.

MelJuSo cells were transfected with various mRFP-tagged ORP1L variants as indicated. Cells were fixed and stained for CD63 or LAMP1. The right panel shows a zoom-in of the region where the vesicles locate. n>100; bar represents 10 µm.

S2C

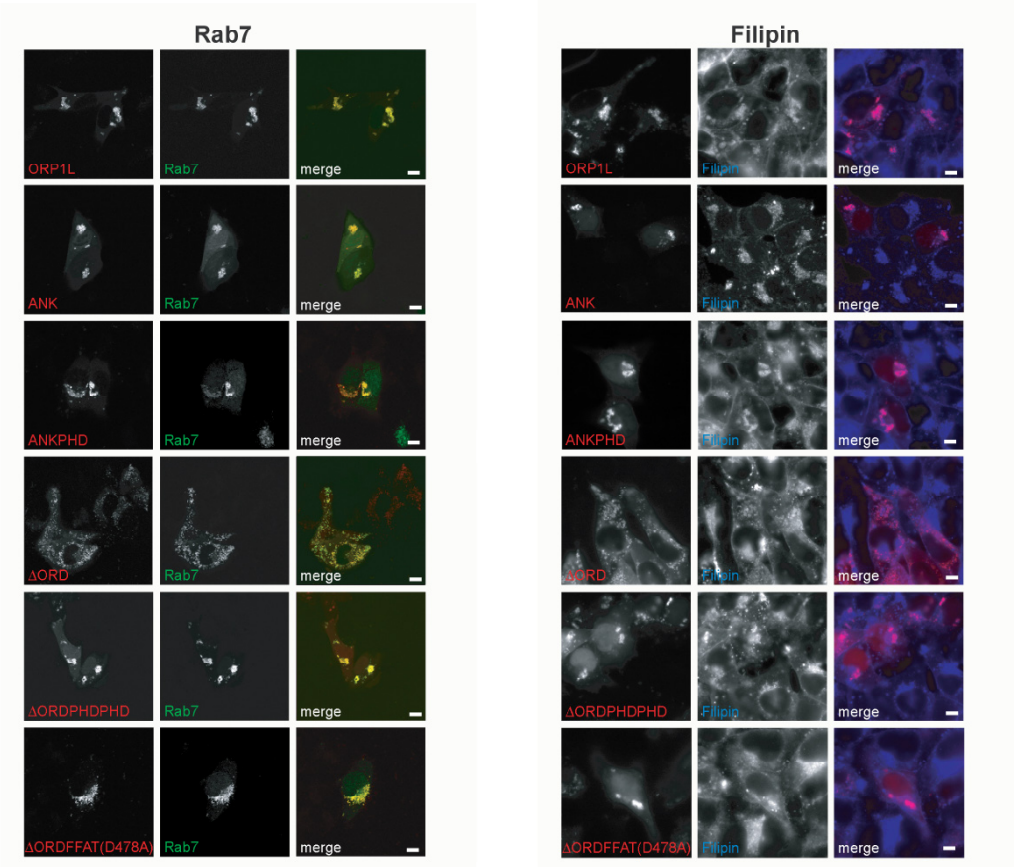


Figure S2C. ORP1L and variants label Rab7 and cholesterol positive vesicles.

MelJuSo cells were transfected with various mRFP-tagged ORP1L variants as indicated. Cells were fixed and stained for Rab7 or for cholesterol by filipin. n> 80; bar represents 10 µm.

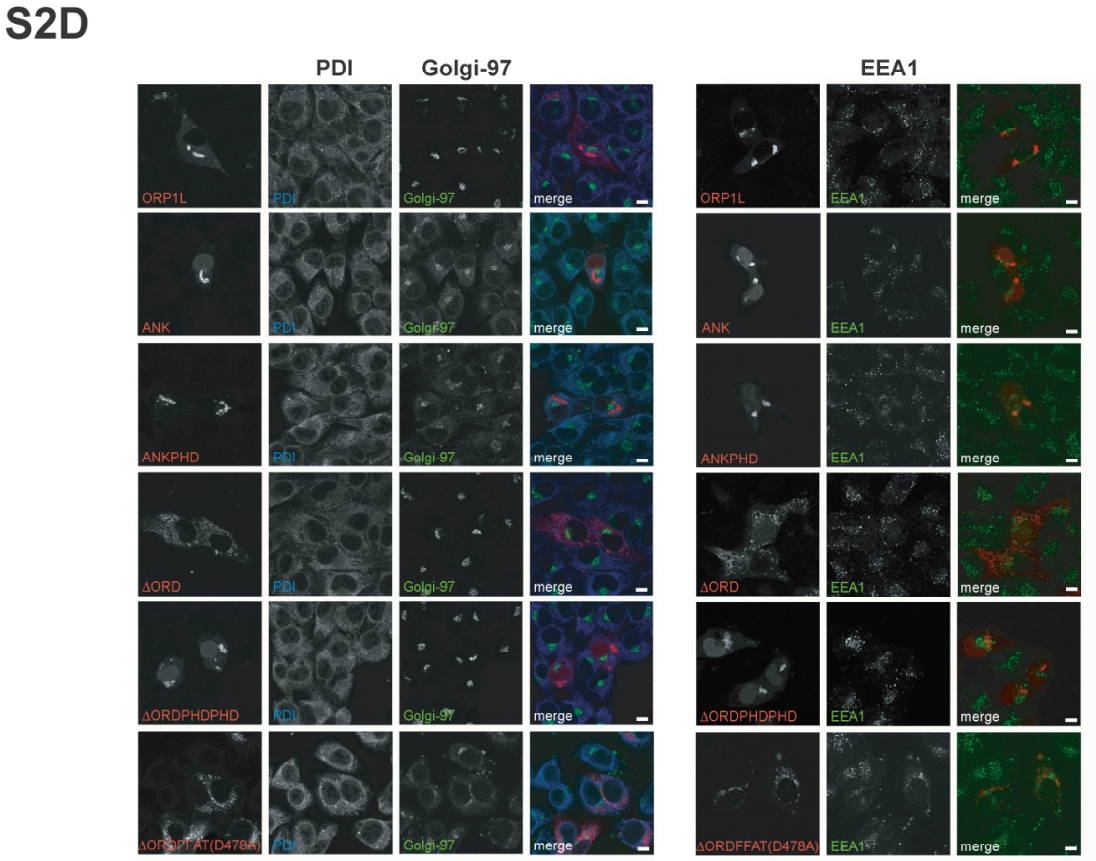


Figure S2D. ORP1L and variants do not label ER, Golgi or early endosomes.

MelJuSo cells were transfected with various mRFP-tagged ORP1L variants as indicated. Cells were stained and labeled for the ER marker PDI, Golgi marker Golgi-97 or (right panel) the early endosomal marker EEA1. n>100 for each panel; bar represents 10 µm.

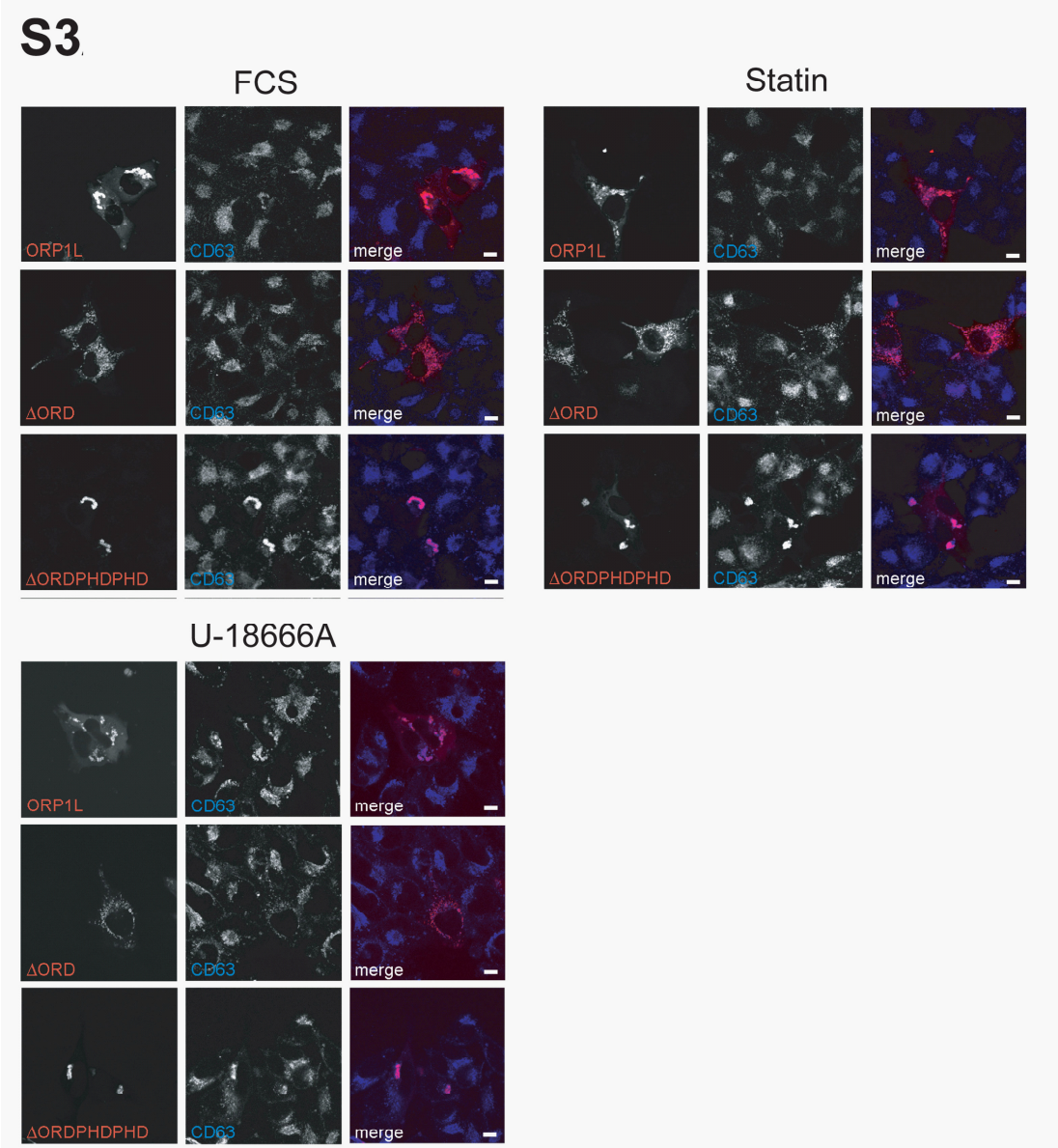


Figure S3. Chemical manipulation of cholesterol levels and location ORP1L variants on late endosomes.

MelJuSo cells were transfected with various mRFP-labeled ORP1L variants as indicated, before intracellular cholesterol levels were decreased (Statin) or increased (U-18666A). Cells were fixed and stained for the late endosomal marker CD63, as indicated. n>50; bar represents 10 µm.

Figure S4. Control sensitized emission FRET and FLIM experiments, the effect of NPC1 silencing on ORP1L conformation and vesicle distribution of ORP1L mutants.

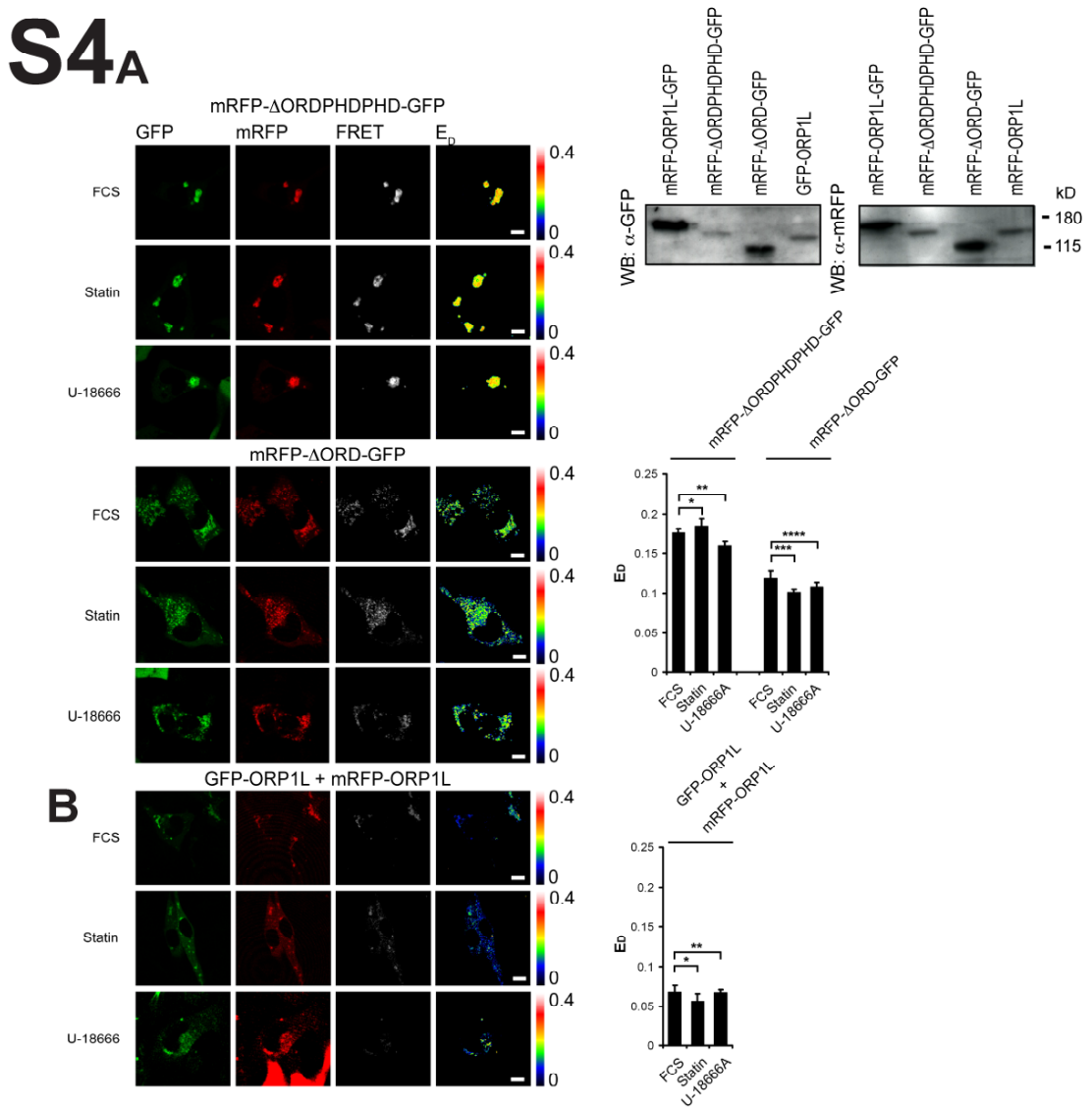


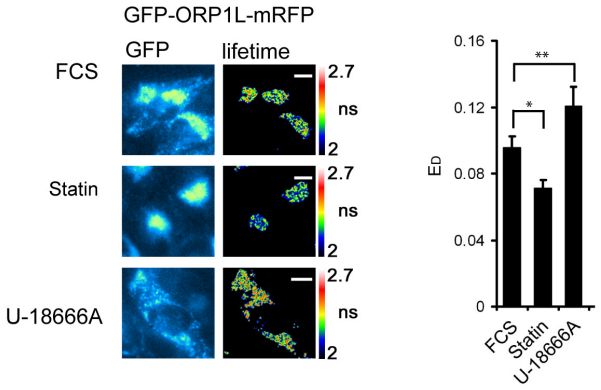
Figure S4A. Sensitized emission confocal FRET for ORP1L variants and cholesterol level manipulations.

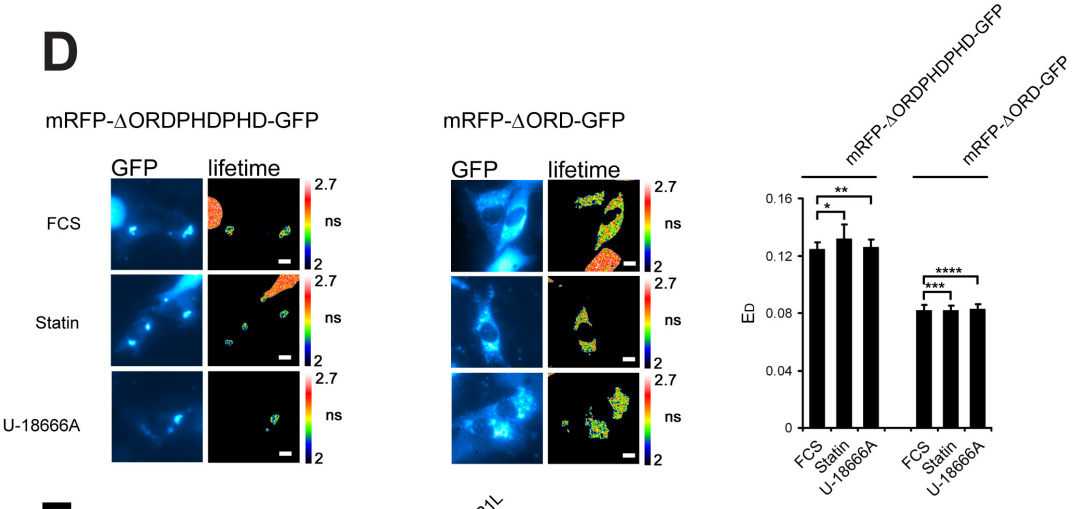
MelJuSo cells were transfected with GFP-ΔORDPHDPHD-mRFP or GFP-ΔORD-mRFP and sensitize emission was determined under control conditions (FCS), conditions of cholesterol depletion (Statin) or cholesterol accumulation (U-18666A). Cells were co-cultured with control cells expressing GFP or mRFP only, which were used to control for bleed-through and indirect excitation (not shown). Left panel: for the different constructs (as indicated), the GFP channel (after excitation with 488 nm light), the mRFP signal (after excitation with 568 nm laser light), FRET (after correction for bleed through and indirect excitation) and donor FRET efficiency (E_D) is shown. A color LUT directly reveal differences in donor FRET efficiency. Bar represents 10 µm. Right top panel: The constructs tested in Fig S4A-D were expressed, separated by SDS-PAGE and Westernblotting and probed with antibodies against GFP or mRFP, as indicated. The molecular weight standards are indicated. Right bottom panel: Donor FRET efficiency E_D plotted from 8 measurements per condition. Shown is mean + SEM. (*p=0.33; **p=0.11; ***p=0.10; ****p=0.29)

Figure S4B. Sensitized emission confocal FRET to test clustering GFP-ORP1L and mRFP-ORP1L under different conditions of cholesterol manipulation.

MelJuSo cells were transfected with the two constructs GFP-ORP1L and mRFP-ORP1L and co-cultured with control cells expressing GFP or mRFP only. Left panel: two control cells expressing mRFP only are shown in the bottom panel. Cells were cultured under the various conditions of cholesterol manipulation before GFP, corrected mRFP, FRET and donor FRET efficiency were measured, as described above. Bar represents 10 µm. Right panel: quantification of donor FRET efficiency E_D calculated from 9 measurements per condition. Shown is mean + SEM. (*p=0.39; **p=0.98).

S4c





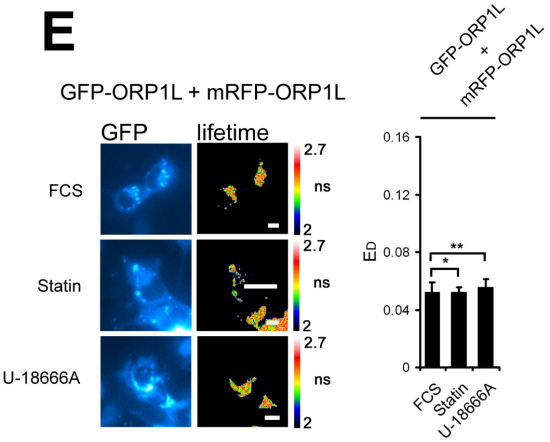


Figure S4C and S4D. FLIM to detect conformational changes in ORP1L variants in response to cholesterol level manipulations.

MelJuSo cells were transfected with GFP-ORP1L-mRDP (C), GFP-ΔORDPHDPHD-mRFP or GFP-ΔORD-mRFP (D) and GFP fluorescence life-time was determined under control conditions (FCS), conditions of cholesterol depletion (Statin) or cholesterol accumulation (U-18666A). Left panel: cells were co-cultured with control cells expressing GFP only as an internal control for GFP life-time not involved in a FRET pair. FLIM was measure by wide-field microscopy. Panel 'GFP' shows the GFP signal, 'FLIM' the fluorescence life time in ns, visualized using a color LUT. Bar represents 10µm. Right panel: quantification of donor FRET efficiency E_D for the FRET constructs calculated from 20 measurements per condition. Shown is mean + SEM. (For C: (*p=4,9*10-7; **p=9.5*10-12. For D: *p=0.28; **p=0.74; ***p=0.98; ****p=0.83).

Figure S4E. FLIM measurements to test clustering of GFP-ORP1L and mRFP-ORP1L under different conditions of cholesterol manipulation.

MelJuSo cells were transfected with the two constructs GFP-ORP1L and mRFP-ORP1L and co-cultured with control cells expressing GFP only before exposure to conditions of cholesterol manipulation, as described above. Left panel: wide-field image of GFP fluorescence (panel 'GFP') and life-time detection, shown in false colors for life-time differences as shown by color LUT. Bar represents 10 µm. Right panel: Calculated donor FRET efficiency E_D under the different conditions of cholesterol manipulation from 20 measurements. Shown is mean + SEM. (*p=0.94; **p=0.63).

S4F

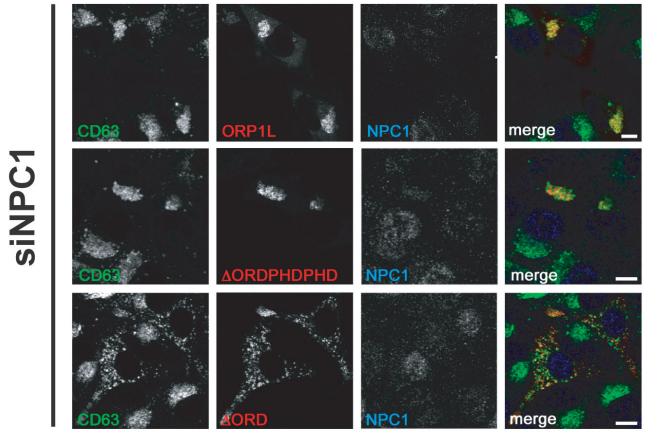


Figure S4F. Silencing NPC1 and location of ORP1L variants on CD63 containing endosomes.

MelJuSo cells were transfected with siRNA for NPC1 and 48 hrs later with the various mRFP-labeled ORP1L constructs as indicated. After another 24 hours, cells were fixed and stained for the late endosomal marker CD63 and NPC1 to control for actual silencing. n>100; bar represents 10 µm.

G

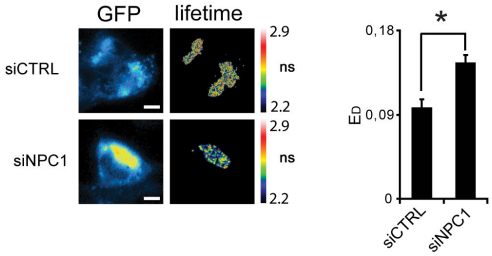


Figure S4G. ORP1L conformation in NPC1-deficient cells as detected by FLIM.

mRFP-ORP1L-GFP -expressing MelJuSo cells were transfected with control (siCTRL) or NPC1 (siNPC1) siRNAs. Left panel: GFP fluorescence detected the distribution of the ORP1L-containing vesicles by wide-field microscopy. GFP lifetime was detected by FLIM. The lifetime was determined (in ns) and plotted in false colour LUT. Scale bars, 10 µm. Right panel: donor FRET efficiencies (E_D) as calculated from the FLIM data. The mean and SD from 75 cells analyzed in three independent experiments is shown (*p=3.1*10-16).

H

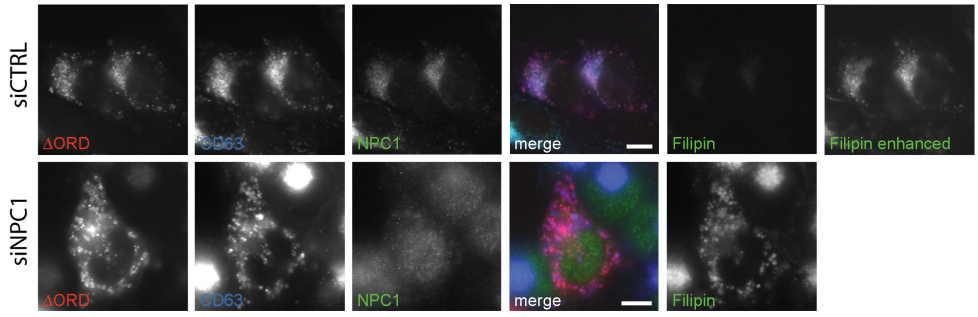


Figure S4H. Late endosomal scattering in NPC1-deficient cells.

MelJuSo cells were transfected with control siRNA or siRNA for NPC1 and 48 hrs later with mRFP-ΔORD. 24 hours later, cells were fixed and stained the late endosomal marker CD63, NPC1 (as control) and filipin to detect cholesterol. Microscopy images were made under identical settings. An additional image for filipin made after long exposure is shown ('Filipin enhanced') to show that control cells also contain cholesterol. n>50; bar represents 10 µm.

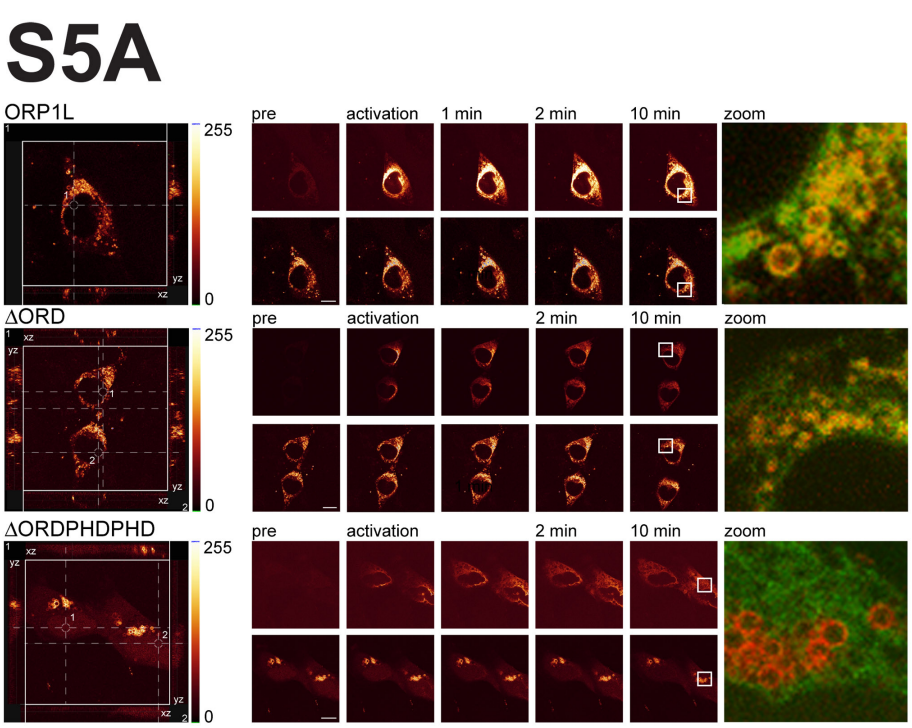


Figure S5. ORP1L mediated recruitment VAP-A from the ER and the release of p150^{Glued} from RILP

Figure S5A. ORP1L recruits VAP-A from the ER.

PA-GFP tagged VAP-A in mRFP-ΔORDPHDPHD, -ΔORD or -ORP1L expressing MelJuSo cells was photoactivated with a 405nm light to follow transport of ER located PA-GFP/VAP-A to late endosomes by time-lapse microscopy. Firstly, a z-stack of cells was made to identify a location for selective photoactivation of the ER pool of VAP-A. Left panel shows an x-y, x-z and y-z projection through the site of photoactivation (the 405nm laser spot position shown as a circle). Cells were followed by time-lapse confocal microscopy and various snapshots of the mRFP and GFP channels, prior and post-photoactivation of PA-GFP/VAP-A, are shown. Images presented in glow-over/under mode to represent different fluorescent intensities. Right panel is a zoom-in on late endosomes (indicated by the box) and merge of the mRFP and GFP channel. n>10 for each condition. Scale bars, 10µm. Movies are shown in Supplemental M1-3.

Figure S5B. VAP-A recruitment by ΔORD and release of p150^{Glued} from RILP. MelJuSo cells were transfected with GFP-RILP, mRFP-ORP1L constructs (as indicated) and HA-tagged VAP-A before fixation and staining with anti-HA and anti-p150^{Glued} antibodies before 4-color confocal microscopy. The box in the images indicates the zoom-in region shown in overlay colors as the fourth panel. The right panel shows p150^{Glued}. ΔORD recruits VAP-A and excludes p150^{Glued} from RILP resulting in scattered vesicles.

S6

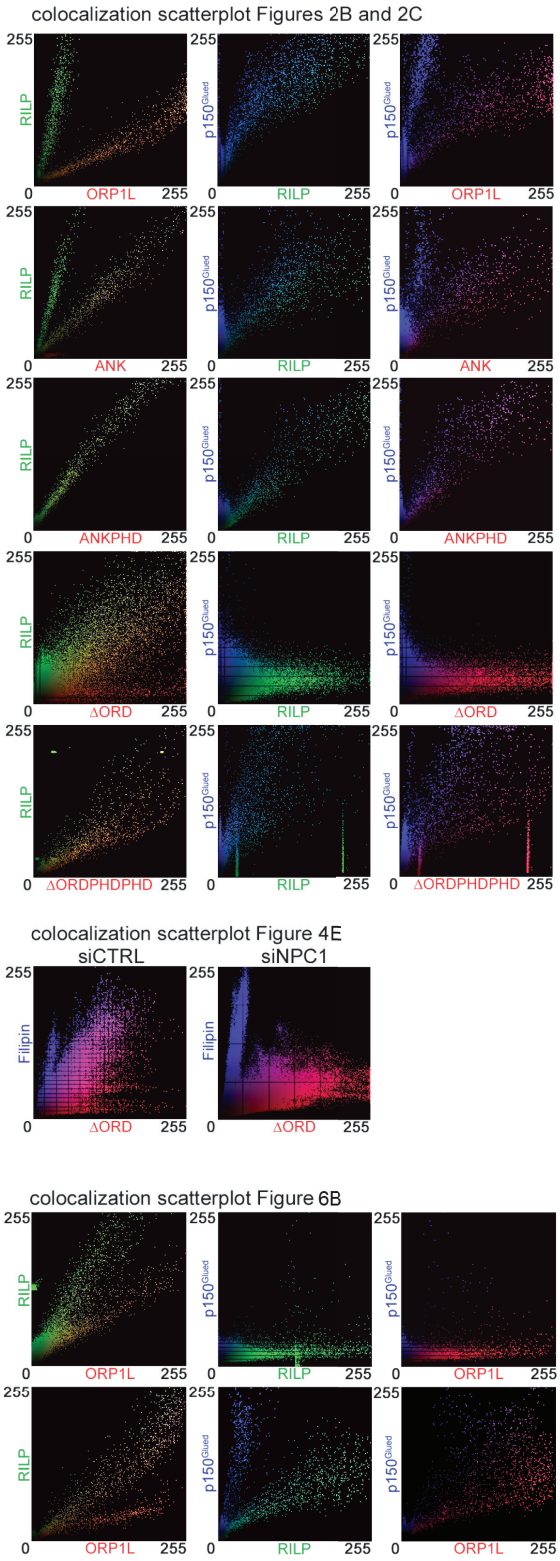


Figure S6. 2D-pixel analyses for co-localization of markers.

The confocal microscopy images shown in Figure 2BC, 4E and 6B were analyzed pixel-by-pixel for co-localization (intensity correlation analysis) of the markers indicated using Image J software, with WCIF plug-ins (http://www.uhnresearch.ca/facilities/wcif/imagej/). Proteins analyzed are shown along the X- and Y-axis of the scatterplot in the color of analysis. Co-localization is indicated by a correlation in the X-Y axis.

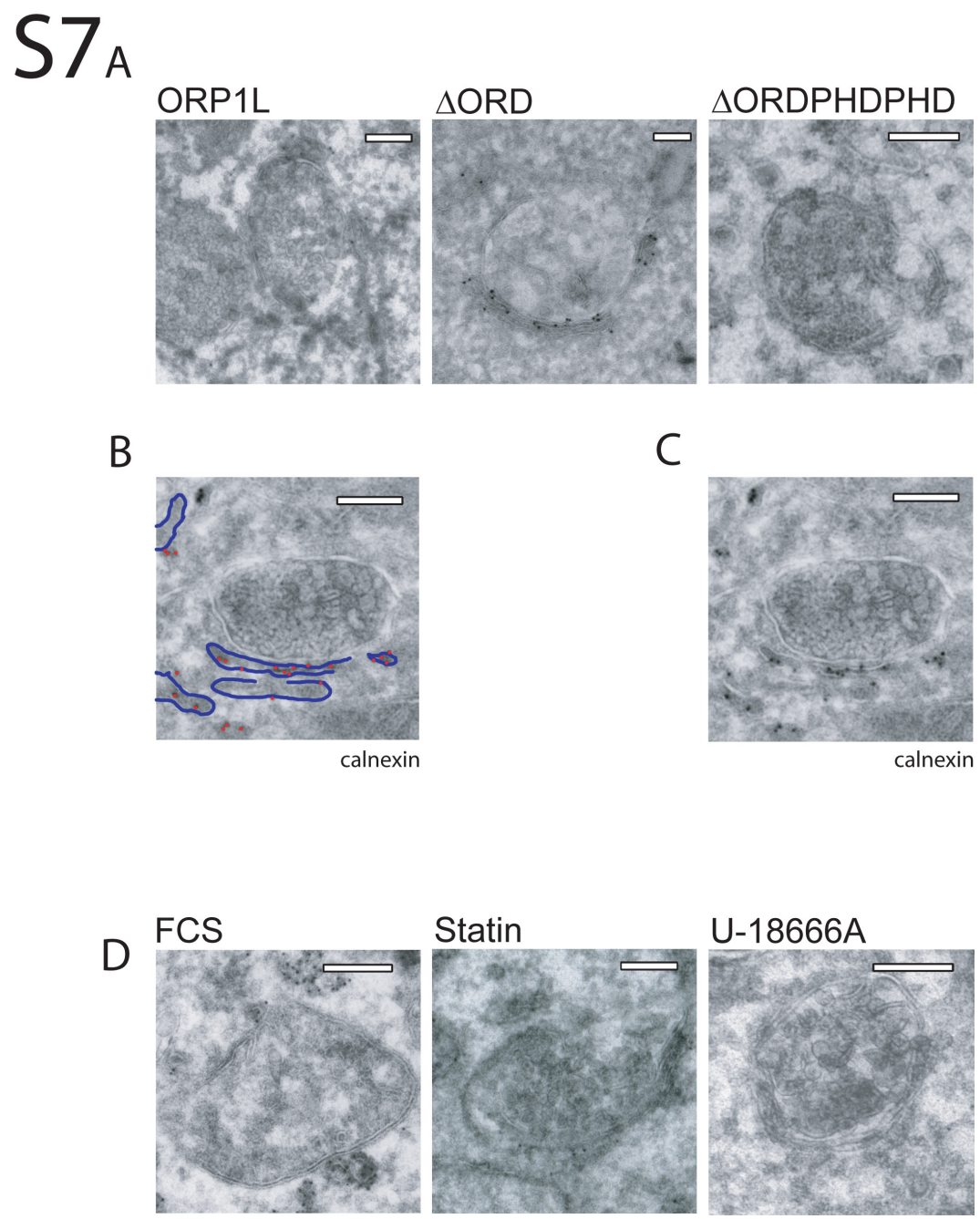
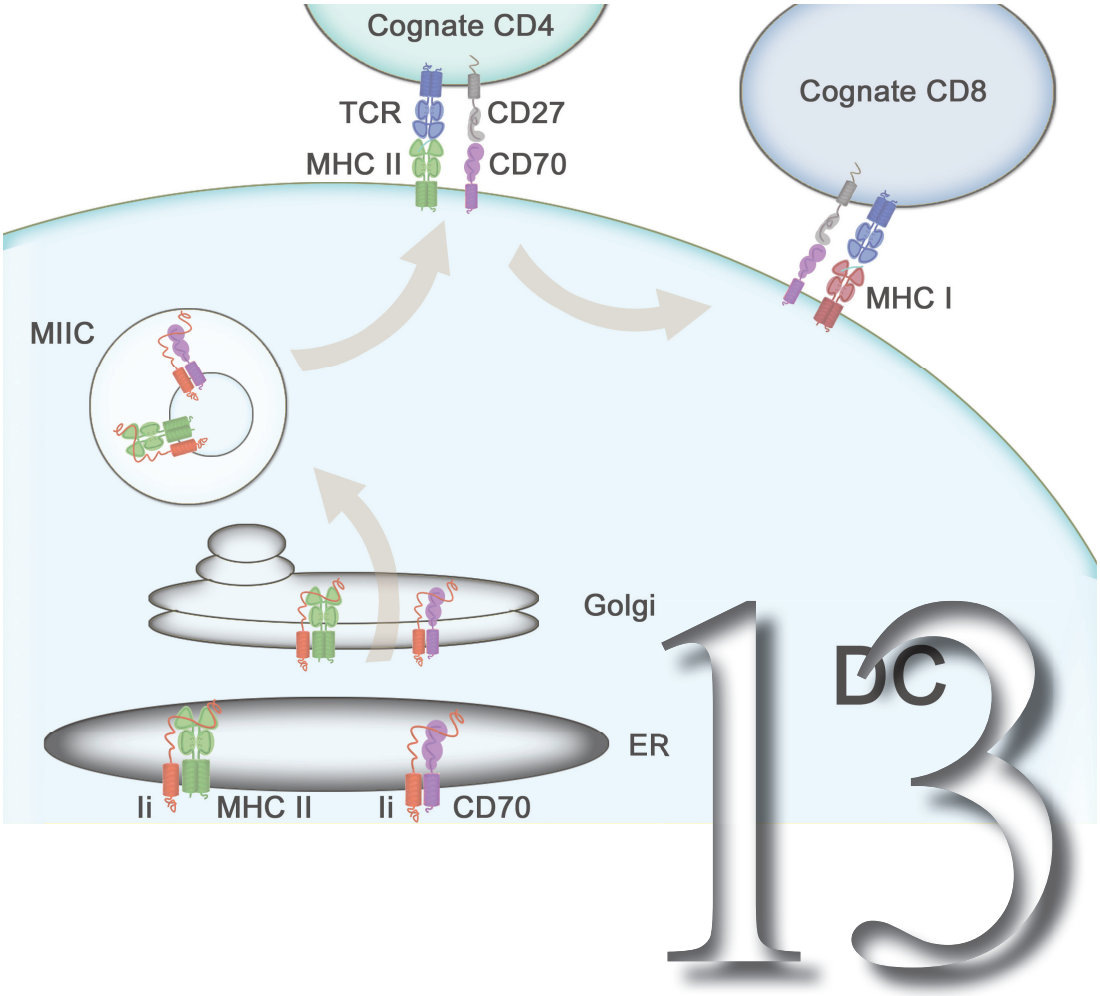


Figure S7. Cholesterol, the ER and multivesicular bodies, as visualized by immuno electronmicroscopy.

(**A**) Electronmicrographs of multivesicular bodies in MelJuSo cells expressing HA-VAP and different variants of GFP-ORP1L, as indicated. Cells were fixed and cryosections stained with anti-HA antibodies detected with 15 nm gold particles. These images correspond to Figure 6C. Bar: 200 nm.
(**B**) Electronmicrographs of multivesicular bodies in MelJuSo cells expressing GFP-ΔORD. Cryosections were labelled with anti-calnexin antibodies detected by 15 nm gold particles. The gold particles are highlighted by red dots and the ER membrane by a blue line. Bar: 200 nm.
(**C**) Original electronmicrograph from multivesicular bodies in MelJuSo cells expressing GFP-ΔORD. Cryosections were labelled with anti-calnexin antibodies detected by 15 nm gold particles. Image corresponds to Figure S6B. Bar: 200 nm.
(**D**) Electronmicrographs of multivesicular bodies in HA-VAP and GFP-ORP1L expressing MelJuSo cells exposed to different cholesterol manipulating conditions, as indicated. Cells were fixed and stained with anti-HA antibodies marked by 15 nm gold particles. These images correspond to Figure 6E. Bar: 200 nm.

Invariant chain controls CD70 transport in dendritic cells and thereby regulates CD8+ T cell priming

Submitted



Invariant chain controls CD70 transport in dendritic cells and thereby regulates CD8+ T cell priming

Anna M. Keller[a§], Wilbert Zwart[b], Gerda van der Horst[a], Victor Peperzak[a], Evert de Vries[a], Hans Janssen[b], Shalin H. Naik[a], Jacques Neefjes[b] and Jannie Borst[a]

Abstract
CD70 is a Tumor Necrosis Factor family member that is expressed by mature dendritic cells and provides T cell costimulatory signals. Strict regulation of CD70 cell surface expression is essential to maintain T cell homeostasis and immunological tolerance. We report here that the Invariant chain (Ii, CD74), a well-known chaperone for major histocompatibility complex (MHC) class II molecules, regulates transport and function of CD70. In cells lacking the MHC class II presentation pathway, CD70 was transported to the plasma membrane, but co-expression of Ii directed CD70 towards late endosomes/lysosomes. In cells with features of professional antigen presenting cells, CD70 and endogenous Ii were co-transported to the late endosomal/lysosomal MHC class II compartment. Fluorescence resonance energy transfer studies documented a physical interaction between the two molecules. In activated dendritic cells, Ii controlled the kinetics and level of CD70 cell surface expression and thereby dictated the extent of CD8+ T cell clonal expansion. We propose that directional and temporal control of CD70 cell surface expression by Ii serves to set the threshold for CD8+ T cell priming.

Introduction

Dendritic cells (DCs) are specialized antigen presenting cells that can initiate clonal expansion of antigen-specific T cells and drive their differentiation into effector cells. To become optimal elements for such T cell priming, DCs need to mature and acquire expression of costimulatory molecules. These include CD70, a Tumor Necrosis Factor (TNF) family member that is the ligand of the T-cell costimulatory receptor CD27 (Goodwin *et al*., 1993; Tesselaar *et al*., 1997). CD70 expression in DCs is induced in response to Toll-like receptor- and/or CD40 stimulation (Sanchez *et al*., 2007). In vivo, such stimulation takes place when a DC has encountered a pathogen and contacted a CD40 ligand-expressing CD4+ T cell. These interactions condition the DC for optimal CD8+ T cell priming by the collective induction of CD80, CD86 and CD70 (Bullock and Yagita, 2005). These costimulatory ligands bind to CD28 and CD27 respectively, which make non-redundant contributions to clonal expansion of CD8+ T cells (Hendriks *et al*., 2003). CD27-CD70 costimulation not only impacts on the CD8+ T cell response, but also promotes CD4+ T cell clonal expansion and the development of CD8+ T cell helper- and memory programming functions in CD4+ T cells (Soares *et al*., 2007; Xiao *et al*., 2008).

After acute infection, CD70 cell surface expression is low, highly transient and most pronounced on DCs and Bcells in lymphoid organs and at the site of infection (Hendriks *et al*., 2005). Strict control of CD70 cell surface expression is required to maintain T- and B cell homeostasis, as demonstrated by the phenotype of transgenic mice with constitutive CD70 expression on B cells or DCs (Arens *et al*., 2001; Keller *et al*., 2008). Deliberate chronic stimulation of CD27 in these mice results in seemingly spontaneous conversion of naive T cells into effector cells, which culminates in a lethal combined T- and B cell immunodeficiency (Tesselaar *et al*., 2003). Control of CD70 cell surface expression apparently ensures that the pro-survival input through CD27 signaling is limited and occurs specifically upon immune activation. Deliberate transgenic expression of CD70 on immature DCs suffices to convert CD8+ T cell tolerance into immunity, which further underlines the importance of strict regulation of CD70 expression (Keller *et al*., 2008).

Divisions of Immunology[a] and Cell Biology[b],
The Netherlands Cancer Institute, 1066 CX Amsterdam, The Netherlands
Running title: Invariant chain controls CD70 transportClassification: Biological sciences
Correspondence: Jannie Borst, Division of Immunology, The Netherlands Cancer Institute, Plesmanlaan 121, 1066 CX Amsterdam, The Netherlands; e-mail: j.borst@nki.nl, telephone: +31-20 5122056; fax: +31-20-5122057
[§]Current address: London Research Institute, Cancer Research UK, London WC2A 3PX, UK

Abbreviations: a.a., amino acids; APCs, antigen presenting cells; BFA, brefeldin A; BM, bone marrow; CFSE, carboxyfluorescein succinimidyl ester; c, conventional; CLSM, confocal laser scanning microscopy; CLQ, chloroquine; CIITA, Class II transactivator; DC, dendritic cell; E_D, donor FRET efficiency; EGFP, enhanced green fluorescent protein; EM, electron microscopy; ER, endoplasmic reticulum; Flt3L, fms-like tyrosine kinase 3 ligand; FRET, fluorescence resonance energy transfer; h, human; Ii, invariant chain; L, ligand; LPS, lipopolysaccharide; m, murine; MHC, major histocompatibility complex; MIIC, MHC class II compartment; mRFP, monomeric red fluorescent protein; OVA, ovalbumin; PI, propidium iodide; TCR, T cell antigen receptor; TLR, Toll-like receptor; TNF, tumor necrosis factor; WT, wild-type.

We have previously shown that in DCs, CD70 cell surface expression is not only regulated by selective transcription of CD70 mRNA, but also by specific intracellular routing of the CD70 protein (Keller *et al*., 2007). In maturing DCs, newly synthesized CD70 was found to be transported to late endosomal/lysosomal MHC class II-containing compartments known as MIICs (Neefjes *et al*., 1990; Peters *et al*., 1991). These are the compartments in which MHC class II is loaded with antigenic peptides derived from extracellular sources. MIICs are essentially secretory lysosomes that upon contact between a DC and an antigen-specific T cell are polarized towards the contact site and fuse with the plasma membrane (Boes *et al*., 2002; Kleijmeer *et al*., 2001). This process allows for coordinated recruitment and simultaneous delivery of CD70 and MHC class II molecules to the immunological synapse with cognate CD4+ T cells (Keller *et al*., 2007).

We report here that the specific routing of CD70 to the MIIC is dictated by the Invariant chain (Ii, CD74). Ii is widely known as the obligate chaperone of MHC Class II molecules (Cresswell, 1994). Ii pairs with MHC class II in the endoplasmic reticulum (ER) and directs it to the MIIC by virtue of unique sorting signals in its cytoplasmic tail (Lotteau *et al*., 1990; Odorizzi *et al*., 1994). By determining the transport of MHC class II molecules, Ii directs both their loading with antigenic peptides and their delivery to T cells. Since MHC class II presents peptides exclusively to CD4+ T cells, the function of Ii has thus far only been examined in the context of CD4+ T cell responses (Bikoff *et al*., 1993; Viville *et al*., 1993; Wong and Rudensky, 1996). The novelty of our present work lies in three aspects: 1) We define a novel chaperone function for Ii in showing that it escorts the TNF family member CD70 to MIICs. 2) We show that by directing CD70 to MIICs, Ii controls kinetics and levels of CD70 cell surface expression in maturing DCs. 3) We demonstrate that this is the mechanism by which Ii controls CD8+ T cell clonal expansion. The global concept into which these data fit is that Ii serves to tightly regulate cell surface expression of CD70, which sets the threshold for CD8+ T cell activation and is thus crucial for the prevention of unwarranted T cell responses. Moreover, we propose that directional and temporal control of CD70 cell surface expression by Ii serves to coordinate CD4+ T cell help for the CD8+ T cell response.

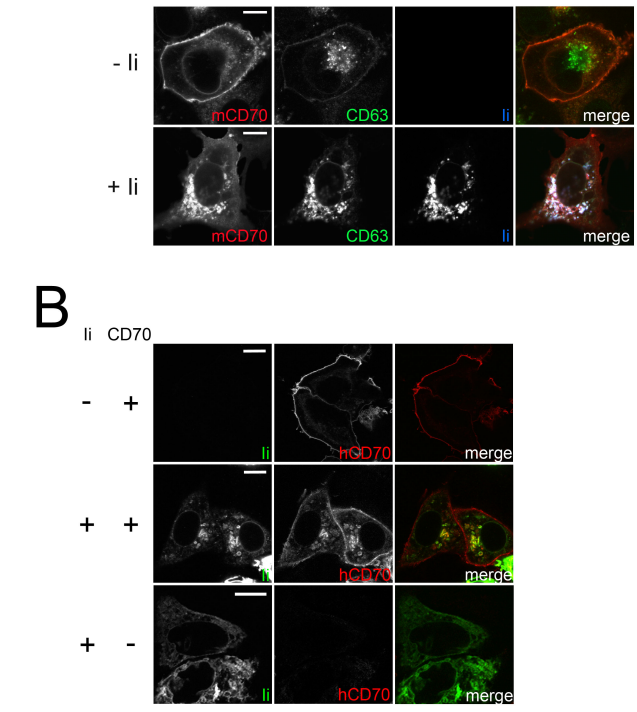


Figure 1. Localization of CD70 in HeLa cells.

(**A**) Murine (m)CD70. HeLa cells were transfected to express mCD70 without (top panel) or with (bottom panel) Ii, fixed, permeabilized and stained sequentially with anti-CD63-FITC (green), rat anti-mCD70 (FR70) and goat anti-rat Ig-Alexa 568 (red), mouse anti-human Ii (Bu45) and goat anti-mouse Ig-Alexa 633 (far red, shown as blue) and examined by CLSM. The merged image shows signals from all three channels and reveals co-localization of mCD70, CD63 and Ii as a white color. The scale bars equal 10 µm. Images are representative of 80%-93% of mCD70+ cells imaged in two independent experiments (n>30). (**B**) Human (h)CD70. HeLa cells were transfected to express hCD70 alone (top panel), CD70 and Ii (middle panel), or Ii alone (bottom panel), fixed and stained with mouse anti-human Ii (Bu45) and goat anti-mouse Ig-Alexa 488 (green), followed by mouse anti-hCD70 (2F2) and goat anti-mouse Ig-Texas Red (red) and examined by CLSM. The merged image shows signals from the two channels and reveals co-localization of hCD70 and Ii as a yellow color. The scale bars equal 10 µm. Images are representative of data obtained in two independent experiments (n>20).

Results

Ii directs CD70 to late endosomes/lysosomes in cells that lack the MHC class II presentation machinery

We previously observed that CD70 travels by default to the plasma membrane in HeLa cervix carcinoma cells that do not express MHC class II and its associated presentation machinery. However, upon CIITA co-expression in these cells, CD70 was directed towards late endosomes/lysosomes (Keller *et al*., 2007). CIITA directs the expression of a multitude of genes that are characteristic for professional antigen presenting cells (Chang and Flavell, 1995). One of these is Ii, which was tested for its potential involvement in CD70 transport. Upon expression of murine (m)CD70 in HeLa cells, the great majority of molecules resided at the plasma membrane and did not colocalize with the late endosomal/lysosomal marker CD63 (Peters *et al*, 1991), as demonstrated by confocal laser scanning microscopy (CLSM) (Fig. 1A). In contrast, when mCD70 was co-expressed with Ii, a major proportion of mCD70 molecules localized, together with Ii, in intracellular compartments that labeled for CD63 (Fig. 1A). Similar results were obtained when Ii was co-expressed with human (h)CD70 (Fig. 1B). Moreover, in the same HeLa cells, Ii stayed in the endoplasmic reticulum (ER) when it was expressed in absence of CD70 (Fig. 1B). This is in accordance with its described ER retention in absence of MHC class II (Marks *et al*., 1990). From these findings, we conclude that Ii redirects CD70 from the default transport route and targets it to late endosomes/lysosomes instead, analogous to what it does for MHC class II. Moreover, CD70 can alleviate ER retention of Ii in absence of MHC class II.

CD70 and Ii co-localize in MIIC in cells with the characteristics of professional antigen presenting cells

Next, the human melanoma cell line Mel JuSo was employed as model cell line because it expresses all components of the MHC class II antigen presentation pathway (Pieters *et al*., 1991). In Mel Juso cells, a fusion protein of mCD70 and monomeric Red Fluorescent Protein (mRFP) co-localized with endogenous Ii in intracellular vesicles that labeled for CD63 (Fig. 2A). Untagged hCD70 similarly co-localized with Ii (Supplementary Fig. S1A). To examine the subcellular localization of CD70 and Ii in more detail, immuno-electron microscopy (EM) was performed on Mel Juso cells stably expressing untagged mCD70. Immuno-EM of cryo-sections revealed the characteristic morphology of MIICs, which is essentially that of a multivesicular body with a delimiting outer membrane enveloping a multitude of internal vesicles (Peters *et al*., 1991). CD70 co-localized with Ii in MIICs and also resided at the plasma membrane (Fig. 2B). Organelles and gold grains are indicated for further clarification in Supplementary Fig. S1B. Staining was specific in that nucleus or mitochondria were not labeled for either CD70 or Ii (Fig. 2B and data not shown). CD70 was also detected in the Golgi apparatus (results not shown), in agreement with earlier observations (Keller *et al*., 2007). We conclude that CD70, when expressed in cells with the characteristics of professional antigen presenting cells, co-localizes with Ii in MIICs.

CD70 and Ii physically interact

To examine a possible direct interaction between Ii and CD70, we performed FRET measurements in living cells. FRET is the energy transfer from

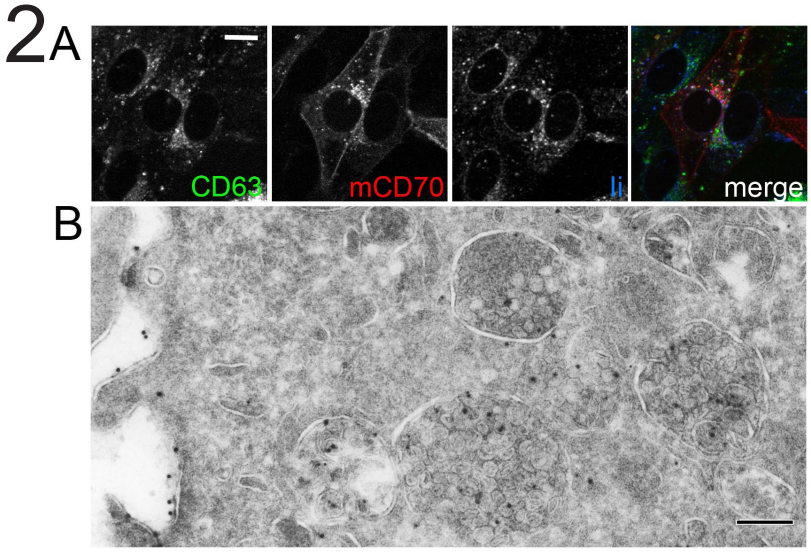


Figure 2. Colocalization of mCD70, Ii and CD63 in Mel JuSo cells.

(**A**) Mel JuSo cells were transfected to express mCD70-mRFP (red), fixed, permeabilized and stained sequentially with mouse anti-human Ii (Bu45) and goat anti-mouse Ig-Alexa 647 (far red, shown as blue) and with anti-CD63-FITC (green) and examined by CLSM. The scale bar equals 10 µm. Images are representative of 2 independent experiments (n>30).

(**B**) Mel JuSo cells, stably expressing mCD70 were fixed and processed for immuno-EM. Sections were stained for mCD70 with FR70 mAb (large gold) and for endogenous human Ii with ICN1 polyclonal (small gold). The scale bar equals 200 nm.

a donor fluorophore to a suitable acceptor fluorophore, which can only be detected when the fluorophores are within 80 Å from each other (Forster *et al*., 1948). Any significant FRET signal is therefore indicative of a physical interaction. Enhanced green fluorescent protein (EGFP) was fused to Ii as donor and mRFP to CD70 as acceptor fluorophore and these chimeric proteins were expressed in HeLa cells. By this approach, we have previously demonstrated physical interactions between HLA-DR and HLA-DM (Zwart *et al*., 2005). To control for spectral overlap between the fluorophores, the test HeLa cells were cultured together with control cells expressing Histone 2B (H2B)-EGFP or H2B-mRFP only (Fig. 3A, panels I, II) FRET between Ii-EGFP and CD70-mRFP was detected by CLSM as the sensitized emission of mRFP following energy transfer from EGFP (van Rheenen *et al*., 2004) (Fig. 3A, panel III). The sensitized emission images were corrected for spectral leak through of EGFP into the mRFP channel and indirect excitation of mRFP by the GFP-specific laser, using the independent H2B-fluorophore proteins, defining the remaining signal in the same sample as genuine FRET between Ii-EGFP and CD70-mRFP (Fig. 3A, panel IV). FRET was related to

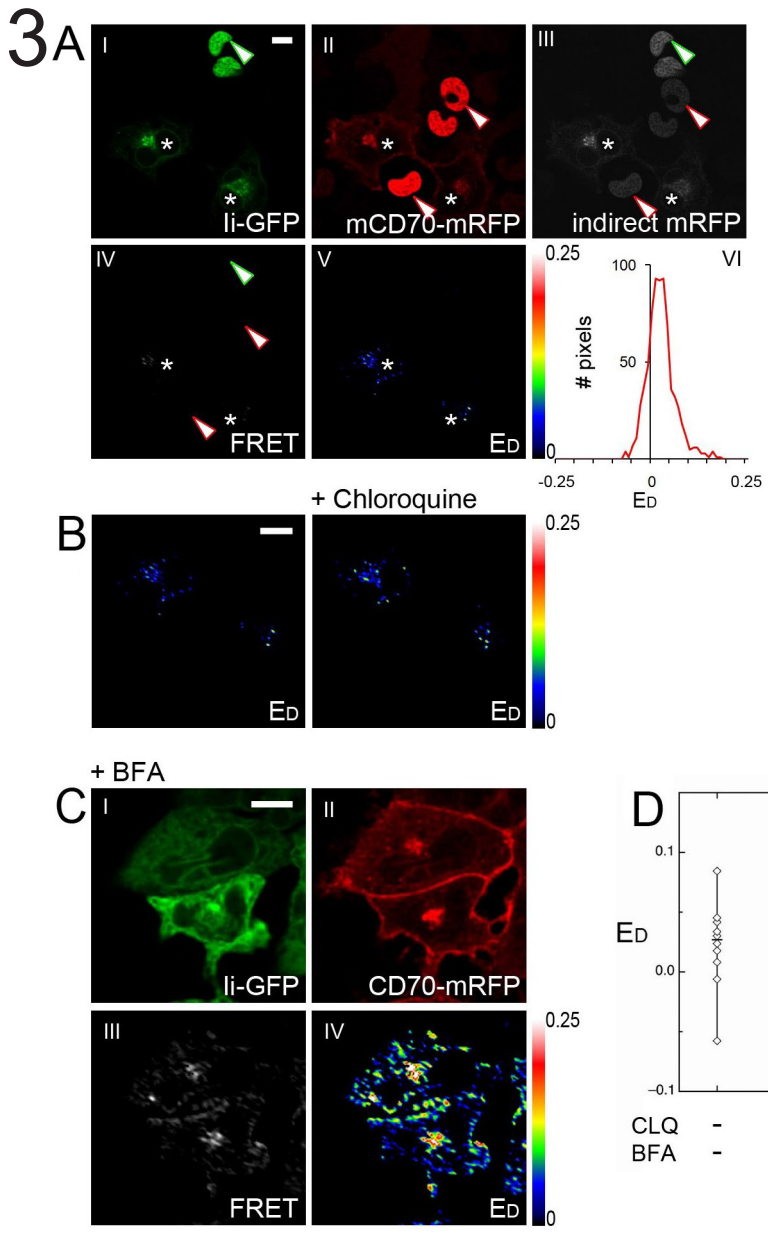


Figure 3. Physical interaction between CD70 and Ii.

(**A**) HeLa cells were transfected to co-express Ii-EGFP and mCD70-mRFP (asterisks). Control cells expressing either H2B-EGFP or H2B-mRFP were mixed into the same culture (arrowheads). All panels represent the same sample, with Panel I showing Ii-EGFP and H2B-EGFP in the green channel, Panel II mCD70-mRFP and H2B-RFP in the red channel, Panel III the sensitized emission of mRFP following its activation by EGFP, Panel IV the corrected FRET signal beween Ii-EGFP and mCD70-mRFP, Panel V the calculated donor FRET efficiency (E_D) and Panel VI the E_D value of each pixel in a histogram. The false color look up table in panel V represents E_D values from 0 to 0.25, equaling 0-25% FRET efficiency. (**B**) Zoom-in on cells depicted in Fig. 3A, as delineated by the white frame in panel V. E_D is shown before and after treatment of the sample with chloroquine. (**C**) HeLa cells co-expressing Ii-EGFP and mCD70-mRFP were treated with BFA and incubated at 20°C. Panels depict the indicated signals from the same sample.

(**D**) E_D values from multiple samples in differentexperiments under conditions as in Fig. 3B and 3C, in which each data point represents one cell. BFA, brefeldin A; CLQ, chloroquine. Significant differences were determined with two-tailed Student's test (*p = 0.05).

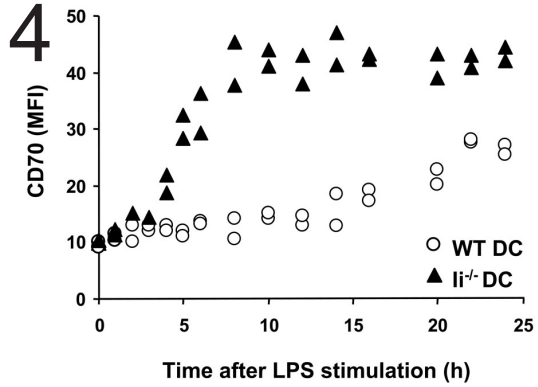


Figure 4. BM-derived, Flt3L generated WT and Ii-/- DCs were stimulated with LPS for the indicated time periods and CD70 cell surface expression was examined by flow cytometry. MFI (mean fluorescence intensity) of 10 equals background fluorescence, as determined by an Ig isotype control antibody. Data points represent values obtained in two independent experiments with pooled samples (n=2).

the total fluorescence emitted by the donor fluorophore to yield the donor FRET efficiency (E_D), which is the best reflection of intermolecular interaction by rendering the FRET signal donor-concentration independent (Fig. 3A, panel V). Panel VI shows the distribution of E_D values of the pixels in panel V. Mean FRET efficiency between CD70 and Ii was 2%. We neutralized MIIC by adding the lysosomotropic base chloroquine to cells while imaging (Zwart *et al*., 2005). This did not alter FRET efficiencies (Fig. 3B) and therefore excludes any effect of acidic pH in MIICs on fluorophore emission or FRET.

Ii binds MHC class II in the ER and escorts it subsequently through the Golgi apparatus to MIICs (Cresswell, 1994). We considered that Ii might similarly bind CD70 in the ER. To synchronize transport of such putative complexes, we treated cells with brefeldin A (BFA) to accumulate newly synthesized proteins in the ER (Klausner *et al*., 1992). Subsequently, BFA was removed and cells were cultured at 20°C. This allows protein egress from ER to the Golgi, but not further due to inhibited membrane trafficking at this temperature (de Graaf *et al*., 2004). Under these conditions, FRET efficiency between Ii-EGFP and CD70-mRFP in the Golgi area was 8% (Fig. 3C,D). Taken together, the FRET measurements indicated that Ii physically interacts with CD70 and thus transports it to MIICs.

Ii determines the kinetics and extent of CD70 cell surface deposition in primary DCs

Next, we extended our observations from model cell lines to primary DCs. As discussed, cDCs acquire CD70 protein expression upon their maturation in response to CD40 and/or TLR stimulation (Sanchez *et al*., 2007). To determine the impact of Ii on CD70 membrane expression, we compared DCs from wild-type (WT) and Ii-deficient (Ii-/-) mice (Viville *et al*., 1993). Immature DCs, generated from murine bone marrow (BM), were activated with the TLR ligand lipopolysaccharide (LPS) and CD70 cell surface expression was examined by flow cytometry throughout the next 24 h. The kinetics and extent of CD70 cell surface deposition following DC activation differed greatly between WT and Ii-/- DCs. In Ii-/- DCs, CD70 was found at the cell surface at earlier time points than in WT DCs (Fig. 4). In addition, CD70 reached a higher level of steady-state cell surface expression in matured Ii-/- DCs than in WT DCs (Fig. 4). Activated MHC class II-/- DCs expressed similar levels of CD70 at the cell surface as WT DCs (data not shown), indicating that MHC class II did not regulate CD70 transport.

Ii regulates subcellular distribution of CD70 in DCs, independent of the presence of MHC class II

We have previously found that colocalization of CD70 and MHC class II could best be appreciated in recently activated DCs, in which CD70 is newly synthesized (Keller *et al*., 2007). To determine the subcellular localization of CD70 in WT versus Ii-/- DCs, we therefore used DCs stimulated with LPS for 4 h. They were simultaneously loaded with ovalbumin (OVA) protein to allow for antigen presentation to OVA-specific OT-II CD4+ T cells. OT-II T cells and

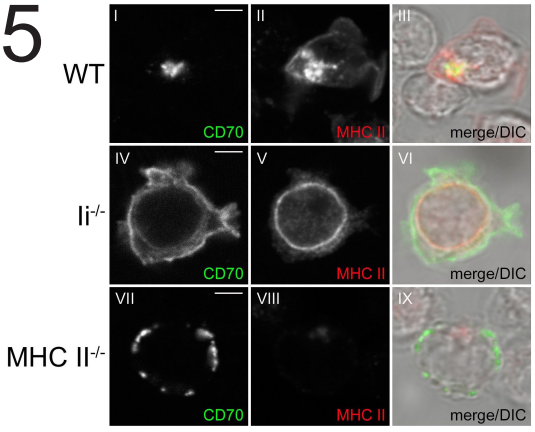


Figure 5. Transport of CD70 in primary DCs.

BM DCs from WT (I-III), Ii-/- (IV-VI) or MHC class II-/- (VII-IX) mice were loaded with OVA protein, matured with LPS and allowed to form conjugates with naive OT-II CD4+ T cells for 1 h. Cells were fixed, permeabilized and stained with rat anti-mCD70 (FR70) and goat anti-rat Ig-Alexa 488 (green), followed by rabbit anti-MHC class II (JV2) and goat anti-rabbit Ig-Alexa 568 (red). Images are representative of 70-76% of DCs analyzed in two independent experiments (n>30). DIC = differential interference contrast image. The scale bars equal 5 µm.

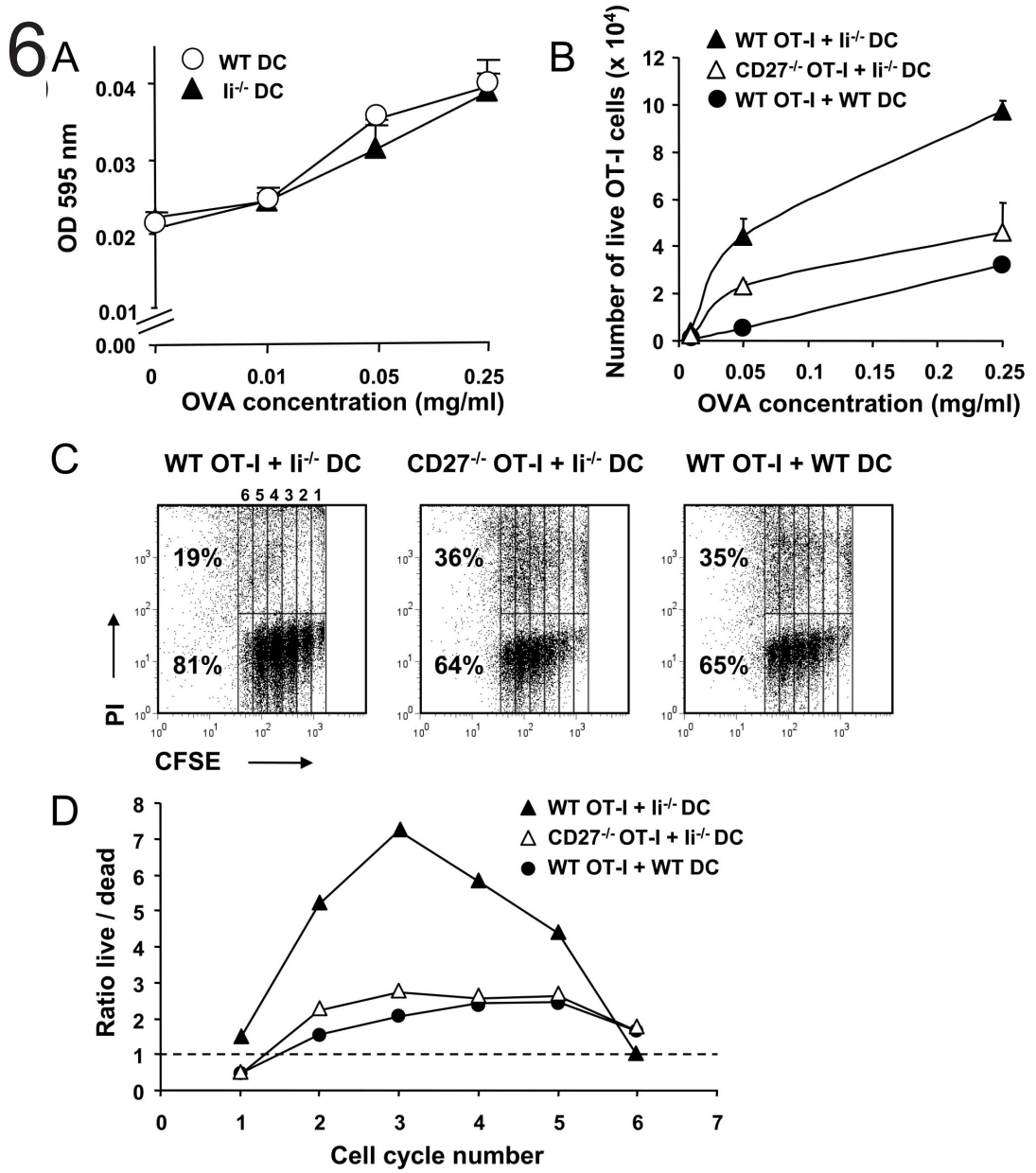


Figure 6. Impact of Ii-guided CD70 transport in CD8+ DCs on CD8+ T cell priming.

(**A**) Antigen presentation assay. CD8+ splenic DCs from WT or Ii-/- mice were loaded with OVA protein, matured with LPS and cocultured with B3Z T cells that in response to TCR stimulation by the H-2Kb/OVA257-264 complex expresses β galactosidase, which is quantified as the OD595 of its CPRG substrate. Shown are the average OD values of triplicate wells (+ SD). The experiment is representative of three. (B,C,D). OVA loaded, LPS matured CD8+ splenic DCs from WT or Ii-/- mice were co-cultured for 65 h with CFSE labeled WT or CD27-/- OT-I T cells.
(**B**) Total numbers of PI excluding, live OT-I T cells after culture with DCs loaded with different OVA concentrations. Data points represent means of duplicate measurements; error bars indicate range of values obtained.
(**C**) Flow cytometric analysis of CFSE versus PI staining of OT-I T cells cultured with DCs loaded with 0.25 mg/ml OVA. The percentage of dead cells (PI+) and live cells (PI-) of the total pool of divided T cells (diluted CFSE) is indicated. Numbered gates denote consecutive cell division cycles.
(**D**) Ratio (based on means of duplicate measurements) of live versus dead cells in the indicated division cycles, as defined in (C). The results shown are representative of three independent experiments.

DCs were co-cultured for 1 h, which allowed for synapse formation in case of WT DCs. In most OT-II T cell conjugates with WT DCs, MHC class II and CD70 co-localized in internal vesicles that were polarized towards the contact point with the T cell (Fig. 5, panels I-III). In case of Ii-/- DCs, the subcellular localization of both CD70 and MHC class II were dramatically altered. MHC class II located to the nuclear envelope and surrounding network that represents the ER and was absent from MIICs and the plasma membrane (Fig. 5, panel V). This concurs with the described role of Ii in transport of MHC class II out of the ER (Marks *et al*., 1990). In contrast to MHC class II, CD70 had a pronounced plasma membrane localization in a large proportion of Ii-/- DC (Fig. 5, panel IV). This indicates that also in primary DCs, Ii is required to re-direct CD70 from the default transport route to MIICs. No conjugates between CD4+ OT-II T cells and Ii-/- DC were found (Fig. 5, panel VI), in accordance with the dramatic ER retention of MHC class II observed and the reported decreased cell surface deposition of MHC class II/peptide complexes in Ii-/- antigen presenting cells (Viville *et al*., 1993; Bikoff *et al*., 1993). Interestingly, in MHC class II-/- DCs that still express Ii (Cosgrove *et al*., 1991), CD70 accumulated in vesicles (Fig. 5, panel VII) that were MIICs according to CD63

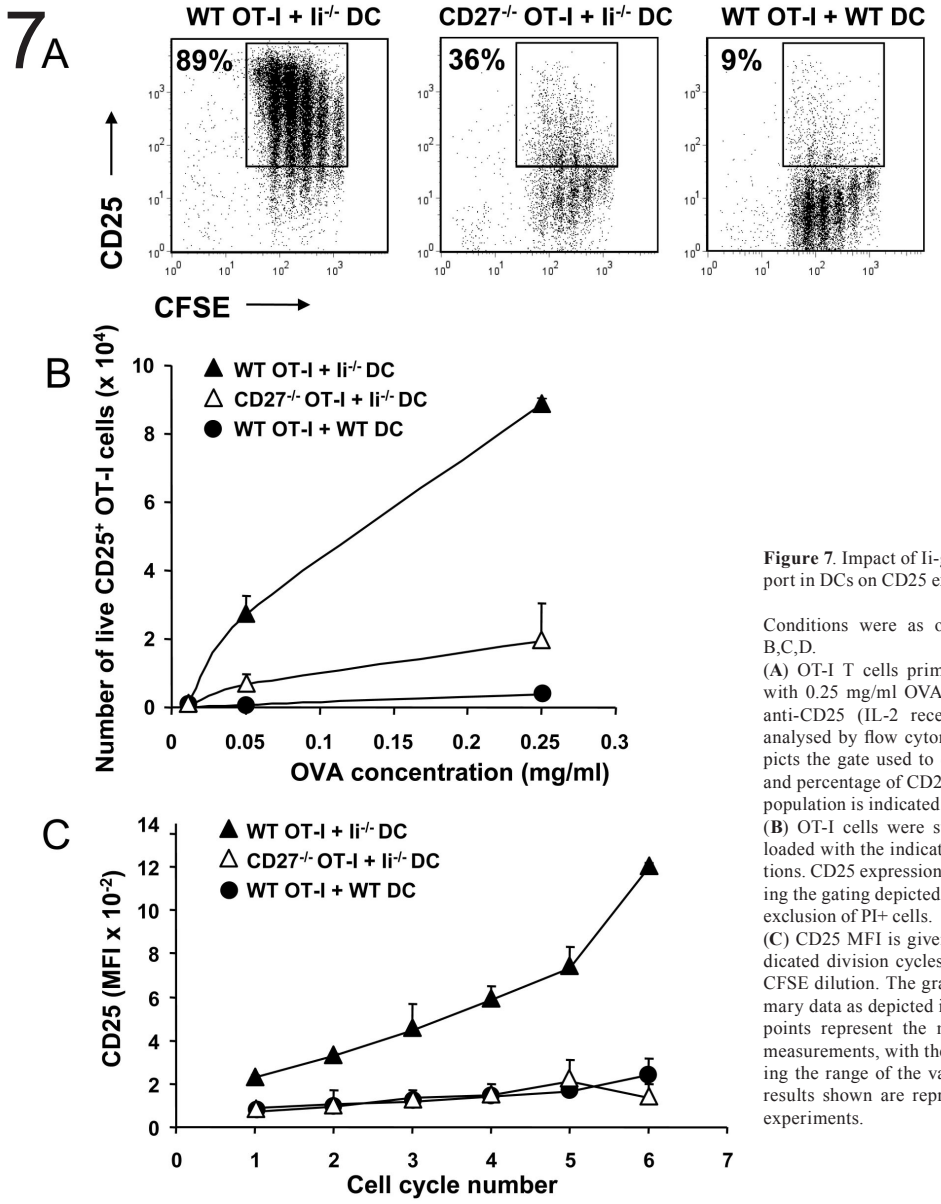


Figure 7. Impact of Ii-guided CD70 transport in DCs on CD25 expression.

Conditions were as outlined for Fig. 6 B,C,D.
(**A**) OT-I T cells primed by DCs loaded with 0.25 mg/ml OVA were stained with anti-CD25 (IL-2 receptor α) mAb and analysed by flow cytometry. The box depicts the gate used to define CD25+ cells and percentage of CD25+ cells in the total population is indicated.
(**B**) OT-I cells were stimulated with DC loaded with the indicated OVA concentrations. CD25 expression was monitored, using the gating depicted in Fig. 7A and with exclusion of PI+ cells.
(**C**) CD25 MFI is given of cells in the indicated division cycles, as determined by CFSE dilution. The graph is based on primary data as depicted in Fig. 7A. The data points represent the means of duplicate measurements, with the error bars indicating the range of the values obtained. The results shown are representative of three experiments.

content (results not shown). These vesicles remained evenly distributed throughout the cytoplasm in the presence of OT-II CD4+ T cells (Fig. 5, panel IX), consistent with a lack of synapse formation in the absence of MHC class II. We conclude that in primary DC, Ii transports CD70 to MIICs, also when MHC class II is not present.

Ii-regulated CD70 transport determines the efficiency of CD8+ T cell cross-priming

Having found that Ii determines the kinetics and extent of CD70 cell surface expression in maturing DCs, we examined the impact of Ii on CD8+ T cell priming. For this purpose, we used CD8+ DCs, which are most efficient at cross-presentation (Heath *et al*., 2004). To examine whether WT and Ii-/- LPS-matured CD8+ DCs had a similar capacity to cross-present OVA protein, we used a read out with B3Z T cells that express β-galactosidase in response to TCR triggering by the H-2Kb/OVA257-264 complex (Sanderson and Shastri, 1994). The extent of TCR stimulation was dependent on the concentration of OVA protein added to the DCs, indicating specific cross-presentation (Fig. 6A). There was no difference between the capacity of WT and Ii-/- DCs to elicit a response from B3Z cells. We conclude that Ii-deficiency did not affect the ability of CD8+ DCs to generate the OVA257-264 peptide from intact OVA protein and to present it in MHC class I.

To determine the capacity of these DCs to prime a CD8+ T cell response, they were matured, loaded with OVA protein and cultured with CD8+ OT-I T cells, which are specific for the H-2Kb/OVA257-264 complex. WT and CD27-/- OT-I T cells were used, to determine the contribution of CD27-CD70 interaction to the CD8+ T cell response. After 2.5 days, cultures were stained with propidium iodide (PI) and viable OT-I T cells were enumerated (Fig. 6B). At all concentrations of OVA antigen used, total numbers of live WT OT-I T cells were significantly higher after priming by Ii-/- DCs as compared to WT DCs. The increase in live cell numbers largely depended on CD27-proficiency of OT-I T cells, indicating that it was driven by CD27-CD70 interactions (Fig. 6B).

The OT-I T cells had been labeled with carboxyfluorescein succinimidyl ester (CFSE) to determine the ratio of live versus dead cells per cell division. Overall, a lower percentage of WT OT-I T cells died upon priming by Ii-/- DCs as compared to WT DCs. This effect was completely reversed when OT-I cells lacked CD27 (Fig. 6C). Plotting the ratio of live versus dead cells in each division cycle revealed that Ii expression by DCs did not affect cell cycle progression of OT-I T cells, but promoted their survival in each successive division (Fig. 6D). Improved OT-I T cell survival was fully dependent on CD27, indicating that it was determined by the enhanced CD70 expression on Ii-/- DCs (Fig. 6D).

Since the IL-2 receptor has been implicated in driving survival of activated T cells (D'Souza and Lefrancois, 2003), we examined the expression of CD25 (IL-2 receptor α chain) on OT-I T cells in the cultures. Ii-/- DCs induced CD25 expression on a dramatically higher percentage of WT OT-I T cells than did WT DCs (Fig. 7A). CD25 up-regulation was largely CD27-dependent and reflected at a range of OVA concentrations (Fig. 7B). Levels of CD25 increased with each successive cycle in a CD27-CD70 dependent manner (Fig. 7C). These data demonstrate that in absence of Ii, surface levels of CD70 on DCs increase, which promotes CD27-driven clonal expansion of primed CD8+ T cells. CD27-CD70 interactions induce and amplify CD25 expression and concomitantly support T cell survival throughout successive division cycles.

Discussion

The magnitude and nature of costimulation provided by professional APCs determines the fate of primed T cells. We have shown previously that in DCs, delivery of CD70 to the immunological synapse with CD4+ T cells is coordinated with MHC class II antigen presentation by means of their shared, regulated transport via MIICs (Keller *et al*., 2007). Here, we reveal that CD70 is guided to MIICs by Ii, the chaperone protein known to escort MHC class II molecules to the same late endosomal/lysosomal compartment.

The chaperone function of Ii for MHC class II is well documented and many details about the interaction between these molecules are known (Cresswell, 1994; Jasanoff *et al*., 1998). Ii contains an arginine-based ER retention motif in its cytoplasmic tail and does not easily exit the ER unless this motif has been covered by pairing with other proteins (Michelsen *et al*., 2005). Upon import into the ER, Ii forms a homotrimer and interacts with three MHC class II α/β heterodimers to form a nonameric complex, which can be transported to the Golgi. Di-leucine-based motifs in the cytoplasmic tail of Ii subsequently direct the complex to MIICs (Cresswell, 1994; Michelsen *et al*., 2005). This may occur directly from the trans-Golgi network, but can also involve routing via the plasma membrane (McCormick *et al*., 2005). Ii also performs such a chaperone function for CD1d (Kang and Cresswell, 2002; Jayawardena-Wolf *et al*., 2001) and - as recently documented - for the neonatal Fcg receptor (Ye *et al*., 2008), which are both closely related to MHC molecules. The chaperone function of Ii for CD70 is unusual in this context, since the overall structure of

TNF family members is very different from that of MHC-like molecules (Banner *et al*., 1993; Locksley *et al*., 2001).

Our FRET data indicate that CD70 and Ii interact directly. The overall structural homology between CD70 and Ii may facilitate their interaction. Both are type II transmembrane glycoproteins, with a cytoplasmic tail of 22-28 amino acids (a.a.) and an extracellular (luminal) domain of about 150 a.a (Goodwin *et al*., 1993; Tesselaar *et al*., 1997). Moreover, Ii is a trimer and CD70, like other TNF family members, is most likely a trimer as well. However, the exact mechanism of CD70-Ii interaction must be distinct from MHC class II-Ii interaction, given the structural differences between CD70 and MHC class II. In case of the MHC class II α/β heterodimer, the peptide binding groove binds the CLIP region of Ii (Jasanoff *et al*., 1998). CD70 does not have an analogous CLIP-binding region, as predicted based on the crystal structure of TNF (Banner *et al*., 1993) and related proteins. Moreover, we could not co-immunoprecipitate the CD70-Ii complex from lysates prepared with different mild detergents from Mel JuSo cells or DCs, while MHC class II-Ii complexes could successfully be isolated under the same conditions (results not shown). Possibly, the transmembrane segment of Ii participates in binding to CD70, since it also supports binding to MHC class II (Castellino *et al*., 2001). Further studies are required to determine which regions in CD70 and Ii are involved in their interaction.

We have demonstrated here that CD70 exits from the ER and travels to the cell surface in absence of Ii. This is in agreement with the lack of known retention- or sorting motifs in its cytoplasmic tail. The sole expression of Ii sufficed to re-direct CD70 to late endosomal/lysosomal compartments. Conversely, CD70 expression sufficed to alleviate ER retention of Ii. This suggests that the two proteins form a complex in the ER and then travel to the Golgi. The strong increase in FRET signal between Ii and CD70 in the Golgi after pretreatment of cells with BFA supports this concept. The FRET signal between CD70-mRFP and Ii-GFP was much lower in MIICs than in the Golgi after BFA treatment. This suggests that interactions between CD70 and Ii are lost upon arrival in MIIC, likely due to degradation of Ii (Cresswell, 1994).

We not only found a novel chaperone function of Ii, but also provide the first evidence that Ii regulates the MHC class I-restricted CD8+ T cell response. Since Ii is generally perceived as a unique chaperone for MHC class II, it is not expected to impact on MHC class I-restricted CD8+ T cell responses. Ii-/- mice have impaired antigen presentation to CD4+ T cells. This is consistent with qualitative and quantitative alterations in MHC class II/peptide complex formation and reduced expression of MHC class II on the surface of professional antigen presenting cells in these mice (Viville *et al*., 1993; Bikoff *et al*., 1993). We now show that by acting as a chaperone for CD70, Ii regulates CD8+ T cell cross-priming by CD8+ DCs. Whereas Ii-deficiency did not have an impact on MHC class I-restricted antigen presentation, it did alter the threshold for CD8+ T cell priming. At all concentrations of OVA protein tested, CD8+ T cell clonal expansion was more pronounced when cells were primed by Ii-/- DCs than by WT DCs. This effect was CD27-dependent, indicating that is was due to enhanced CD70 cell surface expression on Ii-/- cDCs. During a normal acute infection, CD70 is transiently expressed and at very low levels (Hendriks *et al*., 2005). Constitutive cell surface expression of transgenic CD70 on B cells or DCs led to a CD27-dependent turnover of naïve T cells into effector cells, with a dramatic impact on T cell homeostasis (Arens *et al*., 2001; Tesselaar *et al*., 2003; Keller *et al*., 2008). Transgenic expression of CD70 on tolerogenic steady-state conventional DCs sufficed to render them capable of priming anti-viral or anti-tumor immune responses (Keller *et al*., 2008). These data indicate that CD27-CD70 interactions can lower the threshold for T cell priming. The present study underlines this: disruption of the intracellular retention of CD70 in DCs by Ii deficiency lowered the antigen concentration required for CD8+ T cell cross-priming.

Several lines of evidence suggest that CD70 expression is an important aspect of CD40-mediated DC "licensing", i.e. giving DC the potential to prime an effective CD8+ T cell response (Ridge *et al*., 1998). Upon cognate interactions with CD4+ T cells, DCs gain the ability to recruit CD8+ T cells, resulting in preferential interaction of CD8+ T cells with DCs that are licensed by CD4+ T cells (Beuneu *et al*., 2006; Castellino *et al*., 2006). Such licensing is rapid and dependent on CD40-CD40L interactions (Ridge *et al*., 1998), which in turn induce high cell surface levels of CD70 (Sanchez *et al*., 2007). In view of these data and our findings, we propose the following scenario: When triggered by pathogen-derived signals, a DC synthesizes CD70 protein, which is directed towards MIICs by its chaperone Ii. When such a maturing DC encounters a cognate CD4+ T cell, these two cells form an immunological synapse. MIICs bring CD70 and MHC class II towards this contact point and TCR signaling induces CD40L, while CD27 gives survival input. As result of subsequent CD40-CD40L interaction between the DC and the CD4+ T cell, CD70 production in the DC is enhanced and pro-survival signaling by the CD27-CD70 pair is enforced. After delivery to the synapse, CD70 diffuses over the plasma membrane (Keller *et al*., 2008) and becomes available for triggering CD27 on the recruited CD8+ T cells. In this way, Ii-directed transport of CD70 not only coordinates MHC class II antigen presentation with delivery of the CD27-CD70

costimulatory signal to CD4+ T cells, but also temporally controls delivery of the same signal to cognate CD8+ T cells.

Materials and Methods

Mice

Wild-type, Ii-/- (Viville *et al*., 1993), MHC II-/- (Cosgrove *et al*., 1991), OT-I, OT-II (Li *et al*., 2001) and CD27-/- (Hendriks *et al*., 2000) mice on a C57BL/6 background were used at 6-12 weeks of age. OT-I mice are transgenic a TCR recognizing OVA257-264 peptide in the context of H-2Kb and OT-II mice are transgenic for a TCR recognizing OVA323-339 in the context of I-Ab. Mouse experiments were performed in agreement with national and institutional guidelines.

Antibodies

Monoclonal antibodies (mAb) used were: anti-CD8α, 53-6.7; anti-CD11c, HL3; anti-CD24, M1/69; anti-CD25, PC61; anti-CD45R/B220, RA3-6B2; anti-CD63, MEM-259; anti-mCD70, FR70; anti-hCD70, 2F2 (Hintzen *et al*., 1994); anti-human Ii, Bu45; anti-I-A^b, AF6-120.1; anti-HLA-DR, 1B5 (Neefjes *et al*., 1990). Polyclonal rabbit sera used were: anti-I-A^bβ, JV2 (Bryant *et al*., 1999); anti-human Ii, ICN1 (Morton *et al*., 1995); anti-mouse Ii, S22 (Koch *et al*., 1987). For flow cytometry, antibodies conjugated to FITC, PE, allophycocyanin (APC), Pacific Blue or tandem conjugate peridinin chlorophyll protein (PerCP)-Cy5.5 were used. All mAb were obtained from BD Biosciences, eBioscience, or prepared as purified Ig from available hybridomas. For CLSM, MEM-259 was used as FITC conjugate, other antibodies were used as purified Ig or serum and detected by secondary antibodies, conjugated to fluorochromes (Molecular Probes), as indicated.

Flow cytometry

DCs and T cells were washed in PBS and cells were incubated with fluorochrome-conjugated mAbs. Incubations were performed in staining buffer (PBS, 1% BSA, 0.01% sodium azide) for 30 min on ice. PI was used for identification of dead cells. Cells were analyzed using a FACSCalibur (BD Biosciences) in combination with FlowJo software (Tree Star). For all stainings of DCs, cells were pre-incubated with Fc Block (mAb to CD16/CD32, 2.4G2, BD Biosciences).

Cell isolation and culture

Human melanoma cell line Mel JuSo, human cervix carcinoma cell line HeLa and their stably transduced or transfected derivatives were grown in IMDM (Gibco-BRL) supplemented with 8% FCS, penicillin and streptomycin. DCs were generated from BM as described (Naik *et al*., 2005). Briefly, BM was flushed from tibiae and femurs and erythrocytes were lysed on ice for 1 min in 0.14 M NH4Cl, 0.017 M Tris-HCl pH 7.2. Cells were cultured for 8-10 days at 1.5-3 x 106 cells/ml in presence of 300 ng/ml murine Flt3L (generated in-house) in RPMI 1640 (Gibco-BRL) supplemented with 10% FCS, penicillin, streptomycin and 50 μM 2-mercaptoethanol. Splenic DCs were separated by density gradient (Naik *et al*., 2003). Briefly, spleens were digested for 20 min at room temperature with Collagenase type 3 (Worthington) and DNAase I (Roche) and subsequently incubated with 10 mM ethylenediaminetetraacetic acid (EDTA) in PBS. To prevent DC maturation during the isolation, all subsequent procedures were performed at 0°C to 4°C in PBS/EDTA. Light-density cells, which constituted 5% of the total nucleated spleen cells, were selected by centrifugation in a medium containing Nycoprep 1.077 (Axis-Shield). DCs were isolated from spleen by collagenase D (Roche) digestion (2.5 mg/ml in Hanks' Balanced Salt Solution) followed by separation on OptiPrep gradient according to manufacturer's instructions (Axis-Shield, Norway). DCs were further purified by magnetic separation on auto-MACS, using anti-CD11c (N418)-labeled MACS beads (Miltenyi Biotec GmbH, Germany), or by flow cytometry using the FACSAria (BD Biosciences). For flow cytometric sorting of CD8+ DCs, OptiPrep-selected splenic DCs were incubated with antibodies specific for CD11c, CD8α, CD24 and CD45R/B220 conjugated to APC, PerCP-Cy5.5, PE or Pacific Blue and selected based on the CD11c+ CD8+ CD24+ CD45R/B220- phenotype. DCs were matured by incubation with 1 μg/ml LPS of Escherichia coli serotype 055:B5 (Sigma-Aldrich) in RPMI supplemented with 10% FCS, penicillin, streptomycin and 50 μM 2-mercaptoethanol and, if applicable, concomitantly loaded with OVA protein (Sigma Aldrich) at 40 μM or the indicated concentrations for 4 h at 37oC and eventually washed with medium. OVA-specific MHC class I-restricted OT-I T cells or MHC class II restricted OT-II T cells were purified from spleens or pooled spleens and lymph nodes of naïve mice using the Mouse T Lymphocyte Enrichment Set (BD Biosciences).

Co-culture of DCs and T cells

Purified OT-II T cells were added to LPS matured, OVA-loaded splenic DCs at a 4:1 ratio in medium in a 96-well round bottom plate and centrifuged for 1 min at 200 g. After co-culture for 1 h, cells were allowed to adhere to poly-L-lysine (Sigma Aldrich) coated coverslips, fixed and processed for CLSM analysis. For OT-I T cell stimulation, CD8+ splenic DCs were loaded with OVA protein (Sigma Aldrich) and simultaneously matured with LPS for 2 h and then washed with RPMI, 8% FCS. DCs and OT-I T cells were co-cultured for 65 h in 96 well round bottom plates at 5 x 103 and 5 x 104 cells per well, respectively. OT-I T cells had been labeled with CFSE (5 μM), following the manufacturer's protocol (Invitrogen, Molecular Probes). Prior to flow cytometry, 5 x 103 blank calibration particles (BD Biosciences) were added per well and PI was added to determine cell viability. For the B3Z T cell assay (Sanderson and Shastri, 1994), CD8+ splenic DCs were loaded with OVA protein in the presence of LPS for 90 min at 37°C. DCs and B3Z cells were co-cultured in triplicate overnight in 96 well round bottom plates at 5 x 103 and 5 x 104 cells per well, respectively. The cell mixture was lysed with PBS containing 1 mM MgCl2, 0.125% Nonidet P-40 and 0.155 mM chlorophenol red β-D galactopyranoside (CPRG; Calbiochem). Next, the plates were incubated at 37°C for 30 min and then at 4°C for 48 h. The OD595 was measured using a Wallac Victor2 1420 multilabel counter plate reader (Perkin Elmer).

Constructs and gene transfer

The Mel JuSo cell line stably expressing mCD70 was generated by retroviral transduction as described (Keller *et al*., 2007). Transient transfection of Mel Juso or HeLa cells with mCD70 cDNA (Tesselaar *et al*., 1997), hCD70 cDNA (Goodwin *et al*., 1993) and human Ii-p31 cDNA (all in pcDNA3 expression vector) was performed using Fugene 6 Transfection Reagent (Roche). For FRET experiments, constructs were used encoding mCD70 fused to mRFP and Ii-p31 fused to EGFP. mCD70 cDNA was cloned into pmRFP-N1 and Ii into pEGFP-N1 (Clontech) in the same reading frame as mRFP and EGFP, respectively. pmRFP-N1 was derived from pEGFP-N1 by replacing the EGFP coding sequence with the mRFP coding sequence using BamH I and Not I sites. pcDNA3 encoding Histone 2B-GFP (H2B-GFP), or a variant construct in which the GFP coding sequence was replaced with the mRFP coding sequence (H2B-mRFP) were used as controls for FRET experiments (van Rheenen *et al*., 2004).

CLSM

HeLa cells transfected with Ii and/or CD70 cDNA were allowed to attach to glass coverslips for 24 h. DCs were allowed to attach for 1 h to coverslips coated with poly-L-lysine (Sigma Aldrich). Cells were washed in PBS containing 1 mM MgCl2 and 1 mM CaCl2, fixed for 10 min with 3.7% paraformaldehyde in PBS and permeabilized for 3 min with 0.1% Triton X-100 in PBS. Non-specific binding sites were blocked for 30 min using 1% BSA in PBS. Incubations were performed with antibodies diluted in blocking buffer for 45 min, after which coverslips were washed and incubated for 30 min with the appropriate secondary antibodies diluted in blocking buffer. Coverslips were washed, mounted in Vectashield (Vector Laboratories) and viewed under a Leica TCS NT confocal laser-scanning microscope (Leica Microsystems). Images with two fluorochromes were taken by simultaneous scanning and images with three fluorochromes were taken by sequential scanning. Antibody cross-reactivity was excluded since non-specific combinations of primary and secondary antibodies did not show any staining (data not shown).

Immuno-electron microscopy

Mel JuSo cells stably expressing mCD70 were fixed for 2 h in a mixture of 2% paraformaldehyde and 0.2% glutaraldehyde in 60 mM PIPES, 25 mM HEPES, 2 mM MgCl2, 10 mM EGTA, pH 6.9 and processed for ultrathin cryosectioning as described (Calafat *et al*., 1997). For immunolabelling, the sections were incubated for 10 min with 0.15 M glycine in PBS and for 10 min with 1% BSA in PBS to block free aldehyde groups and prevent aspecific antibody binding, respectively. Sections were incubated with anti-Ii rabbit polyclonal Ig ICN1 and 10 nm protein-A conjugated colloidal gold (EM lab, University of Utrecht) all in 1% BSA in PBS. Next, sections were fixed in 1% glutaraldehyde and blocked with glycine and BSA in PBS, incubated with anti-mCD70 mAb FR70 for 1 h, followed by rabbit anti-rat Ig adsorbed against mouse Ig, followed by 15 nm protein-A conjugated gold probe. Next, the cryosections were embedded in uranylacetate and methylcellulose and examined with a Philips CM 10 electron microscope (FEI Eindhoven, The Netherlands).

FRET imaging

Hela cells were cultured on coverslips for 48 h. At 24 h prior to imaging, cells were transfected to express Ii-EGFP and CD70-mRFP. Mel JuSo cells stably transfected to express H2B-GFP or H2B-mRFP were added to the culture for leak-through corrections and internal

controls as described (Zwart *et al*., 2005). For imaging, coverslips were placed in 2 ml bicarbonate-buffered saline (140 mM NaCl, 5 mM KCl2, 2 mM MgCl2, 1 mM CaCl2, 23 mM NaHCO3, 10 mM D-glucose, 10 mM HEPES pH 7.3) and analyzed in a tissue culture chamber at 37°C, 5% CO2. FRET between EGFP and mRFP was determined by calculating the sensitized emission (the mRFP emission upon EGFP excitation), using separately acquired donor and acceptor images as described previously (van Rheenen *et al*., 2004). In short, images were acquired on a DM-Ire2 inverted microscope fitted with TCS-SP2 scan head (Leica Microsystems). Three images were collected: EGFP excited at 488 nm and detected at 495-550 nm; indirect mRFP excited at 488 nm and detected at 580-650 nm and direct mRFP excited at 568 nm and detected at 580-650 nm. Because of considerable overlap of EGFP and mRFP spectra, mRFP emission was corrected for leak-through of EGFP emission and for direct excitation of mRFP during EGFP excitation. FRET was calculated from these data (Forster, 1948), with shade-correction and smoothening of images. Sensitized emission (FRET) was calculated using correction factors obtained from cells expressing either GFP or mRFP alone, which were included for every image. The apparent donor FRET efficiency (E_D) was calculated by relating the FRET signal to the total emission signal of the donor fluorophore, after which the E_D image was overlaid with a false color look up table. By this approach, differences in FRET efficiency can be measured with an accuracy of 0.5% (Zwart *et al*., 2005). For graphic representation, the E_D was calculated for each pixel from the raw data files of the represented cell and was exported to Microsoft Excel. In this program, the amount of pixels was related to the corresponding E_D and plotted as a histogram. Brefeldin A (GolgiPlug, BD Biosciences) was added to the cells for 6 h, washed off and cells were subsequently incubated for 1 h at 20oC. Chloroquine (200 μM) was added to the cells for 2 min prior to imaging, as indicated. This suffices to neutralize late endosomes/lysosomes (Zwart *et al*., 2005 and results not shown).

Acknowledgements

We thank the personnel of the experimental animal-, flow cytometry- and CLSM facilities of the Netherlands Cancer Institute for assistance, E. Veraar, K. Jalink and P. Kujala for help with various experiments, B. Dubois, D. Kaiserlian for Ii-/- mice, N. Koch for antibodies and A. Berns for critically reading the manuscript. This work was supported by grants from the Dutch Cancer Society and The Netherlands Organization for Scientific Research to J.N. and J.B.

Footnotes

A.M.K., W.Z., G.v.d.H., V.P., E.d.V., H.J., S.N., and V.P. performed research and analyzed data. A.M.K., W.Z., J.N. and J.B designed research. A.M.K. and J.B. wrote the paper.
The authors declare no conflict of interest.
This article contains supplemental information.

References

Arens R, Tesselaar K, van Schijndel GMW, Baars PA, Pals ST, Krimpenfort P, Borst J, van Oers MHJ, van Lier RAW (2001) Constitutive CD27/CD70 interaction induces expansion of effector-type T cells and results in IFNgamma-mediated B cell depletion. Immunity 15: 801-812

Banner DW, D'Arcy A, Janes W, Gentz R, Schoenfeld HJ, Broger C, Loetscher H, Lesslauer W (1993) Crystal structure of the soluble human 55 kd TNF receptor-human TNF beta complex: implications for TNF receptor activation. Cell 73: 431-445

Beuneu H, Garcia Z, Bousso P (2006) Cutting edge: cognate CD4 help promotes recruitment of antigen-specific CD8 T cells around dendritic cells. J Immunol 177: 1406-1410

Bikoff EK, Huang LY, Episkopou V, van Meerwijk J, Germain RN, Robertson EJ (1993) Defective major histocompatibility complex class II assembly, transport, peptide acquisition, and CD4+ T cell selection in mice lacking invariant chain expression. J Exp Med 177: 1699-1712

Boes M, Cerny J, Massol R, Op den Brouw M, Kirchhausen T, Chen J, Ploegh H (2002) T-cell engagement of dendritic cells rapidly rearranges MHC class II transport. Nature 418: 983-988.

Bryant PW, Roos P, Ploegh HL, Sant AJ (1999) Deviant trafficking of I-Ad mutant molecules is reflected in their peptide binding properties. Eur J Immunol 29: 2729-2739.

Bullock TN, Yagita H (2005) Induction of CD70 on dendritic cells through CD40 or TLR stimulation contributes to the development of CD8+ T cell responses in the absence of CD4+ T cells. J Immunol 174: 710-717.

Calafat J, Janssen H, Stahle-Backdahl M, Zuurbier AE, Knol EF, Egesten A (1997) Human monocytes and neutrophils store transforming growth factor-alpha in a subpopulation of cytoplasmic granules. Blood 90:1255-1266

Castellino F, Han R, Germain RN (2001) The transmembrane segment of invariant chain mediates binding to MHC class II molecules in a CLIP-independent manner. Eur J Immunol 31: 841-850.

Castellino F, Huang AY, Altan-Bonnet G, Stoll S, Scheinecker C, Germain RN (2006) Chemokines enhance immunity by guiding naive CD8+ T cells to sites of CD4+ T cell-dendritic cell interaction. Nature 440: 890-895.

Chang CH, Flavell RA (1995) Class II transactivator regulates the expression of multiple genes involved in antigen presentation. J Exp Med 181: 765-767.

Cosgrove D, Gay D, Dierich A, Kaufman J, Lemeur M, Benoist C, Mathis D (1991) Mice lacking MHC class II molecules. Cell 66: 1051-1066.

Cresswell P (1994) Assembly, transport and function of MHC class II

molecules. Annu Rev Immunol 12: 259-293

de Graaf P, Zwart WT, van Dijken RA, Deneka M, Schultz TK, Geijsen N, Coffer PJ, Gadella BM, Verkleij AJ, van der Sluijs P, van Bergen en Henegouwen PM (2004) Phosphatidylinositol 4-kinase beta is critical for functional association of rab11 with the Golgi complex. Mol Biol Cell 15:2038-2047.

D'Souza WN, Lefrancois L (2003) IL-2 is not required for the initiation of CD8 T cell cycling but sustains expansion. J Immunol 171: 5727-5735

Förster T (1948) Zwischemolekulare energiewanderung und fluoreszenz. Ann Physik 2: 55-67

Goodwin RG, Alderson MR, Smith CA, Armitage RJ, Vandenbos T, Jerzy R, Tough TW, Schoenborn M, Davies-Smith T, Hennen K, Falk B, Cosman D, Baker E, Sutherlands GR, Grabstein KH, Giri JG, Beckmann MP (1993) Molecular and biological characterization of a ligand for CD27 defines a new family of cytokines with homology to tumor necrosis factor. Cell 73: 447-456

Heath WR, Belz GT, Behrens GMN, Smith CM, Forehan SP, Parish IA, Davey GM, Wilson NS, Carbone FR, Villadangos J (2004) Cross-presentation, dendritic cell subsets, and the generation of immunity to cellular antigens. Immunol Rev 199: 9-26

Hendriks J, Gravestein LA, Tesselaar K, van Lier RA, Schumacher TN, Borst J (2000) CD27 is required for generation and long-term maintenance of T cell immunity. Nat Immunol 1: 433-440

Hendriks J, Xiao Y, Borst J (2003) CD27 promotes survival of activated T cells and complements CD28 in generation and establishment of the effector T cell pool. J Exp Med 198: 1369-1380

Hendriks J, Xiao Y, Rossen JWA, van der Sluijs KF, Sugamura K, Ishii N, Borst J (2005) During viral infection of the respiratory tract, CD27, 4-1BB, and OX40 collectively determine formation of CD8+ memory T cells and their capacity for secondary expansion. J Immunol 175: 1665-1676

Hintzen RQ, Lens SM, Koopman G, Pals ST, Spits H, van Lier RA (1994) CD70 represents the human ligand for CD27. Int Immunol 6: 477-480

Jasanoff A, Wagner G, Wiley DC (1998) Structure of a trimeric domain of the MHC class II-associated chaperonin and targeting protein Ii. EMBO J 17: 6812-6818

Jayawardena-Wolf J, Benlagha K, Chiu Y-H, Meher R, Bendelac A. (2001) CD1d endosomal trafficking is independently regulated by an intrinsic CD1d-encoded tyrosine motif and by the invariant chain. Immunity 15: 897-908

Kang SJ, Cresswell P (2002) Regulation of intracellular trafficking of human CD1d by association with MHC class II molecules. EMBO J 21: 1650-1660

Keller AM, Groothuis TA, Veraar EAM, Marsman M, Maillette de Buy Wenniger L, Janssen H, Neefjes J, Borst J (2007) Costimulatory ligand CD70 is delivered to the immunological synapse by shared intracellular trafficking with MHC class II molecules. Proc Natl Acad Sci USA 104: 5989-5994

Keller AM, Schildknecht A, Xiao Y, van den Broek M, Borst J (2008) Expression of costimulatory ligand CD70 on steady-state dendritic cells breaks CD8+ T cell tolerance and permits effective immunity. Immunity 29: 934-946

Klausner RD, Donaldson JG, Lippincott-Schwartz J (1992) Brefeldin A: insights into the control of membrane traffic and organelle structure. J Cell Biol 116: 1071-80

Kleijmeer M, Ramm G, Schuurhuis D, Griffith J, Rescigno M, Ricciardi-Castagnoli P, Rudensky AY, Ossendorp F, Melief CJM, Stoorvogel W, Geuze HJ (2001) Reorganization of multivesicular bodies regulates MHC class II antigen presentation by dendritic cells. J Cell Biol 155: 53-63.

Koch S, Schultz A, Koch, N. (1987) The production of recombinant HLA-DR beta and invariant chain polypeptides by cDNA expression in E. coli. J Immunol Methods 103: 211-220

Li M, Davey GM, Sutherland RM, Kurts C, Lew AM, Hirst C, Carbone FR, Heath WR (2001) Cell-associated ovalbumin is cross-presented much more efficiently than soluble ovalbumin *in vivo*. J Immunol 166: 6099-6103

Locksley RM, Killeen N, Lenardo MJ (2001) The TNF and TNF receptor superfamilies: integrating mammalian biology. Cell 104: 487-501

Lotteau V, Teyton L, Peleraux A, Nilsson T, Karlsson L, Schmid SL, Quaranta V, Peterson PA (1990) Intracellular transport of class II MHC molecules directed by invariant chain. Nature 348: 600-605

Marks MS, Blum JS, Cresswell P (1990) Invariant chain trimers are sequestered in the rough endoplasmic reticulum in the absence of association with HLA class II antigens. J Cell Biol 111: 839-855

McCormick PJ, Martina JA, Bonifacino JS (2005) Involvement of clathrin and AP-2 in the trafficking of MHC class II molecules to antigen-presenting compartments. Proc Natl Acad Sci USA 102: 7910-7915

Michelsen K, Yuan H, Schwappach B (2005) Hide and run. Arginine-based endoplasmatic reticulum-sorting motifs in the assembly of heteromultimeric membrane proteins. EMBO Rep 6: 717-722

Morton PA, Zacheis ML, Giacoletto KS, Manning JA, Schwarz BD (1995) Delivery of nascent MHC class Ii-invariant chain complexes to lysosomal compartments and proteolysis of invariant chain by cysteine proteases precedes peptide binding in B-lymphoblastoid cells. J Immunol 154: 137-150

Naik S, Vremec D, Wu L, O'Keeffe M, Shortman K (2003) CD8α+ mouse spleen dendritic cells do not originate from the CD8α- dendritic cell subset. Blood 102: 601-604

Naik SH, Proietto AI, Wilson NS, Dakic A, Schnorrer P, Fuchsberger M, Lahoud MH, O'Keeffe M, Shao QX, Chen WF, Villadangos JA, Shortman K, Wu L. (2005) Cutting edge: generation of splenic CD8+ and CD8- dendritic cell equivalents in Fms-like tyrosine kinase 3 ligand bone marrow cultures. J Immunol 174: 6592-6597

Neefjes JJ, Stollorz V, Peters PJ, Geuze HJ, Ploegh HL (1990) The biosynthetic pathway of MHC class II but not class I molecules intersects the endocytic route. Cell 61: 171-183

Odorizzi GC, Trowbridge IS, Xue L, Hopkins CR, Davis CD, Collawn JF (1994) Sorting signals in the MHC class II invariant chain cytoplasmic tail and transmembrane region determine trafficking to an endocytic processing compartment. J Cell Biol 126: 317-330

Peters P J, Neefjes JJ, Oorschot V, Ploegh HL, Geuze HJ (1991) Segregation of MHC class II molecules from MHC class I molecules in the Golgi complex for transport to lysosomal compartments. Nature 349: 669-676

Pieters J, Horstmann H, Bakke O, Griffiths G, Lipp J (1991) Intracellular transport and localization of major histocompatibility complex class II molecules and associated invariant chain. J Cell Biol 115: 1213-1223.

Ridge JP, Di Rosa F, Matzinger P (1998) A conditioned dendritic cell can be a temporal bridge between a CD4+ T-helper and a T-killer cell. Nature 393: 474–478

Sanchez PJ, McWilliams JA, Haluszczak C, Yagita H, Kedl RM (2007) Combined TLR/CD40 stimulation mediates potent cellular immunity by regulating dendritic cell expression of CD70 *in vivo*. J Immunol 178: 1564-1572

Sanderson S, Shastri N (1994) LacZ inducible, antigen/MHC-specific T cell hybrids. Int Immunol 6: 369-376

Soares H, Waechter H, Glaichenhaus N, Mougneau E, Yagita H, Mizenina O, Dudziak D, Nussenzweig MC, Steinman RM (2007) A subset of dendritic cells induces CD4+ T cells to produce IFN-g by an IL-12-independent but CD70-dependent mechanism *in vivo*. J Exp Med 204: 1095-1106

Tesselaar K, Arens R, van Schijndel GMW, Baars PA, van der Valk M, Borst J, van Oers MHJ, van Lier RAW (2003) Lethal T cell immunodeficiency induced by chronic costimulation via CD27-CD70 interactions. Nat Immunol 4: 49-54.

Tesselaar K, Gravestein LA, van Schijndel GM, Borst J, van Lier RA (1997) Characterization of murine CD70, the ligand of the TNF receptor family member CD27. J Immunol 159: 4959-4965

van Rheenen J, Langeslag M, Jalink K (2004) Correcting confocal acquisition to optimize imaging of fluorescence resonance energy transfer by sensitized emission. Biophys J 86: 2517-2529

Viville S, Neefjes J, Lotteau V, Dierich A, Lemeur M, Ploegh H, Benoist C, Mathis D (1993) Mice lacking the MHC class II-associated invariant chain. Cell 72: 635-648

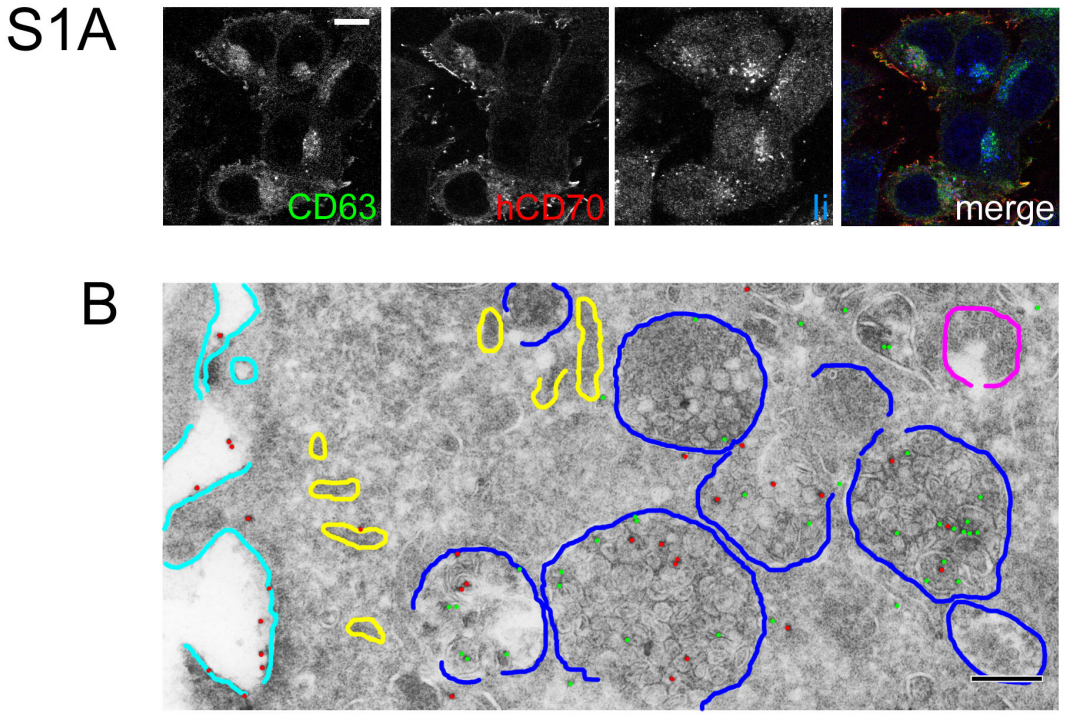
Wong P, Rudensky AY (1996) Phenotype and function of CD4+ T cells in mice lacking invariant chain. J Immunol 156: 2133-2142

Xiao Y, Peperzak V, Keller AM, Borst J (2008) CD27 instructs CD4+ T cells to provide help for the memory CD8+ T cell response after protein immunization. J Immunol 181: 1071-1082

Ye L, Liu X, Rout SN, Li Z, Yan Y, Lu L, Kamala T, Nanda NK, Song W, Samal SK, Zhu X (2008) The MHC Class II-associated invariant chain interacts with the neonatal Fcg receptor and modulates its trafficking to endosomal/lysosomal compartments. J Immunol 181: 2572-2585.

Zwart W, Griekspoor A, Kuijl C, Marsman M, van Rheenen J, Janssen H, Calafat J, van Ham M, Janssen L, van Lith M, Jalink K, Neefjes J (2005) Spatial separation of HLA-DM/HLA-DR interactions within MIIC and phagosome-induced immune escape. Immunity 2: 221-233.

Supplemental data



Supplemental Figure S1.

(**A**) Colocalization of hCD70, Ii and CD63 in Mel JuSo cells. Mel JuSo cells were transiently transfected with hCD70, fixed and stained with rabbit anti-Ii (S22) followed by goat anti-rabbit Ig-Alexa 647 (blue), mouse anti-hCD70 (2F2) followed by goat anti-mouse Ig-TexasRed (red) and anti-CD63-FITC Ii (green) and examined by CLSM. The merged image shows signals from all three channels and reveals co-localization of hCD70, CD63 and Ii as a white color. The scale bar equals 10 µm. Images are representative of data obtained in two independent experiments (n>20).
(**B**) Immuno-EM image of Mel JuSo cells stably expressing mCD70, as presented in Figure 2B, now highlighting in false colors CD70 (red) and Ii (green) gold labelling. Indicated are the plasma membrane (cyan), ER (yellow), mitochondria (purple) and multivesicular bodies (blue). The scale bar equals 200 nm.

Summary and Discussion antigen presentation

summary

14

Summary and discussion: antigen presentation

For a cell to communicate information about its internal health and status to the immune system, a sophisticated cellular machinery has originated for distinct antigenic subclasses; peptides and lipids from intra- and extracellular origins. CD1 presents lipids from both exogenous and endogenous origins, while for peptides two distinct molecular pathways have developed, namely MHC class I (for endogenous and viral peptides) and MHC class II (for peptides from extracellular origins) (reviewed in Chapter 9). While MHC class I is expressed in all nucleated cells, MHC class II is only expressed in specialized antigen-presenting cells. MHC class II molecules, including HLA-DR, assemble in the ER, where it associates with its specific chaperone, Invariant chain (Ii). Together with Ii, HLA-DR is transported to late endosomal/lysosomal compartments, where it meets peptides taken up through the endocytic route and processed by lysosomal peptidases. These MHC class II bearing late endosomal/lysosomal compartments, or MIIC, share a typical morphology; a limiting membrane surrounded structure with multiple internal vesicles. In these MIIC, the remainder of Ii, Class II-associated invariant chain peptide (CLIP), is exchanged for an antigenic peptide. This process is facilitated by another chaperone, HLA-DM. After the peptide is loaded on HLA-DR, the complex can be transported to and presented on the plasma membrane. Here, the complex is recognized by CD4+ T cells.

To gain insights into the process of antigen loading, we monitored the interaction between HLA-DR and HLA-DM in living cells (Chapter 10). Cell lines were constructed containing HLA-DR/CFP, HLA-DM/YFP and Ii, in which we measured Fluorescence Resonance Energy Transfer (FRET) in the MIIC. FRET is the radiationless energy transfer from a donor, in this case CFP, to a suitable acceptor, in this case YFP. Since this biophysical phenomenon only takes place when the fluorophores are in close proximity, a detection of FRET signal is indicative for a physical interaction. Interestingly, we found interaction between HLA-DR and HLA-DM only to occur on the internal vesicles of the MIIC and not on the limiting membrane. Since HLA-DR/HLA-DM interactions are essential for antigen loading, we defined a specific antigen-loading micro environment within this lysosomal structure. This micro environment within the MIIC is specifically disrupted by pathogens, such as *Salmonella typhimurium*. The bacterium actively prevents the formation of internal vesicles in its own phagosomal/lysosomal structure and thereby actively enables a local immune escape. Whether the antigen-loading subdomain can be generalized among different HLA-DR isoforms and if the effects we described in HEK293 cells can also be observed in specialized antigen-presenting cells, are still open questions.

In antigen loading and presentation, vesicular movement is essential. The vesicles containing cargo from extracellular origins need to encounter and fuse with lysosomal compartments in order to degrade the cargo. Likewise, after MHC class II molecules are transported to this late endosomal/lysosomal structure and the antigen is loaded, the antigen-loaded MHC class II needs to be transported to the plasma membrane in order to present its antigenic information. One of the proteins directly involved in these transport processes is Rab7. Rab7 is a member of the Rab GTPase superfamily, and is essential for minus-end microtubule organizing centre (MTOC)–directed transport. For MTOC-directed transport and perinuclear vesicle localization, Rab7 needs to associate to Rab7-interacting lysosomal protein (RILP) and oxysterol-binding protein-related protein 1L (ORP1L) (Chapter 11). Both RILP and ORP1L are effectors of Rab7 and can simultaneously bind to GTP-loaded Rab7. RILP can directly interact with the dynactin projecting arm $p150^{Glued}$, which is required for dynein motor recruitment to these vesicular structures.

ORP1L function is, however, required in an unexpected fashion. We have shown that ORP1L can alter its conformation as a response to binding cholesterol (Chapter 12). In a non-cholesterol-associated conformation, ORP1L can recruit VAP (an ER resident protein) to interact with ORP1L *in trans*. VAP subsequently removes $p150^{Glued}$ from the Rab7-RILP-ORP1L complex and the vesicle localizes at the cell periphery. If cholesterol levels are high on the cytosolic leaflet of these vesicles, ORP1L does not recruit VAP, preventing a dissociation of $p150^{Glued}$ which leads to a clustering of these vesicles at the perinuclear region. Thus, the cholesterol levels regulate ORP1L conformation which regulates vesicular positioning in the cell.

A clear message from this chapter is that low resolution techniques, such as light microscopy, should not be over interpreted. One would conclude from the CLSM data in this paper that the endoplasmatic reticulum can fuse with lysosomal compartments. Monitoring now the same structures using electron mi-

croscopy led to the conclusion that the endoplasmatic reticulum alligns to, rather then fuses with, vesicular compartments. What factors enable this allignment, and thereby the VAP/ORP1L interactions, remains to be discovered. The formation of this endoplasmatic recitulum/vesicle synapse may be governed solely by VAP/ORP1L interactions, but could also be mediated by thus far unknown proteins. Also more processes may be regulated at this endoplasmatic recitulum/vesicle contact site, next to the removal of the $p150^{Glued}$ subunit from the motor complex, which are currently under investigation.

Another point of discussion is whether bacteria make use of the cholesterol-dependence of vesicle localization and possibly lysosomal maturation. This could be the case for *Salmonella typhimurium*. This bacterium secretes the factor SseJ, that induces an esterification of cholesterol. Although no data has been published about the physiological role of this cholesterol esterification, it may be related to the ORP1L-mediated vesicle localization. Through this modification, the cholesterol moiety may not be recognisable for ORP1L, preventing the maturation of the phagosome. This way, the cholestrol-driven vesicle-localization in cells can be influenced and manipulated by bacteria in order to survive in host cells.

Next to chaperoning MHC class II, Ii can also have an influence on other factors. We have shown that Ii directly and functionally interacts with CD70, a Tumor Necrosis Factor (TNF)-related costimulatory ligand that - via its receptor CD27 - directs CD4+ and CD8+ T cell responses (Chapter 13). In the absence of Ii, CD70 transports by default to the plasma membrane. When Ii is coexpressed, CD70 can interact with Ii in the ER, after which Ii targets CD70 to the MIIC. Ii controls the kinetics and extent of CD70 cell surface expression and thereby regulates delivery of CD27-mediated survival signals to CD8+ T cells via MHC Class I. Additionally, now that both antigen-loaded MHC class II and CD70 are on the same structure, fusion of the vesicle with the plasma membrane results in a spatially and temporally restricted delivery of both an antigen-loaded complex and a costimulatory response. This way, CD4+ T cells can not only detect the antigen-loaded MHC class II, but also in the same complex allow the buildup of an immunological synapse between CD27 and CD70, which serves to activate CD4+ T cells to provide help for the CD8+ T cell response and to dictate the extent of CD8+ T cell clonal expansion.

The results presented here illustrated an antigen-loading microdomain within MIIC and showed how the Rab7/RILP/ORP1L complex cooperatively orchestrates motor complex recruitment and vesicle positioning. In addition, we described that Ii mediates CD70 targeting to the MIIC, where timed and controlled delivery of both antigen-loaded MHC class II and CD70 determines CD4+ and CD8+ T cell responses. Still, a number of questions remain unanswered. What factors define the antigen-loading microdomain? What renders the internal vesicles of the multivesicular structure functionally different from the limiting membrane? Candidate factors are CD63 and CD82, tetraspanin molecules that are described to localize mainly on the internal vesicles of the MIIC and are reported to directly interact with both HLA-DR and HLA-DM. Another question raised concerns the existence of other potential factors which might directly influence antigen loading and transport, possibly fine-tuning the sophisticated MHC class II pathway. This would also pave the way to developing novel chemical inhibitors which could be applied in the clinical setting to treat MHC class II presentation-related diseases, such as auto-immune diseases and certain leukemias. Another obvious question is covering all the chapters discussed here: to what degree do these seemingly different processes interconnect? Do vesicles destined to fuse with lysosomes expose high cholesterol levels on their cytosolic leaflet, and after antigen loading and CD70 acquisition decrease their cholesterol content, in order to move to and fuse with the plasma membrane?

Further research will certainly focus on these and other questions, shedding light on the complex and tightly regulated cellular machinery involved in MHC class II antigen presentation.

Nederlandse samenvatting Curriculum Vitae & List of Publications

Every science begins as philosophy and ends as art.
Will Durant, The Story of Philosophy, 1926

Nederlandse Samenvatting

Binnen celbiologie zijn veel verschillende technische benaderingen beschikbaar om het gedrag van eiwitten te bestuderen. De getrokken conclusies weerspiegelen echter niet altijd het gedrag van het bestudeerde eiwit in zijn physiologische context. Hoewel biochemie zeer waardevol is gebleken in het bestuderen van eiwit-eiwit interacties, geeft deze benadering geen informatie over het dynamisch gedrag van deze eiwitten in de levende cel. De lokalisatie van een eiwit binnen de cel kan het gedrag van zo'n eiwit sterk beïnvloeden en wanneer cellen worden opengebroken om zo naar eiwit-eiwit interacties te kijken, gaat deze cellulaire context verloren. Verder gaat de mogelijke betrokkenheid van andere eiwitten bij het stabiliseren van deze interacties door lysis ook verloren. Deze nadelen treden niet op wanneer levende cellen worden bestudeerd met behulp van fluorescentie microscopie. Conventionele fluorescentie microscopie geeft echter alleen informatie over de lokalisaties van de bestudeerde eiwitten op een maximale resolutie van 250 nm. Bij visualisatie met deze resolutie impliceert colocalisatie alleen niet noodzakelijk interactie, maar slechts een redelijk kleine afstand van de twee eiwitten ten opzichte van elkaar. Hoewel hoge resoluties wel kunnen worden bereikt met behulp van elektronen microscopie, staat deze techniek niet toe de dynamiek van de interacties te bestuderen. Tevens kan fixatie van de cellen leiden tot artefacten.

Biofysische microscopische technieken, zoals Fluorescent Resonance Energy Transfer (FRET), staan hoge-resolutie analyse van zowel eiwit-eiwit interacties als van eiwit conformatie status in levende cellen en in real time toe. Op deze wijze kunnen dynamische processen van eiwit-interacties en -vouwing in hun natuurlijke omgeving, namelijk de intacte levende cel, gevisualiseerd worden met een unieke gevoeligheid en nauwkeurigheid.

In de volgende twee onderzoekslijnen worden methodes toegepast die gebruik maken van dit biofysisch fenomeen.

Anti-oestrogeen resistentie via oestrogeen receptor-fosforylering en verhoogde co-activator niveaus

Borstkanker is de meest voorkomende vorm van kanker bij vrouwen, met meer dan een miljoen nieuw gediagnosticeerde gevallen wereldwijd elk jaar. Aangezien de groei van de meerderheid van alle borsttumoren afhankelijk is van oestrogeen receptor-alpha (ERα) activiteit, wordt therapie standaard gericht op het remmen van deze hormoongevoelige transcriptie factor. Een grote vooruitgang bij de behandeling van borstkanker patiënten werd geboekt met de komst van tamoxifen. Tamoxifen werd in 1966 ontwikkeld en uiteindelijk geïntroduceerd in de kliniek. Dit medicijn kan competeren met oestradiol, het natuurlijke ligand van de oestrogeen receptor, waardoor het de functie van de receptor kan remmen. Tamoxifen bleek zeer succesvol te zijn en heeft inmiddels de levens van miljoenen borstkanker patiënten wereldwijd gered, door de kans op terugkeer van de ziekte met 50% te verminderen. Bij de patiëntengroep waarbij de ziekte terugkomt, zelfs na behandeling met tamoxifen, vindt zodoende resistentie tegen dit medicijn plaats. De achterliggende mechanismen die verantwoordelijk zijn voor deze resistentie zijn nog niet volledig begrepen en daardoor onderwerp van veel onderzoeken.

Eén oorzaak van tamoxifen resistentie blijkt de activatie van de Proteïne Kinase A (PKA) signaleringsroute te zijn. PKA kan de oestrogeen receptor fosforyleren op serine 305, een residu dicht bij de kleine flexibele scharnier regio ('hinge') in ERα. Deze fosforylatie is er verantwoordelijk voor dat tamoxifen wordt herkend als een activator van transcriptie en tumorgroei, in plaats van de remmer die tamoxifen dient te zijn (beschreven in de hoofdstukken 1 en 2).

Artsen bepalen hun medicijnkeuze van anti-oestrogene stoffen, zoals tamoxifen, op basis van een empirisch bepaalde volgorde en niet afhankelijk van individuele kenmerken van de tumor. Het vaststellen van predictive selectiecriteria, waarbij de effectiviteit van anti-oestrogene stoffen kan worden voorspeld, kan helpen bij het afstemmen van endocriene therapie op elke patiënt. Op deze manier wordt de selectie van de meest optimale eerstelijns behandeling mogelijk. Om dit te bereiken, hebben we hier onderzocht wat de criteria zijn waaraan een cel moet voldoen om resistentie tegen anti-oestrogenen te ontwikkelen.

Als eerste onderzoek binnen dit proefschrift, wordt het moleculaire mechanisme beschreven waarmee de fosforylatie van serine 305 op ERα resistentie tegen tamoxifen induceert (hoofdstuk 3). De oestrogeen receptor bindt aan p160 familieleden (waaronder steroïde receptor coactivator 1 ; SRC-1) binnen het transcriptie complex. ERα kan deze interactie met SRC-1 aangaan door middel van haar twee transactivatie regio's, AF-1 en AF-2. Terwijl de AF-1 functie van ERα hormoon onafhankelijk is, wordt de AF-2 geactiveerd door oestradiol binding. Deze interacties

van ERα met SRC-1 zijn een eerste en essentiële stap in de vorming van een actief transcriptie complex en dus ERα activiteit. We maakten gebruik van een fusie van ERα met Cyaan Fluorescent Eiwit ('CFP')en van SRC-1 met Geel Fluorescent Eiwit ('YFP'). Met deze fusie-eiwitten hebben we Fluorescence Resonance Energy Transfer (FRET) gemeten tussen ERα en SRC-1. FRET is de stralingsloze energie-overdracht vanaf een donor fluorofoor naar een geschikte acceptor fluorofoor en is sterk afhankelijk van de afstand tussen deze twee fluoroforen. Op deze manier konden veranderingen in oriëntatie en vouwing binnen het ERα/SRC-1 complex bestudeerd worden. Na tamoxifen behandeling kon SRC-1 nog steeds binden aan ERα via de AF-1 regio, terwijl de AF-2 interactie verloren ging. Wanneer serine 305 van een tamoxifen-gebonden ERα gefosforyleerd was, wijzigde de AF-2 van ERα haar oriëntatie ten opzichte van SRC-1. In deze gewijzigde oriëntatie kon RNA polymerase II gerecruteerd en het transcriptie complex geactiveerd worden, wat resulteerde in tamoxifen-resistentie.

De oestrogeen-gereguleerde transcriptie en celdeling bleek complexer te zijn dan gedacht, toen in 1996 een tweede oestrogeen receptor werd ontdekt; de oestrogeen receptor beta (ERβ). De expressie van ERα en ERβ verschilt in diverse menselijke weefsels, variërend van exclusieve expressie van ERβ in de hersenen en de dikke darm, tot aan onderling verschillende niveaus van ERα en ERβ in andere weefsels, waaronder borstweefsel. Bij borstkanker is de exacte rol van ERβ nog onderwerp van discussie, maar hoge expressie niveaus zijn wel gecorreleerd met een goede prognose. Een mogelijke verklaring voor het positieve effect van ERβ niveaus op prognose is een remming van de activiteit van ERα door ERβ in een hetero-dimeer complex.

Terwijl ERα aan SRC-1 kan binden via zijn ligand onafhankelijke transactivatie regio (AF-1), mist ERβ deze capaciteit (hoofdstuk 4). Dit onvermogen om een interactie aan te gaan met SRC-1 op een ligand onafhankelijke wijze bleek de oorzaak te zijn voor de lagere transactivatie capaciteit van ERβ ten opzichte van ERα. Ook de zwakke gestimuleerde reactie van ERα op tamoxifen, een essentiële stap in tamoxifen-resistentie, komt niet voor in ERβ en kon worden toegeschreven aan de AF-2 van ERβ. Bij ERα bleek de AF-1 samen met de specifieke scharnier regio ('hinge') essentieel om een maximale AF-2 activiteit te bereiken.

Nieuwe anti-oestrogenen, elk met specifieke kenmerken en functionaliteit, worden voortdurend ontwikkeld en geïntroduceerd in de kliniek. Nadat we het mechanisme van tamoxifen-resistentie geïnduceerd door PKA hadden onderzocht, ontstond de vraag welke alternatieve anti-oestrogene stoffen zouden kunnen worden toegepast wanneer tamoxifen niet meer werkt. Om deze vraag te beantwoorden werden zeven anti-oestrogene stoffen getest, allen momenteel in fase III klinische testfase of onlangs geïntroduceerd in de kliniek (zie hoofdstuk 5). We testten de effecten van zowel PKA- als MAP-kinase activatie op anti-oestrogeen functie. Van beide kinases is gerapporteerd dat ze de effectiviteit van tamoxifen beïnvloeden, wat in deze gevallen leidt tot resistentie. Beide kinases hebben andere posities op ERα die ze kunnen modificeren: terwijl PKA activatie leidt tot een fosforylatie van ERα op serine residuen 236 en 305, leidt MAP kinase activatie tot fosforylatie van ERα op serine 118. De gevoeligheid van deze zeven anti-oestrogenen voor kinase activatie werd getest door gebruik te maken van een FRET benadering, waarbij een YFP gekoppeld werd aan de N-terminus van ERα en een CFP aan de C-terminus. Door hetzelfde ERα molecuul met deze twee fluoroforen te labelen, kan een verandering in de ER-vouwing gemeten worden, wat geregistreerd wordt door verschillen in FRET signaal. Een verandering in FRET signaal bleek indicatief te zijn voor een geïnactiveerde ERα. Door het meten van een al dan niet veranderd FRET signaal, kon het effect van kinase activiteit op de functionaliteit van anti-oestrogenen bepaald worden. Op deze manier werd een profiel gecreëerd, waarin voor elke anti-oestrogeen kon worden aangegeven welke specifieke fosfo-modificaties leidden tot resistentie van de receptor tegen deze stof.

Niet alleen kinase activiteit, maar ook expressie niveaus van co-activatoren zijn beschreven betrokken te zijn bij de resistentie tegen anti-oestrogene stoffen. Om de gevoeligheid van nieuwe anti-oestrogenen voor deze variabelen te testen, werden vijf anti-oestrogenen geselecteerd vanuit de subgroepen voor MAPK en PKA gevoeligheid (hoofdstuk 6). De co-activatoren waarvan werd getest of verhoogde niveaus effect hadden op anti-oestrogeen functie, waren SRC-1 en cycline D1. Vorige studies hebben namelijk beschreven dat resistentie tegen tamoxifen correleert met hoge expressie niveaus van SRC-1. Daarnaast is het cycline D1 gen geamplificeerd in 15% van de borsttumoren en is het eiwit in verhoogde niveaus aanwezig in 40% van de tumoren. Deze co-activatoren werden apart getest, maar ook in combinatie met elkaar. Verder werd een mogelijke synergie met PKA-activiteit bestudeerd voor inductie van resistentie.

Ook binnen deze studie hebben we een FRET-gebaseerd profiel van combinaties kunnen construeren, waarin de resistentie tegen elke anti-oestrogeen kon worden aangegeven. Verder hebben we uitvoerig gekeken naar de resistentie tegen arzoxifene en GW-5638, die werd geïnduceerd door verhoogde cycline D1 niveaus. Beide medicijnen zijn momenteel in de fase III klinische testfase. Verhoogde cycline D1 niveaus leidde in arzoxifene-behandelde cellen tot reporter gen activatie en tot groei van de ERα afhankelijke MCF-7 borstkanker cellijn. Dit bleek echter

niet het geval te zijn wanneer cycline D1 tot overexpressie werd gebracht in cellen die behandeld werden met GW-5638. Dit laatst genoemde medicijn bleek te leiden tot oestrogeen receptor afbraak, zelfs wanneer de oestrogeen receptor een resistente vouwing had. Deze data gaf aan dat oestrogeen receptor degradatie een dominante factor is boven resistentie. Uit een studie door anderen waarin tamoxifen en arzoxifene behandeling bij borstkanker patiënten vergeleken werd, blijkt dat tamoxifen-behandelde patiënten een betere prognose hadden dan degenen die behandeld werden met arzoxifene. Echter, aangezien 40% van de borsttumoren verhoogde cyclin D1 niveaus hebben, kan deze overexpressie een causale rol spelen in de ongunstige reactie van deze patiënten op arzoxifene.

Studies door anderen hebben een verband aangetoond tussen de PAK-1 expressie niveaus en tamoxifen-resistentie bij patiënten. Bovendien werd een mogelijke fosforylatie van ERα-Serine 305 door PAK-1 gesuggereerd, wat verantwoordelijk zou zijn voor deze vorm van resistentie. Deze hypothese werd door ons getest, waarbij we PAK-1 expressie niveaus gevisualiseerd hebben in patiënten, in combinatie met PKA-activiteit en ERα-S305 fosforylatie (hoofdstuk 7). Hoewel de PAK-1 niveaus wel correleerden met tamoxifen-resistentie, bleek dit onafhankelijk te zijn van ERα-S305 specifiek signaal. Actief PKA signaal bleek echter te correleren met ER-S305 signaal, wat een functionele relatie tussen deze eiwitten impliceert. Belangrijker is dat de combinatie van deze drie antilichamen een derde van alle patiënten identificeerde als niet-reagerend op tamoxifen behandeling. Deze combinatie van antilichamen kan zodoende helpen om patiënten te geselecteren die een alternatieve endocriene behandeling zouden moeten krijgen.

De resultaten in dit proefschrift beschrijven het moleculaire mechanisme van de PKA-geïnduceerde resistentie tegen tamoxifen en verduidelijken de functionele verschillen tussen de twee ER isovormen. Verder zijn er profielen geschetst voor anti-oestrogeen resistentie geïnduceerd door ERα-fosforylering en co-activator niveaus en hebben we een algoritme geïntroduceerd waarmee we tamoxifen-resistentie bij een derde van alle borstkankerpatiënten kunnen voorspellen.

Toch blijven een aantal vragen nog onbeantwoord. Of de resistentie profielen die we geschetst hebben voor de geteste anti-oestrogenen ook geldig zijn in de kliniek is nog steeds een belangrijke openstaande vraag. Hoewel de FRET profielen geverifieerd zijn in transactivatie-proeven en celgroei experimenten, kunnen weefselkweek gebaseerde experimenten nooit de complexiteit van het menselijk lichaam omvatten. Bovendien kunnen metabolieten van de gebruikte anti-oestrogenen onvoorspelbare effecten op de ER-functie en stabiliteit hebben. Aangezien het moeilijk is om toegang te krijgen tot materiaal van de patiënten die behandeld zijn met deze nieuwe anti-oestrogenen en de follow-up van deze patiënten nog grotendeels onvolledig is, is de vertaling van de hier geschetste profielen naar een klinische toepassing nog niet mogelijk.

De inductie van transcriptie door ERα-S305P gebonden aan tamoxifen kan resulteren in de activatie van een specifieke subset van genen, die uniek zijn ten opzichte van de oestradiol of tamoxifen geïnduceerde genen. Door identificatie van deze genen kunnen de causale factoren voor de gestimuleerde celdeling en een ongunstige prognose gevonden worden. Verder kunnen deze geactiveerde genen ook dienen als additionele predictieve markers die kunnen worden toegepast in de kliniek. Het definiëren van deze genen en hun celbiologische rol bij de ontwikkeling van resistentie tegen anti-oestrogene stoffen is een uitdaging die nog moet worden aangegaan.

Naast SRC-1 eiwit niveaus kunnen ook die van SRC-2 en SRC-3 een rol spelen bij de ontwikkeling van anti-oestrogeen resistentie. Dit mede, omdat deze eiwitten erg veel op elkaar lijken en omdat er voor SRC-3 niveaus al een correlatie is gevonden met tamoxifen resistentie. Momenteel wordt een mogelijke rol van deze eiwitten bij anti-oestrogeen resistentie verder onderzocht, zowel in cellijnen als in tumor materiaal afkomstig van patiënten.

Zoals hierboven aangegeven, kunnen we met gebruik van drie antilichamen een substantiële groep van tamoxifen-resistente patiënten identificeren. Het vinden van markers die tamoxifen-resistentie bij de resterende groep van borstkanker patiënten kan voorspellen wordt één de grootste uitdagingen voor de nabije toekomst, waarvan de eerste stappen nu gezet worden.

Antigeen belading, vesiculaire structuur positionering en costimulatie

Cellen geven continu informatie over hun interne gezondheid door aan het immuunsysteem. Om dit mogelijk te maken zijn geavanceerde mechanismen ontstaan voor verschillende kenmerken die kanker maar ook een bacteriële of virale infectie kunnen aanduiden; peptiden en lipiden van zowel intra- als extracellulaire oorsprong. CD1 moleculen presenteren lipiden van zowel cel-eigen als van buiten de cel ori-gine, terwijl voor presentatie van peptiden zich twee afzonderlijke cellulaire routes hebben ontwikkeld, namelijk de MHC klasse I route (voor cel-eigen en virale peptiden) en de MHC klasse II route (voor peptiden van extracellulaire oorsprong, zoals bacteriën) (beschreven in hoofdstuk

9). MHC klasse I komt tot expressie in alle kern-bevattende cellen. MHC klasse II daarentegen kan alleen gevonden worden in gespecialiseerde antigeen presenterende cellen. MHC klasse II moleculen, waaronder HLA-DR, worden gevormd in het endoplasmatisch reticulum, waar ze een interactie aangaan met een specifieke chaperone genaamd invariante keten (Ii). Samen met Ii wordt HLA-DR getransporteerd naar laat-endosomale / lysosomale compartimenten. Hier kan HLA-DR peptiden aan zich binden, die opgenomen zijn via de endocytotische route en verwerkt zijn door lysosomale peptidases. Deze MHC klasse II positieve laat-endosomale / lysosomale compartimenten, of MIIC, hebben een typische morfologie; een membraan omgeven structuur met meerdere interne blaasjes. In deze MIIC wordt Ii afgebroken met uitzondering van een kleine peptide sequentie; klasse II-geassocieerde invariante keten peptide ('CLIP'). Een andere chaperone, HLA-DM, zorgt voor een vervanging van CLIP aan de peptide-bindingsplaats op HLA-DR voor een opgenomen peptide. Nadat het peptide is geplaatst op HLA-DR, kan het complex vervoerd worden naar en fuseren met de cel membraan, waarna het peptide gepresenteerd kan worden aan CD4 positieve T cellen.

Om inzicht te krijgen in het proces van anti-geen belading, hebben we de interactie tussen HLA-DR en HLA-DM bestudeerd in levende cellen (hoofdstuk 10). Om dit mogelijk te maken werden cellijnen gemaakt die HLA-DR/CFP, HLA-DM/YFP en Ii produceren. In deze cellen hebben we Fluorescentie Resonance Energy Transfer (FRET) gemeten in de MIIC. FRET is de stralingsloze energie-overdracht van een donor, in dit geval Cyaan Fluorescent Eiwit ('CFP') naar een geschikte acceptor, in dit geval Geel Fluorescent Eiwit ('YFP'). Aangezien dit biofysische verschijnsel alleen plaatsvindt wanneer de fluoroforen dicht bij elkaar zijn, is een detectie van FRET signaal indicatief voor een fysieke interactie tussen deze twee eiwitten. De interactie tussen HLA-DR en HLA-DM bleek alleen gevonden te worden op de interne blaasjes van de MIIC, en niet op de omringende membraan structuur. Aangezien HLA-DR/HLA-DM interacties essentieel zijn voor antigeen belading, hebben we met deze techniek een specifiek antigeen-beladings subdomein binnen de lysosomale structuur gedefinieerd. Deze micro-omgeving binnen de MIIC wordt specifiek verstoord door pathogenen, zoals *Salmonella typhimurium*. De bacterie voorkomt actief de vorming van de interne blaasjes binnen haar eigen phagosomale / lysosomale structuur, wat haar in staat stelt om actief en lokaal aan het immuun systeem te ontsnappen.

Binnen het proces van antigeen belading en presentatie is het transport van de membraan-omgeven blaasjes van essentieel belang. De blaasjes met lading van buiten de cel moeten met lysosomale compartimenten fuseren om afbraak van de lading mogelijk te maken. Ook MHC klasse II complexen worden naar deze late endosomale / lysosomale structuren getransporteerd, waar het antigeen wordt geladen. Als MHC klasse II met antigeen beladen is moet het vervolgens naar de plasmamembraan getransporteerd worden om de antigenen te presenteren aan het imuunsysteem.

Eén van de eiwitten die rechtstreeks betrokken is bij dit proces van transport is Rab7. Rab7 is lid van de Rab GTPase superfamilie van eiwitten en is essentieel voor minus-end "microtubule organizing centre" (MTOC)-gericht vervoer van transport structuren, wat resulteerd in een transport van deze blaasjes naast de cel kern. Voor MTOC-gericht vervoer en de localisatie van vesiculaire structuren naast de celkern moet Rab7 interacties aangaan met Rab7-interacterend lysosomale eiwit (RILP) en oxysterol-bindend eiwit-gerelateerd eiwit 1L (ORP1L) (hoofdstuk 11). Zowel RILP als ORP1L zijn effectoren van Rab7 en kunnen tegelijkertijd aan actief (GTP geladen) Rab7 binden. RILP kan op diens beurt rechtstreeks aan $P150^{Glued}$ binden, een eiwit wat vereist is voor de vorming van een actief dyneïne motor complex aan deze vesiculaire structuren en voor MTOC-gericht vervoer.

ORP1L functie is echter betrokken bij vesiculaire structuur-localisatie op een andere, onverwachte manier. ORP1L bleek cholesterol te kunnen binden, wat ervoor zorgt dat de conformatie van ORP1L verandert (hoofdstuk 12). Wanneer ORP1L geen cholesterol heeft gebonden, kan deze een interactie aangaan met VAP (een endoplasmatisch reticulum eiwit) om *in trans* met ORP1L te interacteren. VAP verwijdert vervolgens $P150^{Glued}$ uit het Rab7-RILP-ORP1L complex, wat ervoor zorgt dat de vesiculaire structuur zich aan de rand van de cel bevindt. Als het cholesterol gehalte hoog is aan de cytosolaire zijde van deze blaasjes kan ORP1L geen interactie aan gaan met VAP, wat ervoor zorgt dat $P150^{Glued}$ niet loslaat van het complex. Als gevolg hiervan zullen deze blaasjes zich opeenhopen naast de cel kern. Zo bepaalt cholesterol de conformatie van ORP1L, wat op zijn beurt de positionering van vesiculaire structuren in de cel bepaalt.

Naast zijn functie als chaperone voor MHC klasse II, kan de invariante keten ook een invloed uitoefenen op andere factoren. Ii bleek rechtstreeks en functioneel bindt aan CD70, een costimulatoire ligand dat - via zijn receptor CD27 – de response van CD4 en CD8 positieve T cellen bepaalt (hoofdstuk13). Als Ii niet tot expressie komt, is CD70 vooral te vinden aan de cel membraan. Wanneer invariante keten wel tot expressie komt kan deze binden aan CD70 in het endoplasmatisch reticulum, waarna het Ii/CD70 complex samen naar het MIIC getransporteerd wordt. Op deze manier bepaalt Ii de kinetiek en de hoeveelheid van de CD70 aan het celoppervlak en regelt daarmee de signalering naar CD27 op CD4 positieve T cellen maar ook crosspriming naar CD8 positieve T cellen.

Dit bepaalt de mate van klonale expansie van CD8 positieve T cellen. Omdat MHC klasse II en CD70 zich beiden op dezelfde structuur bevinden, resulteert de fusie van de vesiculaire structuur met de plasmamembraan in een gelijktijdige aflevering van zowel een antigeen-geladen complex als een costimulatoire reactie. Op deze manier kunnen CD4 positieve T cellen niet alleen het antigeen-geladen MHC klasse II herkennen, maar ook de interactie tussen CD27 en CD70 vindt zo plaats binnen dezelfde immunologische synaps.

De resultaten die beschreven staan in dit proefschrift laten een antigeen-beladings subdomein binnen MIIC zien en beschrijven hoe het Rab7/RILP/ORP1L complex de recrutie van het motor complex en daarmee de positie van vesiculaire structuren in de cel bepaalt. Daarnaast wordt beschreven hoe het MIIC gedeeld wordt met CD70, wat bepaald wordt door de gezamenlijke CD70/MHC klasse II chaperone Ii. Dit resulteert in een getimede en gecontroleerde aflevering van zowel antigeen-beladen MHC klasse II als CD70, wat leidt tot een CD4 positieve en CD8 positieve T cel reactie. Toch blijft een aantal vragen nog onbeantwoord. Zoals de vraag welke factoren het antigeen-beladings subdomein bepalen? Met andere woorden: wat maakt de interne blaasjes van deze structuren functioneel anders dan de omringende membraan? Kandidaat-factoren zijn CD63 en CD82, tetraspanin moleculen waarvan beschreven is dat deze zich voornamelijk bevinden op de interne blaasjes van de MIIC en waarvan gerapporteerd is dat ze rechtstreeks binden aan zowel HLA-DR als HLA-DM. Een andere openstaande vraag is of er andere factoren zijn die rechtstreeks invloed op antigeen belading en vesicle transport kunnen uitoefenen, voor een eventuele “fine-tuning” van de MHC klasse II route. Deze nieuw geïndentificeerde factoren zouden chemisch geremd kunnen worden, wat uiteindelijk zou kunnen worden toegepast in de kliniek voor de behandeling van MHC klasse II antigeen presentatie-gerelateerde ziekten, zoals auto-immuunziekten en leukemie. Verder is belangrijk in hoeverre deze ogenschijnlijk verschillende processen en bevindingen te koppelen zijn tot een groter geheel. Hebben blaasjes bestemd voor fusie met lysosomen een hoog cholesterolgehalte aan hun cytosolaire zijde om fusie met lysosomen mogelijk te maken, om na antigeen belading en CD70 opname hun cholesterol gehalte te verlagen, en daardoor naar de plasma membraan te bewegen en er mee te fuseren?

Verder onderzoek zal zich richten op deze en andere vragen om zo licht te werpen op de complexe en uiterst nauwkeurig gereguleerde processen die betrokken zijn bij MHC klasse II antigeen presentatie.

Curriculum Vitae

Wilbert Zwart werd geboren op 26 augustus 1980 te Putten. Na het behalen van het VWO diploma aan het Christelijk College Groevenbeek te Ermelo in 1998 begon hij hetzelfde jaar aan de studie Biologie te Utrecht. Tijdens deze studie liep hij stage in de afdeling Moleculaire Celbiologie/EMSA van de Universiteit Utrecht, onder begeleiding van Dr. Petra de Graaf in de groep van Dr. Paul van Bergen en Henegouwen. Tijdens deze stage werd de rol van Rab11/PI4Kβ interactie in de regulatie van vesiculair transport onderzocht. Een tweede stage heeft hij gevolgd op de afdeling Tumor Biologie aan het Nederlands Kanker Instituut, in de groep van Prof. Dr. Jacques Neefjes onder begeleiding van Dr. Alexander Griekspoor. Tijdens deze stage onderzocht hij de interactie van HLA-DR en HLA-DM binnen levende cellen en de manupulatie van deze interactie door *Salmonella typhimurium*.

De studie Biologie werd in augustus 2003 afgerond, waarna hij begon aan een promotie-onderzoek in de groep van Dr. Rob Michalides op de afdeling Tumor Biologie aan het Nederlands Kanker Instituut. Het promotie project was gericht op onderzoek naar het moleculaire mechanisme van anti-oestrogeen resistentie bij borstkanker. Tijdens deze promotie periode kreeg hij de gelegenheid om uitvoerig samen te werken met andere vakgroepen binnen en buiten het Nederlands Kanker Instituut. Veel interacties werden onderhouden met de groep van Jacques Neefjes waar hij bijdroeg aan onderzoek naar het proces van antigen belading en vesuculair transport.

Voor het onderzoek tijdens zijn promotieperiode, beschreven in dit proefschrift, kreeg hij in januari 2009 de Antoni van Leeuwenhoekprijs uitgereikt. Tot het najaar van 2009 zal hij in de groep van Dr. Rob Michalides op het NKI werkzaam blijven als postdoc, waarna hij zijn studies naar predictie van response op anti-hormonale behandeling bij borstkanker zal voortzetten in de groep van Dr. Jason Carroll gevestigd aan de University of Cambridge te Engeland.

List of Publications

M Kok, **W Zwart**, C Wigerup, R Fles, M Hauptmann, LJ Van 't Veer, LFA Wessels, J Neefjes, O Stål, SC Linn, G Landberg and R Michalides.
Predictive algorithm for tamoxifen resistance in breast cancer patients based on PAK1 and PKA-induced phosphorylation of ERα at serine 305.
Submitted

W Zwart, M Rondaij, K Jalink, ZD Sharp, MA Mancini, J Neefjes and R Michalides.
Resistance to anti-estrogen arzoxifene is mediated by overexpression of Cyclin D1.
Submitted

W Zwart[+], R de Leeuw[+], M Rondaij, J Neefjes, MA Mancini and R Michalides.
The AF-1 and hinge region of Estrogen Receptor cooperate in the quantitative response to estradiol and tamoxifen.
In preparation for resubmission

M Carraz, **W Zwart**, T Phan, R Michalides and L Brunsveld. Use of synthetic LXXLL-motif peptides to inhibit Estrogen Receptor α – coactivator interactions in human cells.
Submitted

N Rocha, C Kuijl[+], R Kant[+], L Janssen, D Houben, H Jansen, **W Zwart*** and J Neefjes*.
Late endosomal positioning by dynein motors and ER contact site formation controlled by cholesterol sensor ORP1L.
* corresponding author
Submitted

AM Keller, **W Zwart**, G van der Horst, SH Naik, J Neefjes and J Borst.
The invariant chain controls intracellular transport of CD70 in dendritic cells and thereby regulates CD8+ T cell priming.
Submitted

W Zwart, A Griekspoor, V Berno, K Lakeman,K Jalink, M Mancini,J Neefjes and R Michalides.
PKA-induced resistance to tamoxifen is associated with an altered orientation of ERalpha towards co-activator SRC-1.
EMBO J. 2007 Aug 8;26(15):3534-44.

W Zwart,A Griekspoor, M Rondaij, D Verwoerd,J Neefjes and R Michalides.
Classification of anti-estrogens according to intramolecular FRET effects on phospho-mutants of estrogen receptor alpha.
Mol Cancer Ther. 2007 May;6(5):1526-33.

Continued on next page

Continued from previous page

A Griekspoor, **W Zwart**, J Neefjes and R Michalides.
Visualizing the action of steroid hormone receptors in living cells.
Nucl Recept Signal. 2007 Mar 9;5:e003

M Johansson[+], N Rocha[+], **W Zwart**, I Jordens, L Janssen, C Kuijl, VM Olkkonen and J Neefjes.
Activation of endosomal dynein motors by stepwise assembly of Rab7–RILP–p150^{Glued}, ORP1L, and the receptor βIII spectrin.
J Cell Biol. 2007 Feb 12; 176 (4):459-71.

A Griekspoor, T Margarido, **W Zwart**, R Michalides.
Review of: BRCA1 and cyclin D1: gate keepers in hormone responsive tissues?
Breast Cancer Online, Volume 9, Issue 04 Apr 2006, e16

W Zwart[+], A Griekspoor[+], J Neefjes. Presenting antigen presentation in living cells using biophysical techniques. Curr Opin Microbiol. 2005 Jun;8(3):338-43.

W Zwart[+], A Griekspoor[+], C Kuijl, M Marsman, J van Rheenen, H Janssen, J Calafat, M van Ham, L Janssen, M van Lith, K Jalink, J Neefjes.
Spatial separation of HLA-DM/HLA-DR interactions within MIIC and phagosome-induced immune escape. Immunity. 2005 Feb;22(2):221-33.

P de Graaf, **W Zwart**, RA van Dijken, M Deneka, TK Schulz, N Geijsen, PJ Coffer, BM Gadella, AJ Verkleij, P van der Sluijs and PM van Bergen en Henegouwen.
Phosphatidylinositol 4-kinasebeta is critical for functional association of rab11 with the Golgi complex.
Mol Biol Cell. 2004 Apr;15(4):2038-47.

[+] equal contribution